Charles University in Prague
Faculty of Mathematics and Physics

Doctoral Thesis

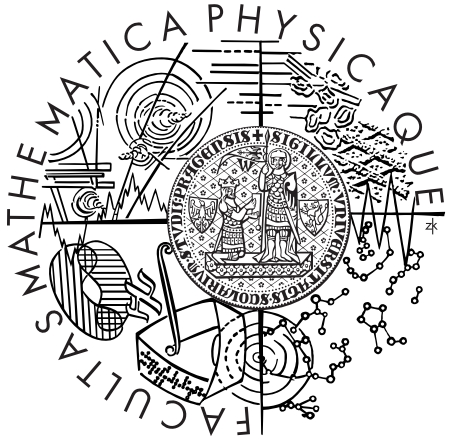

Jiří Kvita

Measurement of Differential Cross-Sections in the $t\bar{t} \to \ell$+jets Channel at $\sqrt{s} = 1.96$ TeV with the DØ Experiment at Fermilab

Institute of Particle and Nuclear Physics
Charles University, Prague, Czech Republic

Supervisor: **Doc. RNDr. Rupert Leitner, DrSc.**

Study Programme: Physics
Subject Field: F9 – Subnuclear Physics

to my parents

and Καικα

Prohlašuji, že jsem disertační práci vypracoval samostatně a výhradně s použitím citovaných pramenů. Souhlasím se zapůjčováním práce.

I declare that I have completed the presented thesis by myself and used only the mentioned literature. I agree with using the thesis.

V Praze dne 2. ledna 2009

Jiří Kvita

"Yesterday's sensation is today's calibration and tomorrow's background."

— Richard Phillips Feynman [1]

Acknowledgments

I would like to thank my supervisor Rupert Leitner for providing me with the opportunity to join the DØ experiment, for his guidance, support and physics insight; and also to the Prague DØ Group leaders Miloš Lokajíček (and his "What you don't finish now, you won't finish ever") and Vladislav Šimák.

The author would like to thank many people who have helped with ideas, discussions, suggestions and encouragements throughout the analysis. While it is impossible to list them all, the author still feels indebted to them so much that a few names have to be mentioned. Thanks belong above all

to Aurelio Juste, for his slide no. 5 from 24$^{\text{th}}$ February 2004 DØ winter physics workshop, where top quark p_{T} as uncovered topic caught my attention; for his encouragements, and for all the fun and privilege of working with him for two years within the JES group, for his dedication and tireless search of truth and precision, for his team spirit a contagious joy of a team work;

to Michael Begel for his tireless interest and discussions; for motivating, trusting in me and supporting me, for all his ideas and critical and truly scientific attitude without compromises, for pushing me and teaching me the beauty of differential spectra;

to Yvonne Peters, Jochen Cammin, Su-Jung Park, Daniel Wicke, and Thorsten Schliephacke for their immense patience with making my preselection consistent; for data processing and their readiness to help at any time; to Gavin Hesketh for his help on unfolding and the interpretation; to Amnon Harel for his insight into differential measurements, MC@NLO and systematics ideas; to Saša Kupčo for his advice on QCD and unfolding and all the coffees in DAB1.

Many people have helped with advice, technical issues and critical remarks, including Frédérique Badaud, Frédéric Déliot, Dmitri Denisov, Denis Gele, Robert Harrington Ulrich Heintz, Pieter Houben, Ia Iashvili, Oldřich Kepka (not only with pQCD discussions:), Marc-André Pleier, Lisa Shabalina, Denis Shpakov, Jonas Strandberg, Christian Schwanenberger, Petr Vokáč (for all the computing!) Michele Weber, and those I forgot.

The life in Fermilab and elsewhere would not have been what it has been without colleges and friends from the Czech DØ team, namely Kamil Augsten, Zdeněk Hubáček, Vlasta Hynek, Saša Kupčo, Roman Otec, Karel Soustružník and Petr Vokáč; Czech and Slovak friends Marian, Miro & Anya, Olda, Roman & Lucia; and many friends from all over the world, which are also impossible to be mentioned as a complete list; Anatoly, Robert, Carsten, Helena, Piyali, Renata, Dan, Murilo, Bilge, Dag, Ana, Andrés, Mikko, Tuula, Martina, Edgar, Marion, Florent, Paola, Krisztián, Mikołaj, Jeremie, Jessica, Duncan, Sarosh, Thorsten, Amnon and Orit.

The author's travels and stays in Fermilab were kindly supported by grants of the MŠMT (Ministry of Education, Youth and Sports) , Czech Republic (INGO 1P05LA257), the Center for Particle Physics, the Institute of Particle and Nuclear Physics of Faculty of Mathematics and Physics of the Charles University in Prague; and the Fermilab International Fellowship Program. I am especially grateful to George Ginther for all his help and understanding during my fellowship at Fermilab, as well as to Fermilab directorate, particle physics division, DØ spoke personnel, physics coördinators and physics and algorithm groups conveners for having had the opportunity to work so closely with them. Special thanks belong to the kind support of prof. Jiří Hořejší and the IPNP DØ Prague Group grant coördinator Karel Soustružník.

Last but not least, many thanks belong to my dear parents and all my dear friends, who have supported me and accompanied me in both presence and spirits throughout the years.

Preface

The analysis presented in this thesis focuses on kinematic distributions in the $t\bar{t}$ system and studies in detail selected differential cross sections of top quarks as well as the reconstructed $t\bar{t}$ pair, namely the top quark transverse momentum and the $t\bar{t}$ system mass.

The structure of the thesis is organised as follows: first the Standard Model of the particle physics is briefly introduced in Chapter 1, with relevant aspects of electroweak and strong interactions discussed. The physics of the top quark and its properties are then outlined in Chapter 2, together with the motivation for measuring the transverse top quark momentum and other kinematic-related variables of the $t\bar{t}$ system.

The concepts of present-day high energy physics collider experiments and the explicit example of Fermilab Tevatron collider and the DØ detector in Chapters 3 and 4 are followed by the description of basic detector-level objects, i.e. tracks, leptons and jets, in Chapter 5; their identification and calibration following in next chapter with the emphasis on the jet energy scale in Chapter 6 and jet identification at the DØ.

The analysis itself is outlined in Chapter 7 and is structured so that first the data and simulation samples and the basic preselection are described in Chapter 8 and 9, followed by the kinematic reconstruction part in Chapter 10. Chapter 11 on background normalisation and Chapter 12 with raw reconstructed spectra results (at the detector-smeared level) are followed by the purity-based background subtraction method and examples of signal-level corrected spectra in Chapter 13.

Next, the procedure of correcting measured spectra for detector effects (unfolding) is described in Chapters 14–15, including migration matrix studies, acceptance correction determination as well as the regularised unfolding procedure itself. Final differential cross sections are presented in Chapter 16 with the main results in Figures 16.19–16.20.

Summary and discussion close the main analysis part in Chapter 17, supplemented by appendices on the wealthy of analysis control plots of the $t\bar{t} \to \ell$+jets channel, selected DØ event displays and finally the list of publications and references.

Preliminary results of this analysis have been documented in DØ internal notes [UnfoldTop], [p17Top], [p14Top]; as well as presented at conferences [APS08], [APS05]. The author has also been a co-author of more than 135 DØ collaboration publications since 2005.

The author has taken part in the jet energy scale calibration efforts performing final closure tests and deriving a correction to jet energy offset due to the suppression of the calorimeter signal. The author has also co-performed the ϕ-intercalibration of the hadronic calorimeter and co-supervised the electromagnetic ϕ-intercalibration; recently has also been involved in maintaining the jet identification efficiencies measurement as a JetID convener.

During the years in Fermilab, many events have taken place in the course of the analysis in persuasion, including more than 170 shifts served for the DØ detector with

or without the beam, 168 talks presented with mixed results and reactions; and tens of thousands of code lines in C (and sometimes perhaps even really C++) written while terabytes of data were processed, analysed, and sometimes also lost. It has been a long but profoundly enriching chapter of my life.

Abbreviations Used

CC	Central cryostat (calorimeter).
CFT	Central fiber tracker.
CH	Coarse hadronic (radially deeper) part of the DØ calorimeter.
DCA	Distance of closest approach (e.g. of a track and a vertex).
EC	End-cap calorimeter.
EM	Electromagnetic (e.g. part of the calorimeter).
FH	Fine hadronic (earlier) part of the DØ calorimeter.
FSR	Final state radiation.
HitFit	Kinematic fitter used in this analysis.
ICR	Inter-cryostat region.
ICD	Inter-cryostat detector.
ISR	Initial state radiation.
JES	Jet energy scale (procedure for jet energy correction).
JetID	Jet identification.
JSSR	Jet shifting, smearing and removal (a procedure to correct simulated jets).
MB	Minimum-bias (events triggered by luminosity monitors coincidence).
MC	Monte Carlo, simulated events or the simulation procedure itself.
MET	Missing E_{T} (calorimeter-based missing transverse energy).
MPF	Missing E_{T} projection fraction method (used e.g. for jet response measurement).
MPI	Multiple parton interactions.
PV	Primary interaction vertex.
SMT	Silicon microstrip tracker.
SV	Secondary vertex (usually of long-lived particles decay) identified by tracking algorithms.
NNm	(Artificial) neural net b-tagging algorithm at the medium operation point (NN output cut of 0.65).
UE	Underlying event, part of the collision not associated with the hard scattering process; both soft (of proton remnants) and hard (from multi-parton interactions).
ZB	Zero-bias (events triggered by the accelerator bunch crossing signal).

Contents

List of Tables

Chapter 1

The Standard Model of Particle Physics

1.1 Overview

In the current picture of physics, interactions are understood to be mediated by four forces, the strong, electromagnetic, weak and gravitational. In all present-day high energy physics experiments, the standard gravity can be safely neglected, and only strong and unified electroweak forces can be considered.

During the 20^{th} century, the Standard Model (SM) of the microcosm has evolved into a compact gauge theory with a particular mechanism of electroweak symmetry breaking. While it describes our world to an astonishing precision, there already is a mounting evidence it is not a complete and ultimate model of nature.

The current particle content of the SM, three lepton and quark families, gluons mediating the strong interactions, and electroweak gauge bosons $W^{\pm}$, Z, has been experimentally verified in many ways, leaving the existence of the Higgs boson (the only fundamental scalar particle), or the electroweak symmetry breaking (EWSB) mechanism in general, unanswered as to-date.

1.2 Electroweak Interactions

In the unified picture of electromagnetic and weak interactions, lepton and quark fields are required to be locally invariant under a specific local phase transformation of the $SU(2)_{\text{L}} \times U(1)$ group, which leads to the introduction of four gauge bosons, which can be combined to particles known as photon, $W^{\pm}$ and Z bosons.

In fact, a very specific choice of the gauge invariance, namely that only left handed chiral components of fermion fields form doublets w.r.t. the $SU(2)_{\text{L}}$ group, lead naturally to the parity violation in weak interaction (a fact, that only left handed chiral fields couple to W bosons, and that fields coupling to the Z boson are different for left and right handed components). However odd this choice may seem at a first glance, it is supported by a wealth of experimental data, and the individual components of the electroweak interaction Lagrangian were actually introduced before the unification scheme was discovered.

Left and right chiral field components are treated as independent fields, and the unifying mechanism is valid only for massless fermions. Mass terms are obtained as a result of adding specific Yukawa interaction terms with a complex scalar field with a special form of a potential [2].

An important feature of the SM is that it forbids flavour changing neutral currents (couplings of fermions to the Z boson is diagonal in flavour eigenstates) at the tree level; and the prediction of special self couplings of gauge bosons $W^{\pm}$, Z and γ, namely that there is no coupling including only Z and γ while there is a specific structure of trilinear WWW, WWZ, ZZZ and $WW\gamma$ as well as quadratic $WW\gamma\gamma$, $WWZ\gamma$, $WWZZ$ and $WWWW$ couplings.

1.3 Strong Interactions

1.3.1 QCD as a Gauge Theory

Quantum chromodynamics (QCD) as currently the deepest theory of strong interactions is based on the non-Abelian local gauge invariance under the group $SU_c(3)$, where c stands for the new quantum number colour.

The QCD Lagrangian contains the quark-gluon interactions as well as gluon self-interactions, a novel feature compared to the quantum electrodynamics, but in some sense already present in electroweak interactions in vector boson couplings. The fact that gluons carry the colour charge and that they interact with each other has profound consequences on the theory properties, usage, regime of applications and resulting predictions. The QCD Lagrangian can be written as

$$\mathcal{L}_{QCD} = \sum_q \bar{\Psi}_q \gamma_\mu \left[i\partial^\mu + g_S A_a^\mu \frac{\lambda_a}{2} - m_q \right] \Psi_q - \frac{1}{4} \mathrm{Tr}\left[G^{\mu\nu} G_{\mu\nu} \right],$$

where the sum runs over all quark fields types, λ_i are 3×3 colour matrices, generators of the $SU(3)$ group, A_a^μ, $a = 1, .., 8$ are gluon vector fields, g_S is the fundamental strong coupling constant and field strength tensor and the covariant derivative can be expressed as

$$G_{ab}^{\mu\nu}(x) \equiv \frac{1}{ig}[D_a^\mu(x), D_b^\nu(x)], \qquad D_a^\mu(x) \equiv \partial^\mu - ig_S A_a^\mu(x).$$

Such Lagrangian is form-invariant under the local rotation in the colour space

$$\mathcal{S}(x) \equiv \exp\left[i\omega_a(x) \frac{\lambda_a}{2} \right]$$

of the colour-triplet quark field

$$\Psi \equiv (\psi_1, \psi_2, \psi_3),$$

i.e. the physical content of the theory does not change after such local rotation of quark fields with corresponding transformation of gauge fields in a similar way as Maxwell equations have the freedom in choosing the calibration condition.

From the practical point of view, perturbative QCD (pQCD) offers Feynman rules for the computation of basic cross-sections and various QCD corrections to SM processes. The key idea is that despite the quark confinement, the asymptotic freedom allows one to employ perturbative calculations at momentum scales where the QCD coupling constant is small enough to make us confident in the convergence of the perturbation series.

1.3.2 Running Coupling Constant

The renormalisation of QCD leads similarly as in QED to the concept of a running coupling constant, the dependence of $\alpha_S \equiv g_S^2/4\pi$ on the renormalisation scale μ_R. The dependence can be computed in pQCD to some order in the power of α_S, leading to the so-called QCD β-function, defined as

$$\beta(\alpha_S(\mu_R^2)) = \mu_R^2 \frac{\partial \alpha_S}{\partial \mu_R^2} \qquad (1.3.1)\,,$$

$$\beta(\alpha_S(\mu_R^2)) = -b(\mu_R^2)\,\alpha_S^2\,[1 + b'(\mu_R^2)\alpha_S + \mathcal{O}(\alpha_S^4)]$$

The remarkable feature of the running coupling formula in QCD is the finding that α_S *decreases* as the momentum scale increases, leading to asymptotically free theory in the limit of $\mu_R^2 \to \infty$. On the other hand, the rise of α_S at low energies leads to the phenomenon of quarks confinement within hadrons and to the fact that it is not possible to use pQCD at large distances, i.e. low momentum scales. Consequently, the theoretical knowledge on proton structure is limited, and at the moment it is not possible to compute its mass from first principles.

The running of $\alpha_S(\mu_R^2)$ is in fact a dependence of a dimension-less quantity on a dimension-full parameter. To introduce a proper auxiliary scale, one can e.g. integrate the renormalisation group equation 1.3.1 and define Λ_{QCD} as an integration constant for some chosen value of Q, usually m_Z:

$$\log \frac{\mu_R^2}{\Lambda_{\mathrm{QCD}}^2} = -\int\limits_{\alpha_S(\mu_R^2)}^{\infty} \frac{\mathrm{d}\xi}{\beta(\xi)} = \int\limits_{\alpha_S(\mu_R^2)}^{\infty} \frac{\mathrm{d}\xi}{b\,\xi^2\,[1 + b'\xi + \cdots]}$$

Measuring $\alpha_S(\mu_R^2)$ at some scale, one can fix Λ_{QCD}, which actually does not depend on the scale μ_R^2 itself. It can be regarded as a fundamental constant, once the renormalisation scheme, number of flavours available at the scale and the perturbation order used are specified. Its value of about 200 MeV defines the pole at which the coupling constant diverges to infinity, and can be regarded as the upper limit on the distance above which pQCD does not make sense anymore. The value corresponds to approximately 1 fm, the size of a proton, and thus corresponds to scales which the theory does not try to attempt to describe by means of pQCD anyway. In the lowest order

$$b_0 = \frac{11 n_c - 2 n_f}{3}$$

where n_c is number of colours and n_f number of flavours with masses below μ, and

$$\alpha_S(\mu_R^2) = \frac{4\pi}{b_0 \log \frac{\mu_R^2}{\Lambda_{\mathrm{QCD}}^2}}\,.$$

1.3.3 Quark Model

In its basic formulation, interaction of a probe with a composite hadron object can be regarded as scattering of the probe on parton constituents, which are almost free in the high momentum transfer limit, and the total cross section can be written as an incoherent sum of cross sections on individual scattering centres. In this idea of Feynman constituents, parton distribution functions (PDF's; the probability of finding a parton i in the hadron carrying a momentum fraction x of the original hadron) $f_i(x)$ are introduced in the high-momentum hadron frame. In an improved picture, pQCD allows an evolution of the distribution functions in the momentum scale and thus a non-zero virtuality of the parton entering the scattering process.

1.3.4 Factorisation

The main idea of the factorisation theorem is the possibility to separate the non-perturbative part of the scattering process (and include it into the distribution functions), and the perturbative, computable part, of the cross-section.

The assumption is that one can separate short distance physics of the hard process not only from the subsequent non-perturbative hadronisation at large distances (and therefore at low momentum scales), but also from the soft scale physics of parton distribution functions $f_{q/H}$, which one cannot derive in pQCD, but for which it is possible to predict the evolution in the momentum scale. Whenever there is a factorisation, there is an evolution, either of parton distribution functions or of fragmentation functions.

Writing down the inelastic cross-section for colliding hadrons A, B, one has to take into account all possible initial parton states a, b and integrate the parton cross-section over their momentum fraction distributions

$$\sigma_{AB}(S,\mu,\mu_F) = \sum_{a,b} \int_{\Omega} \mathrm{d}\hat{s}\,\mathrm{d}x_1\mathrm{d}x_2\, f_{a/A}(x_2,\mu_F)\, f_{b/B}(x_1,\mu_F)\, \hat{\sigma}_{ab}(\hat{s},\mu,\mu_F)\, \delta(x_1x_2S-\hat{s})$$

where μ is the renormalisation scale and μ_F the factorisation scale. If interested in exclusive particle states, proper convolutions with fragmentation functions have to be included.

When studying e.g. the Drell–Yan production of a dilepton pair cross-section as a function of the pair mass ($\hat{s} \equiv m_{ll}^2$), one can obtain

$$\frac{\mathrm{d}\sigma_{AB}(m_{ll}^2,\mu,\mu_F)}{\mathrm{d}m_{ll}^2} = \sum_{a,b} \int_{\Omega} \mathrm{d}x\, f_{a/A}(x,\mu_F)\, f_{b/B}(\xi/x,\mu_F)\, \hat{\sigma}_{ab}(m_{ll}^2,\mu)$$

with $\xi \equiv m_{ll}^2/S$. Deriving the double-differential cross-section formula w.r.t. to the pair mass and rapidity, constrains on PDF's can result from a comparison to data.

1.3.5 DGLAP Evolution Equations

While parton distribution functions cannot be computed directly from first principles at the moment, the underlying theory successfully predicts their evolution as a function of some factorisation scale μ_F, which has the meaning of the maximal allowed virtuality of a parton inside the hadron, by including the most relevant pieces of the physics of the initial parton evolution.

From the independence of physical observables on the factorisation scale, it is possible to obtain the evolution equations for parton distribution functions [4]

$$\frac{\mathrm{d}}{\mathrm{d}\log\mu_F^2}\begin{pmatrix} f_{q_i}(x,\mu_F^2) \\ f_g(x,\mu_F^2)\end{pmatrix} = \sum_j \int_x^1 \frac{\mathrm{d}z}{z} \begin{pmatrix} \mathcal{P}_{q_iq_j}(z) & \mathcal{P}_{q_ig}(z) \\ \mathcal{P}_{gq_j}(z) & \mathcal{P}_{gg}(z)\end{pmatrix} \begin{pmatrix} f_{q_i}(x/z,\mu_F^2) \\ f_g(x/z,\mu_F^2)\end{pmatrix}$$

and write perturbative expansions in terms of the strong coupling

$$\mathcal{P} = \alpha_S\mathcal{P}^{(0)} + \alpha_S^2\mathcal{P}^{(1)} + \alpha_S^3\mathcal{P}^{(2)} + \cdots .$$

1.3.6 Practical QCD

What is calculable with the tools provided by pQCD is some particular process cross-section at the parton level for on-shell quarks. However, looking beyond the leading

order (LO), there are not only divergences coming from the ultraviolet region, which can be regularised and renormalised by standard field theory techniques, but also infrared (present however also in quantum electrodynamics) and (as a novel feature) collinear singularities, when partons are emitted with low energy or collinearily with respect to the parent parton.

A specific class of soft and collinear divergences can be cancelled by adding real and virtual contributions at the level of cross-sections (Kinoshita-Lee-Nauenberg, [3]). The idea is to add cross-sections of different parton configurations, which however lead to the same experimentally observable final state. It is e.g. impossible to resolve experimentally an almost collinear or very low energetic gluon from a final state where no radiation occurred. Roughly speaking, soft and collinear divergences in the initial state partons evolution can be absorbed into parton distribution functions, and soft and parallel divergences in the final state cancel between various final states with the same (indistinguishable) experimental signature. Divergences from virtual corrections cancel with divergences in the real emission where the emitted parton is very soft or collinear and would not be observed as an isolated hard jet. Resulting cross-section with some cuts on jets separation and minimum jet energy is also finite. The KLN theorem allows to safely combine these features.

As already indicated, after the KLN, One is still left with a subset of soft and collinear emission divergences, which can be removed by including them into the re-definition of parton distribution functions by introducing some factorisation scale μ_F, leading to the evolution equations for PDF's. One should keep in mind that the evolution includes only a subset of soft and collinear physics and neglects more complicated interactions of e.g. soft initial gluon interacting with the final state.

Illustrating the above ideas on an example, one can measure e.g. the proton structure function $F^{\gamma/N}$ in ep collisions. In order to compare to the calculation, one can write schematically [5]

$$F^{\gamma/N} = C^{\gamma/\tilde{q}} \otimes f_{\tilde{q}/N}\,, \tag{1.1}$$

where the convolution is a short-hand for the integration over the parton momentum fraction and $f_{\tilde{q}/N}$ is the (finite) probability of finding a parton q in hadron N. The (unknown) parton cross-section $C^{\gamma/\tilde{q}}$ has to be infrared (IR) safe (not sensitive to soft gluon emissions), and in fact the whole r.h.s. must be free of divergences. While the parton in the above cross-section is allowed to have some non-zero virtuality (therefore denoted as $\tilde{q}$ instead of q in the formula), with pQCD Feynman rules one can only compute cross-sections for on-shell partons, resulting in IR singularities.

To treat this problem, let us use one more factorisation trick to extract the IR-safe cross-section using the idea of partons within partons, by writing the hypothetical cross-section of photon on a quark:

$$F^{\gamma/q} = C^{\gamma/\tilde{q}} \otimes f_{\tilde{q}/q}\,. \tag{1.2}$$

Here, $F^{\gamma/q}$ is the divergent cross-section which one can formally calculate in pQCD. The idea is to interpret $f_{\tilde{q}/q}$ as probability of finding an off-shell parton inside an on-shell parton, while $C^{\gamma/\tilde{q}}$ is the desired IR-safe cross-section one desires to extract and plug into the original factorisation formula 1.1. It is possible to absorb the divergent part of $F^{\gamma/q}$ into $f_{\tilde{q}/q}$, which actually closely correspond to QCD branching functions. One can expand all quantities into series in powers of α_{S}, and by comparing terms at proper orders perform the deconvolution to obtain $C^{\gamma/\tilde{q}}$. Having arrived at the finite IR-safe $C^{\gamma/\tilde{q}}$ and substituting it into 1.1 one can experimentally resolve the distribution

functions $f_{\tilde{q}/N}(x, \mu_F)$ (tilde will be suppressed in following formulas), where μ_f^2 has the meaning of a maximal virtuality of the parton allowed to enter the hard process.

Having measured the parton distribution functions, one can assume their universality and apply similar procedure with Eq. 1.1 and 1.2 to another observable so that it is possible to actually *predict* another quantity and compare it to the measurement. Therefore, to make a prediction beyond the LO, two physical processes and two calculations are needed, first to measure PDF's, and the other one to make the comparison; in both cases one needs to perform the trick with partons-within-partons model to absorb divergences in the pQCD cross-section into the splitting functions (and of course make sure real and virtual emissions cancel as well).

To isolate poles in cross-section, one has to perform at least part of each calculation analytically, while the rest can be performed numerically. Various techniques are used for NLO predictions, e.g. phase space slicing or subtraction methods. While a technicality, it is an important and a necessary part of the theory for predicting exclusive quantities and differential cross-sections.

1.3.7 QCD Cross-Section at NLO

According to the factorisation theorem, the cross-section for two colliding hadrons can be written as a convolution of the parton cross-section and probability density functions for finding a parton with a given momentum fraction inside the parent hadron in a schematic formula

$$\sigma_{AB} = \sum_{a,b} f_{a/A} \otimes f_{b/B} \otimes \hat{\sigma}_{ab}$$

As outlined in the previous section, the parton cross-section $\hat{\sigma}_{ab}$ can be easily computed at LO. However, at NLO, $\hat{\sigma}_{ab}$ is in fact not known as the incoming partons a, b are allowed to be off-shell (due to evolution of parton distribution functions), while what is straightforwardly calculable is the cross-section for on-shell initial partons only. There are more fundamental problems of divergences in σ_{AB} of two different types: $1/\epsilon^2$ divergences which actually cancel after adding virtual and real emissions at the level of cross-sections (in the latter case also needs to integrate out the real gluon). This is due to the Kinoshita-Lee-Nauenberg (KLN) theorem, which roughly states that $\sigma_{\text{real+virt}}$ is without the leading divergence. Still, one is left with divergences coming in fact from parallel gluon emissions. It turns out that these can be in fact absorbed into the definition of parton distribution functions.

Denoting σ the cross-section for on-shell partons and $\hat{\sigma}$ for off-shell partons, using partons-within-partons distributions functions it is possible to define the following factorisation-like relation

$$\sigma_{cd} = f_{\tilde{a}/c} \otimes f_{\tilde{b}/d} \otimes \hat{\sigma}_{ab}\,.$$

Structure functions of partons within partons $f_{a/b}$ (probability of finding an off-shell parton in an on-shell parton) are pQCD-calculable (and contain $1/\epsilon$ divergences), as well as the on-shell cross-section σ (also $1/\epsilon$ divergent). The interest is to extract from this formula the cross-section for off-shell partons and see whether the divergences in f and σ cancel to give a finite $\hat{\sigma}$. It truly turns out to be so, and $\hat{\sigma}$ can be derived at different orders as follows. In the lowest order, one obtains simply

$$\sigma^{(0)} = f^{(0)} \otimes f^{(0)} \otimes \hat{\sigma}^{(0)} = \hat{\sigma}^{(0)}\,,$$

as $f^{(0)}$'s are just δ-functions at LO. At NLO, the expression reads

$$\sigma^{(\text{NLO})} = \sigma^{(0)} + \sigma^{(1)} = (f^{(0)} + f^{(1)}) \otimes (f^{(0)} + f^{(1)}) \otimes (\hat{\sigma}^{(0)} + \hat{\sigma}^{(1)})\,.$$

Let $\sigma^{(1)}$ be of the pQCD order of $\mathcal{O}(\alpha^n)$, then the relevant piece the expression is

$$\sigma^{(1)} = f^{(0)} \otimes f^{(0)} \otimes \hat{\sigma}^{(1)} + f^{(0)} \otimes f^{(1)} \otimes \hat{\sigma}^{(0)} + f^{(1)} \otimes f^{(0)} \otimes \hat{\sigma}^{(0)} + \mathcal{O}(\alpha^{n+1}) \,.$$

Noting explicitly the parton indices, this is in fact

$$\sigma^{(1)} = \hat{\sigma}^{(1)} + f^{(1)}_{\tilde{a}} \otimes \hat{\sigma}^{(0)} + f^{(1)}_{\tilde{b}} \otimes \hat{\sigma}^{(0)} + \mathcal{O}(\alpha^{n+1})$$

and the desired cross-section for off-shell partons reads

$$\hat{\sigma}^{(1)} = \sigma^{(1)} - f^{(1)}_{\tilde{a}} \otimes \hat{\sigma}^{(0)} - f^{(1)}_{\tilde{b}} \otimes \hat{\sigma}^{(0)} + \mathcal{O}(\alpha^{n+1}) \,.$$

The point is that divergences in $\sigma^{(1)}$ cancel out (here without an explicit calculation nor proof) with divergences in $f^{(1)}$, leading to a finite $\sigma^{(\mathrm{NLO})}_{ab}$ which are ready to be substituted into the σ_{AB} factorisation formula. The $f^{(1)}$ distribution functions are closely related to $\frac{1}{\epsilon}\mathcal{P}$, where $\mathcal{P}$ are the QCD splitting functions (DGLAP kernels).

1.3.8 Scale Choice

Renormalisation group equation formulates the fact that no physical observable can depend on the renormalisation scale. However, working in a finite order of the perturbation theory, one is often left with a non-negligible scale dependence of e.g. the cross-section, facing thus the problem of an explicit scale choice.

In the production of heavy quarks, one has not only the scale of the typical energy of the process, but also of the heavy quark mass itself. This leads to less clearly motivated scale choices as well as possibly large sensitivity of the result to the chosen scale.

Usually, scales are selected to be the p_{T} of e.g. the first hard parton in case of the dijet production (an example of a dynamic scale), or top quark mass (constant scale choice), or a mixture of constant and dynamical scales. The dependence of theory predictions on the scale choice is usually examined by varying the scale by some factor, traditionally (but not necessarily sufficiently large) of 2, and very often the factorisation and renormalisation scales are set equal, though they are in principle independent.

1.3.9 Jets

Final state partons are often strongly boosted w.r.t. the central-mass system, and therefore hadrons originating from partons are expected to be collimated around the original parton direction. Experimentally, this is observed as distinct sprays or jets of particles, rather than uniformly distributed hadrons. The importance of jets is that as long as the energy flow is studied, one deals IR-safe variables. It is a sensible question to ask how many jets can be produced, while it is not IR-safe nor experimentally observable to ask on a specific number of partons.

Infrared safety roughly means insensitivity to the long range physics, independence from soft processes. It can be formulated in terms of observables based on n partons as follows:

$$\lim_{\lambda \to 0} \mathcal{S}_{n+1}(p_q, \ldots, (1-\lambda)p_n, \lambda p_{n+1}) = \mathcal{S}_n(p_q, \ldots, p_n) \,,$$

i.e. for an IR-safe observable, one cannot experimentally distinguish between a final state of n partons, and a similar situation where an additional soft gluon emission or a collinear splitting occurred.

Various algorithms are widely used to find and define jets from basic building object. The important thing is to use prescriptions which are IR-safe and possible to be defined

for partons, stable particles as well as clusters of energies or tracks at the detector level, in as much similar and consistent way as possible. Among most often used algorithms are cone jet finders and their IR-safer improved versions based on clustering using angular metrics; and k_T-algorithms based on respectful transverse momenta of seeds.

1.4 Electroweak Symmetry Breaking

All the above discussion on gauge theories as the fundamental principle generating electroweak and strong interactions involved an important assumption of massless fermions , and in fact also the gauge bosons. However, it is experimentally evident that objects and particles do have mass. The trouble with fermion and vector boson mass terms in Lagrangians is that they are not locally gauge invariant w.r.t. $SU_{\mathrm{L}}(2)$ (although nothing prevents the theory builder to include them into the QCD Lagrangian), and thus would spoil the EW Lagrangian construction. Other means of obtaining mass terms have to be sought.

At the time of writing this thesis, the simplest way was the introduction of a doublet of complex scalar fields with a potential preventing one to conclude a straight forward particle interpretation of the new sector. However, performing a reparametrisation of the potential and realising one has to make a specific choice of the ground state (symmetry breaking), an elegant way of adding masses to gauge bosons emerges. Moreover, from symmetry reasons one is eligible to write also fermion's Yukawa couplings to this scalar sector, which lead not only to interaction terms but also Dirac mass terms for both leptons and quarks.

Currently, there is almost no doubt that also neutrinos have masses, and that their chiral eigenstates do not exactly correspond to helicity eigenstates. Right-handed neutrinos would only couple to the Higgs field in the SM. Moreover, one can write a Majorana neutrino mass term which would mean neutrino is its own antiparticle. It is still not resolved whether neutrinos are of Dirac or Majorana type, and what their masses are, the mixing matrix is fairly well-known (except for θ_{13}) but the mass splitting hierarchy is not fully resolved yet.

1.5 Fermions Mixing

As the coupling of the Higgs field to fermions is in general not diagonal in flavours, the corresponding flavour and mass bases and eigenstates are different, physically meaning that fermions can mix between families. This mixing is well-observed in weak interactions of quarks, while all experimental evidence supports perturbative conservation of individual family lepton numbers for charged leptons. However, non-zero neutrino masses allow neutrino mixing, experimentally observed in neutrino oscillation results. Moreover, if neutrino is its own antiparticle (i.e. of the Majorana type), a neutrino-less double β-decay ($0\nu\beta\beta$) would be possible, which would consequently violate the sacred lepton number conservation law.

The quark mixing matrix, known as the CKM matrix, is fairly well understood, though still an active field of research and extensive consistency checks. An interesting feature is that it contains (in the case of three quark families) one complex phase responsible for the combined charge and parity (CP) symmetry violation in the SM. New physics features may emerge via virtual particles in quantum loops of penguin diagrams contribution to rare flavour-changing processes in meson decays.

1.6 Problems of the SM

Standard Model describes very successfully a wide range of experimental data to a remarkable precision over large kinematics and energy regions. Despite this, there are many hints for the fact that it might be only an effective theory at the several hundreds GeV scale of some more general framework which may emerge at the TeV scale. Briefly discussing the current problems of the SM, it is the problem of hierarchy, the fact that the EWSB scale of the Higgs sector is much smaller than the Planck scale, and that loop corrections to the Higgs mass from Higgs self-couplings, top quark and W loops require a fine-tuning of the bare Higgs mass. There is also the problem of baryogenesis, matter prevailing antimatter in the observed Universe, and the magnitude of the CP violation in the SM is not sufficient to explain it. From cosmology, there is a strong evidence for dark matter, cosmological constant and perhaps also inflation driven by a scalar field, for which there are no suitable candidates in known particle world. Well-established non-zero neutrino masses require extension of the SM to account for neutrino mixing and the possibility of another CP-violating phase. There is still the unresolved question whether neutrinos are Dirac or Majorana particles. While the SM provides good description of the fermion sector, it does not explain the vastly different masses nor the number of families. Why is the charge magnitude of a compound object like proton equal to the one of electron? From a conceptual point of view, gravity described as curvature of the space-time is treated in a vastly different way than the other interactions. Why is the energy density of the cosmological constant non-vanishing, but much smaller than any relevant particle physics scales? Why is the Universe and main physics constants so well and fine-tuned for the existence of life?

Chapter 2

Top Quark

As the heaviest elementary particle known to-date, top quark is an interesting object to study both as an excellent QCD and electroweak laboratory and as a probe for new physics. Top quark is the main background to many analyses at LHC and Tevatron experiments, and any non-standard production or decay properties directly translate to sensitivities of searches for new phenomena, yields or measurements precision.

Top quark's large mass may suggest possible connections to the physics of the electroweak symmetry breaking via its large coupling to the Higgs boson, or by being part of the mechanism itself. Top quark short decay time provides a unique window to a bare quark system, with reduced final state radiation effects.

Precision measurements of top quark properties and production (mass, cross section, decay) can set constrains on Higgs boson mass or limit proposed extensions of the Standard Model.

2.1 Production

Due to the large top quark mass of about 170 GeV, the only relevant accelerator capable to produce top quark pairs before the LHC turn-on has been Tevatron, where the pairs production via the strong interaction is dominated by the quark-antiquark annihilation (85%), accompanied also by the gluon-gluon fusion (15%), see Figure 2.1 for the basic set of contributing processe. Recently, also the evidence for electroweak production of single top quarks has been reported by DØ at Run II [18].

Even before the top quark discovery, there had been limits to the top mass based on corrections to electroweak observables compared to LEP data. As LHC is effectively a gluon-gluon collider in design as a proton-proton collider, the $q\bar{q}$ channel will contribute by only about 10% at the LHC.

The $t\bar{t}$ productions cross section is predicted to be about 7.61 pb for $m_t = 171$ GeV at Tevatron and roughly 900 pb at the LHC [21]. Current average of DØ measurements yields 7.42 $\pm$0.53 (stat) $\pm$ 0.46 (syst) $\pm$ 0.50 (lumi) pb [19] for $m_t = 170$ GeV.

Theoretical uncertainties stem e.g. from the kinematic close to the threshold region and soft gluon resummation and are already at the level of combined experimental cross section errors.

Recently also the NLO $t\bar{t}$+a hard jet ($t\bar{t}$j) production cross section has been computed [20] and the process will be very important at LHC. Single top quark production via electroweak interactions can be factorised into s and t channels and a W-gluon fusion process. Standard strong top pair production is a background to the single-top production already at Tevatron.

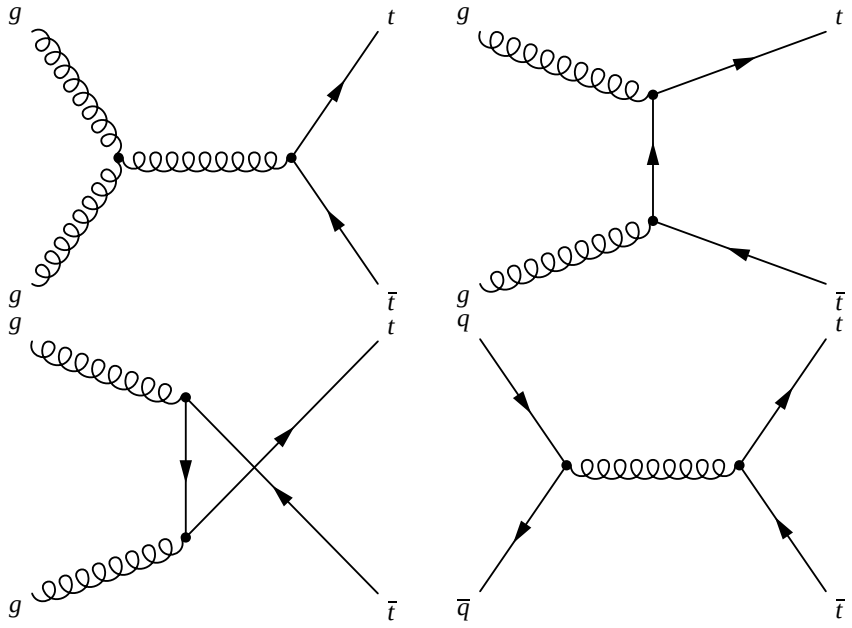

Figure 2.1: Subprocesses contributing to the $t\bar{t}$ production in the leading order of the pQCD (altered according to [38]).

2.2 Decay

Top quark decays almost exclusively into the W boson and b quark as the $|V_{tb}|$ is expected to be very close to 1. (which is confirmed by observations) while $|V_{ts}|$ and $|V_{td}|$ are much smaller. There is also a possible decay mode to $Wb\gamma$, which (although suppressed by the electromagnetic interactions constant α) can be an important background for rare processes at LHC. The experimental classification of the $t\bar{t}$ final state is determined by the way the two W bosons decay, distinguishing the all-jets channel where both W's decay hadronically, lepton+jets channel (see Figure 2.2 for an illustration) where one W decays to a lepton (electron or muon) and a neutrino, and dilepton channels where both W's decay leptonically. See Figure 2.3 for the branching ratios pie diagram. Decays involving the tau lepton are usually included in leptonic or hadronic final states depending on the way the tau lepton decays, or studied dedicatedly by special experimental techniques addressing the difficulties of the τ-lepton identification.

2.3 Properties

2.3.1 Top Quark Mass

Most of top quark characteristics are governed by its high mass. Due to a simple dimensional analysis, top quark width due to its electroweak decay has to depend on its mass as

$$\Gamma_t \propto m_t^3 \, G_F \,,$$

which evaluates at approximately 60 GeV, although a large correction is expected from the limited phase space due to the large mass of the W boson, and so the exact calcu-

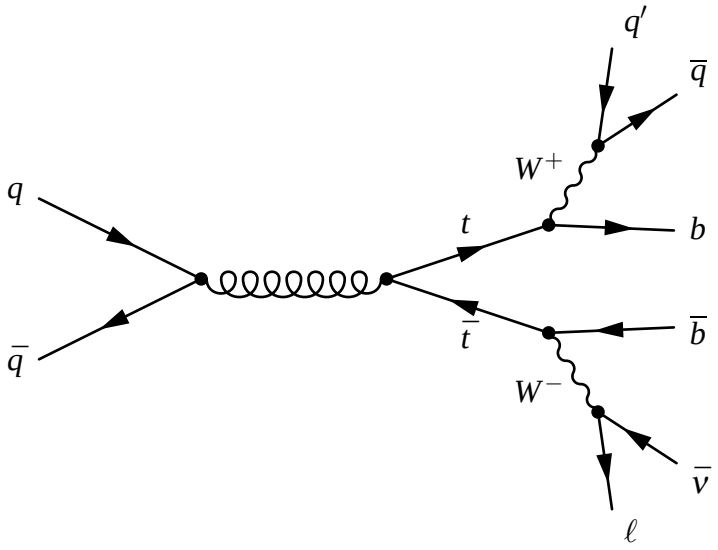

Figure 2.2: An example of the $t\bar{t}$ decay into ℓ+jets. Created using [39].

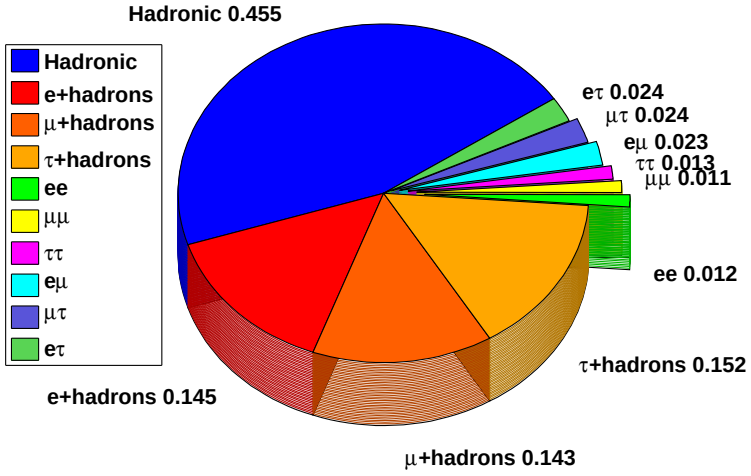

Figure 2.3: $t\bar{t}$ decay branching ratios according to the W bosons decay modes, using numbers from [78].

lation yields a theory value of about 1.4 GeV via [22]

$$\Gamma_t = \frac{G_F m_t^3}{8\pi\sqrt{2}} \left(1 - \frac{m_W^2}{m_t^2}\right)^2 \left(1 + 2\frac{m_W^2}{m_t^2}\right) \left[1 - \frac{2\alpha_s}{3\pi}\left(\frac{2\pi^2}{3} - \frac{5}{2}\right)\right] .$$

Large width corresponds to a short life time of $\Gamma_t^{-1} \approx 4.7 \times 10^{-25}$ s and a characteristic length scale of about 0.14 fm, which is much smaller than the typical hadronisation length $\Lambda_{\mathrm{QCD}}^{-1} \propto 1$ fm. Therefore, top quark is expected not to hadronise, and form neither topponium nor t-mesons, and rather behave as a heavy bare unstable particle. This has important consequences, in e.g. preservation of the t-$\bar{t}$ spin correlations in top quark decay products and an access to a kinematics of a heavy bare quark system at a hight momentum scale.

The precision knowledge of top-quark mass has important consequences on fitting the Higgs mass in precision EW data, as the top quark has strongest coupling to the Higgs boson. However, there is a large ambiguity on the top quark mass definition and substantial difference between the pole mass (defined as the complex pole of renormalised quark propagator) and renormalised (running) top quark mass (physical mass in the Lagrangian, depending on the renormalisation scheme). Such mass definition choice ambiguity can lead up to 10 GeV differences [15], and to complicated question on what top mass is in fact being measured in experiments. Due to most of the methods using kinematic variables, the general consensus or belief is that it is the pole mass which is being extracted from the measurement. Due to non-perturbative reasons, there is an intrinsic uncertainty on top mass of about Λ_{QCD}, called the renormalon problem (top pole mass linearly sensitive to the IR scale, as there is in fact no pole in quark propagator due to confinement) [16], [17].

2.3.2 Top Quark and $t\bar{t}$ System Transverse Momentum and Mass Spectra

Top quark transverse momentum distribution has been studied among other kinematic variables by the DØ collaboration at Run I in the beautiful top quark mass paper [31] with the data set of 125 pb^{-1}. Kinematic variables are expressed at the detector-smeared level compared to HERWIG prediction after the detector simulation. Kinematic fit was employed to fully reconstruct the $t\bar{t}$ system, and further variables like the $t\bar{t}$ system mass, and $t\bar{t}$ system related angular variables (the difference between the two top quarks in the azimuthal angle and pseudorapidity) were also studied. From 91 preselected events (7 with a muon tag)[1], 77 converged in the kinematic fitter with $\chi^2 < 10$ (5 with μ tag), out of which about 25 were attributed to the signal in the lepton+jets channel. The measured smeared spectrum is reproduced in Figure 2.4. Both leptonic and hadronic top quark p_{T}'s were used.

Dedicatedly, top quark p_{T} spectrum was studied by the CDF collaboration at Run I [32], based on a dataset of 106 pb^{-1}. The analysis included corrections for detector resolution effects (unsmearing, know also as unfolding). Out of 61 selected events in the lepton+jets final states, about 32 were considered as background, and the unfolding was performed using a likelihood technique with HERWIG truth top quark p_{T} distribution as the measure of migration (referred to as "response" in the paper). The smeared result in 10 bins and unfolded result in 4 bins are reproduced in Figure 2.5. Only the

[1] At Run I, the DØ detector did posses a central magnetic field nor a precise silicon-based detector allowed to measure displaced vertices of long-living B-mesons. These had been identified (tagged) based only on their semi-leptonic decays.

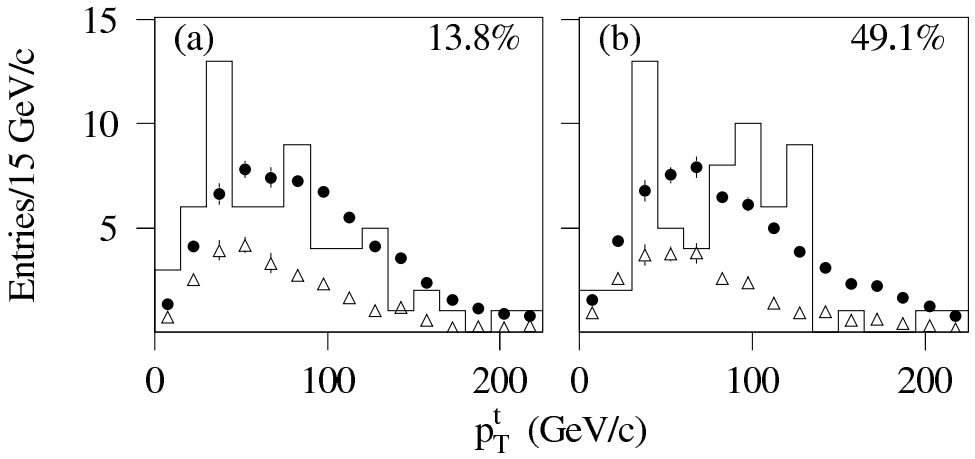

Figure 2.4: DØ Run I smeared top quark p_{T}; data (line), expected signal+background (full circles) and background only (open triangles) for floating (left) and fixed (right) top quark mass in the kinematic fitter ($m_t = 173.3\,\mathrm{GeV}$). Figure reproduced from [31].

hadronic top quark p_{T} was used due to a large correlation to the leptonic top quark p_{T}.

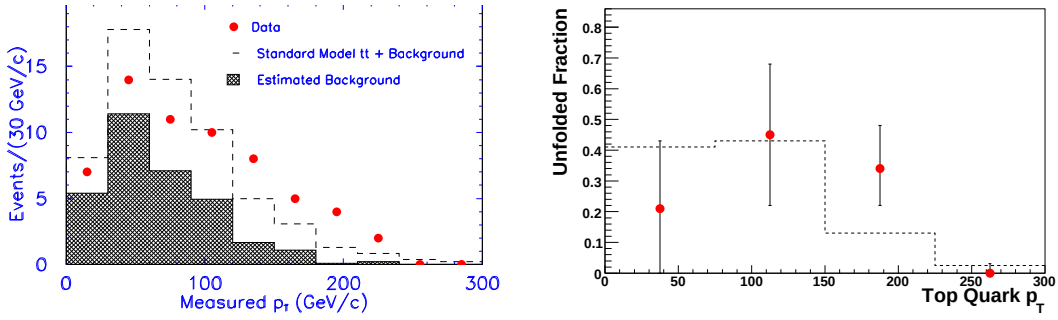

Figure 2.5: CDF Run I measurement; Left: smeared top quark p_{T} spectrum (shaded: background, dashed line: total prediction, red points: data). Right: Unfolded and acceptance-corrected data distribution (points) compared to HERWIG prediction (line); left plot reproduced from and right plot created using results table in [32].

The searches for $t\bar{t}$ resonances have been also performed by the two collider experiment setting the limits on Z' mass of the order of 700 GeV [23], [24].

2.3.3 Other Properties

There is a predicted phenomenon of a top-quark charge asymmetry for the top quark pair production in hadron-hadron collisions, being an NLO effect (see Figure 2.6), which is in essence the asymmetry in counting (anti)top quarks moving along positive or negative z axis defined by e.g. the proton beam.

$$\mathcal{A} = \frac{\sigma_t(y_t > 0) - \sigma_t(y_t < 0)}{\sigma_t(y_t > 0) + \sigma_t(y_t < 0)}\,.$$

The asymmetry stems from the interference term between diagrams with one and two gluon exchange. Experimentally, it can be measured as forward–backward asymmetry in number of charged leptons, i.e. looking at positive and negative rapidities:

$$\mathcal{A}_{\mathrm{FB}} = \frac{N_l(y_l > 0) - N_l(y_l < 0)}{N_l(y_l > 0) + N_l(y_l < 0)}\,.$$

The asymmetry has been measured by DØ and CDF collaborations [25] [26] and is consistent with the SM.

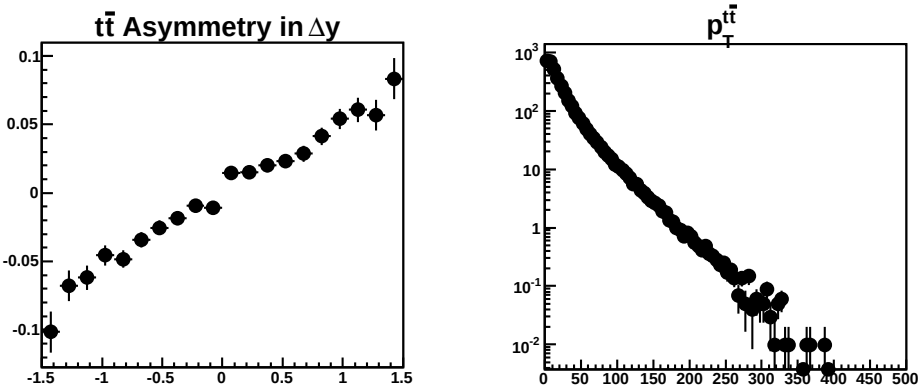

Figure 2.6: $t\bar{t}$ asymmetry in the top quark rapidity (left) and the transverse momentum spectrum of the $t\bar{t}$ pair (right) as predicted by MC@NLO at the parton level.

Due to the short top quark lifetime, its spin is directly translated into correlations between the decay products and could be measured by looking at $t\bar{t}$ spin correlations.

The W helicity in top quark decays can provide a direct test of the V-A structure of weak interactions and has been measured by Tevatron experiments [27], [28]. W boson is expected to be left-handed or transverse but almost never right-handed (in the limit of $m_b \to 0$) with $F_0 \approx 0.70$, $F_- \approx 0.30$, $F_+ \approx 0$.

There are many more kinematic distributions related to individual top quarks as well as the $t\bar{t}$ system, which have not been so far tested experimentally against theoretical predictions, while many new physics can easily change their distributions (e.g. $t\bar{t}$ resonances, top quark anomalous magnetic moment). This fact is the main motivation behind the presented study.

Chapter 3

Tevatron

3.1 Accelerators as Experimental Tools

High energy physics studies fundamental particles, their interactions, underlying forces and the dynamics determining the properties of compound objects; it searches for new forces and particles and phenomena not described by current theory. New models are often related to large energy scales, i.e. shorter distances, and looking closer to smaller and smaller distances requires correspondingly higher energies. With current centre-of-mass energies of Tevatron's proton-antiproton collisions of about 2 TeV, distances of about 10^{-19} m are being probed, which will become about 10^{-20} m at LHC with energies of 14 TeV.

The study of small objects requires large experimental setups, both on the side of accelerators which prepare and collide high energy particle beams, and detector devices, which take detailed snapshots of collisions so that teams of physicists can analyse the collisions and search for unique events. This requires high statistics and therefore large densities of particles in the beam and high collision rates, i.e. large beam luminosities.

3.2 Colliders

Lepton-hadron collisions are a useful tool to study the structure of hadrons with a simple projectile and were used in proton structure discovery in analogy with Rutherford-Geiger-Marsden experiments where α particles probed the structure of gold atoms. Lepton-hadron collisions had been used at SLAC and DESY to probe the structure of the proton.

In the current picture, hadron-hadron collisions are parton-parton colliders[1], i.e. they collide quark and gluons at random fractions of the original hadron momentum, providing an automatic energy scan for the search of new particles at unknown scales or probing shorter distances with increased beam energy.

Lepton-lepton collisions are the cleanest type of interactions used e.g. to precisely measure properties of a known resonance at certain mass (LEP, SLAC, KEK).

The above ideas have been followed in last years of the particle physics history, leading to the discovery of W and Z bosons in proton-proton collisions, their properties determination at electron-positron collider LEP, with current searches for the mechanism of the electroweak symmetry breaking mechanism at Tevatron and LHC, while a linear electron-positron collider is being planned to measure properties of new objects one hopes to observe at LHC. It is amusing to observe that most of recent

[1] Although there is also a significant diffractive part of the cross section, both elastic and inelastic.

fundamental fermions (c, b, t, ν_τ) were discovered on the New Continent, while bosons (W, Z, evidence for gluon) were first observed in Europe. One is still left with the open question on the particular mechanism of the electroweak symmetry breaking, whether the Higgs boson exists and what are the Higgs sector properties.

3.3 Tevatron

Tevatron is a proton-antiproton collider operating at the centre of mass energy of 1.96 TeV[2]. Tevatron is in fact only the last accelerator in the whole chain of linear and circular machines at Fermilab. It consists of 377 + 395 dipoles and 180 quadrupoles aligned around the circumference of $2\pi \times 1$ km.

The beam structure is organised into 36 proton and 36 antiproton bunches colliding head-on in interaction places. Bunches are grouped into three super-bunches of 12. The radio-frequency field (RF) of 53.104 MHz of the one accelerating cavity defines a so-called RF bucket, a stable region in longitudinal phase space along which a bunch can be placed. An accelerator tick is defined as 7 buckets, there are 159 ticks per turn, bunch spacing is 3 ticks (two empty ticks between two bunches) evaluating at 396 ns of the bunch spacing. The 36 bunches around the circumference revolving in about 21 μs generate an average collision rate of about 1.7 MHz.

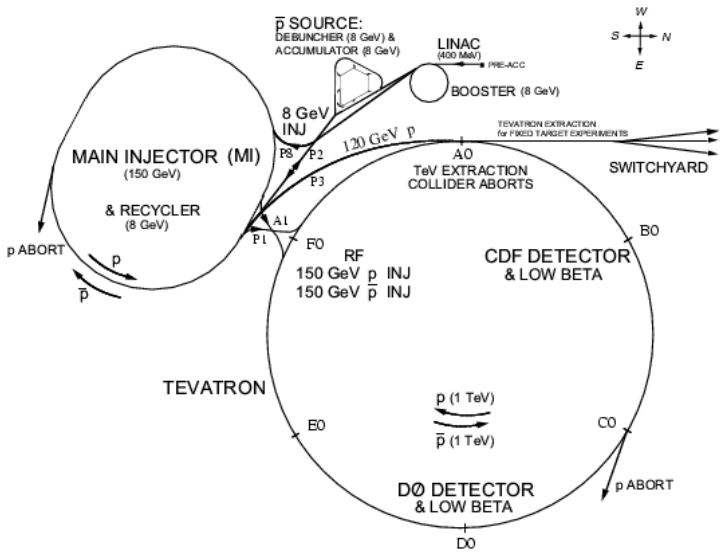

Figure 3.1: Accelerator Layout

3.4 Accelerator Complex

The acceleration process starts at a bottle of hydrogen, the source of H^- ions, which are pre-accelerated by the Cocroft-Walton electrostatic accelerator to 750 keV, transferred to Linac (400 MeV) and to Booster (8 GeV), where the two electrons are stripped off and protons are being accelerated for the Main Injector, which accelerates particles to 150 GeV and injects them into Tevatron, where the final acceleration to a beam energy

[2] 1.8 TeV at Run I period 1992–1996, while Run II is planned for years 2001–2008.

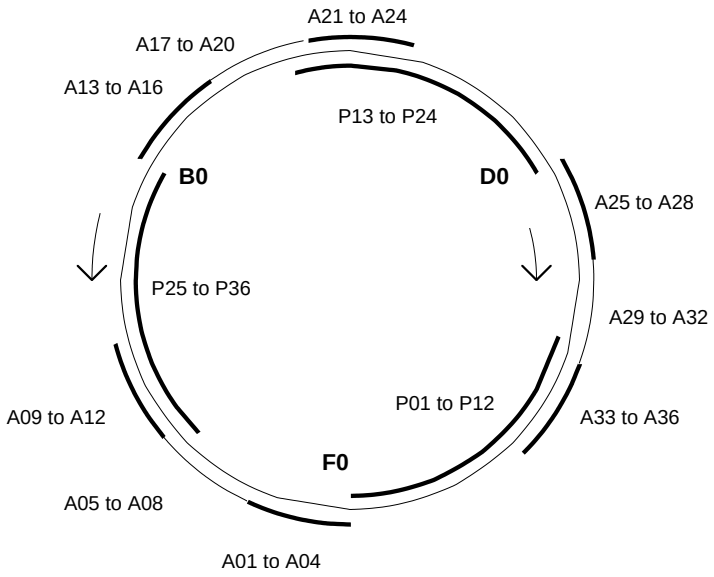

Figure 3.2: Tevatron Bunch Structure

of 0.980 TeV takes place. There are two main interaction points of low beam emittance, where detector facilities CDF and DØ are located.

3.5 Antiproton Source

Protons from the Main Injector are also used for antiprotons production via a nickel target, after which a lithium (least-dense conductor) lens with large radial magnetic field gradient (produced by an electric current flowing along the beam) selects antiprotons [7]. Antiprotons are then transferred to Debuncher and Accumulator, the beam is cooled stochastically in Debuncher and then also by an electron beam in Recycler. Pelletron is a Van der Graff generator, electron accelerator, and a recycler in one. The electron beam generated by the Pelletron is used for electron cooling of the antiprotons in the Recycler.

Main Injector is a synchrotron built specially for the Run II period and replaced the former Main Ring, which was a Tevatron's pre-accelerator in the same (Tevatron) tunnel. It is amusing to note there was a bypass of the Main Ring around the CDF detector, while Main Ring was literally passing through DØ's outer hadronic calorimeter cryostat, causing so-called "Main Ring events" (beam-halo interactions) which had to be removed by special ϕ-cuts.

3.6 Acceleration Phases

The acceleration period in Tevatron takes about 1.3 min and brings protons and antiprotons from the injected energy of 150 GeV to the beam energy of 0.980 TeV (flat-top). Next, squeeze follows, when quadrupoles near detector regions tightly focus the beam. In the initiate collisions phase, electromagnetic separators near collision points change their voltage and helical orbits of protons and antiprotons (which are otherwise kept apart) begin to overlap to start collisions. In the remove halo phase, Tevatron collimators remove proton and antiproton beam halos.

3.7 Luminosity

Luminosity is the quality factor of the collider reflecting the size and density of beams as well as the frequency of collisions, and determines the observed rate of interactions of a specific type knowing the cross section σ for the process by

$$\frac{\mathrm{d}N}{\mathrm{d}t} = \sigma \mathcal{L}\,.$$

Luminosity can be expressed in terms of number of protons and antiprotons in a bunch N_p, number of bunches N_B, frequency of collisions f and beam sizes at interaction point σ_p as [8]

$$\mathcal{L} = \frac{f N_B N_p N_{\bar{p}}}{2\pi(\sigma_p^2 + \sigma_{\bar{p}}^2)}\,\mathcal{F}(\sigma_l/\beta^*)\,,$$

where $\mathcal{F}$ is a form factor depending on σ_l/β^*, the ratio of bunch length to the beta function at the interaction point. The integrated luminosity

$$L \equiv \int \mathcal{L}\,\mathrm{d}t$$

reflects the total collider performance over a certain period of time. During the Run I period, Tevatron delivered about $120\,\mathrm{pb}^{-1}$, while Run II goal is aiming up to $8\,\mathrm{fb}^{-1}$ with more than $5\,\mathrm{fb}^{-1}$ delivered already as at the end of 2008.

Typical initial (store-begin) luminosities at Tevatron Run IIa were about $10^{32}\,\mathrm{cm}^{-2}\,\mathrm{s}^{-1}$, exceeding $3{\cdot}10^{32}$ at the Run IIb phase.

With time, luminosity decreases because of beam-beam effects in interaction points and near parasitic collision points, where beam separation is small, and also due to intra-beam scattering. Thus, number of particles per bunch decreases and bunches grow wider in the plane transverse to the beams. Protons experience stronger beam-beam effect, the number of protons per bunch is about five times bigger than number of antiprotons per bunch. In good stores, about 50% of antiprotons injected to Tevatron are 'burned' by the collisions processes at interactions points.

At 1.96 TeV centre-of-mass energy, the total proton-antiproton cross section can be decomposed into the following values according to the individual subprocesses: about 22.8 mb for the diffractive cross section (both elastic and inelastic), 60.7 mb for the inelastic, out of which 48.3 mb is the hard scattering process [9], [10].

The luminosity delivered by the accelerator division to each experimental site is large that the recorded one due to finite time needed to prepare experiments for physics after collisions are initiated, but also due to operational inefficiencies. The overall efficiencies of both experiments have been about 90%. Out of the recorded luminosity, only a part of data is selected for analyses, based on careful data quality checks which make sure that all subdetectors worked properly and without outstanding problems so that the data can be trusted for entering physics analyses.

Chapter 4

The DØ Detector

4.1 Detectors In High Energy Physics

In general, the design of a high energy physics detector can focus on the performance of tracking, calorimetry, particle identification, muon detection, very forward (diffractive) physics, or e.g. energy/mass resolution optimisation; and reflects itself in specific detector assembly features and geometry. Current HEP experiments usually aim at varied physics programmes (especially at hadron-hadron colliders), and are thus often built as multipurpose sets of sub-detectors to study the wealth of physics collisions provided by the collider/accelerator, ranging from meson and baryon physics using almost exclusively tracking to high-p_{T} physics of jets and electroweak physics, which requires many physics object to be identified. In either case, rare events are of special interest, and the concept of triggering, i.e. selecting from millions of events in a second only interesting cases and writing them to a tape of a limited band width, has to be used in on-line electronics and data acquisition systems. In this chapter, the experimental setup at the Fermilab Tevatron collider from the point of view of the DØ detector is described before moving to the subject of the physics analysis using this device.

4.2 DØ Experiment Overview

The DØ detector [11], [12] is a multipurpose device to analyse proton-antiproton collisions at the Tevatron Collider at Fermi National Accelerator Laboratory in the USA. From the unpolarised beams and symmetrical beam energies, it has a cylindrical symmetry and is radially segmented into specialised sub-detectors providing tracking, calorimetry and muon identification (see Figure 4.1 for the basic overview).

4.3 Tracking

The tracking system is in the heart of the detector as close to the beryllium beam pipe as possible and has been the major subject of upgrade to the DØ Run II detector. Also, for the Run IIb phase, an additional Layer 0 silicon detector has been added. Many identification algorithms rely on the tracking performance in terms of either directly tracks, or higher level objects like primary or secondary vertices. Electron/photon identification, muon matched to the interaction vertex, jet confirmation to the primary vertex, b-tagging and τ identification are the basic object definitions which highly benefit from good tracking performance.

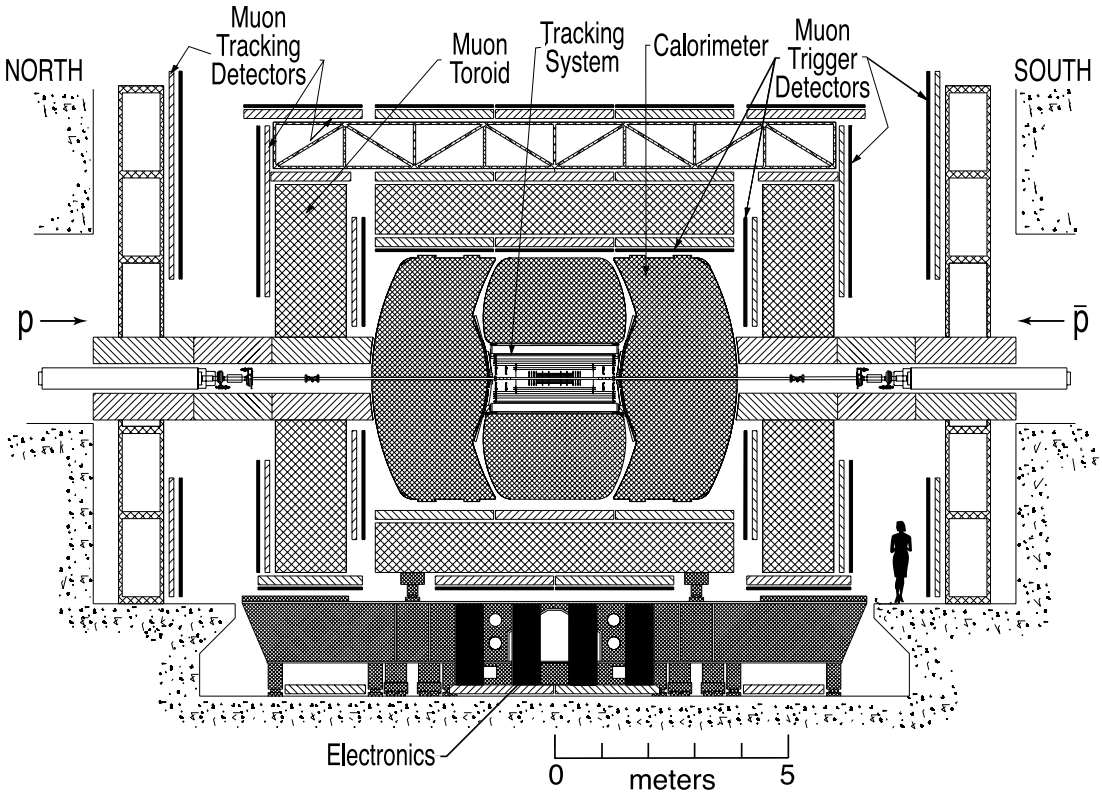

Figure 4.1: DØ Run II Detector.

The tracking is provided by silicon and fiber detectors (see Figure 4.2), which together can find the position of the primary interaction within 35 μm along the beam direction; and can tag b-jets with an impact parameter resolution of about 15 μm in the plane transverse to the beam.

4.3.1 Silicon Microstrip Tracker

Reliable and good resolution tracking detector is an essential tool for many physics goals of the Run II Tevatron programme, ranging from Higgs, top and electroweak physics to almost purely tracking-based heavy flavour physics.

DØ's Silicon Microstrip Tracker (SMT) is housed in 2 T field superconducting central solenoid (Cu/Nb/Ti) running with the current of about 4.7 kA. The solenoid is about $0.9\,X_0$ (radiation lengths) thick in the radial direction. SMT is read out by about 840k channels providing the largest data flow of all DØ sub-detectors.

Geometrically, the detector consists of six concentric barrel modules of 4 silicon layers with insertions of F-disk modules of 12 double-sided wedge detectors, and with special disks located at the end of the tracking cylinder (H-discs; with 24 wedges with two back-to-back single-sided sensors) to provide tracking at high $|\eta|$ (see Figure 4.3). Disks are mounted on beryllium rings and the full support is provided by two carbon-fiber cylinders.

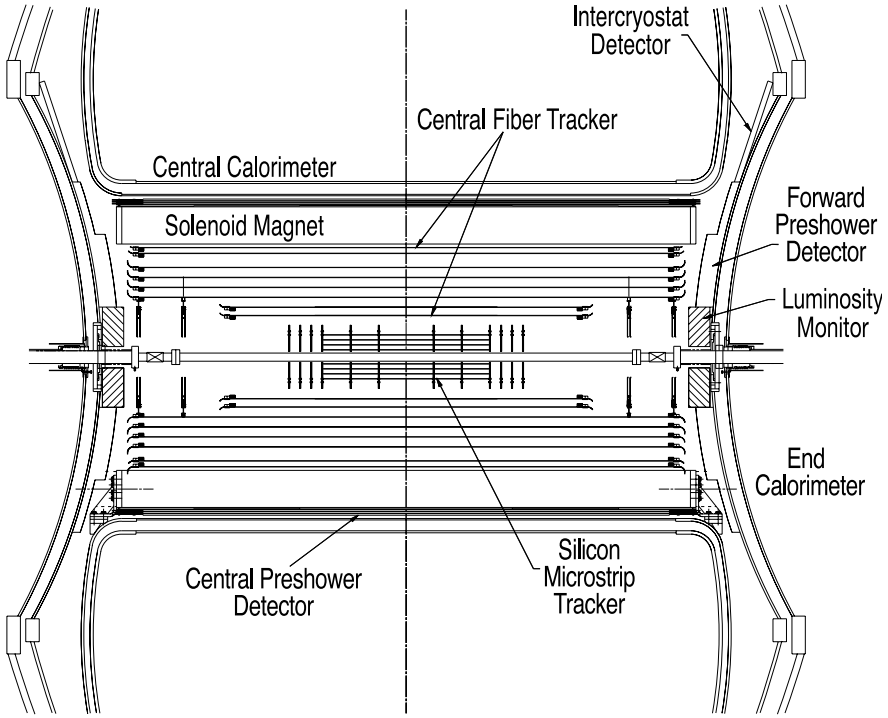

Figure 4.2: DØ Tracking Detectors

4.3.2 Central Fiber Tracker

Central Fiber Tracker (CFT) is based on the technology of wave length shifter fibers and Visible Light Photon Counters, which work in the avalanche mode at 9 K. CFT in fact comprises three detectors: CFT itself of 8 barrels (axial, stereo doublet layers) of 77,000 fibers of 0.83 mm in diameter, Central Preshower (CPS) consisting of 1 axial, 2 stereo (7000 channels); and Forward Preshower (FPS) consisting of 2MIP and 2 shower layers with 15,000 channels. Their function is tracking and supplemental calorimetry. FPS contains a $2X_0$ absorber and a detecting device composed of strips of scintillation fibers of the same kind as CFT.

Basic preshower unit is a hollow scintillator strip with a signal fiber inside, leading the signal to electronics. The fiber is a wave length shifter, so that the light from the scintillator does not simply pass through the fiber, but is re-emitted from blue to green in a random direction, increasing thus the probability for total reflection based transport.

VLPC cassette houses solid state photon detectors at a bias voltage 6–8 V with quantum efficiency for light of about 80%. They are located in a cryostat of 9K and convert light to electrons. In principle, these are photo-diodes converting photons in the intrinsic region to electron-hole pair. Hole drift knocks-out electrons from surrounding atoms and causes an avalanche. Electron accelerates back through gain region, avalanching other electrons, making gains of 20,000–60,000 achievable.

4.4 Luminosity Monitor

The luminosity monitor (LM) measures the luminosity delivered by the Tevatron collider to the DØ interaction region using the observed average number of inelastic colli-

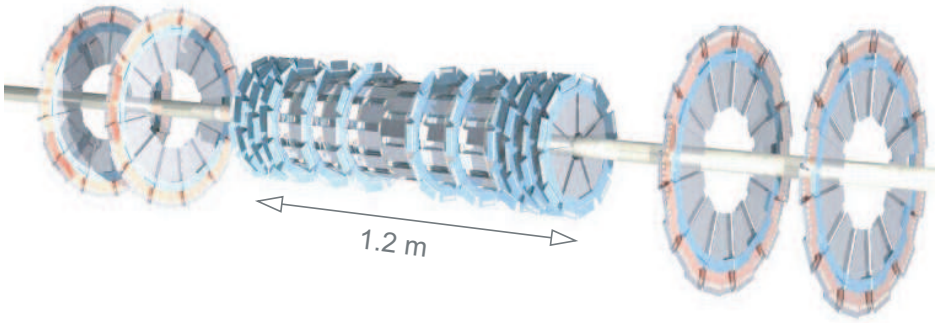

Figure 4.3: DØ Silicon Microstrip Tracker – a perspective view.

sions per beam crossing N^{inel} and the effective inelastic cross section $\sigma_{\text{eff}}^{\text{inel}}$ according to $\mathcal{L} \equiv f\frac{N^{\text{inel}}}{\sigma_{\text{eff}}^{\text{inel}}}$ where f is the beam crossing frequency. The luminosity detector consists of 24 scintillation-based counters symmetrically around the beam and read-out using PMT's. The detector is located between calorimeter cryostat walls close to the beam pine.

The delivered luminosity is calculated for each accelerator tick using the number of measured LM coincidences and an effective $p\bar{p}$ cross section via

$$\mathcal{L} = \frac{f/159}{\sigma_{\text{eff}}} \sum_{\text{tick}\, i=1}^{159} \log\left(1 - \frac{\Delta\text{LM}_i}{\Delta\text{tick}/159}\right)$$

where f is the Tevatron revolution frequency, ΔLM_i is the scalar count from LM for tick i and Δtick is the length of the luminosity block in 132 ns ticks [13].

4.5 Calorimetry

The energy measurement of showers of particles is provided by three calorimetry devices housed in separated cryostats, denoted as Central (CC) and End Cap (EC) Calorimeters (see Figure 4.5). In the radial direction (see the one-quarter cross section of the calorimeter in Figure 4.6 with lines of selected detector projective η) Electromagnetic (EM) part is followed by Fine Hadronic (FH) and Coarse Hadronic (CH) sections to contain most of the showers produced in $p\bar{p}$ collisions at Tevatron energies.

The calorimetry is based on the process of charge particles ionising the liquid argon active medium, while shower is developped and contained in uranium, copper and steel passive materials. The basic calorimeter unit (Figure 4.7) consists of a 2.3 mm wide Lq-Ar gap, 3 mm absorber plate and a copper readout pad surrounded by a G10 insulator coated with a high resistive epoxy. The signal pad observes a reflected charge of the particle trace in the liquid argon due to the voltage of 2000 V between the pad and the absorber plate.

Fine segmentation in the angular space $\Delta\phi \times \Delta\eta$ of 0.1×0.1 is doubled in the third EM layer to 0.05×0.05, being at the depth of the shower maximum at Run I (however, there is unfortunately more dead material in front of calorimeters at Run II, related e.g. to the addition of the solenoid and the tracking detectors).

In total, about 50,000 cells are being read-out from the device. Signal is magnified in charge preamplifiers at the cryostats and then shaped on baseline subtractor boards

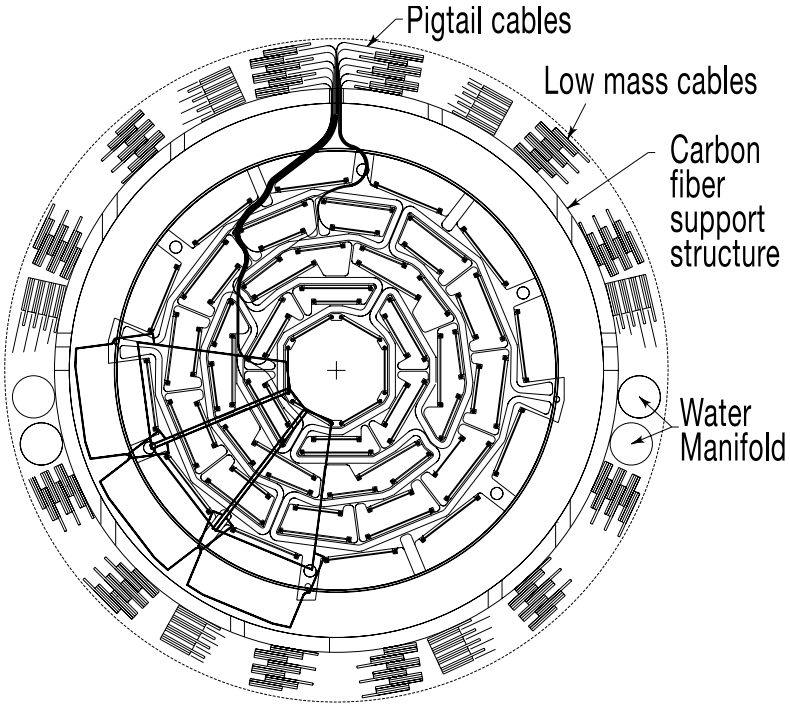

Figure 4.4: DØ Silicon Microstrip Tracker – cross section of a disk/barrel module.

(BLS) and stored for up to $4\,\mu$s in an analog way in switched capacitors arrays (SCA's) until readout (Level 2) decision comes, and signal is then digitised outside the detector. A faster analog-summed signal serves as input to Level 1 and Level 2 trigger decision framework, using trigger towers of approximate granularity of 0.2×0.2 in the $\eta \times \phi$ space.

The preamplifier outputs a signal integral with a rising time of about 450 ns and a recovery time of about $15\,\mu$s. The shaper uses about 260 ns of the signal from the gap (about 2/3 of the collected charge). Shaped signal of a peak at about 320 ns and a recovery time of about $1.2\,\mu$s is sampled every 132 ns and in order to subtract the baseline of the previous collision, signal from the time of 396 ns earlier is subtracted on BLS.

The integration time at Run I was long enough to collect almost all the charge generated along the particle path in the gap. However, at Run II, the electron drift time across the gap of 450 ns is even longer than the interval between two bunch crossings of 396 ns, and so a pile-up of signal from the previous collision occurs in general, therefore the baseline subtraction (there is ideally no physics-related base line subtraction in the crossing of the first bunch of the super-bunch). Differences in the charge collection due to module-by-module variation and possible geometry imperfections translate to the signal variation; this effect has become important at Run II to the extend that a cell-level calibration procedure had to be developped to account for part of the effect [ϕCalib].

Between the central and end-cap cryostats, the inter-cryostat detector (ICD) is placed to provide energy sampling supplemental measurement in the region of $1.1 < |\eta| < 1.4$ based on the technology of scintillating tiles, wavelength-shifting fibers and photomultipliers (PMT's).

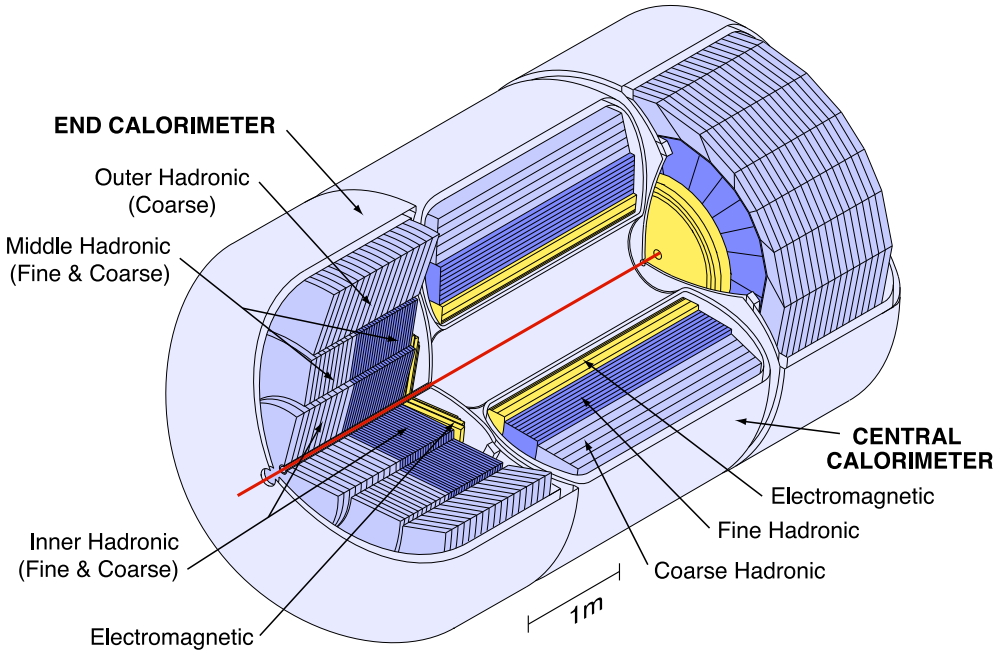

Figure 4.5: DØ Run II Liquid Argon Calorimeter.

4.6 Muon Systems

Located radially in the outermost part of the detector, the purpose of muon chambers is to detect muons, which as nearly minimum ionising particles penetrate even the calorimeter.

Central muon system is equipped with three layers (A, B, C) of proportional drift tubes (PDT's) used already during the Run I period, covering the η range up to about 1. In addition, new forward muon system based on three layers of mini drift tubes (MDT's) with shorter electron drift time was installed, extending the coverage up to $|\eta| < 2$ and including also scintillation counters (Figure 4.8) for triggering, and additional shielding. For the overview of PDT and MDT muon systems, see the Figure 4.9.

An iron-core toroidal magnetic field between A and B layers enables the muon momentum measurement. The central toroid is a square annulus of about 1 m thick iron starting radially about 318 cm from the beam with 20 coils of 10 turns each, the end toroids with 8 coils of 8 turns each. The magnetic field reaches about 1.9 T.

Muon systems do not only detect muons, but all possible charge particles which penetrate the calorimeter, like high energy jets which were not fully contained in the calorimeter, as well as pions which have not developped the hadron shower. There are also cosmic muons, which can however be easily identified due to "wrong" timing and usual off-center tracks.

4.7 Forward Proton Detector

Although not important for this analysis, the DØ detector has been equipped with the device for diffractive physics studies, often referred to as Roman Pots. These scintillating fiber detectors measure elastically scattered (anti)protons at large pseudorapidities and can be used as triggers of diffractive events, where at least one of colliding hadrons does not break.

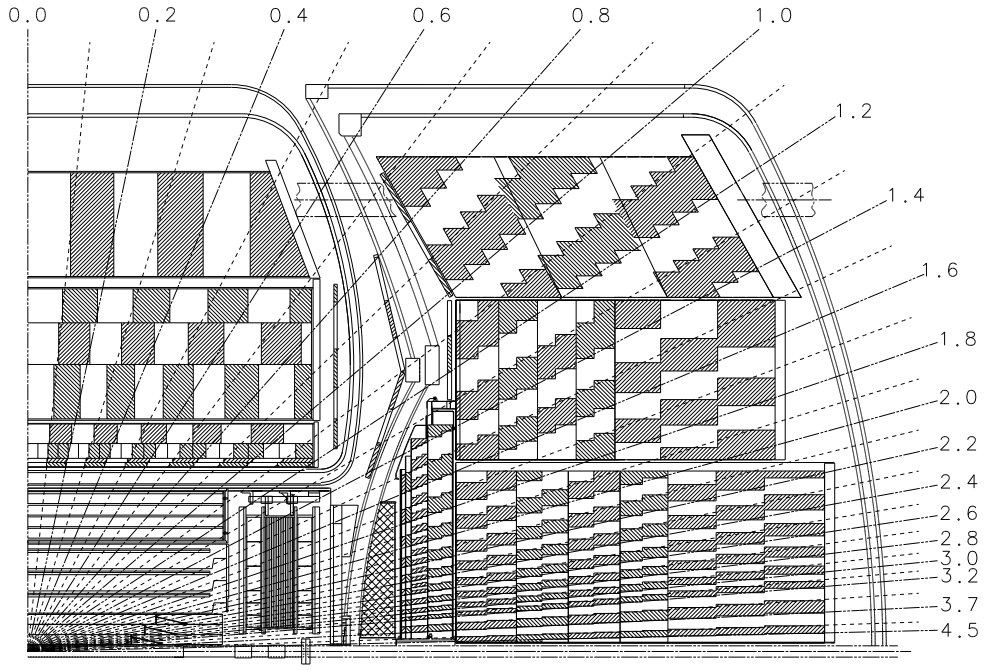

Figure 4.6: DØ calorimeter projective towers.

4.8 Data Acquisition and Triggering

Total 36 bunches spread per 12 in 3 super-bunches with the revolution time of 21 μs yield the average crossing frequency of 1.7 MHz. The typical L1/L2/L3 input trigger rates at the Tevatron Run II have typically been 1.7 MHz/2.5 kHz/1 kHz, the output rates about 2500/1000/100 Hz, limited by the rate data can be written to a tape. Available decision times at L1/L2/L3 are about 4.2 μs/100 μs/50 ms [14].

Therefore, the L1 decision is hardware based and uses simple signatures so that the decision can be made in 3.5 μs. L1 trigger framework (TFW) collects the information from L1 trigger devices and prescales triggers which have a rate too high to write every event they trigger. TFW receives 256 inputs (trigger bits) from various detector outputs to form individual triggers. 128 bits can be programmed as AND/OR physics triggers.

The L2 decision is software based and is performed within 100 μs; basic physics objects like leptons, jets and even tracks can be compared to template patterns and L2 cuts (e.g. on jet p_{T}) can be performed. The L3 trigger can already run simplified versions of reconstruction algorithms and provide more effective triggering.
Triggering is an essential part of high luminosity high energy physics experiments as it is of great importance not to lose rare events over the common ones. Fast decision and cuts are therefore crucial, although they can lead to important biases due to finite (and often worse) resolution of the trigger-level object.

When the L3 trigger decision is positive, event fragments are sent from each readout-crate single board computer (SBC) to a selected L3 farm node, which then combines (builds) the event (see Figure 4.10 for the DAQ network configuration). Finally, events are sent to a reconstruction farm and stored in tapes. For the data flow diagram, see Figure 4.11.

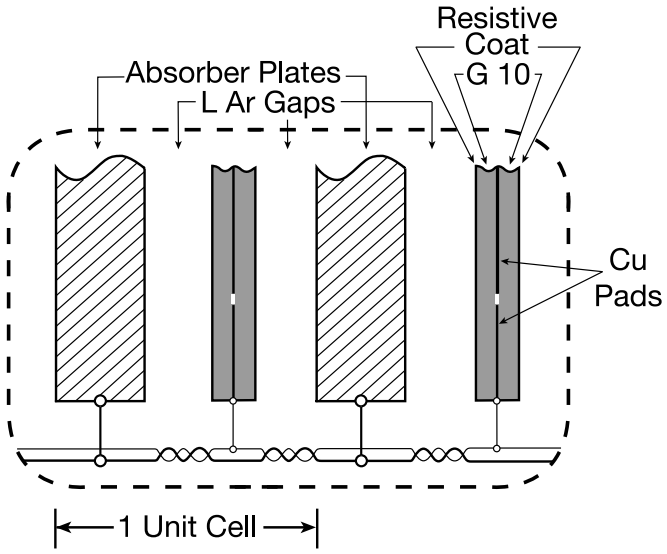

Figure 4.7: DØ calorimeter cell unit.

4.8.1 The Data Flow

Data flow from each of the sub-detector is buffered in a readout crate (controlled by a controller crate) until L2 Accept decision arrives. Then data is passed to a L3 filter, which checks whether it passes the L3 decision, and then sends it to the back-end part of the data acquisition system. There, collector/router duplicates the event, one copy going to a data distributor which sends it to on-line examines applications, while the other copy goes to one of 4 data loggers which send data to disks, to be kept there for up 2 days. Finally, data is sent via Enstore to SAM storage system in Feynman Computing Center (FCC).

A readout crate consists of several subparts. There is a controller card which can communicate to L2 and trigger framework, and data cards holding L1 data buffers (usually 16 events). If buffers are full, trigger framework is notified about L1 busy, and trigger frameworks stops reading the data. L2 buffers are usually 8 events deep. If the L2 decision comes, data is moved to the output buffer by the single board computer (SBC), which sends data via Ethernet to L3 Linux farm nodes. If an output buffer fills up, a L2 busy signal is send, and no more L2 accepts are then coming, while L1 buffers can still be filled with new events. Therefore, L2 busy is not a dead time unless it induces L1 busy.

Routing master is a specialised SBC which decides to what farm node should all other SBC's send their event fragments. If there are no L3 farm nodes available, the L3 disable state happens. Event tags from all event fragments have to match in every L3 farm node for current event.

On each L3 farm, an Event Builder collects all event fragments to build the event from the event buffers. Complete event goes to filter shells which send them to the back-end.

4.8.2 Controls

Central Coordination Process (COOR) controls all system configurations and run transitions, making sure client requests are not in conflict. Via COOR, store-end and store-begin commands are issued, as well as a serial command link initialisation (clears

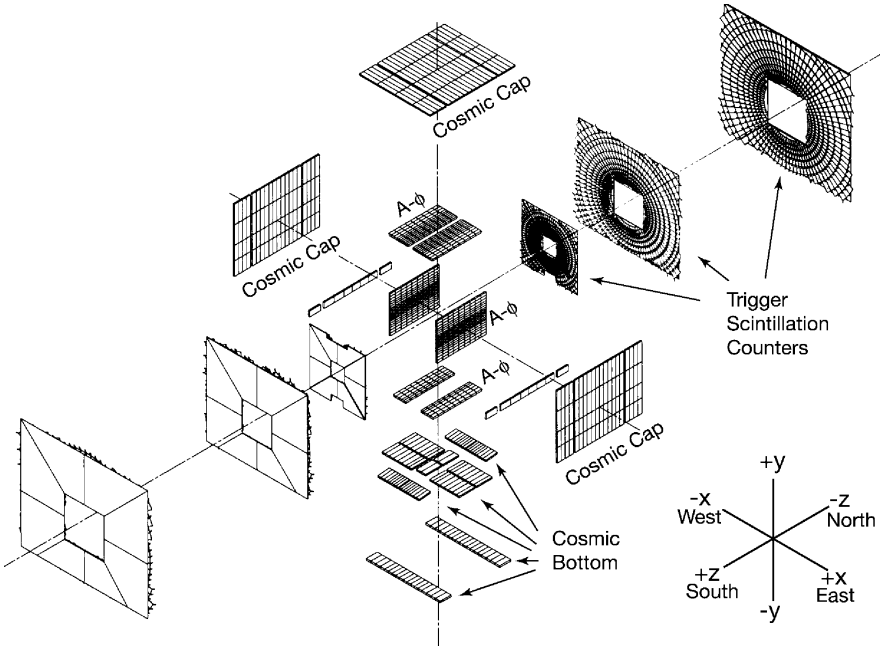

Figure 4.8: DØ muon systems – scintillators.

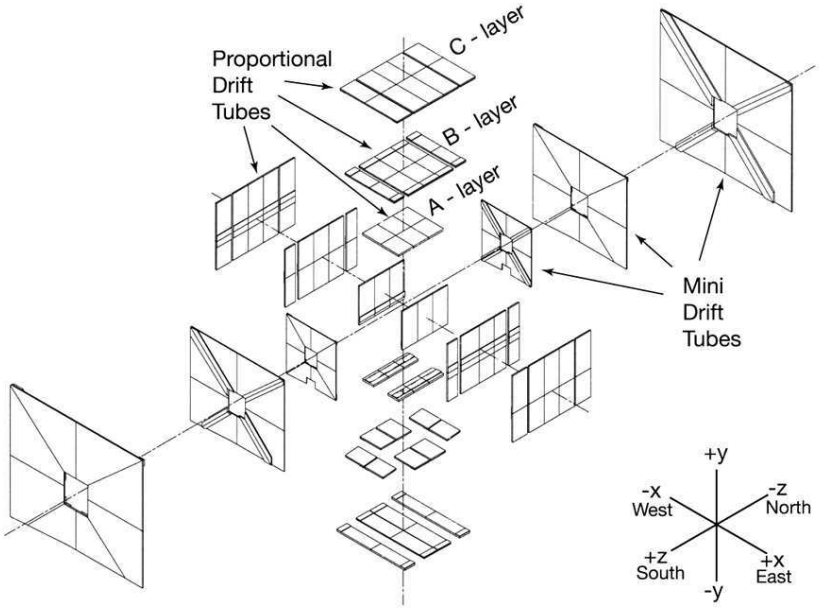

Figure 4.9: DØ muon systems – wire chambers.

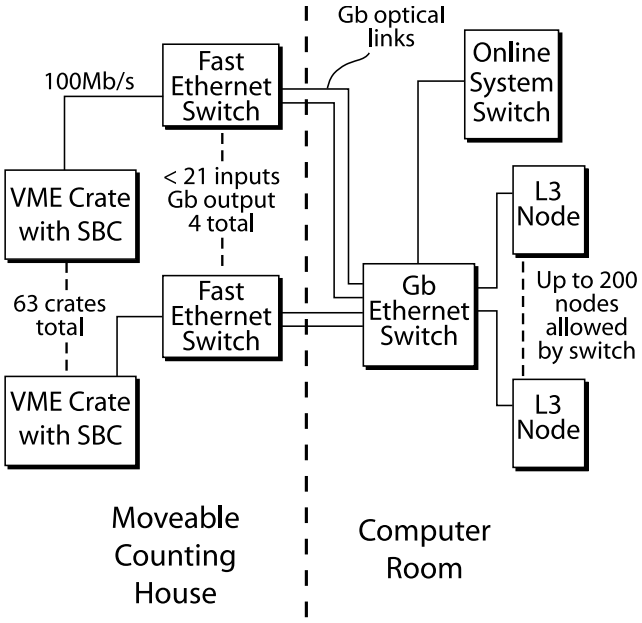

Figure 4.10: DØ DAQ system network configuration.

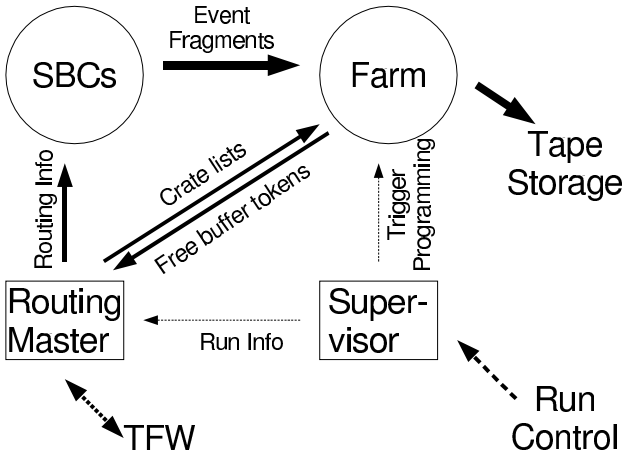

Figure 4.11: DØ DAQ system data flow.

buffers in all crates) or initialisation of the trigger framework. Clients like `taker` can download requested trigger list while `crater` controls what crates should be included in the run. When COOR starts, it reads configuration from a resource file so that to know what crates are available. Significant Events System (SES) monitors the health of the DØ DAQ system (both hardware and software), catching and displaying alarms and important DAQ transitions. The central process is the SES server with helper processes like alarm watcher or alarm display.

Chapter 5

Object Identification

5.1 Primary Vertex

The primary interaction vertex (PV) is selected based on tracks with $p_{\mathrm{T}} > 0.5\,\mathrm{GeV}$ and at least 2 SMT hits. Further criteria include a track distance of closest approach (DCA) to the beam spot, namely the DCA significance $\mathrm{DCA}/\sigma_{\mathrm{DCA}} > 5$ [40]. Several algorithms are combined into an adaptive vertex finding procedure. The hard scatter vertex is selected from the candidates list by minimising the probability that it is only a minimum bias (MB) vertex using MB templates [41].

First, the logarithm of the tracks p_{T} distribution is used to determine whether a track is compatible with a MB track hypothesis upon the assumption that PV tracks have higher p_{T} by constructing the track MB probability as

$$\mathcal{P}(p_{\mathrm{T}}) \equiv \frac{\int_{\log p_{\mathrm{T}}}^{\infty} \mathcal{F}\mathrm{d}\mathcal{F}}{\int_{\log 0.5}^{\infty} \mathcal{F}\mathrm{d}\mathcal{F}}$$

with $\mathcal{F}(p_{\mathrm{T}}) \equiv \log p_{\mathrm{T}}$ being the MB track p_{T} spectrum template. Instead of taking as the MB probability simply the product for track belonging to the vertex

$$\xi \equiv \prod_{k=1}^{N_{\mathrm{trk}}} \mathcal{P}_{MB}^{\mathrm{track}}(k)\,,$$

it is rather a more complex definition which is however independent of the number of tracks N_{trk}:

$$\mathcal{P}_{MB} \equiv \xi \sum_{\mathrm{k}=1}^{N_{\mathrm{trk}}} \frac{(-\log \xi)^k}{k!}\,.$$

5.2 Jet Reconstruction and Identification

5.2.1 Jet Algorithms

Hadronic final states manifest themselves in the detector as showers of particles which are combined by a jet algorithm.

The Run II cone algorithm [42] uses the four-momentum combination scheme to merge objects into jets, based on a metric in the physics rapidity and ϕ. Resulting jets are in general massive.

The right-handed Cartesian coordinate system is used with the positive z axis coinciding with the proton beam direction. Protons are going from the north. The y axis is pointing upwards at $\phi = \pi/2$ measured from the x axis and the azimuthal θ is measured from the positive z axis, $\theta \in \langle 0,\, \pi \rangle$, $\phi \in \langle 0,\, 2\pi \rangle$. Pseudorapidity

$$\eta \equiv -\log \tan \frac{\theta}{2}$$

only approximates the Lorentz invariant rapidity

$$y_{\text{jet}} = \frac{1}{2} \ln \frac{E + p_z}{E - p_z} = \frac{1}{2} \ln \frac{1 + \beta_z}{1 - \beta_z} \,,$$

$$p_z = E \, \frac{e^{2y} - 1}{e^{2y} + 1} = E \tanh y = m \sinh y$$

The four-momentum of a calorimeter cell is defined using the measured cell energy and its direction w.r.t. the primary interaction vertex

$$P_{\text{cell}} \equiv E_{\text{cell}}(1,\, \vec{n}_{\text{cell}}) \,.$$

$$\vec{n}_{\text{cell}} = (\sin\theta \cos\phi,\, \sin\theta \sin\phi,\, \cos\theta) \qquad |\vec{n}_{\text{cell}}| = 1 \,,$$

A calorimeter projective tower consists of cells within a projective direction and with the signal 2.5 σ above the cell noise (pedestal mean value). The associated tower momentum is

$$P_{\text{tower}} = (E_{\text{tower}},\, p_{\text{tower}}) \equiv \sum_{\text{cells}} P_{\text{cell}} \,.$$

Run II uses Improved Legacy Cone Algorithm where an object i is defined to be within a cone C if

$$\sqrt{(y_i - y_C)^2 + (\phi_i - \phi_C)^2} \leq R$$

Finally, jet momentum is defined as

$$P_{\text{jet}} = (E_{\text{jet}},\, p_{\text{jet}}) \equiv \sum_{\text{towers}} P_{\text{tower}}$$

$$p_{\text{T}} \equiv \sqrt{p_x^2 + p_y^2} = |\vec{p}| \sin\theta \,, \qquad |\vec{p}| = p_{\text{T}} \cosh\eta \,.$$

The jet algorithm starts with calorimeter towers as seeds and also adds mid-points between the seeds (to improve the IR-safety) and iteratively combines protojets until a stable cone axis is reached. Then, jets with a large energy share are either split or merged depending on the sharing fraction and the jet axis is recomputed.

A p_{T} cut on the final collection of jets of 6 GeV is applied, in order to remove low-p_{T} jets highly contaminated by noise. This cut performance is affected by the jet resolution, which is very poor in the low-p_{T} region. As the cut is based on uncorrected jet energy while the correction is typically of the order of 1.6 depending on jet energy and its location in the calorimeter, the effect of the cut thus propagates to a higher p_{T} region and additional p_{T} cuts have to be applied at the analysis level, also due to the fact that the effect in data is not fully described by the simulation. See Section 6.12 for details on how the effect is dealt with.

5.2.2 Good Jet Definition

The main problem is to distinguish a real physical jet from an electron, photon, or a cluster of energy in the calorimeter which comes e.g. from uranium/electronics noise.

To define a good jet, several variables are used [43], among them the jet electromagnetic fraction (EMF, fraction of energy in the EM calorimeter) to be typically greater than 0.05 and smaller than 0.95; and coarse hadronic energy fraction (CHF) of a jet not to exceed usually 0.4 (outer calorimeter regions being prone to out-of-cryostat noise). Particular cuts values slightly vary with the jet detector η. For jets in data, a special condition on the ratio of the reconstructed jet energy and of a matched L1 object is also required to be about 0.5 for central jets, with the variable defined as $L1_{\text{ratio}} \equiv \frac{p_{\text{T}}^{\text{L1}}}{p_{\text{T}}^{\text{reco}}(1-\text{CHF})}$ [44].

Having reconstructed calorimeter jets, their energies need to be corrected for imperfect detector response and other various detector and instrumental effects. This procedure, jet energy scale calibration (JES), is described in detail in Chapter 6.

5.2.3 JetID Efficiency

The efficiency of finding a good jet having observed a calorimeter jet is measured using a tag-and-probe method (see reference [JetID]) with a calorimeter jet as a tag of a presumably dijet event, and a recoiling tracking-based jet (track jet), which serves as a probe. An example of such an event is in Figure 5.4.

The idea is that calorimetry and tracking are provided by independent sub-detectors, and so searching for a calorimeter jet close to a well-defined track jet can be used to measure the jet reconstruction efficiency, i.e. how often one observes and reconstructs a jet as a cluster of calorimeter cells when it is expected to have a physical energy deposit in the calorimeter. This way the jet reconstruction efficiency is defined. Having observed a calorimeter-based jet, one can then ask how often it passes good jet criteria, defining the JetID efficiency. Examples of jet reconstruction and identification efficiencies in different η regions are in Figures 5.1-5.2.

Due to differences in the JetID efficiency between the data and simulation, a scale factor is derived for the simulation to match the overall efficiency in data. Examples of the scale factor fitted by a constant in p_{T} for various probe jet η bins are in Figure 5.3.

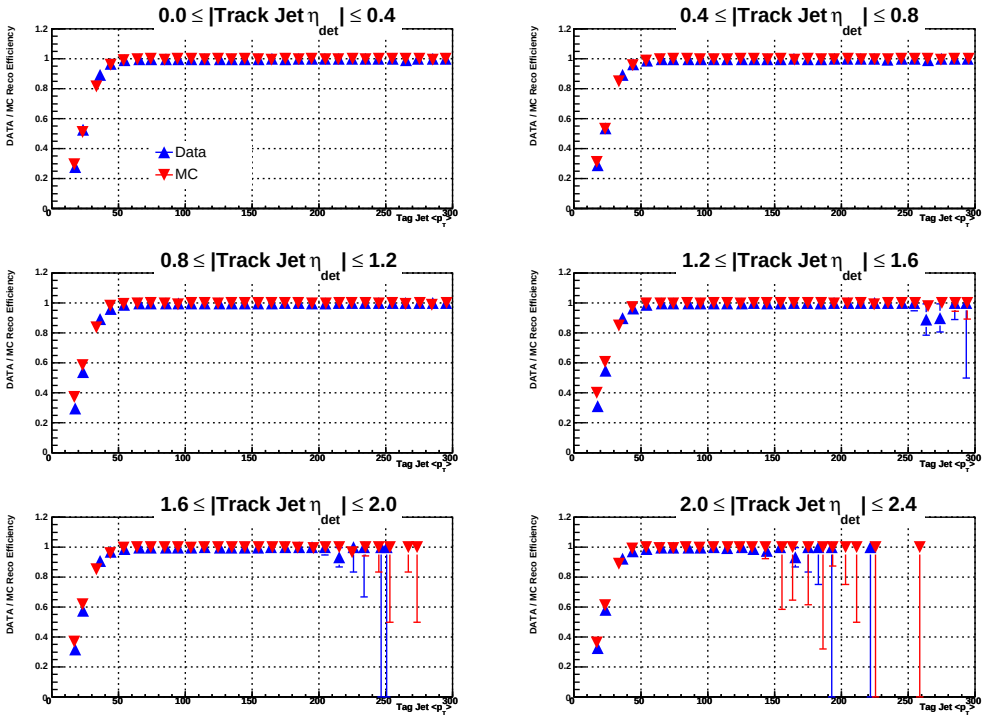

Figure 5.1: Cone 0.5 jets `Reco` efficiency.

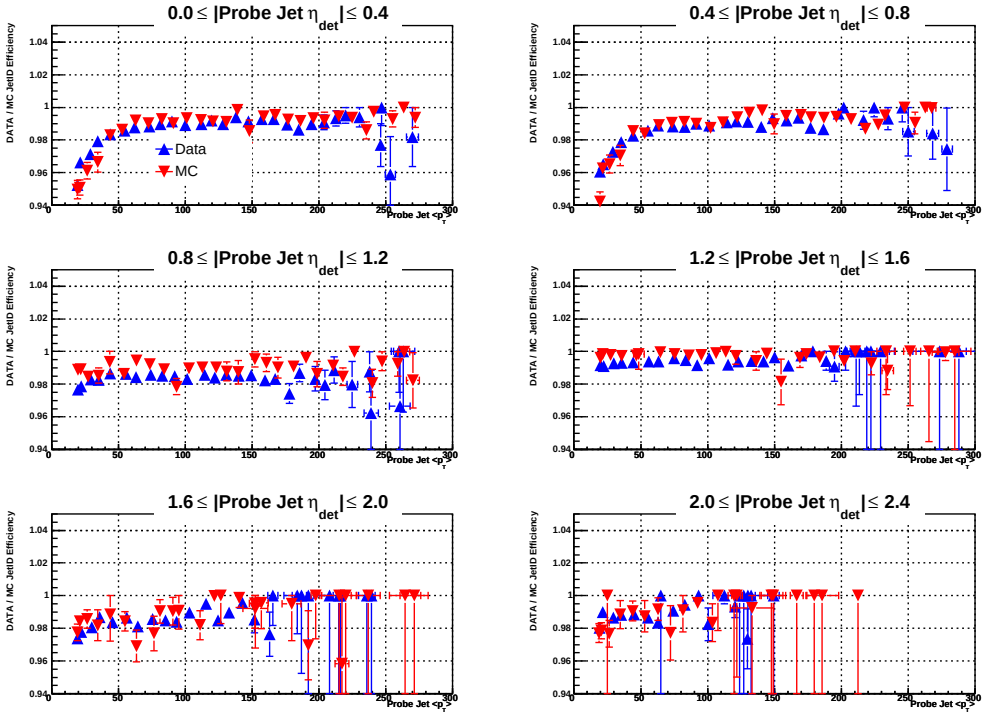

Figure 5.2: Cone 0.5 jets `JetID` efficiency.

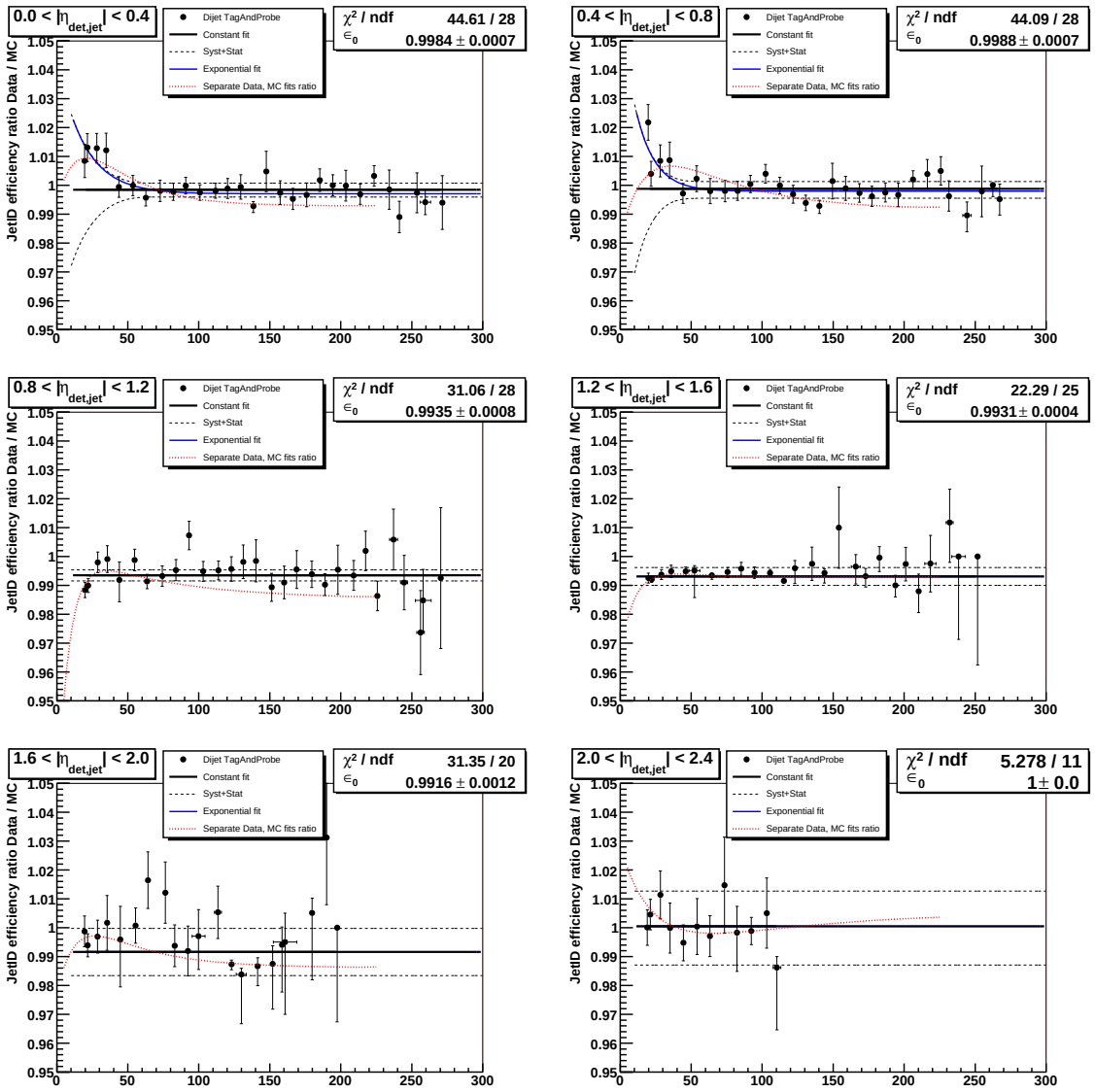

Figure 5.3: Jet ID data/simulation efficiency scale factor.

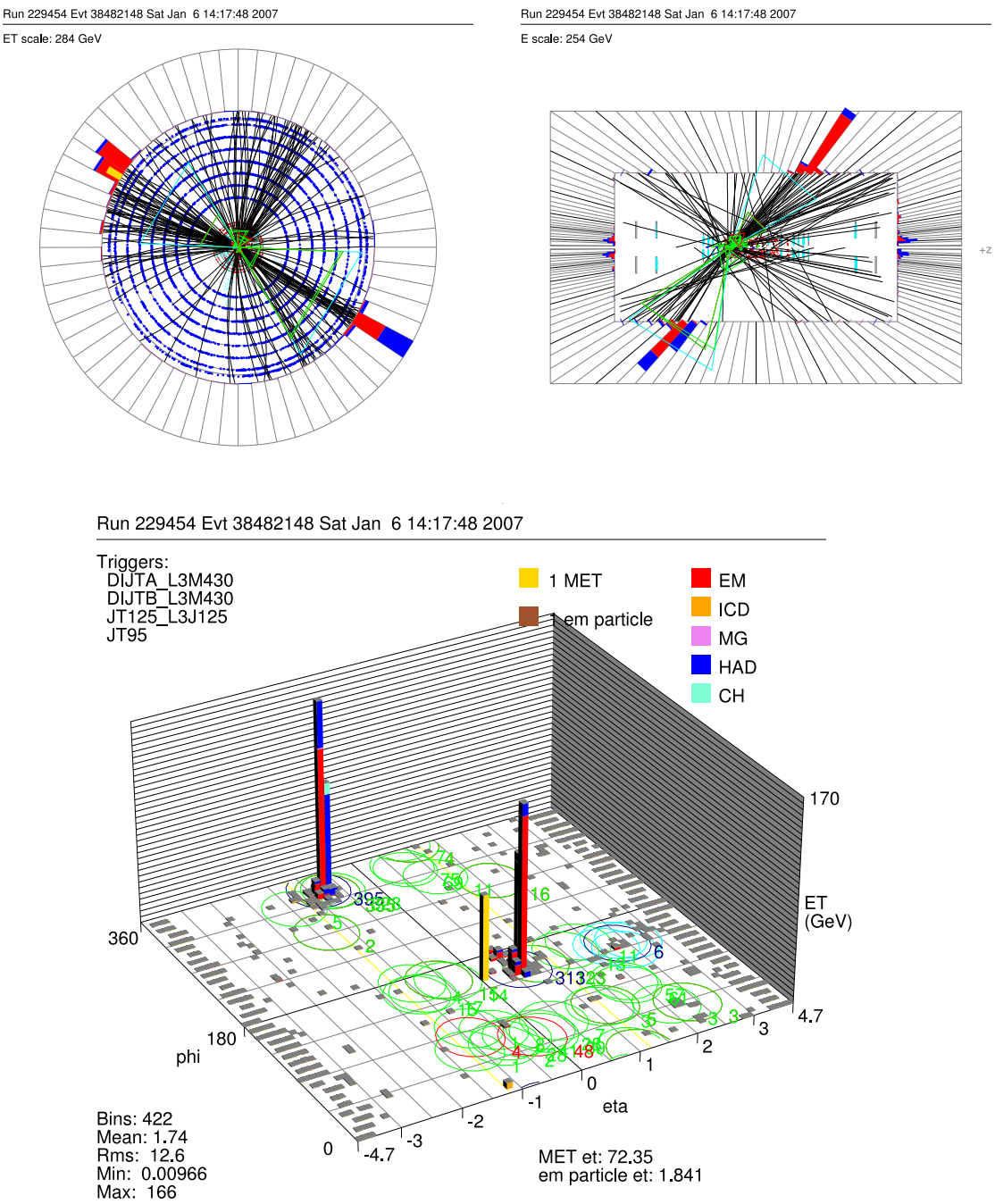

Figure 5.4: An example of a Run IIb dijet event used for the tag-and-probe method for JetID efficiency measurements. Run 229454, Event 38482148. Inst. luminosity: 1.77, Probe emf: 0.867, Probe chf: 0, JES-corrected $p_{\mathrm{T}}^{\mathrm{probe}}$: 354 GeV, Probe η_{det}: 0.641. The probe jet passed the good jet criteria.

5.3 Electron Identification

Electrons are identified as energy clusters mostly in the electromagnetic part of the calorimeter (at least 90 %), with a matched track of $p_{\mathrm{T}} > 5\,\mathrm{GeV}$ as measured by the tracking detector, and whose shower energy profile is consistent with the electromagnetic shower. This is ensured via a cut on the so-called H-matrix variable computed by inverting a 7×7 covariance matrix $\mathcal{H}$ of seven input variables (shower energies in the 4 physical calorimeter depths, shower width in finest third layer, $\log E_{\mathrm{shower}}$ and the logarithm of the primary vertex z position; [46], section B.3) determined in the simulation and applied on the measured shower to construct [47]

$$\mathrm{Hmx7} \equiv (\vec{v}_{\mathrm{meas}} - \vec{v}_{\mathrm{MC}})^T \; \mathcal{H}^{-1} \; (\vec{v}_{\mathrm{meas}} - \vec{v}_{\mathrm{MC}}) \qquad \text{with}$$

$$\mathcal{H}_{ij} \equiv \frac{1}{N} \sum_{n=1}^{N} \left[x_i^{(n)} - \langle x_i^{(n)} \rangle \right] \left[x_j^{(n)} - \langle x_j^{(n)} \rangle \right] , \quad N = 7$$

and requiring the Hmx7 χ^2-like variable to be smaller than 50. A tight electron candidate ([45], section 4.2) is defined by further cuts as follows. A cut on the fraction of energy in the annular region in the calorimeter around the electron axis of $0.2 < R \equiv \sqrt{\Delta\eta^2 + \Delta\phi^2} < 0.4$ is required to be smaller than 15% of the energy in the core $R < 0.2$ (isolation cut). Further, the electron likelihood ([46]) is constructed from several EM-shower and tracking variables based on signal and background templates of variables with small correlation as

$$\mathcal{L}(\vec{x}) \equiv \frac{\mathcal{P}_{\mathrm{sig}}(\vec{x})}{\mathcal{P}_{\mathrm{sig}}(\vec{x}) + \mathcal{P}_{\mathrm{bkg}}(\vec{x})} , \qquad \mathcal{P}_{\mathrm{sig/bkg}}(\vec{x}) \equiv \prod_{k=1}^{N_{\mathrm{vars}}} \mathcal{P}^k_{\mathrm{sig/bkg}}(x_k)$$

and is required to be greater than 0.85 to pass the tight electron definition criterion.

Next, E/p track match is performed by extrapolating each track within 0.5×0.5 in the $\eta \times \phi$ space and matching angularly the EM cluster and the track impact to the EM3 layer of the calorimeter by computing $\chi^2 = (\Delta\phi/\sigma_\phi)^2 + (\Delta z/\sigma_z)^2$ and requiring it to be greater than 0.

The main source of background in the electron identification are jets which fragmented mainly to neutral pions, resulting in deposit mostly in the electromagnetic calorimeter with a matched track; and photons with a fake associated reconstructed track.

5.4 Muon Identification

Several muon definitions are available providing various quality of the muon candidate [48]. In any approach, muons are identified by dedicated three-layer muon chambers outside the calorimeter with the aid if iron-core toroid magnet. Specific timing condition for different layers are applied together with the requirement of the muon being matched to a track in the inner detector. Good muons have to be isolated from jets by at least 0.5 in the $\eta \times \phi$ space (see the metrics defined in electron isolation). A tight muon is tagged when the energy deposited in calorimeter within the annular region of $0.1 < R < 0.4$ contains less than 8% of the muon p_{T} and if momenta of all tracks except for the matched one add up to less than 6% of the reconstructed muon p_{T}.

The main backgrounds come from fake isolated muons coming originally from jets and not the hard process, muons mimicked by high energy jets punching through the

calorimeter system, and cosmic muons, which are however largely reduced by the central track requirement.

Beam-spot position is used to correct muon p_{T} for muons with no hits in the central silicon tracker.

5.5 Missing Transverse Energy

At hadron colliders, the event momentum along the beam axis is usually not known due to arbitrary fractions of parton energies of the original hadron energy (although one can measure quark energy fractions e.g. in dijet events from rapidities of jets). In complex final states, the momentum conservation in the transverse plane one can be used to indirectly identify a signature of a hard neutrino in the event.

The missing transverse energy is computed as the negative vectorial sum of transverse cell energies in the calorimeter above a give threshold ([49]). It needs to be corrected for muons which leave only a minor calorimeter deposit and are fully measured only in muon systems.

Transverse momentum and transverse energy for any object is defined as

$$E_{\mathrm{T}}^{\mathrm{cell}} \equiv E^{\mathrm{cell}} \sin\theta^{\mathrm{cell}} .$$

As a vector in $x-y$ plane, the missing energy is defined as

$$\vec{\not{E}}_{\mathrm{T}} = -\sum_{E_{\mathrm{T}}^{\mathrm{cell}}>0.1\,\mathrm{GeV}} \vec{E}_{\mathrm{T}}^{\mathrm{cell}} ,$$

where $\vec{E}_{\mathrm{T}}^{\mathrm{cell}} \equiv (E_x^{\mathrm{cell}}, E_y^{\mathrm{cell}}, 0) = E_{\mathrm{T}}^{\mathrm{cell}}(\cos\phi^{\mathrm{cell}}, \sin\phi^{\mathrm{cell}}, 0)$.

The missing transverse energy is largely sensitive to noise in the calorimeter, which is significant especially in the outer parts (coarse hadronic, CH) near the cryostat wall. Therefore, missing energy includes the CH cells only when such are part of a reconstructed jet. Further, the missing energy is corrected for additional energy scale factors applied on objects in the event (jets, electrons, muons).

Due to unpolarised beams delivered by the Tevatron accelerator, the missing transverse energy should be symmetrical around the beam axis, any remaining asymmetry coming from uncalibrated detector features and noise.

5.6 b-Jets Identification (Tagging)

Finding a jet which contains (originates from) a b hadron has become a powerful and essential tool in most recent high physics experiments. Heavy-flavour tagger algorithms (b, c) can help to improve signal-to-background ratios provided it is expected that the signal should to be enriched in the heavy flavour. This is exactly the case of top quark physics, where one expects two b-jets in $t\bar{t}$ events.

There are several ways of evaluating the probability that a jet originates from a b quark, based on the decay channel of the resulting B hadron. One of them is soft lepton tagging (SLT) using leptons within the jet coming from semi-leptonic B-decays. More profound are lifetime and secondary-vertex taggers (SVT) analysing the presence of the displaced decay vertex of the B hadron due to its sufficiently long life time of about $c\tau \approx 500\,\mu$m. Such vertex can be reconstructed by the inner silicon detector and its significance and quality can serve as input parameters for several tagging algorithms.

The neural network tagger (NN tagger, [50]) used in this analysis is based on seven input variables as follows:

- Decay length significance of the secondary vertex (SV);
- Weighted combination of the tracks' impact parameter significances;
- Probability that the jet originates from the primary vertex (PV);
- χ^2 per degree of freedom of the SV; Number of SV found in the jet.
- Number of tracks used to reconstruct the SV; Mass of the SV;

Several operation points defined by different cuts on the NN output variable are supported and provided with tagging efficiency and the fake rate. This analysis makes use of the medium operation point (NNm) corresponding to the NN cut of 0.65. This still provides the analyser with excellent b-tagging efficiency of more than 60% in most of the kinematical range. The efficiency to tag a c jet is about 15% and for the medium (12% for the tight operation point), and fake rates (tagging a light jet) are below 2%.

5.6.1 Taggability

To disentangle instrumentation (e.g. tracking inefficiency) effects from the tagger algorithm performance, the tagging efficiency is measured on jets which are marked as taggable.

Jet is called taggable if it is a good jet with $p_{\mathrm{T}} > 15\,\mathrm{GeV}$ and within the pseudorapidity region of $|\eta| < 2.5$, and if it matches a track-based jet with the following properties: [51]

- It has at least two tracks with at least one hit in the SMT sub-detector.
- At least one track with $p_{\mathrm{T}} > 1\,\mathrm{GeV}$, other with $p_{\mathrm{T}} > 0.5\,\mathrm{GeV}$.
- $|r_{xy} - \mathrm{DCA}| < 0.2\,\mathrm{cm}$, $|z - \mathrm{DCA}| < 0.4\,\mathrm{cm}$.

where DCA is the distance of closest approach of a track to the primary interaction vertex (PV).

The important thing is that taggability may also depend on the physics sample, whereas tagging efficiency should not, therefore the b-tagging efficiency is measured only for taggable jets.

5.6.2 Tagging the Simulation

As the b-tagging efficiency in the data is not described well by the simulation (being higher in the latter), the simulation in this analysis has been tagged using data-based parametrisations of the tagging efficiency (so-called tag-rate functions, TRF's). The flavour of the simulation jet is determined by an angular matching to heavy flavour mesons, an appropriate TRF is selected (b, c or light flavour) and jet is tagged randomly according to the TRF evaluated at given jet p_{T} and η. The shape of the TRF's for b, c and light jets are in Figure 5.5.

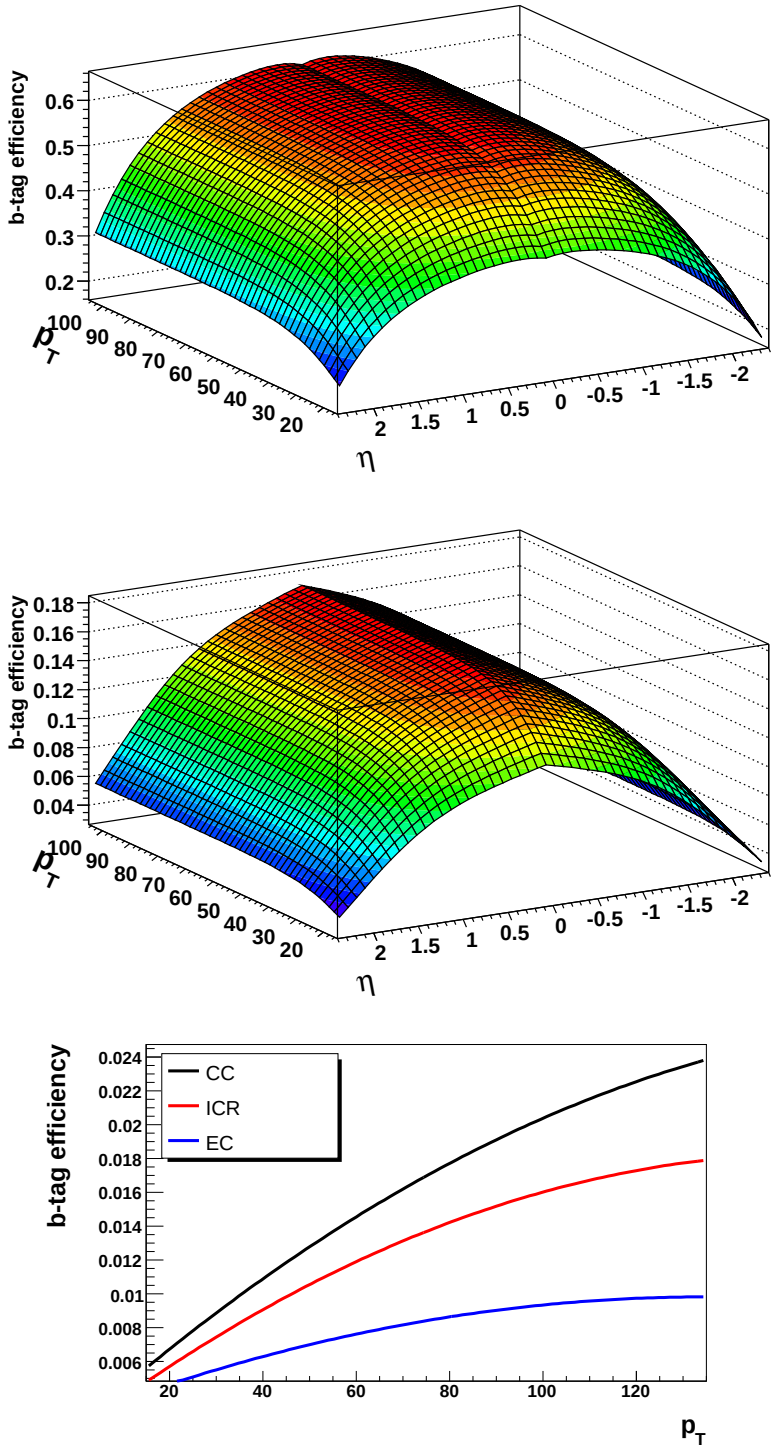

Figure 5.5: DØ's certified tag rate functions (parametrised tagging efficiencies) for b (top), c (middle) and light (bottom) jets extracted from data b-tagging efficiencies and applied to the simulation in order to reproduce the correct average tagging rate as in data.

5.7 The Underlying Event

Underlying event (UE) is defined as all processes not directly related to the hard scatter process. This includes the soft UE part related to hadron remnants, as well as a possible hard component coming from multiple parton interactions (MPI).

Due to the high luminosity and high bunch densities, several hadron-hadron interactions may occur during a single bunch crossing. Such situation is called multiple interactions (MI) and can be experimentally observed as several primary interaction vertices.

At the DØ, pile-up is a term describing signal in the detector coming from the previous collision (e.g. charge flow in the calorimeter due to finite drift time of electrons in the liquid argon). This, together with the noise, contributes to the total readout signal.

Chapter 6

Jet Energy Scale

The aim of the jet energy scale procedure [p17JES] is to calibrate observed calorimeter jet energies as close as possible to the particle level, i.e. before entering the detector. This can be only performed on average and is a subject to uncertainties, as already is the measured (fluctuated) jet energy in the calorimeter.

Due to an imperfect detector simulation as well as effects in instrumentation which are not fully understood or described, jet energy scale at the DØ is measured separately for data and simulation on special physics samples.

The two Run II jet algorithms of cone sizes $\mathcal{R} = 0.7$ and $\mathcal{R} = 0.5$ were calibrated individually. Most physics analyses use smaller cone sizes, although most QCD analyses make use of the larger cone. As cone 0.7 jets are expected to have better resolution they are a possible area of improvement for single top searches.

The importance of the jet energy scale for this analysis is obvious realising that in the $t\bar{t} \to \ell$+jets final state one expects two light-quark jets from the hadronic decay of one of the W bosons, two b-jets from the weak top quark decays and possible additional jets from initial and final state radiation or multiple interactions. The precision calibration of jet energies directly translates to the resolution of combined quantities like the $t\bar{t}$ system mass or top quark transverse momentum.

6.1 Overview

The basic idea is to correct consistently and step-by-step the measured raw jet energy to the particle jet level using a sub-corrections factorisation which in its basic form can be written as

$$E_{\text{jet}} = \frac{E_{\text{raw}} - \mathcal{O}}{\mathcal{R}_{\text{jet}}\,\mathcal{S}}\,.$$

Here Offset $\mathcal{O}$ stands for the energy in the jet originating from noise, pile-up and multiple interactions, $\mathcal{R}_{\text{jet}}$ denotes the detector energy response to the jet and showering $\mathcal{S}$ corrects for the energy of particles leaving and entering the original jet cone.

In practice, corrections are derived sequentially on top of each other in order to avoid possible interference. As will be shown later, this formula is still an approximation, as interplay between corrections as well as further subtle effects lead to the realisation that these are only estimations of each true sub-correction due to biases introduced by methods of their determination. Estimated corrections are therefore denoted with a hat $\hat{\mathcal{O}}$, $\hat{\mathcal{R}}_{\text{jet}}$ in an approximate formula for the particle jet energy

$$\hat{E}_{\text{jet}} = \frac{E_{\text{raw}} - \hat{\mathcal{O}}}{\hat{\mathcal{R}}_{\text{jet}}\,\hat{\mathcal{S}}}\,.$$

Corrections estimates will later be brought to their true unbiased values $\mathcal{O}$, $\mathcal{R}_{\text{true}}$ as described in following subsections.

6.2 Jet Offset

Offset is the part of the jet energy which is coming from different processes leaving energy deposit in the same calorimeter region as the reconstructed jet. In order to further properly correct the raw jet energy, such offset needs to be subtracted.

Offset has been measured on two data samples described below. Data triggered by the Minimum Bias Trigger (MB), where the Luminosity Monitors are required to fire, is used to determine the energy from random additional $p\bar{p}$ interactions. Data triggered by the Zero Bias Trigger is defined by a simple fire of the bunch-crossing signal. For the Offset measurement, Zero Bias Trigger events with the Luminosity Monitor Veto have been used to determine the contribution to the calorimeter energy density without the presence of a collision.

The offset energy can be decomposed into several contributions according to the origin of the energy deposit. The underlying event (UE) is the energy coming from physics objects not associated with the hard process (both soft and hard, i.e. beam remnants as well as contributions from color-flow connections).

Noise and Pile-up (NP) is the energy coming from the uranium and electronics noise and from signals in the readout still present from previous bunch crossings. Multiple Interaction (MI) contribution is the energy density coming from additional $p\bar{p}$ crossings which could accompany the main hard scatter process.

Offset energy is a function of luminosity, which reflects approximately linearly in the number of reconstructed primary vertices in the event. Starting with an event with one primary vertex, the offset contribution can be written as

$$\text{Offset}(1\text{PV}) = \text{MB}(1\text{PV})\,,$$

$$\text{Offset}(1\text{PV}) = \underbrace{\text{MB}(1\text{PV}) - \text{ZB}(0\text{PV})}_{\text{UE}} + \underbrace{\text{ZB}(0\text{PV})}_{\text{NP}}\,.$$

For two primary vertices one gets

$$\text{Offset}(2\text{PV}) = \text{MB}(1) - \text{ZB}(0) + \text{ZB}(0) + \text{MB}(2) - \text{MB}(1) = \text{UE} + \text{NP} + \text{MI}(1)\,,$$

so in general

$$\text{Offset}(n\text{PV}) = \text{MB}(1) - \text{ZB}(0) + \text{ZB}(0) + \text{MB}(n\text{PV}) - \text{MB}(1) = \text{UE} + \text{NP} + \text{MI}(n\text{PV} - 1)\,.$$

The contribution from the Underlying Event is not attempted to be corrected for as it depends on flavour content and thus the individual physics channel under consideration.

6.3 Suppression Effect on Offset

Due to the uranium and electronics noise in the calorimeter signal, not all cells are used for the reconstruction of physical objects. Without colliding beams, mean values and widths of each channel are measured and these are then used in physics data taking to be subtracted from the read-out signal. Then the suppression takes place: only cells with their signal in the regions $> \mu + n\sigma$ or $< \mu - n\sigma$ are considered. Offset energy has

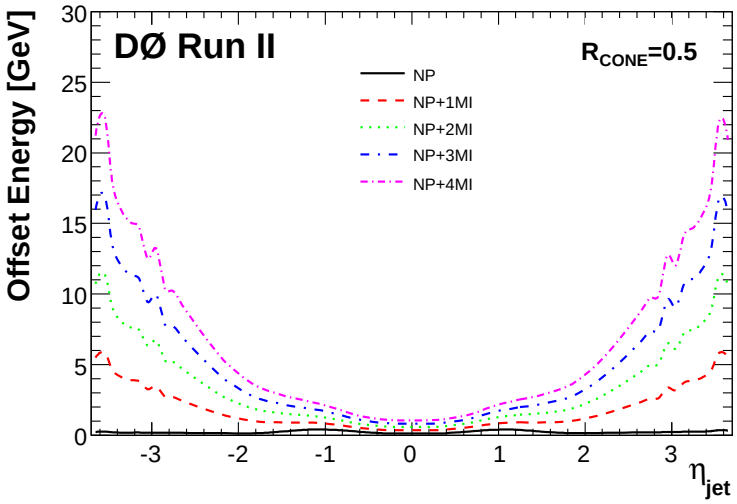

Figure 6.1: Jet offset energy as a function of the detector projective pseudorapidity for $\mathcal{R}_{\text{cone}} = 0.5$ jets; shown are the contributions from noise and pileup (NP) and for various number of multiple interactions of $p\bar{p}$ (MI). Plot taken from [p17JES].

been measured on special ZB and MB triggered data, and such sample is biased towards lower activity in the calorimeter. In a busy physics event containing jets, many cells receive contributions from both the noise and physical signal, and thus some cells which would not have been read out in less busy ZB or MB are read out in the jet environment, being effectively triggered by the additional physics content. Resulting tower and jet energies contain different amounts of the contribution from noise than were previously estimated in offset $\hat{\mathcal{O}}$. Therefore, one has to correct for this suppression effect, either the offset itself, or directly the original offset-subtracted ZB-overlaid energy $E_{\text{ZB}} - \hat{\mathcal{O}}$ to the no-overlay (noZB) level defining the correction factor

$$k_{\mathcal{O}} \equiv \frac{\langle E_{\text{noZB}} \rangle}{\langle E_{\text{ZB}} - \hat{\mathcal{O}} \rangle} \,.$$

Note that E_{noZB} contains the visible energy of particle from both inside and outside the original particle jet cone, but in contrast to E_{ZB} does not contain the energy from noise, pile up or multiple interactions. Therefore, E_{noZB} still needs further corrections for physics particles showering as well as for the detector response.

The $k_{\mathcal{O}}$ correction factor can be determined in a dedicated simulation study employing the same generated γ+jet events once reconstructed with the overlay and once without in. To minimise the matching ambiguity, exactly one jet is required in the noZB sample, and best match in $\Delta\mathcal{R}$ to a jet from the same generator event in the ZB sample is sought. Thus two matchings take place: event-event and jet-jet. Furthermore, a $\Delta\phi$ cut between the jet and photon of 3.0 is required as in the Response measurement.

The size of the correction depends on energy, studied jet η and the jet cone size (see Figure 6.2 for illustration). Furthermore, it has to be derived separately for data and simulation, due to the fact that additional interactions in the simulation have been simulated by overlaying already suppressed ZB events from data, whereas what happens in reality for data is that the total signal is deposited in calorimeter and only

than is suppressed. Therefore, although the offset correction is the same for data and simulation, the suppression effect correction is different.

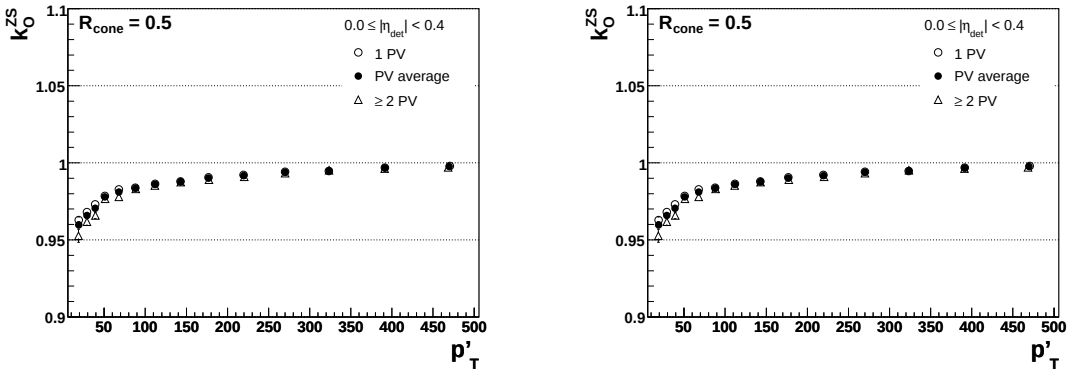

Figure 6.2: Example of a suppression effect correction factor for Offset.

6.4 The MPF Method

A general procedure using a well-measured tag object in terms of energy and the missing transverse energy can be used to calibrate a probe object energy scale. The method is called a missing E_{T} projection fraction method (MPF), and is based on the transverse plane momentum balance. The model case are events with a photon accompanied with a jet, Z+jet events or dijet production.

In each case, a tag object is selected (photon, reconstructed Z or a well-measured central jet) and probe jet energy can be inferred from the following algebra.

Ideally, neglecting intrinsic parton transverse momenta, objects in an event should be balanced in the transverse momentum:

$$\vec{p}_{\mathrm{T}}^{\,\mathrm{tag}} + \vec{p}_{\mathrm{T}}^{\,\mathrm{probe}} = 0\,.$$

In reality, both objects have detector responses to their energies different from 1, resulting in nonzero observed energy imbalance in the transverse plane:

$$\mathcal{R}_{\mathrm{tag}}\,\vec{p}_{\mathrm{T}}^{\,\mathrm{tag}} + \mathcal{R}_{\mathrm{probe}}\,\vec{p}_{\mathrm{T}}^{\,\mathrm{probe}} + \vec{\not{E}}_{\mathrm{T}} = 0\,.$$

Assuming already calibrated energy scale of the tag object ($\mathcal{R}_{\mathrm{tag}} = 1.$) and performing a dot product with the tag transverse momentum, one gets the relation

$$(\vec{p}_{\mathrm{T}}^{\,\mathrm{tag}})^2 + \mathcal{R}_{\mathrm{probe}}\,\vec{p}_{\mathrm{T}}^{\,\mathrm{probe}} \cdot \vec{p}_{\mathrm{T}}^{\,\mathrm{tag}} + \vec{\not{E}}_{\mathrm{T}} \cdot \vec{p}_{\mathrm{T}}^{\,\mathrm{tag}} = 0\,,$$

into which one can plug the ideal balance formula 6.4 arriving at the master MPF formula for the probe object response

$$\mathcal{R}_{\mathrm{probe}} = 1 + \frac{\vec{\not{E}}_{\mathrm{T}} \cdot \vec{p}_{\mathrm{T}}^{\,\mathrm{tag}}}{(\vec{p}_{\mathrm{T}}^{\,\mathrm{tag}})^2}\,.$$

The advantage of this approach is that one only needs the well-measured tag object momentum and the missing transverse energy in the event, no information on the tag object is needed as all the imbalance is transferred into the $\vec{\not{E}}_{\mathrm{T}}$ observable.

6.5 Jet Response

Jet response is measured using the MPF method in γ+jet events (see Figure 6.3), where the photon is absorbed in the electromagnetic part of the calorimeter, and its energy and momentum is thus well-known. The recoiling system should be well-balanced on average with respect to the photon in terms of the transverse momentum.

The event selection closely follows this idea, requiring exactly one jet and one photon back-to-back to each other as realised by a cut on their $\Delta\phi$ of 3.0 (approximately $180 \pm 8°$).

As the amount of activity in the event depends strongly on the observed number of primary vertices (primary interactions), response measurement is restricted only to 1 or 2 such vertices in the event. This ensures lower instantaneous luminosity sample as well as cleaner events with a healthy interpretation of the missing transverse energy to be due to the uncorrected jet energy (response on average smaller then 1).

Response is an approximate logarithmic function of the jet energy, but it would be inconvenient to bin it in such a variable with a poor resolution. Instead, response is measured as a function of the energy estimator $E' \equiv p_{\mathrm{T}}^{\gamma} \cosh \eta_{\mathrm{jet}}$, which combines a well-measured photon transverse momentum and sufficiently stable jet pseudorapidity.

Simultaneously with response itself, average jet energy in each E' bin is measured and the mapping $\mathcal{R}(E') \to \mathcal{R}(E_{\mathrm{jet}})$ is performed. Response is measured for central jets and in given higher rapidity bin is expressed as a product of the central response and an η-correction factor as $\mathcal{R}_{\eta} \equiv \mathcal{R}_{\mathrm{CC}} \mathcal{F}_{\eta}$, the $\mathcal{F}_{\eta}$ factor being obtained by a complex global fit of the relative jet response in given η w.r.t. the central response. Jet response as measured in impure γ+jet events is also corrected for the background contamination.

6.5.1 The MPF Bias Correction

It is important to keep in mind that it is not exactly the jet response which is being measured by the MPF method. Actually, it is the response of the whole hadronic system recoiling with respect to the photon, while the desired response is that of the particle jet, i.e. the visible calorimeter energy of particles from the particle jet. Although requiring the back-to-backness of the two objects, one is still left with topological biases of the MPF method.

A dedicated simulation-based study comparing particle-deposited and original particle jet energies can account for this bias and correct for it, thus leading to a new factor

$$k_{\mathrm{topo}} \equiv \frac{\mathcal{R}_{\mathrm{true}}}{\mathcal{R}^{\mathrm{noZB}}_{\mathrm{MPF},\,\eta}}\,, \qquad \text{with} \qquad \mathcal{R}_{\mathrm{true}} \equiv \frac{E^{\mathrm{visible}}_{\mathrm{ptcl}}}{E_{\mathrm{ptcl}}}$$

being the true particle jet response.
This leads to the jet energy correction formula

$$E^{\mathrm{corr}}_{\mathrm{jet}} = \frac{E_{\mathrm{raw}} - \hat{\mathcal{O}}}{R^{\mathrm{MPF}}_{\mathrm{CC}}\, \mathcal{F}_{\eta}\, k_{\mathrm{topo}}\, \mathcal{S}}\,.$$

6.6 Suppression Effect on Response

Similarly to Offset, there is an effect of the suppression procedure on the response measurement. Consequently, the measured response is not equivalent to the ideal one in the non-overlaid sample. Again, one can correct for the effect by measuring the ratio of responses in the same generator events once in ZB-overlaid and non-overlaid

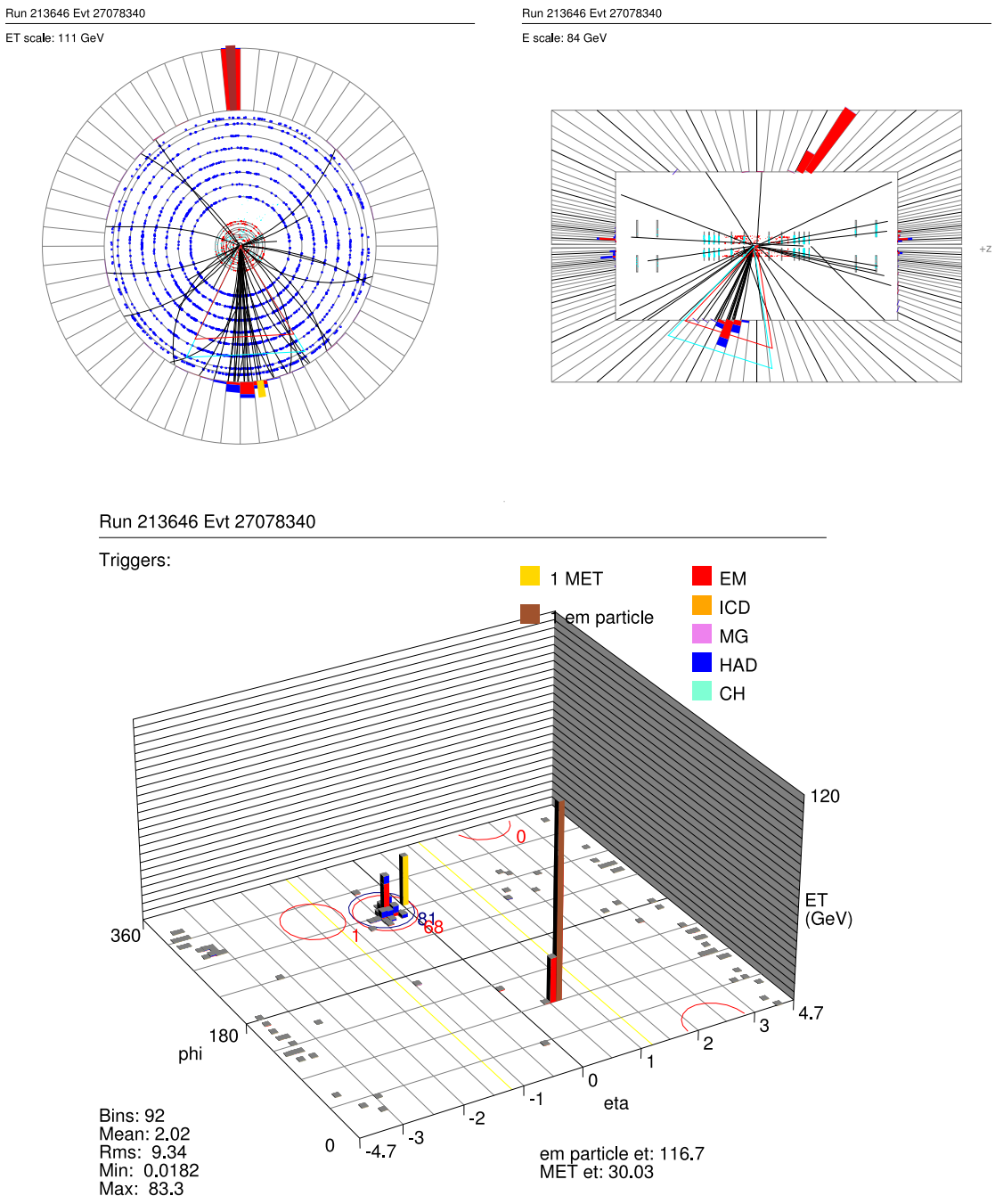

Figure 6.3: An example of a γ+jet event used for data JES derivation, as seen by the DØ detector. A cluster of electromagnetic-calorimeter energy deposit back-to-back to tracks pointing to a hadronic recoil.

reconstructed paths, defining the correction factor as a ratio of averages as one needs to correct the response on average to the noZB level

$$k_{\mathcal{R}} \equiv \frac{\langle \mathcal{R}^{\mathrm{MPF}}_{\mathrm{noZB}} \rangle}{\langle \mathcal{R}^{\mathrm{MPF}}_{\mathrm{ZB}} \rangle} \,.$$

The correction magnitude and shape is illustrated in Figure 6.4.

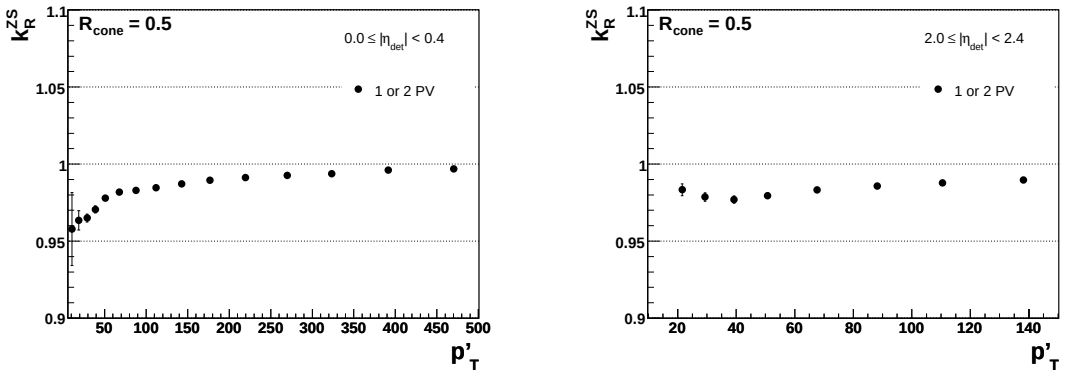

Figure 6.4: An example of the suppression effect correction factor for the jet response.

6.7 Total Suppression Effect

Both $k_{\mathcal{O}}$ and $k_{\mathcal{R}}$ correction factors have been in reality fitted together as a ratio and are being applied as one total correction for the suppression effect, $k_{\mathcal{O}}/k_{\mathcal{R}}$, as illustrated in Figure 6.5.

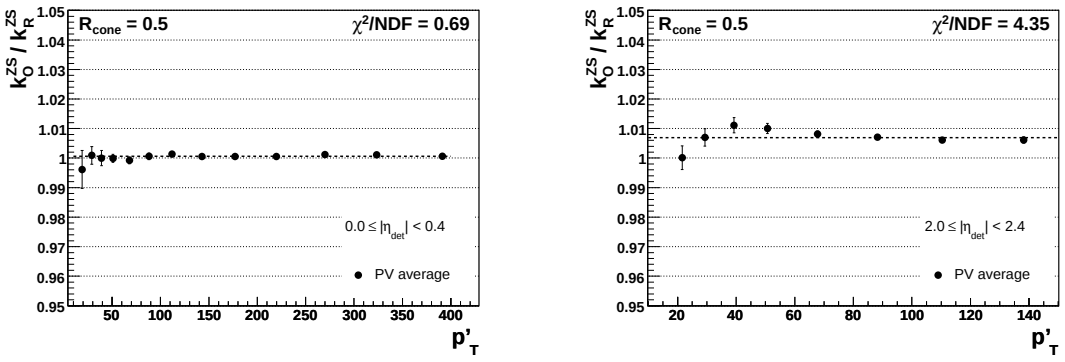

Figure 6.5: An example of the suppression effect correction factor for Offset and Response.

6.8 The Showering Correction

The showering corrections accounts for the fact that particles migrate both from and into the reconstructed (calorimeter) jet cone. For the simulation, showering can be

directly studied by comparing particles energy deposits and the particle jet energy for γ+jets events without the ZB overlay. For data, the showering correction is first estimated by examining jet energy profiles (the energy distribution around the jet axis) by fitting the jet profile using templates of two distinct contributions of different origin: particle-jet (from particles within the particle jet) and non-particle-jet (from underlying event as well as from large angle gluon evolution). The data-based showering is then corrected for the bias of the method using the simulation, where the direct and template-based methods give very close results. The truth showering is thus a ratio of observed particles energies within the calorimeter cone (from both in and out-of-particle-jet-cone contributions) and the total visible particle jet energy

$$\mathcal{S} \equiv \frac{E^{\rm raw}_{\rm noZB}}{E^{\rm visible}_{\rm ptcl}} \,,$$

where $E^{\rm raw}_{\rm noZB}$ contains the visible energy of particles which have reached the calorimeter jet cone from either inside or outside the particle jet cone.

6.9 The Full JES Formula

The final JES formula based on techniques developped for the first time starting with the $1\,{\rm fb}^{-1}$ DØ data sample including all sub-corrections then reads

$$E_{\rm corr} \equiv \frac{E^{\rm raw} - \hat{\mathcal{O}}}{\mathcal{F}_\eta \, k_{\rm topo} \, \hat{\mathcal{R}}_{\rm CC} \; \hat{\mathcal{S}}} \, \frac{k_{\mathcal{O}}}{k_{\mathcal{R}}}$$

and in the fullest form

$$E_{\rm corr} \equiv \frac{E^{\rm raw}_{\rm ZB} - \hat{\mathcal{O}}}{\frac{\mathcal{R}^{\rm ZB}_{{\rm MPF},\eta}}{\mathcal{R}^{\rm CC}_{\rm MPF}} \cdot \frac{\mathcal{R}_{\rm true}}{\mathcal{R}^{\rm noZB}_{{\rm MPF},\eta}} \cdot \mathcal{R}^{\rm CC}_{\rm MPF} \cdot \frac{E^{\rm raw}_{\rm noZB}}{E^{\rm visible}_{\rm ptcl}}} \cdot \frac{\frac{E^{\rm raw}_{\rm noZB}}{E^{\rm raw}_{\rm ZB} - \hat{\mathcal{O}}}}{\frac{\mathcal{R}^{\rm noZB}_{{\rm MPF},\eta}}{\mathcal{R}^{\rm ZB}_{{\rm MPF},\eta}}} = E_{\rm ptcl} \,,$$

truly brings the corrected jet energy to the particle level.

6.9.1 Full Four-momentum Correction

As jets in the Run II jet algorithm have nonzero masses, it is nontrivial to translate the energy correction to the full momentum calibration. In fact, there are more effects like a rapidity bias – the systematical shift of the (pseudo)rapidity of the reconstructed jet with respect to the particle jet, which also have to be corrected for. The procedure described above aims primarily the jet energy calibration, although at various stages the $p_{\rm T}$ balance of objects in the event is employed. The main idea is to correct the energy to the particle jet level, and all corrections are tailored to bring the reconstructed jet energy there in several steps. Dedicatedly to QCD-oriented analyses, special corrections addressing also the specific flavour composition and η-bias were also studied.

6.10 Closure Tests

The purpose of closure tests is to verify the Jet Energy Scale calibration procedure and its performance on a specific physics sample. As a first step, this is the γ+jets same sample most of the JES corrections were derived on.

6.10.1 Direct Closure Tests on the Simulation

The master closure test is the comparison of the simulation reconstructed jet energy to the energy of a matched particle jet. Matching is performed using a metric in $\eta \times \phi$

$$\Delta\mathcal{R} = \sqrt{\Delta\phi^2 + \Delta\eta^2}$$

and imposing the matching cut of $\mathcal{R}_{\rm cone}/2$. This test can be obviously performed only in the simulation, and resulting Direct closure variable

$$\mathcal{D} = \frac{E_{\rm corr}}{E_{\rm ptcl}}$$

is binned in terms of E', $p_{\rm T}^{\gamma}$. There is a subtlety in the means of averaging over events. One can average the whole ratio, or one can average the numerator and denominator separately:

$$\mathcal{D} = \left\langle \frac{E_{\rm corr}}{E_{\rm ptcl}} \right\rangle \qquad \text{or} \qquad \mathcal{D} = \frac{\langle E_{\rm corr}\rangle}{\langle E_{\rm ptcl}\rangle}\,.$$

Due to a finite resolution, the two definitions do not return the same result especially at low $p_{\rm T}$'s due to poor resolution. The appropriate choice of the averaging scheme has to follow the way JES corrections were derived and what variable one expects to close. As the JES procedure has been designed to correct the reconstructed jet energy to the particle jet energy on average, i.e. to $\langle E_{\rm ptcl}\rangle$, the second scheme is being used and the closure performance is illustrated in Figure 6.6.

The explanation for the difference between the two schemes is as follows. Let $E_{\rm corr}$ be the JES-corrected reconstructed jet energy and $E_{\rm ptcl}$ the particle jet energy one ideally corrects to. Let x and y be the random variables describing the fluctuations on corrected reconstructed and particle levels respectively, so that $\langle x\rangle = 0$, $\langle y\rangle = 0$.

What one would naïvely study in the Direct Closure on MC, is the simple event-by-event average testing the closeness of the corrected level to the particle level by filling an histogram with

$$\begin{aligned}
\left\langle \frac{E_{\rm corr}}{E_{\rm ptcl}} \right\rangle &= \left\langle \frac{\langle E_{\rm corr}\rangle + x}{\langle E_{\rm ptcl}\rangle + y} \right\rangle = \left\langle \frac{\langle E_{\rm corr}\rangle + x}{\langle E_{\rm ptcl}\rangle[1 + y/\langle E_{\rm ptcl}\rangle]} \right\rangle \\
&\approx \left\langle \frac{\langle E_{\rm corr}\rangle + x}{\langle E_{\rm ptcl}\rangle}[1 - y/\langle E_{\rm ptcl}\rangle] \right\rangle \\
&= \frac{\langle E_{\rm corr}\rangle}{\langle E_{\rm ptcl}\rangle} - \left\langle \frac{[\langle E_{\rm corr}\rangle + x]\cdot y}{\langle E_{\rm ptcl}\rangle^2} \right\rangle \\
&= \frac{\langle E_{\rm corr}\rangle}{\langle E_{\rm ptcl}\rangle} - \frac{\langle x\cdot y\rangle}{\langle E_{\rm ptcl}\rangle^2}
\end{aligned}$$

Although x and y are random fluctuations, they are not uncorrelated, as fluctuations in energy in particle level and reconstructed (and JES corrected level) are not independent (e.g. the underlying event is common). So in general, $\langle x\cdot y\rangle \neq 0$ and therefore

$$\left\langle \frac{E_{\rm corr}}{E_{\rm ptcl}} \right\rangle \neq \frac{\langle E_{\rm corr}\rangle}{\langle E_{\rm ptcl}\rangle}\,.$$

The point is that what one aims is to correct from $\langle E_{\rm corr}\rangle$ to $\langle E_{\rm ptcl}\rangle$, i.e. on average, so the proper least biased closure test is using the variable $\langle E_{\rm corr}\rangle/\langle E_{\rm ptcl}\rangle$.

6.10.2 Data Closure Tests

To test the JES closure on data, average jet energy as a function of the energy estimator E' was measured for data and a mixture of signal and dijet background simulation samples (combined using a data-based purity) and divided so that the data closure could be compared to the simulation closure, which was already tested using the direct test. Example plots of the data closure are in Figure 6.7, being consistent with unity withing the claimed JES uncertainties.

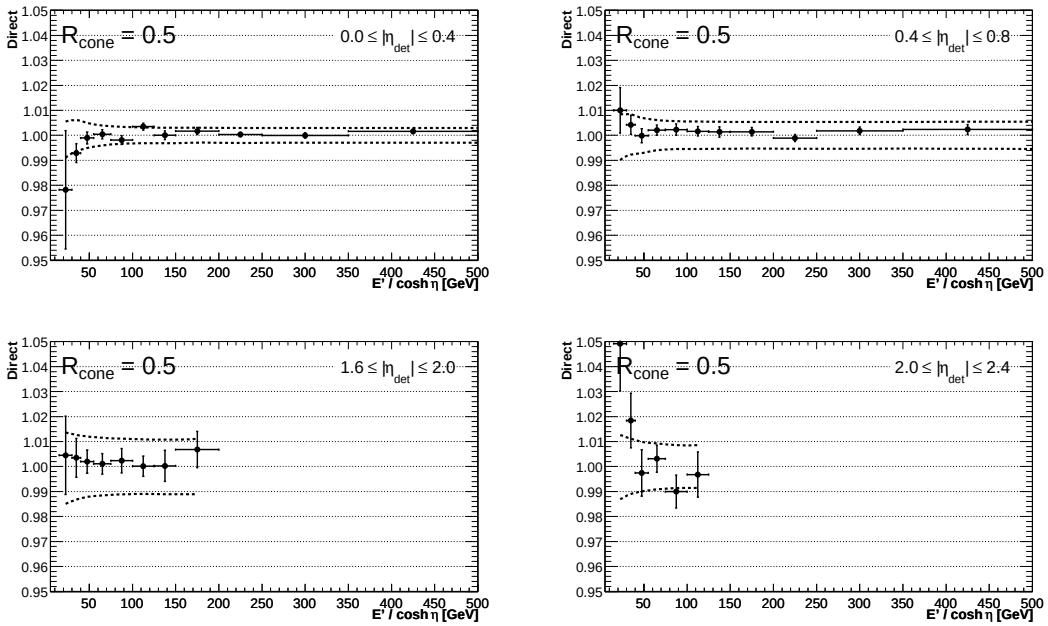

Figure 6.6: Direct closure tests for $\mathcal{R} = 0.5$ jets in the simulation as a function of p'_{T} in different η bins, with photon p_T cuts.

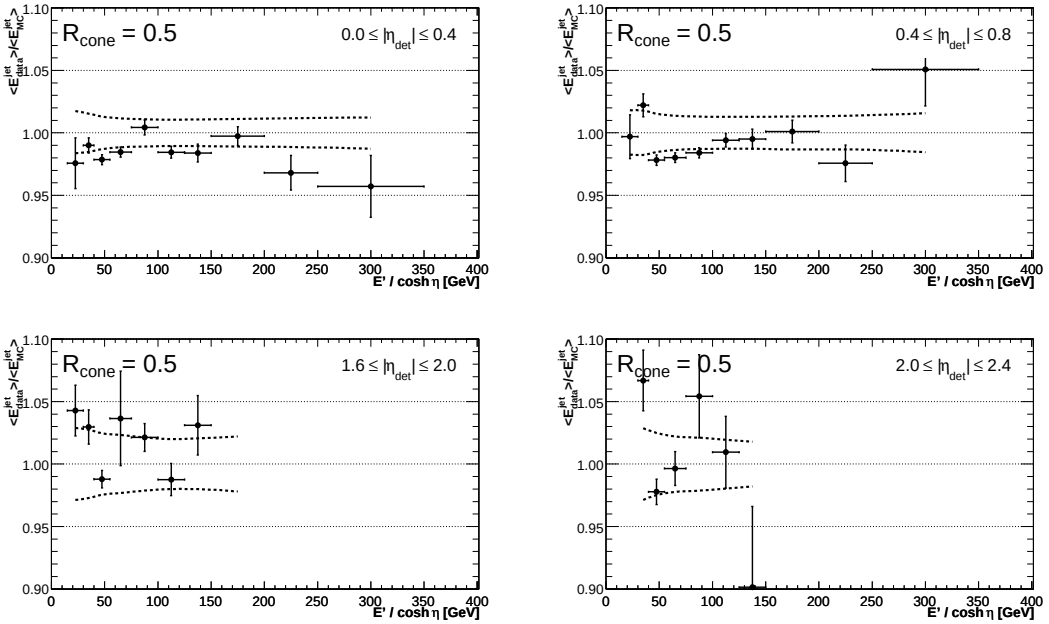

Figure 6.7: $\langle E_{\mathrm{jet}}^{\mathrm{Data}} \rangle / \langle E_{\mathrm{jet}}^{\mathrm{MC}} \rangle$ closure test for $\mathcal{R} = 0.5$ jets between the data and a mixture of signal+background simulation as a function of p'_{T} in different η bins, with photon p_T cuts.

6.11 JES Correction and Uncertainties

The final JES correction factor as a function of jet p_{T} for central ($\eta = 0$) and a selected forward ($\eta = 2$) pseudorapidity is displayed in Figure 6.8; for fixed selected jet p_{T}'s as a function of the rapidity in Figure 6.9. The JES errors decomposition is documented in Figures 6.10–6.11. In general, the correction is of the order of 1.5 and the error is 1–2% in most of the kinematic region.

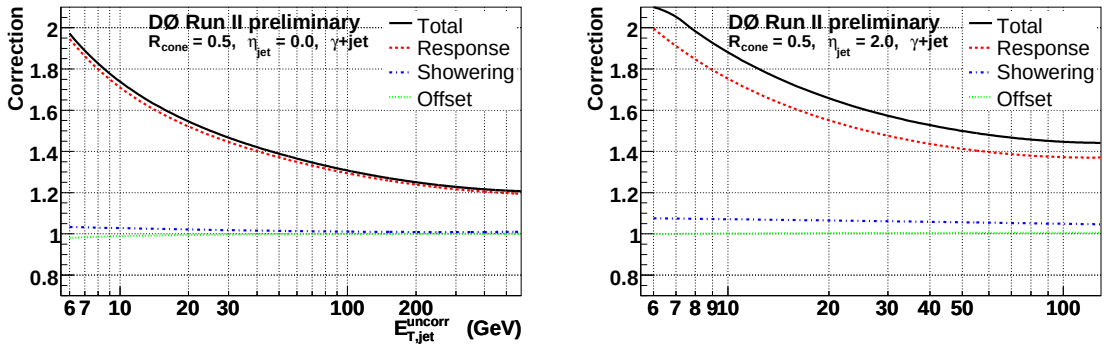

Figure 6.8: JES correction factor in two jet η's of 0. and 2.0 as a function of jet p_{T} for $\mathcal{R}_{\mathrm{cone}} = 0.5$ jets. Plots taken from [p17JES].

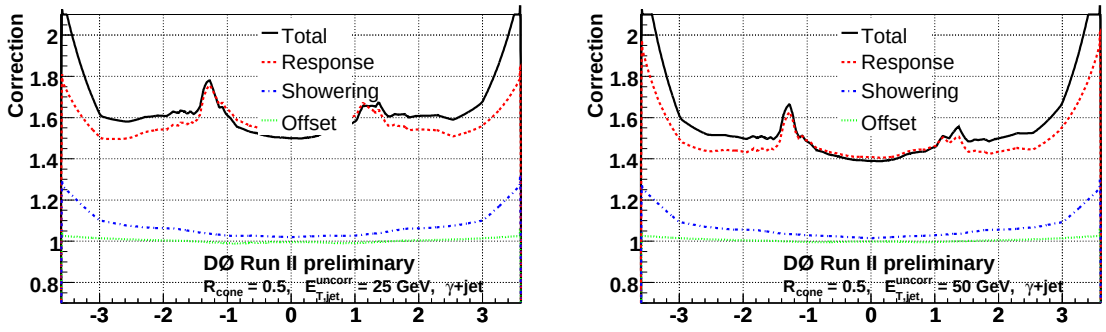

Figure 6.9: JES correction factor for two typical jet p_{T}'s of 25 and 50 GeV as a function of jet η for $\mathcal{R}_{\mathrm{cone}} = 0.5$ jets. Plots taken from [p17JES].

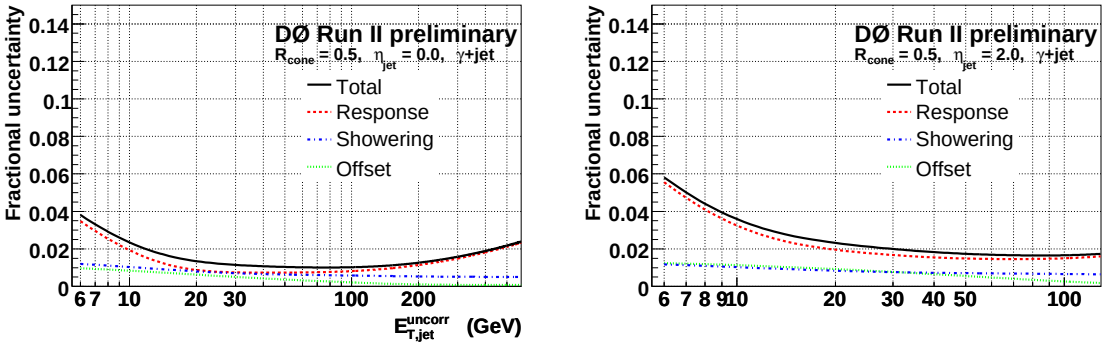

Figure 6.10: JES errors in two jet η's of 0. and 2.0 as a function of jet p_{T} for $\mathcal{R}_{\mathrm{cone}} = 0.5$ jets. Plots taken from [p17JES].

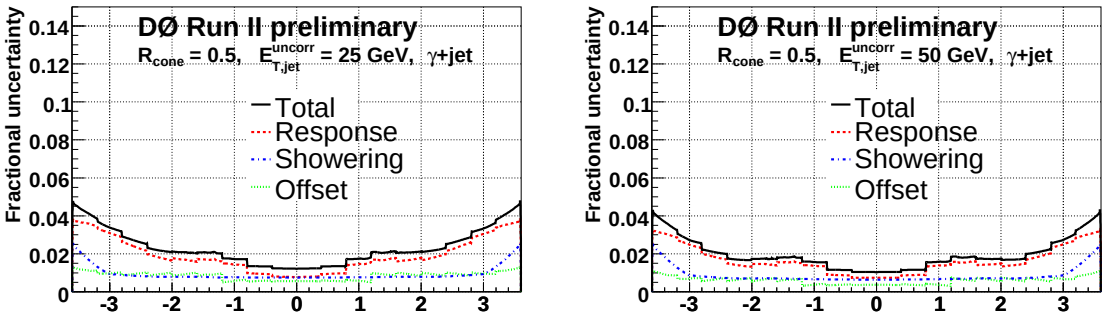

Figure 6.11: JES errors for two typical jet p_{T}'s of 25 and 50 GeV as a function of jet η for $\mathcal{R}_{\mathrm{cone}} = 0.5$ jets. Plots taken from [p17JES].

6.12 Relative Data – Simulation JES Difference

Due to differences in the jet energy scale and resolution between the data and simulation, a general procedure has been developped at the DØ to correct the simulation for related effects [53].

The prescription is based on the observation of the transverse momentum imbalance in γ+jet events using a variable

$$\Delta\mathcal{S} \equiv \frac{p_{\mathrm{T}}^{\gamma} - p_{\mathrm{T}}^{\mathrm{jet}}}{p_{\mathrm{T}}^{\gamma}},$$

which is measured for data and the simulation. Ideally, this quantity would be distributed around some value close to zero (with reconstruction and instrumentation effects shifting the mean), width of which gives one a handle on the jet p_{T} resolution.

Therefore, a procedure to over-smear simulation jet energy using measured resolutions in data and simulation (binned in η and p_{T}) can be developped to add a random fluctuation to the simulation reconstructed jet energy using a Gaussian over-smearing factor according to the resolution difference in the $\Delta\mathcal{S}$ variable between data and simulation:

$$\sigma_{\mathrm{oversmear}} = \sqrt{\sigma^2_{\mathrm{Data}} - \sigma^2_{\mathrm{MC}}}\,.$$

Then, simulation jets are randomly removed based on data jet identification and reconstruction efficiencies to simulate the difference in the efficiencies on average. There are two separate reasons for removing jets: the so-called threshold removing accounts for the fact that due to different resolutions, jets migrate over and below the 6 GeV reconstruction p_{T} cut differently in the data and simulation. Second effect is a slightly smaller efficiency of the data jets to pass the good jet criteria, which is parametrised by a constant in p_{T} and is referred to as plateau removal (see section 5.2.3). The threshold removal is inferred from fitting the profile of the $\Delta\mathcal{S}$ by a convolution of Gaussian and step functions, and the difference of thresholds is extracted from fits; in general data and simulation reach the plateau similarly at p_{T} of about 15 GeV, while differences are visible in the threshold region.

In addition, one can shift the energy scale of jets in the simulation to reproduce the mean value of the $\Delta\mathcal{S}$ variable as in data, this procedure being called shifting, accounting for the relative difference of data and simulation jet energy scales.

The full procedure outlined above is thus called jet shifting, smearing and removal (JSSR) (although this analysis used only the smearing and removing part) and Figures 6.12–6.14 of this section which document the procedure briefly outlined above are taken by the courtesy of authors from [53]. In fact, the Z+jets events are used as the main sample with the large statistics γ+jets events serving as a cross-check and a bridge to higher rapidities.

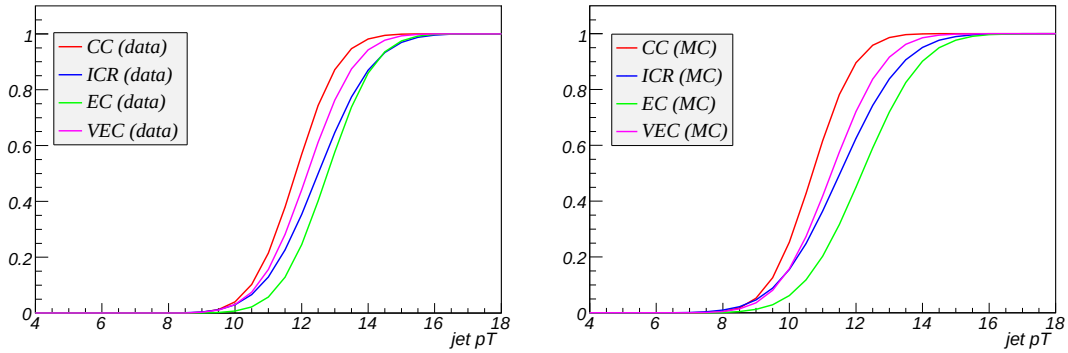

Figure 6.12: Average turn-on curves for the jet reconstruction efficiency in various calorimeter regions for data (left) and simulation (right). The 15 GeV cut on the reconstructed jet p_{T} to be used in most of analyses is motivated by these plots. Taken from [53].

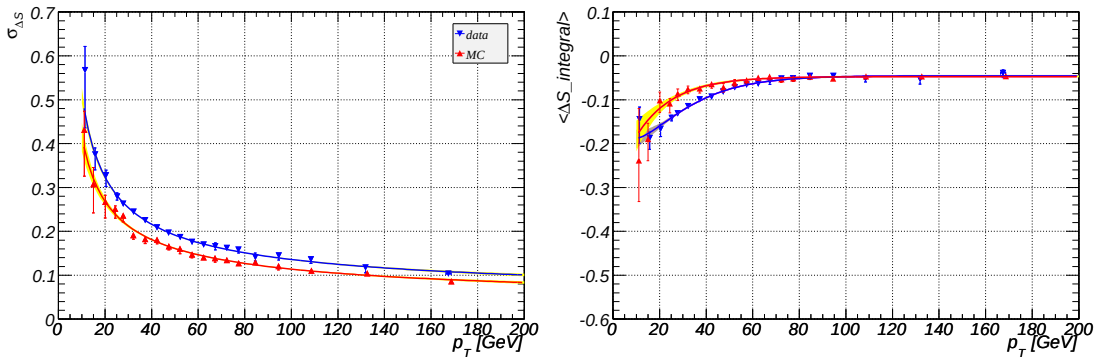

Figure 6.13: The $\Delta\mathcal{S}$ variable resolution (left) and mean (right) in the CC calorimeter part in γ+jet events in data (blue) and simulated (red) events. Plots taken from [53].

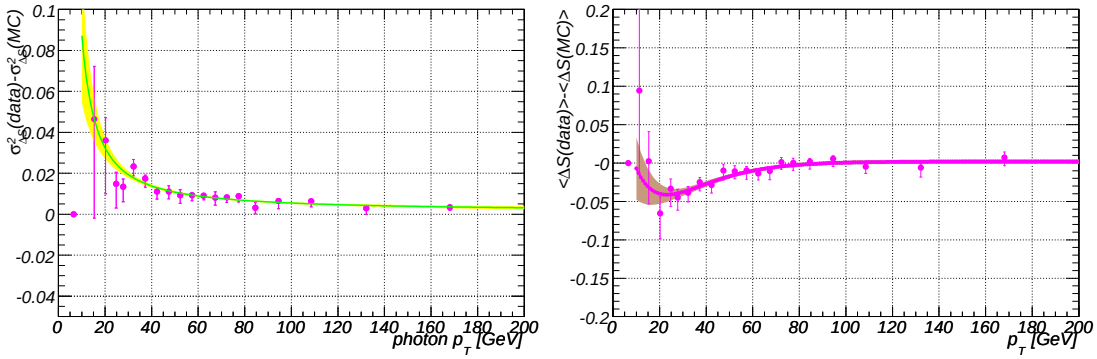

Figure 6.14: Smearing (left; squared) and shifting (right) factors for CC jets derived from γ+jet events using the differences in resolution and mean of the $\Delta\mathcal{S}$ variable as in Figure 6.13. Plots taken from [53].

Chapter 7

$t\bar{t}$ Differential Spectra

7.1 Motivation

The aim of this study is to measure differential spectra in the $t\bar{t}$ pair system produced in $p\bar{p}$ collisions at the 1.96 TeV center of mass energy.

The analysis can be regarded as a complementary study to similar observables in standard QCD analyses in the dijet system, namely one can study the pair invariant mass, transverse momentum spectrum, pair angular correlations as well as individual object spectra.

Many new models predict altered spectra with respect to the Standard Model prediction, which itself is known to a limited precision due to finite orders of perturbative QCD employed in calculations. It is therefore interesting to search for possible deviations in observed spectra and look for new physics or constrain the precision of current theory.

Looking at different $t\bar{t}$ system mass and characteristic transverse momenta, one can view the $t\bar{t}$ production at large momentum scales and check thus short distance physics or look for new physics (e.g. models with $t\bar{t}$ resonances or Z'). Besides the top quark p_{T} spectrum measurement itself, these are also the motivations for this study. Table 7.1 lists several important energy and length scales in GeV, seconds and fm. Many $t\bar{t}$ system related differential distributions were looked at for the first time in the presented study, and provide an important check of the consistency of the experiment and theory of top quark production and decay.

Scale	GeV	Time [s]	Length [fm]
Hydrogen atom ground state	$1.36{\cdot}10^{-8}$	$4.84{\cdot}10^{-17}$	$1.45{\cdot}10^{7}$
Λ_{QCD}	0.1	$6.58{\cdot}10^{-24}$	1.97
Γ_{top}	1.4	$4.70{\cdot}10^{-25}$	0.141
M_Z	90	$7.31{\cdot}10^{-27}$	0.00219
M_{top}	170	$3.87{\cdot}10^{-27}$	0.00116
Tevatron C.M.S. Energy	1,960	$3.36{\cdot}10^{-28}$	0.000101

Table 7.1: Selected energy scales expressed in terms of a characteristic length and time.

Top quark pair production is an important background for many new physics searches at the LHC as well as already at Tevatron (being a source of background for e.g. SM electroweak single-top quark production). For the $t\bar{t}$ pair being produced by the strong interaction, there are significant uncertainties (especially at LHC) on the

total cross-section coming from parton distribution functions due to the finite precision of their evolution prediction and experimental errors. As searches may involve the pair kinematic properties for e.g. topological discriminants, it is important to study the differential spectra of the system to have a detailed understanding before attempting to confirm or exclude new physics signals.

7.2 Strategy

For the purpose of the study, the lepton+jets (ℓ+jets) decay channel of the $t\bar{t}$ system was selected due to its distinct signature of the presence of a high p_{T} lepton and missing transverse energy, but also due to still large statistics compared to dilepton channels. Also, only one unreconstructed object (neutrino) is present, making it possible to employ a reasonable fitting procedure to reconstruct the full event kinematics. Compared to the all-jets channel, one is left with much more reduced background, here stemming mostly from the physics of W/Z+jets production and instrumental background coming from multijet events mimicking an isolated lepton in the detector (either via a highly electromagnetic jet faking an electron, or by an isolated muon coming originally from a jet). The presence of the two jets coming from the b-quark (b-jets) suggests to use some form of a b-tagging algorithm, i.e. identifying jets from heavy quarks and including this information into the event selection (and cut on the number of tagged jets in the event) or also into the fitting procedure (to decrease the number of possible jet permutations).

After the basic event preselection and b-tagging, one is left with a data sample enriched in the $t\bar{t}$ signal. In order to subtract the total background, all possible sources have to be considered and properly normalised. Namely, the number of events coming from the multijet background can be obtained from the so-called Matrix Method (see Section 11.2), which uses the loose and tight lepton isolation with know efficiencies for multijet and W-like sample. The most challenging part is the normalisation of the heavy flavour background accompanying the W/Z production. Aiming the differential spectrum analysis and differential cross-section extraction, such background subtraction has to be ideally performed individually in each bin for each distribution of interest.

Getting to the level of background-subtracted spectra, one can compare them with the signal simulation passed through the full detector simulation. Although already providing an interesting window into the understanding of basic processes involved, such comparison is of limited information value as it depends on possible imperfections in the simulation implementation as well as our knowledge of physics and approximations used in the generation of the hard process, fragmentation or the underlying event.

The most portable experimental result is such which is corrected for all acceptances (triggers, analysis cuts) as well as detector (smearing, mismeasurement) resolution and reconstruction (combinatorics) effects. Such unfolded spectrum can be directly compared to theoretical predictions and can set tighter limits on new physics or constrain current theory describing the process. There is an additional uncertainty coming from the unfolding procedure, which can nevertheless be well studied on the simulation and evaluated by comparing unfolded and truth distributions.

Chapter 8

Data and Simulation Samples

8.1 Data

Data for this analysis were collected by the DØ detector during the Run IIa period, and correspond to the integrated luminosity of $1037.82\,\mathrm{pb}^{-1}$ in the e+jets and $996.27\,\mathrm{pb}^{-1}$ in the μ+jets channel, i.e. approximately $1\,\mathrm{fb}^{-1}$. After the skimming (basic events streaming based on simple event flags like the presence of jets, leptons or firing of specific triggers) [54], 246,153,103 (262,601,935) events which passed the e+jet (μ+jet) triggers (see Tables 8.1-8.2) in the electron (muon) channel were selected for the base ℓ+jets sample to be further a subject to a dedicated $t\bar{t}$ preselection.

8.2 Simulation Samples

8.2.1 $t\bar{t}$ Signal Simulation Sample

As the main signal simulation ("Monte Carlo") sample, LO Alpgen matrix element generator [55] with Pythia [56] parton shower modelling with top quark mass of 170 GeV was used to generate $t\bar{t}$+0lp, $t\bar{t}$+1lp, $t\bar{t}$+2lp samples where 'lp' stands for additional light hard partons. Alpgen contains more diagrams for the additional jet production (e.g. the flavour creation) compared to standard Pythia. The parton distribution functions used were those of the CTEQ6L1 set [60], and a dynamical factorisation scale $\mu_F^2 = m_t^2 + \sum (p_{\mathrm{T}}^{\mathrm{jets}})^2$ was used. Pythia underlying event has been tuned to Tevatron CDF data as explained in [57], nicknamed as "Tune A" and summarised as for Pythia parameters in Table 8.3.

8.2.2 Modelling Issues

Soft underlying event is a part of the Pythia generator, and has been tuned to CDF and DØ data. For the parton shower part, Pythia is also always used as Herwig was not a part of the DØ software at the time of this analysis.

Hard underlying event, caused by possible multiple $p\bar{p}$ collisions, is modelled by overlaying a detector snap-shot containing events from the zero-bias trigger, which is defined by the collision timing only, and may, or may not, contain an additional interaction. The problem is that such an overlay is added to the simulation after passing the detector and, most importantly, after performing the signal suppression of calorimeter cells. Thus, in principle, data and simulation are not at the same footing as for the activity in the calorimeter, because due to a hard-scatter physics signal in real calorimeter data, more of the zero-bias signal can be triggered to be read out, while

Trigger list Version	Trigger name	Integrated luminosity [pb^{-1}]
V8.0 - V9.0	EM15_2JT15	23.49
V9.0 - V10.0	EM15_2JT15	24.96
V10.0 - V11.0	EM15_2JT15	9.81
V11.0 - V12.0	EM15_2JT15	63.40
V12.0 - V13.0	E1_SHT15_2J20	227.80
V13.0 - V13.3	E1_SHT15_2J_J25	55.22
V13.3 - V14.0	E1_SHT15_2J_J30	298.94
V14.0 - V15.0	E1_SHT15_2J_J25	334.20
TOTAL		1037.82

Table 8.1: Integrated luminosity collected with the e+jets trigger and the trigger list version for the Run IIa data-set. Courtesy of [73].

Trigger list Version	Trigger name	Integrated luminosity [pb^{-1}]
V8.0 - V9.0	MU_JT20_L2M0	24.79
V9.0 - V10.0	MU_JT20_L2M0	25.00
V10.0 - V11.0	MU_JT20_L2M0	10.70
V11.0 - V12.0	MU_JT20_L2M0	65.83
V12.0 - V13.0	MU_JT25_L2M0	231.63
V13.0 - V13.2	MUJ2_JT25	31.84
V13.2 - V13.3	MUJ2_JT25_LM3	16.10
V13.3 - V14.0	MUJ2_JT30_LM3	255.94
V14.0 - V14.2	MUJ1_JT25_LM3	0.01
V14.2 - V14.3	MUJ1_JT25_ILM3	21.89
V14.3 - V15.0	MUJ1_JT35_LM3	312.55
TOTAL		996.27

Table 8.2: Integrated luminosity collected with the μ+jets trigger and the trigger list version for the Run IIa data-set. Courtesy of [73].

Parameter	Default	Tune	Meaning
MSTP(81)	1.	1	Turns on multiple parton interactions (MPI).
MSTP(82)	1.	4	Double Gaussian matter distribution.
PARP(82)	1.9	2.0	Cut-off for multiple parton interactions, P_{T0} .
PARP(67)	1.0	4.0	Scale factor that governs the amount of ISR.
PARP(83)	0.5	0.5	Warm Core: 50% of matter in radius 0.4.
PARP(84)	0.2	0.4	Warm Core: 50% of matter in radius 0.4.
PARP(85)	0.33	0.9	Probability that the MPI produces two gluons with color connections to the nearest neighbors.
PARP(86)	0.66	0.95	Probability that the MPI produces two gluons either by PARP(85) or as a closed gluon loop. The remaining fraction consists of $q\bar{q}$ pairs.
PARP(89)	1000.	1800.	Determines the reference energy E_0
PARP(90)	0.16	0.25	Determines the energy dependence of the cut-off p_{T0} as $p_{T0}(E_{\rm cm}) = p_{T0}(E_{\rm cm}/E_0)^{\rm PARP(90)}$.

Table 8.3: Parameters used to tune Pythia underlying event to Tevatron CDF data ("Tune A") [58], [59].

this cannot happen in the case of the present-state simulation. While it would be in principle possible to change this procedure, it has been performed at DØ this way for many years and was not changed and the effect is at least partially being corrected for by dedicated jet energy offset correction, which is derived separately for data and simulation using appropriate unsuppressed or suppressed zero-bias overlays.

8.2.3 Background Samples

The main source of the physics background is the vector boson production with associated jets.

W+jets and Z+jet Backgrounds

In case of the W+jets production, the main background, a perfectly isolated lepton and large missing transverse energy can easily mimic the $t\bar{t}$ signal.

In case of the second background ordered in importance, the Z+jets production, one lepton may escape passing the good lepton criteria, and the event may be thus also mis-classified as containing only one isolated lepton. The $Z \to \nu\nu$ MC sample is not included, as the only way it would pass the preselection is through a jet from initial state radiation faking a lepton, which case is included already in the multijet background [73].

As the analysis under consideration uses b-tagging as one of the main signal/background separation technique, important differences are in the normalisation of separately $W(qq)$, $W(cc)$ and $W(bb)$ backgrounds, i.e. cases, where the W boson production is accompanied by different flavours of additional partons, produced either via flavour creation or as incoming partons.

There are two main approaches on how to generate and model the W production in association with multiple partons: (usually) a tree-level matrix element for the W+n-partons production; and a parton shower algorithm, which generates additional partons via the parton evolution via pQCD branching functions.

Matrix element approach is a fixed-order prescription, usually at tree level, and describes successfully well-separated partons with mutual large transverse momenta.

It preserves all quantum interference between included diagrams, as all the information is described by a hard process matrix element.

Using the parton shower approach, the parton shower evolution (as in e.g. PYTHIA or HERWIG) is used to generate mostly soft partons, collinear with the original parton. Some of the higher logarithmic terms are thus resumed via the ordered Sudakov-factor governed parton shower evolution, while the quantum interference is not exact.

Both approaches are complementary and are needed in order to properly describe different phase-space regions and aspects of the additional jets production. However, there are in general overlaps in the phase-space in the momenta of additional jets generated either by a higher-multiplicity matrix element, or a lower-multiplicity process with a parton shower.

In practice, one cannot simply take the cross section of a simple sum of W+n-partons passed through the parton shower nor simply merge the samples, but a proper matching or weighting scheme has to be applied to avoid the double counting in the phase-space of additional partons [62], [63].

As no virtual corrections are included in either of these approaches, the obtained cross section should be regarded as a Leading Order (LO) one, and additional scale factors ($\equiv k$-factors) to correct the LO yield with the Next-to-LO (NLO) should be are applied[1].

At the DØ, ALPGEN matrix element generator is used to produce W/Z+n-partons samples, and a MLM matching scheme [63] is used to avoid the double-counting w.r.t. PYTHIA parton shower. Samples include the following matched sub-processes: (with $Q \in \{c, b\}$, 'lp' being a light parton);

- W+0lp, W+1lp, W+2lp, W+3lp, W+4lp, W+5lp
- WQQ+0lp, WQQ+1lp, WQQ+2lp, WQQ+3lp
- Z+0lp, Z+1lp, Z+2lp, Z+3lp
- ZQQ+0lp, ZQQ+1lp, ZQQ+2lp

W is then decayed leptonically and Z into corresponding charged dilepton pair. Tauonic decay modes are also allowed, as electron or muon from the tau decay can pass the preselection.

Other Backgrounds

Remaining diboson processes WW, WZ and ZZ were simulated by PYTHIA while the single top quark production via COMPHEP [66]; SM cross sections were used for normalisation as explained in Section 11.3.

8.2.4 MC@NLO

MC@NLO [33], [34] is a unique tool for generating events at the NLO pQCD level. Unfortunately, it had not been included in the full official production of the DØ simulation chain, therefore is was not available to be studied at the level after the detector simulation (technically due to HERWIG, needed for hadronisation, not being supported at DØ Run II phase of this analysis). Still, it is a very useful tool for the NLO parton-level

[1] S. Frixione, KITP Workshop, Santa Barbara Jan 14th 2004: "Standard MC's don't perform well in predicting multi-jet observables, and the practice of multiplying the results by inclusive k-factors is just wrong."

prediction for variables of interest, and as such it is used as a comparison tool to final unfolded spectra. HERWIG version 6.510 [35] was used together with the MC@NLO version 3.2 (without spin correlations in the $t\bar{t}$ system) [36].

8.3 The Multijet Background

The sample representing the background from multijet events where an isolated lepton is faked by either electromagnetic jet passing the electron criteria or by a fake isolated muon coming originally from a jet, was defined as such a part of the data sample, where a lepton passes loose lepton identification criteria, but fails the tight selection (loose-tight, i.e. loose but not tight).

Chapter 9

Selection Cuts in the ℓ+jets Channel

The analysis cuts closely follow those used for the measurement of the $t\bar{t}$ cross section at the DØ with the same data-set [64], [67]. The main difference is that only the $\geq$4-jet analysis bin is being investigated, and that the τ-channels veto is not being applied (while it is used by the cross section analysis due to orthogonality and cross-section combination issues).

The ROOT [68] analysis framework has been extensively used at many stages of the analysis together with DØ's own ROOT-based analysis framework and format CAF (Common Analysis Framework) [69] and finally also ROOT-based ntuples ROC trees [70] (historically named as the format of the Rochester group at the DØ). MS Excell [71] has not been used anywhere in the presented analysis.

9.1 Common Cuts

Basic event quality cuts include the following conditions.

- Require events to be in certified good luminosity block numbers [72].
- Primary vertex position along the beam axis has to be well within the centre of the detector to ensure good tracking: $|z_{\mathrm{PV}}| < 60$ cm with at least 3 reconstructed tracks attached.
- At least 4 jets with $p_{\mathrm{T}} > 20\,\mathrm{GeV}$ within the detector projective pseudorapidity region of $|\eta| < 2.5$.
- Require at least one jet within $|\eta| < 2.5$ with $p_{\mathrm{T}} > 40\,\mathrm{GeV}$.
- For final distributions, at least one of these jets is required to pass the b-tag neural net cut > 0.65, corresponding to NN-medium operation point.

The cut-flow tables for data and the simulation samples in each of the e+jets and μ+jets channels are in Tables 9.1–9.4.

9.2 e+jets Preselection

Further preselection for events to pass the electron+jets channel includes the following criteria (with related variables defined in Section 5.3).

- Require at least one of top group e+jet triggers.
- Require the fully corrected missing transverse energy $\not{E}_{\mathrm{T}} > 20\,\mathrm{GeV}$.
- Track-matched electron with pseudorapidity $\eta < 1.1$, $p_{\mathrm{T}} > 20\,\mathrm{GeV}$.
- EM: emf$>$ 0.9, iso$<$ 0.15, hmx7$<$ 50.
- Tight selection: EMlhood $>$ 0.85, associated track $p_{\mathrm{T}} > 10\,\mathrm{GeV}$.
- Veto another well-contained tight electron above with p_{T} above 15 GeV to suppress the diboson background.
- Veto any isolated μ with p_{T} above 15 GeV.
- $\not{E}_{\mathrm{T}}$–electron $\Delta\phi$ triangular cut to reduce the multijet background:

$$\Delta\phi_{e,\,\not{E}_{\mathrm{T}}} > -0.045 \times \not{E}_{\mathrm{T}} + 0.7\pi$$

- Require the electron reconstructed z coordinate to be close to the primary vertex: $|z_{\mathrm{e}} - z_{\mathrm{PV}}| < 1$ cm.

9.3 μ+jets Preselection

For the muon+jets channel selection path, the following conditions are imposed.

- Require at least one of top group μ+jets triggers.
- Require the fully corrected missing transverse energy $\not{E}_{\mathrm{T}} > 25\,\mathrm{GeV}$.
- Select a tight muon with $|\eta| < 2$, $p_{\mathrm{T}} > 20\,\mathrm{GeV}$.
- Veto another medium isolated muon with p_{T} above 15 GeV to suppress the diboson background.
- Veto any tight electron with p_{T} above 15 GeV.
- $\not{E}_{\mathrm{T}}$–μ $\Delta\phi$ triangular cut to reduce the multijet background:

$$\Delta\phi_{\mu,\,\not{E}_{\mathrm{T}}} > 0.48\pi - 0.033\pi \times \not{E}_{\mathrm{T}}\,.$$

- In case of other central loose ΔR_{jet}-isolated muons with opposite sign, require the pair invariant mass $m_{\mu\mu} \notin (70,\ 110)$ GeV to reject the Z+jets background.
- Require the muon reconstructed z coordinate to be close to the primary vertex: $|z_{\mu} - z_{\mathrm{PV}}| < 1$ cm.

Selection	Events	Relative	Total
Initial	1730769		
Quark_particle_selector	681302	39.364±0.037%	39.364±0.037%
jet_selection: Jet pT $\geq$ 15.00 GeV	681301	100.000±0.000%	39.364±0.037%
jet_selection: Jet JES pT $\geq$ 15.00 GeV	681301	100.000±0.000%	39.364±0.037%
jet_selection: Jet $\lvert\eta_{\rm det}\rvert < 2.50$	681301	100.000±0.000%	39.364±0.037%
jet_selection: Jet ID	681282	99.997±0.001%	39.363±0.037%
jet_selection: EM jets removal	681266	99.998±0.001%	39.362±0.037%
jet_selection: Number of jets $\geq$ 1	681266	100.000±0.000%	39.362±0.037%
leading_jet: Jet pT $\geq$ 0.00 GeV	675755	100.000±0.000%	39.044±0.037%
leading_jet: Jet JES pT $\geq$ 0.00 GeV	675755	100.000±0.000%	39.044±0.037%
leading_jet: Jet ID	675755	100.000±0.000%	39.044±0.037%
leading_jet: EM jets removal	675755	100.000±0.000%	39.044±0.037%
leading_jet: Number of jets $\geq$ 1	675755	100.000±0.000%	39.044±0.037%
loose_electron: Object ID = 10, 11	406282	60.123±0.060%	23.474±0.032%
loose_electron: Calorimeter isolation $\leq$ 0.15	406282	100.000±0.000%	23.474±0.032%
loose_electron: EM fraction $\geq$ 0.9	406282	100.000±0.000%	23.474±0.032%
loose_electron: HMx7 $\leq$ 50	406282	100.000±0.000%	23.474±0.032%
loose_electron: E/P track match probability $>$ 0	406282	100.000±0.000%	23.474±0.032%
loose_electron: Track pT $\geq$ 5	406282	100.000±0.000%	23.474±0.032%
loose_electron: Electron pT $>$ 20.0 GeV	374293	92.126±0.042%	21.626±0.031%
loose_electron: $\lvert\eta^{\rm cal}_{\rm det}\rvert < 1.1$	325537	86.974±0.055%	18.809±0.030%
loose_electron: N electrons $\geq$ 1	325537	100.000±0.000%	18.809±0.030%
veto_muon: N muons $\leq$ 0	325371	99.949±0.004%	18.799±0.030%
veto_electron: N electrons $\leq$ 1	325253	99.964±0.003%	18.792±0.030%
Z of the first primary vertex $<$ 60 cm	320619	98.575±0.021%	18.525±0.030%
N tracks for the first primary vertex $\geq$ 3	320592	99.992±0.002%	18.523±0.030%
vertex_selection: dZ(electron, first PV) $<$ 1 cm	320190	99.875±0.006%	18.500±0.030%
met_selection: MET $\geq$ 20 GeV	284643	88.898±0.056%	16.446±0.028%
Triangle cut (MET, LeadingElectron)	268003	94.154±0.044%	15.485±0.027%
Passed_cuts	235992	88.056±0.063%	13.635±0.026%
passedNjetCut	235992	100.0000±0.00000 %	13.63510±0.02608 %
passedLeadJetPtCut	232937	98.7055±0.02327 %	13.45858±0.02594 %
passedMETCut	232937	100.0000±0.00000 %	13.45858±0.02594 %
passedTriangularCut	232937	100.0000±0.00000 %	13.45858±0.02594 %
passedBasicCuts	142705	61.2633±0.10094 %	8.24518±0.02091 %
passedNjetsAbovePtCut	109546	76.7640±0.11180 %	6.32933±0.01851 %
passedHFChi2Cut	108796	99.3154±0.02491 %	6.28599±0.01845 %

Table 9.1: Merged selection efficiencies for the ALPGEN e+jets signal sample.

Selection	Events	Relative	Total
Initial	1659241		
Remove bad runs and lbns	1396725	84.17855 ± 0.02833 %	84.17855 ± 0.02833 %
Event quality	1351878	96.78913 ± 0.01492 %	81.47569 ± 0.03016 %
jet_selection: Jet pT $\geq$ 15.00 GeV	1351878	100.00000 ± 0.00000 %	81.47569 ± 0.03016 %
jet_selection: Jet JES pT $\geq$ 15.00 GeV	1351878	100.00000 ± 0.00000 %	81.47569 ± 0.03016 %
jet_selection: Jet $\lvert\eta_{\text{det}}\rvert < 2.50$	1351878	100.00000 ± 0.00000 %	81.47569 ± 0.03016 %
jet_selection: Jet ID	1351878	100.00000 ± 0.00000 %	81.47569 ± 0.03016 %
jet_selection: EM jets removal	1351878	100.00000 ± 0.00000 %	81.47569 ± 0.03016 %
jet_selection: Number of jets ≥ 1	1351878	100.00000 ± 0.00000 %	81.47569 ± 0.03016 %
loose_electron: Object ID = 10, 11	1351878	100.00000 ± 0.00000 %	81.47569 ± 0.03016 %
loose_electron: Calorimeter isolation ≤ 0.15	1351878	100.00000 ± 0.00000 %	81.47569 ± 0.03016 %
loose_electron: EM fraction ≥ 0.9	1351878	100.00000 ± 0.00000 %	81.47569 ± 0.03016 %
loose_electron: HMx7 ≤ 50	1351878	100.00000 ± 0.00000 %	81.47569 ± 0.03016 %
loose_electron: E/P track match prob. > 0	1351878	100.00000 ± 0.00000 %	81.47569 ± 0.03016 %
loose_electron: Track pT ≥ 5	1351878	100.00000 ± 0.00000 %	81.47569 ± 0.03016 %
loose_electron: Electron pT > 20.0 GeV	1174782	86.90000 ± 0.02902 %	70.80237 ± 0.03530 %
loose_electron: $\lvert\eta^{\text{cal}}_{\text{det}}\rvert < 1.1$	1174331	99.96161 ± 0.00181 %	70.77519 ± 0.03531 %
loose_electron: N electrons ≥ 1	1174331	100.00000 ± 0.00000 %	70.77519 ± 0.03531 %
veto_muon: N muons ≤ 0	1151925	99.95809 ± 0.00191 %	69.42482 ± 0.03577 %
veto_electron: N electrons ≤ 1	1139894	98.95557 ± 0.00947 %	68.69972 ± 0.03600 %
met_selection: MET ≥ 20 GeV	211394	18.54506 ± 0.03640 %	12.74040 ± 0.02588 %
Triangle cut (MET, LeadingElectron)	72569	34.32879 ± 0.10327 %	4.37363 ± 0.01588 %
PROCESSOR "passed_cuts" (input)	47917	66.02957 ± 0.17581 %	2.88789 ± 0.01300 %
passedNjetCut	47917	100.0000 ± 0.00000 %	2.88789 ± 0.01300 %
passedLeadJetPtCut	26735	55.7944 ± 0.22688 %	1.61128 ± 0.00977 %
passedMETCut	26735	100.0000 ± 0.00000 %	1.61128 ± 0.00977 %
passedTriangularCut	26735	100.0000 ± 0.00000 %	1.61128 ± 0.00977 %
passedBasicCuts	981	3.6693 ± 0.11498 %	0.05912 ± 0.00189 %
passedNjetsAbovePtCut	462	47.0948 ± 1.59368 %	0.02784 ± 0.00130 %
passedHFChi2Cut	419	90.6926 ± 1.35169 %	0.02525 ± 0.00123 %

Table 9.2: Data tight e+jets sample efficiencies.

Selection	Events	Relative	Total
Initial	1730582		
Quark_particle_selector	677292	39.137±0.037%	39.137±0.037%
jet_selection: Jet pT $\geq$ 15.00 GeV	677285	99.999±0.000%	39.136±0.037%
jet_selection: Jet JES pT $\geq$ 15.00 GeV	677285	100.000±0.000%	39.136±0.037%
jet_selection: Jet $\lvert\eta_{\rm det}\rvert < 2.50$	677283	100.000±0.000%	39.136±0.037%
jet_selection: Jet ID	677268	99.998±0.001%	39.135±0.037%
jet_selection: EM jets removal	677265	100.000±0.000%	39.135±0.037%
jet_selection: Number of jets $\geq$ 1	677265	100.000±0.000%	39.135±0.037%
leading_jet: Jet pT $\geq$ 0.00 GeV	674760	100.000±0.000%	38.990±0.037%
leading_jet: Jet JES pT $\geq$ 0.00 GeV	674760	100.000±0.000%	38.990±0.037%
leading_jet: Jet ID	674760	100.000±0.000%	38.990±0.037%
leading_jet: EM jets removal	674760	100.000±0.000%	38.990±0.037%
leading_jet: Number of jets $\geq$ 1	674760	100.000±0.000%	38.990±0.037%
loose_muon: Muon $\lvert\eta_{\rm det}\rvert < 2.00$	674520	99.964±0.002%	38.976±0.037%
loose_muon: Muon quality is medium	589978	87.466±0.040%	34.091±0.036%
loose_muon: Number of layers $\geq$ 3	515463	87.370±0.043%	29.786±0.035%
loose_muon: Veto on cosmic muon	504354	97.845±0.020%	29.144±0.035%
loose_muon: Matched with central track	490663	97.285±0.023%	28.352±0.034%
loose_muon: Muon global fit $\chi^2 < 4$	486103	99.071±0.014%	28.089±0.034%
loose_muon: dca < 0.02 ($n_{\rm SMT} > 0$), dca < 0.2 ($n_{\rm SMT}$) $= 0$)	467062	96.083±0.028%	26.989±0.034%
loose_muon: Muon pT $\geq$ 20 GeV	349051	74.733±0.064%	20.170±0.031%
loose_muon: DeltaR(mu, jet) > 0.5	287648	82.409±0.064%	16.621±0.028%
loose_muon: N muons $\geq$ 1	287648	100.000±0.000%	16.621±0.028%
veto_electron: N electrons $\leq$ 0	287134	99.902±0.006%	16.592±0.028%
Z of the first primary vertex < 60 cm	283222	98.638±0.022%	16.366±0.028%
N tracks for the first primary vertex $\geq$ 3	283210	99.996±0.001%	16.365±0.028%
vertex_selection: dZ(muon, first PV) < 1 cm	282930	99.901±0.006%	16.349±0.028%
met_selection: MET $\geq$ 20 GeV	257010	90.839±0.054%	14.851±0.027%
Triangle cut (MET, LeadingMuon)	236289	91.938±0.054%	13.654±0.026%
Passed_cuts	204558	86.571±0.070%	11.820±0.025%
passedNjetCut	204082	99.7673±0.01065 %	11.79268±0.02452 %
passedLeadJetPtCut	201648	98.8073±0.02403 %	11.65203±0.02439 %
passedMETCut	193343	95.8814±0.04425 %	11.17214±0.02395 %
passedTriangularCut	193343	100.0000±0.00000 %	11.17214±0.02395 %
passedBasicCuts	125828	65.0802±0.10842 %	7.27085±0.01974 %
passedNjetsAbovePtCut	103173	81.9953±0.10832 %	5.96175±0.01800 %
passedHFChi2Cut	98001	94.9871±0.06794 %	5.66289±0.01757 %

Table 9.3: Merged selection efficiencies for the ALPGEN μ+jets signal sample.

Selection	Events	Relative	Total
Initial	248529		
Remove bad runs and lbns	215394	86.66755 ± 0.06819 %	86.66755 ± 0.06819 %
Event quality	207142	96.16888 ± 0.04136 %	83.34722 ± 0.07473 %
jet_selection: Jet pT ≥ 15.00 GeV	207142	100.00000 ± 0.00000 %	83.34722 ± 0.07473 %
jet_selection: Jet JES pT ≥ 15.00 GeV	207142	100.00000 ± 0.00000 %	83.34722 ± 0.07473 %
jet_selection: Jet $\lvert\eta_{\mathrm{det}}\rvert < 2.50$	207142	100.00000 ± 0.00000 %	83.34722 ± 0.07473 %
jet_selection: Jet ID	207142	100.00000 ± 0.00000 %	83.34722 ± 0.07473 %
jet_selection: EM jets removal	207142	100.00000 ± 0.00000 %	83.34722 ± 0.07473 %
jet_selection: Number of jets ≥ 1	207142	100.00000 ± 0.00000 %	83.34722 ± 0.07473 %
loose_muon: Muon $\lvert\eta_{\mathrm{det}}\rvert < 2.00$	207142	100.00000 ± 0.00000 %	83.34722 ± 0.07473 %
loose_muon: Muon quality is medium	207142	100.00000 ± 0.00000 %	83.34722 ± 0.07473 %
loose_muon: Number of layers ≥ 3	207142	100.00000 ± 0.00000 %	83.34722 ± 0.07473 %
loose_muon: Veto on cosmic muon	207142	100.00000 ± 0.00000 %	83.34722 ± 0.07473 %
loose_muon: Matched with central track	207142	100.00000 ± 0.00000 %	83.34722 ± 0.07473 %
loose_muon: Muon global fit $\chi^2 < 4$	207142	100.00000 ± 0.00000 %	83.34722 ± 0.07473 %
loose_muon: dca < 0.02 ($n_{\mathrm{SMT}} > 0$), dca < 0.2 ($n_{\mathrm{SMT}} = 0$)	207142	100.00000 ± 0.00000 %	83.34722 ± 0.07473 %
loose_muon: Muon pT ≥ 20 GeV	112011	54.07450 ± 0.10949 %	45.06959 ± 0.09981 %
loose_muon: DeltaR(mu, jet) > 0.5	111954	99.94911 ± 0.00674 %	45.04665 ± 0.09980 %
loose_muon: N muons ≥ 1	111954	100.00000 ± 0.00000 %	45.04665 ± 0.09980 %
veto_electron: N electrons ≤ 0	111778	99.84279 ± 0.01184 %	44.97584 ± 0.09979 %
Z of the first primary vertex $< 60\,\mathrm{cm}$	111778	100.00000 ± 0.00000 %	44.97584 ± 0.09979 %
N tracks for the first primary vertex ≥ 3	111778	100.00000 ± 0.00000 %	44.97584 ± 0.09979 %
vertex_selection: $\Delta z(\mu$, first PV$) < 1\,\mathrm{cm}$	111778	100.00000 ± 0.00000 %	44.97584 ± 0.09979 %
met_selection: MET ≥ 25 GeV	44487	39.79942 ± 0.14641 %	17.90012 ± 0.07690 %
Triangle cut (MET, LeadingMuon)	31561	70.94432 ± 0.21526 %	12.69912 ± 0.06679 %
Passed_cuts	26983	85.49476 ± 0.19822 %	10.85708 ± 0.06240 %
passedNjetCut	26983	100.0000 ± 0.00000 %	10.85708 ± 0.06240 %
passedLeadJetPtCut	22511	83.4266 ± 0.22637 %	9.05770 ± 0.05757 %
passedMETCut	22511	100.0000 ± 0.00000 %	9.05770 ± 0.05757 %
passedTriangularCut	22511	100.0000 ± 0.00000 %	9.05770 ± 0.05757 %
passedBasicCuts	831	3.6915 ± 0.12567 %	0.33437 ± 0.01158 %
passedNjetsAbovePtCut	393	47.2924 ± 1.73194 %	0.15813 ± 0.00797 %
passedHFChi2Cut	385	97.9644 ± 0.71234 %	0.15491 ± 0.00789 %

Table 9.4: Data tight μ+jets sample efficiencies.

Chapter 10

Kinematic Reconstruction

10.1 The Kinematic Fitter

The kinematics in the lepton+jets final state is not fully known due to the unreconstructed neutrino. Furthermore, objects properties as observed by the detector are mismeasured due to finite experimental resolutions. A kinematic fitter HitFit [77] is therefore applied to reconstruct the $t\bar{t}$ system using reasonable assumptions as additional constraints.

The first constraint is the requirement of equal masses of the hadronic and leptonic reconstructed top quarks. Further two constraints concern the invariant masses of each two objects forming the W boson candidates to be equal to the world average [78]. As the primary aim is not the measurement of the top-quark mass, one can also constrain directly its value, which leads to total of four constraints to fit the neutrino longitudinal momentum. Thus, the fitted χ^2-like expression is either

$$\chi^2_{\text{float}} \equiv \frac{(m_{l\nu b} - m_{jjb})^2}{\sigma_t^2} + \frac{(m_{jj} - m_W)^2}{\sigma_W^2} + \frac{(m_{l\nu} - m_W)^2}{\sigma_W^2} \tag{10.1.1}$$

for floating top quark mass or

$$\chi^2_{\text{fixed}} \equiv \frac{(m_{l\nu b} - m_t)^2}{\sigma_t^2} + \frac{(m_{jjb} - m_t)^2}{\sigma_t^2} + \frac{(m_{jj} - m_W)^2}{\sigma_W^2} + \frac{(m_{l\nu} - m_W)^2}{\sigma_W^2}\,, \tag{10.1.2}$$

for fixed top quark mass in the fitter; with $m_W = 80.4\,\text{GeV}$ and $m_b = 4.6\,\text{GeV}$ and σ_t and σ_W computed from resolutions of individual objects which build up the top or W candidates four-vectors, at momentum and angular scales of individual jets and leptons.

During the fitting procedure, objects are kept at a constant mass and the above constraints are maintained in a scheme where energies of objects are scaled (the other possibility would be to scale the 3-momentum).

10.2 Neutrino Solutions

The evidence of a neutrino coming from the hard process is the large missing transverse momentum (energy) in the calorimeter. While the longitudinal momentum is not known (depending on the parton system boost), the missing energy is used as a starting value for the neutrino transverse momentum component, and the longitudinal is computed from the top quarks mass constraints.

As this condition is a quadratic expressions in measured quantities (momenta and energies), there are in general two neutrino solutions, of which both are tried by the fitter and the one with lower χ^2 is used. Having four jets in the event, there are up to 12 possible permutations, disregarding the possible swap of light jet candidates forming the hadronic W boson candidate.

10.3 Resolutions for the Fitter

The analysis considers only the preselection-based ≥4-jet bin (counting based also on the η acceptance). For the kinematic fitter, only first four p_{T}-leading jets are used as jet-input to the fitter, without the requirement of the η coverage as in the preselection, where the 4-jet bin is defined by counting jets within $|\eta| < 2.5$. Appropriate lepton is passed to the fitter, together with the missing transverse energy as a solution prior for the neutrino p_{T}. As a safe convergence criterion, at least one positive χ^2 (10.1.1) resp. (10.1.2) is required. However, b-tagging is not required to be respected by the fitter, i.e. the fitter-assigned b-jets do not have to coincide to true b-tags; this is to enhance the fitting efficiency. Internally, the neutrino p_z solution with a smaller χ^2 is selected. This leads to up to 12 permutations. Out of the full results list, the one with lowest χ^2 is selected (best χ^2). Distributions of the χ^2 for the best and second best permutations are shown in Figures 10.1 through 10.9.

Resolutions for the fitter used are those as derived for a top-quark mass measurement using an ideogram method, as documented in DØ note [79]. Resolutions were derived using partons matched to reconstructed and JES-corrected jets and parametrised in the jet p_{T} and η. Similarly, resolutions were also derived for both leptons of the electron and muon type. Muon resolution is parametrised as a function of $1/p_{\mathrm{T}}$ as this is the quantity being Gaussian-like distributed when measuring the muon momentum using track-based variables and muon chambers; this is in contrast to jet and electron resolutions being parametrised by usual constant (C), noise (N) and stochastic (sampling, R) terms from the calorimetry-based shower energy measurement.

A specific parametrisations of momentum resolutions was used as described in [79], corresponding to HitFit resolution file version `defaults_june2007`. Lepton angular resolutions used are based on the values from Run I parameters $\sigma_\eta = 0.0071$, $\sigma_\phi = 0.0060$ for electrons and $\sigma_\eta = 0.0001$, $\sigma_\phi = 0.003$ for muons.

10.3.1 Electron Momentum Resolution

Electron momentum resolution is parametrised in terms of p by the form

$$\sigma_e(p) = \sqrt{C^2p^2 + R^2p + N^2}$$

with $C = 0.044$, $R = 0.23$, $N = 0.21$ for $|\eta_e| < 1.1$, evaluating at about 4.5% at $\eta = 0$ for $p = 30\,\mathrm{GeV}$.

10.3.2 Muon Momentum Resolution

Muon momentum resolution is parametrised in terms of $1/p_{\mathrm{T}}$ as

$$\sigma_\mu(1/p_{\mathrm{T}}) = \sqrt{C^2(1/p_{\mathrm{T}})^2 + R^2(1/p_{\mathrm{T}}) + N^2}\,.$$

with $C = R = 0$, $N = 0.002618$ for $|\eta_\mu| < 1.6$ and $C = R = 0$, $N = 0.003511$ for $|\eta_\mu| > 1.6$, which for muon with $p_{\mathrm{T}} = 30\,\mathrm{GeV}$ results in momentum uncertainty of about 8–11% depending on η.

10.3.3 Jets Momentum Resolution

Jet resolution was parametrised as a function of jet p_{T} [80] using a similar formula as for the electrons

$$\sigma_{\mathrm{jet}}(p_{\mathrm{T}}) = \sqrt{C^2 p_{\mathrm{T}}^2 + R^2 p_{\mathrm{T}} + N^2}\,.$$

with parameters listed in Table 10.1. Typically, the jet resolution is $95\%/\sqrt{p_{\mathrm{T}}}$ (p_{T} in GeV) with additional constant and noise terms.

$\lvert\eta_{\mathrm{max}}\rvert$	C	R	N	σ_η	σ_ϕ
0.4	10.0415	0.927	0.0	0.0390	0.0405
0.8	20.0505	0.947	0.0	0.0395	0.0400
1.2	30.1027	0.992	0.0	0.0460	0.0470
1.6	40.0908	0.968	0.0	0.0605	0.0545
2.0	50.0267	0.948	0.0	0.0525	0.0475
2.4	60.0844	0.750	0.0	0.0525	0.0475
99.	70.1556	0.000	4.1	0.0525	0.0475

Table 10.1: Resolution parameters of jets used for the kinematic fit.

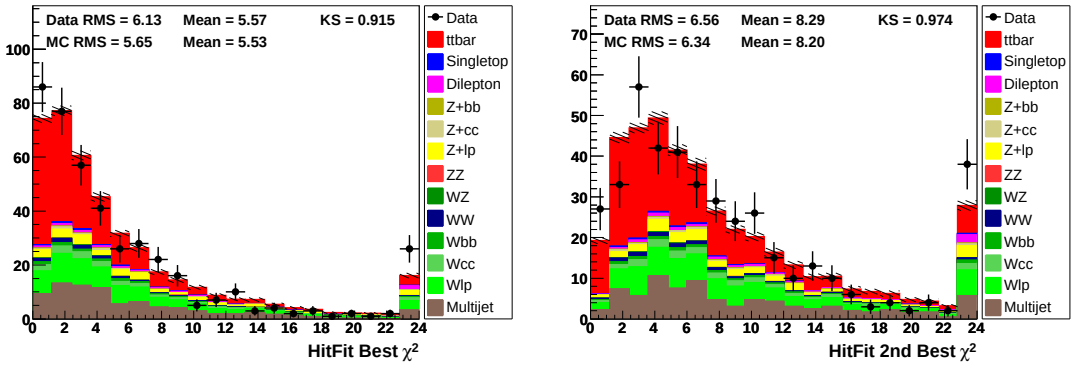

Figure 10.1: Best (left) and second best (right) kinematic fit χ^2 in e+jets untagged data and the simulation.

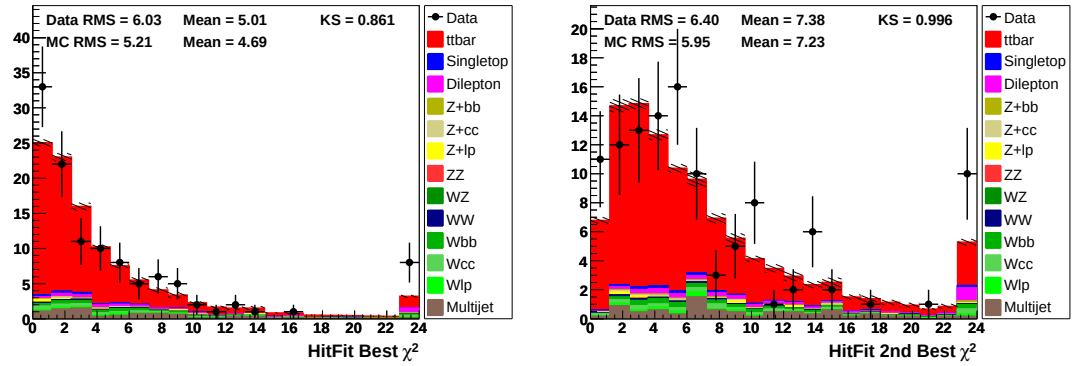

Figure 10.2: Best (left) and second best (right) kinematic fit χ^2 in e+jets single tag data and the simulation.

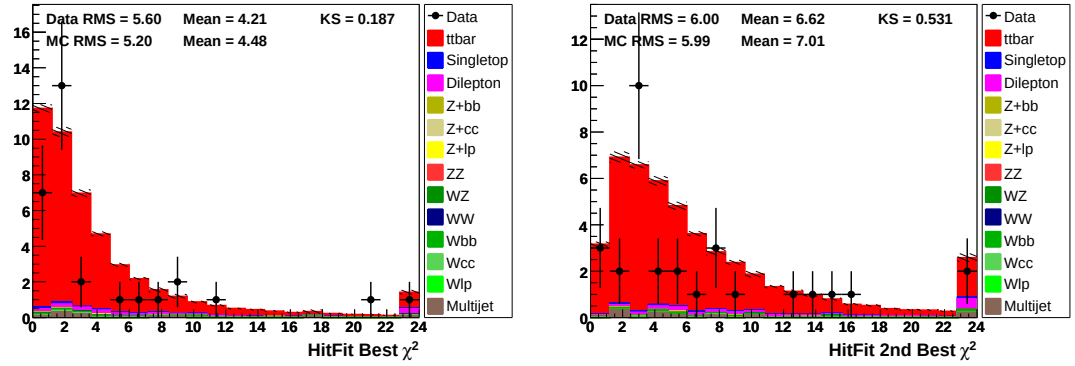

Figure 10.3: Best (left) and second best (right) kinematic fit χ^2 in e+jets $\geq$ 2-tag data and the simulation.

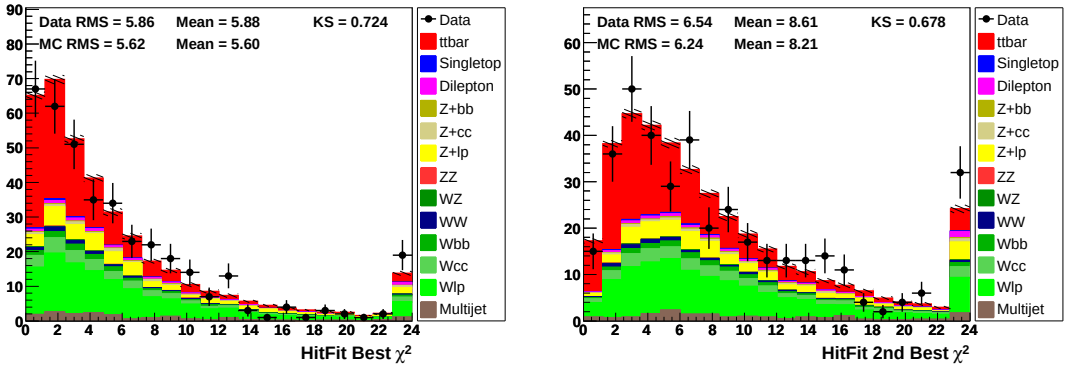

Figure 10.4: Best (left) and second best (right) kinematic fit χ^2 in μ+jets untagged data and the simulation.

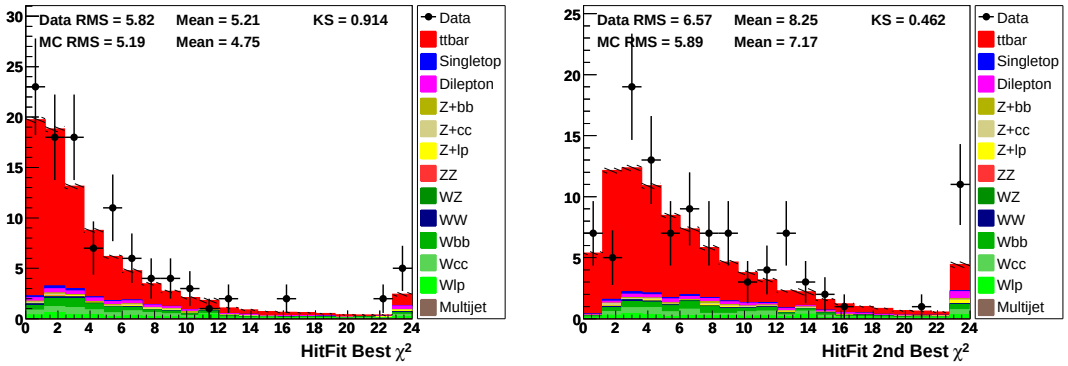

Figure 10.5: Best (left) and second best (right) kinematic fit χ^2 in μ+jets single tag data and the simulation.

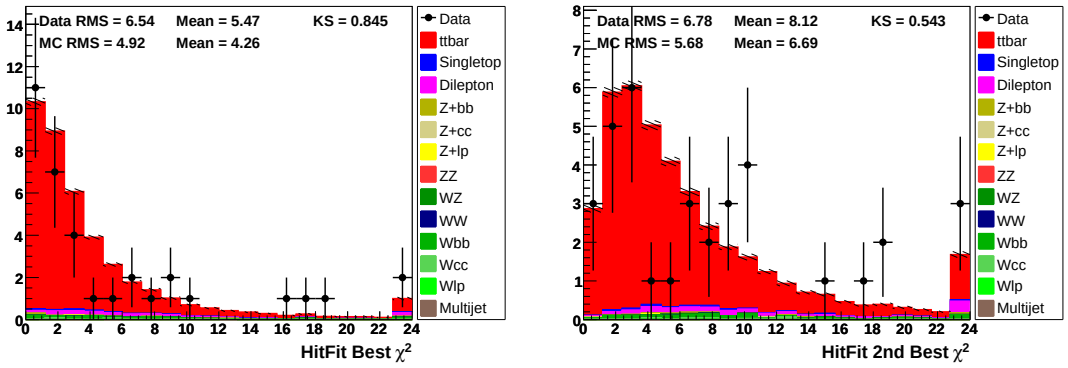

Figure 10.6: Best (left) and second best (right) kinematic fit χ^2 in μ+jets $\geq$ 2-tag data and the simulation.

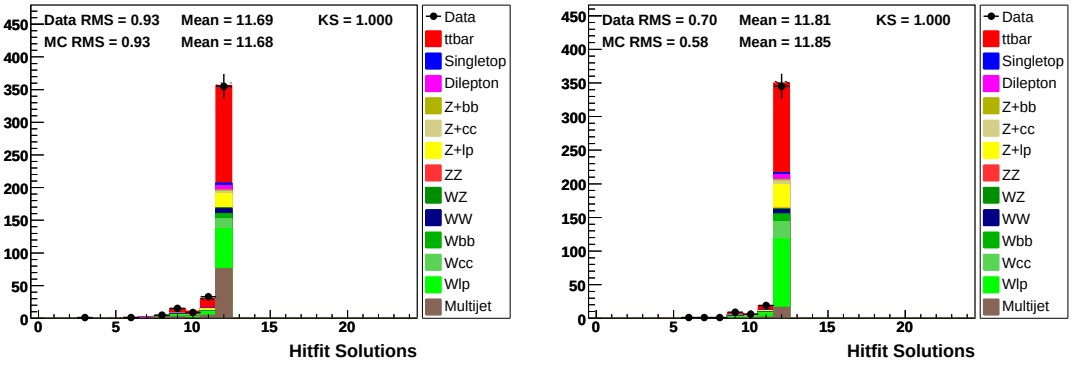

Figure 10.7: Number of HitFit solutions for e+jets (left) and μ+jets (right), untagged data and the simulation.

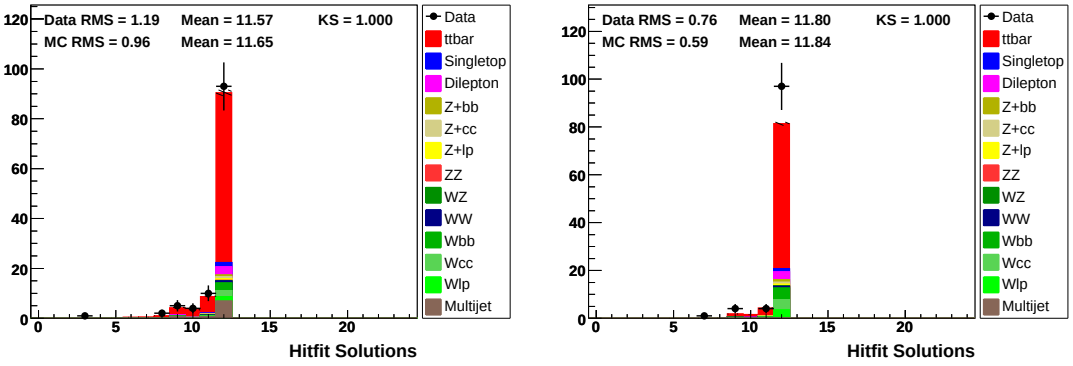

Figure 10.8: Number of HitFit solutions for e+jets (left) and μ+jets (right), NNm single tag data and the simulation.

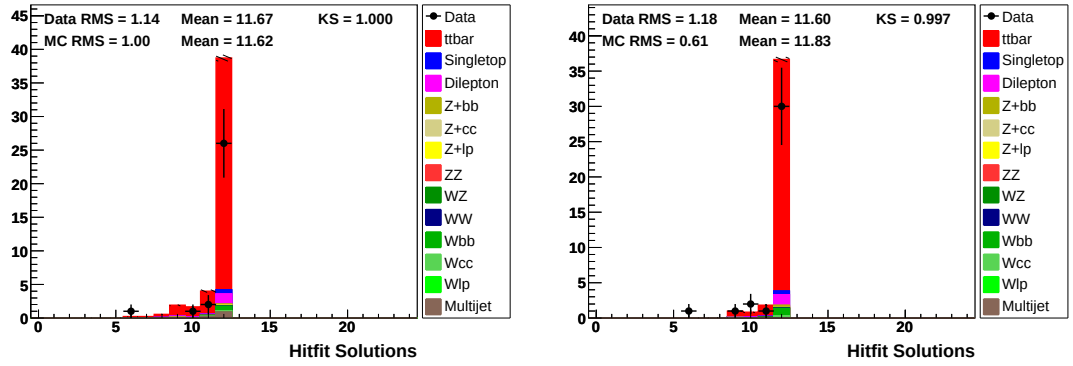

Figure 10.9: Number of HitFit solutions for e+jets (left) and μ+jets (right), NNm $\geq$ 2-tag data and the simulation.

Chapter 11

Samples Normalisation

Various backgrounds are being normalised differently according to the nature, origin, importance and specialties of the given background type. In general, backgrounds either use a theory-predicted cross section or are (partially) normalised to match the total event counts in data.

11.1 Simulations Weights

All simulation-based backgrounds normalised using individual selection efficiencies are corrected for several data/simulation scale factors accounting for differences in efficiencies or selected event profiles by means of weighting the simulation events [64]. This includes reweighting the primary vertex z position, the instantaneous luminosity profile, a scale factor for the overall lepton identification efficiencies; the b-fragmentation model reweighting, Z-boson p_{T} reweighting (for Z+jet samples only), a weight to simulate the trigger effect; and also the good data quality efficiency scale factor of $\epsilon_{\mathrm{DQ}} = 0.9715$ as measured in [74]. In addition, a special weight is assigned to individual Alpgen samples to mix properly the contributions to additional partons from either hard matrix elements or soft Pythia parton shower; this weight also includes the normalisation to the data luminosity. Several weights for the μ+jets case of Alpgen signal are illustrated in Figure 11.1.

11.2 The Matrix Method

The following method has been adopted to estimate the number of multijet (QCD-like) background and W-like events (both the signal $t\bar{t}$ and W+jets background), called the Matrix method.

The idea is that in the QCD-like background, leptons are mimicked by a EM-like jet (faking an electron) or by a muon particle which was the part of the showering jet, but which has appeared as an isolated lepton (e.g. due to multiple scattering, jet angle change due to split/merge etc.). Assuming one can require two different lepton quality selections denoted as loose and tight, tight being a subset of loose, the number or observed events can be written as

$$N_{\mathrm{loose}} = N_{\mathrm{loose}}^{\mathrm{QCD}} + N_{\mathrm{loose}}^{W+t\bar{t}}$$
$$N_{\mathrm{tight}} = N_{\mathrm{tight}}^{\mathrm{QCD}} + N_{\mathrm{tight}}^{W+t\bar{t}}.$$

The efficiencies for each sample to pass the tight criterion after passing the loose, ϵ_{QCD} and $\epsilon_{\mathrm{W+t\bar{t}}}$ can be measured in a separate study in each jet multiplicity bin.

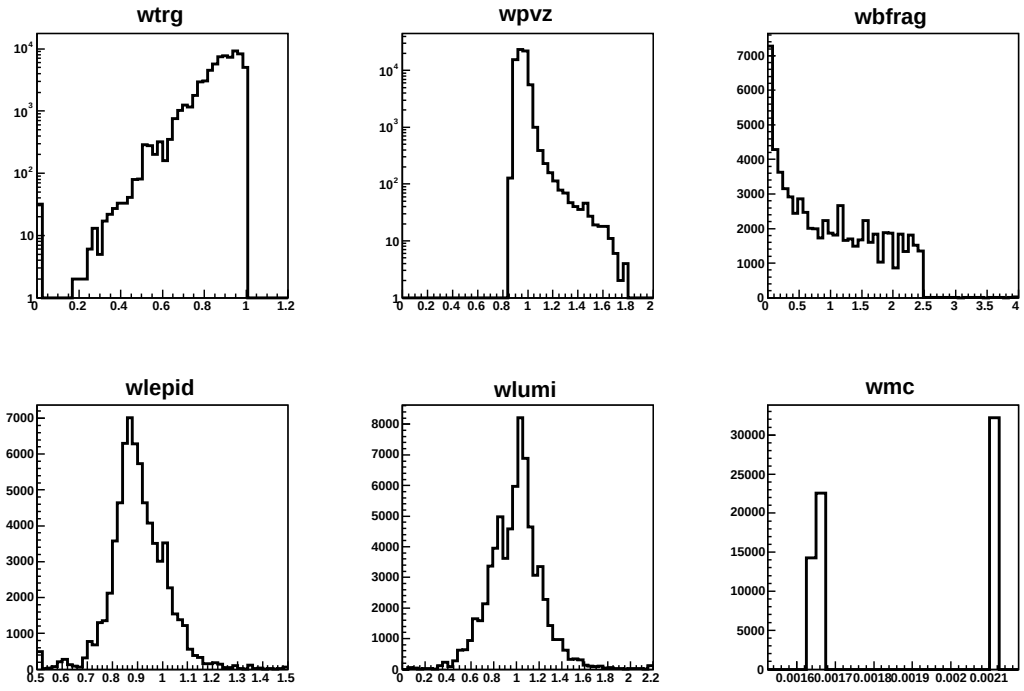

Figure 11.1: Simulation weight for μ+jets ALPGEN signal sample (trigger, z_{PV}, b-fragmentation, lepton-ID scale factor, luminosity reweighting and the matching weight.

ϵ_{QCD} has been measured on a special data sample containing jets and leptons after the standard selection criteria, but with a reversed cut on the missing transverse energy [61]. Such sample is enriched in the multijet background, and the efficiency of passing the tight criterion was fitted in lower region of the missing transverse energy (as signal fraction increases with $\not\!\!E_{\mathrm{T}}$).

The efficiency $\epsilon_{\mathrm{W+t\bar{t}}}$, also denoted as ϵ_{sig}, was measured in simulation. One can rewrite the equation for the tight lepton selection yield as

$$N_{\mathrm{tight}} = \epsilon_{\mathrm{QCD}} N_{\mathrm{loose}}^{\mathrm{QCD}} + \epsilon_{\mathrm{W+t\bar{t}}} N_{\mathrm{loose}}^{W+t\bar{t}}$$

and the set of the two equations can then be solved in terms of $N_{\mathrm{loose}}^{\mathrm{QCD}}$ and $N_{\mathrm{loose}}^{W+t\bar{t}}$, thus leading also to $N_{\mathrm{tight}}^{\mathrm{QCD}}$ and $N_{\mathrm{tight}}^{W+t\bar{t}}$. The desired quantity is the number of multijet events passing the tight lepton preselection

$$N_{\mathrm{tight}}^{\mathrm{QCD}} = \epsilon_{\mathrm{QCD}} \frac{\epsilon_{\mathrm{sig}} N_{\mathrm{loose}} - N_{\mathrm{tight}}}{\epsilon_{\mathrm{sig}} - \epsilon_{\mathrm{QCD}}} \,.$$

Numbers for the relevant efficiencies used in this analysis are in Table 11.1.

11.3 Di-boson Backgrounds and Single Top

Due to their very small cross sections, yields for the double vector bosons production are estimated using SM next-to-leading cross sections of $\sigma_{WW} = 12.0\,\mathrm{pb}$, $\sigma_{WZ} = 3.68\,\mathrm{pb}$ and $\sigma_{ZZ} = 1.42\,\mathrm{pb}$ [65]. Single top production in s and t channels is estimated using COMPHEP [66] cross sections of 0.88 pb and 1.98 pb, respectively.

	e+jets	μ+jets
ϵ_{signal}	0.8399	0.8450
ϵ_{QCD}	0.1940	0.2790
Error on ϵ_{QCD}	0.016	0.048

Table 11.1: Signal and multijet sample tight lepton selection efficiencies used in this analysis.

11.4 Signal Normalisation

The signal simulation samples were normalised before the b-tagging using the DØ's combined measured $t\bar{t}$ cross section of 8.16 pb [67], which is in agreement with the world average and is also consistent with the integrated cross section extracted in this analysis later. Variation of the assumed cross section is later also taken as a systematics. Branching ratios for lepton+jets and dilepton final states used are listed in Table 11.2.

	e+jets	μ+jets
$\text{BR}_{t\bar{t}}$	0.17210	0.17137
$\text{BR}_{\text{dilepton}}$	0.06627	0.06607

Table 11.2: Branching ratios for $t\bar{t} \to \ell$+jets and dilepton final states used for normalising the simulation yields computed using PDG 2006 [78] from individual branching ratios so that at least one electron (muon) is present in the e+jets (μ+jets) final state. Taken from [67].

11.5 Z+jets Backgrounds

The LO cross section stemming from the usage of ALPGEN matrix element and PYTHIA for parton shower, is scaled by NLO/LO k-factors accounting also for the fact of changed heavy flavour admixture at the NLO, as described in [75], which results in $k_{Z\text{lp}} = 1.35$, $k_{Z\text{bb}} = 1.688$ and $k_{Z\text{cc}} = 1.688$, being a combination of a NLO/LO scale factor and a heavy flavour scale factor for Zbb and Zcc.

11.6 W+jets Background

The main idea in normalising the W+jets background is to subtract from the observed number of events the expected signal and all non-W+jets backgrounds and attribute the rest to the W+jets contribution, being the most important background. Heavy-flavour scale factors are applied for Wcc and Wbb samples on top of NLO k-factors of $k_{W\text{bb}} = 1.93$, $k_{W\text{cc}} = 1.93$ as documented in [76].

Normalising the W+jets background before the b-tagging to the data yield subtracted by all other sources of background as well as signal in fact means that one scales the fraction of truth over theory-predicted number of W+jets events (integrated over all bins) by a quantity

$$\alpha_W \equiv \frac{N_{\text{Data}} - N_{t\bar{t}} - N_{\text{non}W}}{k_{Wlp}N_{Wlp} + k_{Wcc}N_{Wcc} + k_{Wbb}N_{Wbb}},$$

where

$$N_{\mathrm{non}W} \equiv k_{Zlp}N_{Zlp} + k_{Zcc}N_{Zcc} + k_{Zbb}N_{Zbb} + N_{tb} + N_{ll} + N_{WW} + N_{WZ} + N_{ZZ} + N_{\mathrm{QCD}}\,.$$

Each W+jets background type expectation before tagging is scaled by α_W, and the computed fraction from the untagged samples is kept for the tagged case, thus for the number of W+jets events after tagging one effectively uses the prediction of average b-tagging efficiency based on the performance of tag rate functions (TRF's; see Section 5.6.2).

11.7 Preselection Yields and Efficiencies

Tables 11.3–11.4 contain the yields and efficiencies for data and signal and background samples in exclusive b-tag bins of 1 and ≥ 2 b-tags for e+jets and μ+jets preselection chain. The inclusive b-tag case ≥ 1 is displayed in Table 11.5. Signal-to-background ratio as predicted by the simulation is also reported. The simulation efficiencies in these tables do not include the simulation weights, but involve the efficiency of a parton selector (deciding the correspondence to the e or μ+jet channel), which is not part of the truth selection efficiency (which also includes all the weights).

In essence, the preselection yields 145 and 141 b-tagged data events in respective e+jets and μ+jets channels with the signal/background ratio in the tagged bin of 3.7, corresponding to the signal fraction of 0.79, predicting total number of signal-like events of 225 out of 286. This is a very clean sample of $t\bar{t}$ events suitable for precision measurements of the detailed kinematics of the final state. As the background overall normalisation is given by the data before the b-tagging, it is a nontrivial check that a good agreement in predicted and observed number of events after tagging is reached in the "SUM" of all estimated background and signal samples (which would ideally match the count in "Data"). In the exclusive b-tagged case, the SUM is often larger then the yield in data by a few events; this is due to the matrix method predicting a negative number of multijet events (consistent with zero, though), which is forced to be greater than 0., thus making the total sum slightly larger then the original data count.

e+jets	=0 tag	=1 tag	≥ 2 tag	Sum
α_{W}	0.71	0.71	0.71	
$\mathrm{t\bar{t}}$ e+jets	56.68	82.17	42.02	180.86
Wlp	68.83	2.00	0.02	70.85
Wbb	4.45	3.50	0.79	8.74
Wcc	15.41	2.97	0.29	18.67
Zlp	25.28	1.01	0.04	26.33
Zbb	1.24	0.81	0.24	2.29
Zcc	3.33	0.85	0.00	4.18
singletop	1.57	1.96	0.71	4.24
dilepton	2.99	4.36	2.01	9.36
WW	7.82	0.89	0.05	8.77
WZ	1.38	0.18	0.05	1.61
ZZ	0.22	0.08	0.02	0.32
Multijet	73.86	7.84	1.08	82.78
SUM	263.06	108.62	47.32	419.00
Data	274.00	115.00	30.00	419.00
$\mathrm{t\bar{t}}$	59.67	86.52	44.03	190.22
W + jets	88.69	8.47	1.10	98.26
Z + jets	29.84	2.67	0.28	32.80
singletop	1.57	1.96	0.71	4.24
diboson	9.43	1.16	0.12	10.70
Multijet	73.86	7.84	1.08	82.78
SUM	263.06	108.62	47.32	419.00
Data	274.00	115.00	30.00	419.00
Eff. $t\bar{t}\ell j$	0.03889	0.05638	0.02883	
Eff. $t\bar{t}\ell\ell$	0.00532	0.00776	0.00359	
$\mathcal{S}/\mathcal{B}$	0.27	3.11	7.92	

Table 11.3: Yields and background composition in exclusively b-tagged NN medium for ≥ 4 jets in e+jets after HitFit, $\sigma_{t\bar{t}} = 8.16$ pb.

μ+jets	=0 tag	=1 tag	$\geq$ 2 tag	Sum
α_{W}	1.26	1.26	1.26	
$\mathrm{t\bar{t}}$ μ+jets	44.00	66.78	36.06	146.83
Wlp	106.46	3.43	0.03	109.93
Wbb	5.91	5.38	1.13	12.42
Wcc	23.56	4.72	0.30	28.59
Zlp	37.15	0.69	0.02	37.85
Zbb	1.34	1.08	0.29	2.71
Zcc	5.14	0.98	0.03	6.15
singletop	1.09	1.43	0.54	3.06
dilepton	2.66	3.65	1.78	8.09
WW	6.46	0.79	0.05	7.30
WZ	1.28	0.25	0.11	1.64
ZZ	0.32	0.04	0.01	0.38
Multijet	19.49	0.00	0.00	19.49
SUM	254.88	89.22	40.35	384.45
Data	241.00	106.00	35.00	382.00
$\mathrm{t\bar{t}}$	46.66	70.43	37.84	154.92
W + jets	135.93	13.53	1.47	150.93
Z + jets	43.63	2.75	0.34	46.72
singletop	1.09	1.43	0.54	3.06
diboson	8.07	1.08	0.17	9.32
Multijet	19.49	0.00	0.00	19.49
SUM	254.88	89.22	40.35	384.45
Data	241.00	106.00	35.00	382.00
Eff. $t\bar{t}\ell j$	0.03158	0.04793	0.02588	
Eff. $t\bar{t}\ell\ell$	0.00495	0.00680	0.00331	
$\mathcal{S}/\mathcal{B}$	0.21	2.98	8.39	

Table 11.4: Yields and background composition in exclusively b-tagged NN medium for ≥ 4 jets in μ+jets after HitFit, $\sigma_{t\bar{t}} = 8.16$ pb.

e+jets	$\geq$0 tag	$\geq$1 tag	$\geq$ 2 tag
α_W	0.71	0.71	0.71
$t\bar{t}$ e+jets	180.86	124.18	42.02
Wlp	70.85	2.01	0.02
Wbb	8.74	4.29	0.79
Wcc	18.67	3.27	0.29
Zlp	26.33	1.05	0.04
Zbb	2.29	1.05	0.24
Zcc	4.18	0.85	0.00
singletop	4.24	2.67	0.71
dilepton	9.36	6.37	2.01
WW	8.77	0.95	0.05
WZ	1.61	0.23	0.05
ZZ	0.32	0.10	0.02
Multijet	82.78	8.92	1.08
SUM	419.00	155.94	47.32
Data	419.00	145.00	30.00
$t\bar{t}$	190.22	130.55	44.03
W + jets	98.26	9.57	1.10
Z + jets	32.80	2.95	0.28
singletop	4.24	2.67	0.71
diboson	10.70	1.28	0.12
Multijet	82.78	8.92	1.08
SUM	419.00	155.94	47.32
Data	419.00	145.00	30.00
Eff. $t\bar{t}\ell j$	0.12409	0.08520	0.02883
Eff. $t\bar{t}\ell\ell$	0.01667	0.01135	0.00359
$\mathcal{S}/\mathcal{B}$	0.76	3.91	7.92

μ+jets	$\geq$0 tag	$\geq$1 tag	$\geq$ 2 tag
α_W	1.26	1.26	1.26
$t\bar{t}$ μ+jets	146.83	102.83	36.06
Wlp	109.92	3.46	0.03
Wbb	12.42	6.51	1.13
Wcc	28.59	5.03	0.30
Zlp	37.85	0.71	0.02
Zbb	2.71	1.37	0.29
Zcc	6.15	1.01	0.03
singletop	3.06	1.97	0.54
dilepton	8.09	5.43	1.78
WW	7.30	0.85	0.05
WZ	1.64	0.35	0.11
ZZ	0.38	0.05	0.01
Multijet	17.05	0.00	0.00
SUM	382.00	129.57	40.35
Data	382.00	141.00	35.00
$t\bar{t}$	154.92	108.27	37.84
W + jets	150.93	15.00	1.47
Z + jets	46.72	3.09	0.34
singletop	3.06	1.97	0.54
diboson	9.32	1.25	0.17
Multijet	17.05	0.00	0.00
SUM	382.00	129.57	40.35
Data	382.00	141.00	35.00
Eff. $t\bar{t}\ell j$	0.10539	0.07381	0.02588
Eff. $t\bar{t}\ell\ell$	0.01507	0.01011	0.00331
$\mathcal{S}/\mathcal{B}$	0.62	3.85	8.39

Table 11.5: Yields and background composition in inclusively b-tagged NN medium for ≥ 4 jets in e+jets and μ+jets after HitFit, $\sigma_{t\bar{t}} = 8.16$ pb.

Chapter 12

Measured Raw Spectra

The following observables in the fully reconstructed $t\bar{t}$ system are studied:

- top quark transverse momentum (two entries per event) p_T^t;
- transverse momentum of the $t\bar{t}$ system $p_T^{t\bar{t}}$;
- $t\bar{t}$ system invariant mass $M_{t\bar{t}}$;
- fitted top-quark mass m_t;
- p_{out} (out-of-plane momentum), the projection of top quark three-momentum onto the direction perpendicular to a plane defined by the other top quark and the beam axis (z) in the laboratory frame (two entries per event), i.e. ([81] pg. 20; [82])
$$p_{\text{out}} \equiv \vec{p}_1 \cdot \frac{\vec{p}_2 \times \hat{z}}{|\vec{p}_2|} \quad \text{and} \quad 1 \leftrightarrow 2\,;$$
- $z_{t\bar{t}} \equiv p_{\text{T}}^{t1}/p_{\text{T}}^{t2}$ and $1 \leftrightarrow 2$ (two entries per event);
- $\chi_{t\bar{t}} \equiv \exp|y_{t1} - y_{t2}|$, related to a similar observable in standard dijet system, which is in the massless limit proportional to $(1+\cos\theta^*)/(1-\cos\theta^*)$ [37];
- azimuthal decorrelation between the two top quarks $\Delta\phi^{t\bar{t}}$;
- and transverse momentum difference between the two top quarks $\Delta p_T^{t\bar{t}}$.

Resulting spectra are studied for the case of a fixed top quark mass in the fitter (χ^2 definition as in Eq. 10.1.2), with the exception of the top quark mass itself which uses the settings where only the proximity of leptonic and hadronic top quark masses is requested based on the χ^2 expression in Eq. 10.1.1. Spectra are presented in Figures 12.1-12.16 with the untagged case (≥ 0 b-tags) followed by distributions with at least one b-tag.

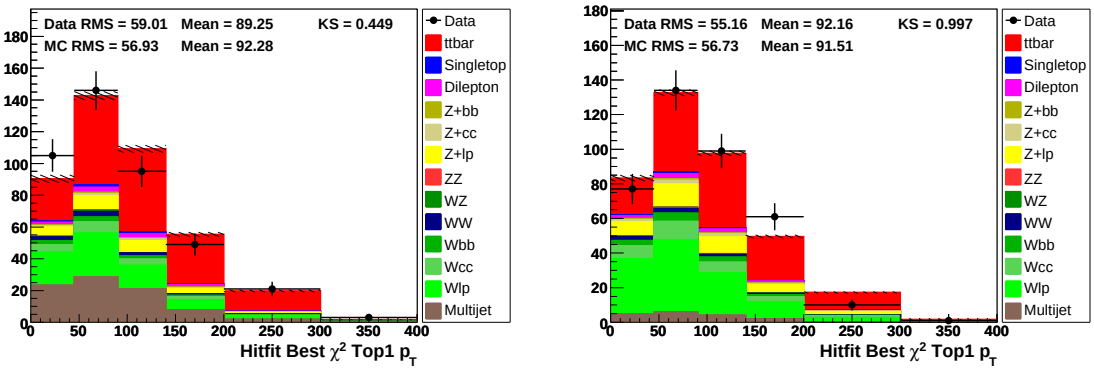

Figure 12.1: Leptonic top p_{T}, e+jets (left) and μ+jets (right), NN-medium ≥ 0 b-tag bin. Signal model: ALPGEN.

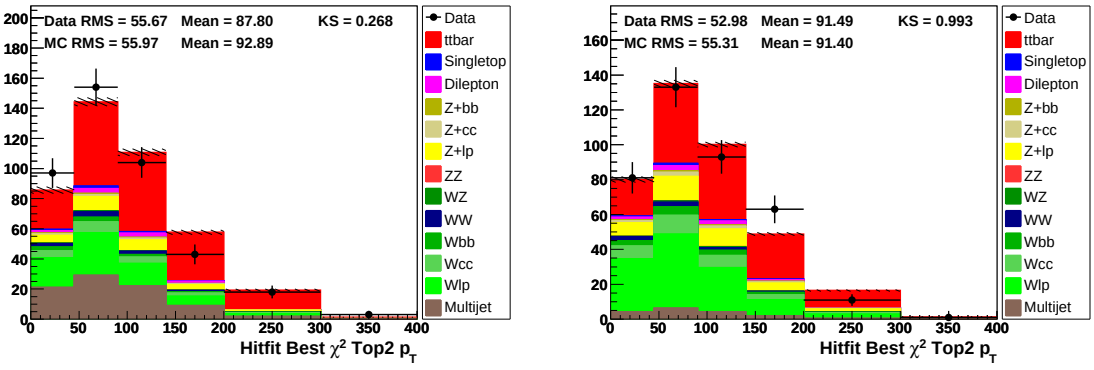

Figure 12.2: Hadronic top p_{T}, e+jets (left) and μ+jets (right), NN-medium ≥ 0 b-tag bin. Signal model: ALPGEN.

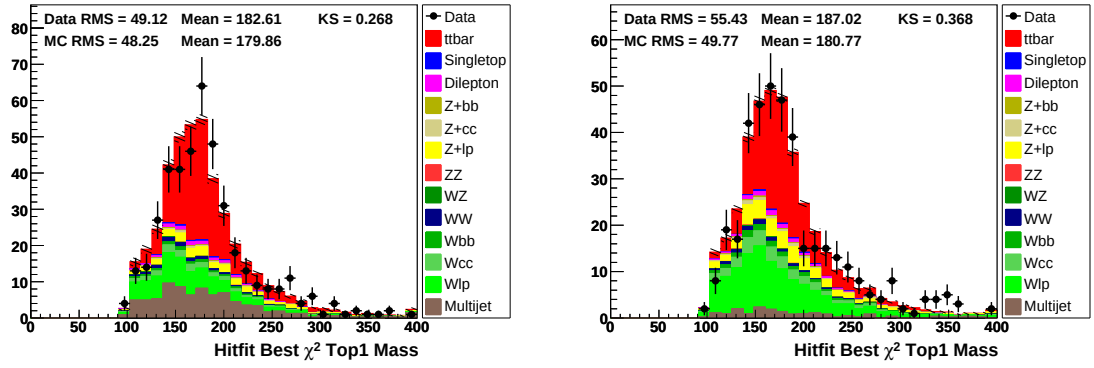

Figure 12.3: Fitted top mass, e+jets (left) and μ+jets (right), NN-medium ≥ 0 b-tag bin. Signal model: ALPGEN.

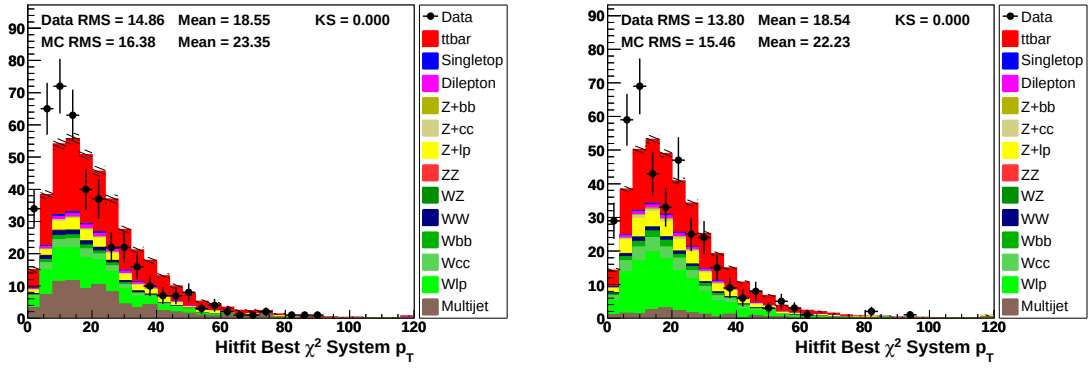

Figure 12.4: $t\bar{t}$ p_{T}, e+jets (left) and μ+jets (right), NN-medium ≥ 0 b-tag bin. Signal model: ALPGEN.

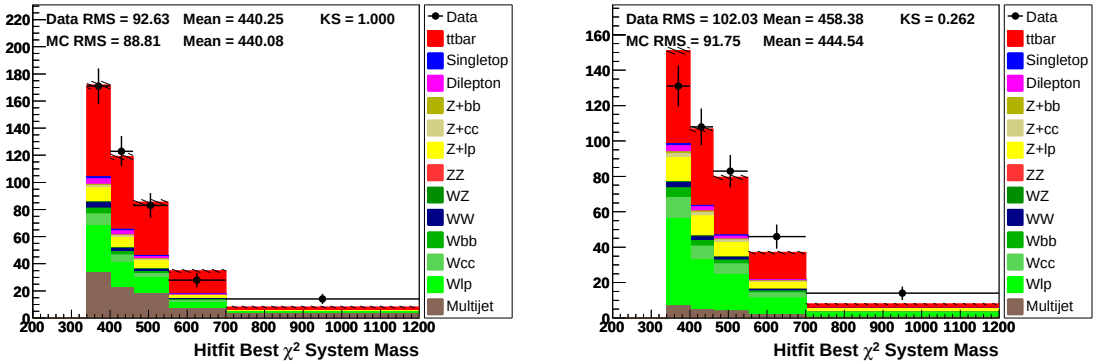

Figure 12.5: $t\bar{t}$ mass, e+jets (left) and μ+jets (right), NN-medium ≥ 0 b-tag bin. Signal model: ALPGEN.

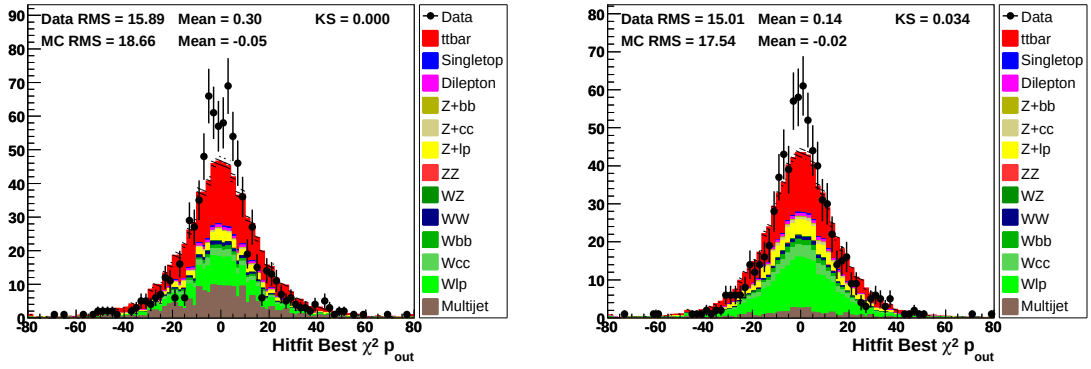

Figure 12.6: p_{out}, e+jets (left) and μ+jets (right), NN-medium ≥ 0 b-tag bin. Signal model: ALPGEN.

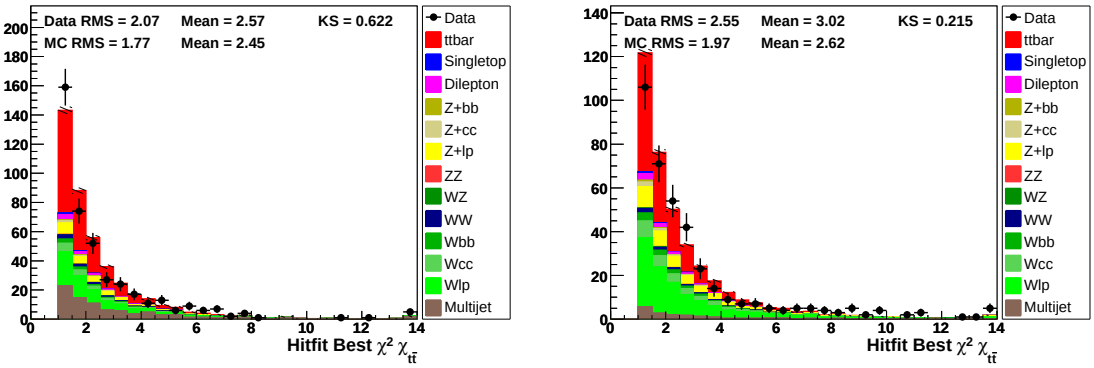

Figure 12.7: $\chi_{t\bar{t}}$, e+jets (left) and μ+jets (right), NN-medium ≥ 0 b-tag bin. Signal model: ALPGEN.

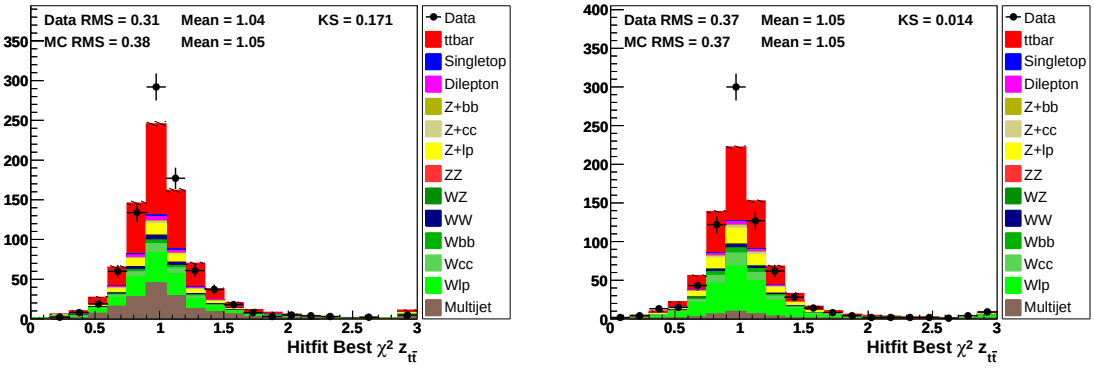

Figure 12.8: $z_{t\bar{t}}$, e+jets (left) and μ+jets (right), NN-medium ≥ 0 b-tag bin. Signal model: ALPGEN.

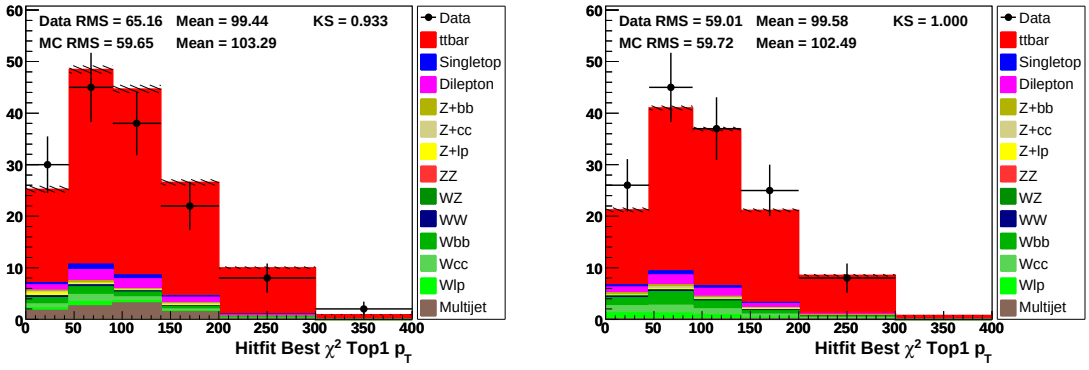

Figure 12.9: Leptonic top p_{T}, e+jets (left) and μ+jets (right), NN-medium ≥ 1 b-tag bin. Signal model: ALPGEN.

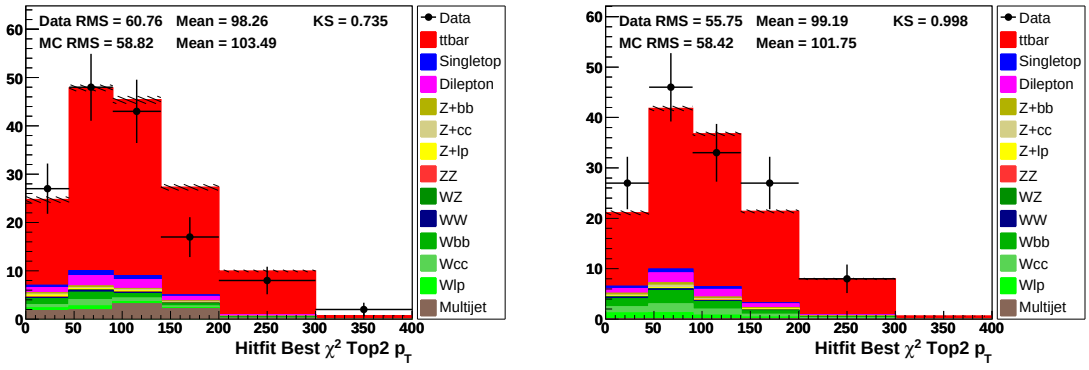

Figure 12.10: Hadronic top p_{T}, e+jets (left) and μ+jets (right), NN-medium ≥ 1 b-tag bin. Signal model: ALPGEN.

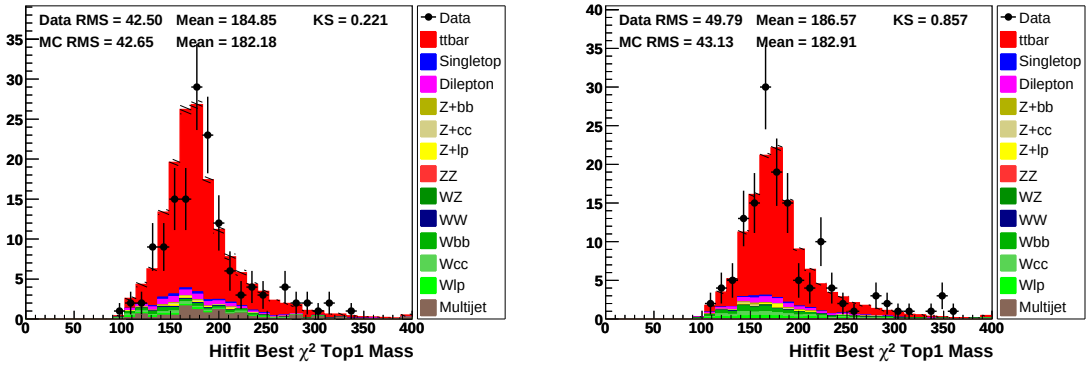

Figure 12.11: Fitted top mass, e+jets (left) and μ+jets (right), NN-medium ≥ 1 b-tag bin. Signal model: ALPGEN.

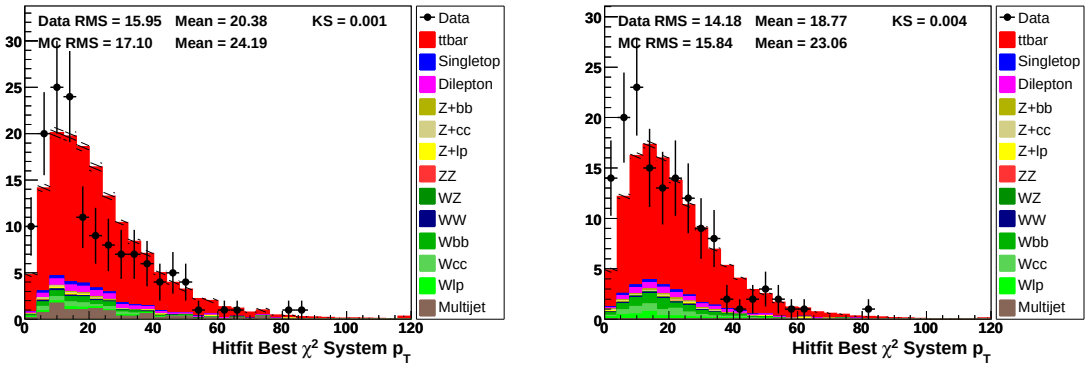

Figure 12.12: $t\bar{t}$ p_{T}, e+jets (left) and μ+jets (right), NN-medium ≥ 1 b-tag bin. Signal model: ALPGEN.

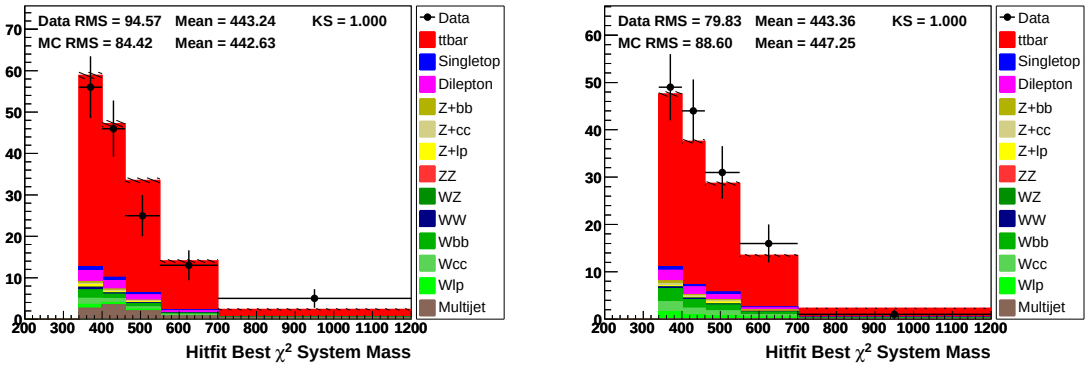

Figure 12.13: $t\bar{t}$ mass, e+jets (left) and μ+jets (right), NN-medium ≥ 1 b-tag bin. Signal model: ALPGEN.

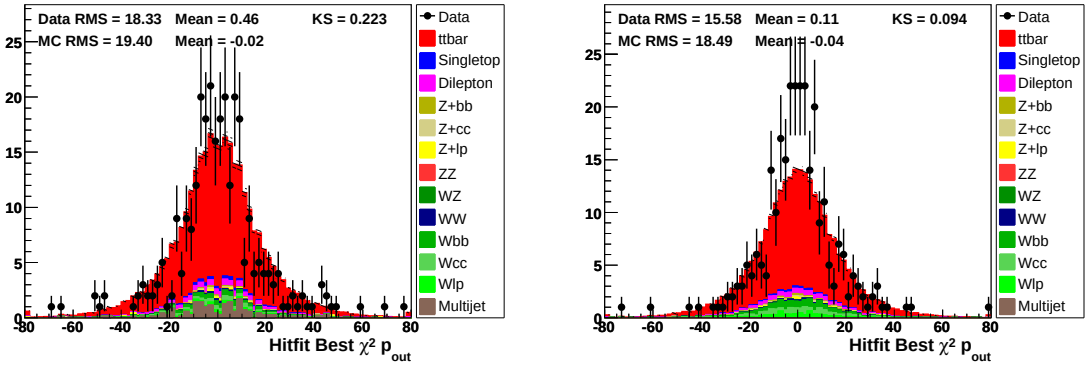

Figure 12.14: p_{out}, e+jets (left) and μ+jets (right), NN-medium ≥ 1 b-tag bin. Signal model: ALPGEN.

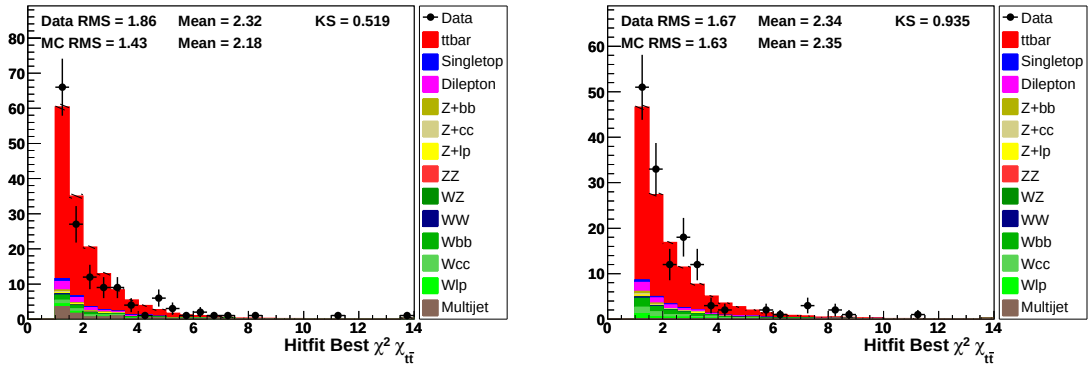

Figure 12.15: $\chi_{t\bar{t}}$, e+jets (left) and μ+jets (right), NN-medium ≥ 1 b-tag bin. Signal model: ALPGEN.

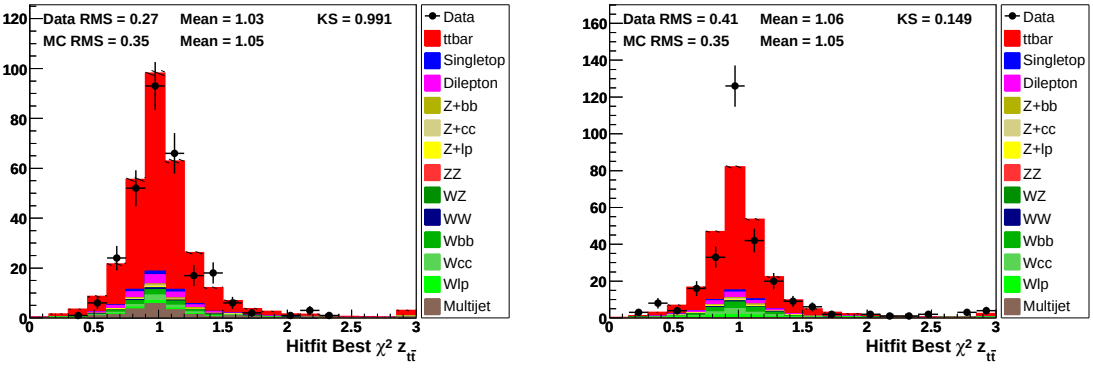

Figure 12.16: $z_{t\bar{t}}$, e+jets (left) and μ+jets (right), NN-medium ≥ 1 b-tag bin. Signal model: ALPGEN.

Chapter 13

Background Subtraction

13.1 Purity Correction

In order to avoid bin-by-bin fluctuations in poorly populated background models (e.g. the multijet sample, which is taken from data), a smooth continuous method to subtract the summed background is employed. Using all modelled backgrounds and the signal Monte Carlo, differential purity is fitted in bins of each variable of interest:

$$\mathcal{P}[x] \equiv \mathcal{S}/(\mathcal{S}+\mathcal{B})[x]$$

and applied as a smooth multiplicative factor to the data distribution. This way, subtracted data, or background-corrected data, distribution is obtained. This is illustrated in Figure 13.1 for the case of leptonic top quark p_{T} in the e+jets channel, including the fit error (which however is not propagated).

13.2 Background-Subtracted Spectra

Figures in this section show distributions of interest before and after the background subtraction using the purity fit technique. Original data is compared to the sum of signal and all background sources while purity-corrected data is compared to signal full detector simulation only.

Figures 13.2-13.10 show the combined ℓ+jets results while plots documenting the purity-based background subtraction in individual e+jets and μ+jets channels are located in Appendix A in Figures A.1-A.18.

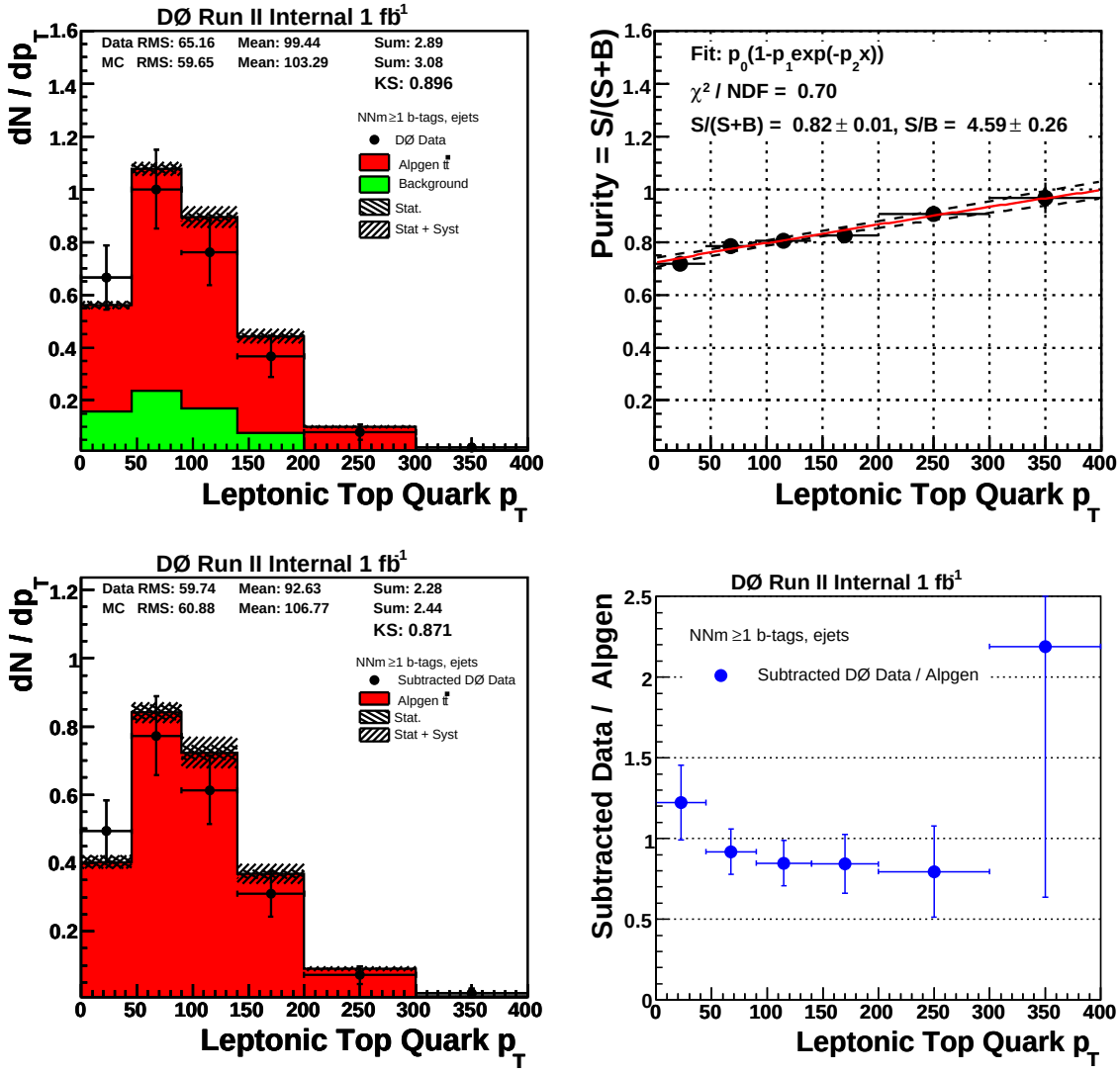

Figure 13.1: Background correction for leptonic top quark p_{T} in e+jets, NN-medium ≥ 1 b-tag bin. Top left: stacked signal and background spectra compared to data. Top right: the purity fit and fit uncertainty (dashed). Bottom left: using the fit, background-subtracted data compared to signal simulation only. Bottom right: subtracted data divided by the signal distribution. Signal model: ALPGEN.

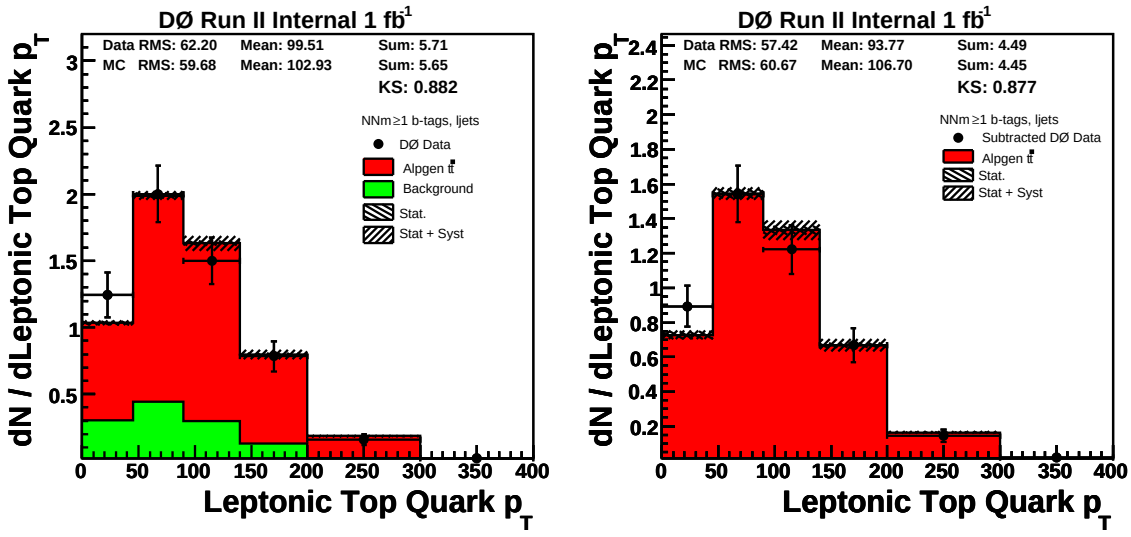

Figure 13.2: Background correction for leptonic top p_{T}, ℓ+jets NN-medium ≥ 1 b-tag bin. Signal model: ALPGEN.

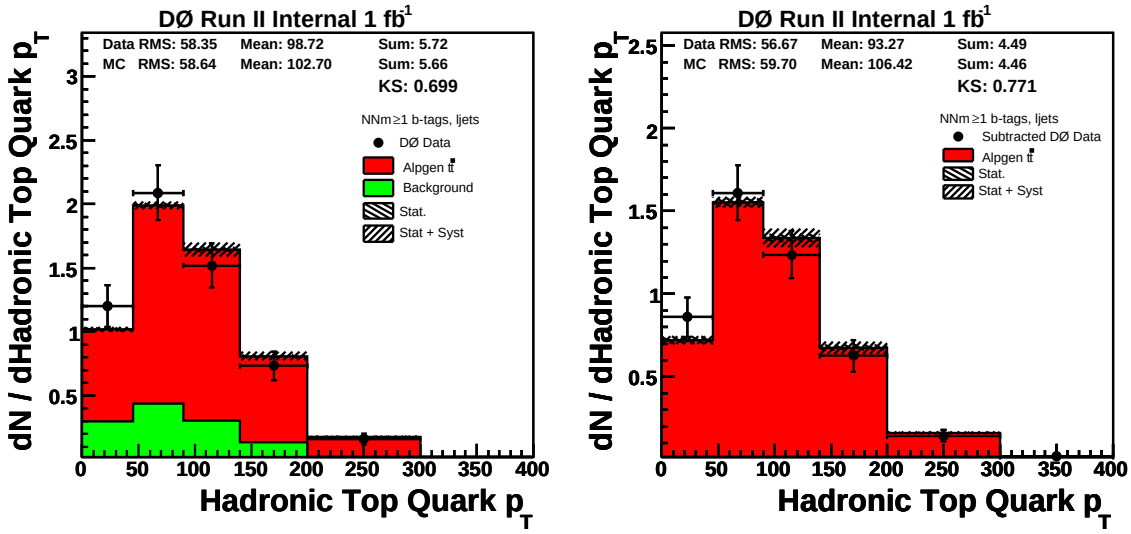

Figure 13.3: Background correction for hadronic top p_{T}, ℓ+jets NN-medium ≥ 1 b-tag bin. Signal model: ALPGEN.

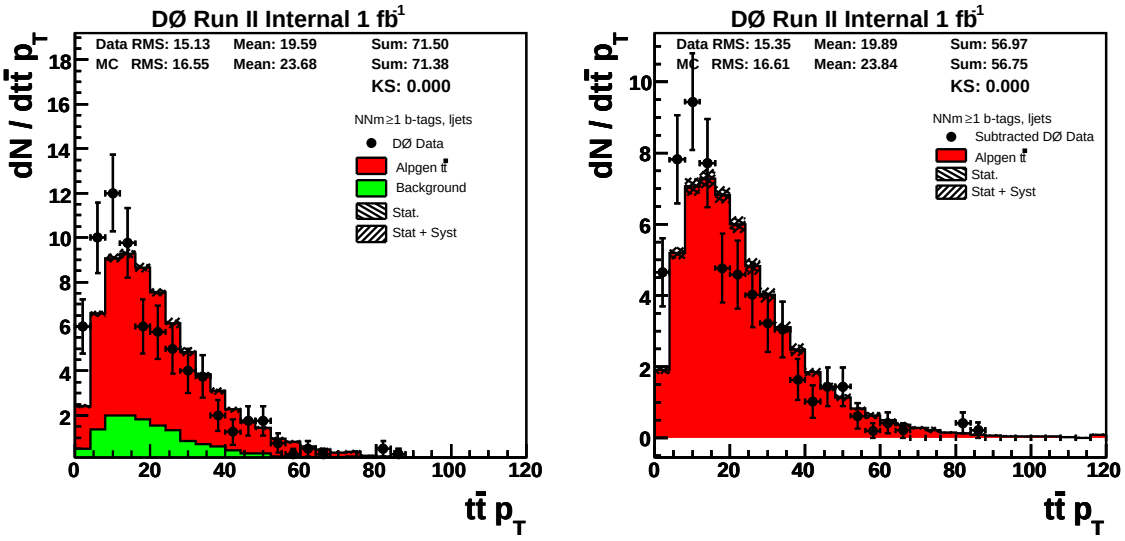

Figure 13.4: Background correction for $t\bar{t}$ system p_{T}, ℓ+jets NN-medium ≥ 1 b-tag bin. Signal model: ALPGEN.

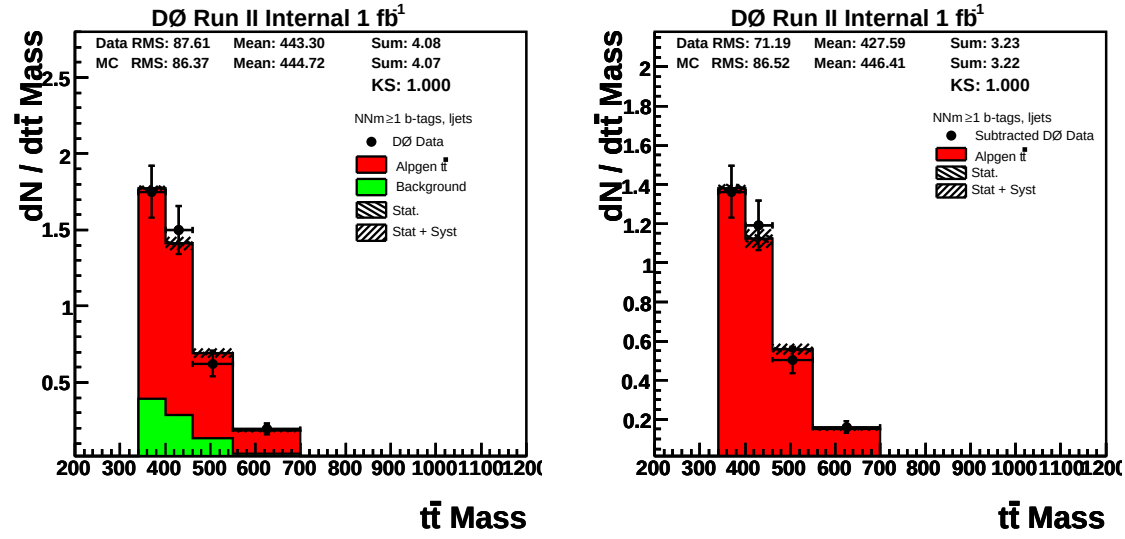

Figure 13.5: Background correction for $t\bar{t}$ system mass, ℓ+jets NN-medium ≥ 1 b-tag bin. Signal model: ALPGEN.

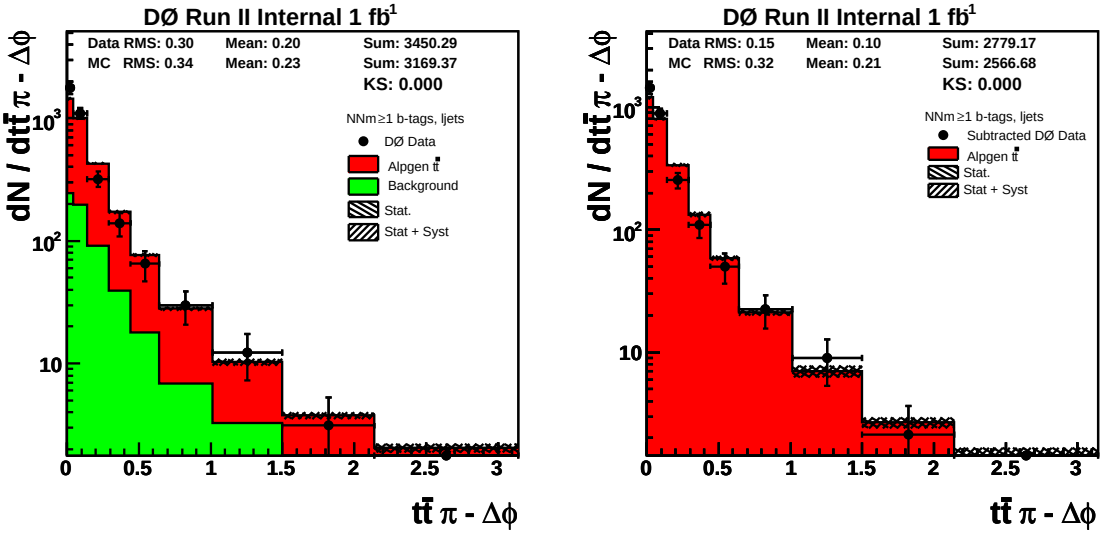

Figure 13.6: Background correction for $\Delta\phi_{t\bar{t}}$, ℓ+jets NN-medium ≥ 1 b-tag bin. Signal model: ALPGEN.

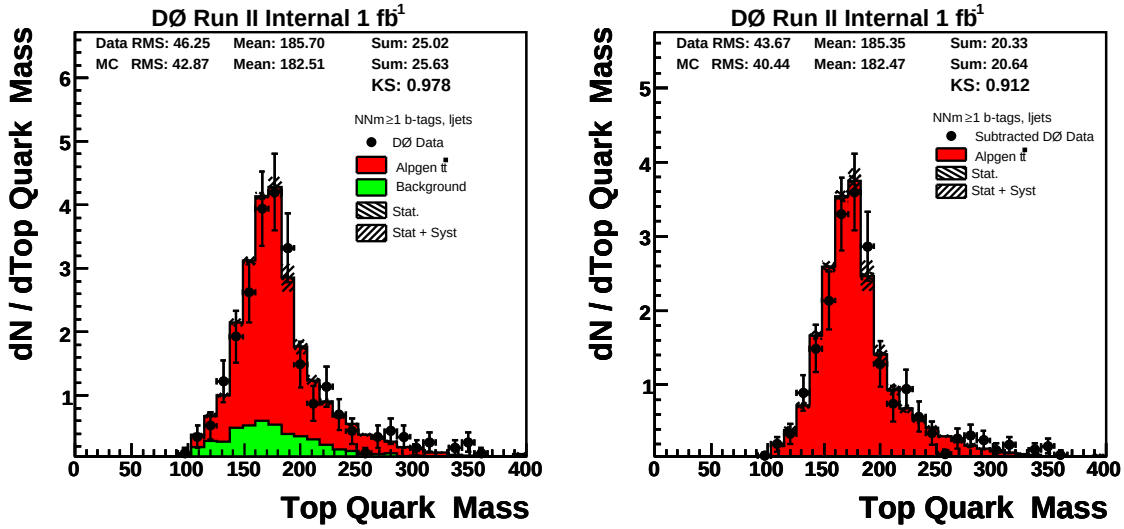

Figure 13.7: Background correction for fitted top mass, ℓ+jets NN-medium ≥ 1 b-tag bin. Signal model: ALPGEN.

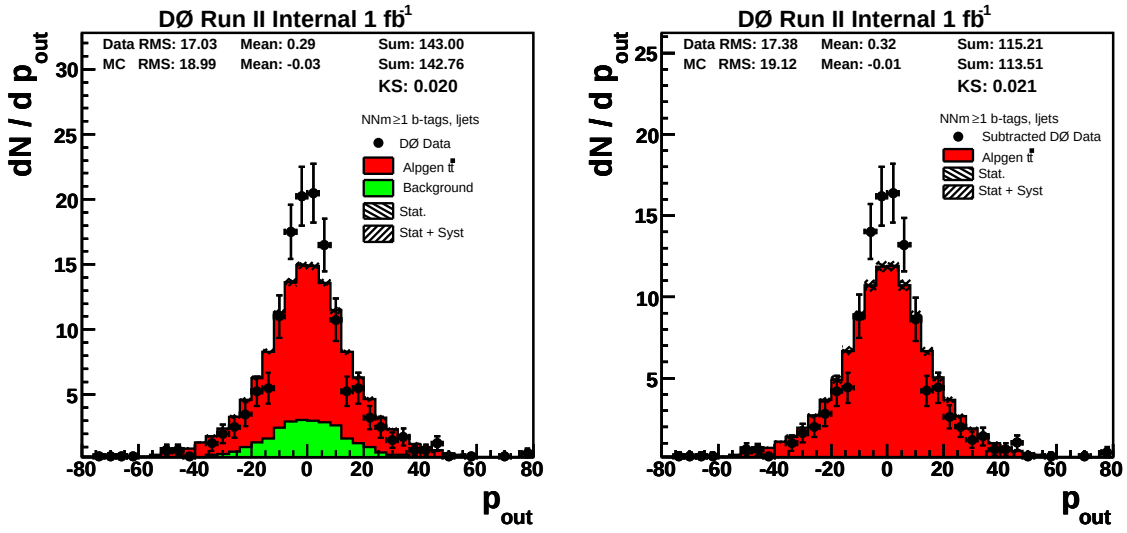

Figure 13.8: Background correction for p_{out}, ℓ+jets NN-medium ≥ 1 b-tag bin. Signal model: ALPGEN.

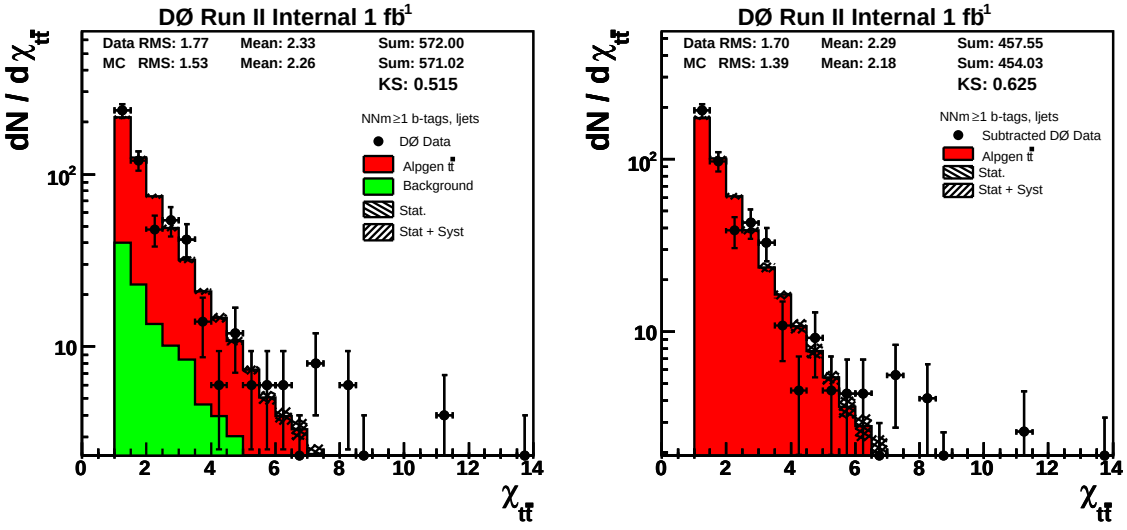

Figure 13.9: Background correction for $\chi_{t\bar{t}}$, ℓ+jets NN-medium ≥ 1 b-tag bin. Signal model: ALPGEN.

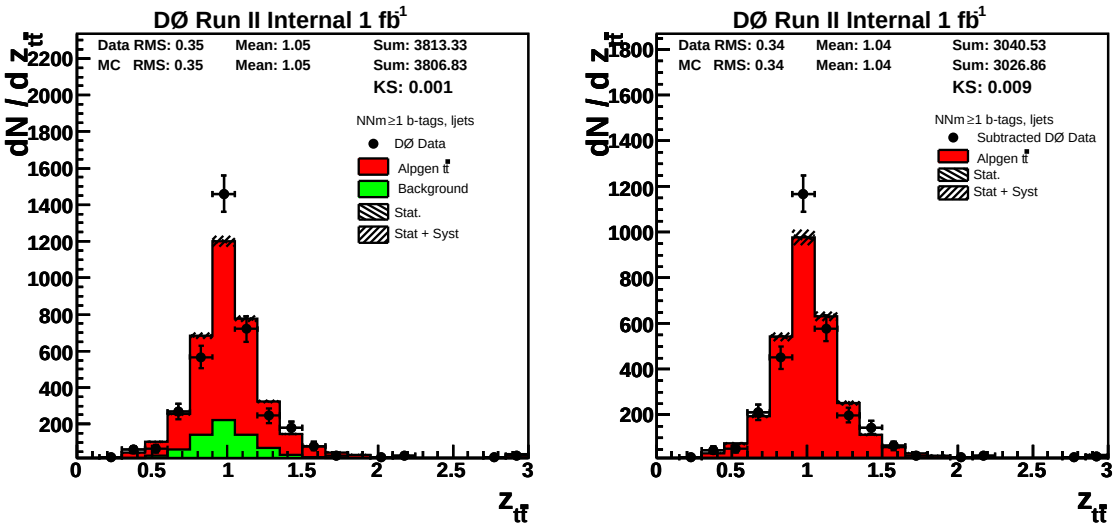

Figure 13.10: Background correction for $z_{t\bar{t}}$, ℓ+jets NN-medium ≥ 1 b-tag bin. Signal model: ALPGEN.

13.3 Comparison of Smeared Spectra to Signal Generators

First result available at this stage of the analysis is the possibility to validate to what extent leading-order generators PYTHIA and ALPGEN describe the differential distributions measured in data. While this comparison involves the purity-based background subtraction which uses the signal and background models shapes, and therefore is not completely model-independent, it still proves to be useful to show the shapes of background-corrected data divided by the signal shape as in Figures 13.11-13.14.

One can conclude that top quark p_{T} spectrum and $t\bar{t}$ system mass are in general well-modelled within a 20% uncertainty (except for the last bin of poorest statistics), while the p_{T} spectrum of the $t\bar{t}$ system is not, possibly because of using a simulation not tuned properly to describe the soft radiation in data.

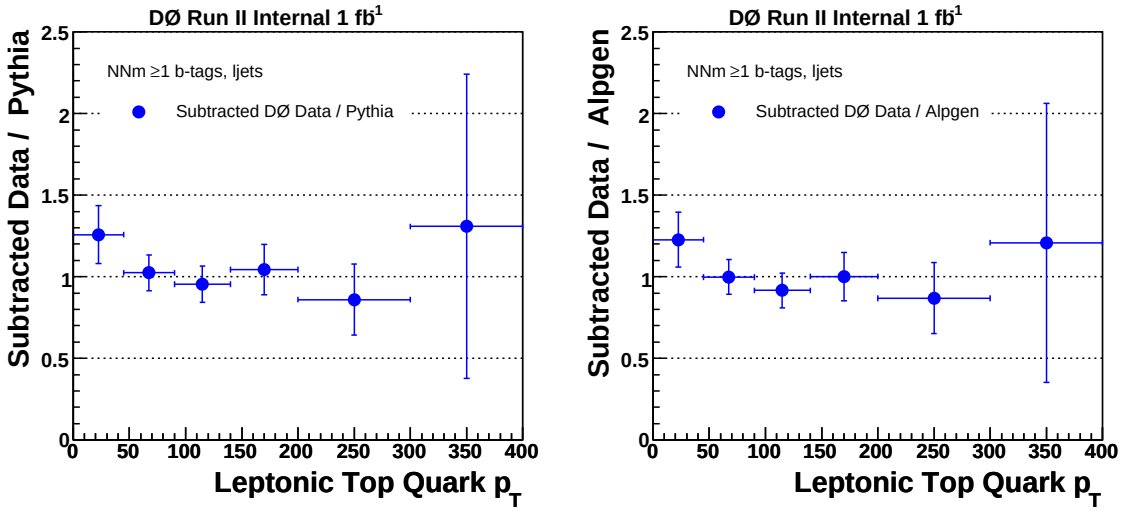

Figure 13.11: Subtracted data divided by the signal simulation for leptonic top p_{T}, ℓ+jets Medium ≥ 1 tag bin. Signal model: PYTHIA (left), ALPGEN (right).

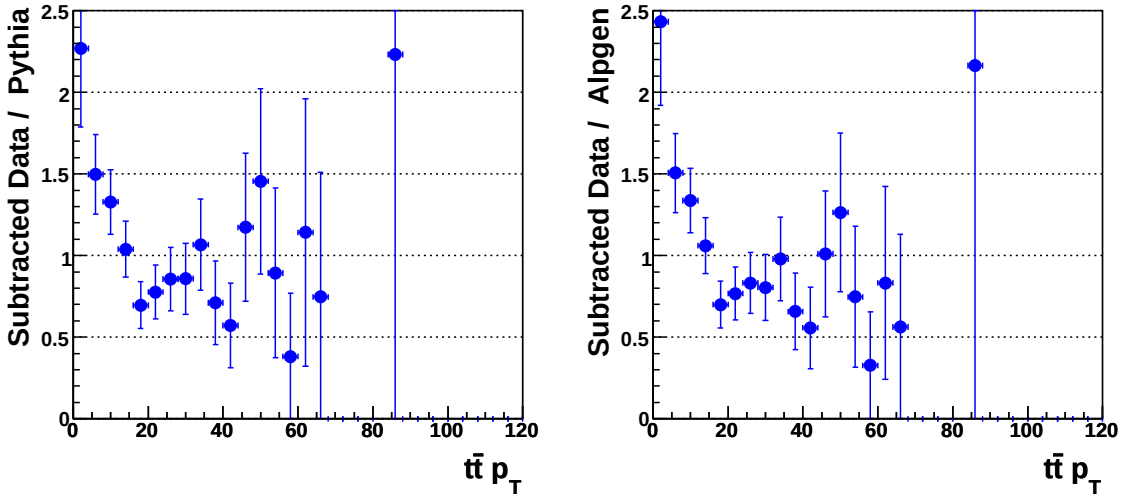

Figure 13.12: Subtracted data divided by the signal simulation for $t\bar{t}$ p_{T}, ℓ+jets Medium ≥ 1 tag bin. Signal model: PYTHIA (left), ALPGEN (right).

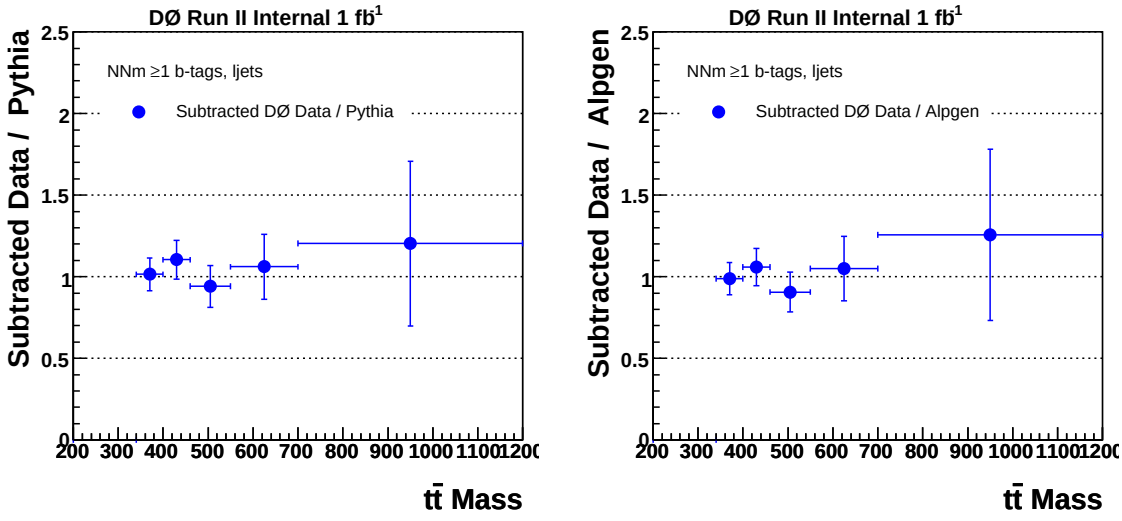

Figure 13.13: Subtracted data divided by the signal simulation for $t\bar{t}$ system mass, ℓ+jets Medium $\geq$ 1 tag bin. Signal model: PYTHIA (left), ALPGEN (right).

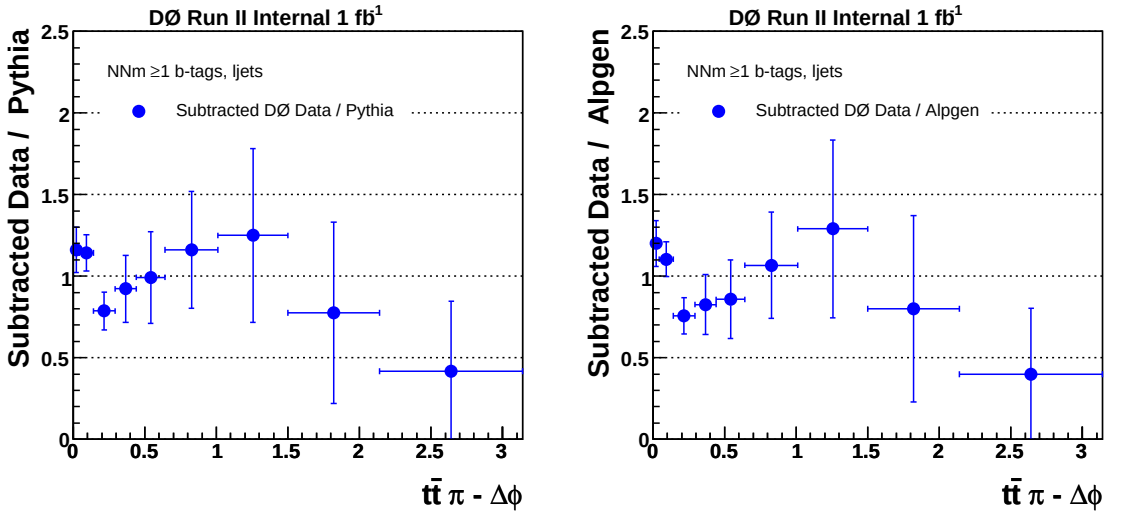

Figure 13.14: Subtracted data divided by the signal simulation for $\Delta\phi_{t\bar{t}}$, ℓ+jets Medium $\geq$ 1 tag bin. Signal model: PYTHIA (left), ALPGEN (right).

Chapter 14

Unfolding

14.1 Top Quark p_{T} Correlations

When studying the top quark p_{T}, the question of which of the leptonic, hadronic, or both, reconstructed p_{T}'s to use in the analysis, and which to unfold. Figure 14.1 shows that the correlation between the two top quark transverse momenta per event is larger than 90%, and also that there is some deviation between the hadronic and leptonic top p_{T} in the lower p_{T} region. This deviation can however be well accounted for by matching the reconstructed spectrum to the truth one using an appropriate migration matrix. Therefore, it was decided to study the leptonic and hadronic top quark p_{T} spectra separately in the unfolding procedure so that not to use the combined spectrum, where the statistical precision would be over-estimated. Also, the JES-related uncertainties appear to be larger for the hadronic top quark p_{T}, therefore the leptonic was selected as the preferred one.

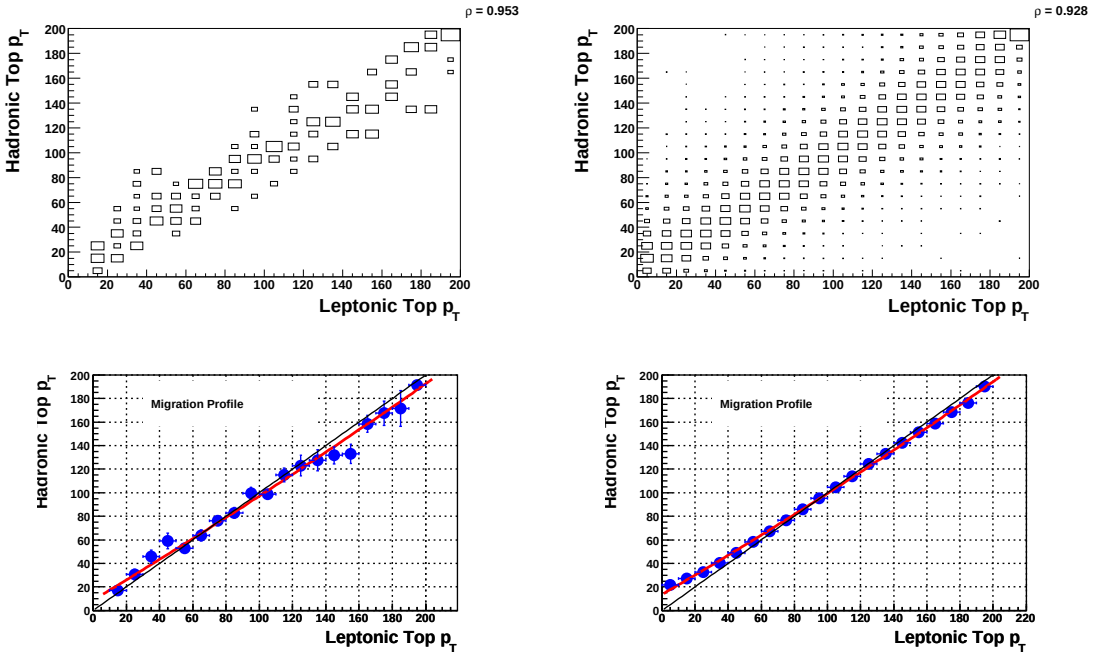

Figure 14.1: Hadronic vs. leptonic top quark p_T spectrum in e+jets for data (left) and ALPGEN (right).

14.2 The Aim of the Spectra Unfolding

The process of unfolding (often also referred to as unsmearing, or deconvolution) aims to reconstruct the spectrum of interest and correct it for finite detector resolution effects.

Due to the complexity of the final state in study (typically four jets, lepton and high missing transverse energy), the often-used ansatz method (which assumes some truth spectrum parametrisation and varies its functional parameters while smearing individual objects using their resolutions until the agreement between smeared level and data is found) is not pursued here. It is instead a regularised migration matrix inversion method which is applied to this particular analysis.

14.3 Correlations and Migration Matrix

The migration matrix is defined as the truth (here parton) versus the reconstructed (reco, as by the kinematic fitter HitFit) scatter plot. Examples of such matrices for the leptonic top quark p_{T} and the $t\bar{t}$ system mass after the b-tagging are in Figures 14.2 and 14.4. The migration purity, i.e. the fraction of events in given truth bin which stays in the same reconstructed bin, is also shown for each variable, being about 60% in most of the bins.

Further interesting properties of the matrix can be studied: the diagonality of the profile, spread (RMS) in each bin, spread divided by bin width (to check whether the binning is adequate), relative resolution here defined as the spread divided by the bin center, as well as profiles of the reconstructed distribution in a given truth bin. These are documented in Figures 14.2-14.5. In general, migration matrices are highly diagonal with a correlation coefficient of about 0.80 for the case of fixed top quark mass in the fitter, while the correlation has been observed to be reduced to about 0.70 by allowing the top mass to float.

For the purpose of merging e+jets and μ+jets channels in order to possibly unfold a larger statistics sample, the properties of each channel migrations matrix have to be studied. This is documented in Figures 14.6 and Figure 14.7, where individual channels migration matrices as well as their ratios are displayed, proving that they are indeed very similar. Therefore, spectra in the merged ℓ+jets channel are later being unfolded using a migration matrix which is a combination of the two migration matrices weighted by the number of b-tagged events in data. A cross-check is performed in Figures 14.8-14.9 in dividing e+jets and μ+jets migration matrix by the merged one to see that the result is a flat distribution with random fluctuations.

14.4 Binning Choice

The binning for the top quark p_{T} and the $t\bar{t}$ system mass distributions was chosen so that the reconstructed level RMS in each truth bin is smaller than the bin width, i.e. by requiring that the binning is coarser that the resolution, as is documented in Figures 14.3–14.5 in bottom left plots, where the width of the reconstructed profile in each truth bin divided by the bin width is indeed below 1.

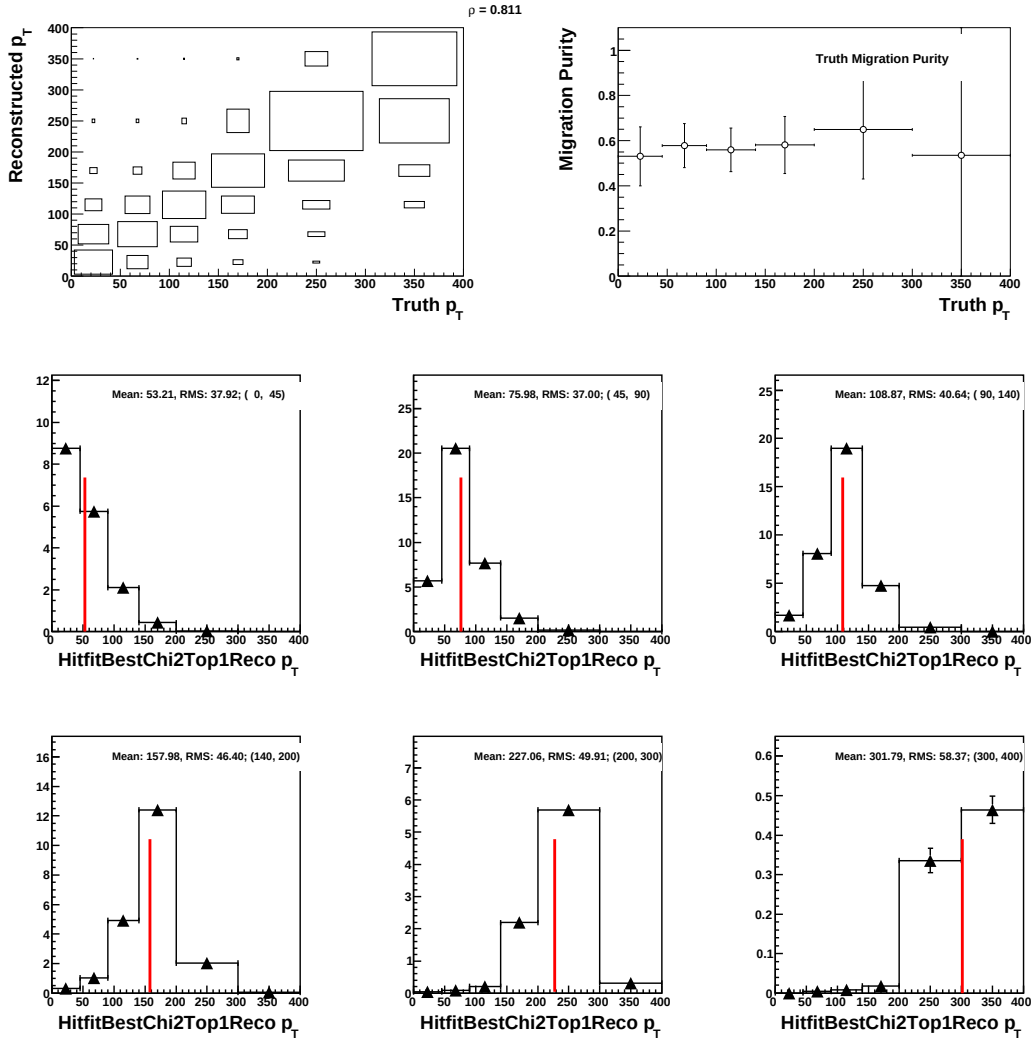

Figure 14.2: Migration matrix (reconstructed versus truth) from ALPGEN e+jets NNm ≥ 1 tag for leptonic top p_{T} (left) and migration matrix purity (right; the fraction of truth events which stay in the same bin). Bottom: reconstructed slices of the migration matrix in various truth bins, not divided by the bin width. The vertical red line in slices is positioned at the mean of the distribution.

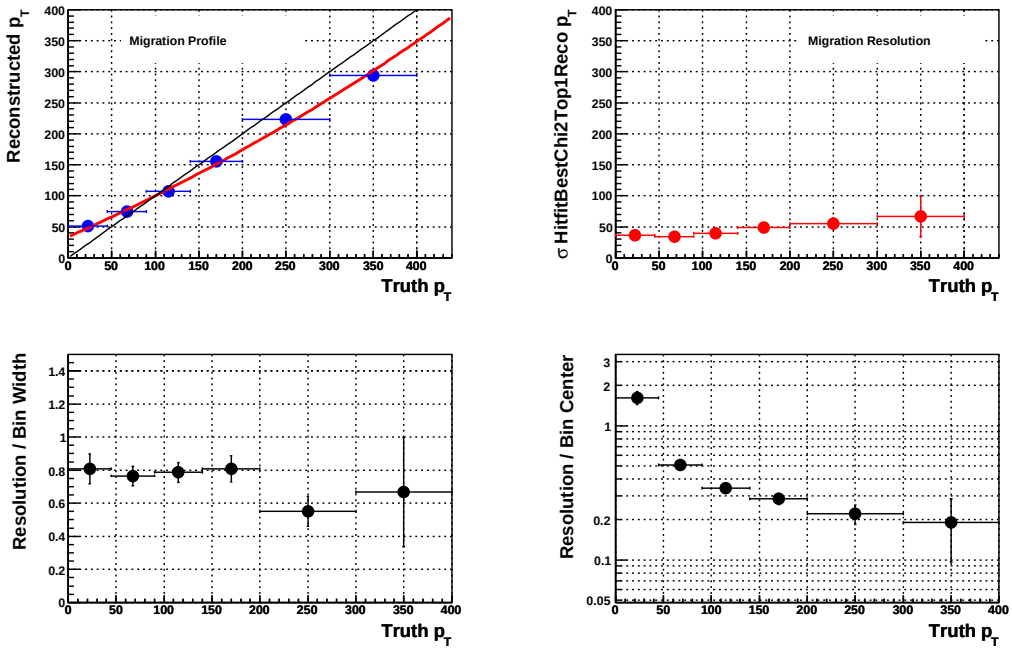

Figure 14.3: Migration matrix profile and absolute and relative reconstructed-level resolutions for the leptonic top quark p_{T} in ALPGEN e+jets. In the profile plot, thin straight line is the diagonal, bold red line a fit to the graph.

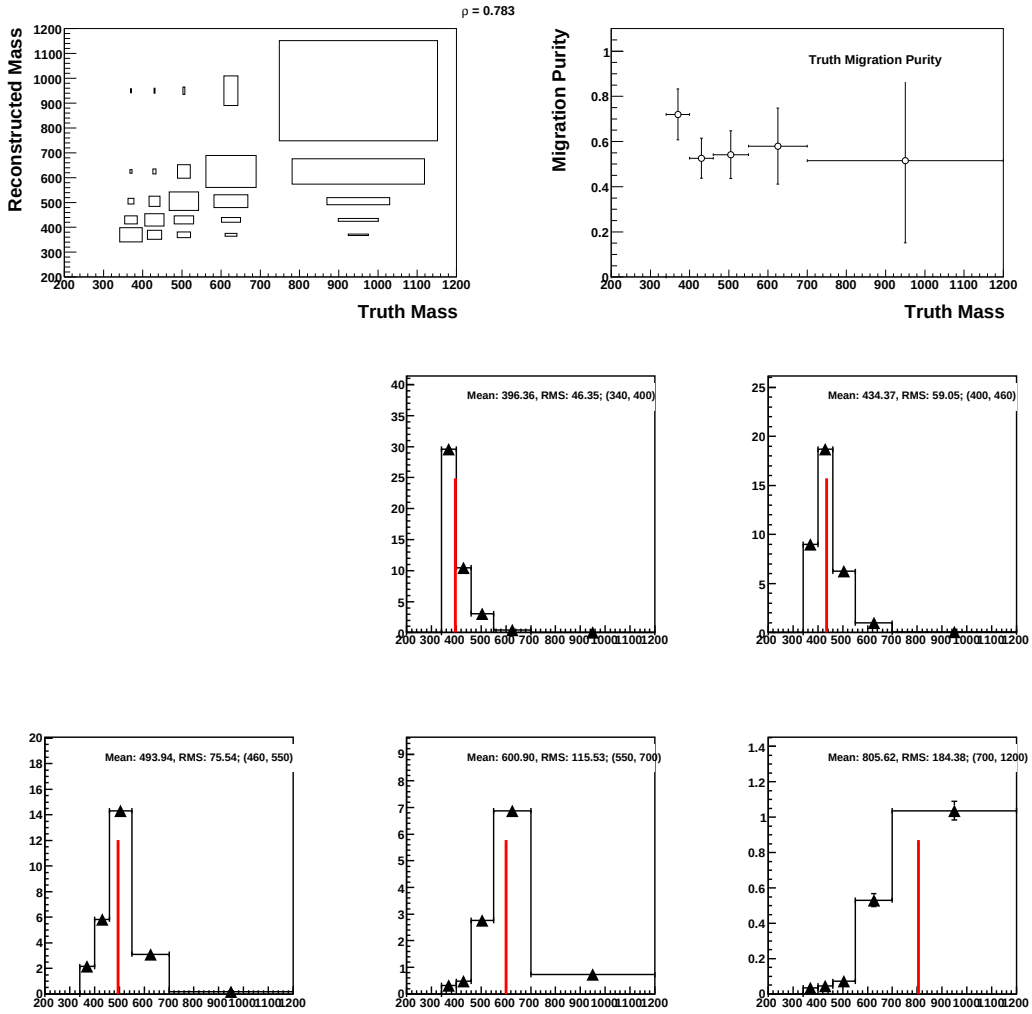

Figure 14.4: Migration matrix (reconstructed versus truth) from ALPGEN e+jets NNm ≥ 1 tag for $t\bar{t}$ system mass (left) and migration matrix purity (right; the fraction of truth events which stay in the same bin). Bottom: reconstructed slices of the migration matrix in various truth bins. The vertical red line in slices is positioned at the mean of the distribution.

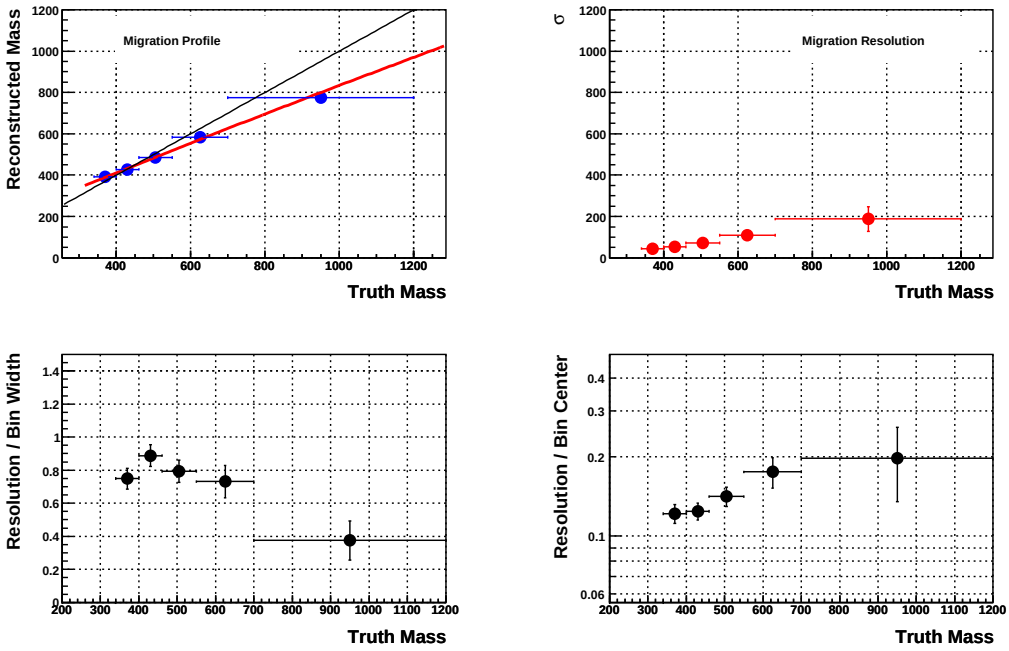

Figure 14.5: Migration matrix profile and absolute and relative reconstructed-level resolutions for the $t\bar{t}$ system mass in ALPGEN e+jets. In the profile plot, thin straight line is the diagonal, bold red line a fit to the graph.

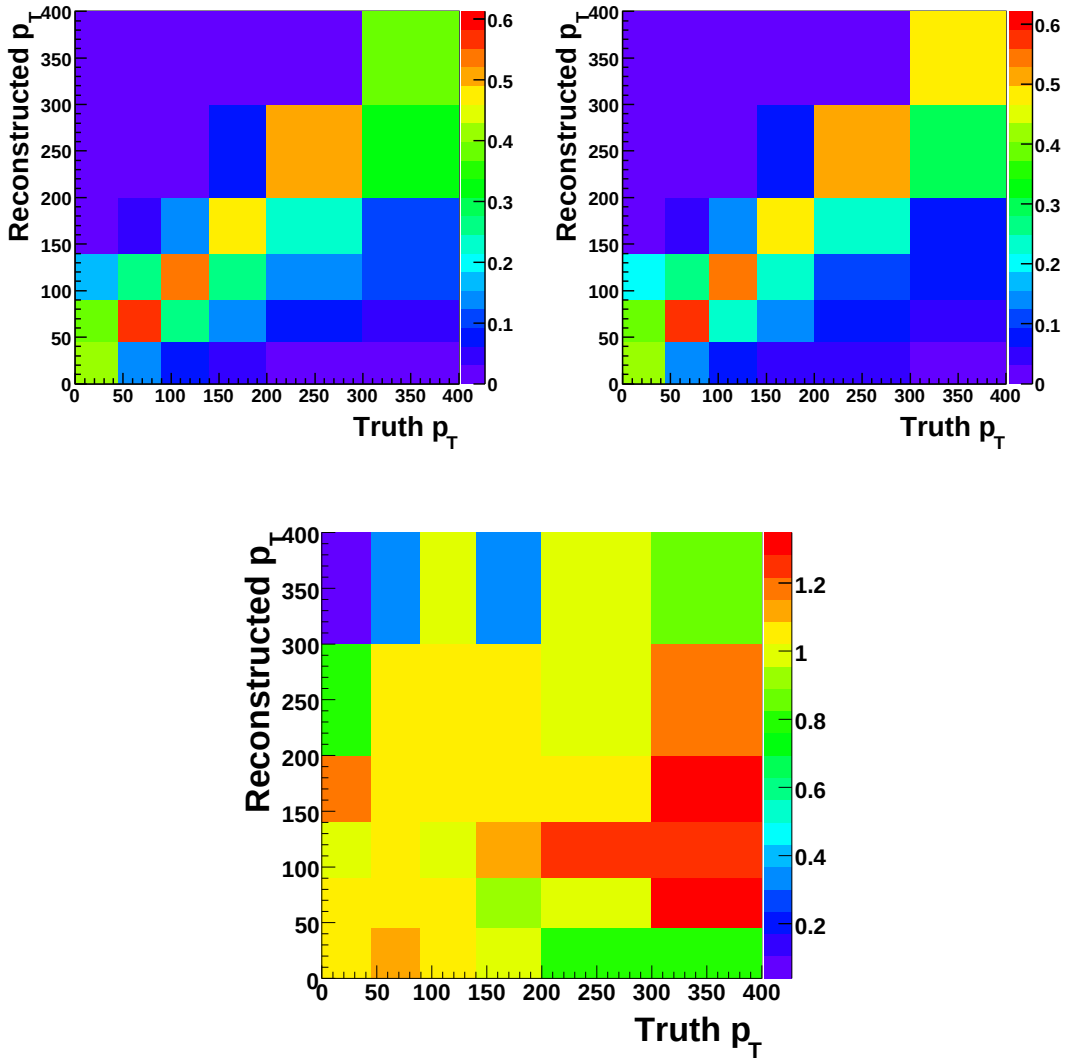

Figure 14.6: Migration matrices for e+jets (top left), μ+jets (top right) and their ratio (bottom) for leptonic top quark p_{T}, showing good uniformity and thus similarity between the channels. Signal model: ALPGEN.

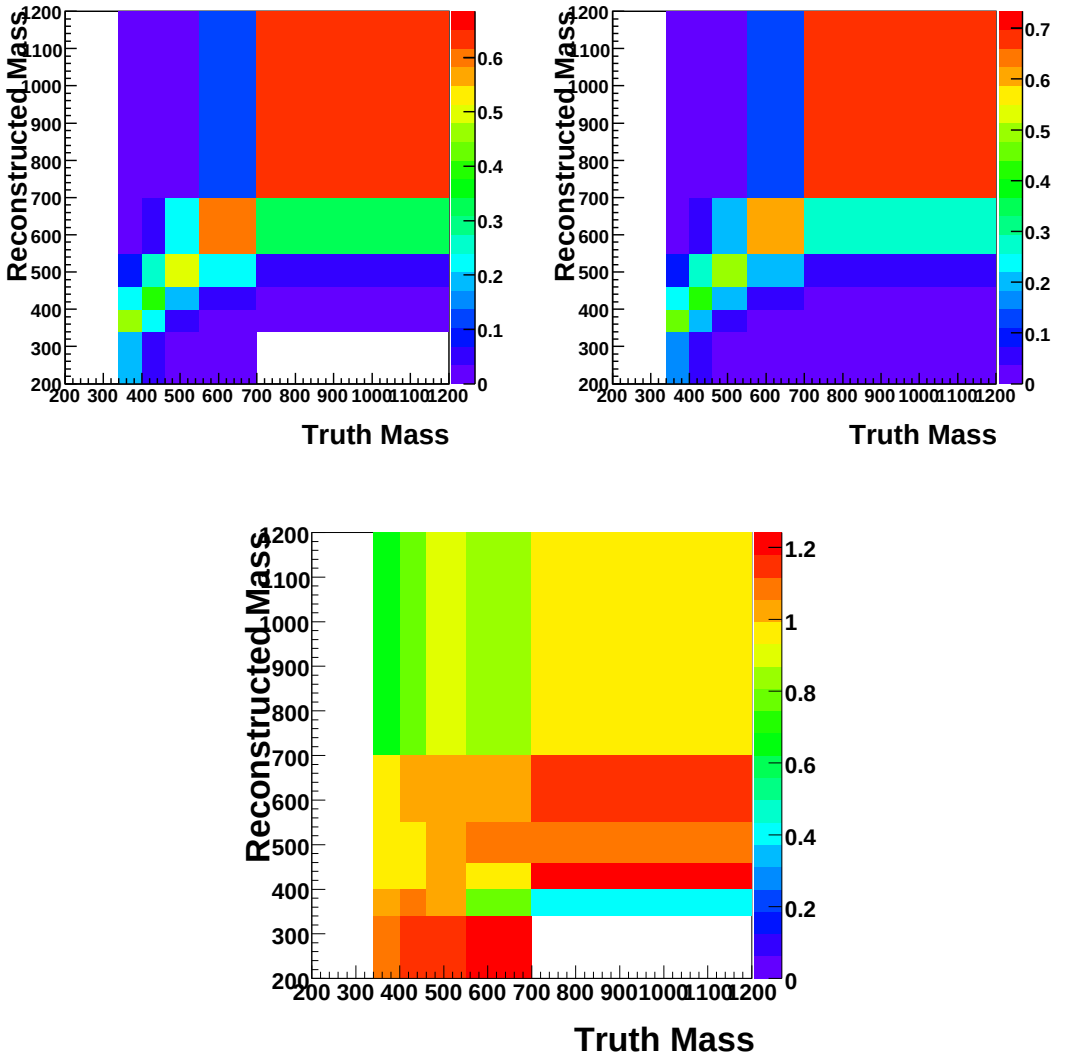

Figure 14.7: Migration matrices for e+jets (top left), μ+jets (top right) and their ratio (bottom) for $t\bar{t}$ system mass, showing good uniformity and thus similarity between the channels. Signal model: ALPGEN.

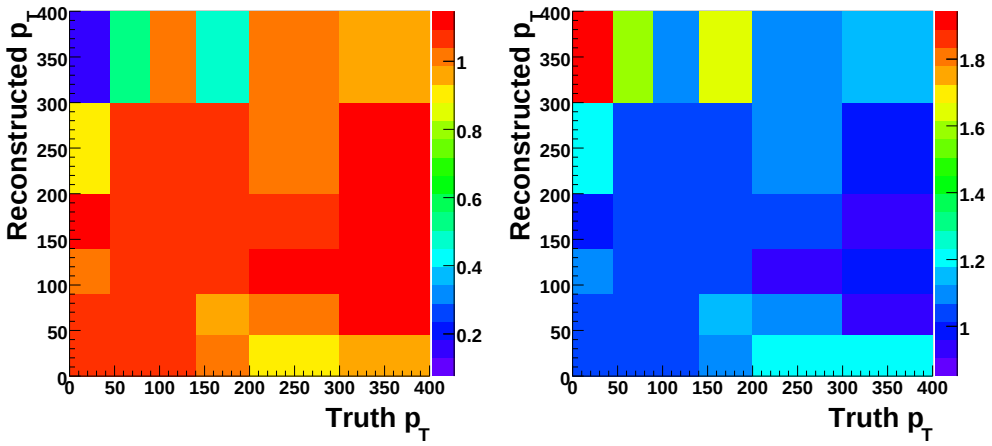

Figure 14.8: Migration matrices for e+jets (left), μ+jets (right) divided by the averaged ℓ+jets migration matrix for leptonic top quark p_{T}, showing the compatibility with a constant distribution with random fluctuations. Signal model: ALPGEN.

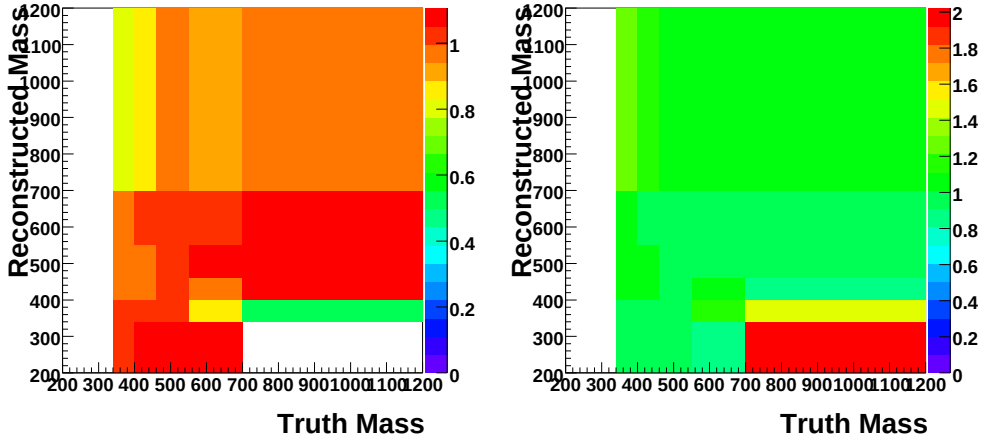

Figure 14.9: Migration matrices for e+jets (left), μ+jets (right) divided by the averaged ℓ+jets migration matrix for $t\bar{t}$ system mass, showing the compatibility with a constant distribution with random fluctuations. Signal model: ALPGEN.

14.5 GURU Unfolding Method

A regularised matrix-inversion method GURU [83] was used for the procedure of unfolding the reconstructed distributions, i.e. correcting for the detector resolution effects. This regularised matrix unfolding technique is based on a singular value matrix decomposition (SVD) [84]. A ready-to use software package by V. Kartvelishvili [83] has been widely used by the high-energy physics community, and a version interfaced to C++ by G. Hesketh [85] was adopted for this analysis.

The main input for the unfolding procedure is the migration matrix $\mathcal{M}$ (usually obtained from the simulation), which is the measure of the migration from a given truth bin to various reconstructed bins

$$\vec{b}_{\rm reco} = \hat{\mathcal{M}}\,\vec{x}_{\rm truth}\,.$$

The original migration matrix $\mathcal{M}$ filled with entries can be normalised to a probabilistic for $\hat{\mathcal{M}}$, holding the fraction of events which migrate from a given truth bin into reconstructed bins.

Ideally, applying $\hat{\mathcal{M}}^{-1}$ on a measured reconstructed distribution would give the unfolded spectrum. However, in the unfolding problem there is a danger of low-significant bins, which can lead to numerical instabilities and quickly oscillating inverted matrix. Therefore, due to finite statistics, $\mathcal{M}$ needs to be regularised and the whole procedure reformulated.

The problem is then to find the best unfolded $\vec{x}$ which minimises the expression

$$\chi^2 \equiv (\hat{\mathcal{M}}\vec{x} - \vec{b}_{\rm meas})^{\rm T}\mathcal{B}^{-1}(\hat{\mathcal{M}}\vec{x} - \vec{b}_{\rm meas})\,,$$

where $\mathcal{B}$ is a covariance matrix of the measured vector $\vec{b}_{\rm meas}$ (usually a diagonal with inverted errors of the measured spectrum).

According to the SVD theorem, a real matrix $\mathcal{A}$ can be diagonalised into a matrix with non-negative diagonal elements $\mathcal{S}$ using two orthogonal matrices

$$\mathcal{A} = \mathcal{U}\mathcal{S}\mathcal{V}^{\rm T}\,.$$

Diagonal elements of $\mathcal{S}$ are called singular values. It turns out that a rank of a matrix is the number of its non-zero singular values; small singular values can be an indication of a low-significant information compatible with zero.

Returning to the problem, as $\mathcal{B}$ is symmetrical, it is possible to diagonalise it with the SVD approach with a single matrix $\mathcal{Q}$

$$\mathcal{B} = \mathcal{Q}\mathcal{R}\mathcal{Q}^{\rm T}\,.$$

Internally, the deviation from the truth (simulation) is in fact unfolded in GURU:

$$\vec{w}:\; w_i = x_i/x_i^{\rm truth}\,.$$

After diagonalising $\mathcal{B}$, the minimisation problem in such a rotated space is simple again:

$$\chi^2 \equiv (\tilde{\mathcal{M}}\vec{w} - \tilde{b}_{\rm meas})^{\rm T}(\tilde{\mathcal{M}}\vec{w} - \tilde{b}_{\rm meas})\,.$$

where

$$\mathcal{R} \equiv {\rm diag}(1/r_i^2)\,, \quad r_i^2 > 0$$

$$\tilde{b}^j_{\rm meas} \equiv \frac{1}{r_i}\sum_j \mathcal{Q}_{ij} b^j_{\rm meas}\,, \qquad \tilde{\mathcal{M}}_{ij} \equiv \frac{1}{r_i}\sum_k \mathcal{Q}_{ik}\mathcal{M}_{kj}\,.$$

The next step is to redefine the problem in order to regularise the minimised χ^2 by adding a term proportional to second derivatives

$$\chi^2 \equiv (\tilde{\mathcal{M}}\vec{w} - \tilde{b}_{\rm meas})^{\rm T}(\tilde{\mathcal{M}}\vec{w} - \tilde{b}_{\rm meas}) + \tau\,(\mathcal{C}\vec{w})^{\rm T}(\mathcal{C}\vec{w})\,,$$

where τ is the regularisation parameter. The second derivatives matrix is motivated by the curvature defined as $\sum_i [(w_{i+1} - w_i) - (w_i - w_{i-1})]^2$, leading to the simple form of

$$C' \equiv \begin{pmatrix} 1 & 1 & \cdot & \cdot & \cdot \\ 1 & -2 & 1 & \cdot & \cdot \\ \cdot & 1 & -2 & 1 & \cdot \\ \cdot & \cdot & 1 & -2 & \cdot \\ \cdot & & & & \ddots \end{pmatrix}.$$

This matrix is however degenerate and cannot be inverted, for which purpose it is modified by a small number $\xi \approx 10^{-4} - 10^{-3}$ to

$$C \equiv \begin{pmatrix} 1+\xi & 1 & \cdot & \cdot & \cdot \\ 1 & -2+\xi & 1 & \cdot & \cdot \\ \cdot & 1 & -2+\xi & 1 & \cdot \\ \cdot & \cdot & 1 & -2+\xi & \cdots \\ \cdot & & & & \ddots \end{pmatrix}.$$

The system is now equivalent to

$$\begin{bmatrix} \tilde{\mathcal{M}} \\ \sqrt{\tau}\mathcal{C} \end{bmatrix} \vec{w} = \begin{bmatrix} \tilde{b} \\ 0 \end{bmatrix}$$

$$\begin{bmatrix} \tilde{\mathcal{M}}\mathcal{C}^{-1} \\ \sqrt{\tau}\,\mathcal{I} \end{bmatrix} \mathcal{C}\,\vec{w} = \begin{bmatrix} \tilde{b} \\ 0 \end{bmatrix}.$$

The unfolded distribution should be smooth, therefore the requirement of a small curvature (second derivatives) is a reasonable constraint used to stabilize the problem. One can now diagonalise $\hat{\mathcal{M}}\mathcal{C}^{-1}$ using SVD with orthogonal matrices $\mathcal{U}$, $\mathcal{V}$:

$$\hat{\mathcal{M}}\mathcal{C}^{-1} = \mathcal{U}\mathcal{S}\mathcal{V}^{\rm T}\,.$$

It is possible to perform a rotation so that to order diagonal elements
$\mathcal{S} = {\rm diag}(s_i), \quad s_i \le s_j \quad i \ge j$. With $\tau = 0$, one retains the original system

$$\mathcal{S}\cdot\vec{z} = \vec{d},$$

where the rotated and rescaled measured reconstructed vector reads

$$\vec{d} \equiv \mathcal{U}^{\rm T}\tilde{b}$$

and the rotated and rescaled unfolded vector

$$\vec{z} \equiv \mathcal{V}^{\rm T}\mathcal{C}\tilde{w}$$

is the solution to the problem in the rotated space. By construction, the inversion of $\mathcal{S}$ is easy

$$\mathcal{S}^{-1} = {\rm diag}(1/s_i)$$

and one can clearly identify the problematic values, which correspond to small values of s_i. The desired result for $\tau \neq 0$ can be written in a compact form

$$z_i^\tau = \frac{d_i s_i}{s_i^2 + \tau} \, .$$

The solution is regularised by τ in a similar way as using e.g. a cutoff in Fourier analyses, singularities due to small s_i's are removed.

The obvious question now arises on how to choose the value of the regularisation parameter τ? For a reasonably measured distribution, only few first d_i's are expected to be significant. Then they should fall quickly and become compatible with zero. The idea is to look for a critical index k (the effective rank of the system) where d_i becomes non-significant and set $\tau \equiv s_k^2$. For this purpose, the plot of $\log |d_i|$ is used as a guidance. The distribution is expected to be falling, and at some point start to be compatible with zero (i.e., to be much smaller than 1, with the error on the quantity being 1 in all bins). By means of the regularisation, only significant solutions will contribute to the matrix inversion and the final unfolded spectrum.

In summary, the inputs to the algorithm are the response matrix from simulation in the form of truth vs. reconstructed bin, and the spectrum to be unfolded. One has to only make the choice of the effective rank of the system based on the distribution of $\log |d_i|$.

14.5.1 The Spectrum Shape Effect

The unfolding bias with the full statistics-based simulation is evaluated for various reweighting schemes of the truth level in the migration matrix, as illustrated in Figure 14.10. The motivation of the amplitude of the order of 20% is the similar level of agreement between data and simulation spectra at the reconstructed level as shown in Section 13.3.

Using variously reweighted migration matrices at the truth level, simulation distributions are unfolded with effective ranks of 3 and 4 in the case of simulation top p_{T} and $t\bar{t}$ mass respectively, and the variation of the resulting shape as tested on ensembles (see Section 14.7) is taken as the shape systematics.

The residual shape effect expresses itself in about 2–5% variation of the unfolded spectrum, compared to the 20% injected variation of the truth spectrum in the migration matrix, therefore proves the stability of the unfolding procedure and confirming that it is mostly the resolution effect being correct for, and that one does not correct "to the simulation spectrum", but rather really accounts for the smearing effects.

The $\log |d_i|$ distributions for various reweighting schemes are in Figures 14.11–14.12 and finally the central shape of the ensembles for top quark p_{T} and $t\bar{t}$ system mass in Figures 14.13–14.14.

14.6 Unfolding the Simulation

The first check to perform is to unfold the simulation distribution and compare the unfolded result to the truth level. This is illustrated in Figures 14.15-14.18. The subtle point is that one cannot reliably unfold a simulation distribution using a migration matrix derived on the same sample. This is due to the fact that the reconstructed spectrum shape as a projection from the migration matrix and the spectrum to be unfolded are the same, and the GURU-unfolded result turns out to be trivially exactly the same as the truth level (the variation of the unfolded/truth is of the order of

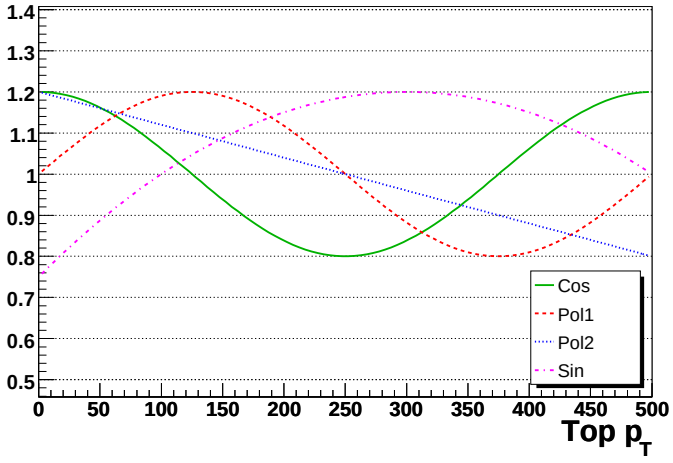

Figure 14.10: Reweighting functions used to modify the truth level weights in the migration matrix for top quark p_{T}.

$2 \cdot 10^{-6}$, at the level of numerical precision); also the $\log |d_i|$ distribution does not show any significance. For this purpose, a technique of reweighting the truth-level spectrum in the migration matrix has been applied to claim a more realistic statement on the unfolding closure. This reweighting is described in Section 14.5.1, as it is also used to evaluate a possible spectrum shape dependence of the unfolded result.

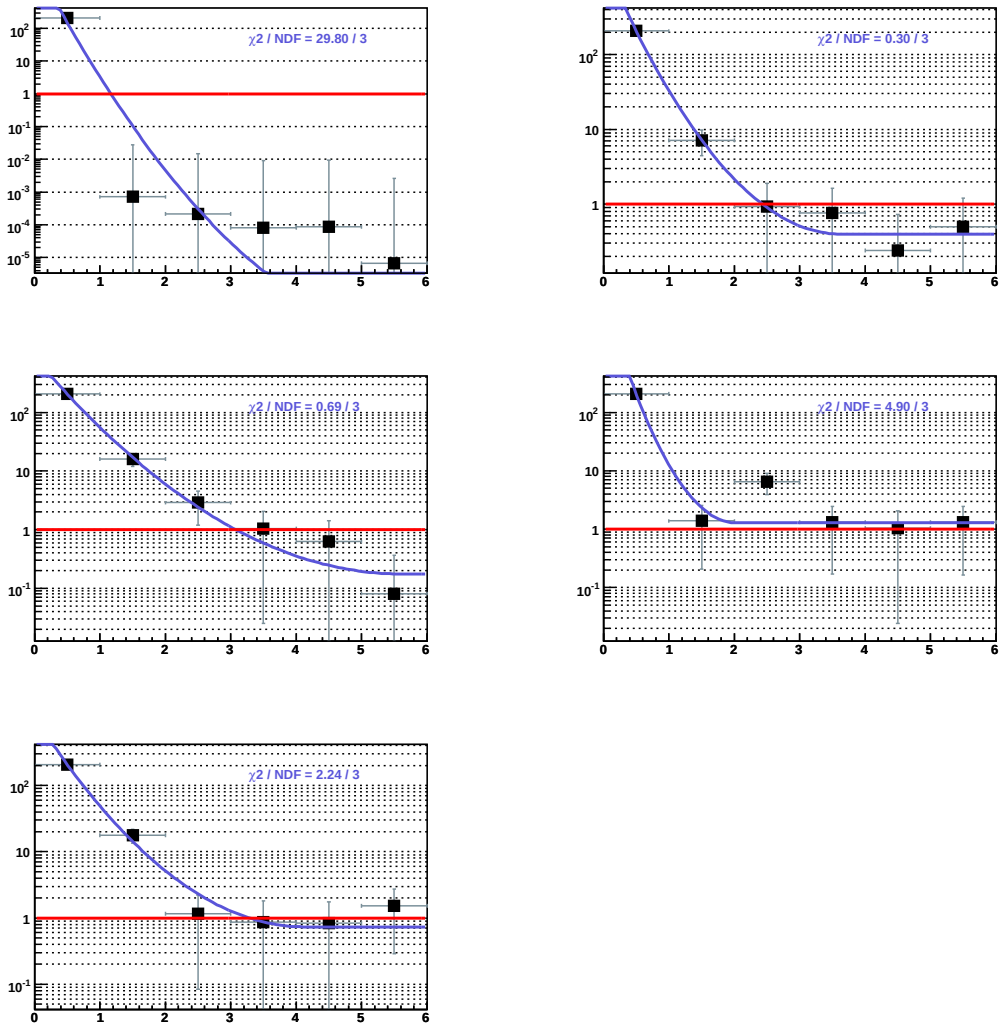

Figure 14.11: GURU's $\log|d_i|$ distribution in leptonic top p_T for full statistics ALPGEN with variously reweighted (at truth level) migration matrices in e+jets.

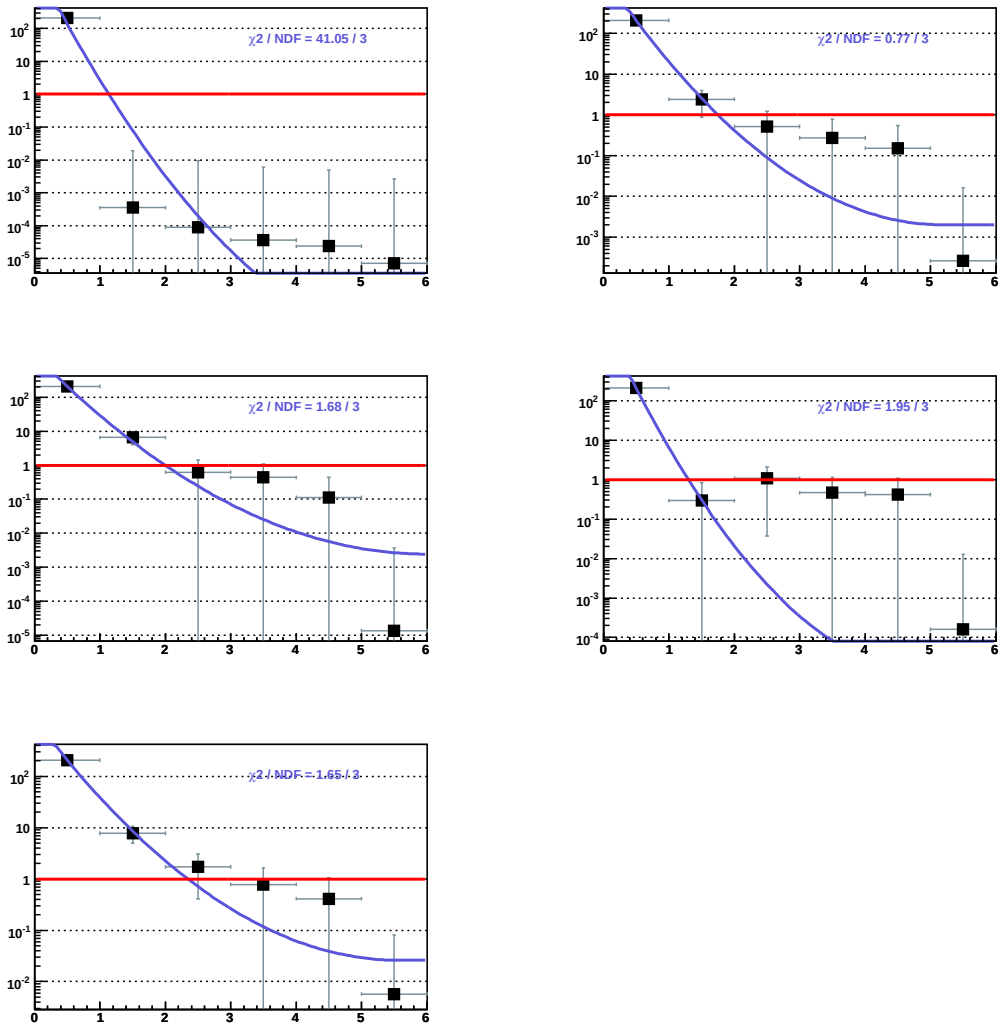

Figure 14.12: GURU's $\log|d_i|$ distribution in $t\bar{t}$ system mass for full statistics ALPGEN with variously reweighted (at truth level) migration matrices in e+jets.

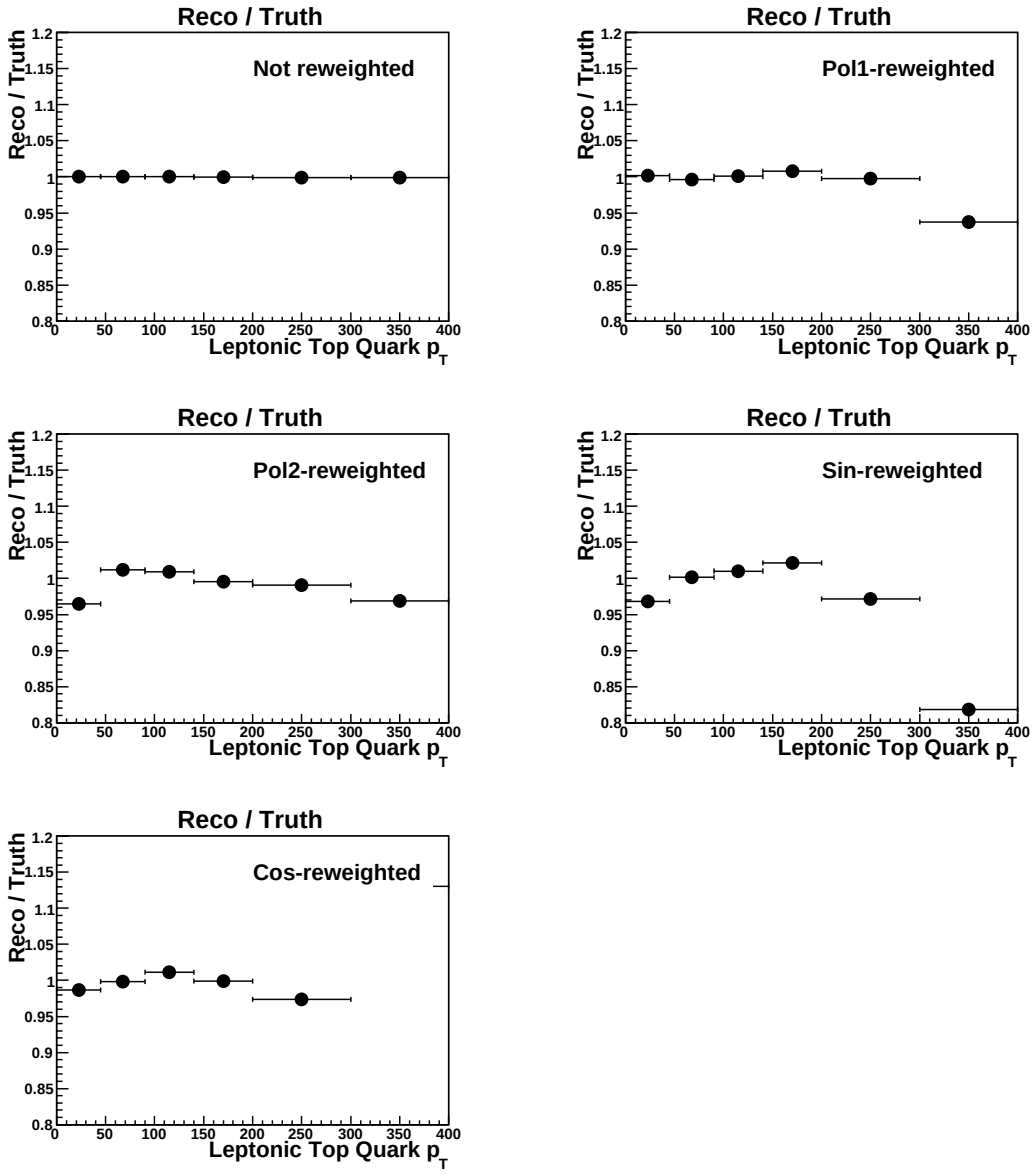

Figure 14.13: Simulation leptonic top p_{T}, unfolded full statistics ALPGEN with variously reweighted (at truth level) migration matrices, effective rank 3 in e+jets.

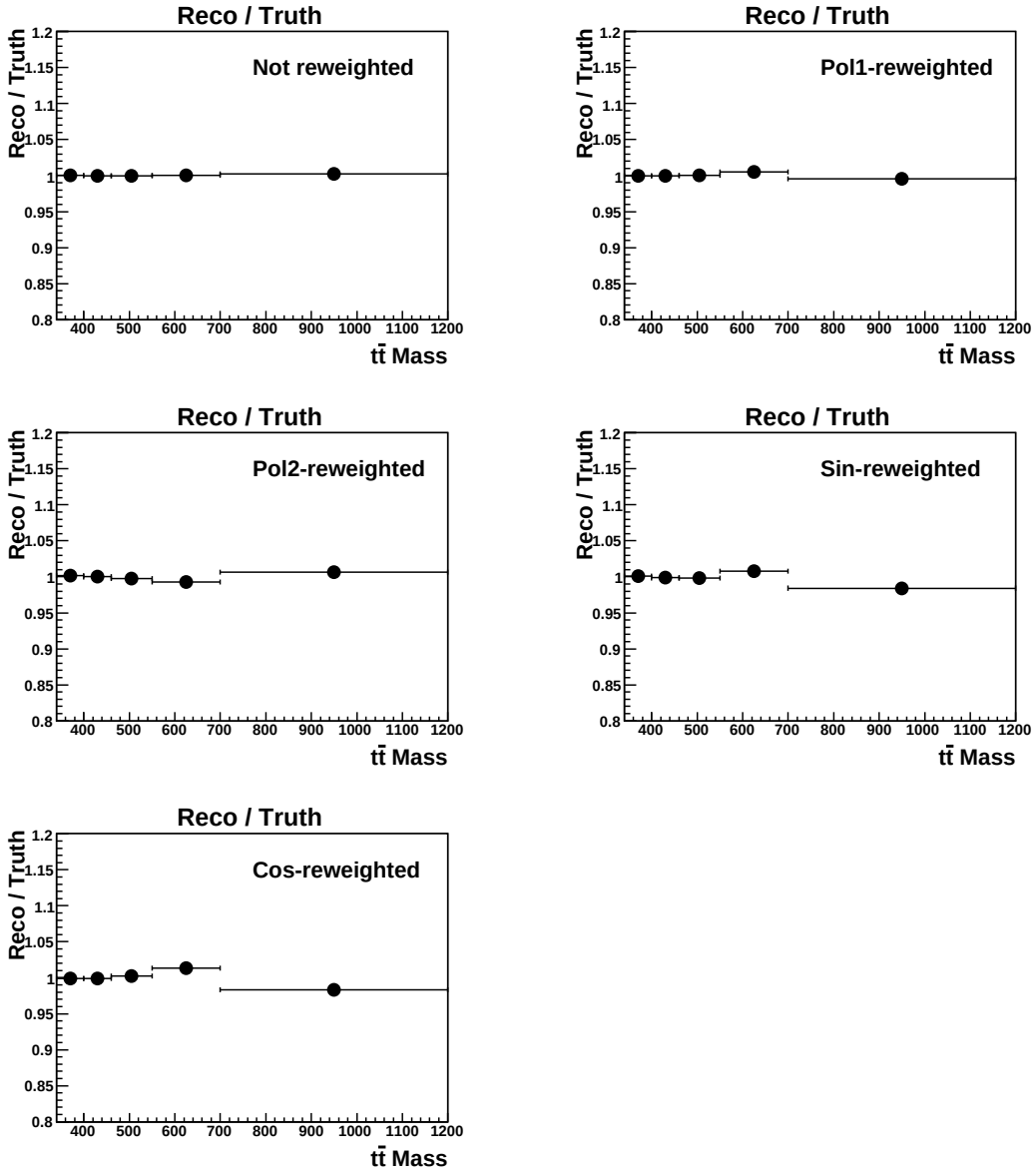

Figure 14.14: Simulation $t\bar{t}$ system mass, unfolded full statistics ALPGEN with variously reweighted (at truth level) migration matrices, effective rank 4 in e+jets.

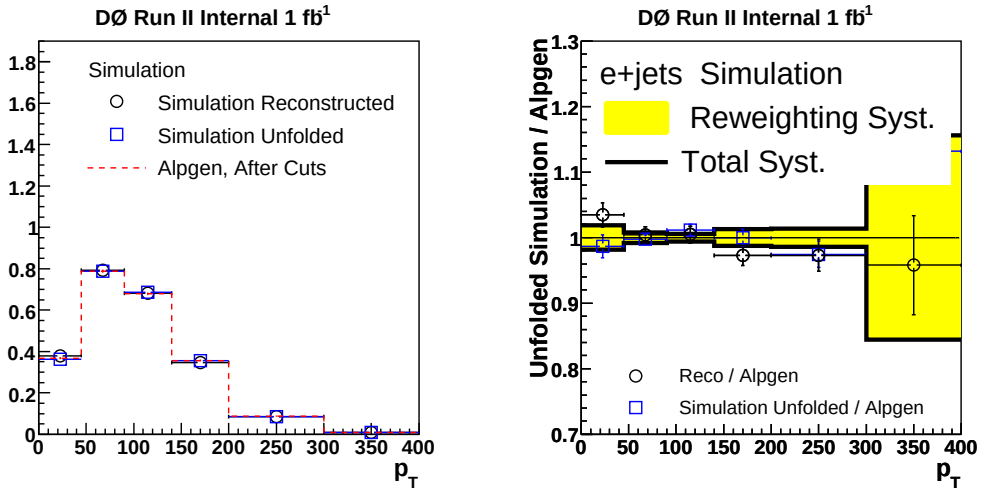

Figure 14.15: Unfolding the simulation leptonic top quark p_{T} spectrum in e+jets using the effective rank of 3. Signal model: ALPGEN, using a cosine-reweighted migration matrix at the truth-level.

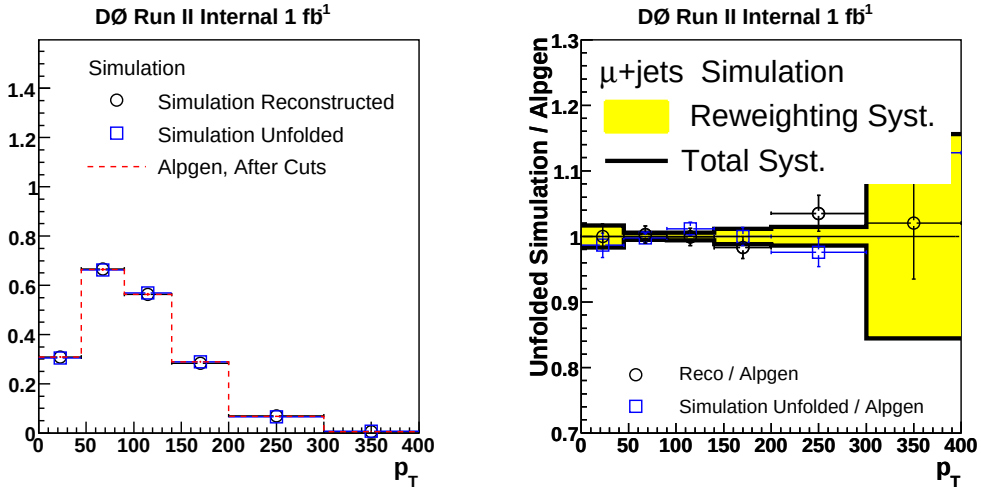

Figure 14.16: Unfolding the simulation leptonic top quark p_{T} spectrum in μ+jets using the effective rank of 3. Signal model: ALPGEN, using a cosine-reweighted migration matrix at the truth-level.

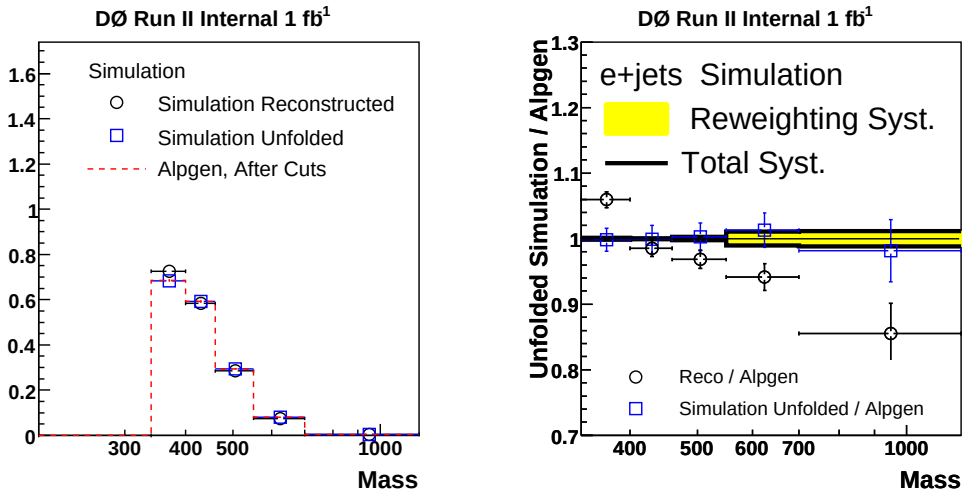

Figure 14.17: Unfolding the simulation $t\bar{t}$ system mass spectrum in e+jets using the effective rank of 4. Signal model: ALPGEN, using a cosine-reweighted migration matrix at the truth-level.

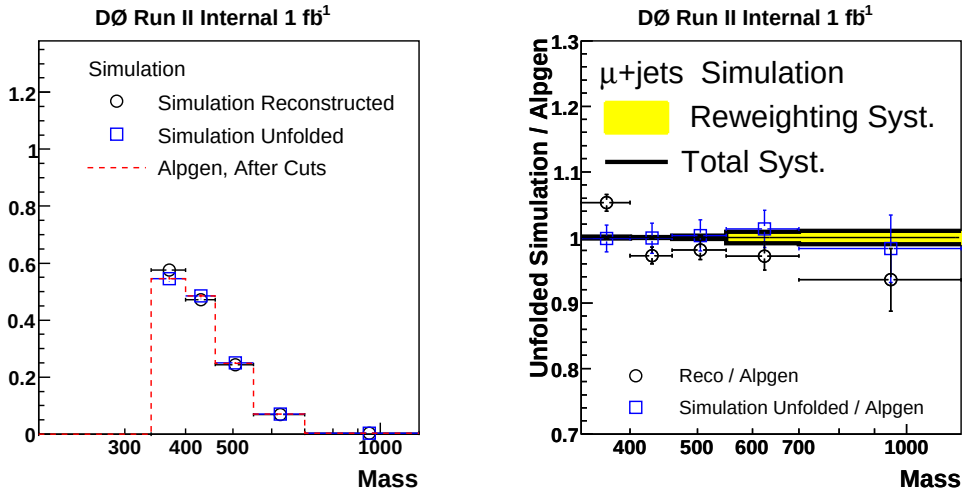

Figure 14.18: Unfolding the simulation $t\bar{t}$ system mass spectrum in μ+jets using the effective rank of 4. Signal model: ALPGEN, using a cosine-reweighted migration matrix at the truth-level.

14.7 Simulation-Based Ensemble Tests

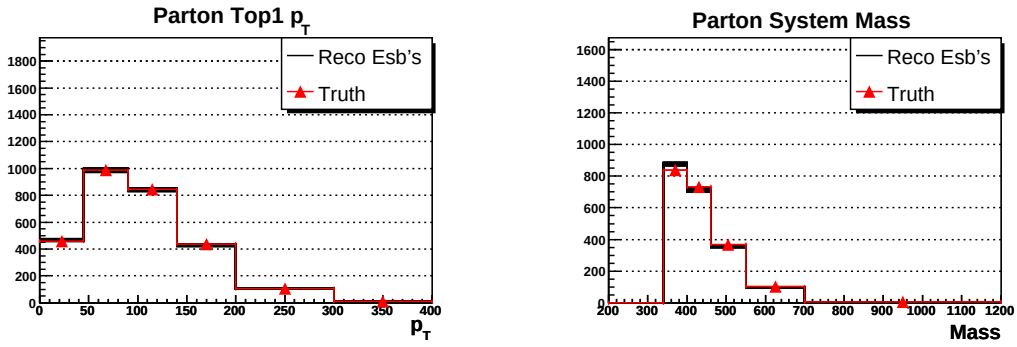

Figure 14.19: Illustration of the simulation-based ensembles, ℓ+jets. Left: leptonic top p_{T}, right: $t\bar{t}$ system mass.

To test the unfolding stability to statistical fluctuations and to check for the unfolding bias (how close is the unfolded spectrum to the truth one), a set of distributions (an ensemble) based on the central spectrum is created.

Ensembles of 1000 members are generated from each of the simulation distribution in study by smearing each bin content by a random number from a Poisson distribution with the mean of the bin content count (i.e. before dividing by the bin width). The ensembles are illustrated in Figure 14.19. Each member is then unfolded and the resulting spectrum shape divided by the truth parton spectrum. The bin-by-bin spread of the ensembles gives one the statistical error on the unfolded distribution, while in simulation one can estimate also the unfolding bias as the deviation of the unfolded spectrum from the truth one. The procedure of deriving the unfolding spread and bias in depicted in Figure 14.20. To test the profiles of the ensembles in each bin, slices of the unfolded/truth distribution are checked for gaussianity in Figures 14.21–14.22.

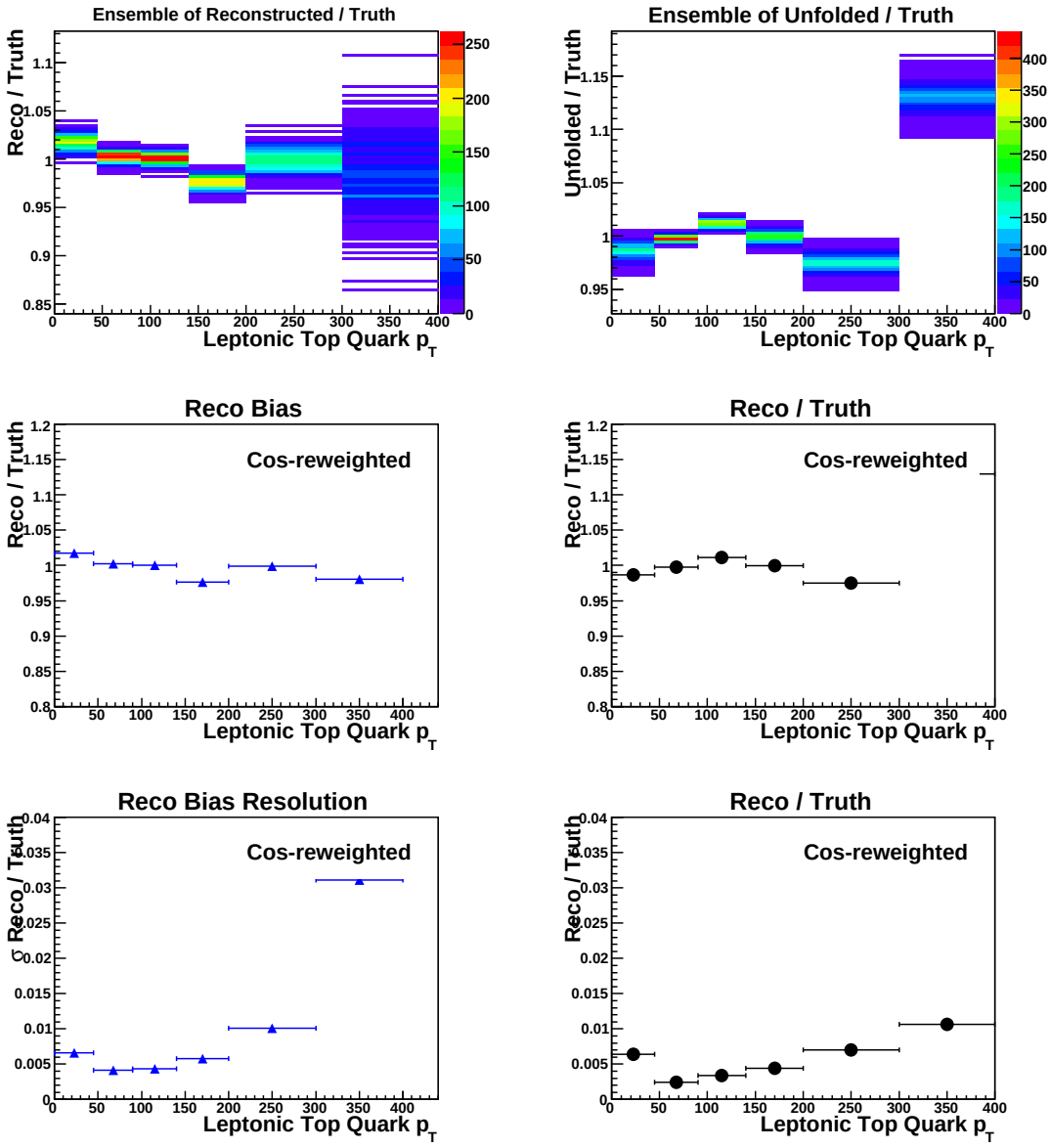

Figure 14.20: Unfolding simulation ensembles for leptonic top p_{T} with ALPGEN migration matrix using the effective rank of 3 in ℓ+jets. Left: reconstructed/truth, right: unfolded/truth. Middle: bias, bottom: spread. Signal model: ALPGEN, using a cosine-reweighted migration matrix at the truth-level.

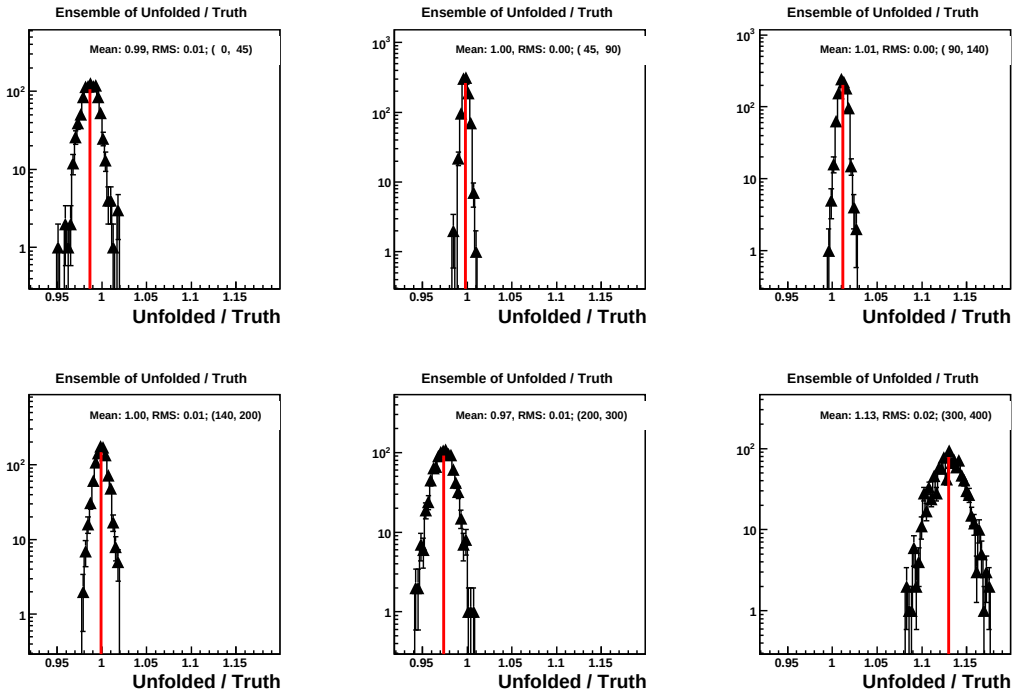

Figure 14.21: Profiles of the unfolded simulation-based ensembles (1000 members) divided by the truth level. Width of the profiles in each bin is used as statistical error for the central unfolded simulation distribution. Leptonic top quark p_{T} spectrum in e+jets using the effective rank of 3. Signal model: ALPGEN, using a cosine-reweighted migration matrix at the truth-level.

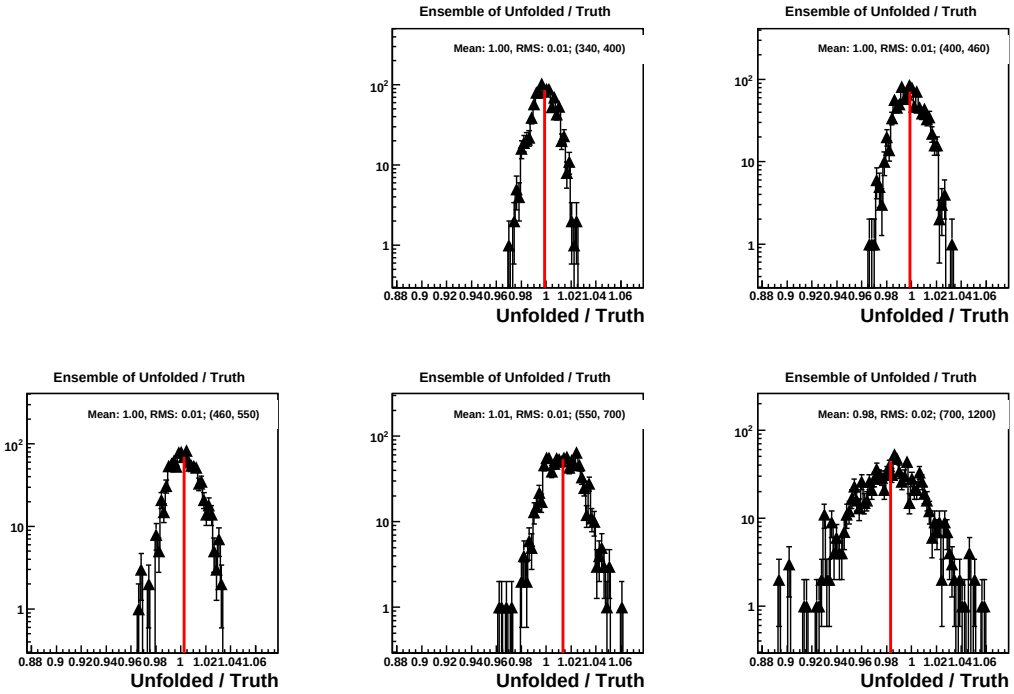

Figure 14.22: Profiles of the unfolded simulation-based ensembles (1000 members) divided by the truth level. Width of the profiles in each bin is used as statistical error for the central unfolded simulation distribution. $t\bar{t}$ system mass spectrum in e+jets using the effective rank of 4. Signal model: ALPGEN, using a cosine-reweighted migration matrix at the truth-level.

14.8 Data-Based Ensemble Tests

While the simulation-based ensembles serve to check the unfolding bias, data-based ensembles are used to derive the statistical error of the unfolded distribution by means of looking at the spread of the unfolded distribution over the ensemble.

Ensembles based on the background-subtracted data distributions (as illustrated in Figure 14.23) are generated in the similar manner as in the case of the simulation, and infolded using the effective rank of 2 for both distribution of interest. The $\log|d_i|$ distributions for various reweighting schemes are in Figures 14.24–14.25. The ensembles processing is illustrated in Figure 14.26 and the central shape of the unfolded data ensembles for top quark p_{T} and $t\bar{t}$ system mass in Figures 14.27–14.32. To test the profiles of the ensembles in each bin, slices of the unfolded/truth distribution are again checked for gaussianity in Figures 14.33–14.34.

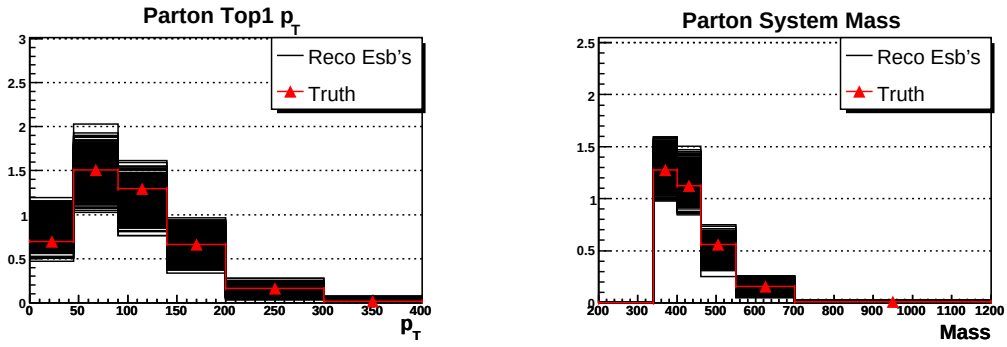

Figure 14.23: Illustration of the data-based ensembles, e+jets. Left: leptonic top p_{T}, right: $t\bar{t}$ system mass.

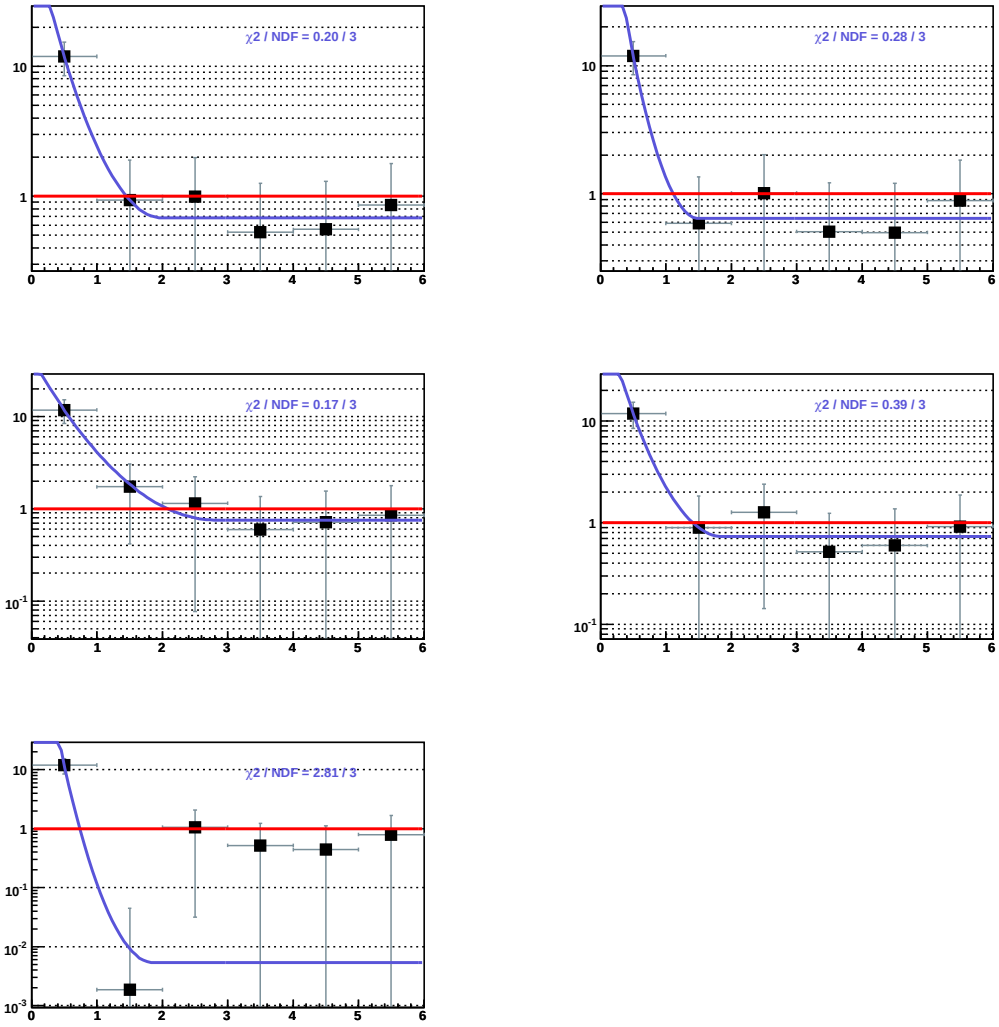

Figure 14.24: GURU's $\log|d_i|$ distribution in leptonic top p_T in data with variously reweighted (at truth level) migration matrices in e+jets.

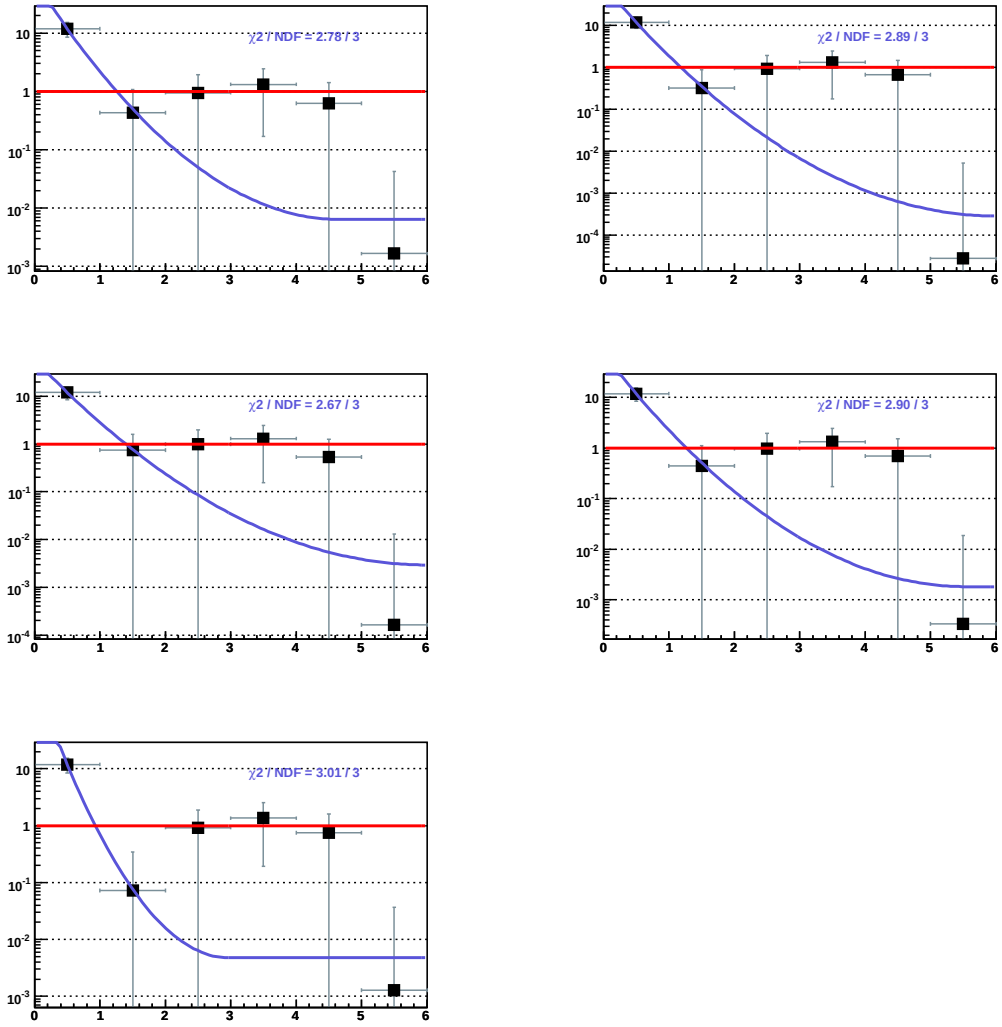

Figure 14.25: GURU's $\log|d_i|$ distribution in $t\bar{t}$ system mass in data with variously reweighted (at truth level) migration matrices in e+jets.

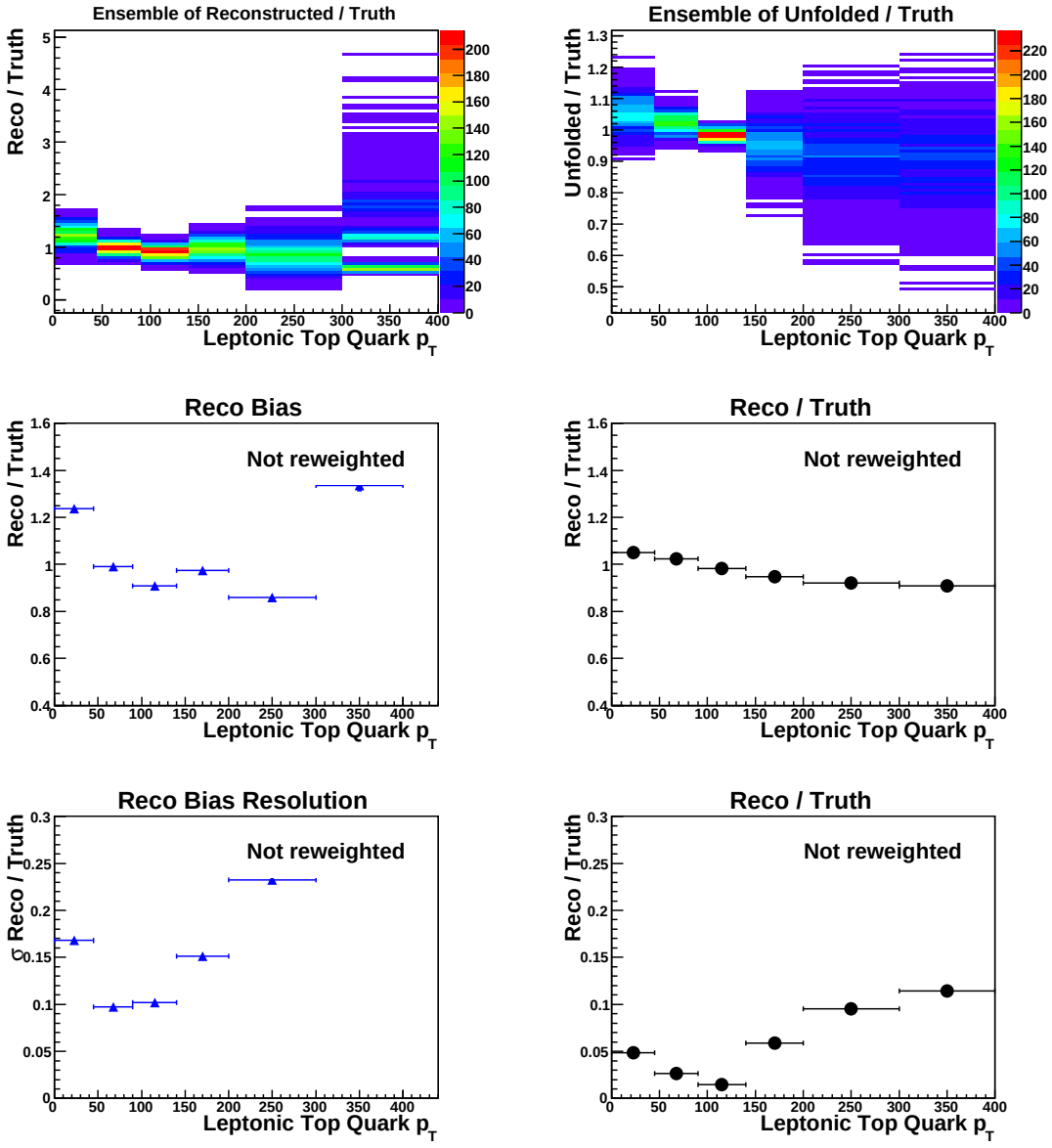

Figure 14.26: Unfolding data ensembles leptonic top quark p_{T} with ALPGEN migration matrix, effective rank of 2 in ℓ+jets. Left: reconstructed/truth, right: unfolded/truth. Middle: bias, bottom: spread.

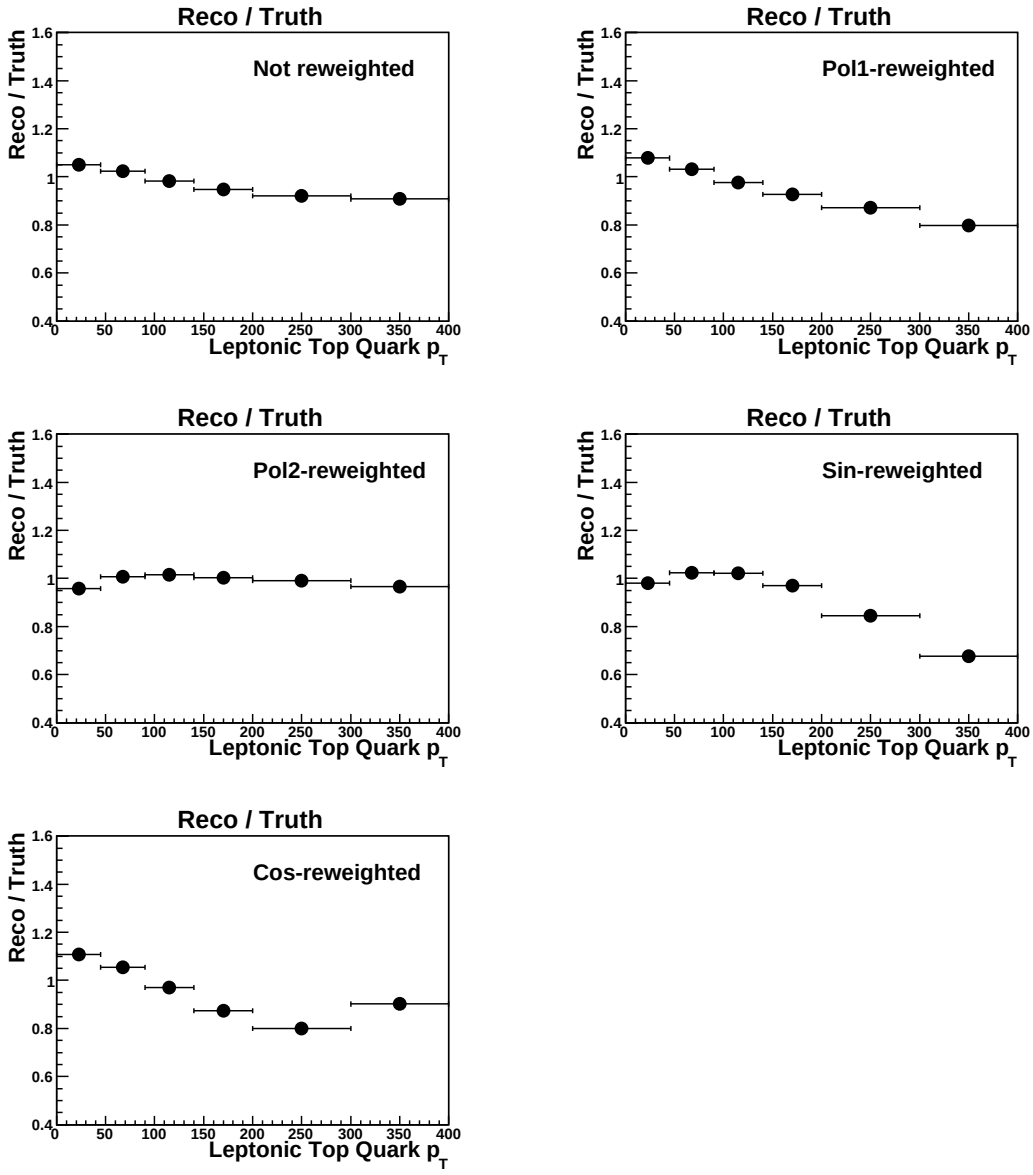

Figure 14.27: Leptonic top p_{T} in data with variously reweighted (at truth level) migration matrices, using the effective rank 2 in ℓ+jets.

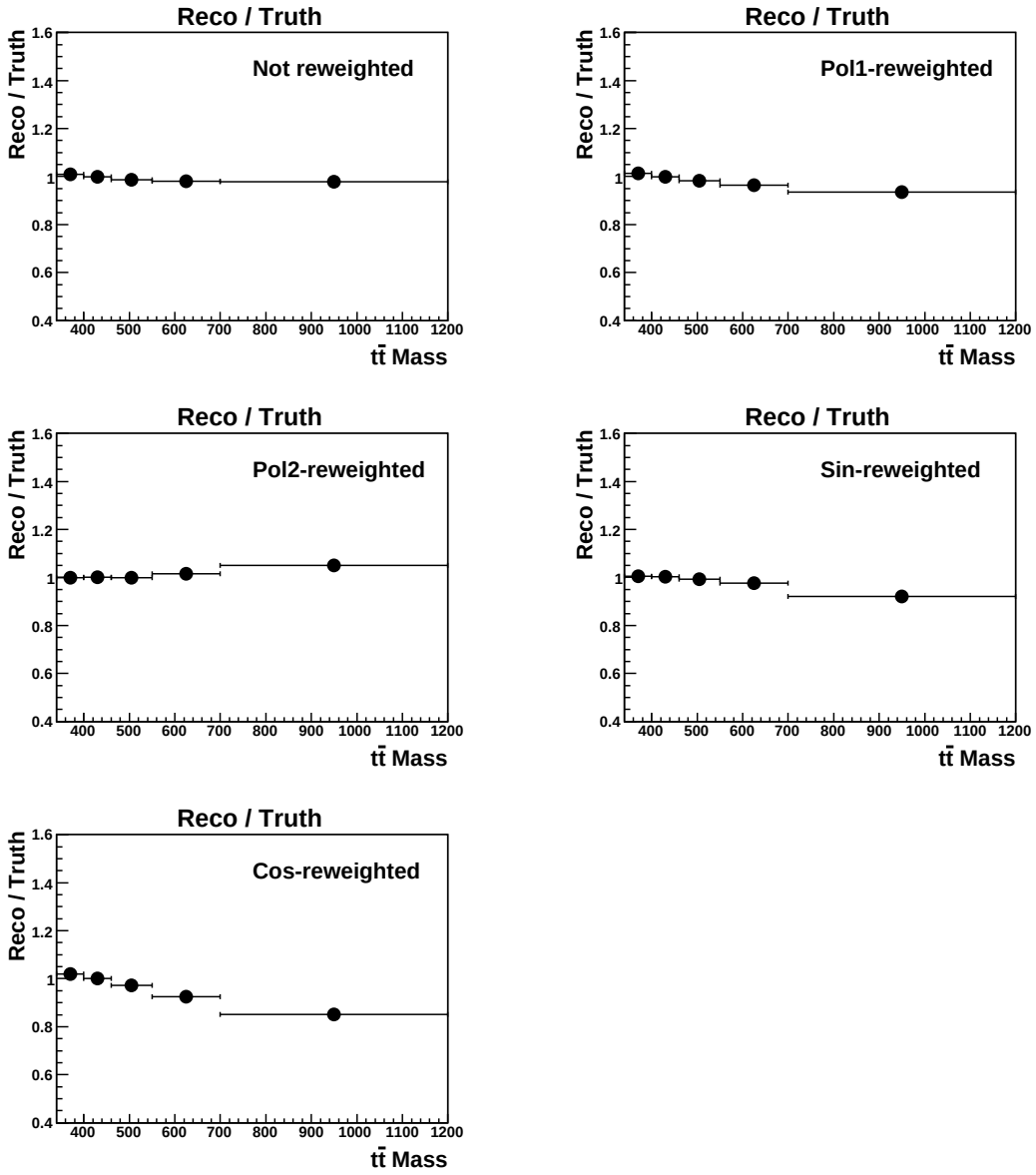

Figure 14.28: $t\bar{t}$ system mass in data with variously reweighted (at truth level) migration matrices, using the effective rank 2 in ℓ+jets.

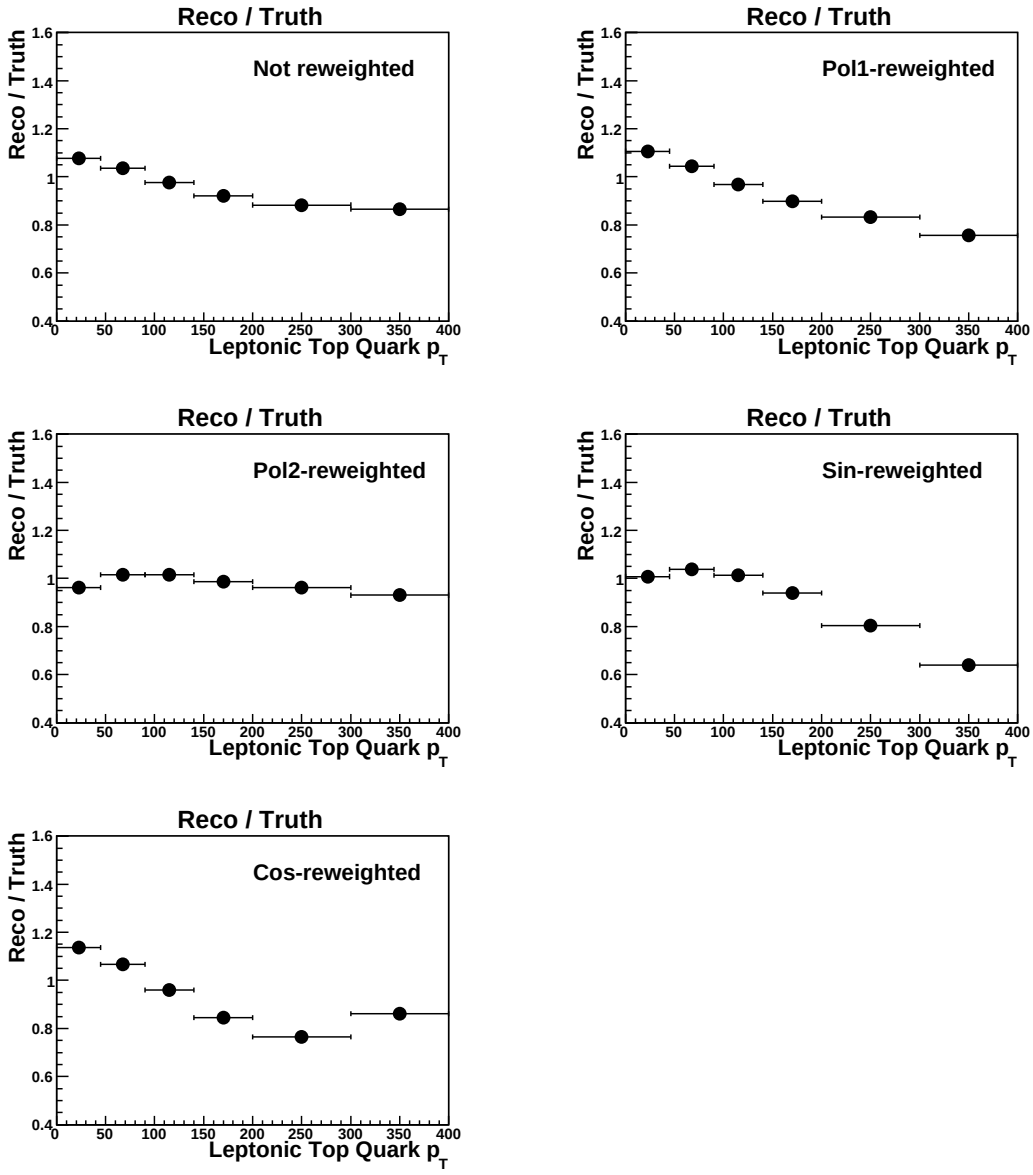

Figure 14.29: Leptonic top p_{T} in data with variously reweighted (at truth level) migration matrices, using the effective rank 2 in e+jets.

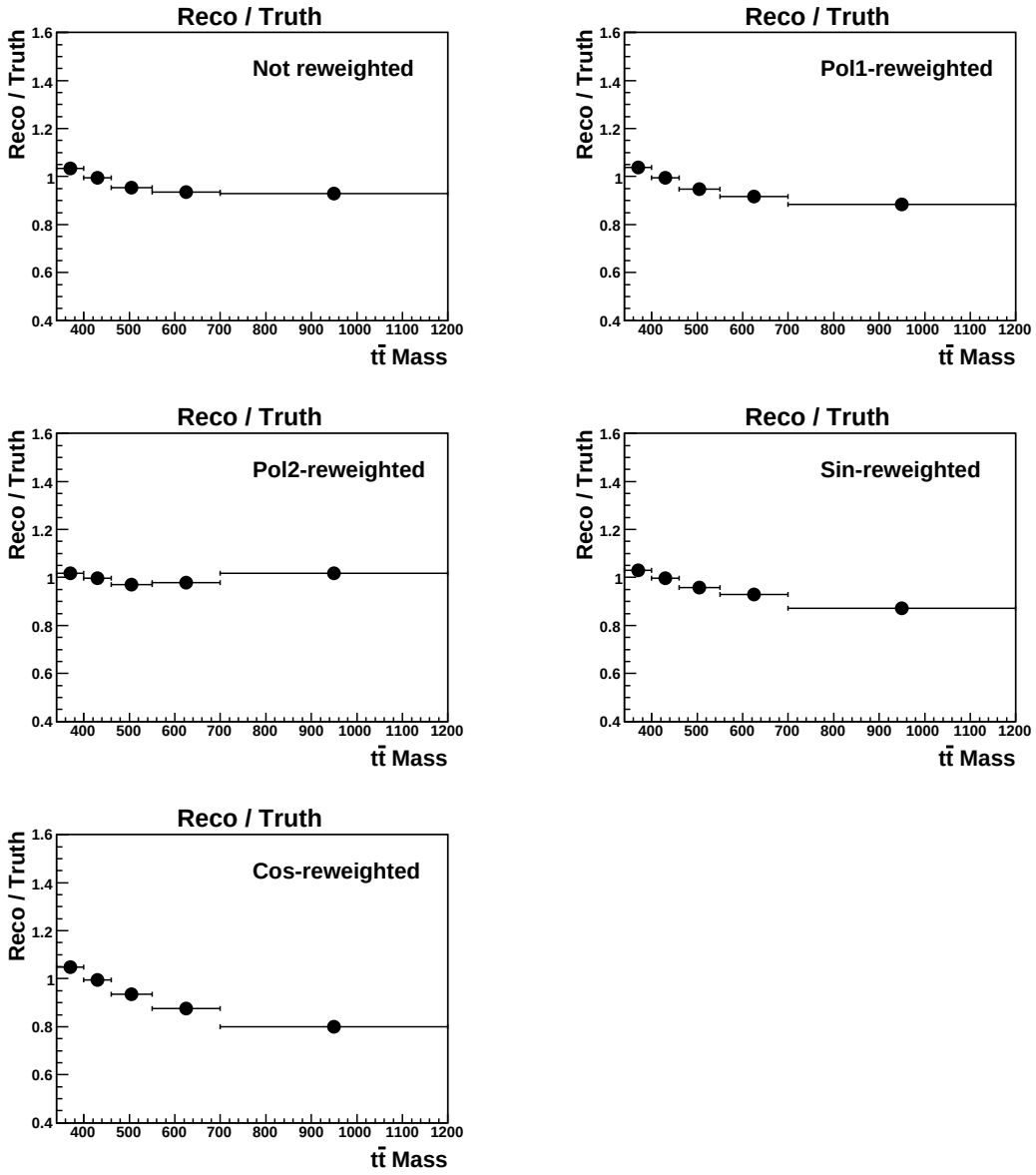

Figure 14.30: $t\bar{t}$ system mass in data with variously reweighted (at truth level) migration matrices, using the effective rank 2 in e+jets.

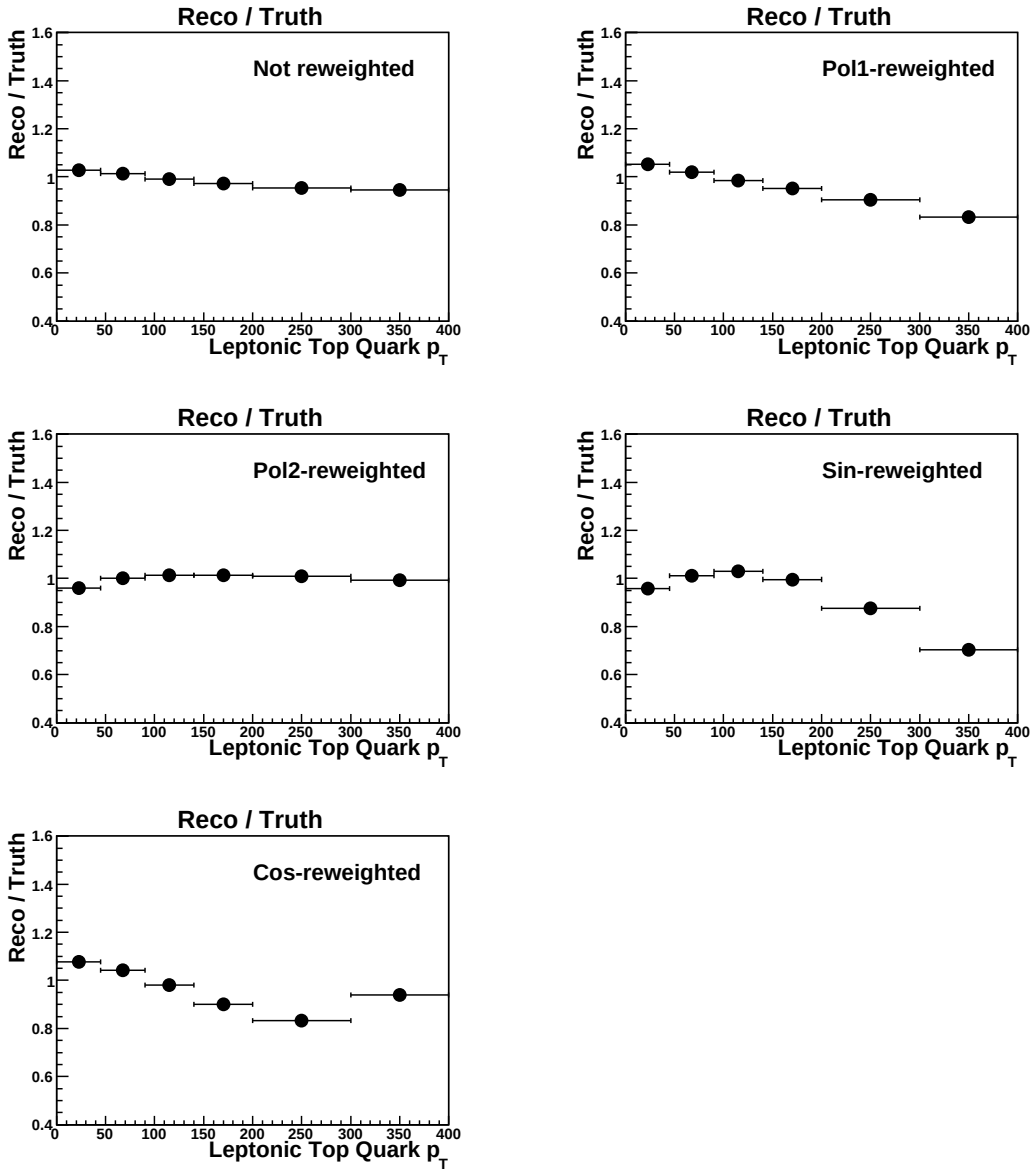

Figure 14.31: Leptonic top p_{T} in data with variously reweighted (at truth level) migration matrices, using the effective rank 2 in μ+jets.

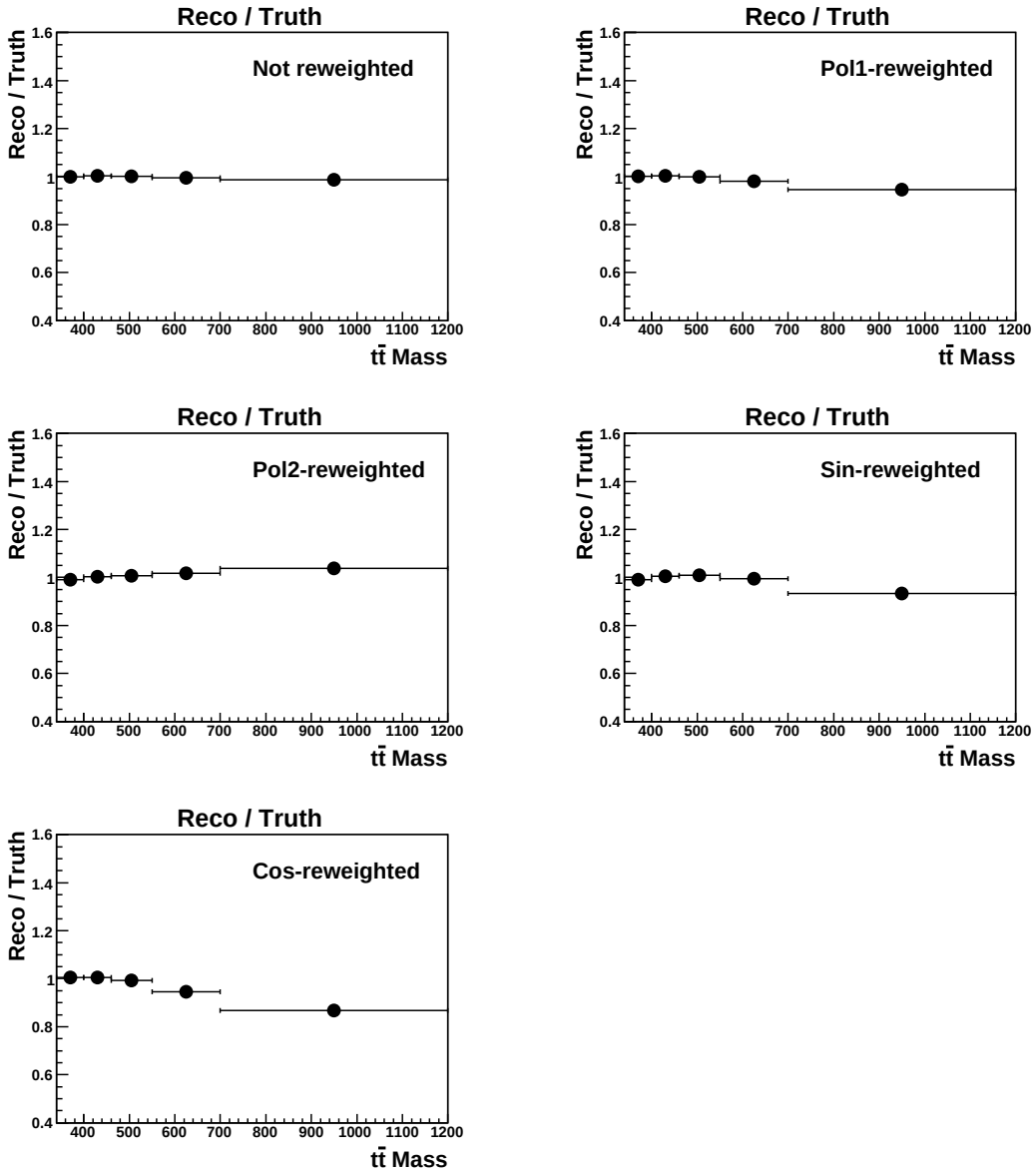

Figure 14.32: $t\bar{t}$ system mass in data with variously reweighted (at truth level) migration matrices, using the effective rank 2 in μ+jets.

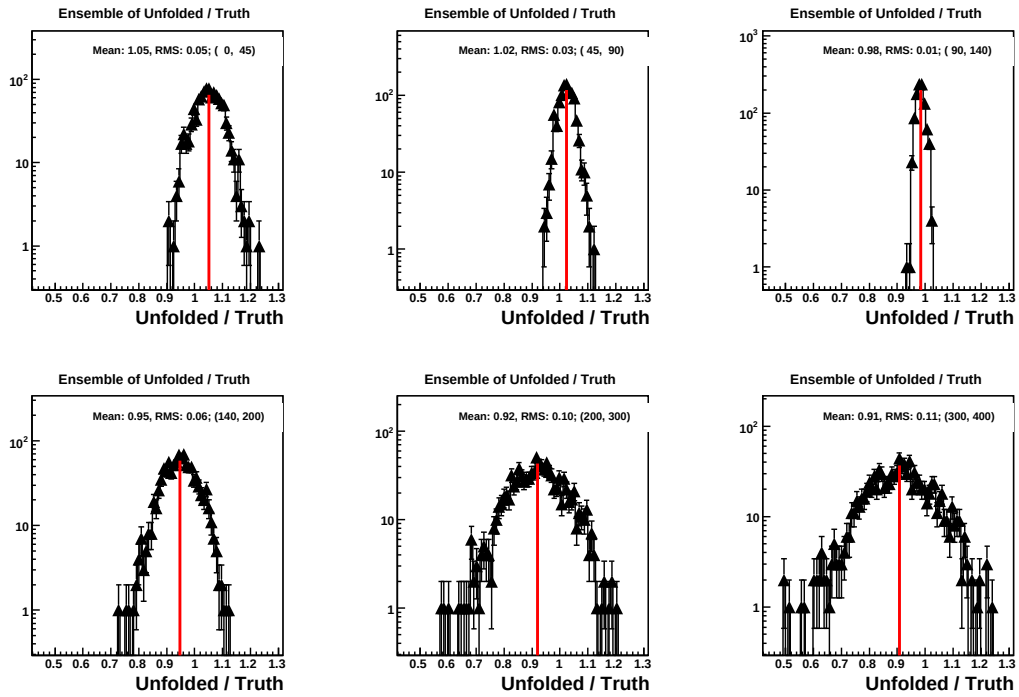

Figure 14.33: Profiles of the unfolded data-based ensembles (1000 members) divided by the truth level. Width of the profiles in each bin is used as statistical error for the central unfolded data distribution. Leptonic top quark p_{T} spectrum in ℓ+jets using the effective rank of 2. Signal model: ALPGEN.

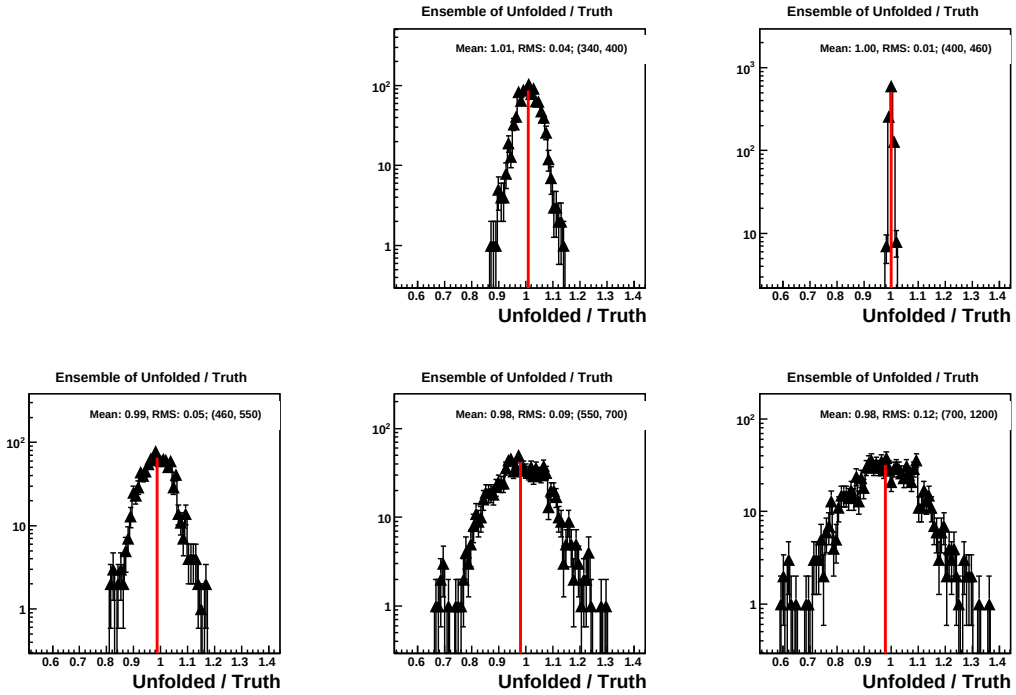

Figure 14.34: Profiles of the unfolded data-based ensembles (1000 members) divided by the truth level. Width of the profiles in each bin is used as statistical error for the central unfolded data distribution. $t\bar{t}$ system mass spectrum in ℓ+jets using the effective rank of 2. Signal model: ALPGEN.

14.9 Unfolding the Data

Data distributions after the purity-based background subtraction are unfolded using the not-reweighted migration matrices from the simulation, while the ensembles-evaluated results based on variously reweighted migration matrix are used as the spectrum shape systematics. The unfolded data (not corrected for the acceptance yet) compared to the truth level ALPGEN after cuts are presented for separate e+jets and μ+jets channels in Figures 14.35-14.36 and for the merged ℓ+jets channel in Figure 14.37 for the case of leptonic top quark p_{T} spectrum and for the $t\bar{t}$ system mass in Figures 14.38–14.40.

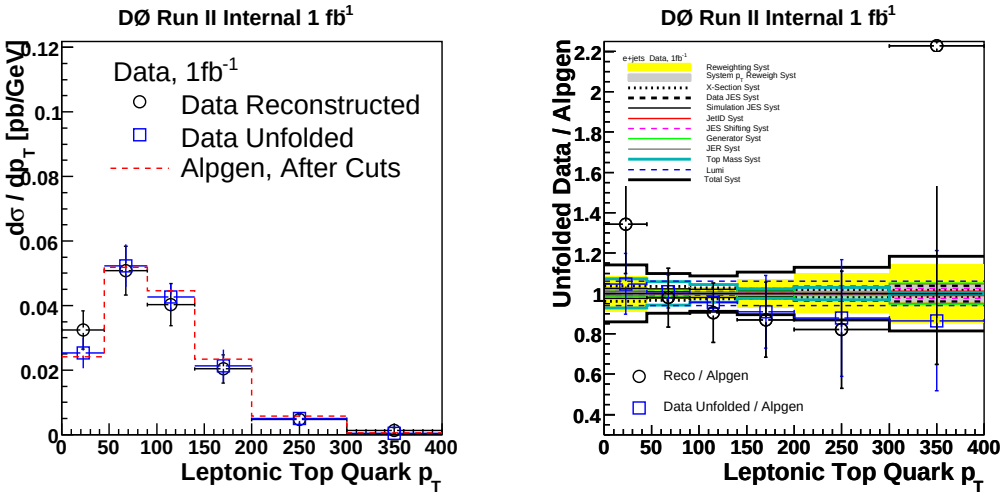

Figure 14.35: Unfolding data leptonic top quark p_{T} spectrum in e+jets using the effective rank of 2. Signal model: ALPGEN.

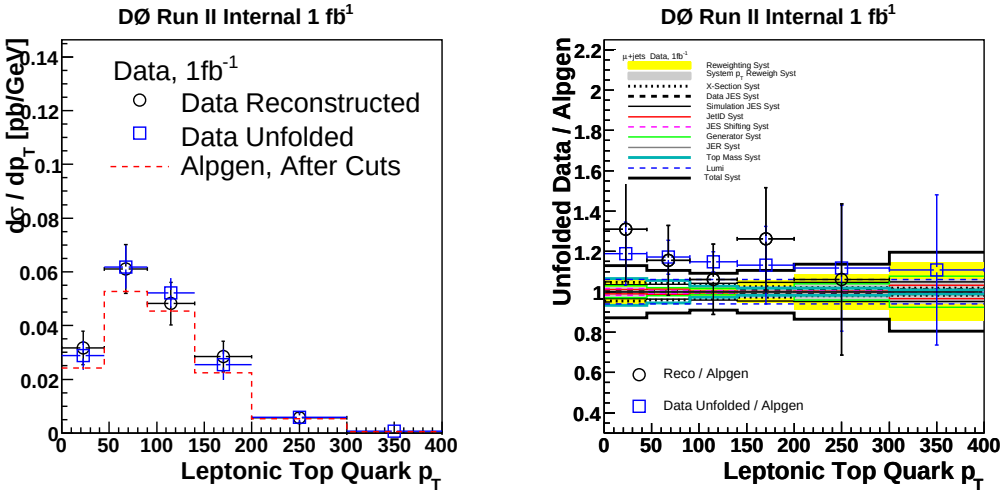

Figure 14.36: Unfolding data leptonic top quark p_{T} spectrum in μ+jets using the effective rank of 2. Signal model: ALPGEN.

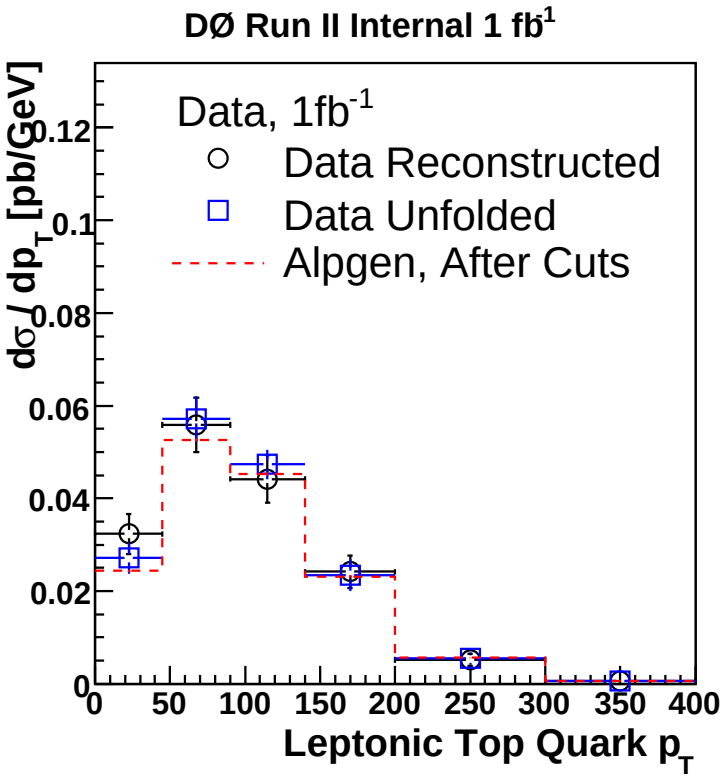

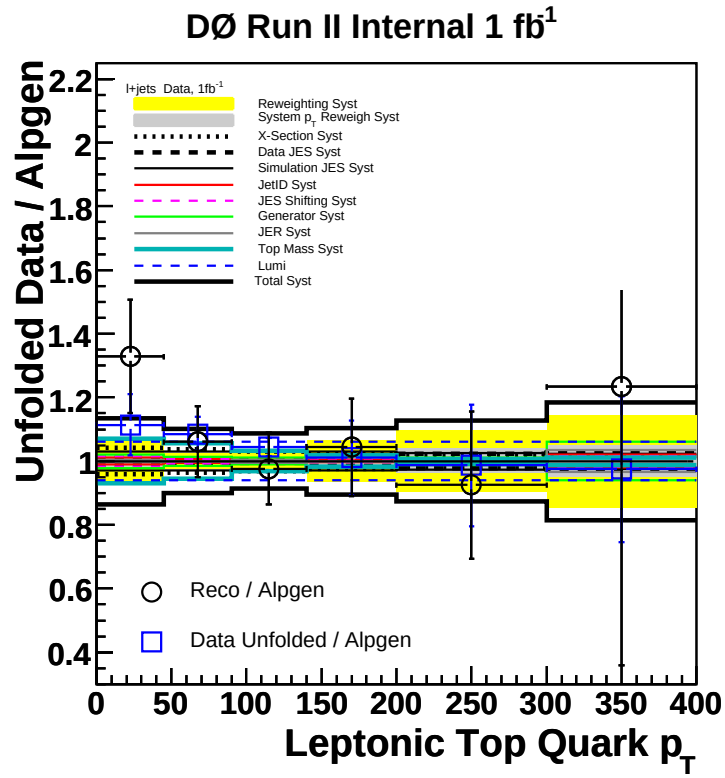

Figure 14.37: Unfolding data leptonic top quark p_{T} spectrum in ℓ+jets using the effective rank of 2. Signal model: ALPGEN.

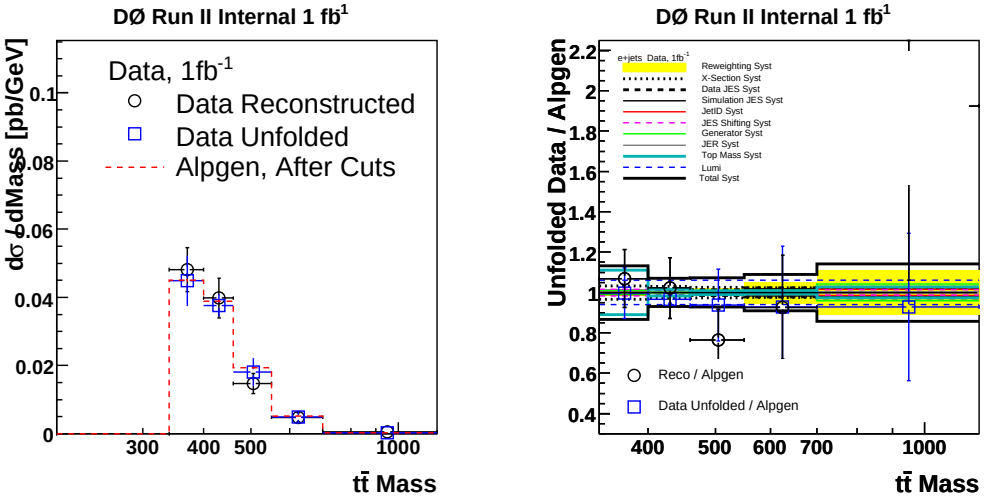

Figure 14.38: Unfolding data $t\bar{t}$ system mass spectrum in e+jets using the effective rank of 2. Signal model: ALPGEN.

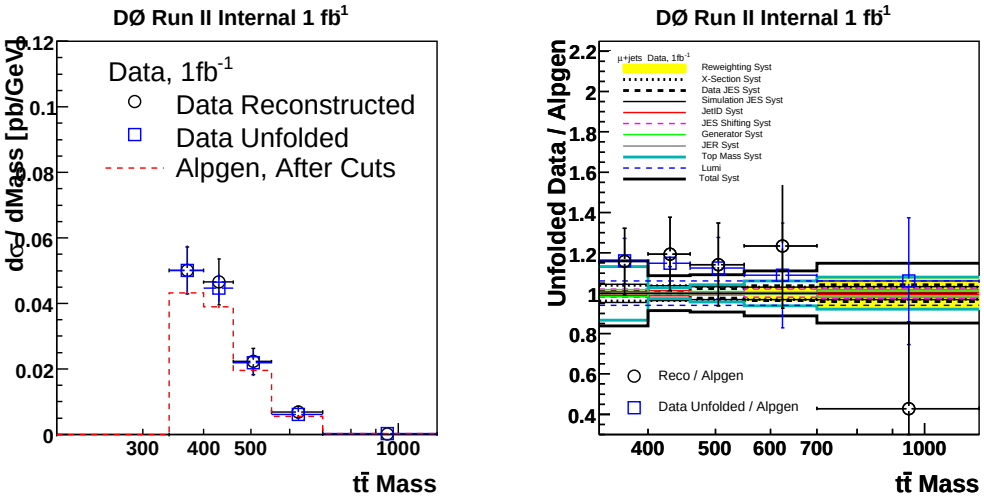

Figure 14.39: Unfolding data $t\bar{t}$ system mass spectrum in μ+jets using the effective rank of 2. Signal model: ALPGEN.

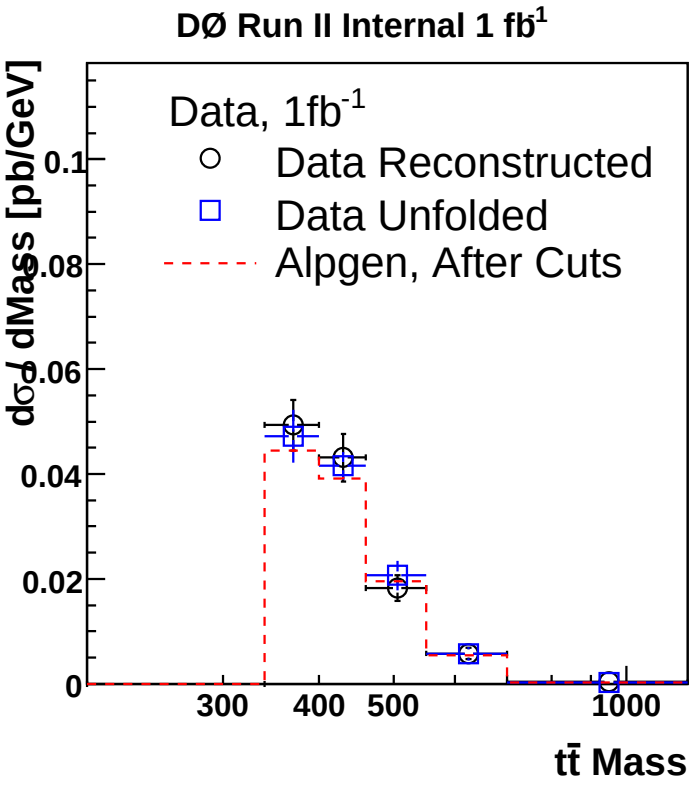

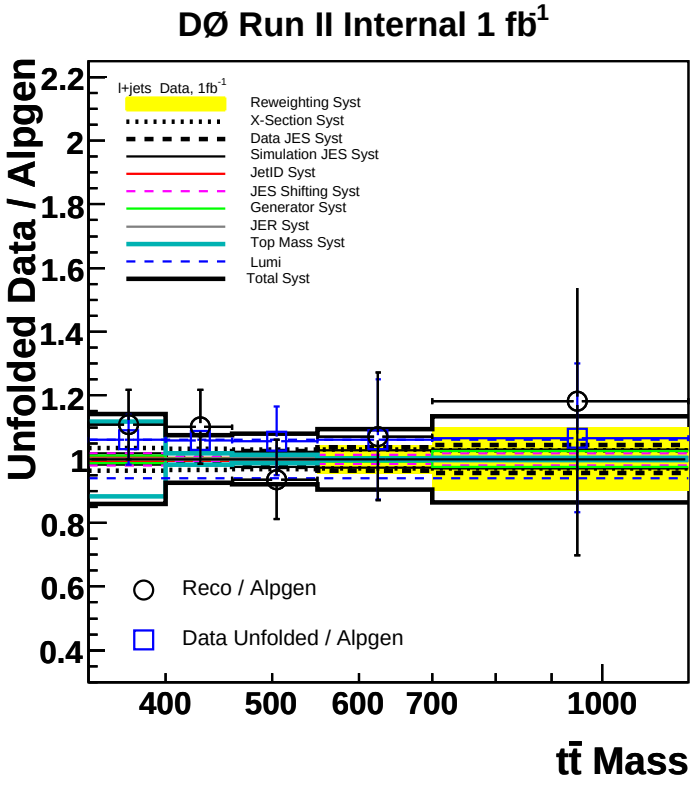

Figure 14.40: Unfolding data $t\bar{t}$ system mass spectrum in ℓ+jets using the effective rank of 2. Signal model: ALPGEN.

Chapter 15

The Acceptance Correction

15.1 Differential Acceptance

The differential acceptance, i.e. the bin-by-bin cuts efficiency in the distribution of interest, is measured using the full simulation ALPGEN $t\bar{t}$ sample and cross-checked with PYTHIA. Each kinematic variable is constructed using the parton level leptonic ($t \to \ell\bar{\nu}_\ell b$) and hadronic ($t \to q\bar{q}'b$) top quarks.

The ratio of the spectrum shape after the selection w.r.t. the shape before the analysis cuts defines the differential *acceptance shaping effect*. The inverse distribution, i.e. spectrum before cuts divided by spectrum after the selection, defines the *acceptance correction* to be applied to the final unfolded distribution, as acceptance is measured on the parton level. Largest effects on rapidity and p_{T}-related variables come from jet and lepton η and p_{T} cuts.

One can fold the selection efficiency into the acceptance shape, or divide by the efficiency to get the shape effect only, such that the inverse (the acceptance correction) does not change the overall normalisation. Second approach is adopted, i.e. in plotting the acceptance shape, "after/before/efficiency" is used. Efficiencies are the combination of the preselection efficiency and the b-tagging efficiency and correspond to numbers in tables in Section 11.7.

To summarise, the acceptance shape is measured as

$$\frac{1}{\epsilon_{\mathrm{Acc}}} \cdot \frac{[\mathrm{d}N/\mathrm{d}X]_{\text{after selection}}}{[\mathrm{d}N/\mathrm{d}X]_{\text{before selection}}},$$

where ϵ_{Acc} is the integral acceptance (and includes the selection efficiencies as well as the b-tagging efficiency). The ALPGEN-based acceptance derived in the inclusive ≥ 1 b-tag bin is used, and later averaged between the e+jets and μ+jets channels for the ℓ+jets. The binned version of the acceptance is used (not the fit).

The derived acceptance shapes for the top quark p_{T}, $t\bar{t}$ system mass and p_{T} are plotted in Figure 15.1. Figure 15.2 shows the acceptances shape ratio between leptonic and hadronic top quark p_{T} for e+jets and μ+jets. Different b-tag bins are compared in Figure 15.3, while the difference between the e+jets and μ+jets channels is studied in Figure 15.4. Acceptance shapes of the $t\bar{t}$ system mass are compared in Figure 15.5, and the PYTHIA and ALPGEN generators are compared in Figures 15.6 and Figures 15.7.

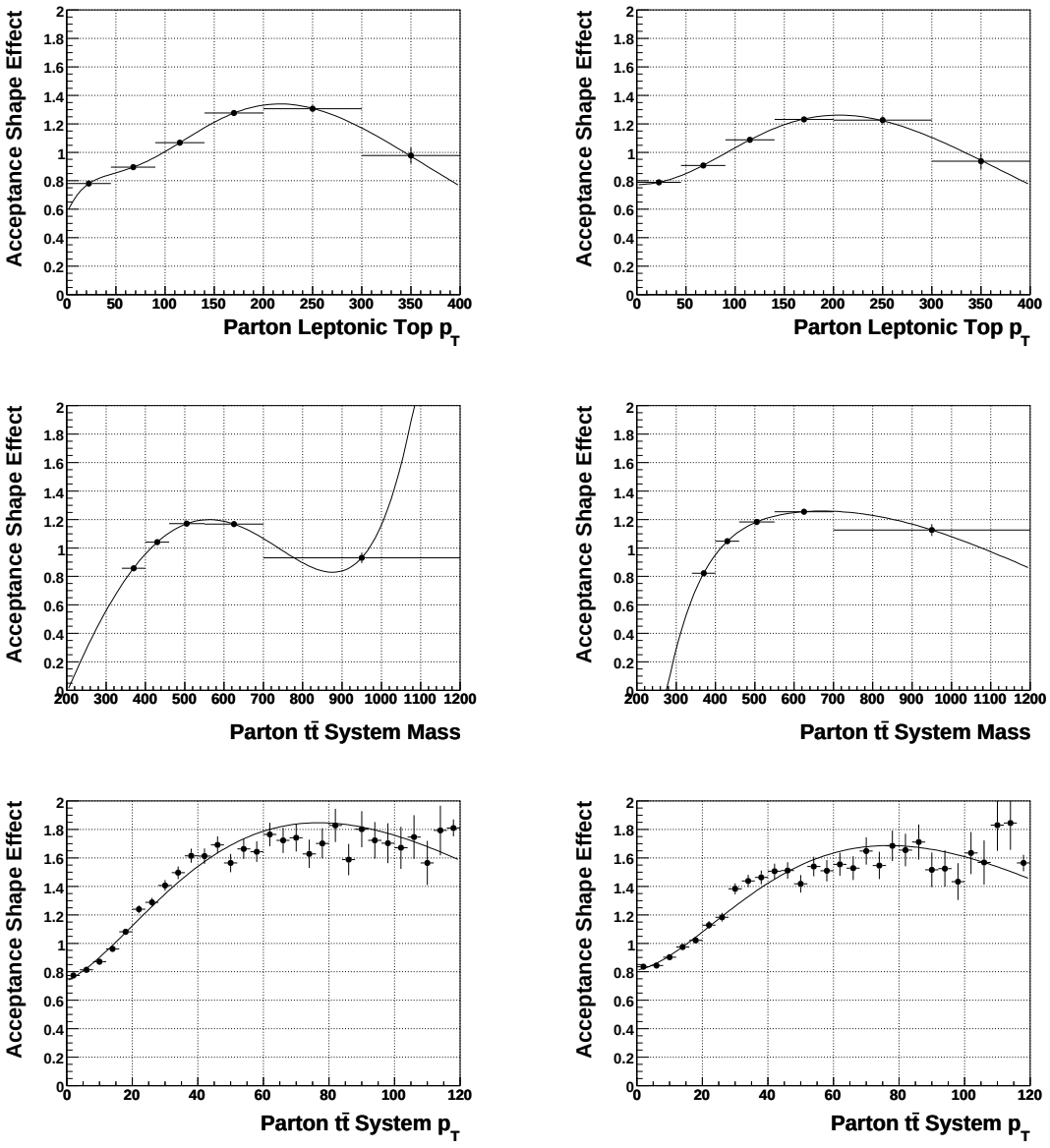

Figure 15.1: From top to bottom, leptonic top quark p_{T} acceptance, $t\bar{t}$ system mass and p_{T} acceptance shapes in e+jets (left) and μ+jets (right) in the ≥ 1 NNm b-tag bin. Signal model: ALPGEN.

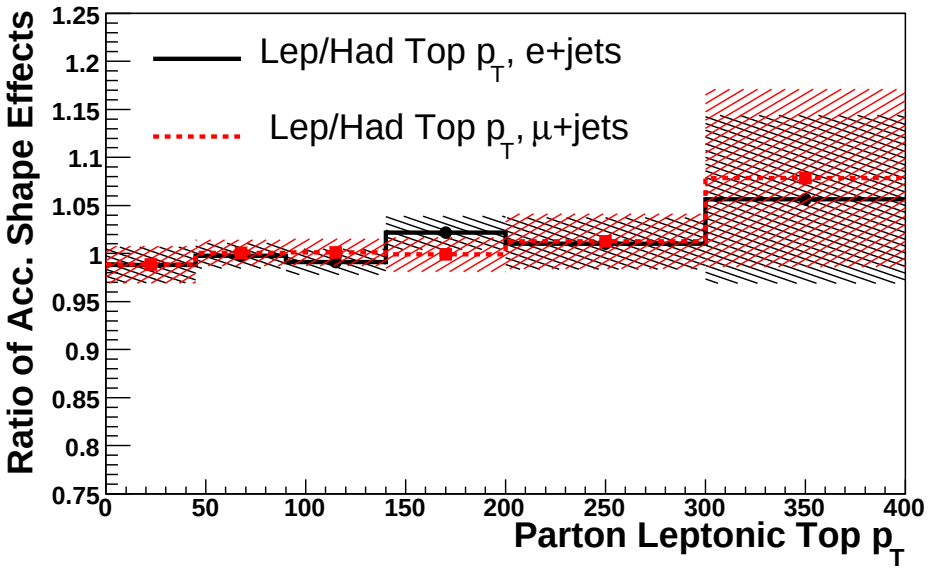

Figure 15.2: Acceptance shapes ratios between the leptonic and hadronic top quark p_{T} for e+jets and μ+jets. Signal model: ALPGEN.

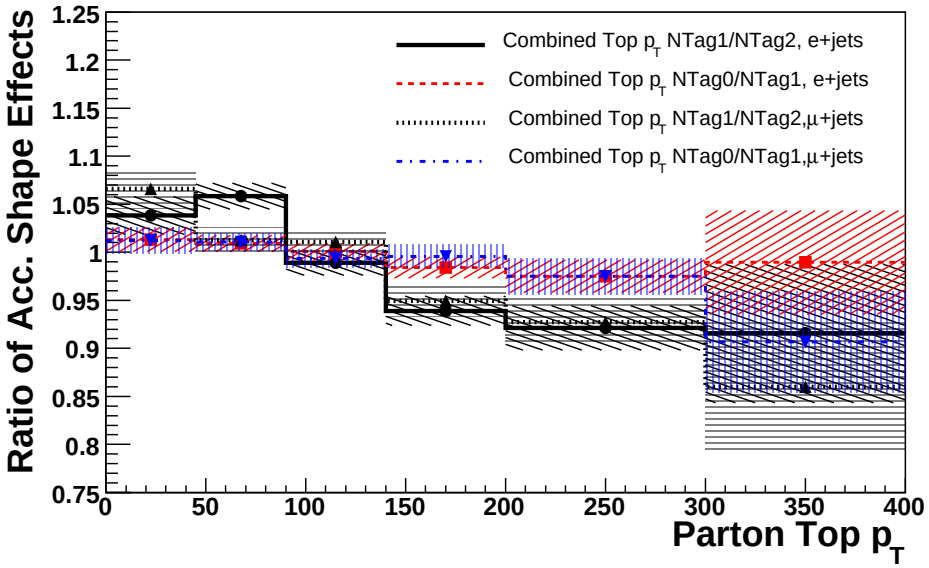

Figure 15.3: Acceptance shape ratios between different b-tag bins for top quark p_{T} in e+jets and μ+jets. Signal model: ALPGEN.

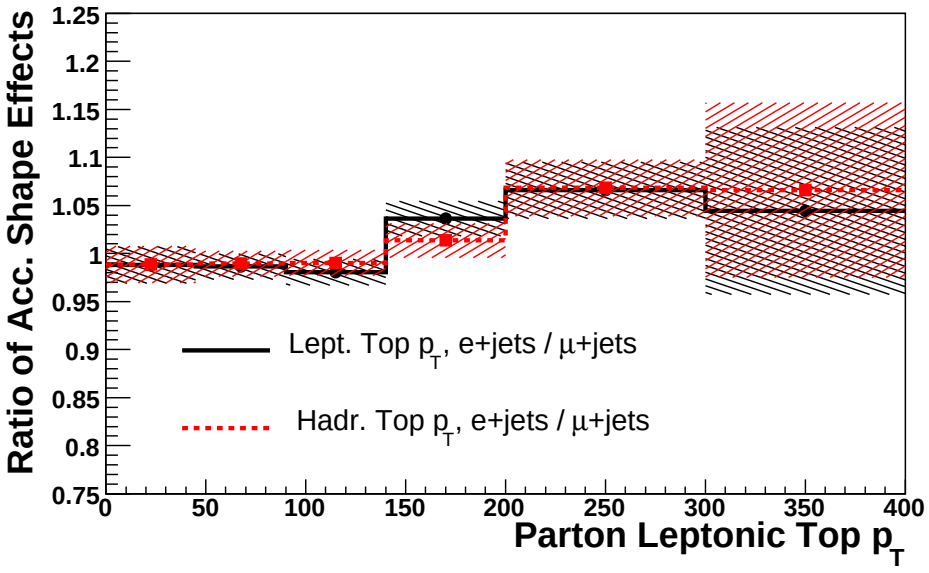

Figure 15.4: Acceptance shape ratios between e+jets and μ+jets for leptonic and hadronic top quark p_{T} in the ≥ 1 NNm b-tag bin. Signal model: ALPGEN.

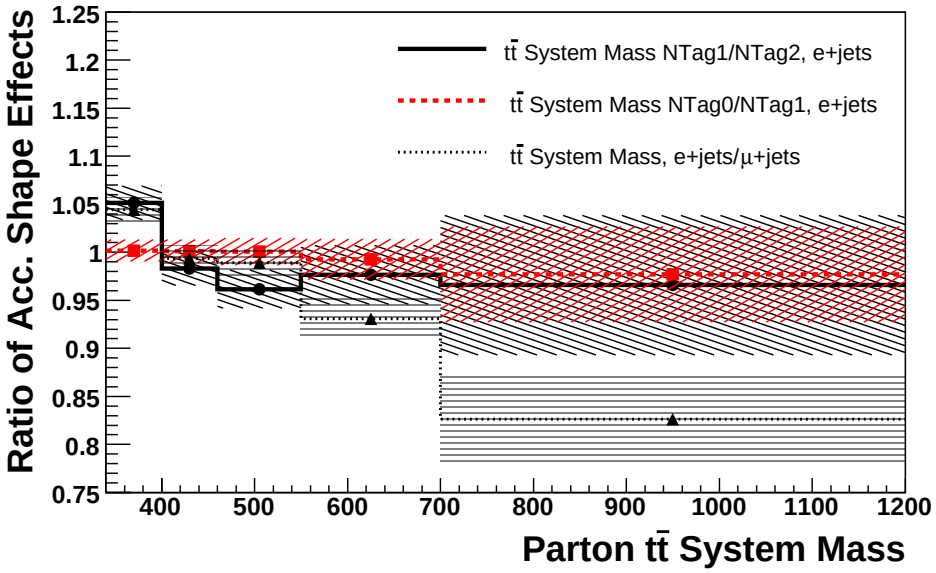

Figure 15.5: Acceptance shape ratios between various b-tag bins and between e+jets and μ+jets for the $t\bar{t}$ system mass. Signal model: ALPGEN.

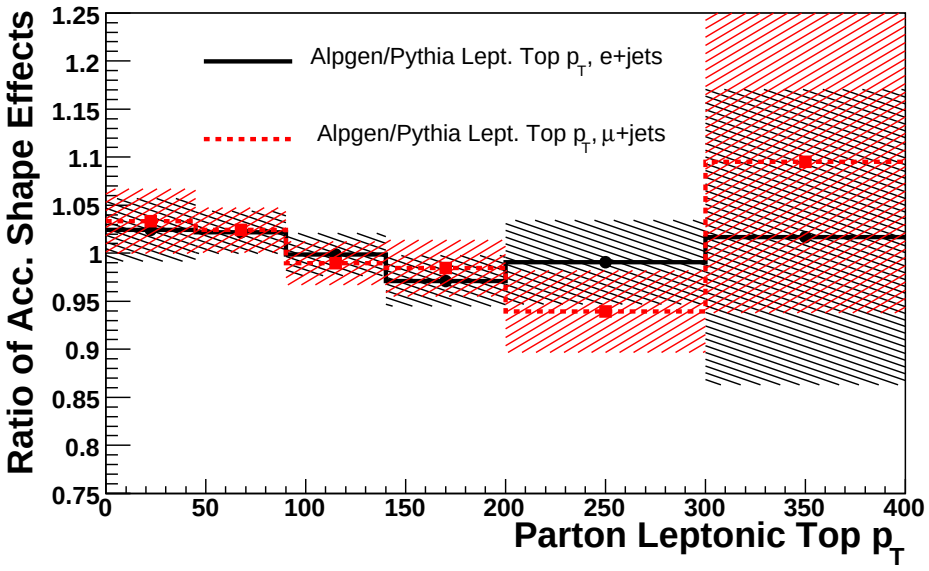

Figure 15.6: ALPGEN and PYTHIA acceptances acceptance shape ratio for top quark p_{T} in e+jets and μ+jets in the ≥ 1 NNm b-tag bin.

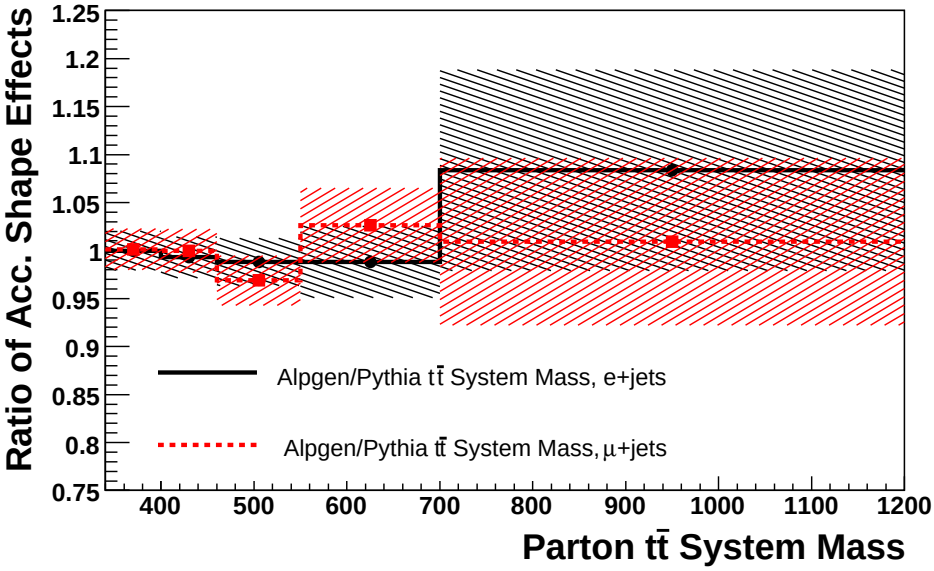

Figure 15.7: ALPGEN and PYTHIA acceptances shape ratio for $t\bar{t}$ system mass in e+jets and μ+jets in the ≥ 1 NNm b-tag bin.

Chapter 16

Final Differential Cross Sections

Final results of the presented study are the background-subtracted b-tagged spectra in the merged ℓ+jets channel after the unfolding and acceptance corrections, scaled to the level of differential cross section in terms of pb/GeV.

16.1 Cross-section normalisation

To translate the result from the spectrum shape measurement $\mathrm{d}N/\mathrm{d}X$ to the truly differential spectrum $\mathrm{d}\sigma/\mathrm{d}X$, the master formula

$$\frac{\mathrm{d}\sigma_{\ell+\mathrm{jets}}}{\mathrm{d}X_j} \equiv \frac{\mathrm{Unfolded}\left[N_j^{\mathrm{observed}} - N_j^{\mathrm{background}}\right]}{\mathcal{L}_{\ell+\mathrm{jets}} \cdot \mathrm{BR}_{\ell+\mathrm{jets}} \cdot \epsilon_{\mathrm{signal}}^{\ell+\mathrm{jets}} \cdot \mathcal{A}_j^{\ell+\mathrm{jets}} \cdot \Delta X_j}$$

was used to compute the differential cross section in a given ℓ+jets channel in the j-th bin of a variable of interest. As the e+jets and μ+jets channels were combined already for unfolding (and averaged acceptance and migration matrix as weighted sums of quantities in individual channels were used), separate factors $\left[\mathcal{L}_{\ell+\mathrm{jets}} \cdot \mathrm{BR}_{\ell+\mathrm{jets}} \cdot \epsilon_{\mathrm{signal}}^{\ell+\mathrm{jets}}\right]^{-1}$ for each channel were computed, and the correction to the dimensionful quantity (measured in pb/GeV) was performed by a sum of the two factors weighted by the number of signal-like events as extracted from data.

16.2 Full Monte Carlo Closure

The full simulation-based closure including the unfolding and acceptance corrections is documented in Figures 16.1–16.4.

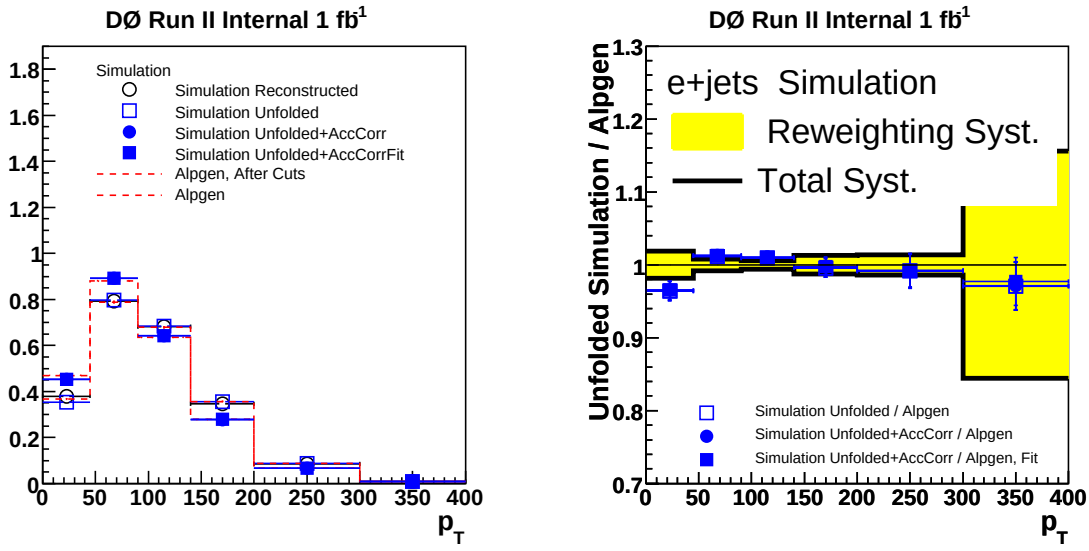

Figure 16.1: Unfolding the simulation leptonic top quark p_T spectrum in e+jets using the effective rank of 3 with "Pol2"-reweighted migration matrix. Signal model: ALPGEN.

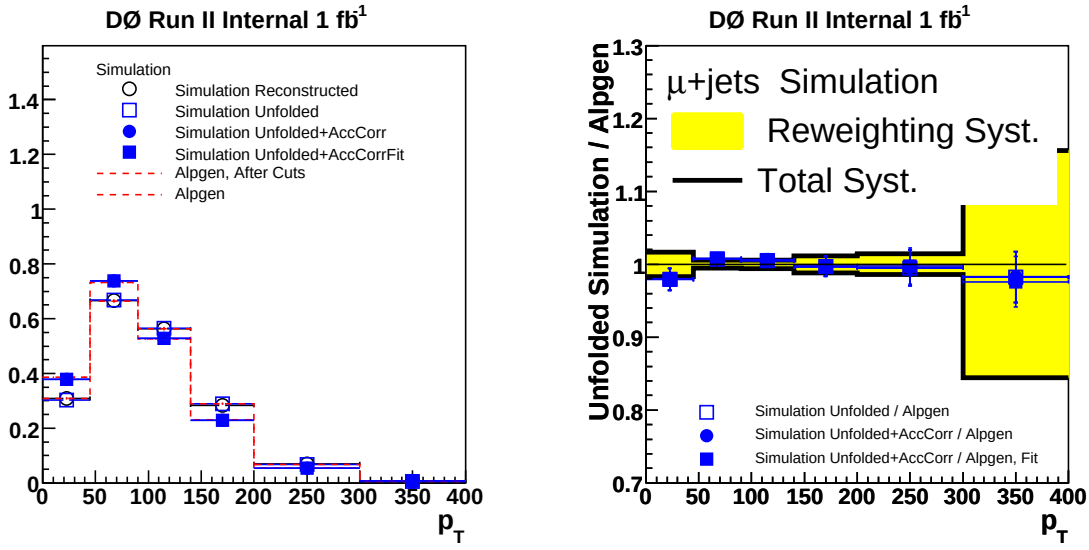

Figure 16.2: Unfolding the simulation leptonic top quark p_T spectrum in μ+jets using the effective rank of 3 with "Pol2"-reweighted migration matrix. Signal model: ALPGEN.

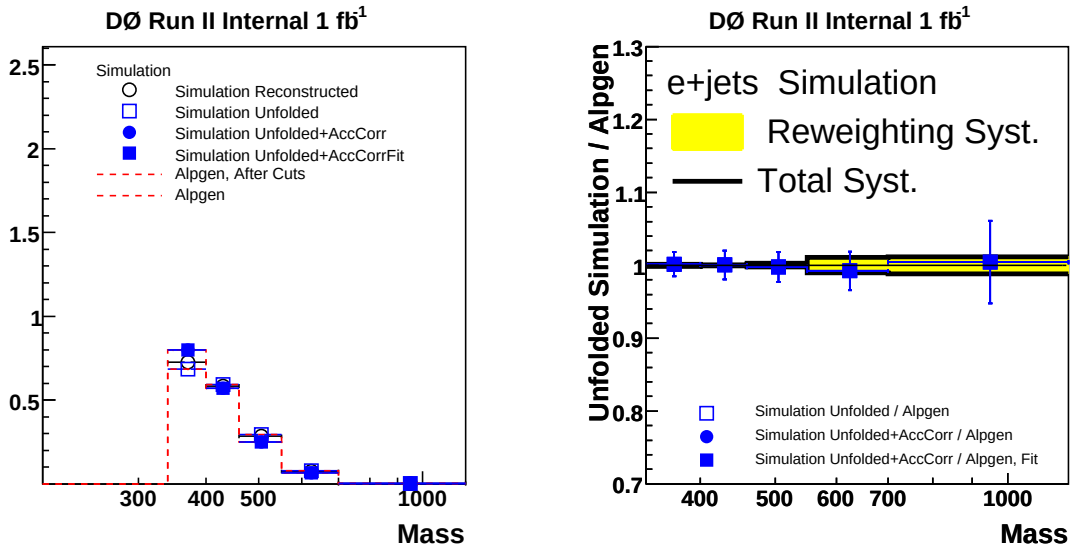

Figure 16.3: Unfolding the simulation $t\bar{t}$ system mass spectrum in e+jets using the effective rank of 4 with "Pol2"-reweighted migration matrix. Signal model: ALPGEN.

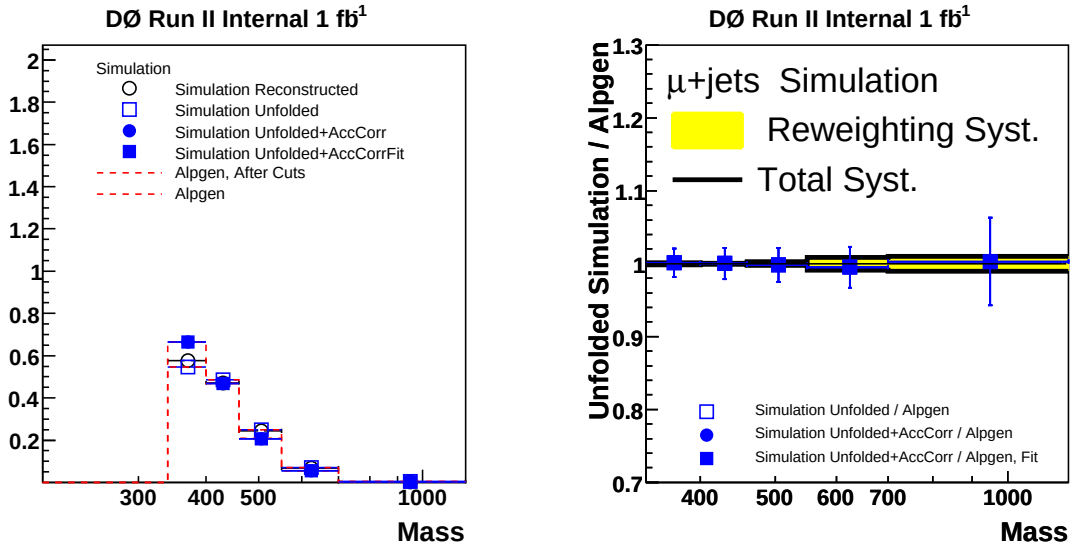

Figure 16.4: Unfolding the simulation $t\bar{t}$ system mass spectrum in μ+jets using the effective rank of 4 with "Pol2"-reweighted migration matrix. Signal model: ALPGEN.

16.3 Systematics Effects

Various sources of possible systematic error were studied and evaluated as the difference of the unfolded differential cross sections normalised to ALPGEN between the central and systematics-varied case. The error of the ratio to ALPGEN was then also propagated into the error of the unfolded distribution itself. In general, systematics are allowed to change the total integrated cross section, and are evaluated for up and down varied systematics. As it is unclear whether a particular shift leads to a higher or smaller cross section (and this can also change over the bins), all such systematics are taken as the maximal difference between the three cases of central and the shifted cases, or taken as a symmetrised error in case of only one systematics available. An appropriate migration matrix was used in each systematics study, for example the one where jet momenta are oversmeared by a varied data-simulation resolution factor in the case of the JER systematics (see below).

- Assumed $t\bar{t}$ cross section is a number entering the normalisation of the signal simulation and also reflects itself in the normalisation of the W+jets background. DØ's combined measured cross section of 8.16 pb was used for the central value and was varied by the experimental errors of $^{+0.95}_{-0.88}$. Only a mild dependence of the extracted cross section on the injected one was observed and the extracted values of 8.17 pb and 8.19 pb (see Tables 16.1–16.2) are in excellent agreement with the injected 8.16 pb. The extracted versus injected cross section is plotted in Figure 16.5. The approximate linear dependence is understandable as the injected cross section affects the assumed purity and influences the integrated cross section (measured on purity-fit background subtracted and unfolded data) in the same direction.

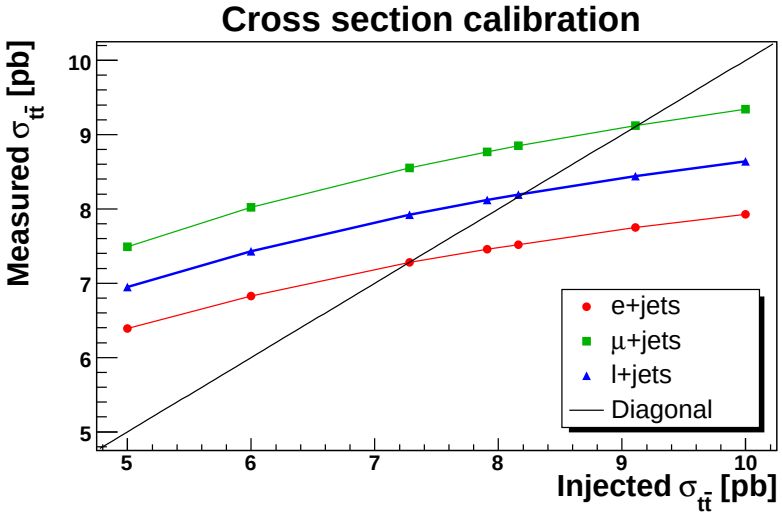

Figure 16.5: Measured cross section as integrated from final unfolded data distribution as a function of the injected cross section (assumed $t\bar{t}$ cross section for the signal simulation). Similar extracted value as the injected occurs around the used value of 8.16 pb.

- Data jet energy scale (data JES) was varied by the total data JES error by $\pm\sigma_{\mathrm{JES}}^{\mathrm{Data}}$

while simulation JES was kept at central so that largest shift between the two can be assigned as the systematics.

- Simulation JES: In the analysis data-set, the simulation JES was shifted by the sum of errors (in quadrature) of both data and MC (because of practical reasons of the top group, where the data/simulation agreement is the primary goal, unlike in this analysis). In order to model independently the MC JES shift effect, unfolded data with JES shifted in the same direction as MC JES were compared; proper MC JES-shifted migration matrices as well as acceptance were used;
- Relative data-simulation JES (JES shifting) was varied by the uncertainty of the fit describing the JES shift between data and simulation.
- Jet energy resolution (JER): The simulation jets are smeared to match the data resolution; the over-smearing factor was therefore varied by its error (see Section 6.12) and corresponding acceptances as well as migration matrices were used.
- Jet identification efficiency difference between data and simulation (Jet-ID) was accounted for by removing from the simulation randomly jets based on the parametrisation of the scale factor on the jet-ID efficiency between the data and the simulation. An uncertainty on the scale factor was varied one way towards the lower simulation efficiency and the unfolded result was again compared to the central case.
- Generator (ALPGEN or PYTHIA) systematics: by default, ALPGEN is the generator used for the signal model and migration matrix. As a systematics, PYTHIA-based migration matrix was used to unfold the data (still background-subtracted using ALPGEN).
- The systematics on the assumed top quark mass was evaluated using signal samples of $m_{\text{top}} = 170$ and 175 GeV while fixing to the corresponding top mass also in the kinematic fitter for signal and data samples. Proper acceptance and migration matrix were consistently used and the systematics was derived as the symmetrised difference between the two cases.
- Luminosity uncertainty of 0.5 pb was assigned to the extracted cross section as a constant uncertainty of $0.5/8.16 = 6.1\%$.

16.3.1 Systematics on Reweighting the $t\bar{t}$ system p_{T}

An important issue is the data/simulation discrepancy in the description of the $t\bar{t}$ system p_{T}. The question is how this failure may influence the level of agreement between the data and simulation in terms of the top quark p_{T} spectrum. For this purpose, simulation was reweighted at the reconstruction level (the reason for not reweighting the truth level is a small correlation between truth and reco for this distribution) as documented in Figure 16.6 so that the system p_{T} spectrum matches the shape in data in separate e/μ+jets channels. Top quark p_{T} spectrum change was observed in terms of reweighted simulation ratio to unchanged data (see Figure 16.7) and the reweighted simulation top quark p_{T} spectrum was then unfolded using the original migration matrix and unfolded results were compared to the same original (not-reweighted) parton level. The idea is that the discrepancy in the data system p_{T} is though to be a reconstruction issue rather than a real difference of the underlying parton spectra. The symmetrised difference between the two unfolded simulation results (see Figure 16.8) was taken as an additional systematics also for the data.

Total Systematics

Dedicated plots describing the relative systematics on the unfolded distributions as the ratio to the ALPGEN prediction are depicted in Figures 16.9–16.14, first in individual e+jets and μ+jets channels for leptonic top quark p_{T} as well as the $t\bar{t}$ system mass, and then also for the final combined ℓ+jets channel.

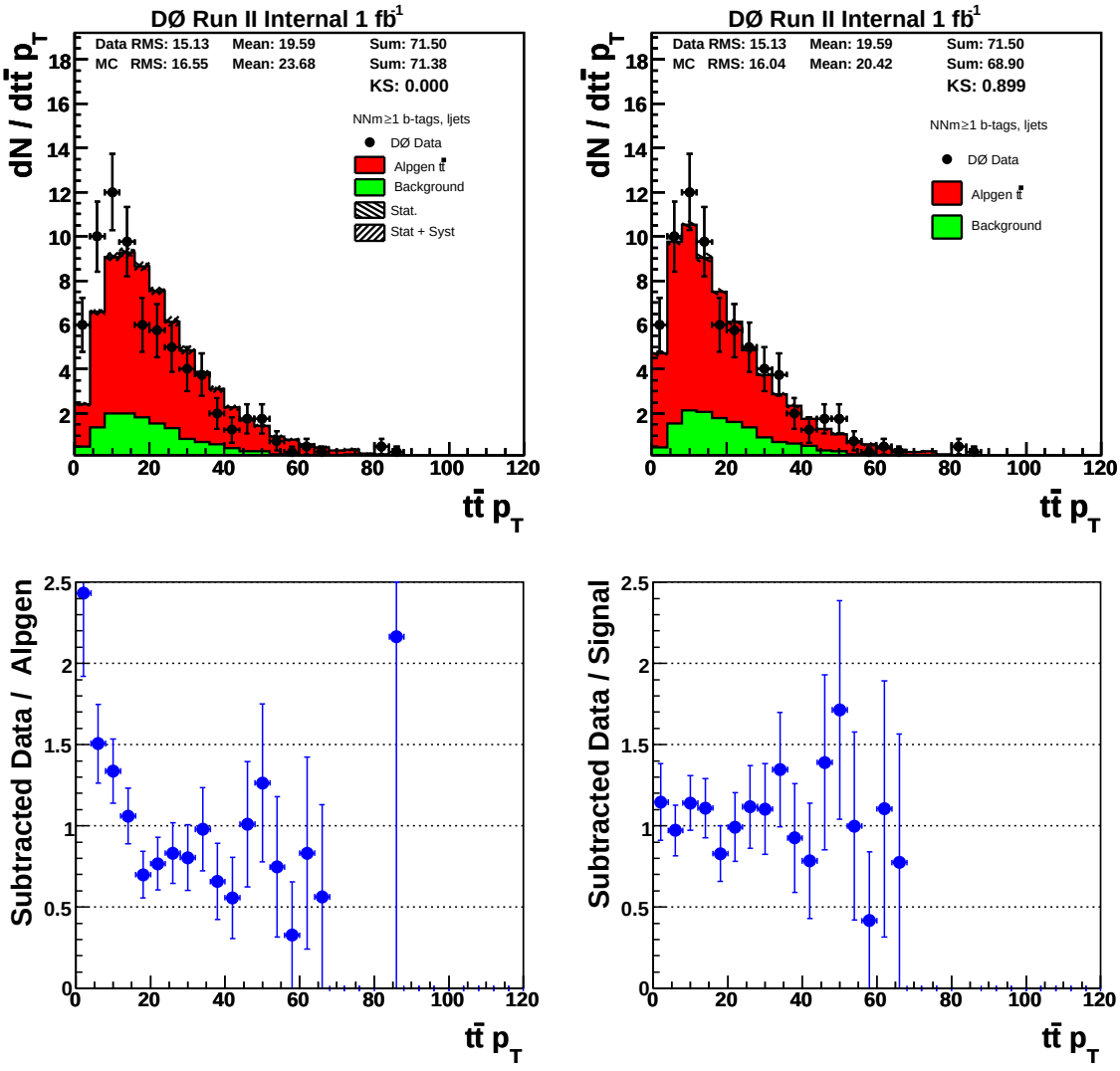

Figure 16.6: Effect of the reweighting of the $t\bar{t}$ system p_{T}. Left: using standard simulation, right: after reweighting $t\bar{t}$ system p_{T} to data. Signal model: ALPGEN.

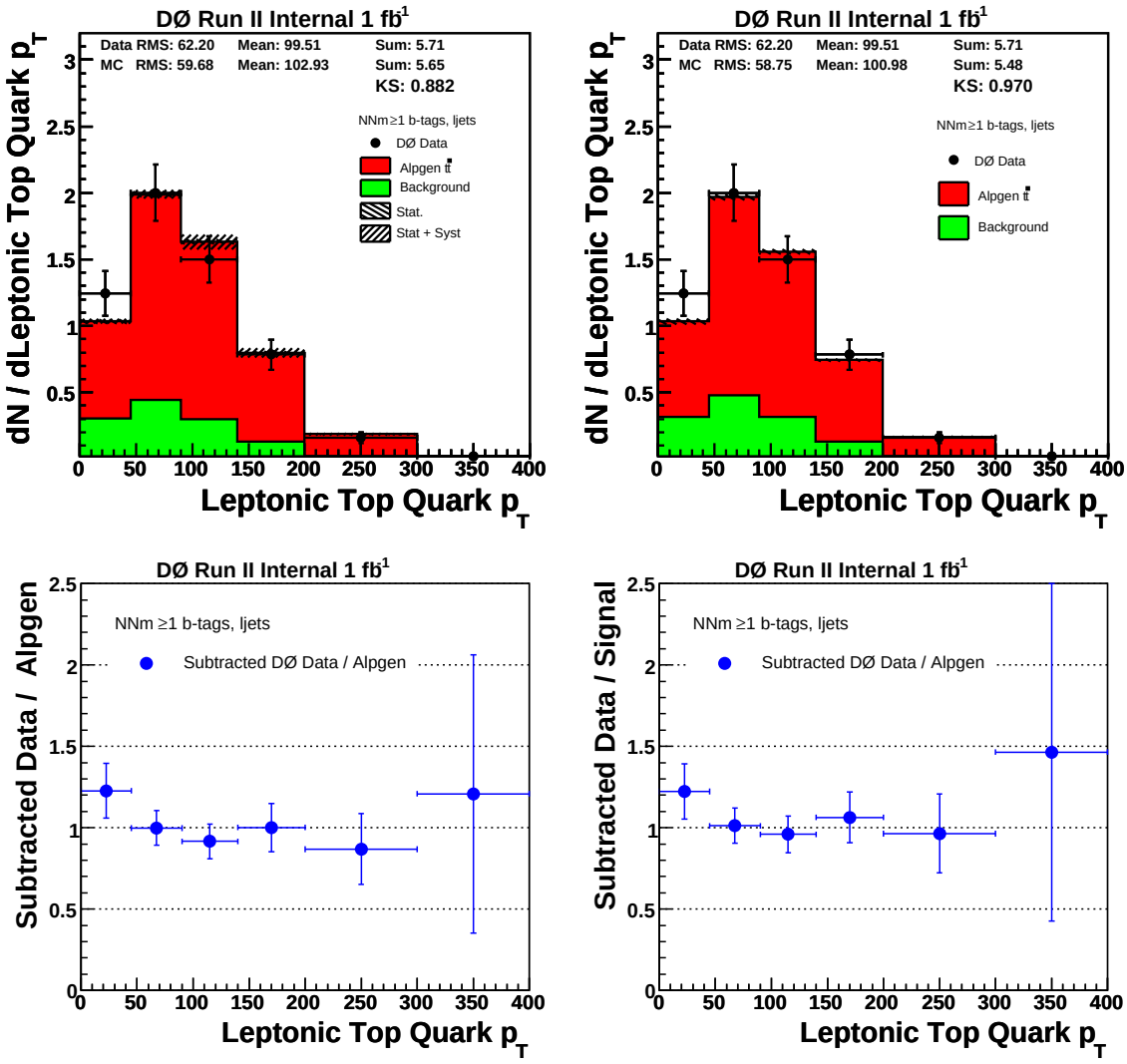

Figure 16.7: Effect of the reweighting of the $t\bar{t}$ system p_{T} on the leptonic top quark p_{T}. Left: using standard simulation, right: after reweighting $t\bar{t}$ system p_{T} to data. Signal model: ALPGEN.

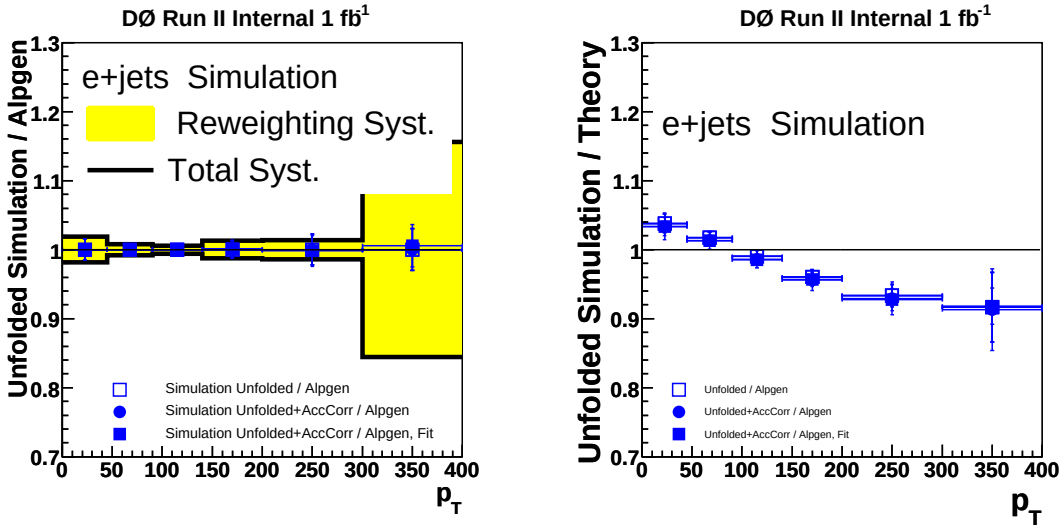

Figure 16.8: Unfolding the simulation leptonic top quark p_T spectrum in e+jets using the effective rank of 3. Left: standard simulation, right: after reweighting the $t\bar{t}$ p_T spectrum at the reconstructed level to match the data. The symmetrised difference between the left and right plots is taken as the $t\bar{t}$ system p_{T}-related systematics and is added to data syst. Signal model: ALPGEN.

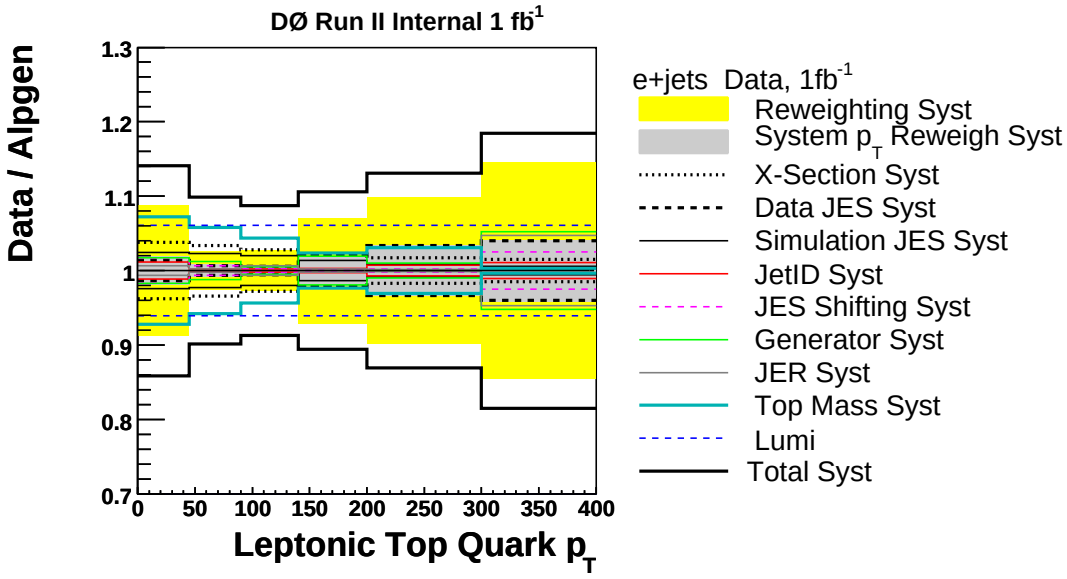

Figure 16.9: Systematics on unfolding data leptonic top quark p_T spectrum in e+jets using the effective rank of 2 for unfolded data / ALPGEN, full thick black symmetrical line is the total systematics.

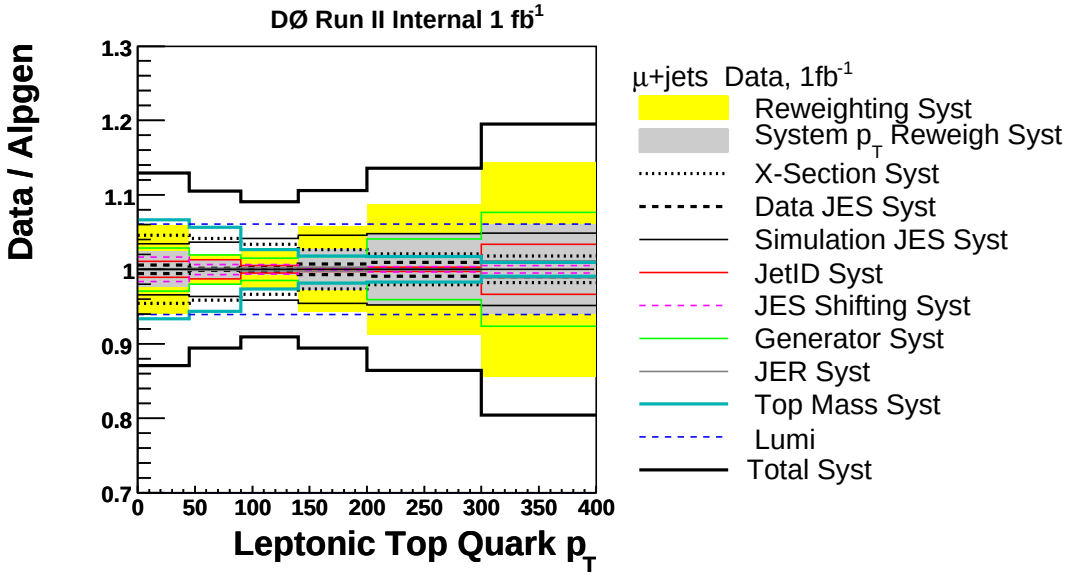

Figure 16.10: Systematics on unfolding data leptonic top quark p_T spectrum in μ+jets using the effective rank of 2 for unfolded data / ALPGEN, full thick black symmetrical line is the total systematics.

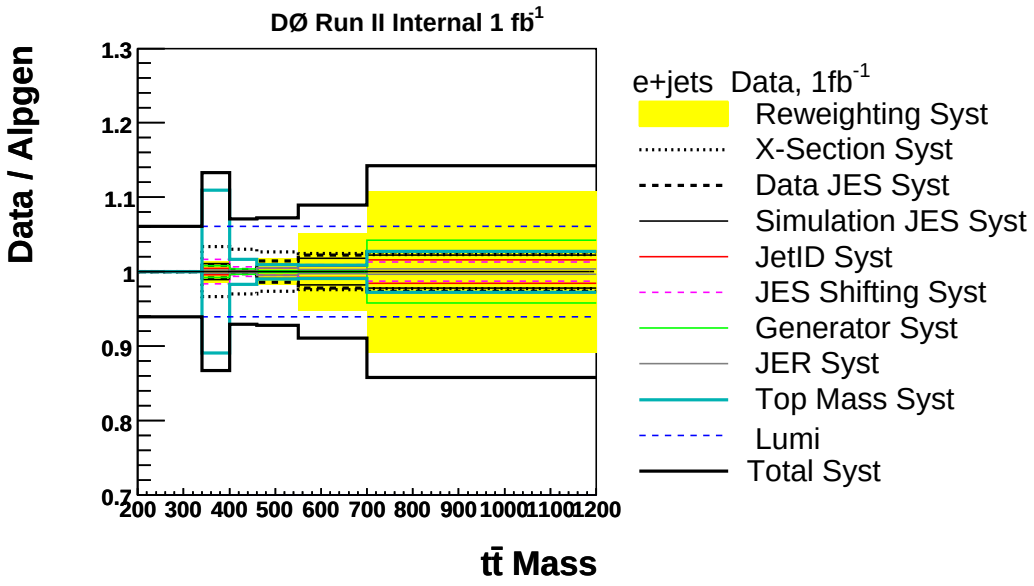

Figure 16.11: Systematics on unfolding data $t\bar{t}$ system mass spectrum in e+jets using the effective rank of 2 for unfolded data / ALPGEN, full thick black symmetrical line is the total systematics.

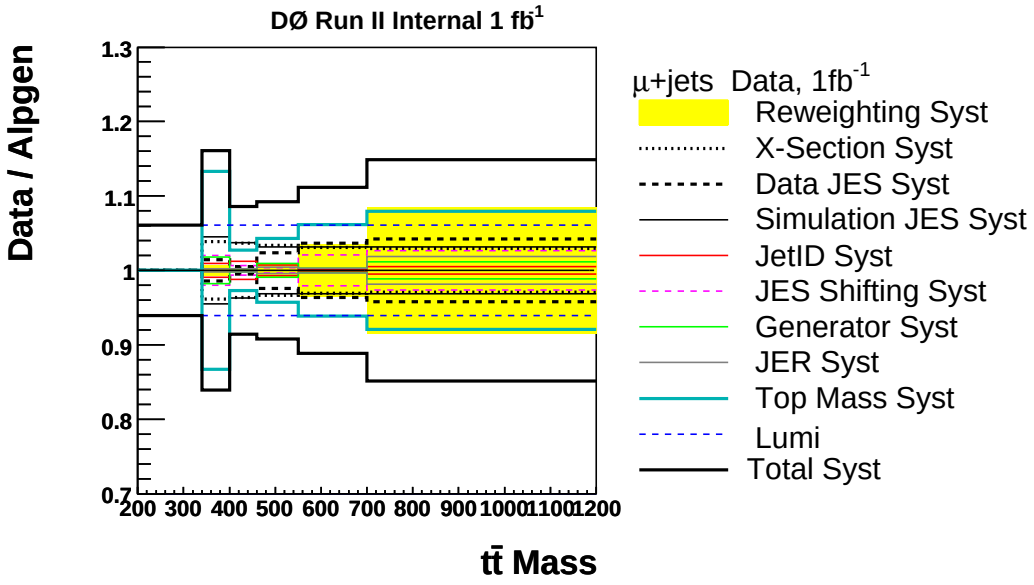

Figure 16.12: Systematics on unfolding data $t\bar{t}$ system mass spectrum in μ+jets using the effective rank of 2 for unfolded data / ALPGEN, full thick black symmetrical line is the total systematics.

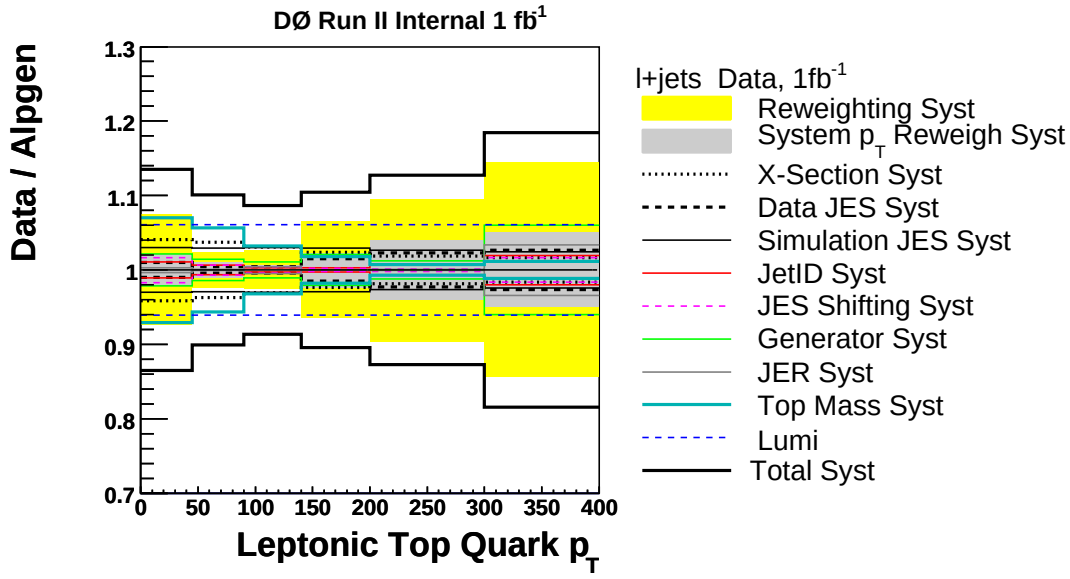

Figure 16.13: Systematics on unfolding data leptonic top quark p_T spectrum in ℓ+jets using the effective rank of 2 for unfolded data / ALPGEN, full thick black symmetrical line is the total systematics.

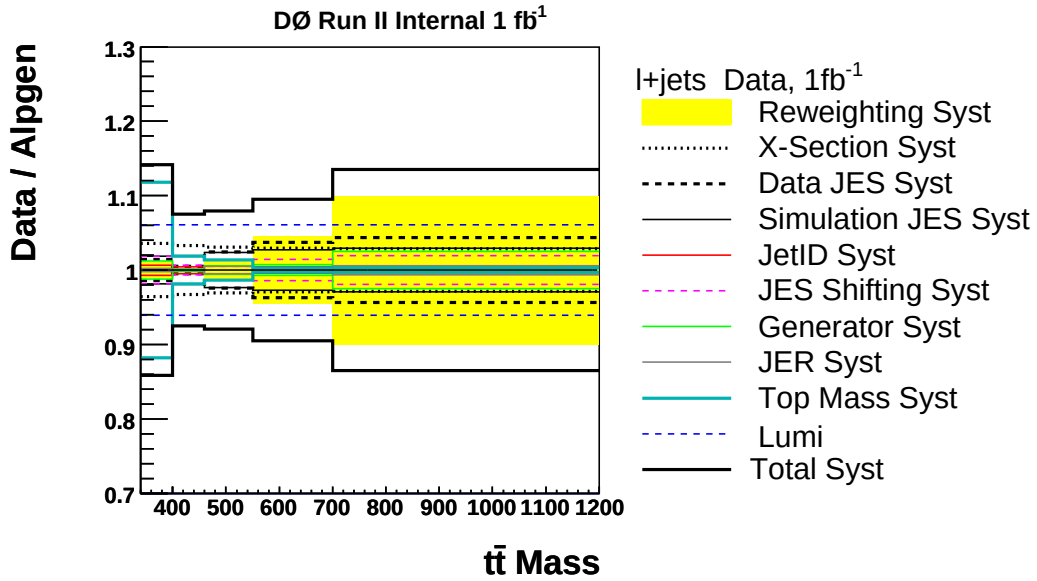

Figure 16.14: Systematics on unfolding data $t\bar{t}$ system mass spectrum in ℓ+jets using the effective rank of 2 for unfolded data / ALPGEN, full thick black symmetrical line is the total systematics.

16.4 Fully Corrected Data

The fully corrected differential cross section for the data, i.e. unfolded data corrected also for the acceptance shape and scaled to pb/GeV, are finally displayed in Figures 16.15–16.20 with the main result from the merged ℓ+jets channel being the Figures 16.19–16.20.

The unfolded spectra are in detail documented in Tables 16.1–16.2 as the list of bin contents as measured and unfolded in data together with the total error, and compared to the central values of ALPGEN and MC@NLO parton levels.

Bins [GeV]	0–45	45–90	90–140	140–200	200–300	300–400	σ_{tot}
Unfolded data	0.0346	0.0633	0.0439	0.0187	0.00438	0.000579	8.22
Total error	0.0042	0.0055	0.003	0.0028	0.001	0.00016	
ALPGEN	0.0315	0.0593	0.0427	0.0187	0.00447	0.000601	7.85
MC@NLO	0.0294	0.058	0.0428	0.018	0.00359	0.000307	7.54

Table 16.1: $\mathrm{d}\sigma/\mathrm{d}p_{\mathrm{T}}$[pb/GeV] for leptonic top quark p_{T}, ≥ 1 b-tags, signal model: Alpgen in ℓ+jets, effective rank 2.

Bins [GeV]	340–400	400–460	460–550	550–700	700–1200	σ_{tot}
Unfolded data	0.0564	0.0398	0.0175	0.00473	0.0003	8.21
Total error	0.006	0.0025	0.0023	0.001	8e-05	
ALPGEN	0.0537	0.0381	0.0169	0.00454	0.000288	7.85
MC@NLO	0.0514	0.038	0.0165	0.004	0.000199	7.54

Table 16.2: $\mathrm{d}\sigma/\mathrm{d}M$[pb/GeV] for $t\bar{t}$ system mass, ≥ 1 b-tags, signal model: Alpgen in ℓ+jets, effective rank 2.

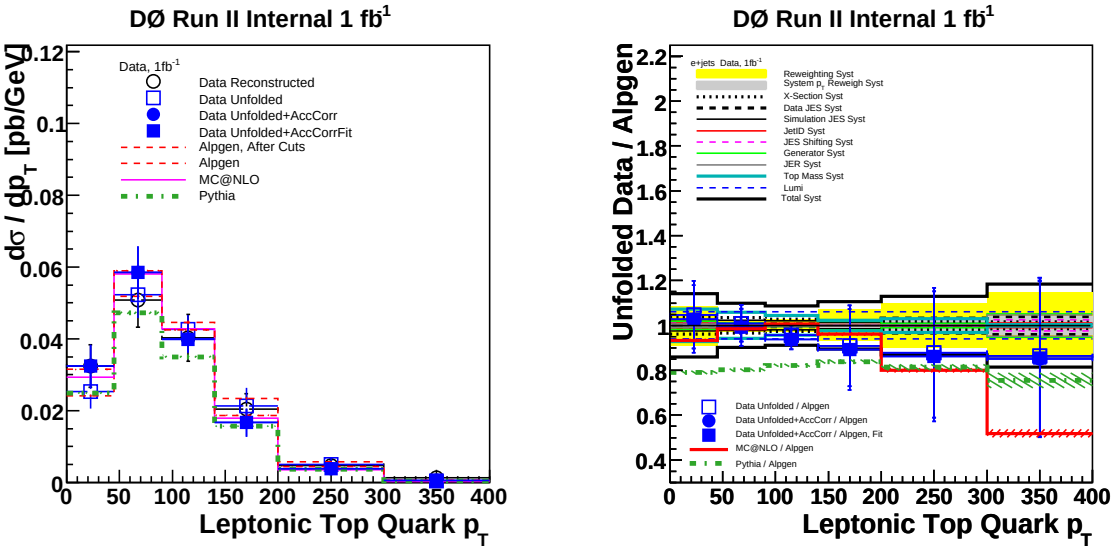

Figure 16.15: Unfolding data leptonic top quark p_T spectrum in e+jets using the effective rank of 2.

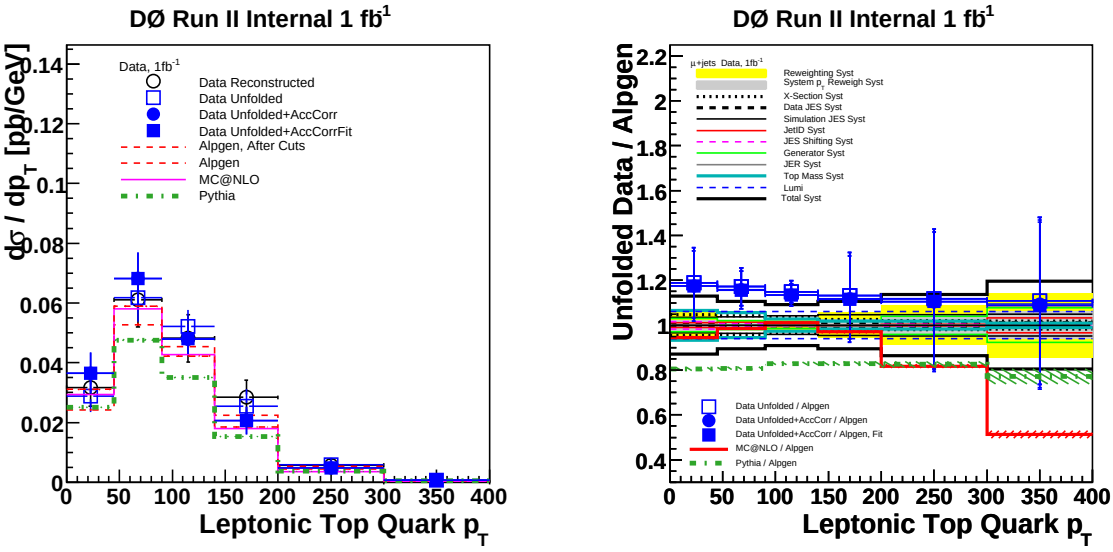

Figure 16.16: Unfolding data leptonic top quark p_T spectrum in μ+jets using the effective rank of 2.

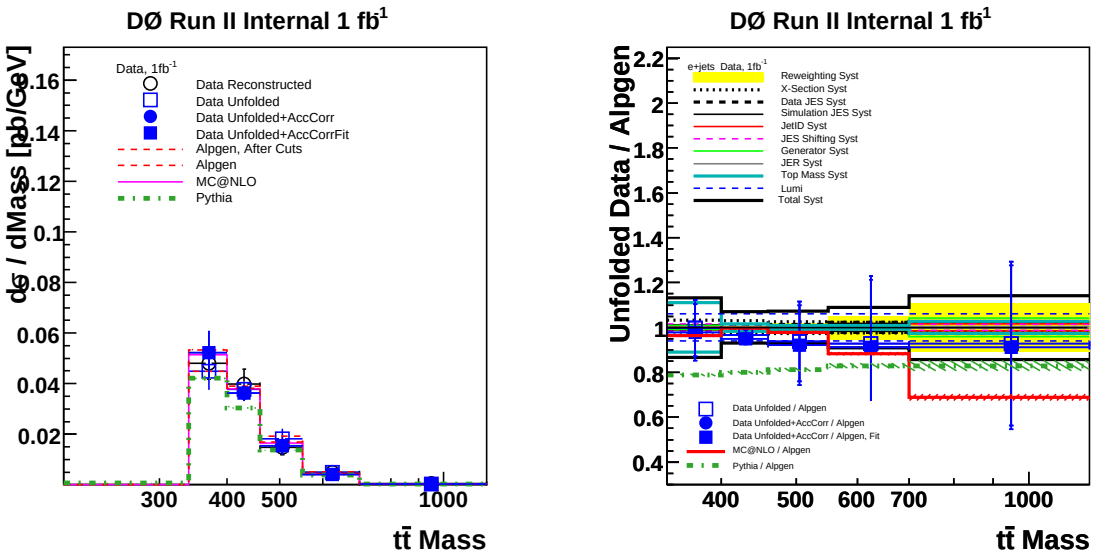

Figure 16.17: Unfolding data $t\bar{t}$ system mass spectrum in e+jets using the effective rank of 2.

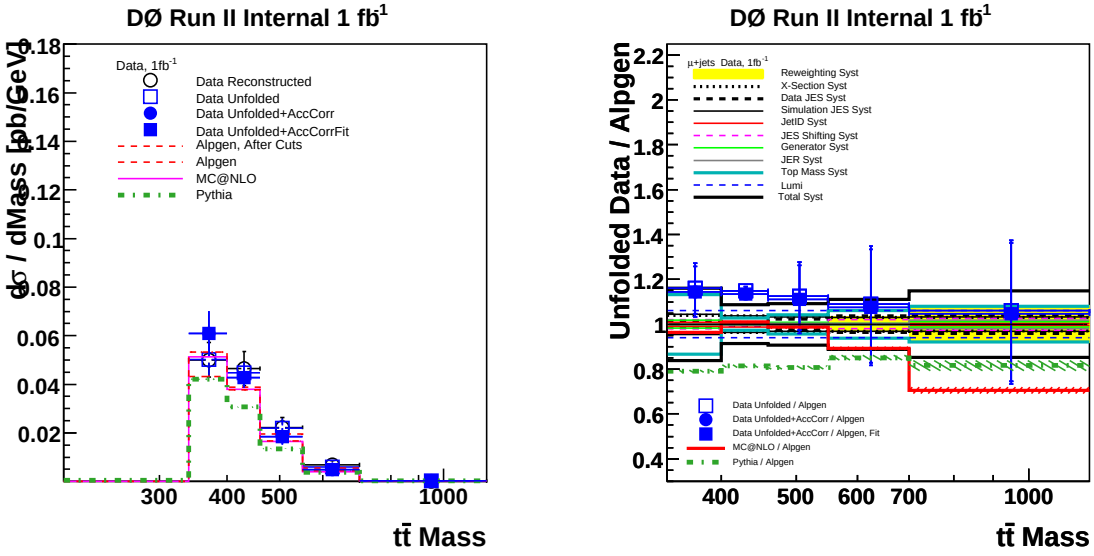

Figure 16.18: Unfolding data $t\bar{t}$ system mass spectrum in μ+jets using the effective rank of 2.

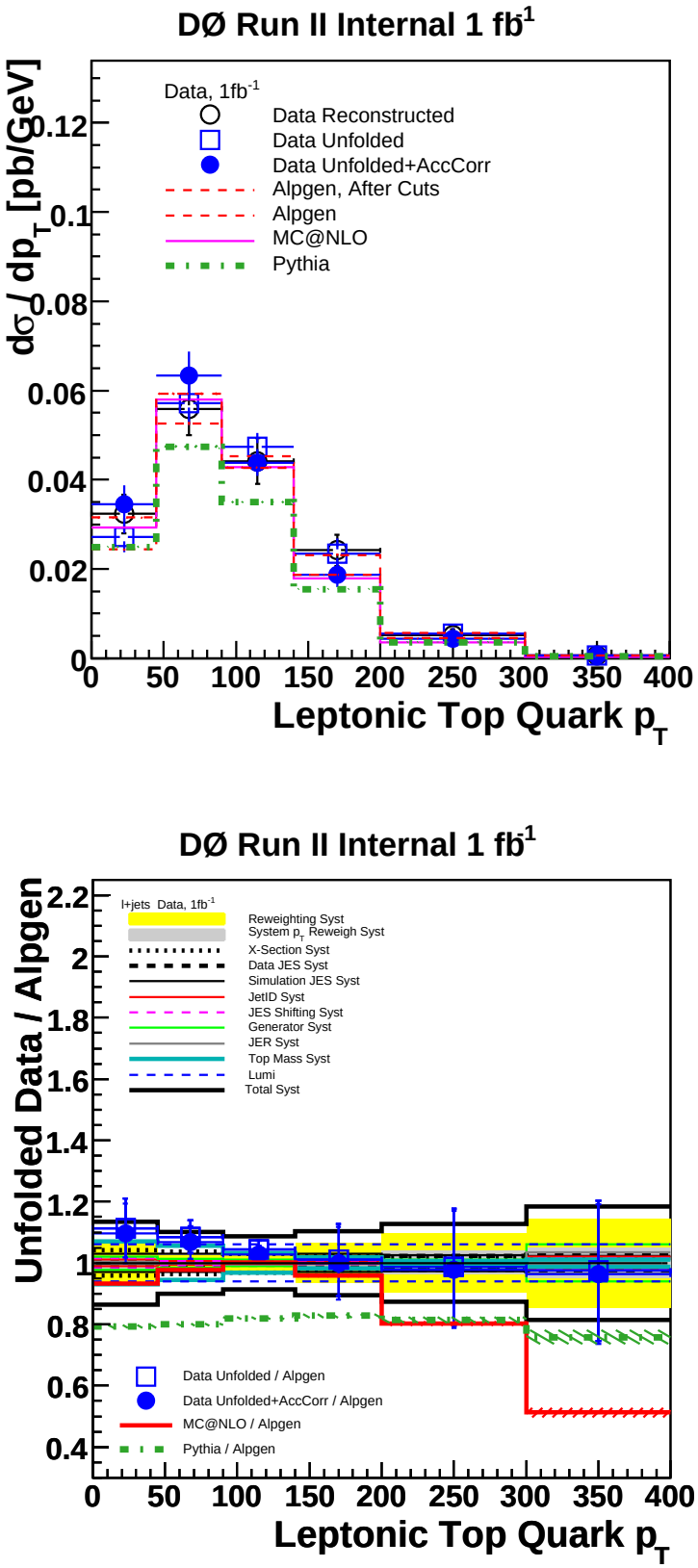

Figure 16.19: Unfolding data leptonic top quark p_T spectrum in ℓ+jets using the effective rank of 2.

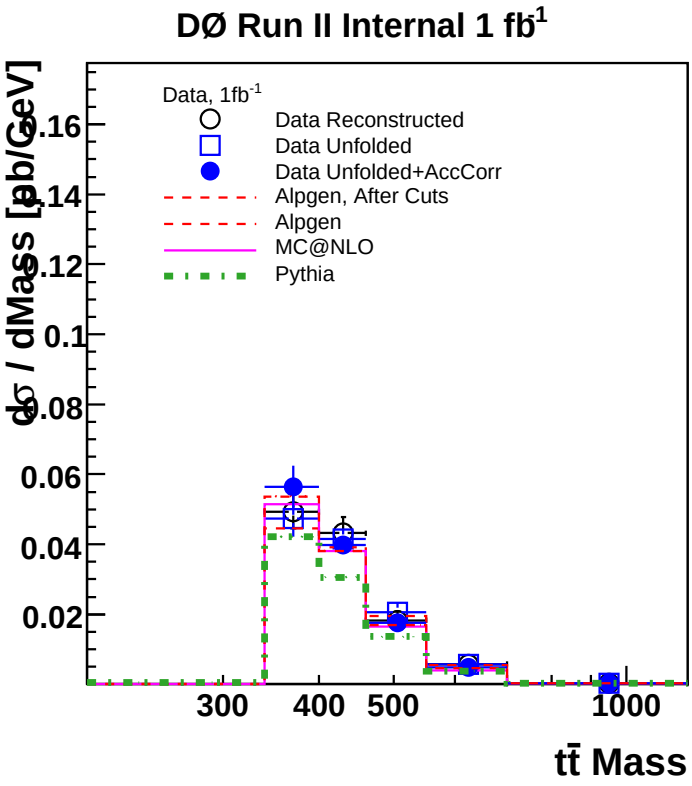

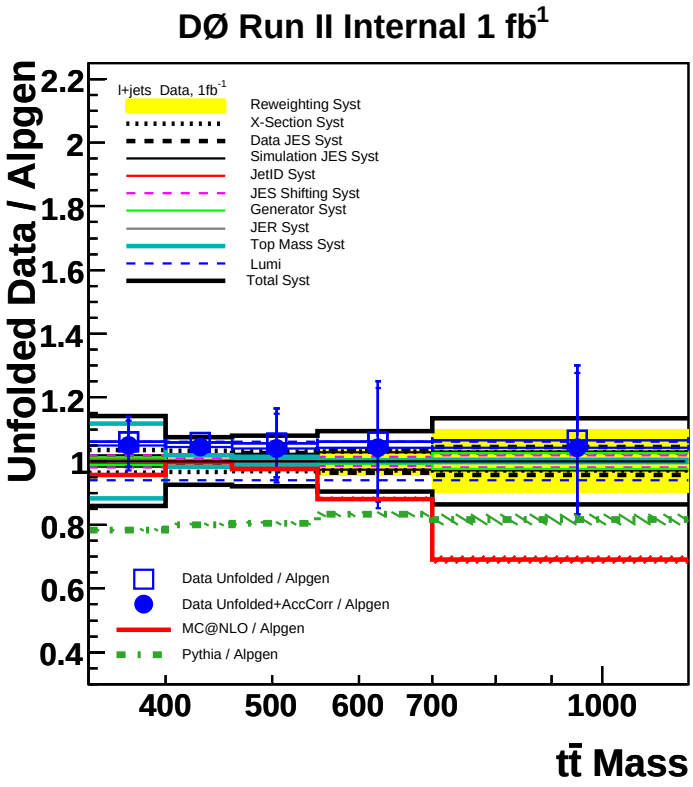

Figure 16.20: Unfolding data $t\bar{t}$ system mass spectrum in ℓ+jets using the effective rank of 2.

Chapter 17

Summary and Conclusions

The measurement of differential distributions shapes in the $t\bar{t}$ system is presented, investigating individual top quark spectra as well as observables related to the $t\bar{t}$ system. The simulation agrees reasonably well with the observed shapes, although some differences are visible. These may be related to the limited description by the LO Pythia event generator, but may also be a combined effect of inadequate tunes of the simulation to the data or hadronisation/fragmentation model.

Out of the wealth of differential distributions, spectra of the top quark transverse momentum and the $t\bar{t}$ pair invariant mass are further unfolded and corrected for the detector resolution and reconstruction effects using a regularised inversion of the migration matrix. Spectra are then corrected for the remaining effect of the differential acceptance shape and scaled to the final units of pb/GeV, therefore resulting in the measurement of differential cross sections in the $t\bar{t} \to \ell + \text{jets}$ channel.

Reasonable agreement is reached w.r.t. the shapes as predicted by the Alpgen parton level, while some discrepancy is observed when comparing to the MC@NLO prediction. This may be partially stemming from a residual model-dependence of the unfolding procedure, which is introduced by using a migration matrix between parton Alpgen and reconstructed (including the fitter) levels. As such, the migration includes particular models of the initial and final state radiation, underlying event as well as the specific Pythia hadronisation model, while these effects are modelled differently in the framework of MC@NLO, which is interfaced to Herwig with its own hadronisation.

An interesting discrepancy is observed in the transverse momentum of the $t\bar{t}$ system already at the reconstructed level (see Figures 12.12 and 13.4). This disagreement was not followed down to the unfolding level, but together with the p_{out} distribution in Figures 12.14 and 13.8 (the variable, defined in Chapter 12, is sensitive to the initial state radiation) the discrepancies may suggest that the tune used in Pythia is not the best suitable for the $t\bar{t}$ environment.

The reconstructed top quark-mass gives one confidence that basic resolutions are similar in data and simulation and that it is adequate to perform the unfolding using the resolutions obtained from the simulation. Various systematics effects were studied as a part of the analysis cross-checks. They are added in quadrature and displayed as a band around the unity. Statistical errors are depicted as points' error bars (obtained from the ensemble tests) of the final unfolded spectra divided by Alpgen.

Finally, the author concludes that the differential spectra shapes in the $t\bar{t}$ system are consistent with the Standard Model and reasonably well described by current event generators. Further analysis based on a larger statistics sample of the full Tevatron Run IIb could have an even larger power to diminish the statistical error and study systematic effects more deeply.

Appendix A

Additional Background Subtraction Plots

This appendix documents the purity fitting procedure for selected distributions in separate e+jets and μ+jets channels. Purity curve as fitted on signal and background models is applied to data points in order to subtract the background from data in a smooth way.

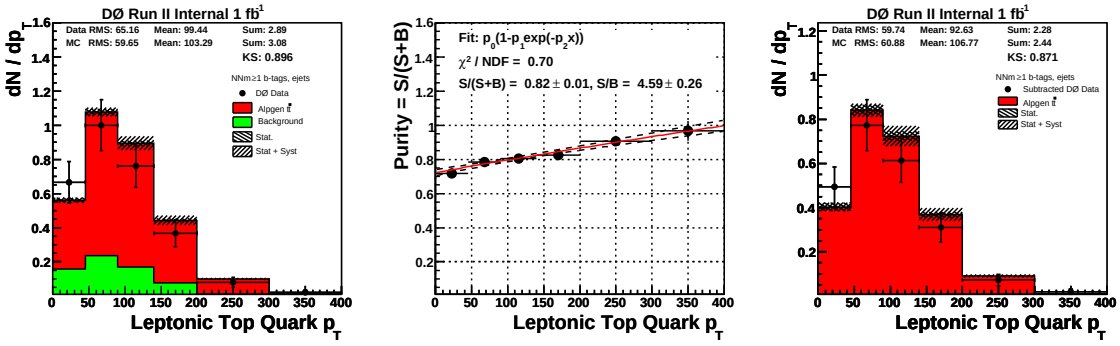

Figure A.1: Background correction for leptonic top p_{T}, e+jets NN-medium ≥ 1 b-tag bin. Signal model: ALPGEN.

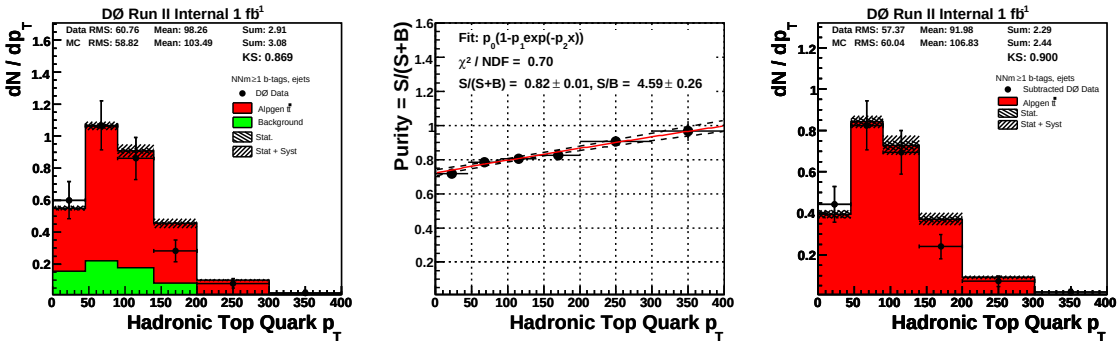

Figure A.2: Background correction for hadronic top p_{T}, e+jets NN-medium ≥ 1 b-tag bin. Signal model: ALPGEN.

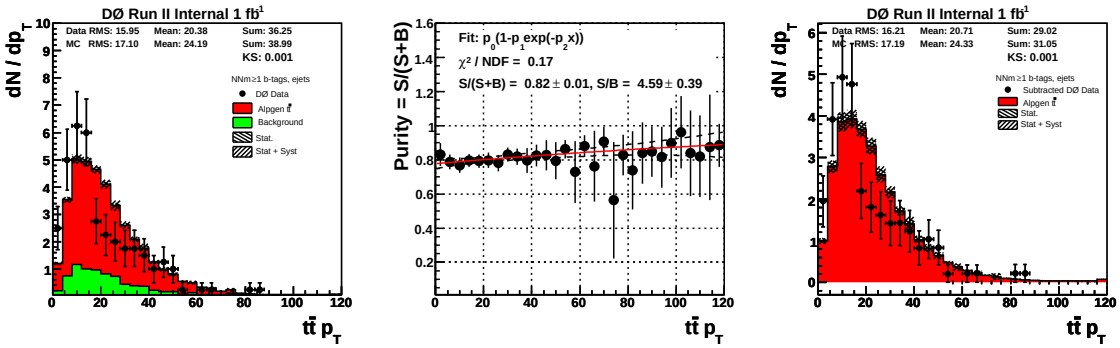

Figure A.3: Background correction for $t\bar{t}$ system p_{T}, e+jets NN-medium ≥ 1 b-tag bin. Signal model: ALPGEN.

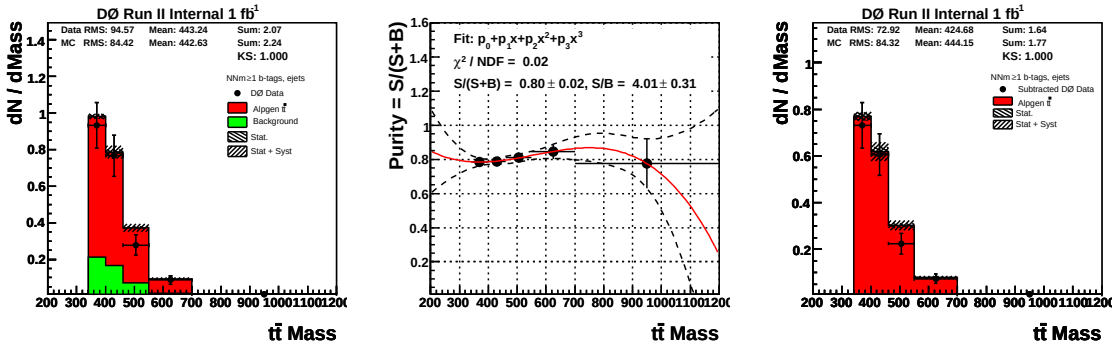

Figure A.4: Background correction for $t\bar{t}$ system mass, e+jets NN-medium ≥ 1 b-tag bin. Signal model: ALPGEN.

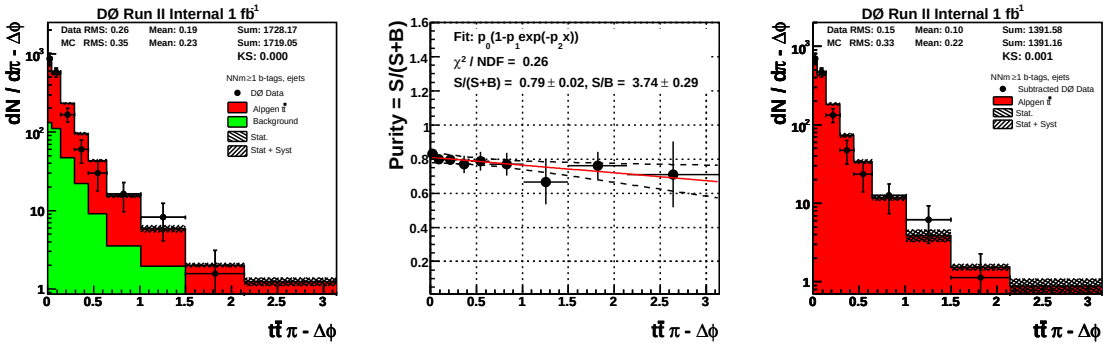

Figure A.5: Background correction for $\Delta\phi_{t\bar{t}}$, e+jets NN-medium ≥ 1 b-tag bin. Signal model: ALPGEN.

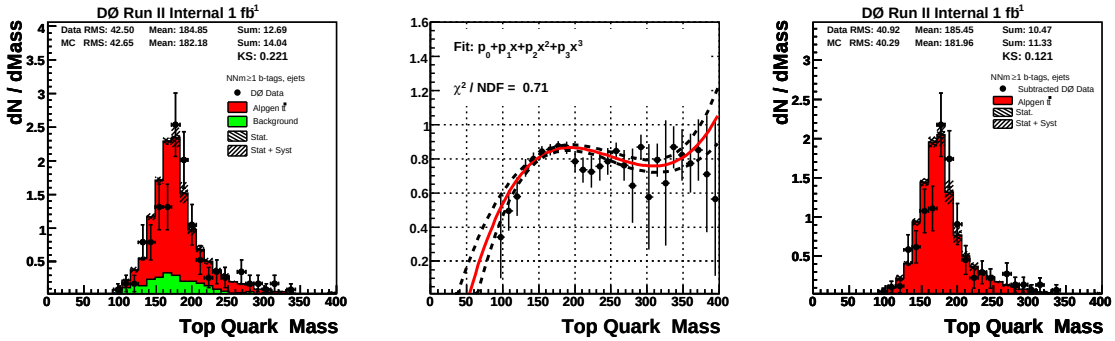

Figure A.6: Background correction for fitted top mass, e+jets NN-medium ≥ 1 b-tag bin. Signal model: ALPGEN.

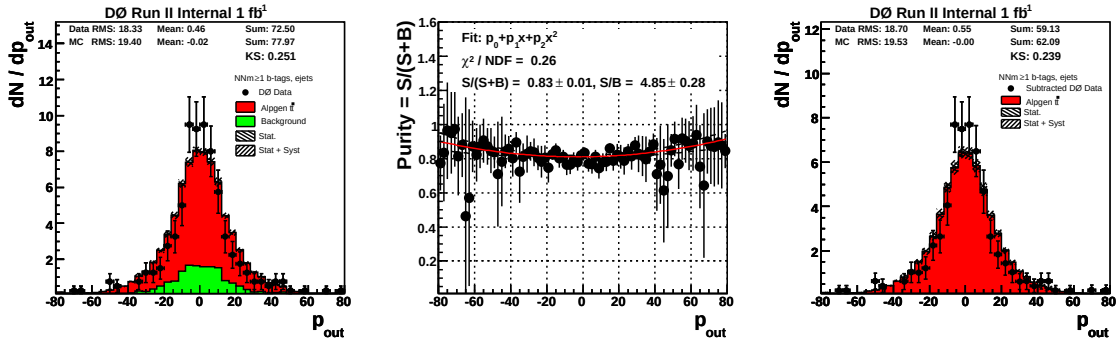

Figure A.7: Background correction for p_{out}, e+jets NN-medium ≥ 1 b-tag bin. Signal model: ALPGEN.

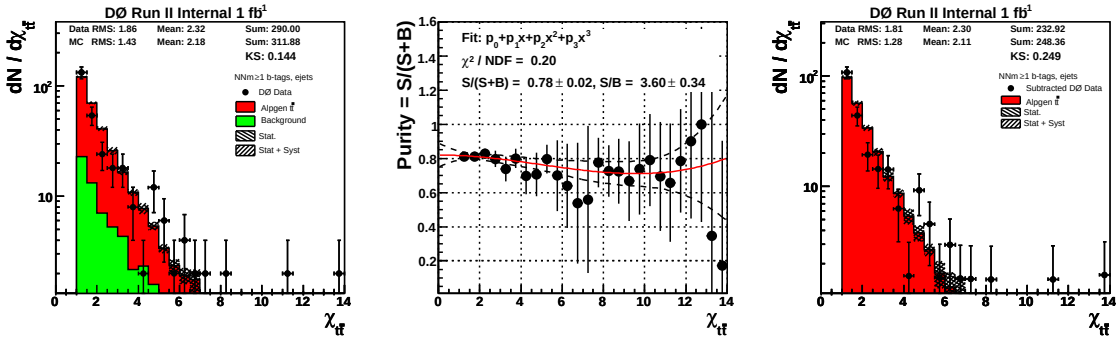

Figure A.8: Background correction for $\chi_{t\bar{t}}$, e+jets NN-medium ≥ 1 b-tag bin. Signal model: ALPGEN.

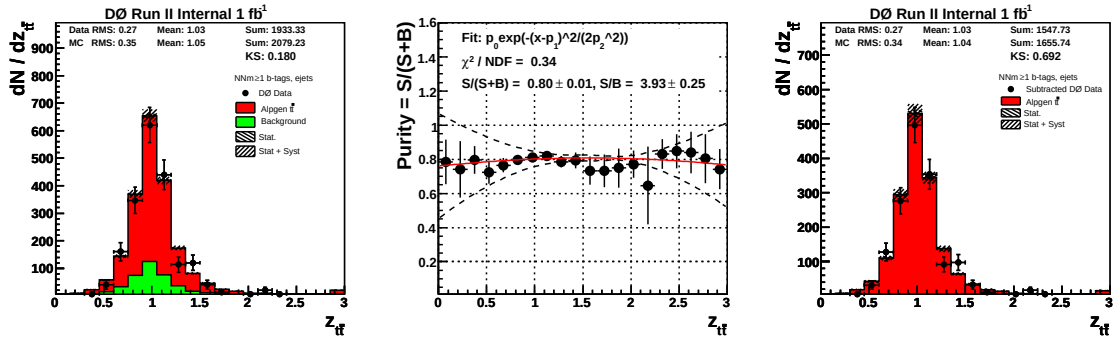

Figure A.9: Background correction for $z_{t\bar{t}}$, e+jets NN-medium ≥ 1 b-tag bin. Signal model: ALPGEN.

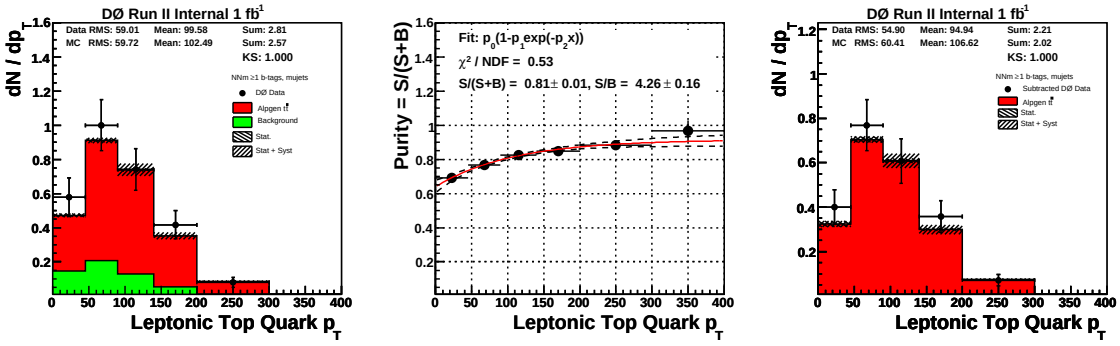

Figure A.10: Background correction for leptonic top p_{T}, μ+jets NN-medium ≥ 1 b-tag bin. Signal model: ALPGEN.

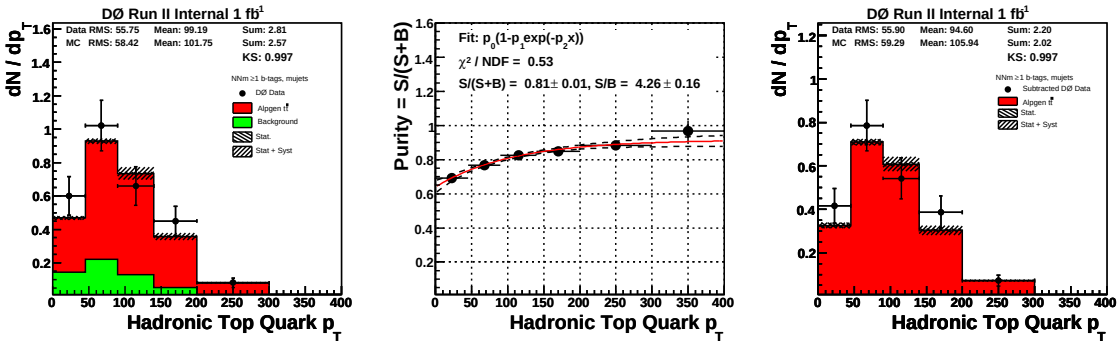

Figure A.11: Background correction for hadronic top p_{T}, μ+jets NN-medium ≥ 1 b-tag bin. Signal model: ALPGEN.

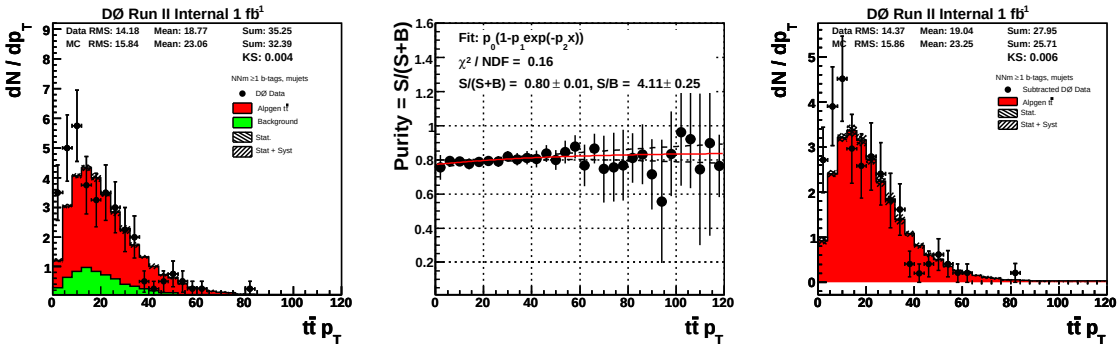

Figure A.12: Background correction for $t\bar{t}$ system p_{T}, μ+jets NN-medium ≥ 1 b-tag bin. Signal model: ALPGEN.

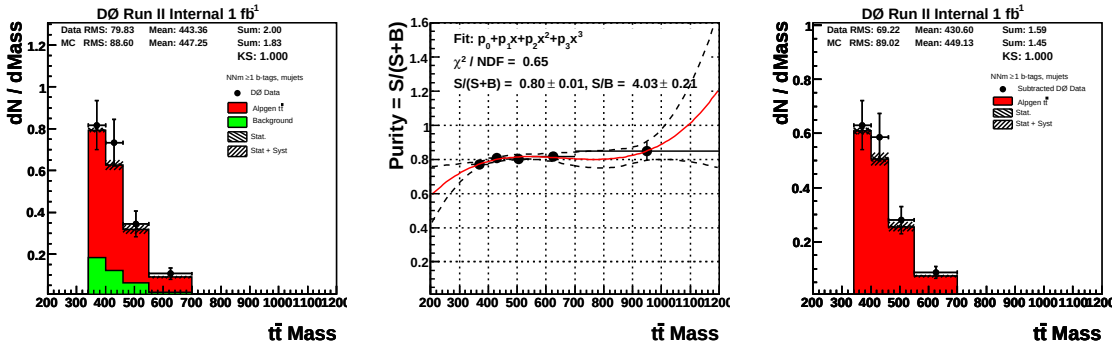

Figure A.13: Background correction for $t\bar{t}$ system mass, μ+jets NN-medium ≥ 1 b-tag bin. Signal model: ALPGEN.

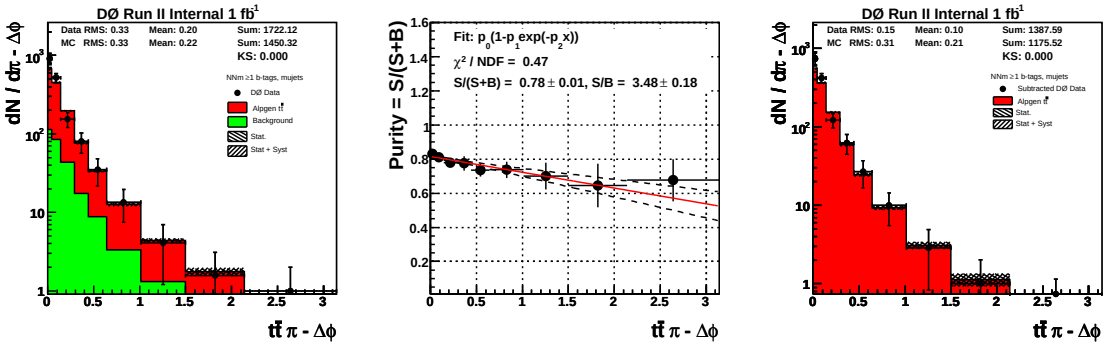

Figure A.14: Background correction for $\Delta\phi_{t\bar{t}}$, μ+jets NN-medium ≥ 1 b-tag bin. Signal model: ALPGEN.

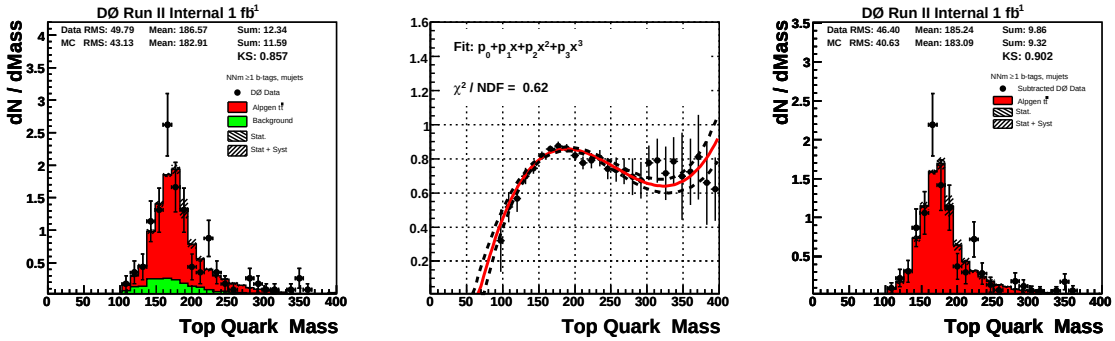

Figure A.15: Background correction for fitted top mass, μ+jets NN-medium ≥ 1 b-tag bin. Signal model: ALPGEN.

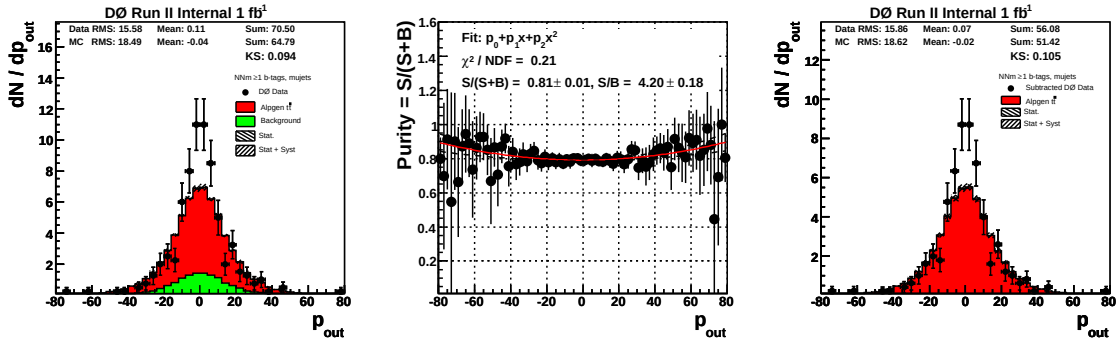

Figure A.16: Background correction for p_{out}, μ+jets NN-medium ≥ 1 b-tag bin. Signal model: ALPGEN.

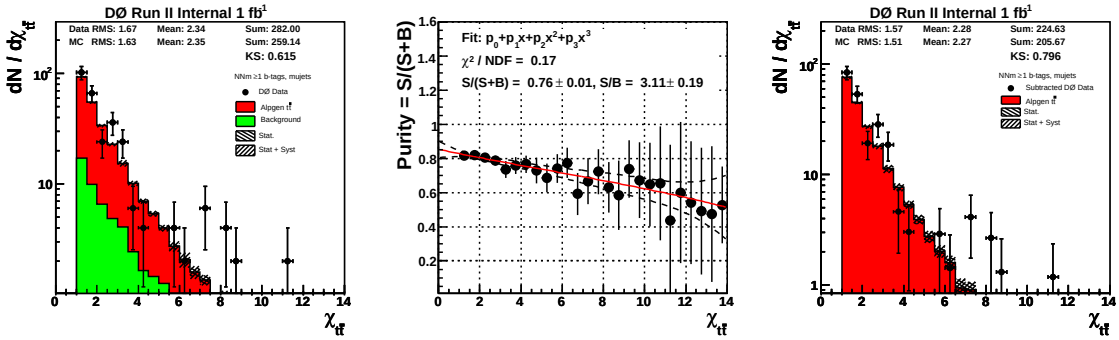

Figure A.17: Background correction for $\chi_{t\bar{t}}$, μ+jets NN-medium ≥ 1 b-tag bin. Signal model: ALPGEN.

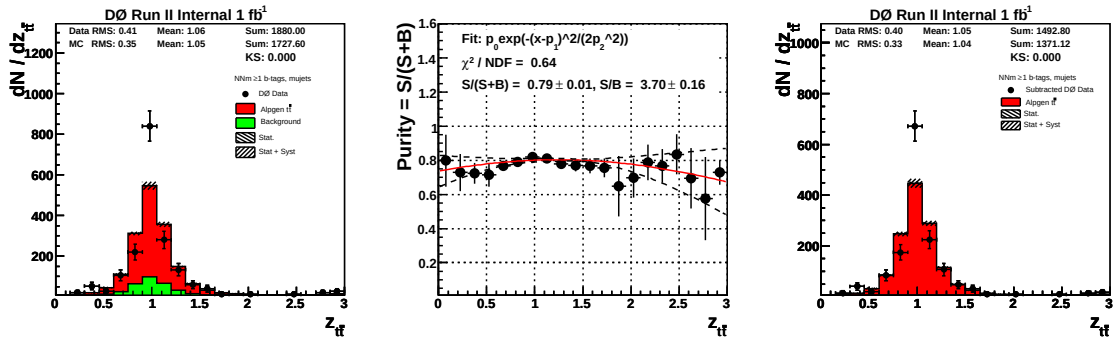

Figure A.18: Background correction for $z_{t\bar{t}}$, μ+jets NN-medium ≥ 1 b-tag bin. Signal model: ALPGEN.

Appendix B

Additional Unfolding Cross-Check Plots

This appendix documents in detail the unfolding results of the leptonic top quark p_{T} and the $t\bar{t}$ system mass for the simulation ℓ+jets channel in Figures B.1–B.2 and data in Figures B.3-B.9 for $e/\mu/\ell$+jets channels using variously reweighted migration matrix at the truth level. The unfolded result is fully corrected for the acceptance and divided by the ALPGEN parton level prediction.

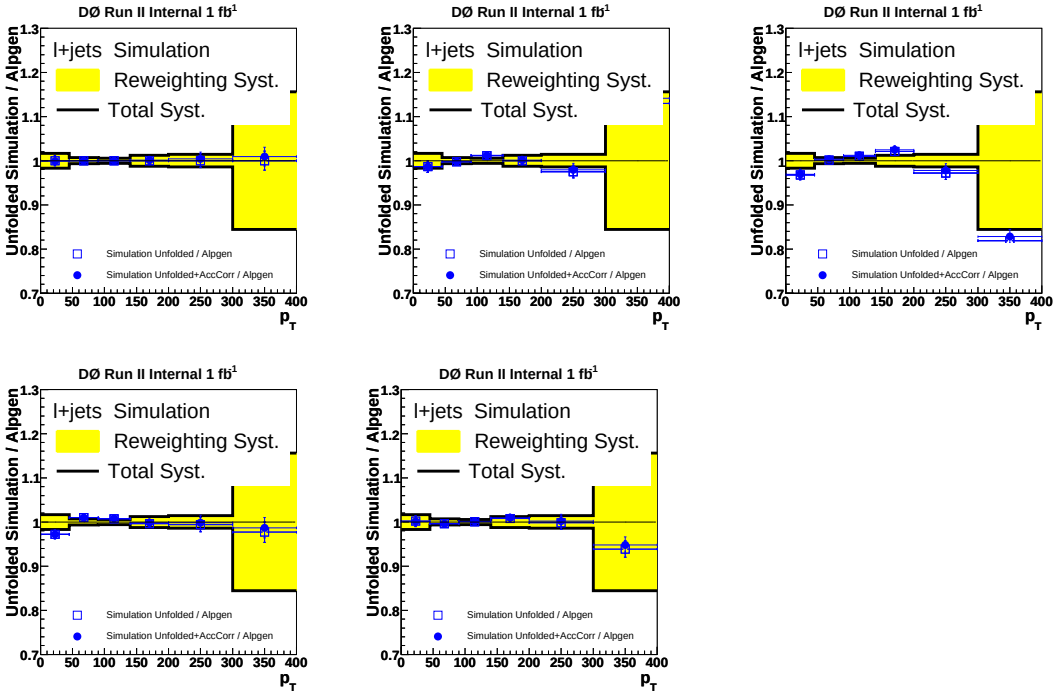

Figure B.1: Leptonic top p_{T}, unfolded full statistics ALPGEN with variously reweighted (at truth level) migration matrices, effective rank 3 in ℓ+jets.

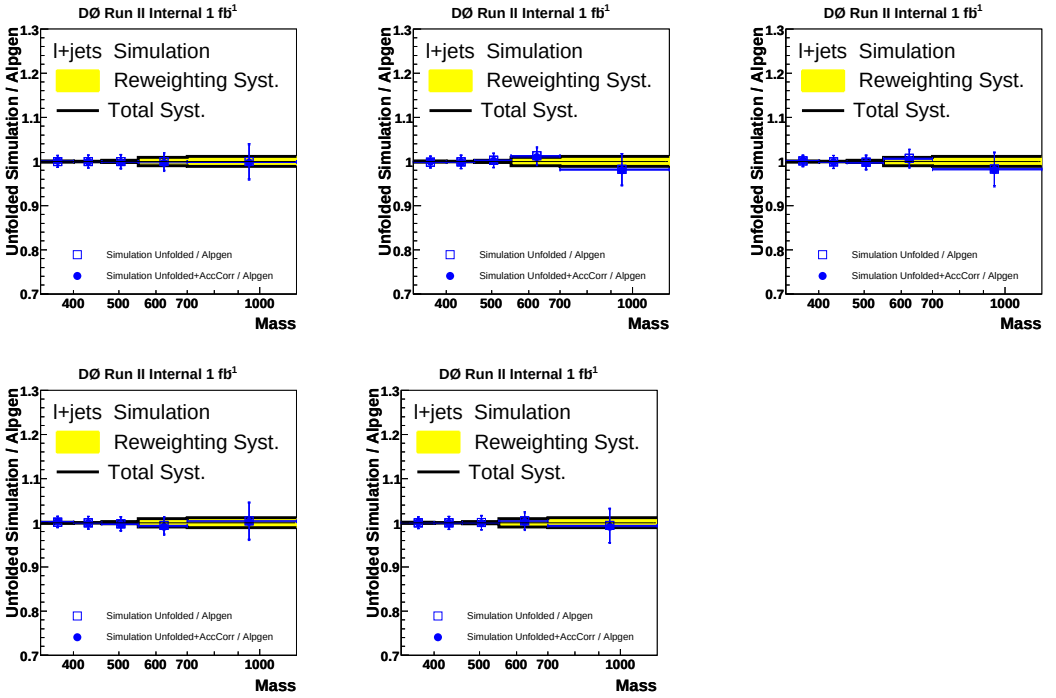

Figure B.2: $t\bar{t}$ system mass, unfolded full statistics ALPGEN with variously reweighted (at truth level) migration matrices, effective rank 4 in ℓ+jets.

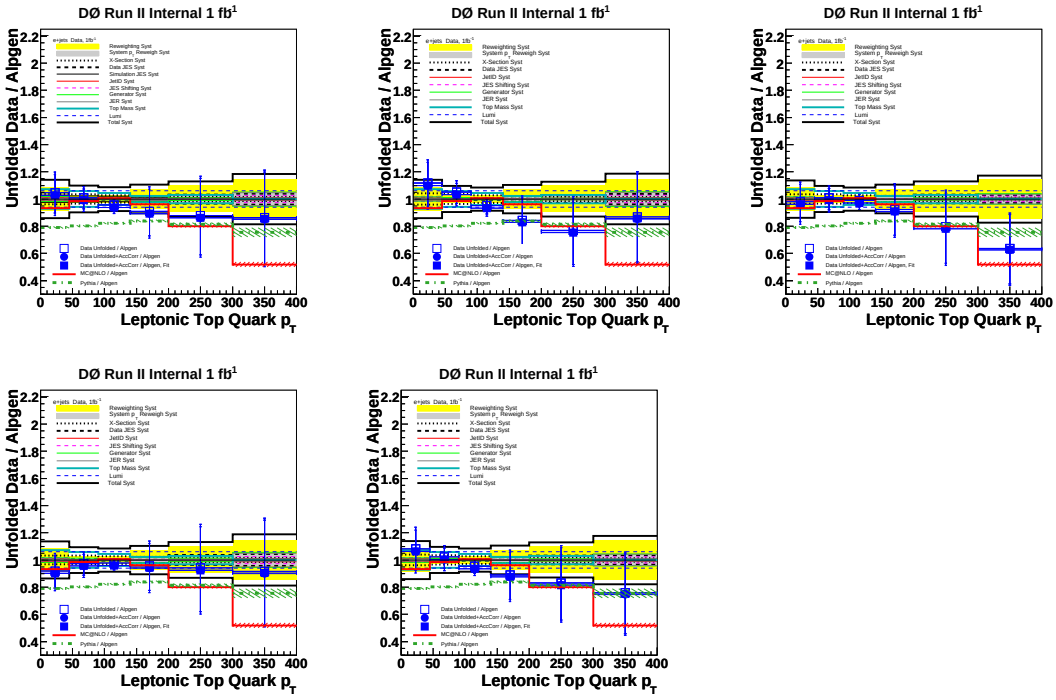

Figure B.3: Data unfolding in $e+$ jets; Reweighting sensitivity, rank 02, leptonic top p_T; for various reweighting of the migration matrix.

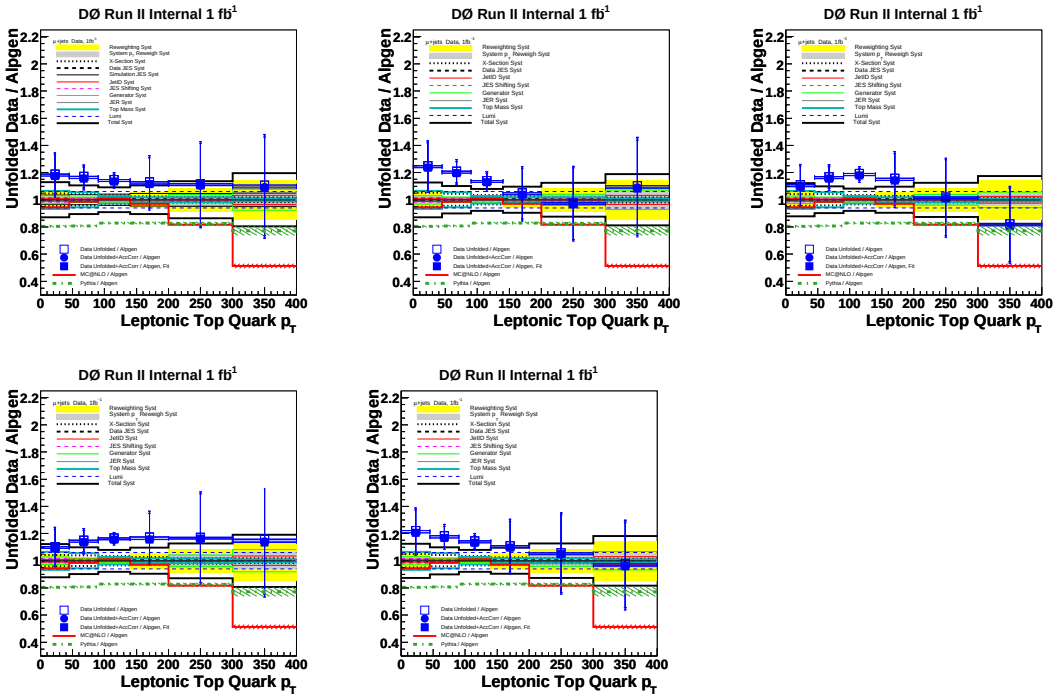

Figure B.4: Data unfolding in $\mu+$ jets; Reweighting sensitivity, rank 02, leptonic top p_T; for various reweighting of the migration matrix.

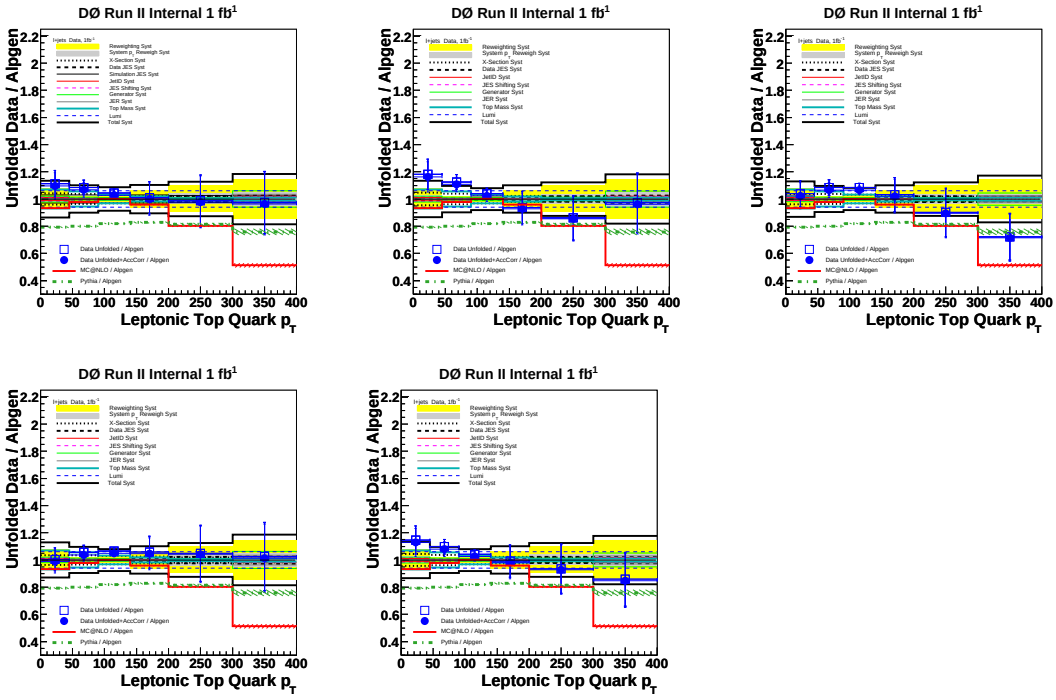

Figure B.5: Data unfolding in ℓ+ jets; Reweighting sensitivity, rank 02, leptonic top p_T; for various reweighting of the migration matrix.

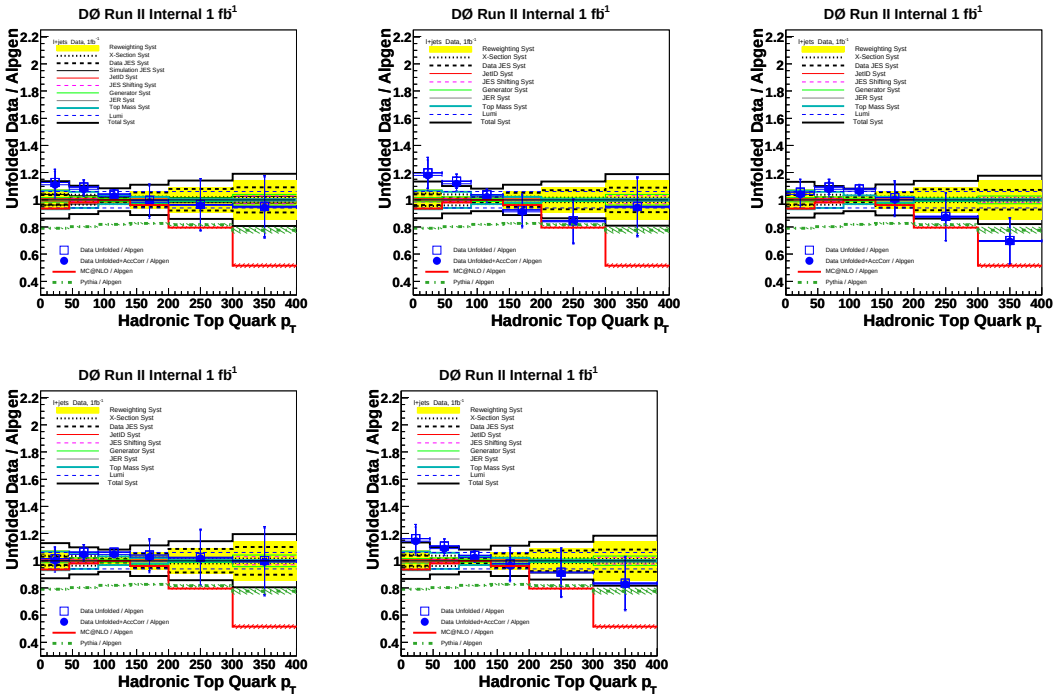

Figure B.6: Data unfolding in ℓ+ jets; Reweighting sensitivity, rank 02, hadronic top p_T; for various reweighting of the migration matrix.

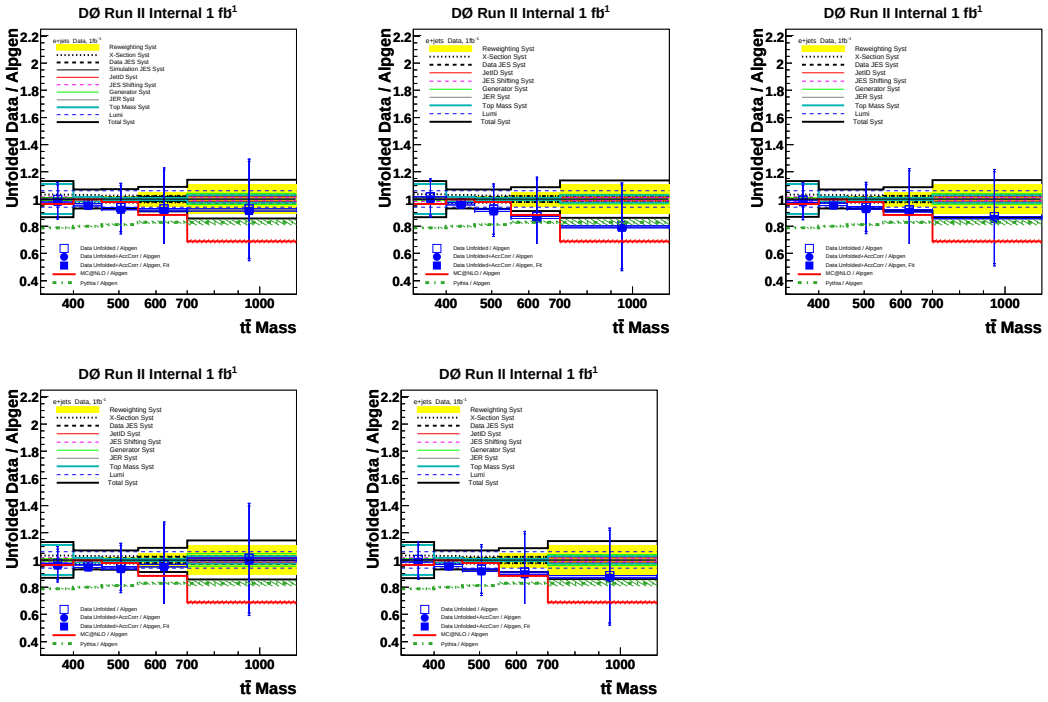

Figure B.7: Data unfolding in $e+$ jets; Reweighting sensitivity, rank 02, $t\bar{t}$ system mass; for various reweighting of the migration matrix.

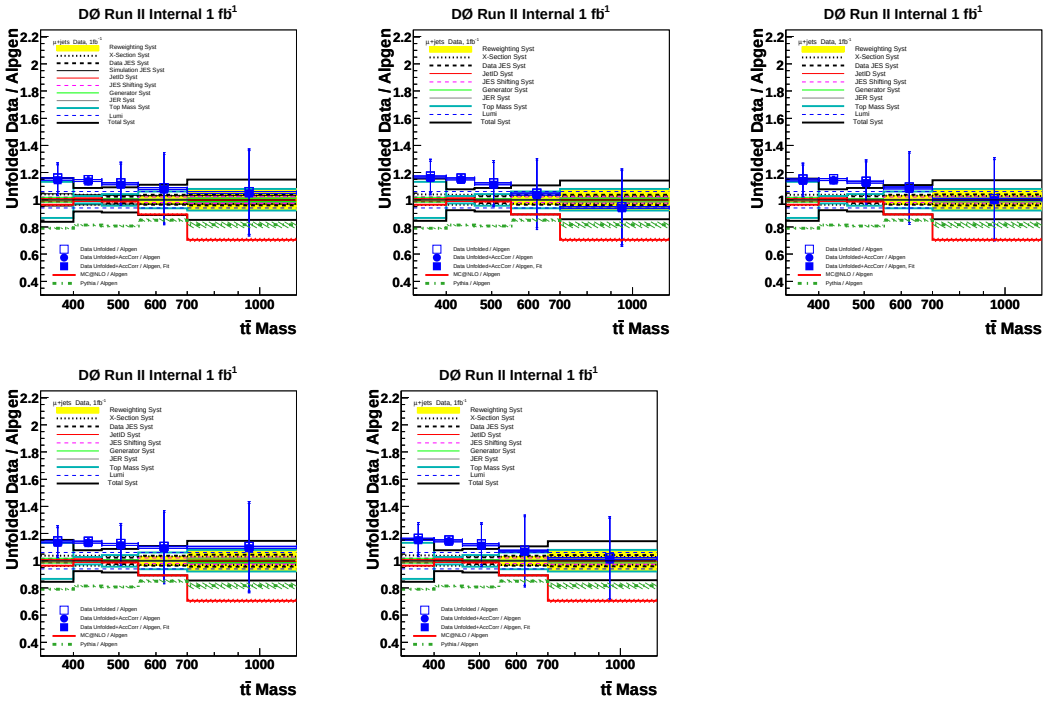

Figure B.8: Data unfolding in $\mu+$ jets; Reweighting sensitivity, rank 02, $t\bar{t}$ system mass; for various reweighting of the migration matrix.

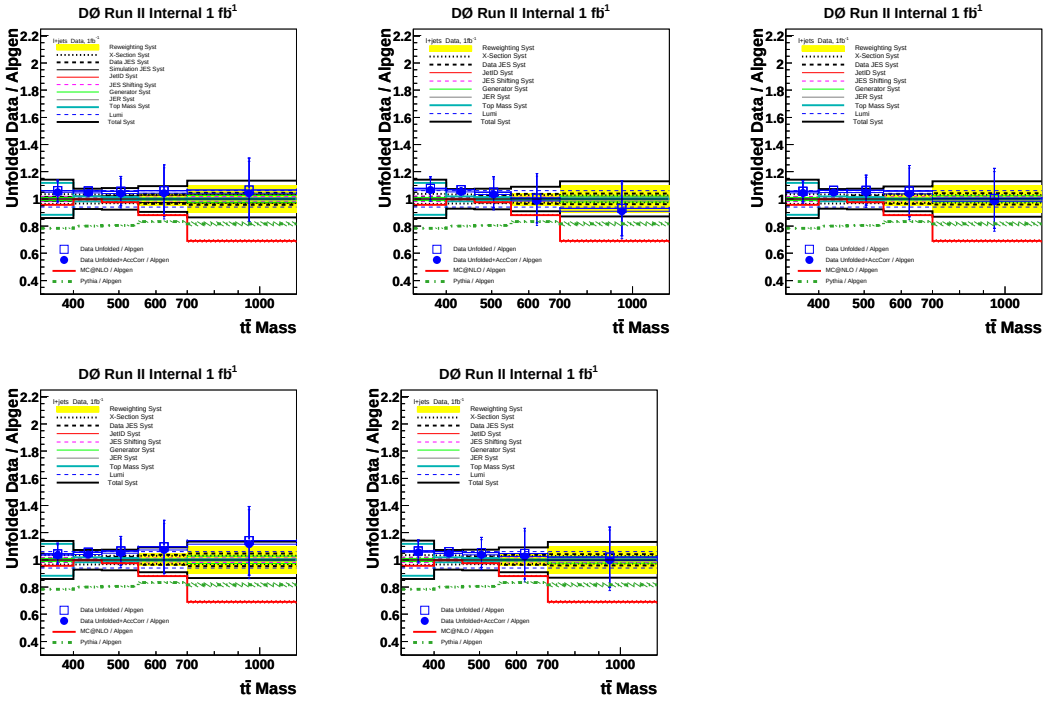

Figure B.9: Data unfolding in ℓ+ jets; Reweighting sensitivity, rank 02, $t\bar{t}$ system mass; for various reweighting of the migration matrix.

Appendix C

Control Plots

This section documents control plots, importance of which is to show the level of agreement between data and predicted background and signal Monte Carlo samples over many kinematic variables of the multiple particles in the $t\bar{t}$ final state. Untagged controls are followed by NN-medium b-tag bins $= 1$ and ≥ 2.

Basic objects' (jets, leptons, compound fitted objects like W) transverse momentum p_{T}, azimuthal angle ϕ (cylindrical symmetry around the beam axis), pseudorapidity η, rapidity y, and objects angular distance in $\mathcal{R} \equiv \sqrt{\Delta y^2 + \Delta\phi^2}$ variables are studied. Transverse mass (used e.g. in W-mass measurements) is computed using the lepton and missing transverse energy

$$M_{\mathrm{T}}^{W} \equiv \sqrt{2E_{\mathrm{T}}^{l}\not{E}_{\mathrm{T}}(1-\cos\Delta\phi_{\vec{l},\vec{\not{E}}_{\mathrm{T}}})}\,.$$

Further topological variables include the aplanarity, sphericity, H_T (the sum of jets' p_{T}'s), H (sum of jets' energies), centrality $\equiv H_T/H$, $\mathcal{C} \equiv 3\,[Q_0Q_1 + Q_0Q_2 + Q_1Q_2]$ (momentum ellipsoid surface area) and $\mathcal{D} \equiv 27\,Q_0Q_1Q_2$ (momentum ellipsoid volume), where Q_i's are eigenvalues of the normalized 3–momentum tensor in the laboratory frame

$$\mathcal{M}^{ab} \equiv \frac{\sum_{i=1}^{n} p_i^a p_i^b}{\sum_{j=1}^{n} p_j^2}\,,$$

where $\vec{p_i}$ are momenta of objects included indexed by i, j while a, b through their momentum space indices. The tensor is symmetrical and can therefore always be diagonalized, and its ordered eigenvalues $Q_1 \leq Q_2 \leq Q_3$ fulfilling

$$Q_1 + Q_2 + Q_3 = 1 \qquad Q_1 > 0\,.$$

are used to define standard aplanarity and sphericity as

$$\mathcal{A} \equiv \frac{3}{2}Q_1 \quad \mathcal{S} \equiv \frac{3}{2}(Q_1 + Q_2)\,.$$

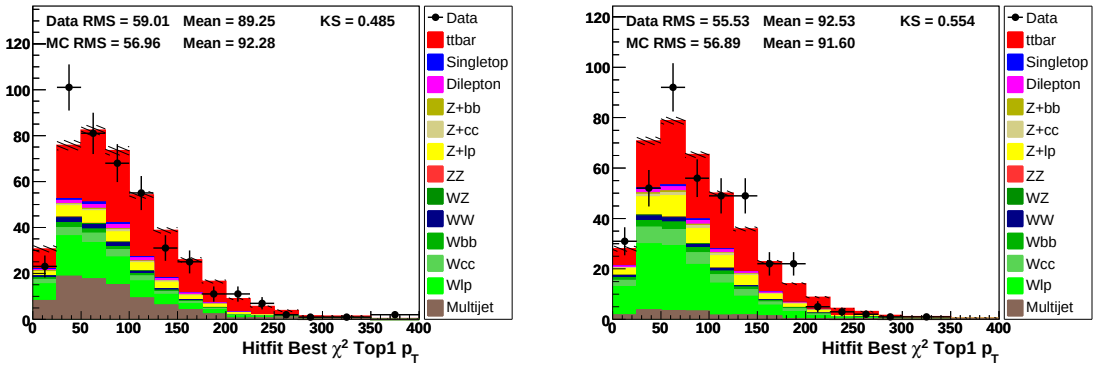

Figure C.1: Leptonic top p_{T}, e+jets (left) and μ+jets (right), NN-medium ≥ 0 b-tag bin. Signal model: ALPGEN.

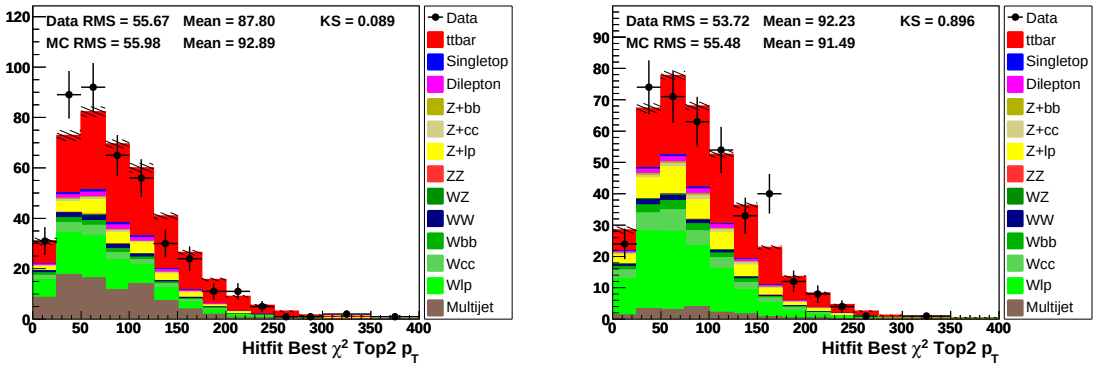

Figure C.2: Hadronic top p_{T}, e+jets (left) and μ+jets (right), NN-medium ≥ 0 b-tag bin. Signal model: ALPGEN.

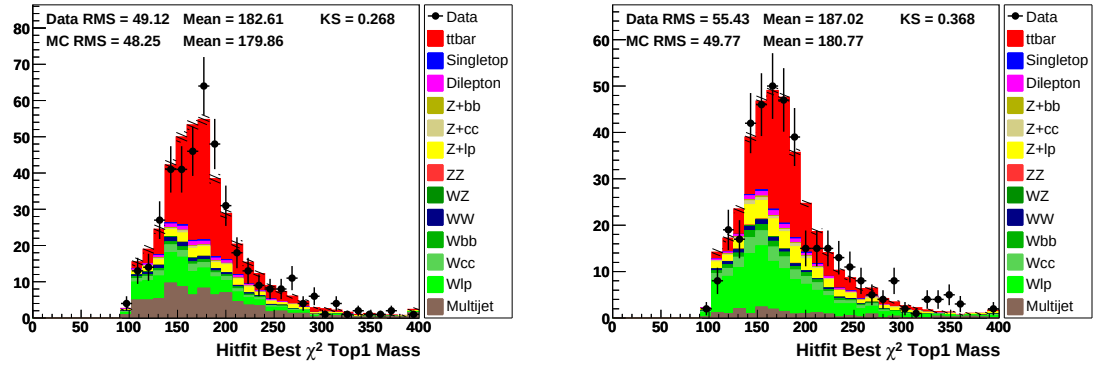

Figure C.3: Fitted top mass, e+jets (left) and μ+jets (right), NN-medium ≥ 0 b-tag bin. Signal model: ALPGEN.

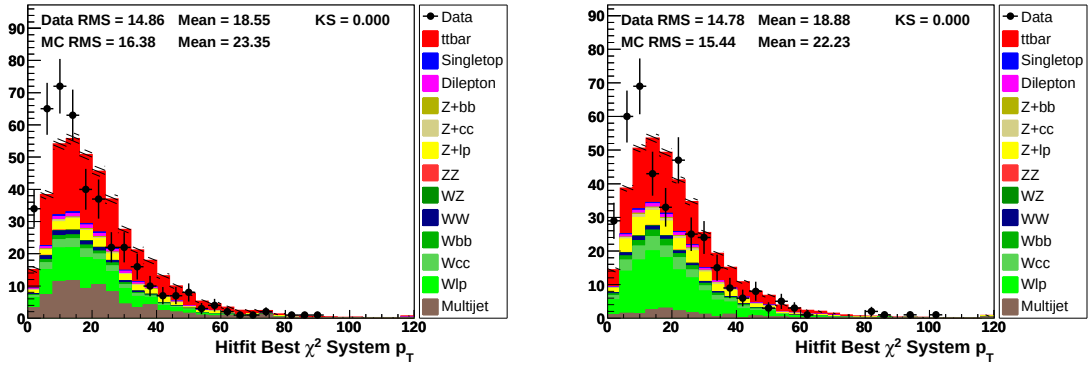

Figure C.4: $t\bar{t}$ p_{T}, e+jets (left) and μ+jets (right), NN-medium ≥ 0 b-tag bin. Signal model: ALPGEN.

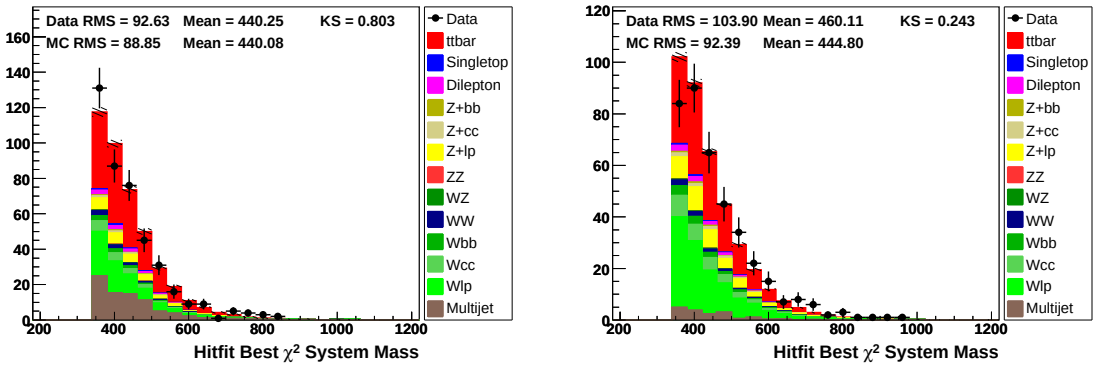

Figure C.5: $t\bar{t}$ mass, e+jets (left) and μ+jets (right), NN-medium ≥ 0 b-tag bin. Signal model: ALPGEN.

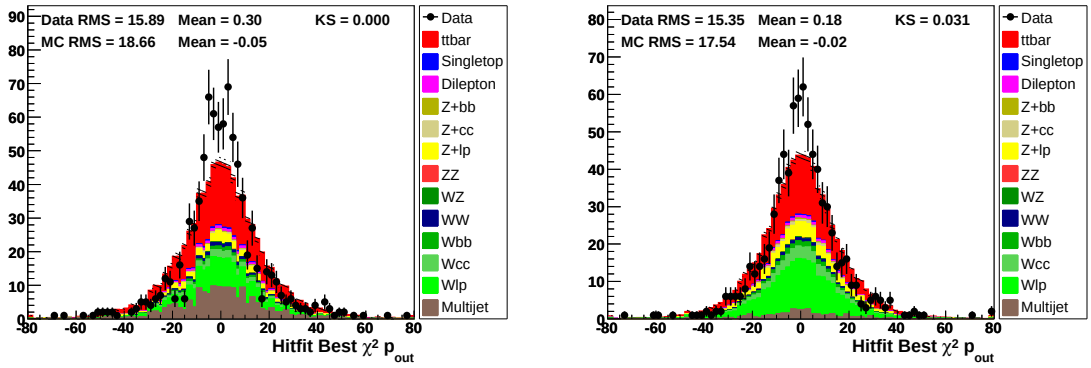

Figure C.6: p_{out}, e+jets (left) and μ+jets (right), NN-medium ≥ 0 b-tag bin. Signal model: ALPGEN.

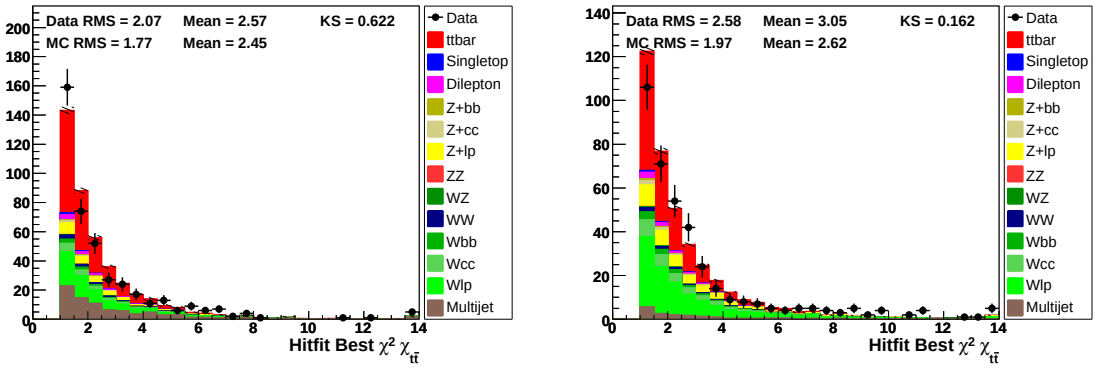

Figure C.7: $\chi_{t\bar{t}}$, e+jets (left) and μ+jets (right), NN-medium ≥ 0 b-tag bin. Signal model: ALPGEN.

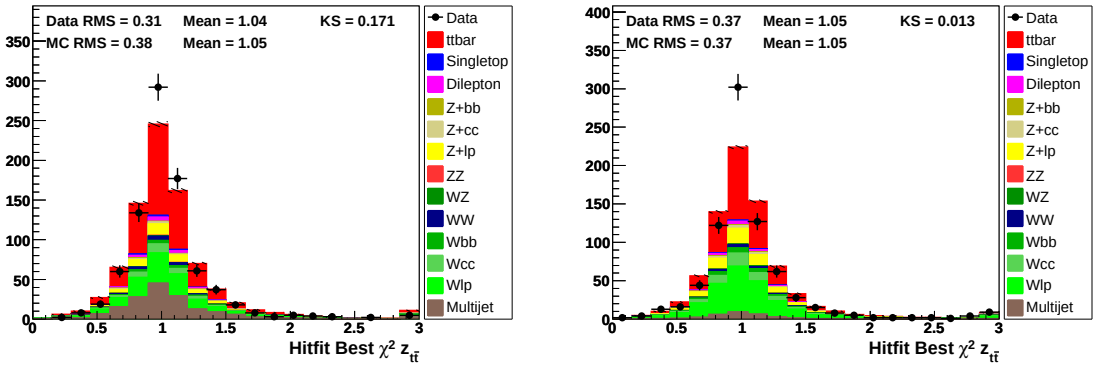

Figure C.8: $z_{t\bar{t}}$, e+jets (left) and μ+jets (right), NN-medium ≥ 0 b-tag bin. Signal model: ALPGEN.

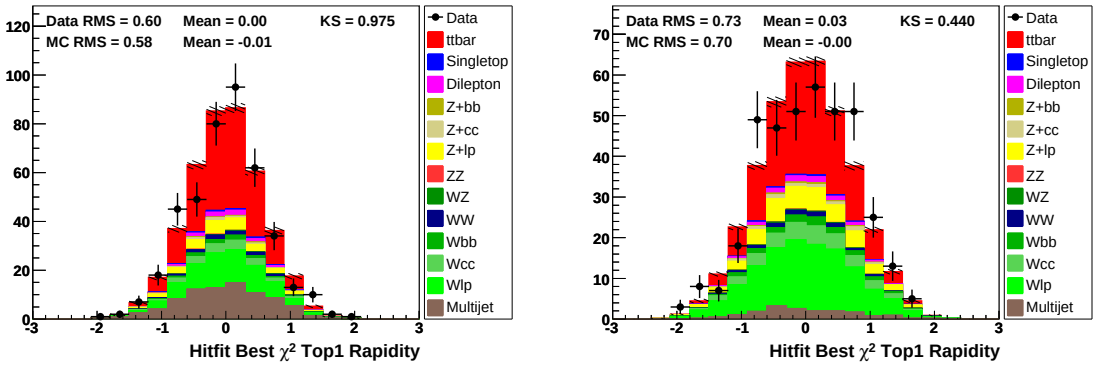

Figure C.9: Leptonic top rapidity, e+jets (left) and μ+jets (right), NN-medium ≥ 0 b-tag bin. Signal model: ALPGEN.

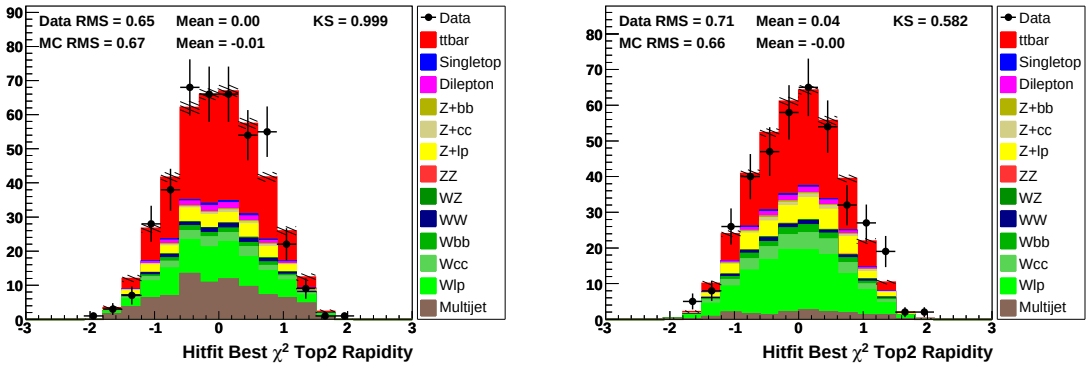

Figure C.10: Hadronic top rapidity, e+jets (left) and μ+jets (right), NN-medium ≥ 0 b-tag bin. Signal model: ALPGEN.

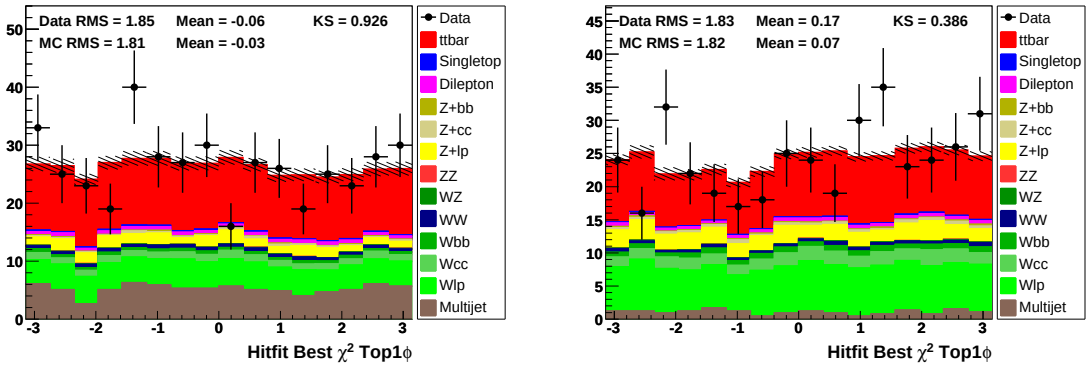

Figure C.11: Leptonic top ϕ, e+jets (left) and μ+jets (right), NN-medium ≥ 0 b-tag bin. Signal model: ALPGEN.

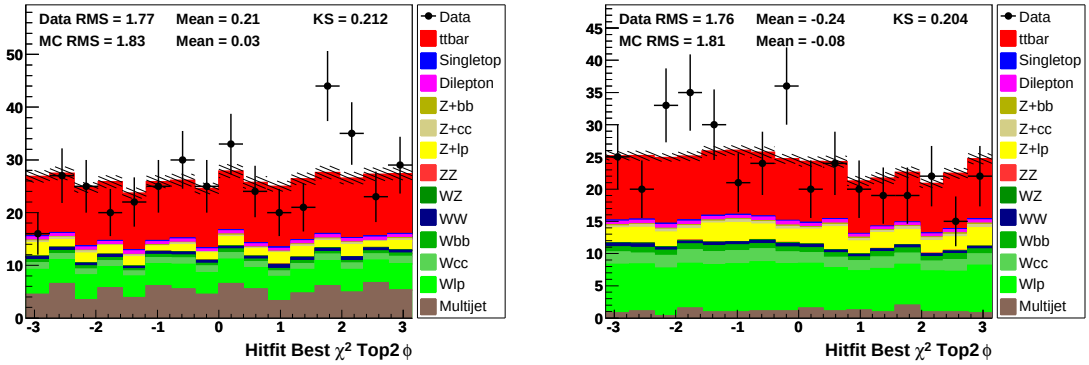

Figure C.12: Hadronic top ϕ, e+jets (left) and μ+jets (right), NN-medium ≥ 0 b-tag bin. Signal model: ALPGEN.

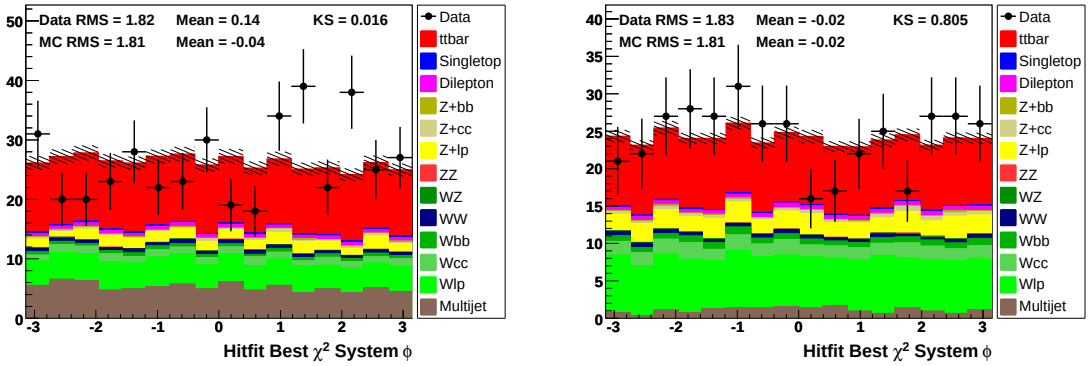

Figure C.13: $t\bar{t}$ ϕ, e+jets (left) and μ+jets (right), NN-medium ≥ 0 b-tag bin. Signal model: ALPGEN.

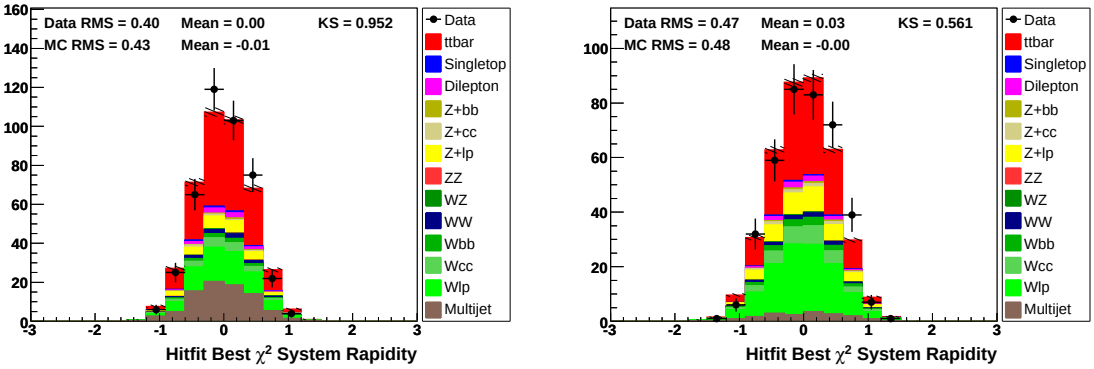

Figure C.14: $t\bar{t}$ rapidity, e+jets (left) and μ+jets (right), NN-medium ≥ 0 b-tag bin. Signal model: ALPGEN.

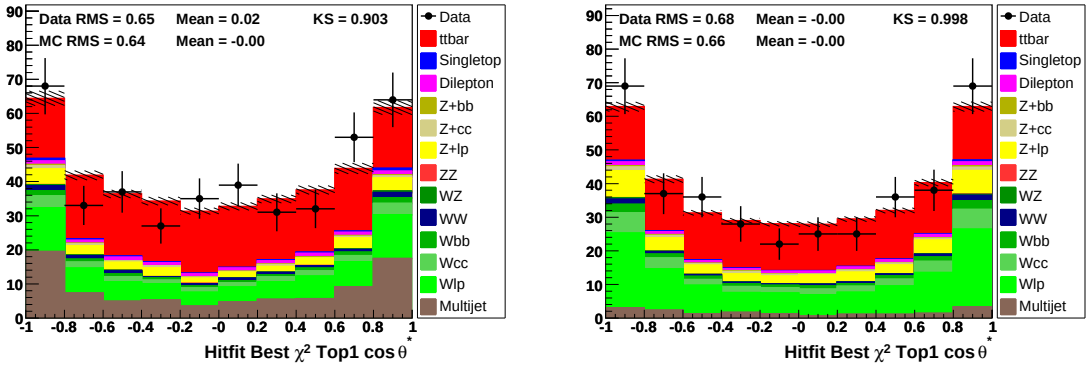

Figure C.15: Leptonic top $\cos\theta^*$, e+jets (left) and μ+jets (right), NN-medium ≥ 0 b-tag bin. Signal model: ALPGEN.

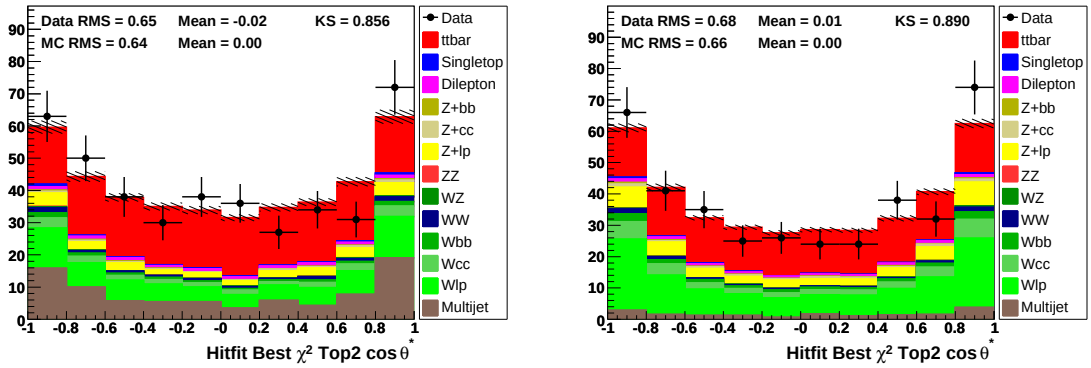

Figure C.16: Hadronic top $\cos\theta^*$, e+jets (left) and μ+jets (right), NN-medium ≥ 0 b-tag bin. Signal model: ALPGEN.

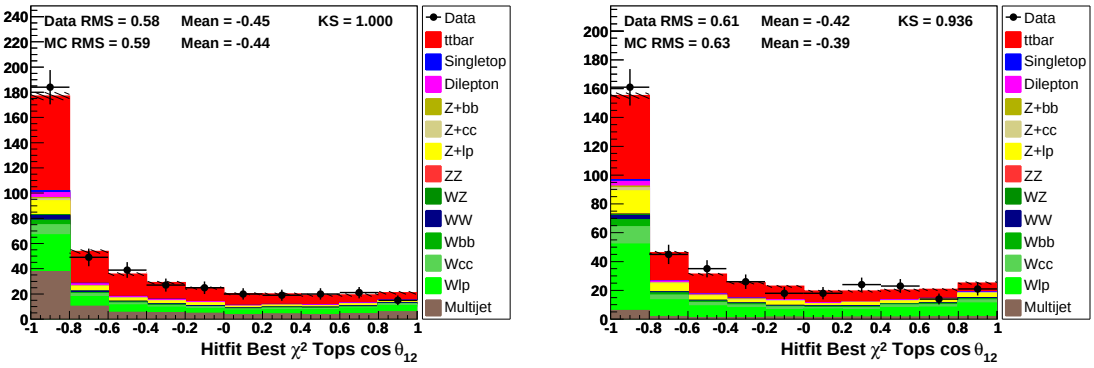

Figure C.17: Opening angle between top quarks, e+jets (left) and μ+jets (right), NN-medium ≥ 0 b-tag bin. Signal model: ALPGEN.

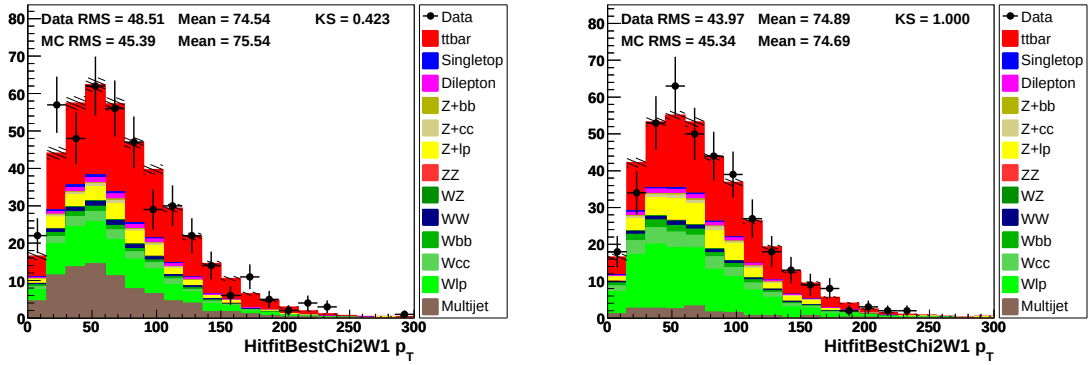

Figure C.18: Leptonic W p_{T}, e+jets (left) and μ+jets (right), NN-medium ≥ 0 b-tag bin. Signal model: ALPGEN.

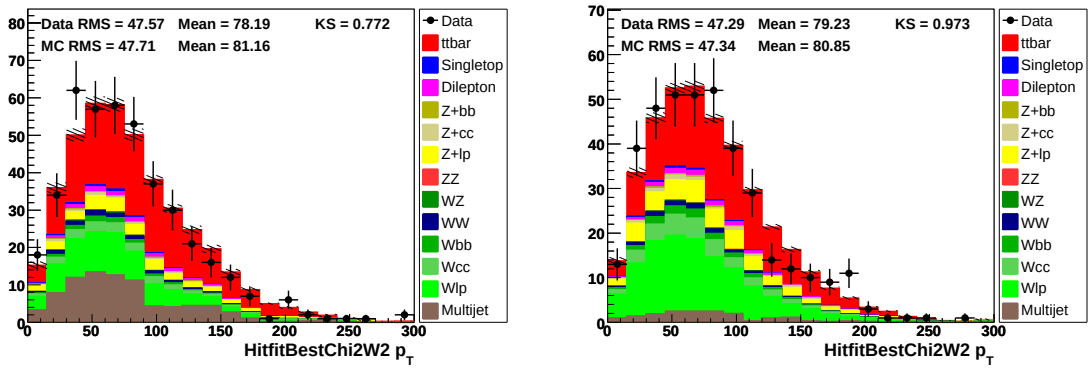

Figure C.19: Hadronic W p_{T}, e+jets (left) and μ+jets (right), NN-medium ≥ 0 b-tag bin. Signal model: ALPGEN.

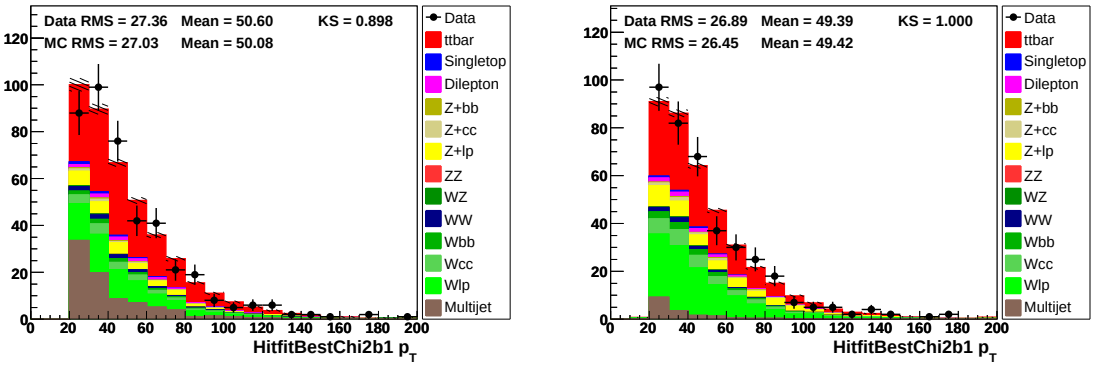

Figure C.20: Leptonic b p_{T}, e+jets (left) and μ+jets (right), NN-medium ≥ 0 b-tag bin. Signal model: ALPGEN.

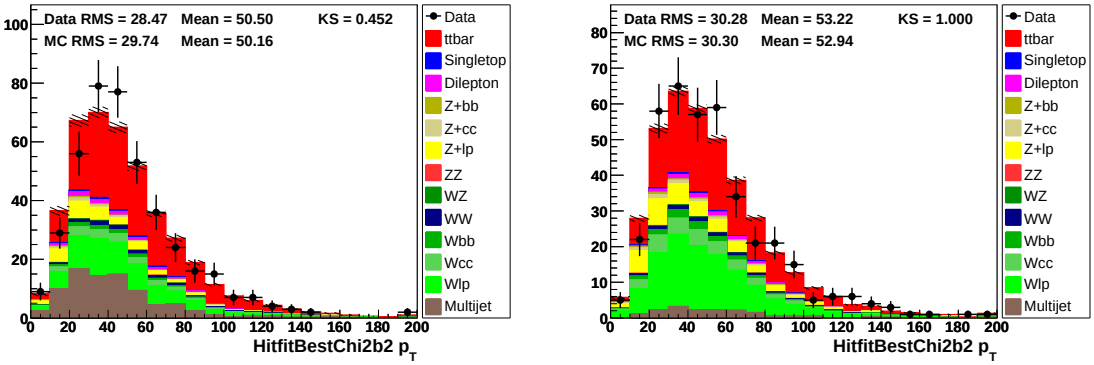

Figure C.21: Hadronic b p_{T}, e+jets (left) and μ+jets (right), NN-medium ≥ 0 b-tag bin. Signal model: ALPGEN.

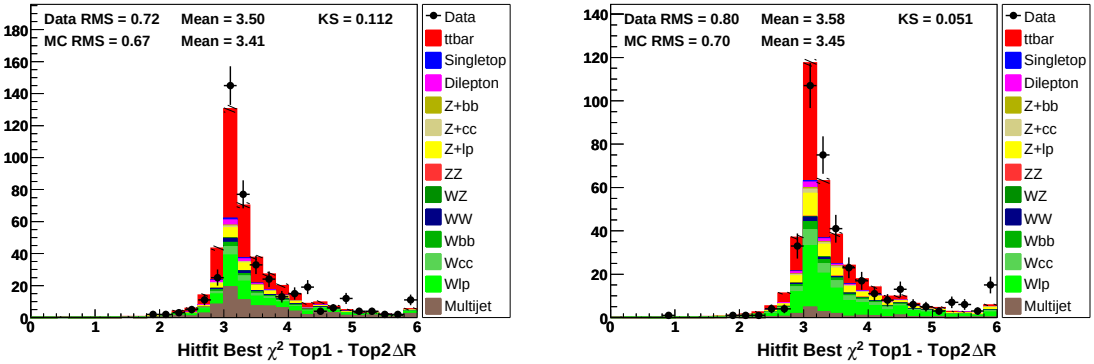

Figure C.22: $\Delta\mathcal{R}_{t\bar{t}}$, e+jets (left) and μ+jets (right), NN-medium ≥ 0 b-tag bin. Signal model: ALPGEN.

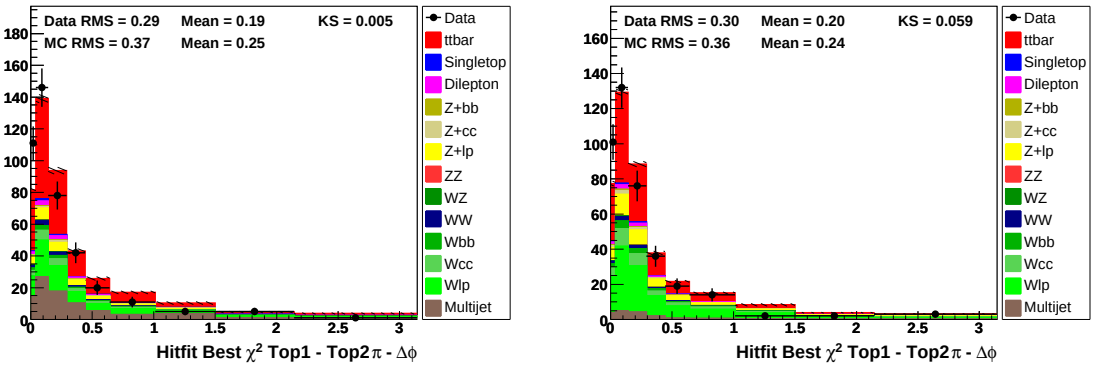

Figure C.23: $\Delta\phi_{t\bar{t}}$, e+jets (left) and μ+jets (right), NN-medium ≥ 0 b-tag bin. Signal model: ALPGEN.

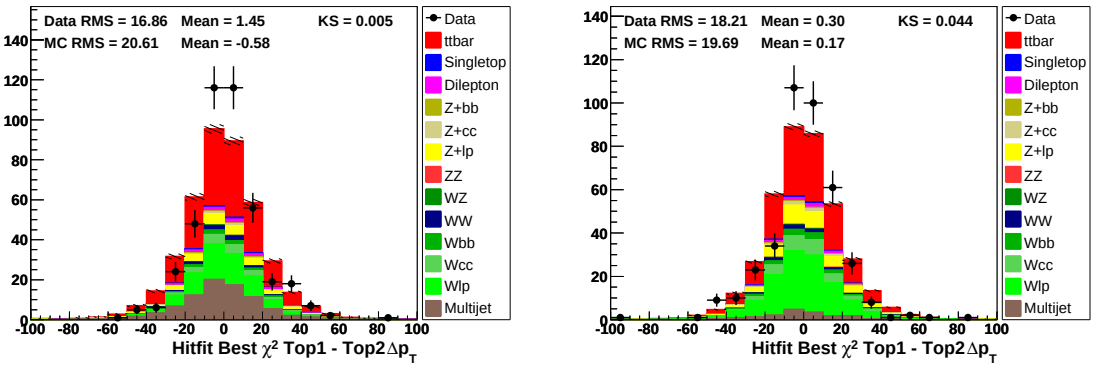

Figure C.24: $\Delta p_{\mathrm{T}}^{t\bar{t}}$, e+jets (left) and μ+jets (right), NN-medium ≥ 0 b-tag bin. Signal model: ALPGEN.

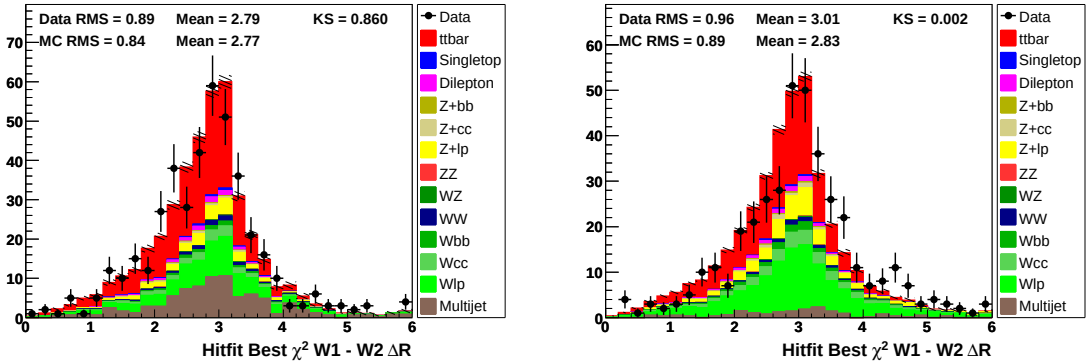

Figure C.25: $\Delta\mathcal{R}_{WW}$, e+jets (left) and μ+jets (right), NN-medium ≥ 0 b-tag bin. Signal model: ALPGEN.

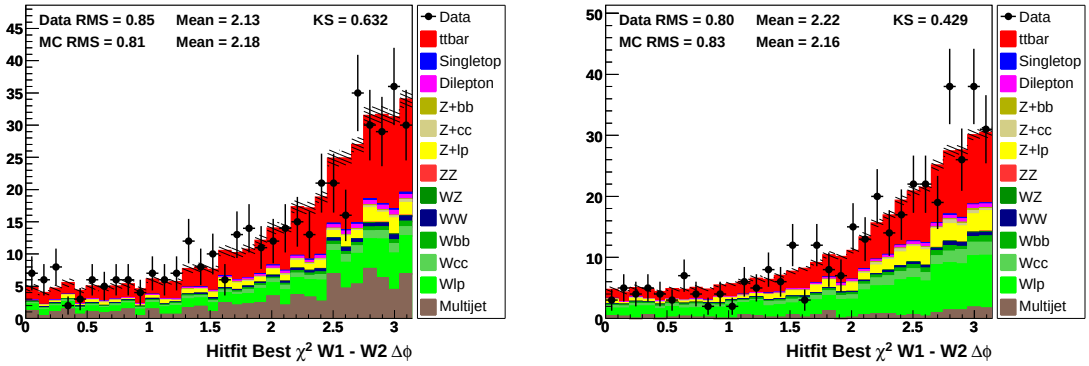

Figure C.26: $\Delta\phi_{WW}$, e+jets (left) and μ+jets (right), NN-medium ≥ 0 b-tag bin. Signal model: ALPGEN.

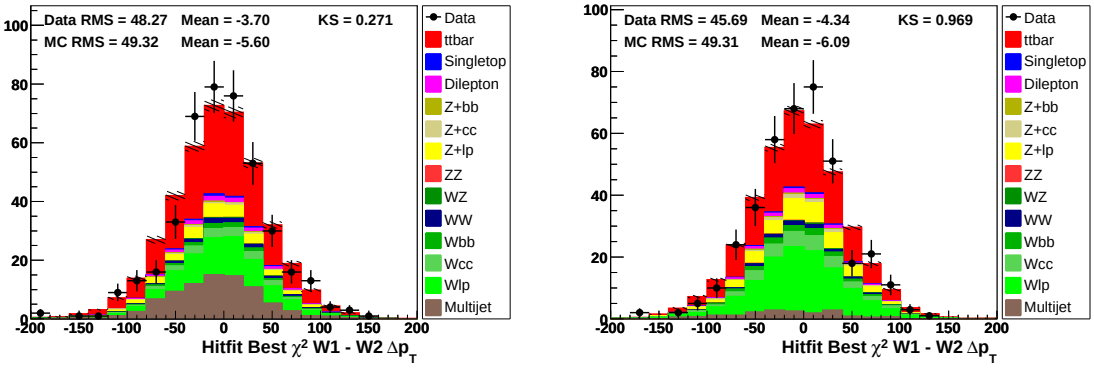

Figure C.27: $\Delta p_{\mathrm{T}}^{WW}$, e+jets (left) and μ+jets (right), NN-medium ≥ 0 b-tag bin. Signal model: ALPGEN.

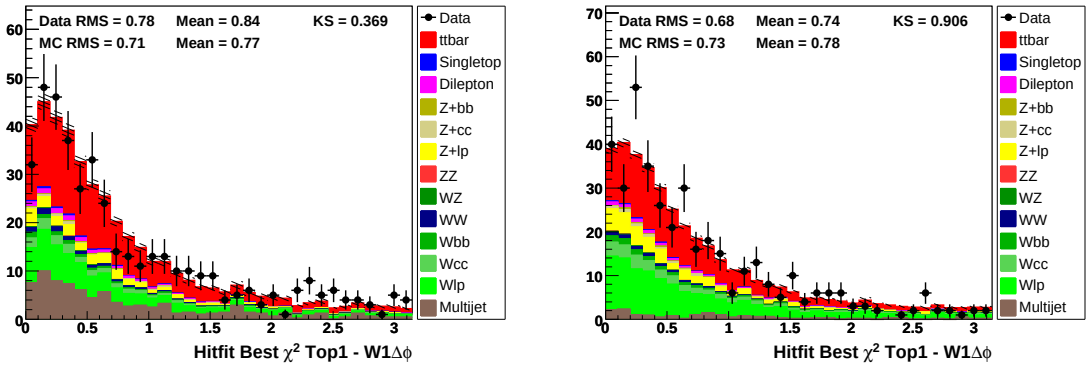

Figure C.28: $\Delta\phi_{t1W1}$, e+jets (left) and μ+jets (right), NN-medium ≥ 0 b-tag bin. Signal model: ALPGEN.

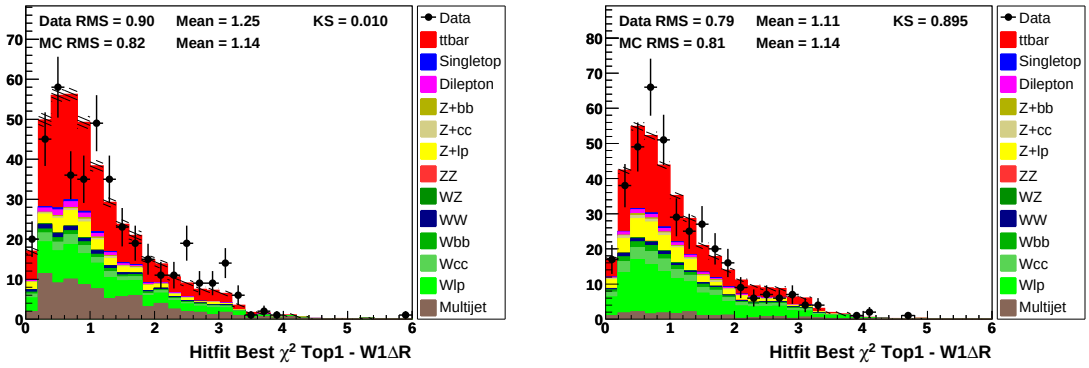

Figure C.29: $\Delta\mathcal{R}_{t1W1}$, e+jets (left) and μ+jets (right), NN-medium ≥ 0 b-tag bin. Signal model: ALPGEN.

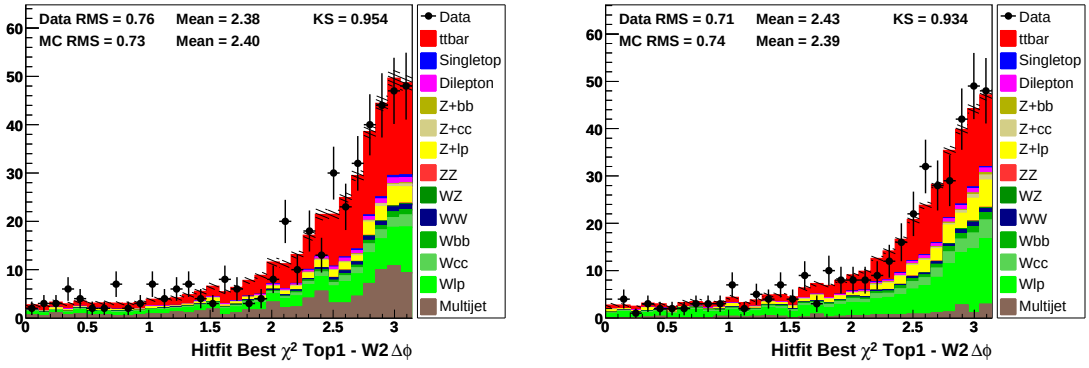

Figure C.30: $\Delta\phi_{t1W2}$, e+jets (left) and μ+jets (right), NN-medium ≥ 0 b-tag bin. Signal model: ALPGEN.

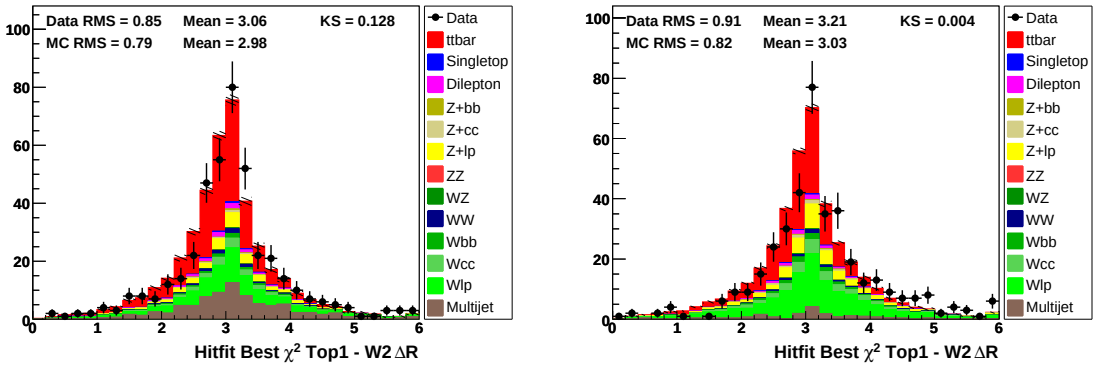

Figure C.31: $\Delta\mathcal{R}_{t1W2}$, e+jets (left) and μ+jets (right), NN-medium ≥ 0 b-tag bin. Signal model: ALPGEN.

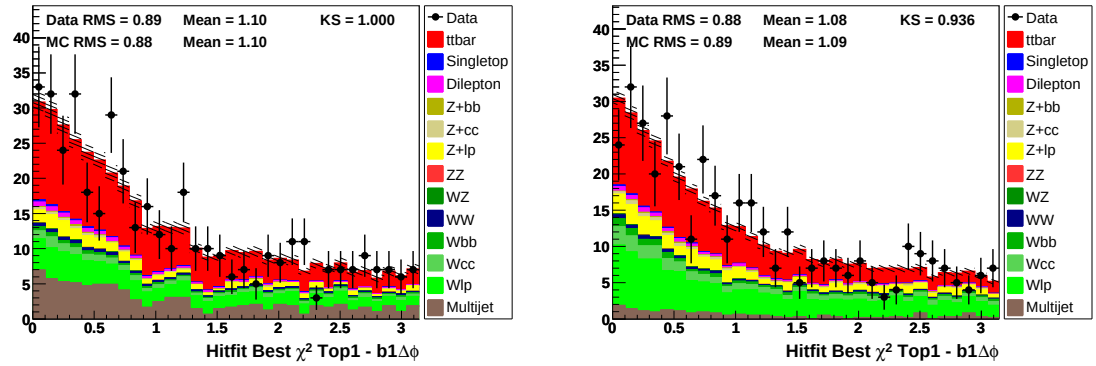

Figure C.32: $\Delta\phi_{t1b1}$, e+jets (left) and μ+jets (right), NN-medium ≥ 0 b-tag bin. Signal model: ALPGEN.

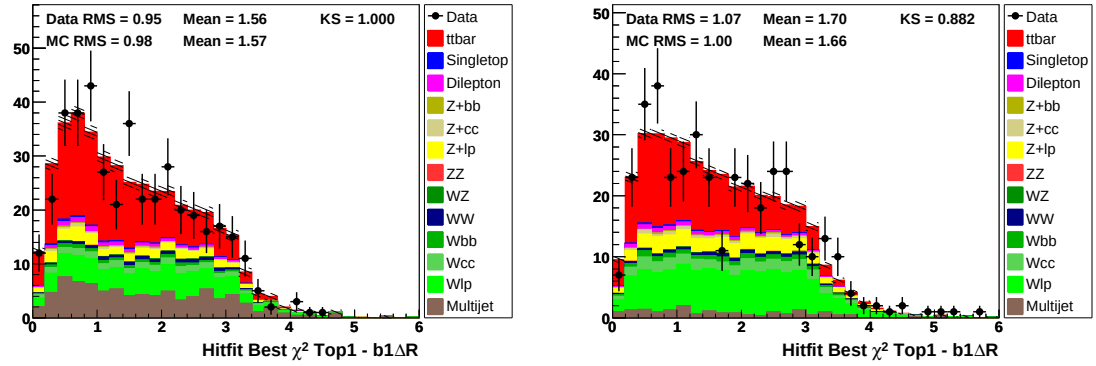

Figure C.33: $\Delta\mathcal{R}_{t1b1}$, e+jets (left) and μ+jets (right), NN-medium ≥ 0 b-tag bin. Signal model: ALPGEN.

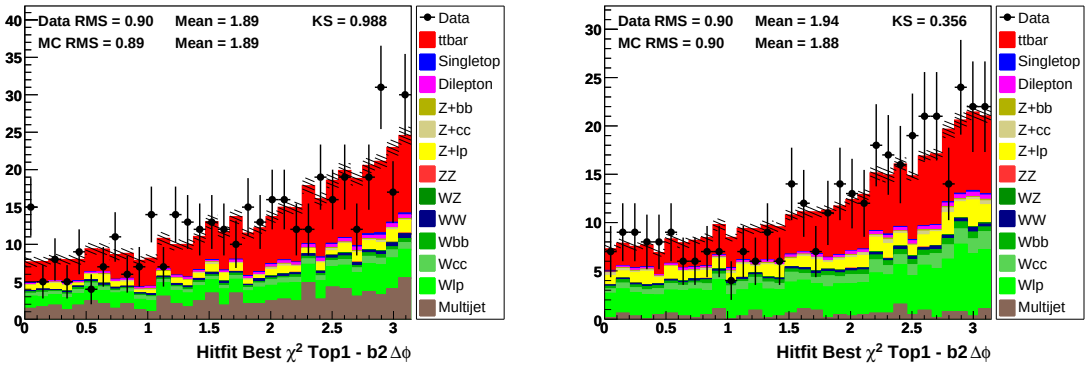

Figure C.34: $\Delta\phi_{t1b2}$, e+jets (left) and μ+jets (right), NN-medium ≥ 0 b-tag bin. Signal model: ALPGEN.

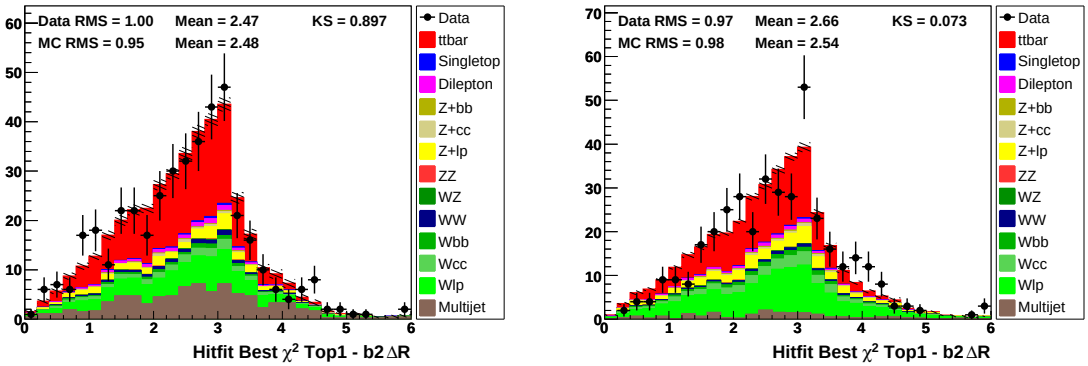

Figure C.35: $\Delta\mathcal{R}_{t1b2}$, e+jets (left) and μ+jets (right), NN-medium ≥ 0 b-tag bin. Signal model: ALPGEN.

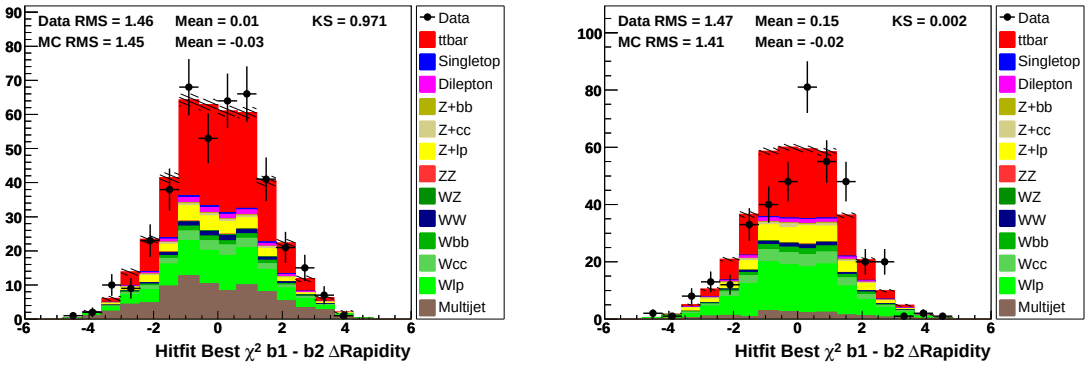

Figure C.36: $\Delta\text{Rapidity}_{b1b2}$, e+jets (left) and μ+jets (right), NN-medium ≥ 0 b-tag bin. Signal model: ALPGEN.

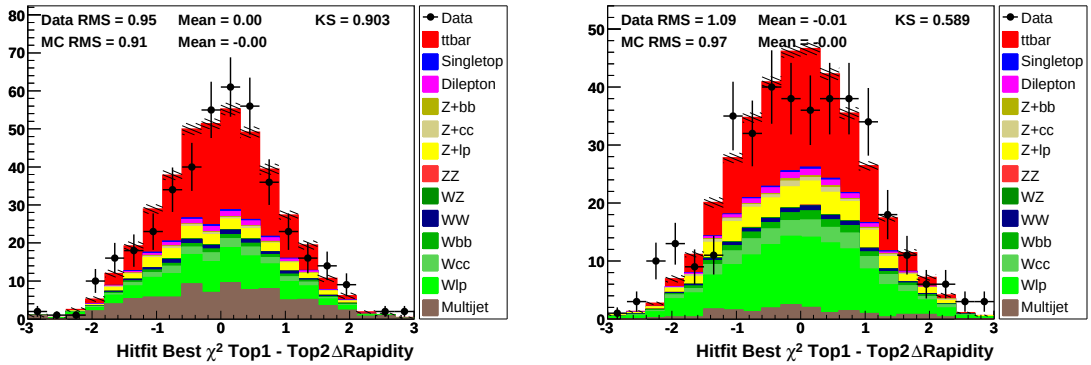

Figure C.37: $\Delta\text{Rapidity}_{t\bar{t}}$, e+jets (left) and μ+jets (right), NN-medium ≥ 0 b-tag bin. Signal model: ALPGEN.

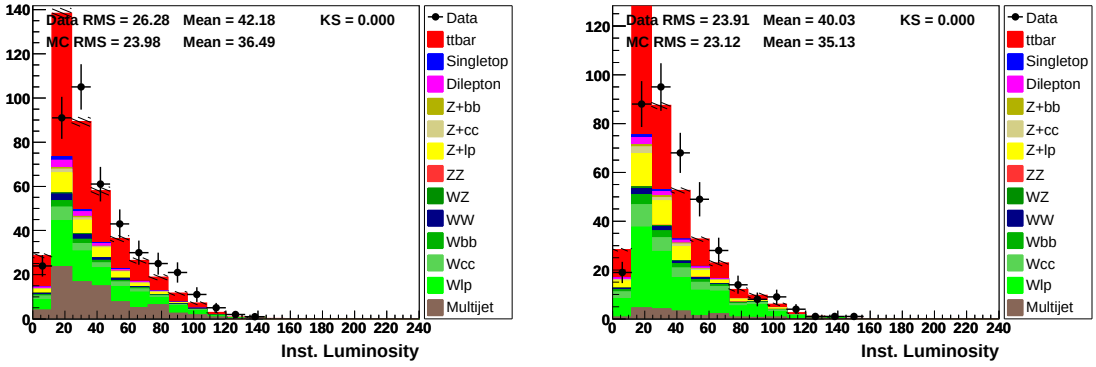

Figure C.38: Instantenous luminosity [$10^{30}\text{cm}^{-2}\text{s}^{-1}$], e+jets (left) and μ+jets (right), NN-medium ≥ 0 b-tag bin. Signal model: ALPGEN.

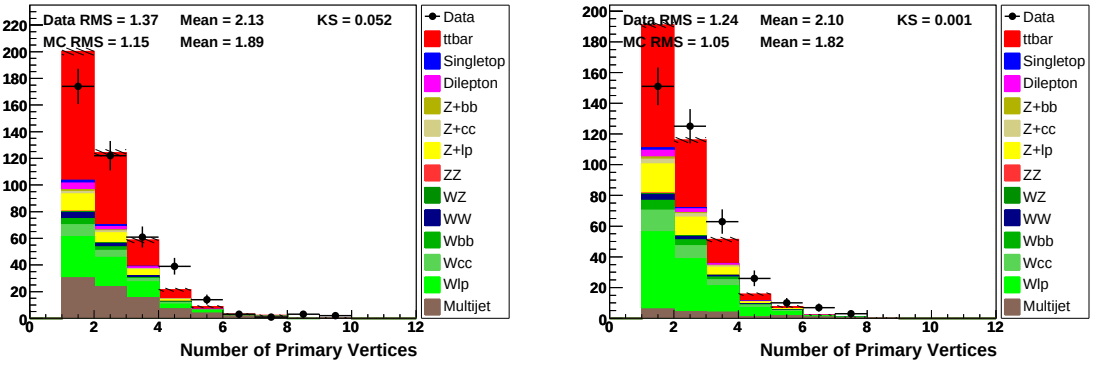

Figure C.39: Number of primary vertices, e+jets (left) and μ+jets (right), NN-medium ≥ 0 b-tag bin. Signal model: ALPGEN.

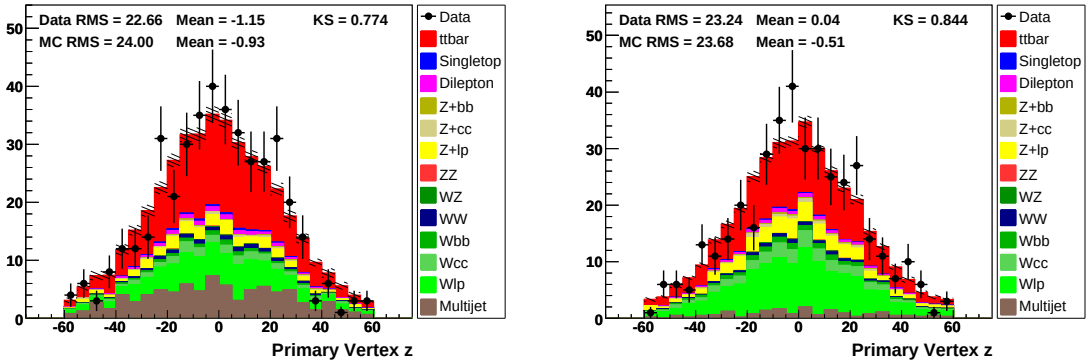

Figure C.40: Primary vertex z coordinate, e+jets (left) and μ+jets (right), NN-medium ≥ 0 b-tag bin. Signal model: ALPGEN.

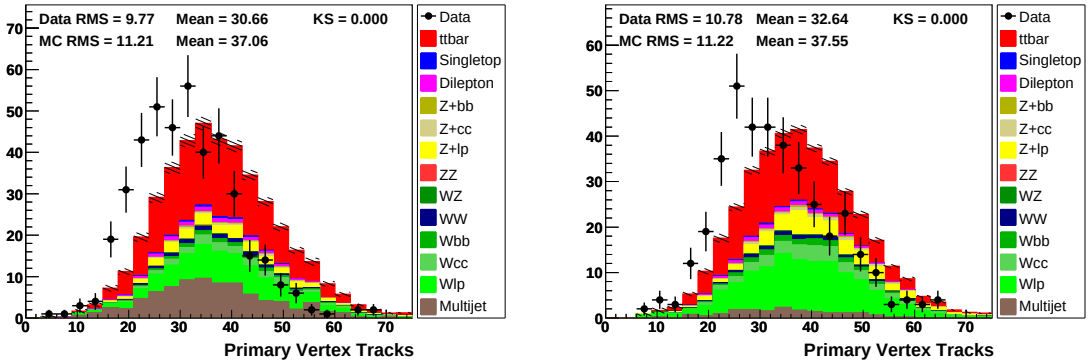

Figure C.41: Number of PV tracks, e+jets (left) and μ+jets (right), NN-medium ≥ 0 b-tag bin. Signal model: ALPGEN.

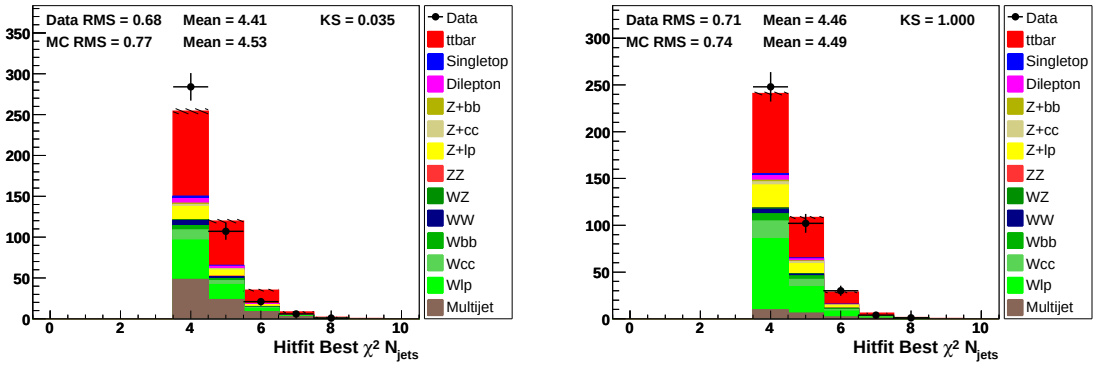

Figure C.42: n_{jets}, e+jets (left) and μ+jets (right), NN-medium ≥ 0 b-tag bin. Signal model: ALPGEN.

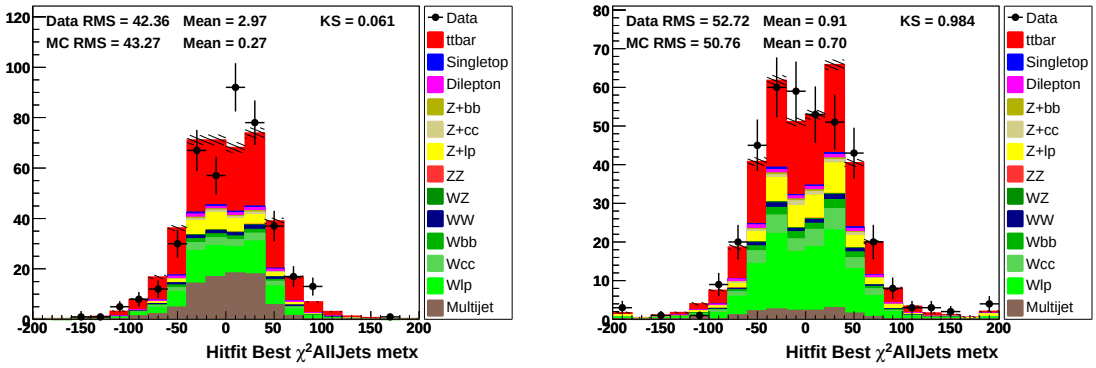

Figure C.43: Missing transverse energy x component, e+jets (left) and μ+jets (right), NN-medium ≥ 0 b-tag bin. Signal model: ALPGEN.

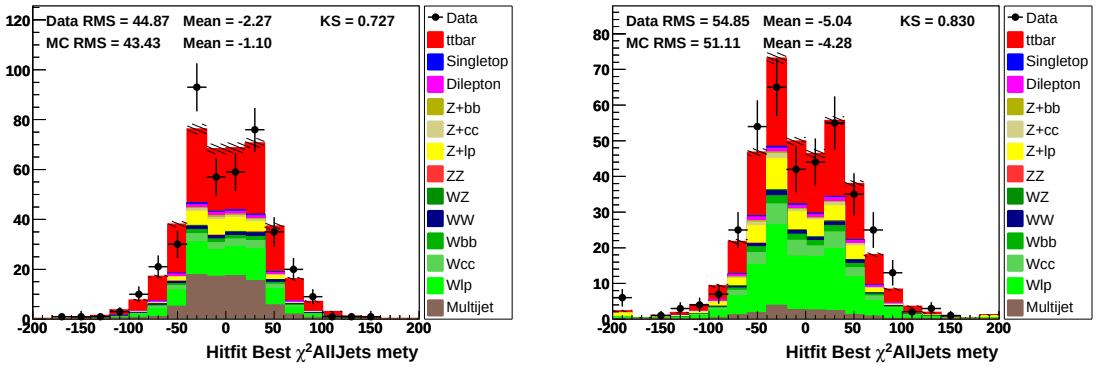

Figure C.44: Missing transverse energy y component, e+jets (left) and μ+jets (right), NN-medium ≥ 0 b-tag bin. Signal model: ALPGEN.

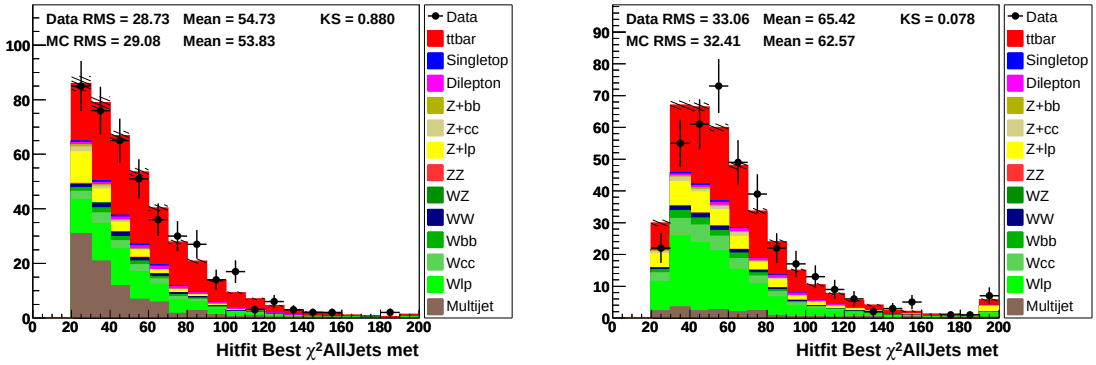

Figure C.45: Missing transverse energy, e+jets (left) and μ+jets (right), NN-medium ≥ 0 b-tag bin. Signal model: ALPGEN.

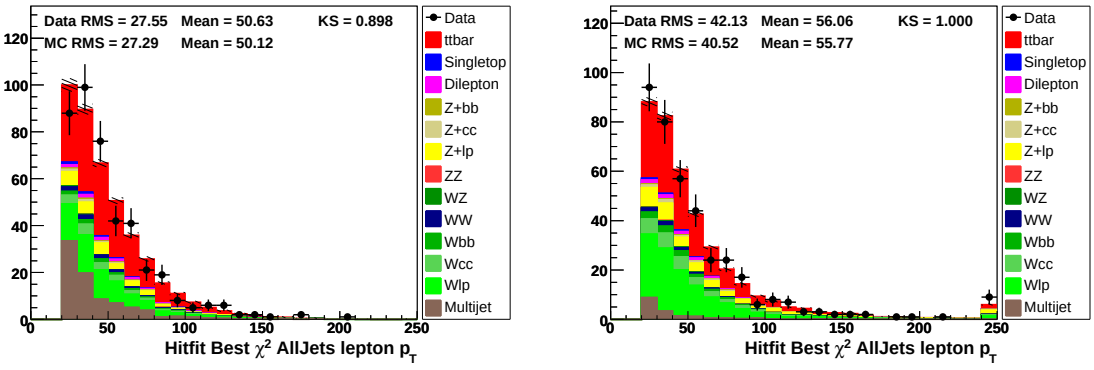

Figure C.46: Lepton p_{T}, e+jets (left) and μ+jets (right), NN-medium ≥ 0 b-tag bin. Signal model: ALPGEN.

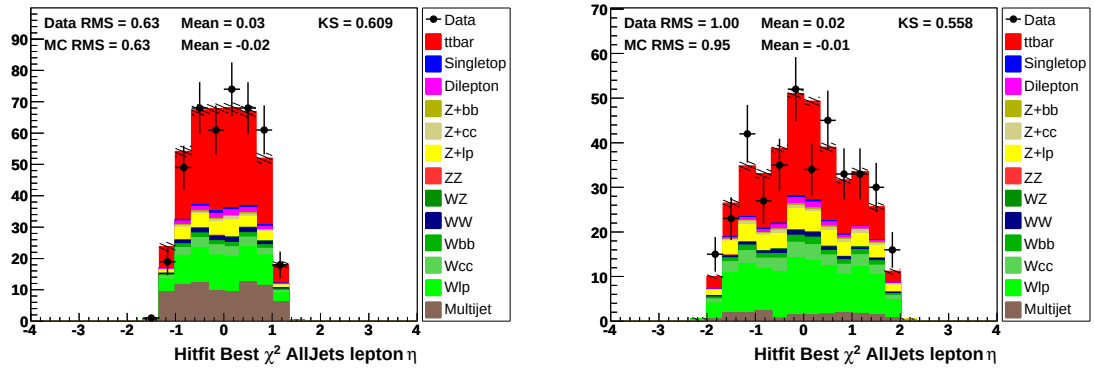

Figure C.47: Lepton η, e+jets (left) and μ+jets (right), NN-medium ≥ 0 b-tag bin. Signal model: ALPGEN.

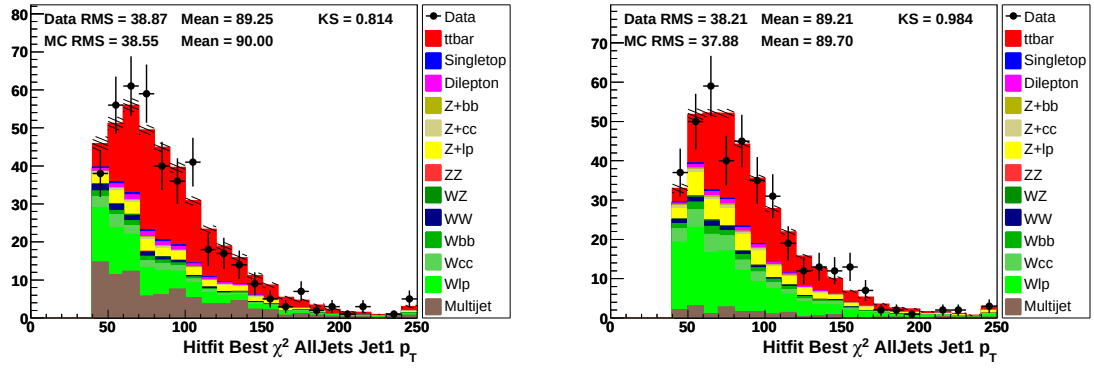

Figure C.48: 1st Jet p_{T}, e+jets (left) and μ+jets (right), NN-medium ≥ 0 b-tag bin. Signal model: ALPGEN.

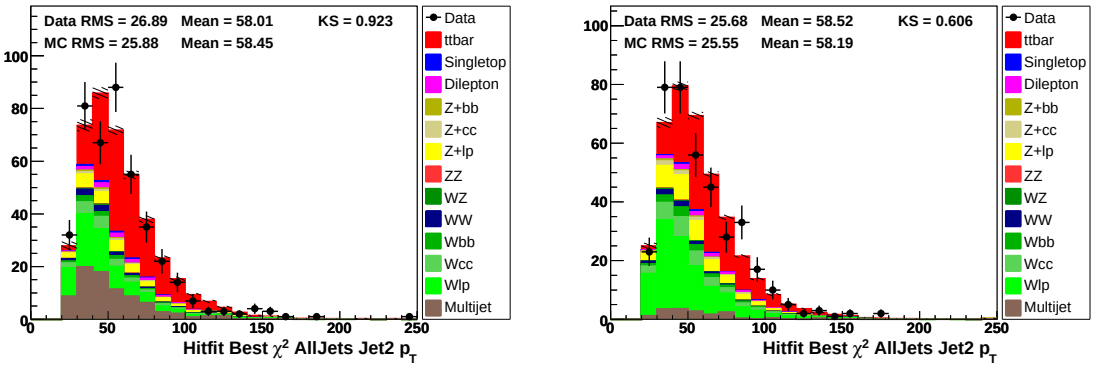

Figure C.49: 2nd Jet p_{T}, e+jets (left) and μ+jets (right), NN-medium ≥ 0 b-tag bin. Signal model: ALPGEN.

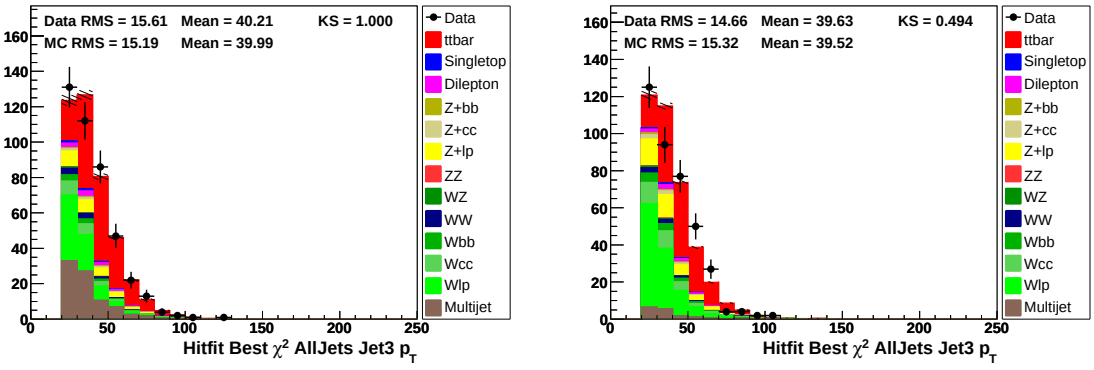

Figure C.50: 3rd Jet p_{T}, e+jets (left) and μ+jets (right), NN-medium ≥ 0 b-tag bin. Signal model: ALPGEN.

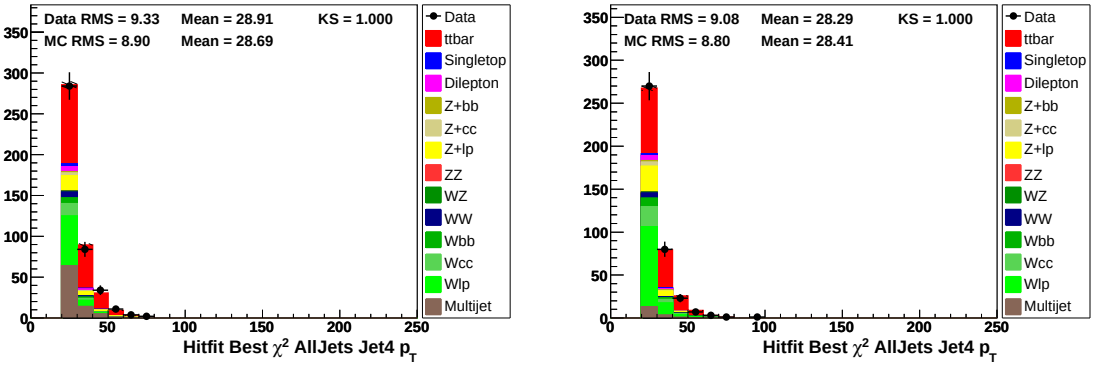

Figure C.51: 4th Jet p_{T}, e+jets (left) and μ+jets (right), NN-medium ≥ 0 b-tag bin. Signal model: ALPGEN.

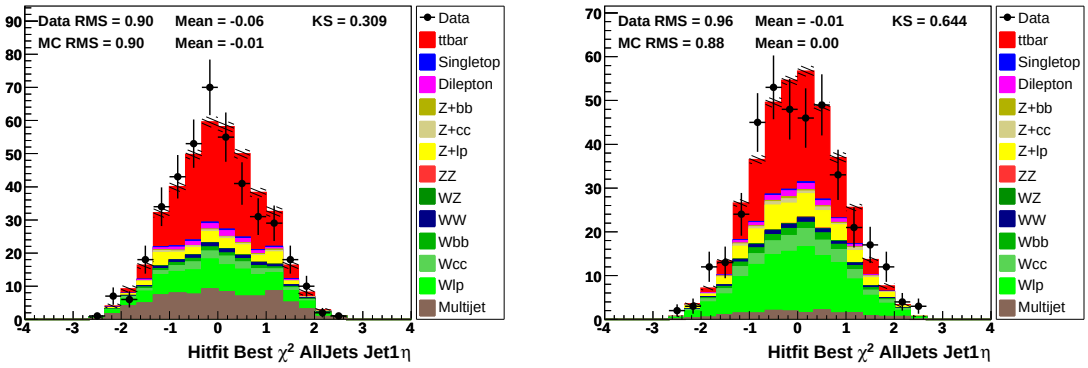

Figure C.52: 1st Jet η, e+jets (left) and μ+jets (right), NN-medium ≥ 0 b-tag bin. Signal model: ALPGEN.

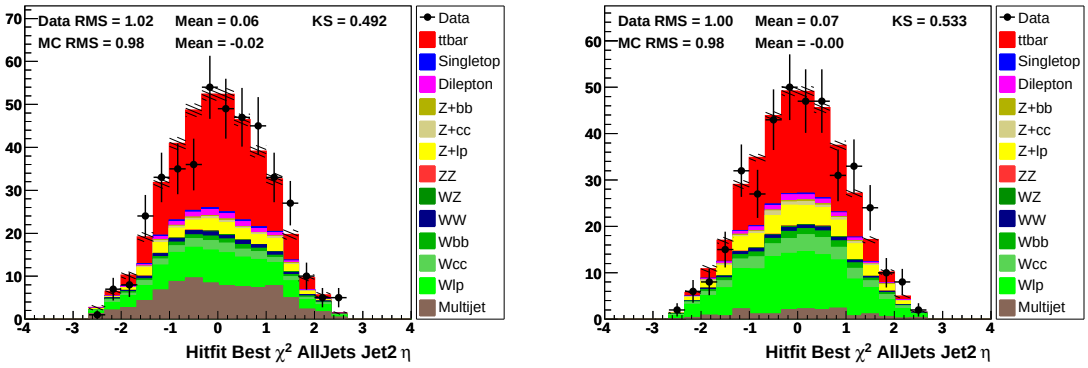

Figure C.53: 2nd Jet η, e+jets (left) and μ+jets (right), NN-medium ≥ 0 b-tag bin. Signal model: ALPGEN.

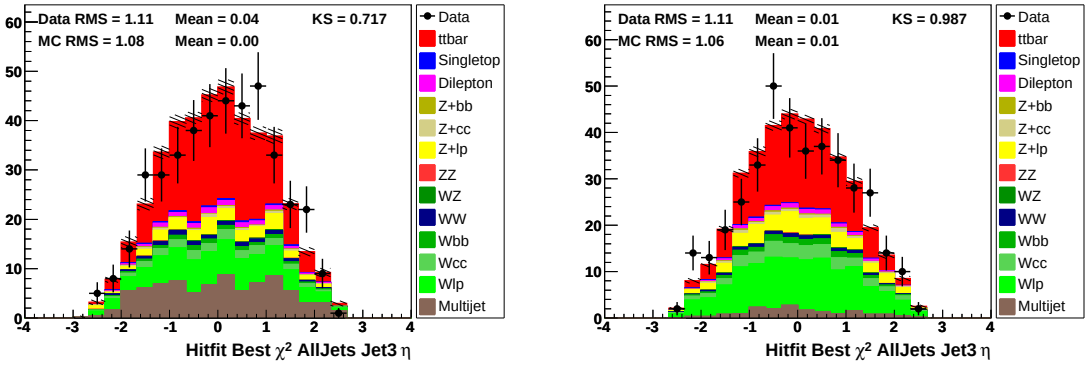

Figure C.54: 3rd Jet η, e+jets (left) and μ+jets (right), NN-medium ≥ 0 b-tag bin. Signal model: ALPGEN.

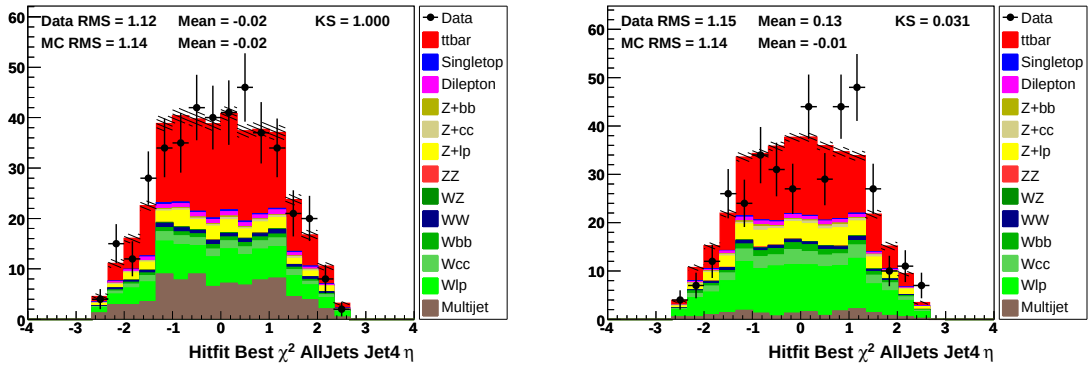

Figure C.55: 4th Jet η, e+jets (left) and μ+jets (right), NN-medium ≥ 0 b-tag bin. Signal model: ALPGEN.

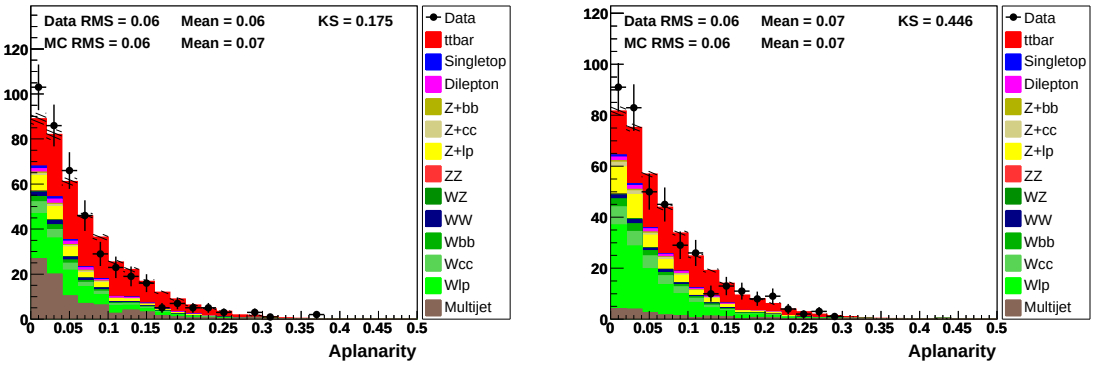

Figure C.56: Aplanarity, e+jets (left) and μ+jets (right), NN-medium ≥ 0 b-tag bin. Signal model: ALPGEN.

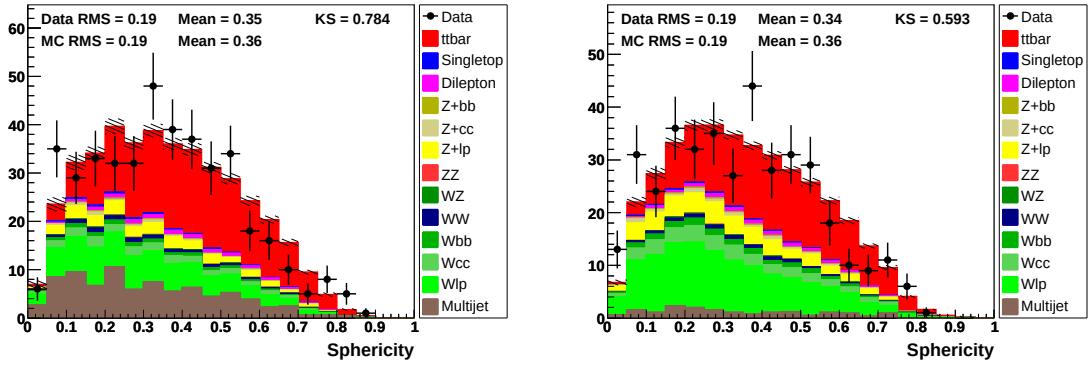

Figure C.57: Sphericity, e+jets (left) and μ+jets (right), NN-medium ≥ 0 b-tag bin. Signal model: ALPGEN.

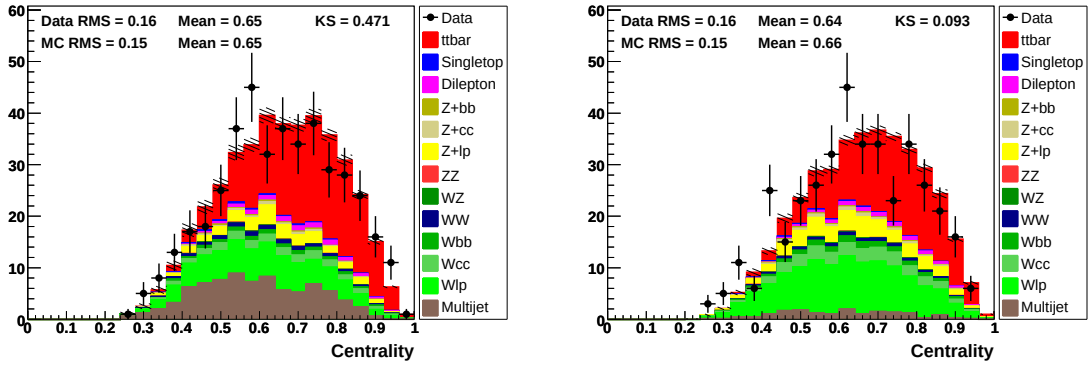

Figure C.58: Centrality, e+jets (left) and μ+jets (right), NN-medium ≥ 0 b-tag bin. Signal model: ALPGEN.

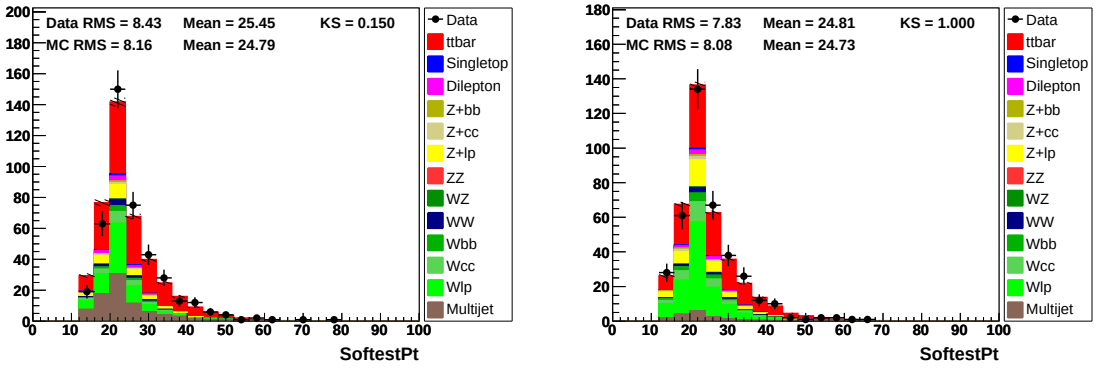

Figure C.59: Softest p_T, e+jets (left) and μ+jets (right), NN-medium ≥ 0 b-tag bin. Signal model: ALPGEN.

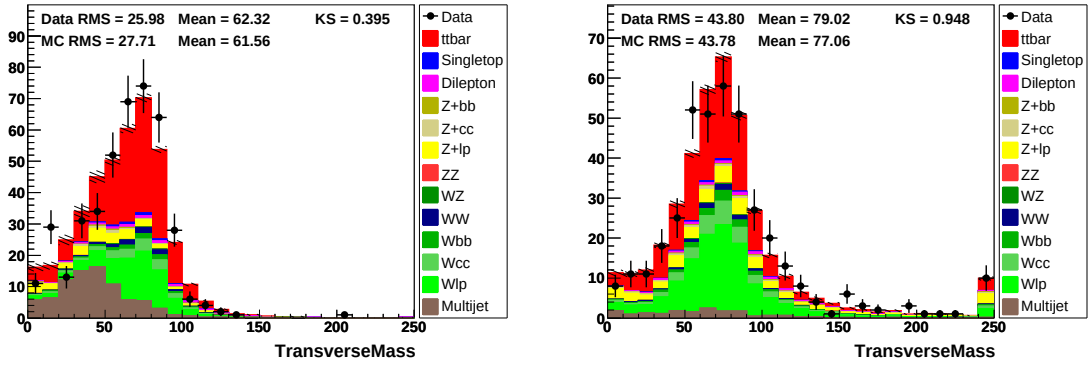

Figure C.60: Transverse mass, e+jets (left) and μ+jets (right), NN-medium ≥ 0 b-tag bin. Signal model: ALPGEN.

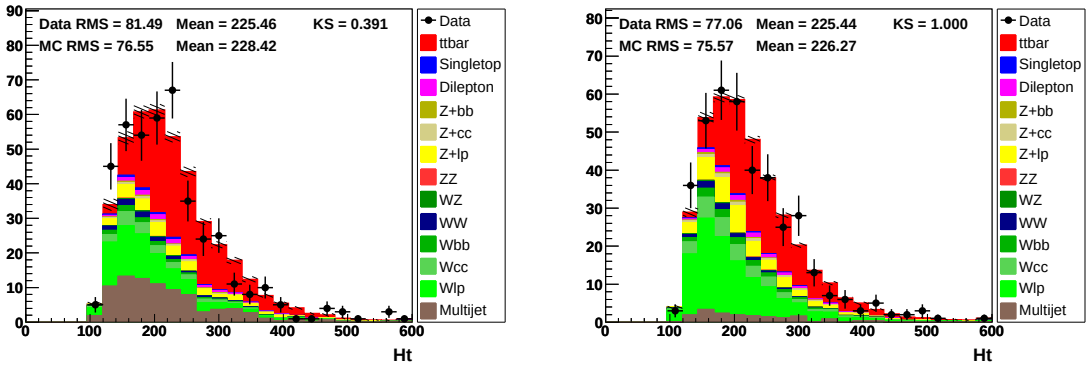

Figure C.61: H_T, e+jets (left) and μ+jets (right), NN-medium ≥ 0 b-tag bin. Signal model: ALPGEN.

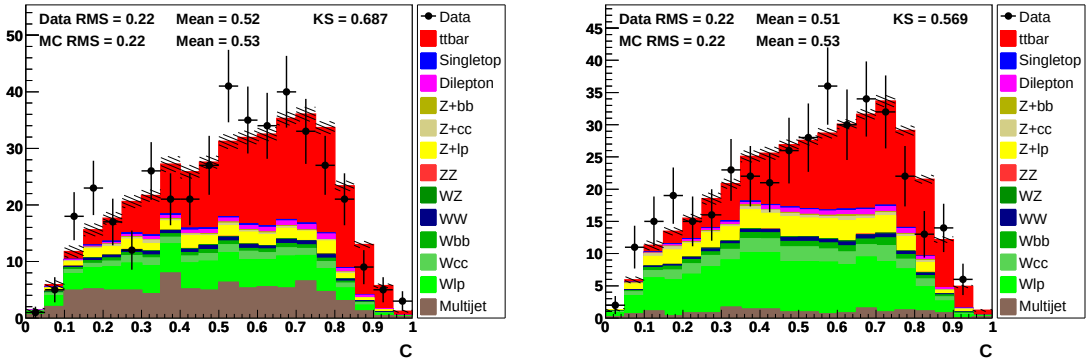

Figure C.62: $\mathcal{C}$, e+jets (left) and μ+jets (right), NN-medium ≥ 0 b-tag bin. Signal model: ALPGEN.

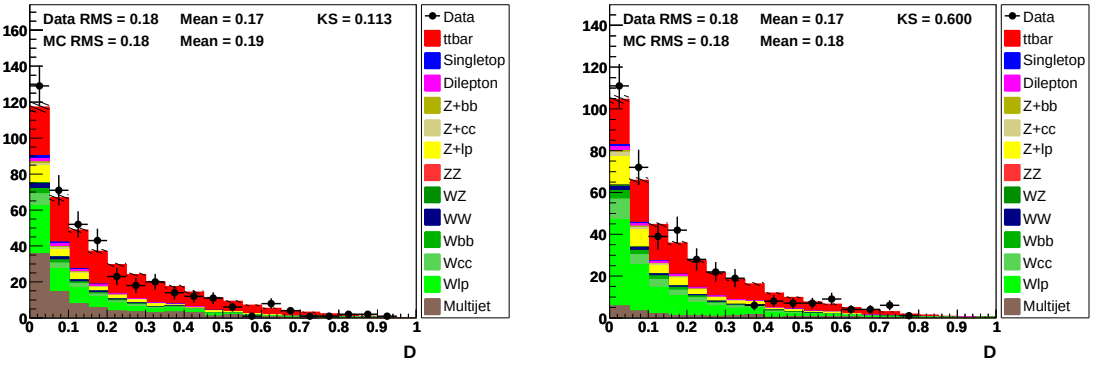

Figure C.63: $\mathcal{D}$, e+jets (left) and μ+jets (right), NN-medium ≥ 0 b-tag bin. Signal model: ALPGEN.

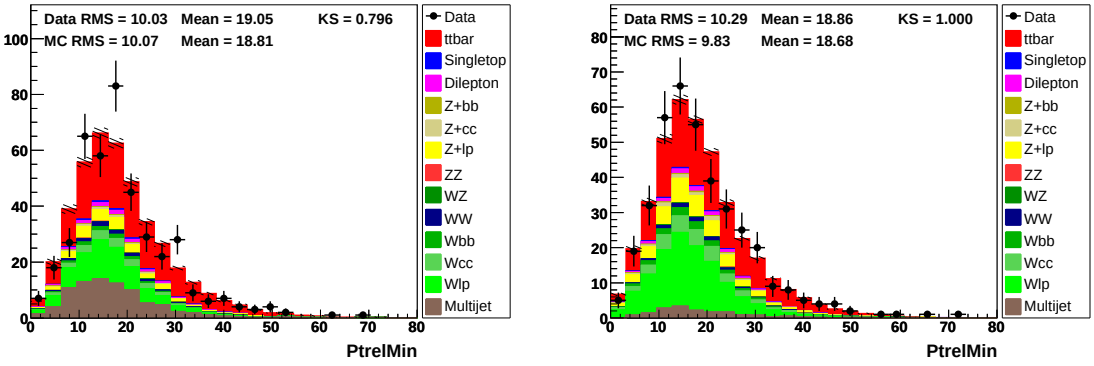

Figure C.64: $p_{T\text{rel.}}^{\text{min}}$, e+jets (left) and μ+jets (right), NN-medium ≥ 0 b-tag bin. Signal model: ALPGEN.

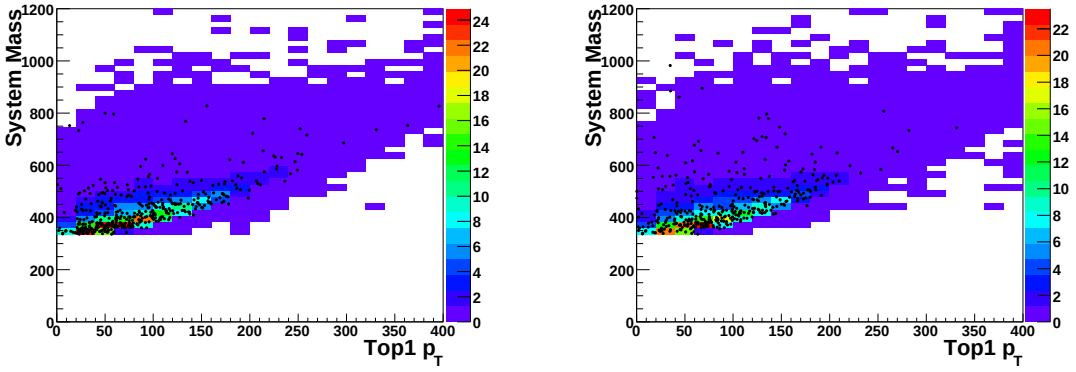

Figure C.65: $t\bar{t}$ system mass vs. leptonic top $p+T$, e+jets (left) and μ+jets (right), NN-medium ≥ 0 b-tag bin. Signal model: ALPGEN.

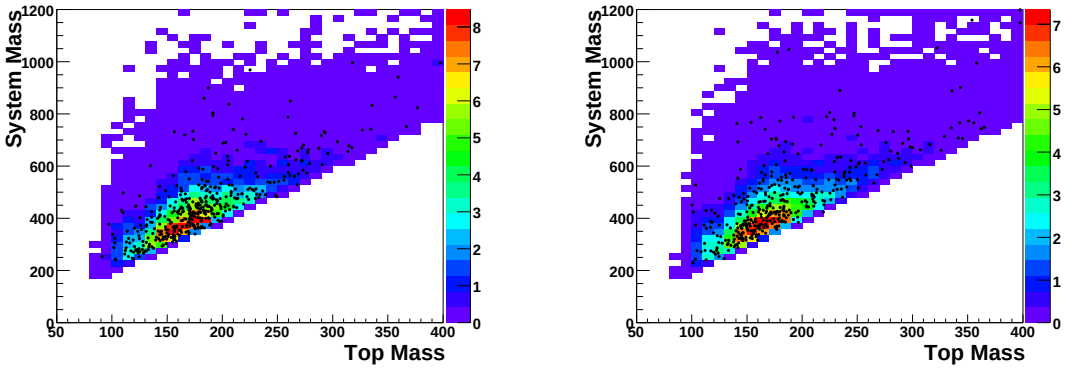

Figure C.66: $t\bar{t}$ system mass vs. top mass, e+jets (left) and μ+jets (right), NN-medium ≥ 0 b-tag bin. Signal model: ALPGEN.

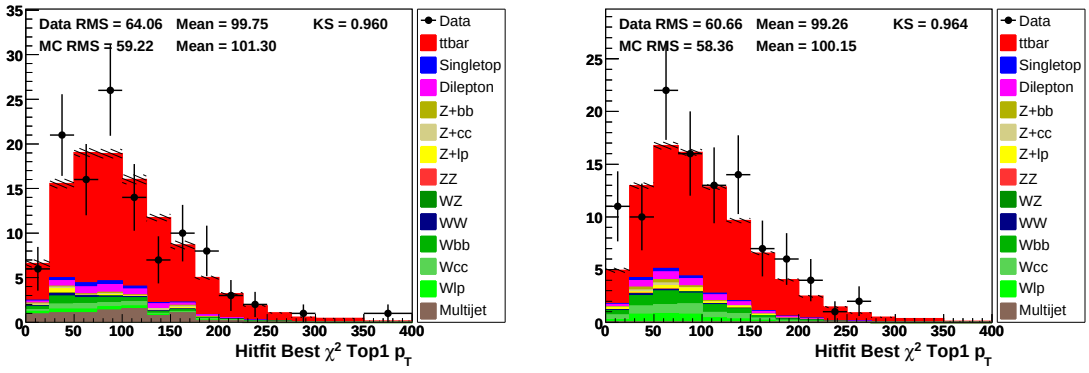

Figure C.67: Leptonic top p_{T}, e+jets (left) and μ+jets (right), NN-medium = 1 b-tag bin. Signal model: ALPGEN.

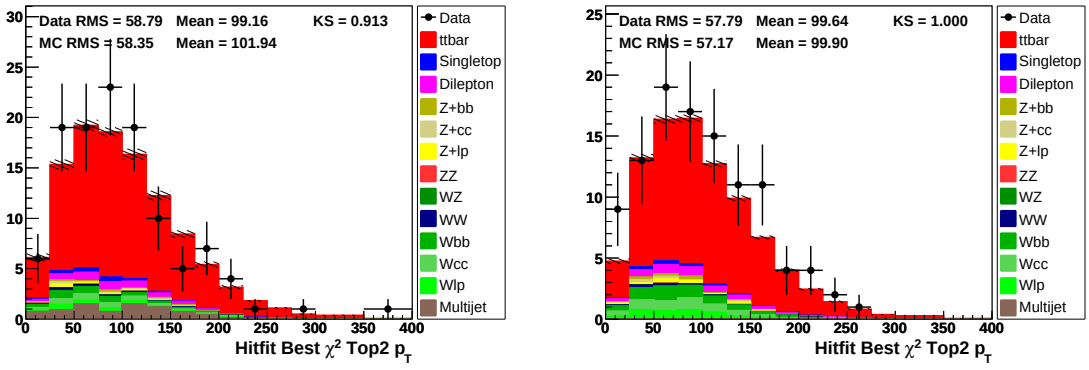

Figure C.68: Hadronic top p_{T}, e+jets (left) and μ+jets (right), NN-medium = 1 b-tag bin. Signal model: ALPGEN.

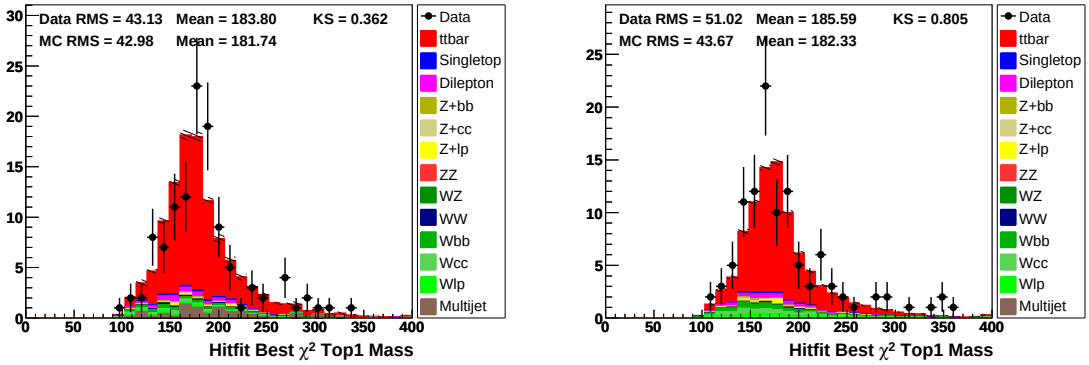

Figure C.69: Fitted top mass, e+jets (left) and μ+jets (right), NN-medium = 1 b-tag bin. Signal model: ALPGEN.

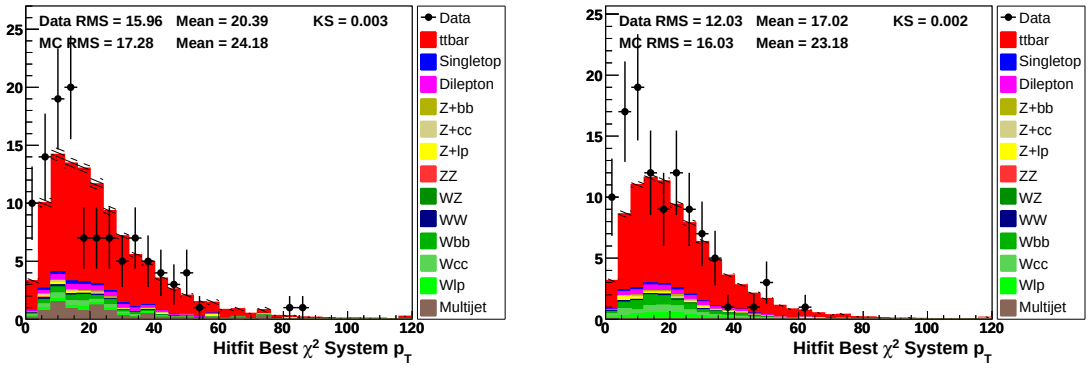

Figure C.70: $t\bar{t}$ p_{T}, e+jets (left) and μ+jets (right), NN-medium = 1 b-tag bin. Signal model: ALPGEN.

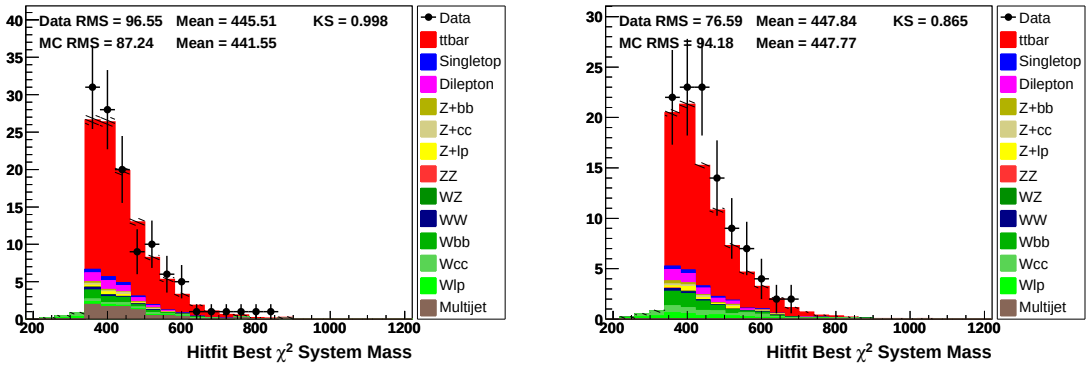

Figure C.71: $t\bar{t}$ mass, e+jets (left) and μ+jets (right), NN-medium = 1 b-tag bin. Signal model: ALPGEN.

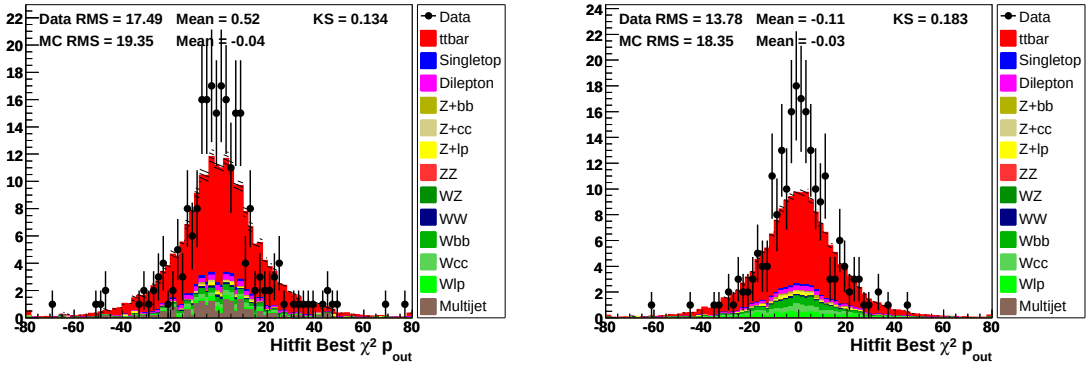

Figure C.72: p_{out}, e+jets (left) and μ+jets (right), NN-medium = 1 b-tag bin. Signal model: ALPGEN.

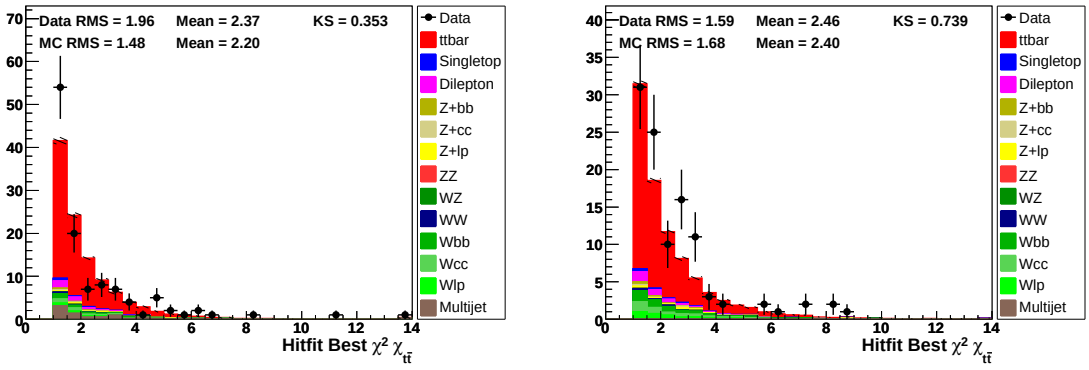

Figure C.73: $\chi_{t\bar{t}}$, e+jets (left) and μ+jets (right), NN-medium = 1 b-tag bin. Signal model: ALPGEN.

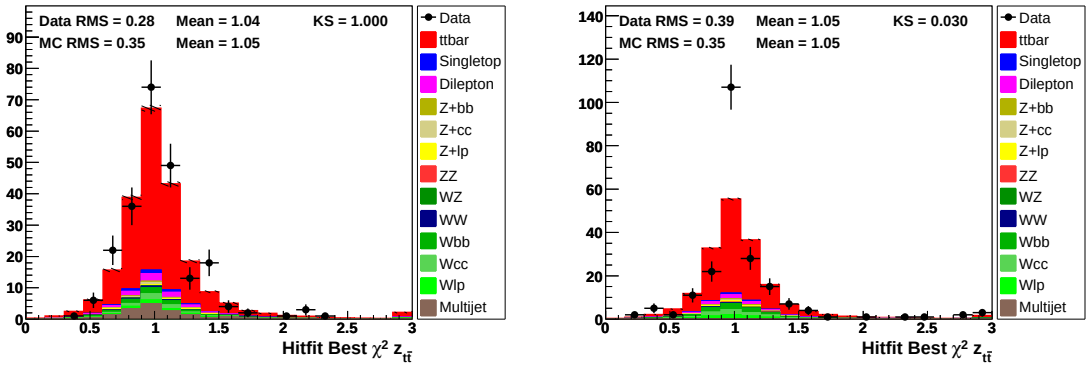

Figure C.74: $z_{t\bar{t}}$, e+jets (left) and μ+jets (right), NN-medium = 1 b-tag bin. Signal model: ALPGEN.

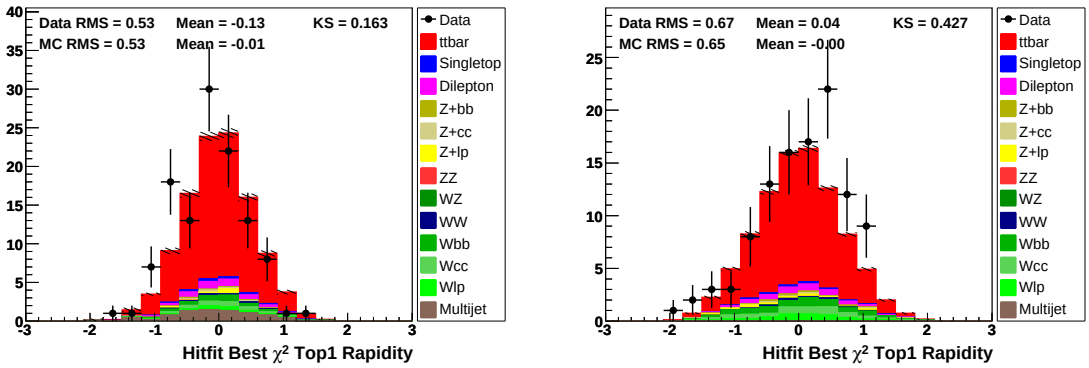

Figure C.75: Leptonic top rapidity, e+jets (left) and μ+jets (right), NN-medium = 1 b-tag bin. Signal model: ALPGEN.

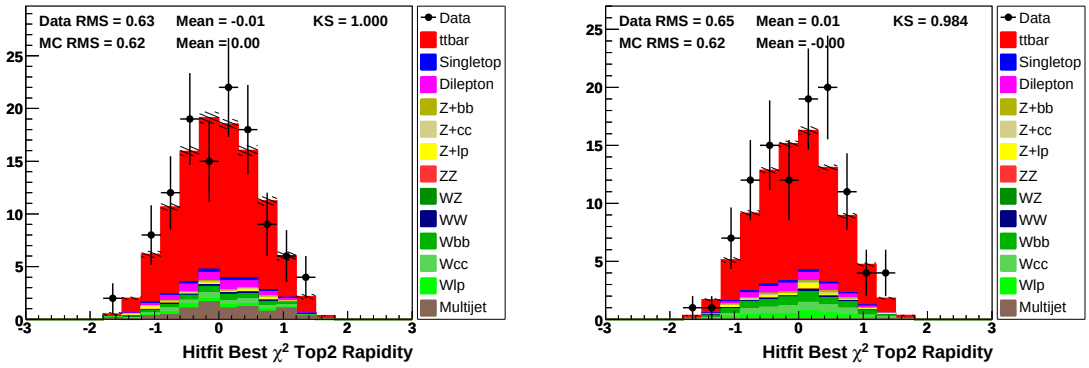

Figure C.76: Hadronic top rapidity, e+jets (left) and μ+jets (right), NN-medium = 1 b-tag bin. Signal model: ALPGEN.

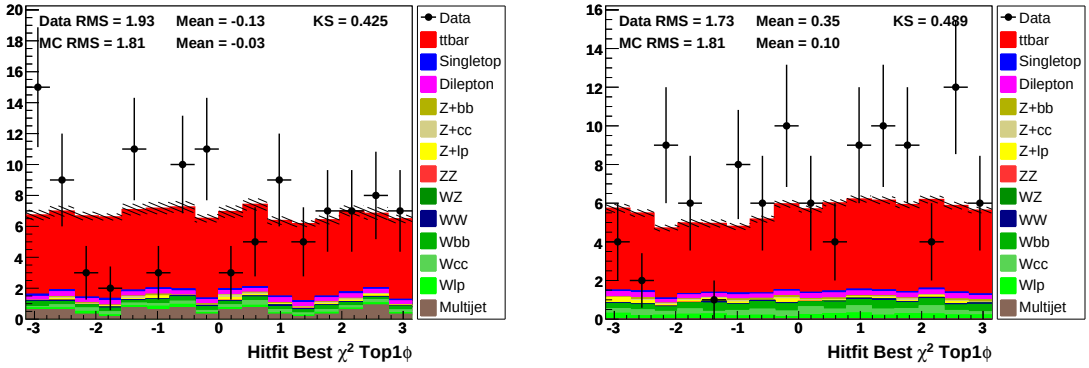

Figure C.77: Leptonic top ϕ, e+jets (left) and μ+jets (right), NN-medium = 1 b-tag bin. Signal model: ALPGEN.

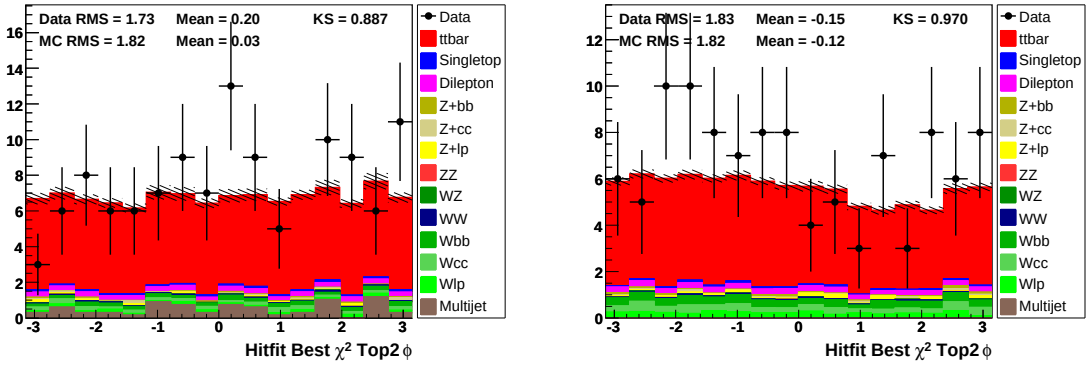

Figure C.78: Hadronic top ϕ, e+jets (left) and μ+jets (right), NN-medium = 1 b-tag bin. Signal model: ALPGEN.

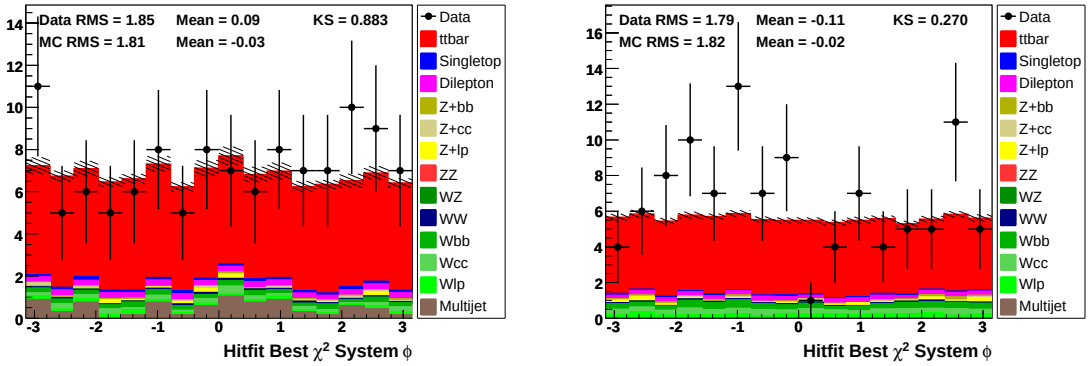

Figure C.79: $t\bar{t}$ ϕ, e+jets (left) and μ+jets (right), NN-medium = 1 b-tag bin. Signal model: ALPGEN.

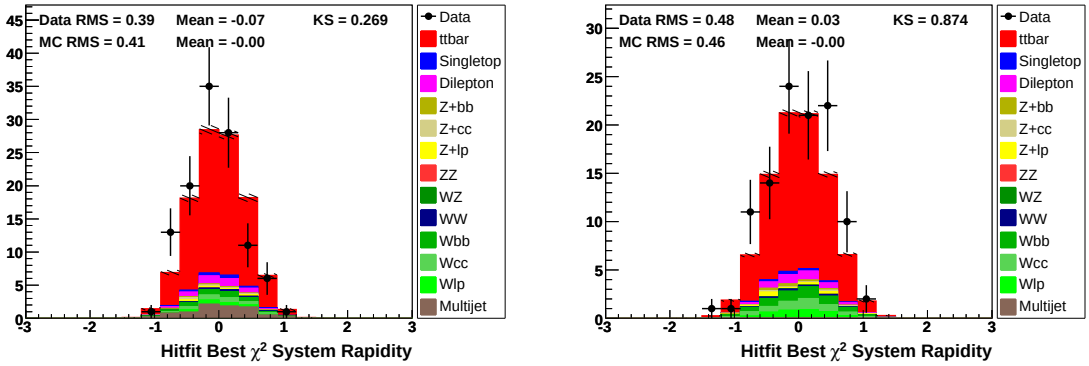

Figure C.80: $t\bar{t}$ rapidity, e+jets (left) and μ+jets (right), NN-medium = 1 b-tag bin. Signal model: ALPGEN.

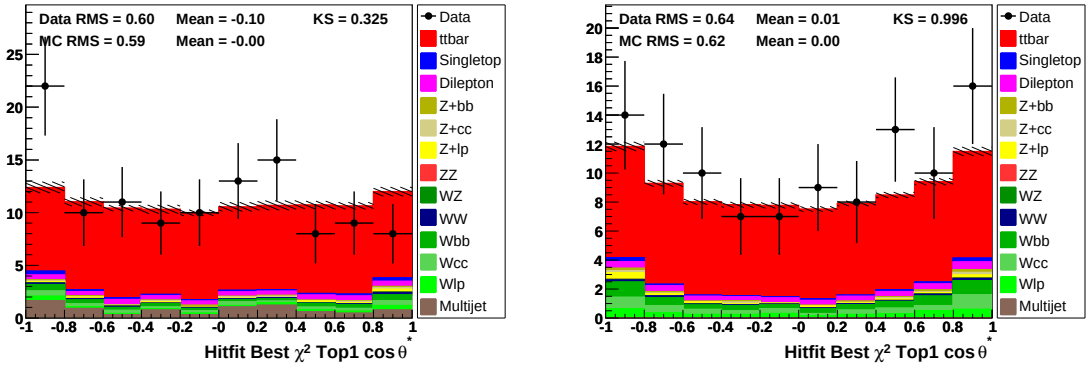

Figure C.81: Leptonic top $\cos\theta^*$, e+jets (left) and μ+jets (right), NN-medium = 1 b-tag bin. Signal model: ALPGEN.

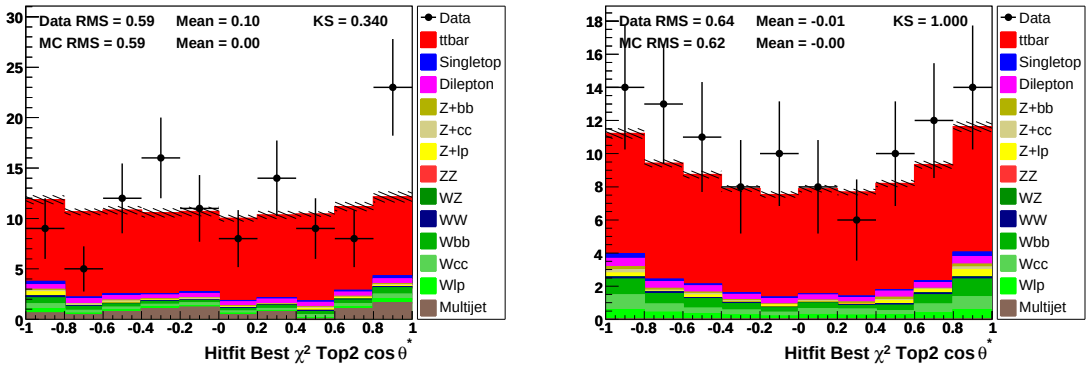

Figure C.82: Hadronic top $\cos\theta^*$, e+jets (left) and μ+jets (right), NN-medium = 1 b-tag bin. Signal model: ALPGEN.

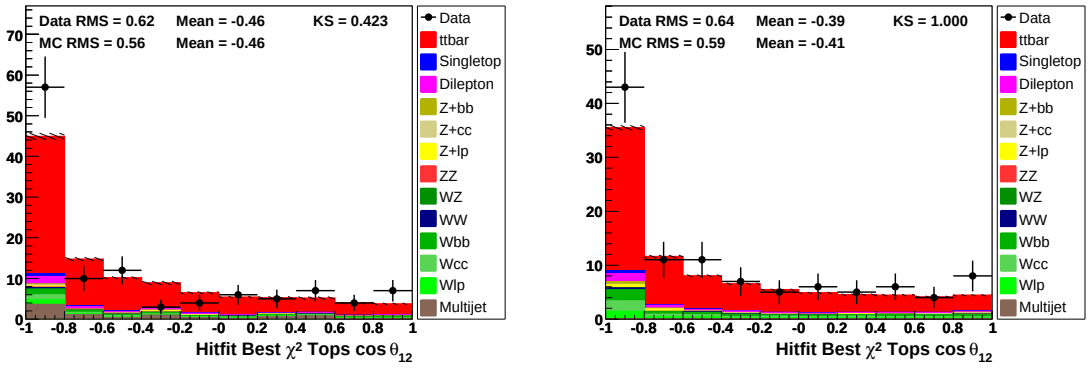

Figure C.83: Opening angle between top quarks, e+jets (left) and μ+jets (right), NN-medium = 1 b-tag bin. Signal model: ALPGEN.

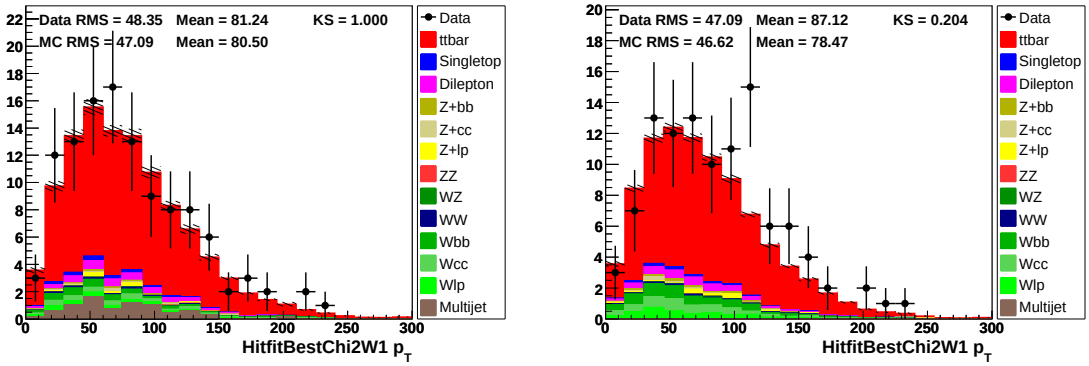

Figure C.84: Leptonic W p_{T}, e+jets (left) and μ+jets (right), NN-medium = 1 b-tag bin. Signal model: ALPGEN.

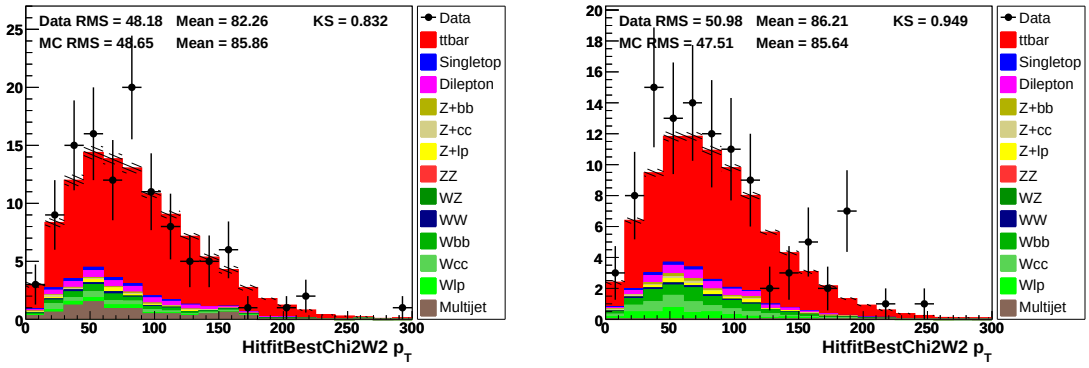

Figure C.85: Hadronic W p_{T}, e+jets (left) and μ+jets (right), NN-medium = 1 b-tag bin. Signal model: ALPGEN.

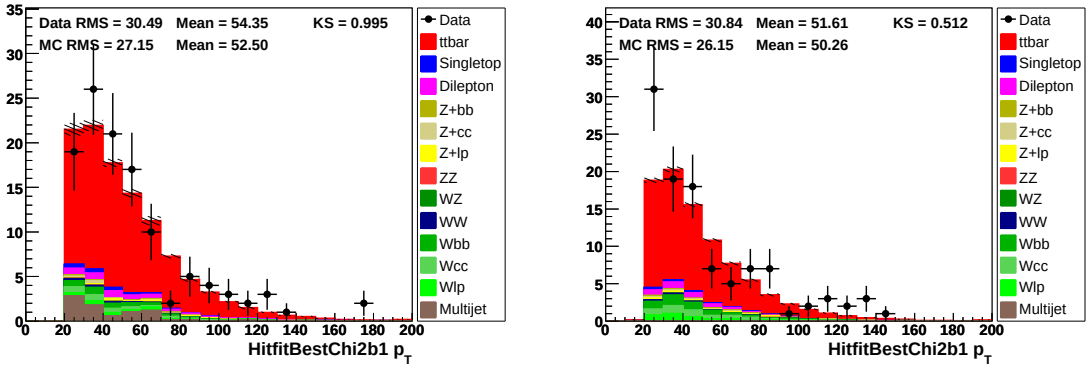

Figure C.86: Leptonic b p_{T}, e+jets (left) and μ+jets (right), NN-medium = 1 b-tag bin. Signal model: ALPGEN.

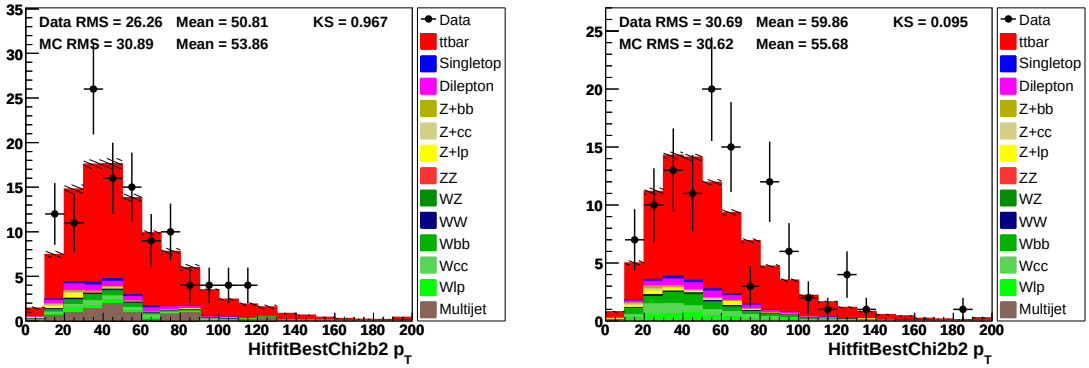

Figure C.87: Hadronic b p_{T}, e+jets (left) and μ+jets (right), NN-medium = 1 b-tag bin. Signal model: ALPGEN.

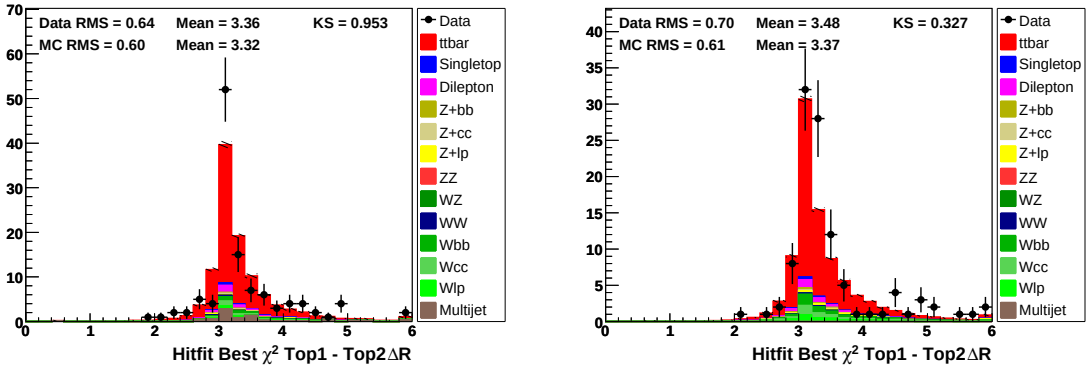

Figure C.88: $\Delta\mathcal{R}_{t\bar{t}}$, e+jets (left) and μ+jets (right), NN-medium = 1 b-tag bin. Signal model: ALPGEN.

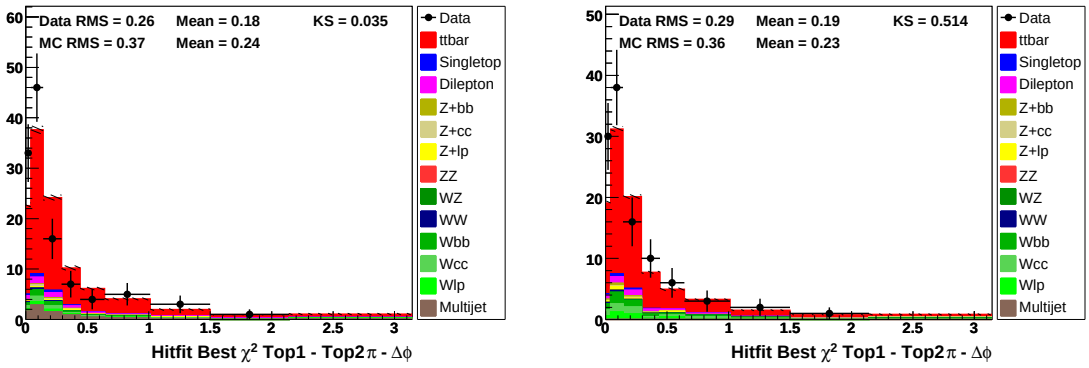

Figure C.89: $\Delta\phi_{t\bar{t}}$, e+jets (left) and μ+jets (right), NN-medium = 1 b-tag bin. Signal model: ALPGEN.

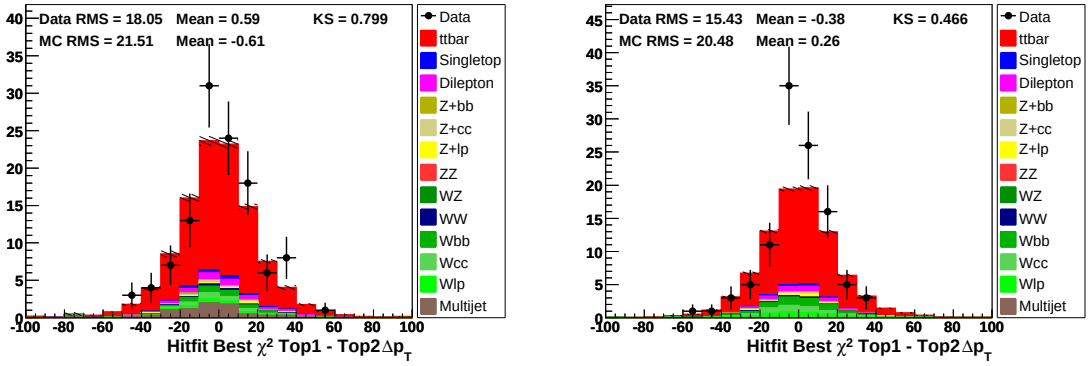

Figure C.90: $\Delta p_{\mathrm{T}}^{t\bar{t}}$, e+jets (left) and μ+jets (right), NN-medium = 1 b-tag bin. Signal model: ALPGEN.

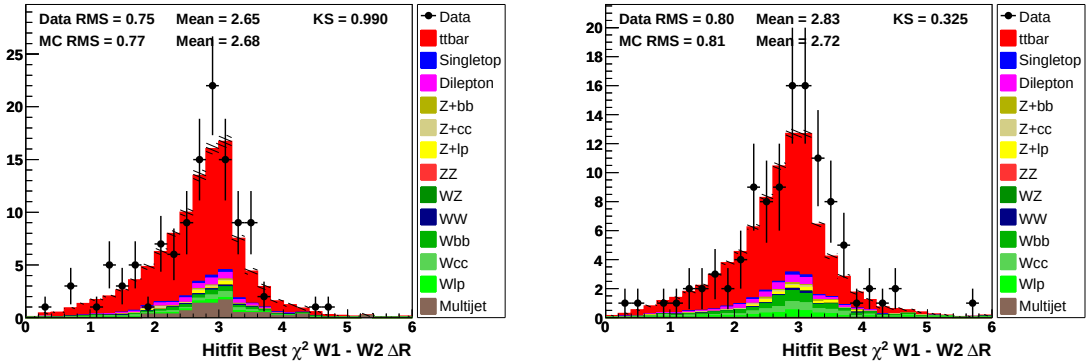

Figure C.91: $\Delta\mathcal{R}_{WW}$, e+jets (left) and μ+jets (right), NN-medium = 1 b-tag bin. Signal model: ALPGEN.

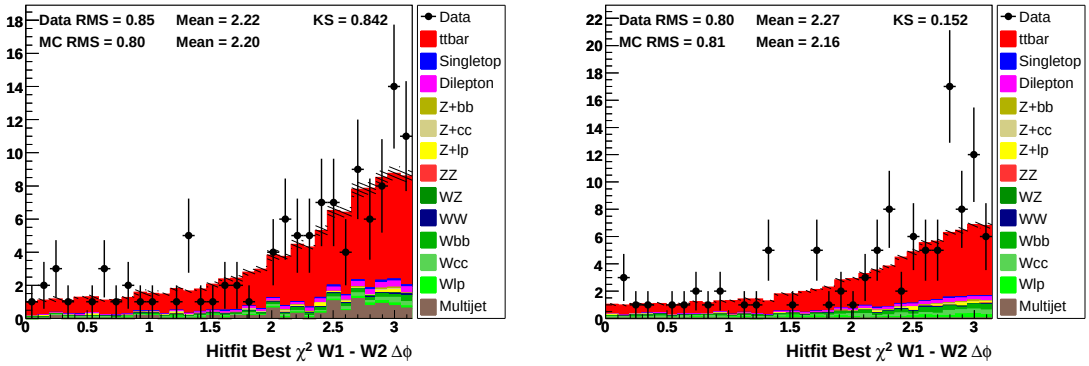

Figure C.92: $\Delta\phi_{WW}$, e+jets (left) and μ+jets (right), NN-medium = 1 b-tag bin. Signal model: ALPGEN.

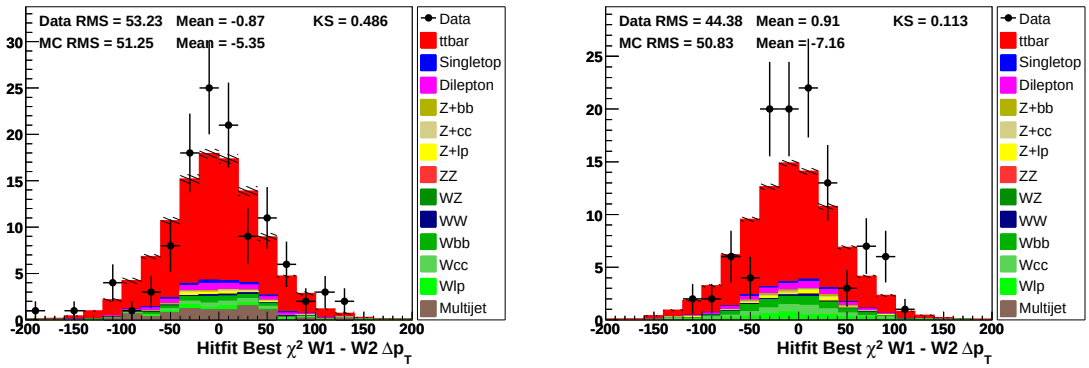

Figure C.93: $\Delta p_{\mathrm{T}}^{WW}$, e+jets (left) and μ+jets (right), NN-medium = 1 b-tag bin. Signal model: ALPGEN.

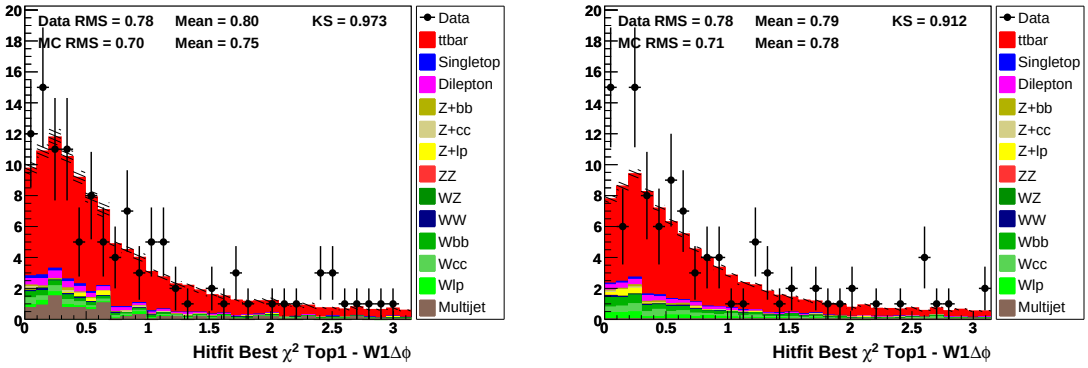

Figure C.94: $\Delta\phi_{t1W1}$, e+jets (left) and μ+jets (right), NN-medium = 1 b-tag bin. Signal model: ALPGEN.

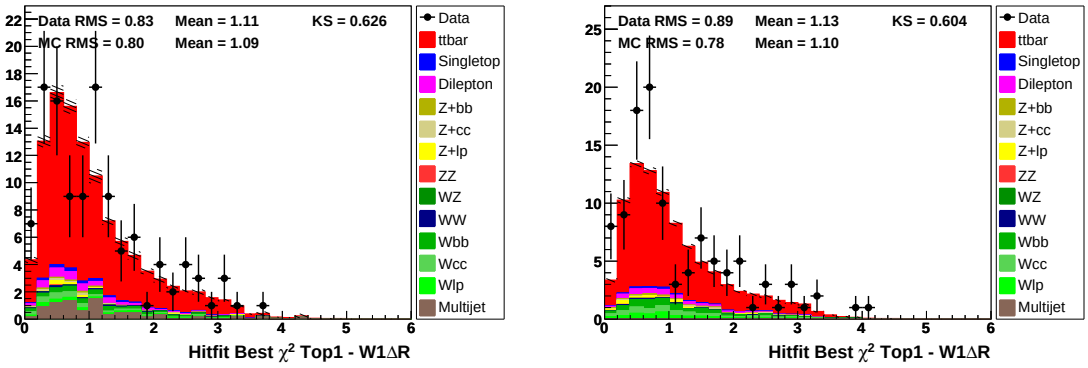

Figure C.95: $\Delta\mathcal{R}_{t1W1}$, e+jets (left) and μ+jets (right), NN-medium = 1 b-tag bin. Signal model: ALPGEN.

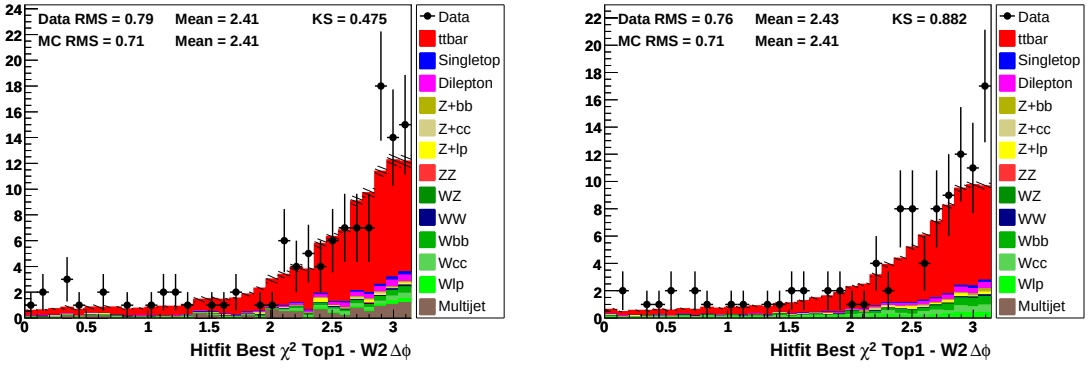

Figure C.96: $\Delta\phi_{t1W2}$, e+jets (left) and μ+jets (right), NN-medium = 1 b-tag bin. Signal model: ALPGEN.

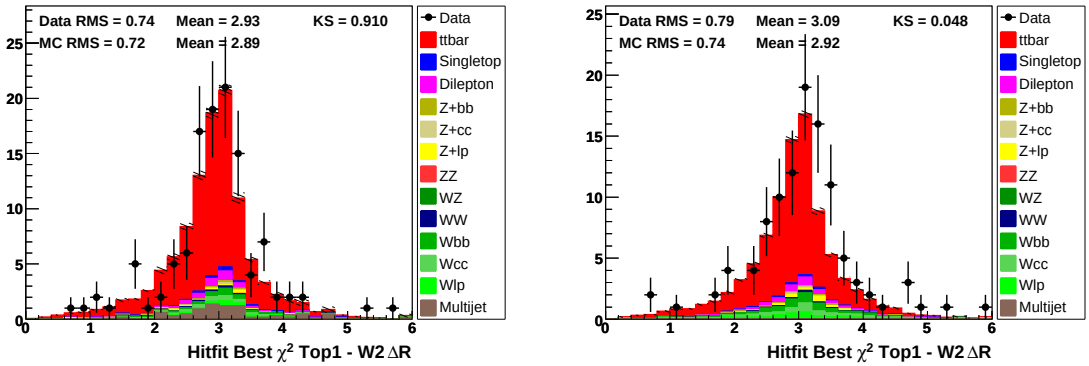

Figure C.97: $\Delta\mathcal{R}_{t1W2}$, e+jets (left) and μ+jets (right), NN-medium = 1 b-tag bin. Signal model: ALPGEN.

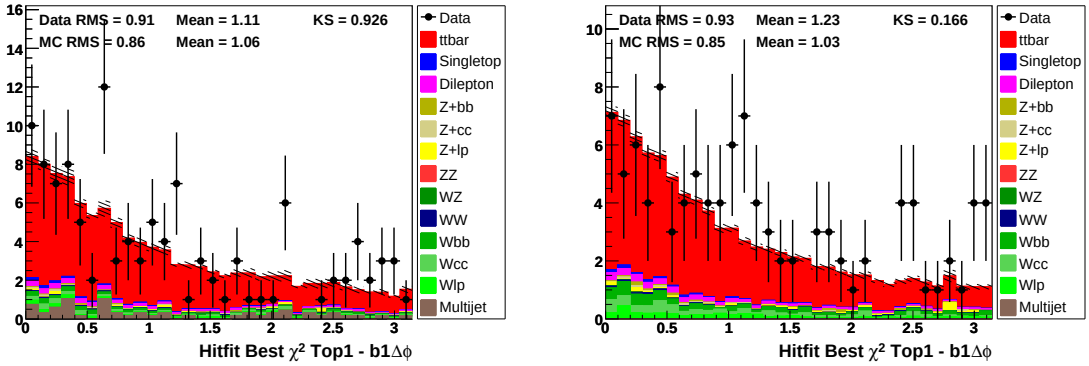

Figure C.98: $\Delta\phi_{t1b1}$, e+jets (left) and μ+jets (right), NN-medium = 1 b-tag bin. Signal model: ALPGEN.

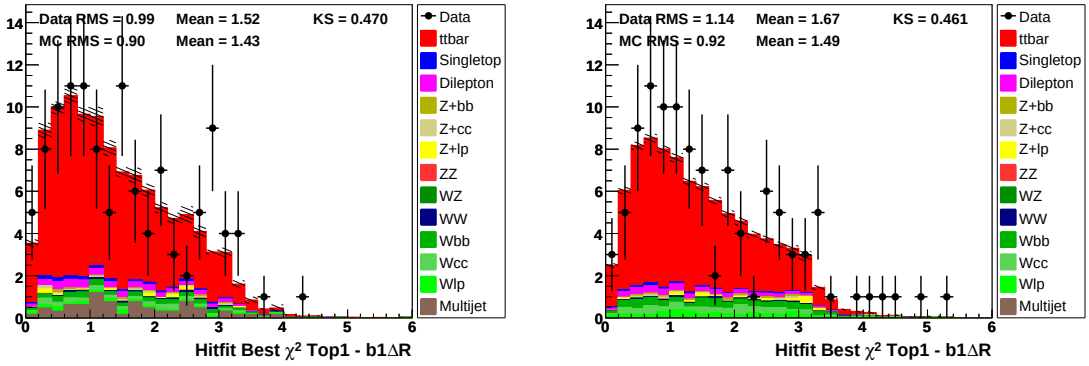

Figure C.99: $\Delta\mathcal{R}_{t1b1}$, e+jets (left) and μ+jets (right), NN-medium = 1 b-tag bin. Signal model: ALPGEN.

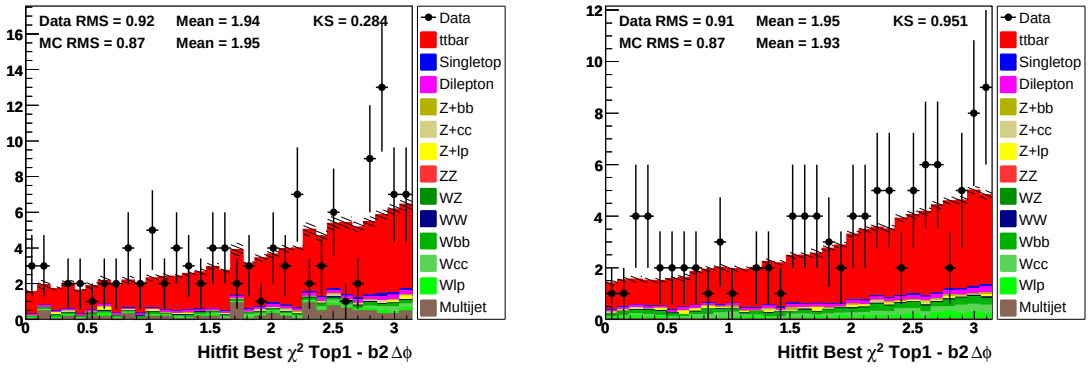

Figure C.100: $\Delta\phi_{t1b2}$, e+jets (left) and μ+jets (right), NN-medium = 1 b-tag bin. Signal model: ALPGEN.

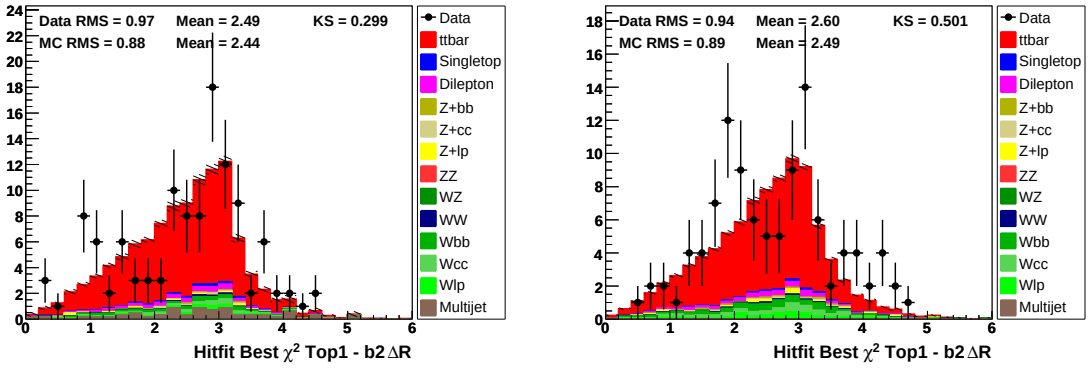

Figure C.101: $\Delta\mathcal{R}_{t1b2}$, e+jets (left) and μ+jets (right), NN-medium = 1 b-tag bin. Signal model: ALPGEN.

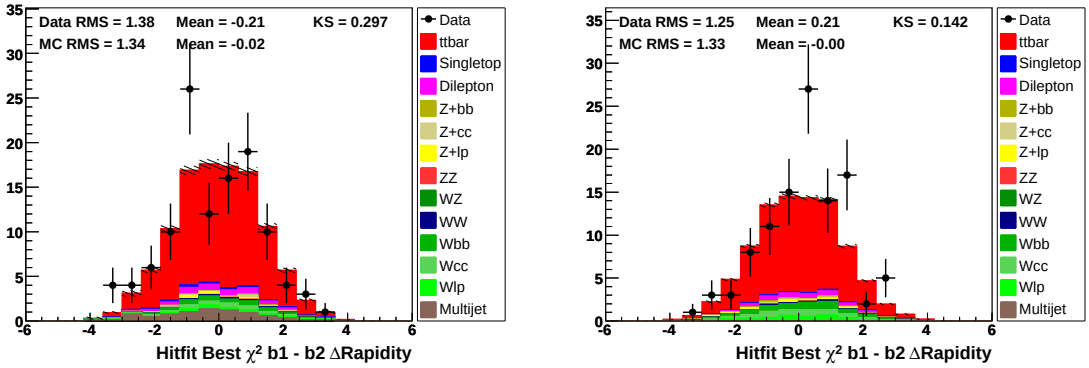

Figure C.102: $\Delta\text{Rapidity}_{b1b2}$, e+jets (left) and μ+jets (right), NN-medium = 1 b-tag bin. Signal model: ALPGEN.

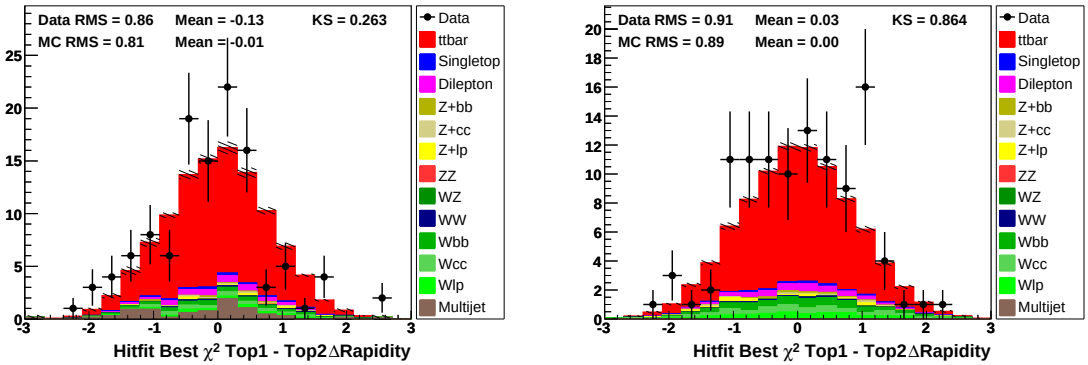

Figure C.103: $\Delta\text{Rapidity}_{t\bar{t}}$, e+jets (left) and μ+jets (right), NN-medium = 1 b-tag bin. Signal model: ALPGEN.

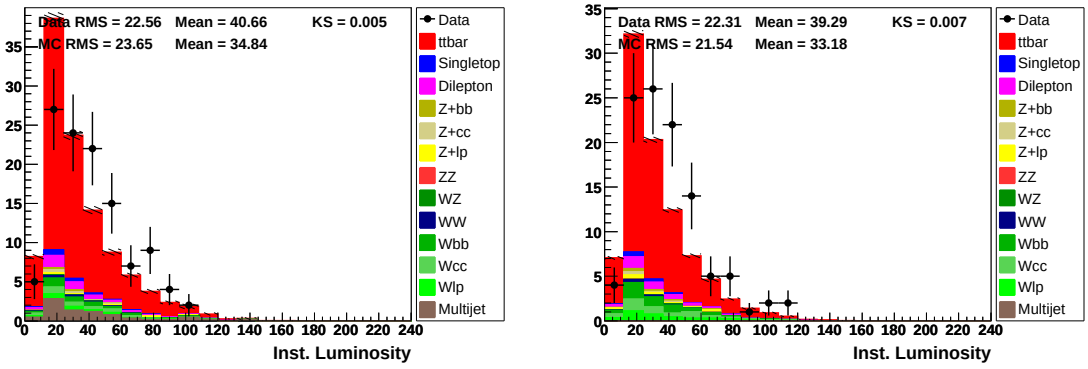

Figure C.104: Instantenous luminosity [$10^{30}\text{cm}^{-2}\text{s}^{-1}$], e+jets (left) and μ+jets (right), NN-medium = 1 b-tag bin. Signal model: ALPGEN.

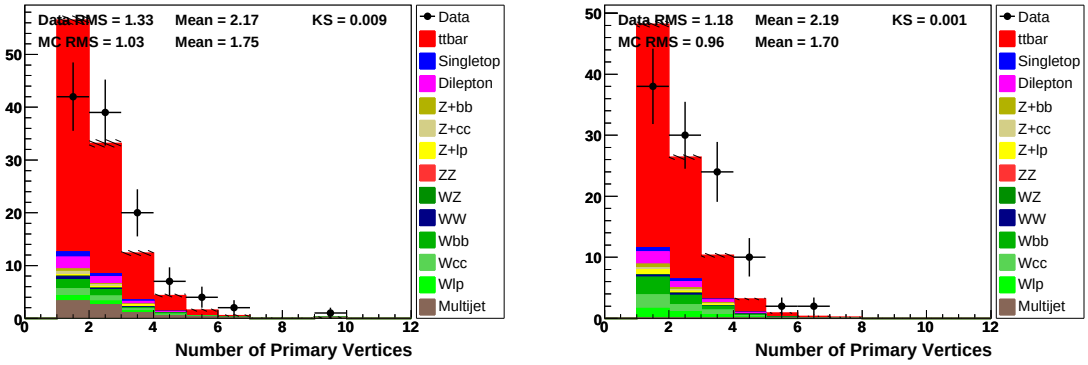

Figure C.105: Number of primary vertices, e+jets (left) and μ+jets (right), NN-medium = 1 b-tag bin. Signal model: ALPGEN.

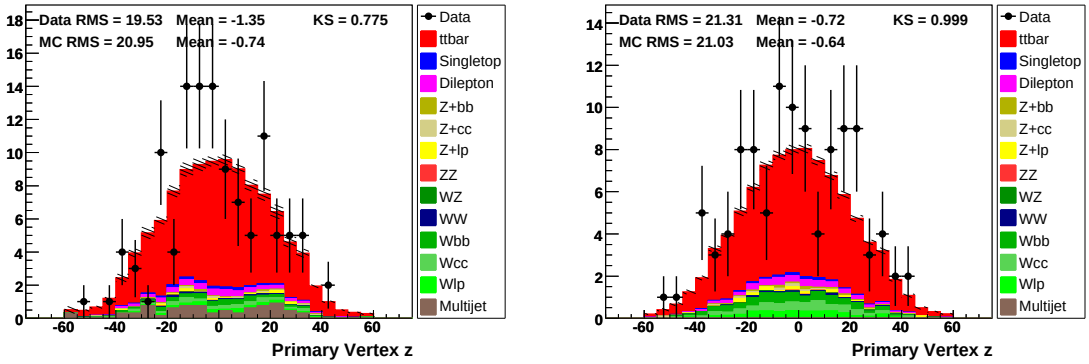

Figure C.106: Primary vertex z coordinate, e+jets (left) and μ+jets (right), NN-medium = 1 b-tag bin. Signal model: ALPGEN.

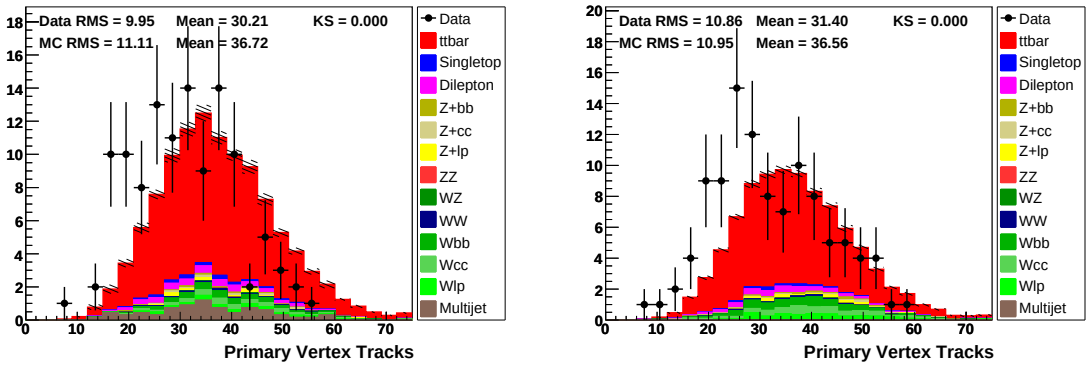

Figure C.107: Number of PV tracks, e+jets (left) and μ+jets (right), NN-medium = 1 b-tag bin. Signal model: ALPGEN.

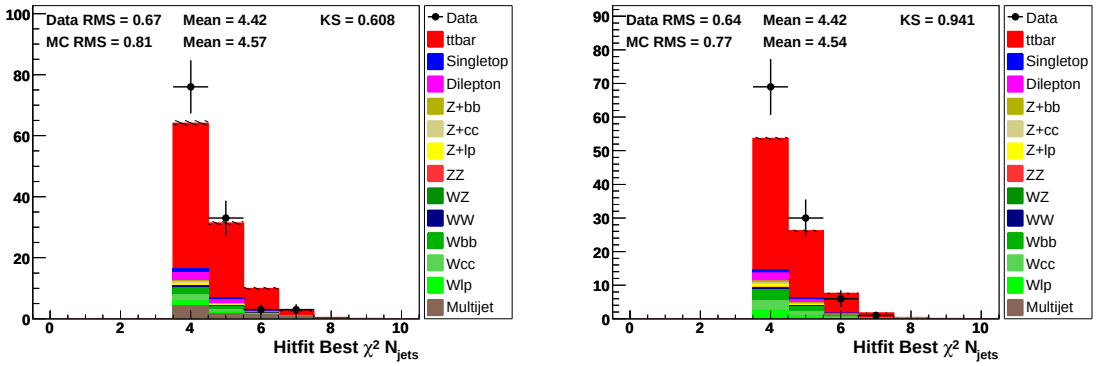

Figure C.108: n_{jets}, e+jets (left) and μ+jets (right), NN-medium = 1 b-tag bin. Signal model: ALPGEN.

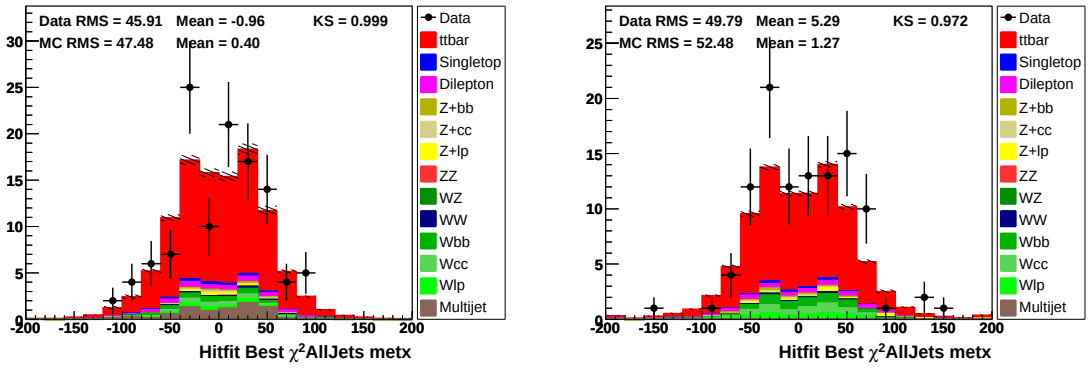

Figure C.109: Missing transverse energy x component, e+jets (left) and μ+jets (right), NN-medium = 1 b-tag bin. Signal model: ALPGEN.

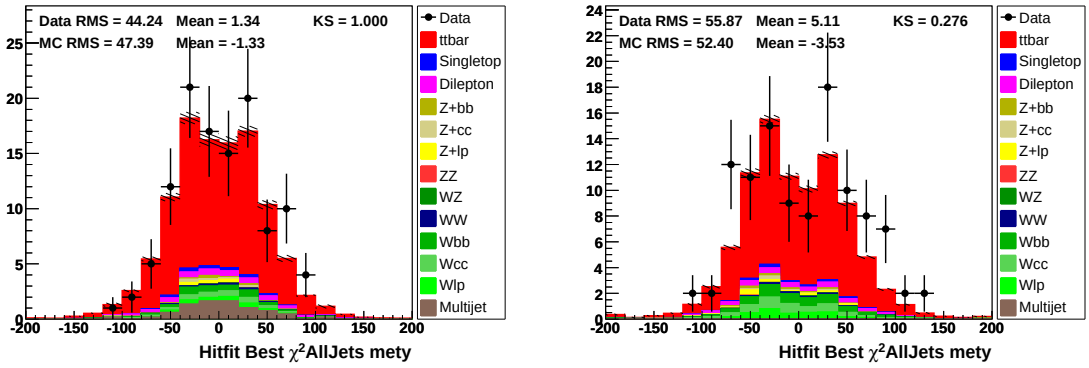

Figure C.110: Missing transverse energy y component, e+jets (left) and μ+jets (right), NN-medium = 1 b-tag bin. Signal model: ALPGEN.

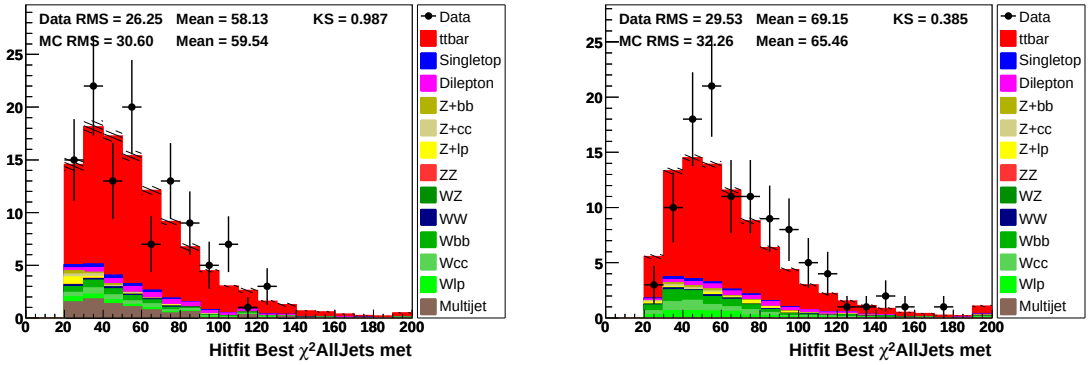

Figure C.111: Missing transverse energy, e+jets (left) and μ+jets (right), NN-medium = 1 b-tag bin. Signal model: ALPGEN.

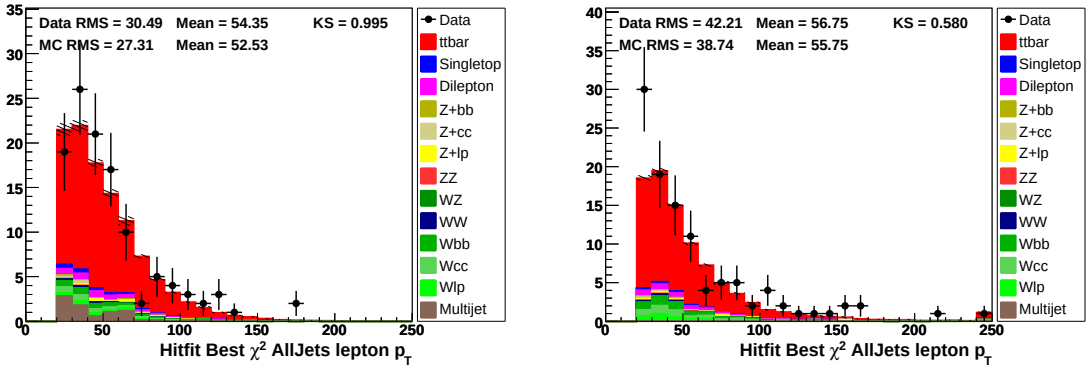

Figure C.112: Lepton p_{T}, e+jets (left) and μ+jets (right), NN-medium = 1 b-tag bin. Signal model: ALPGEN.

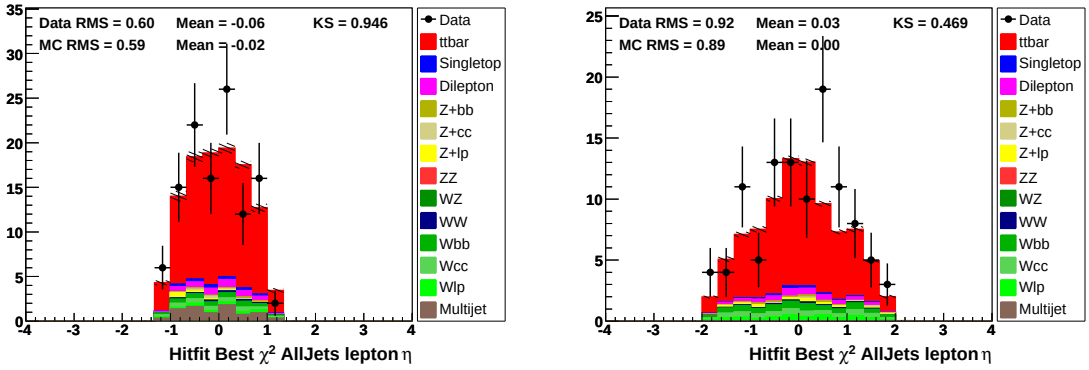

Figure C.113: Lepton η, e+jets (left) and μ+jets (right), NN-medium = 1 b-tag bin. Signal model: ALPGEN.

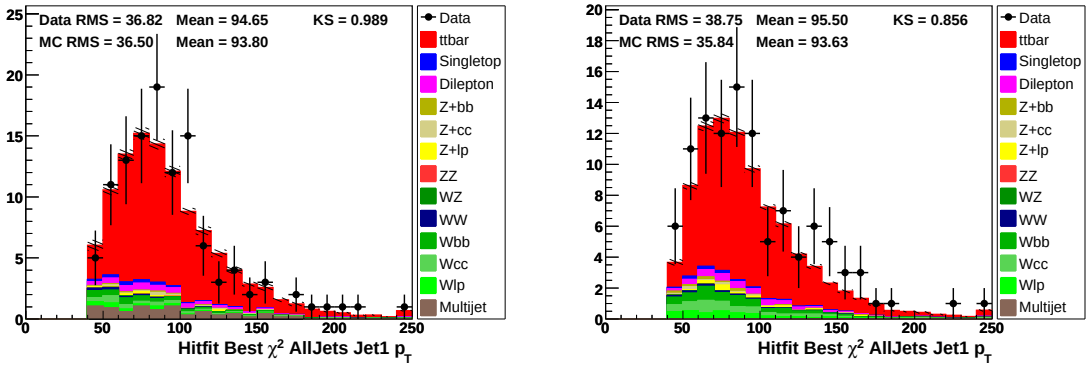

Figure C.114: 1st Jet p_{T}, e+jets (left) and μ+jets (right), NN-medium = 1 b-tag bin. Signal model: ALPGEN.

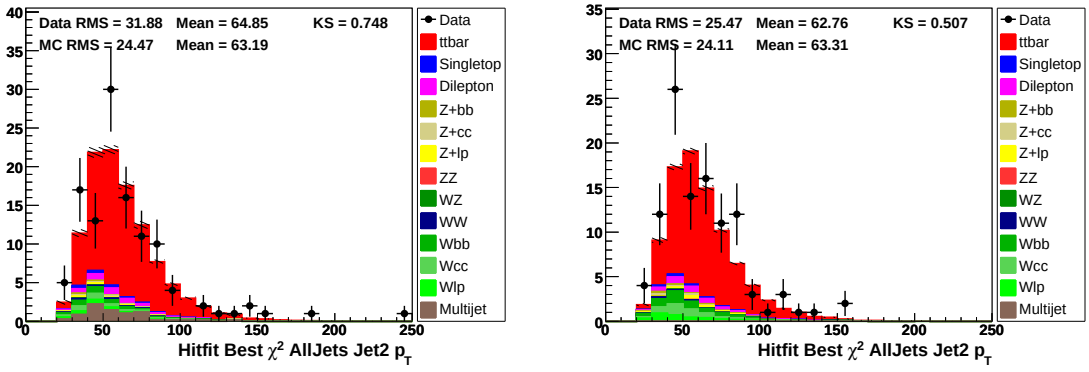

Figure C.115: 2nd Jet p_{T}, e+jets (left) and μ+jets (right), NN-medium = 1 b-tag bin. Signal model: ALPGEN.

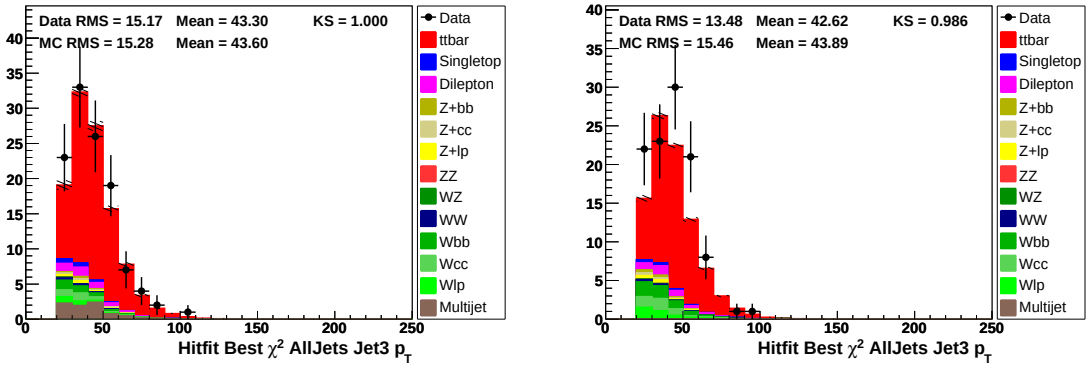

Figure C.116: 3rd Jet p_{T}, e+jets (left) and μ+jets (right), NN-medium = 1 b-tag bin. Signal model: ALPGEN.

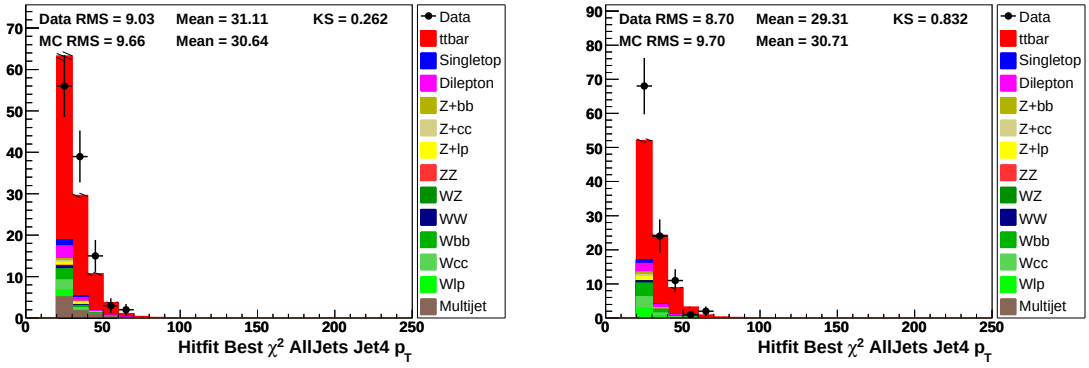

Figure C.117: 4th Jet p_{T}, e+jets (left) and μ+jets (right), NN-medium = 1 b-tag bin. Signal model: ALPGEN.

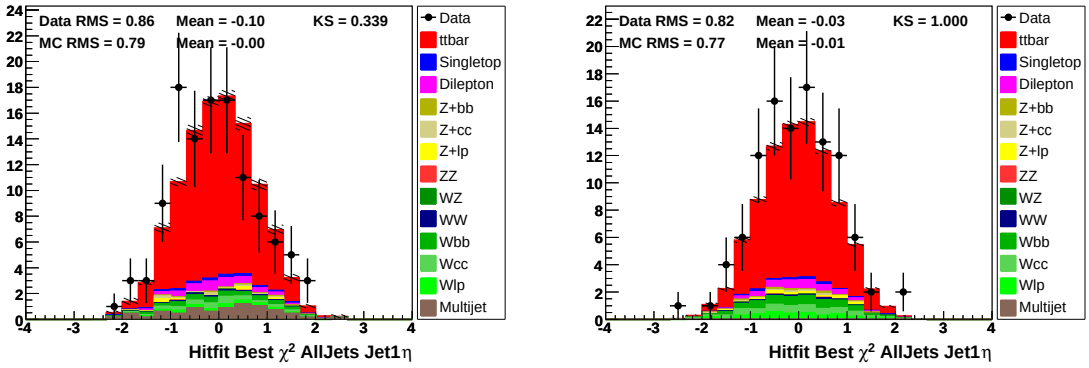

Figure C.118: 1st Jet η, e+jets (left) and μ+jets (right), NN-medium = 1 b-tag bin. Signal model: ALPGEN.

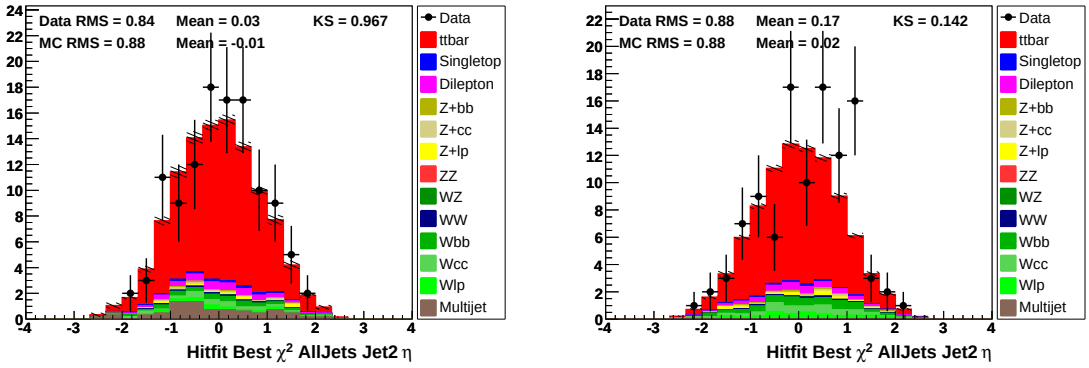

Figure C.119: 2nd Jet η, e+jets (left) and μ+jets (right), NN-medium = 1 b-tag bin. Signal model: ALPGEN.

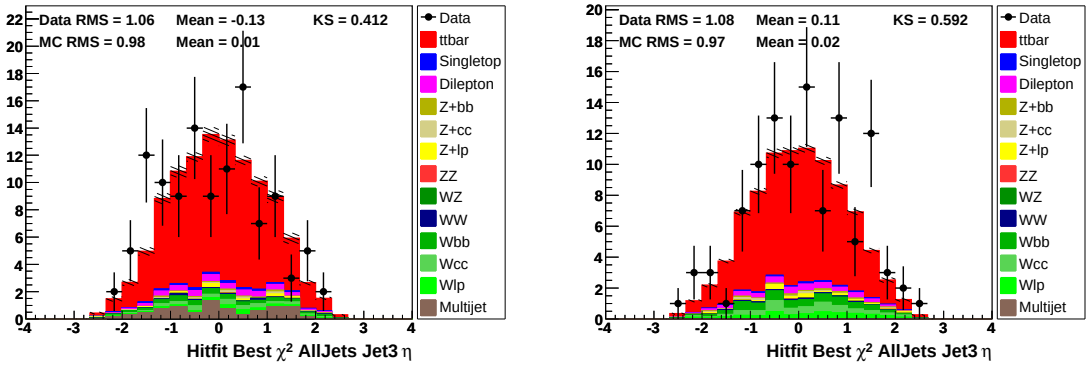

Figure C.120: 3rd Jet η, e+jets (left) and μ+jets (right), NN-medium = 1 b-tag bin. Signal model: ALPGEN.

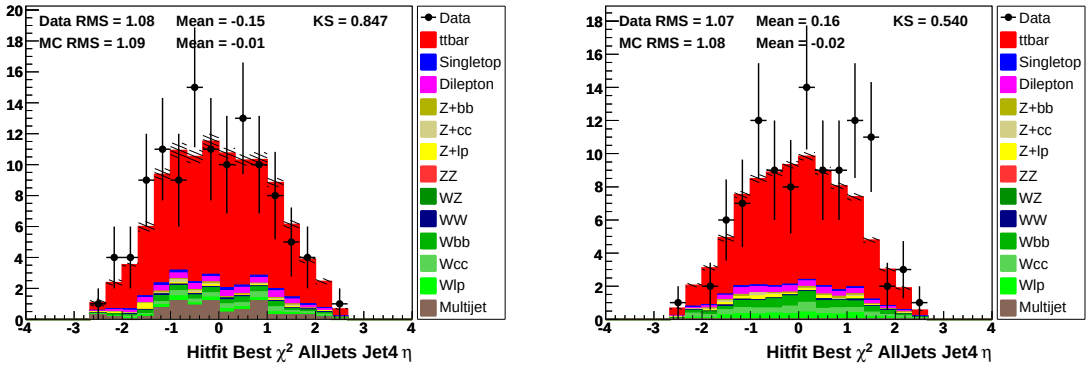

Figure C.121: 4th Jet η, e+jets (left) and μ+jets (right), NN-medium = 1 b-tag bin. Signal model: ALPGEN.

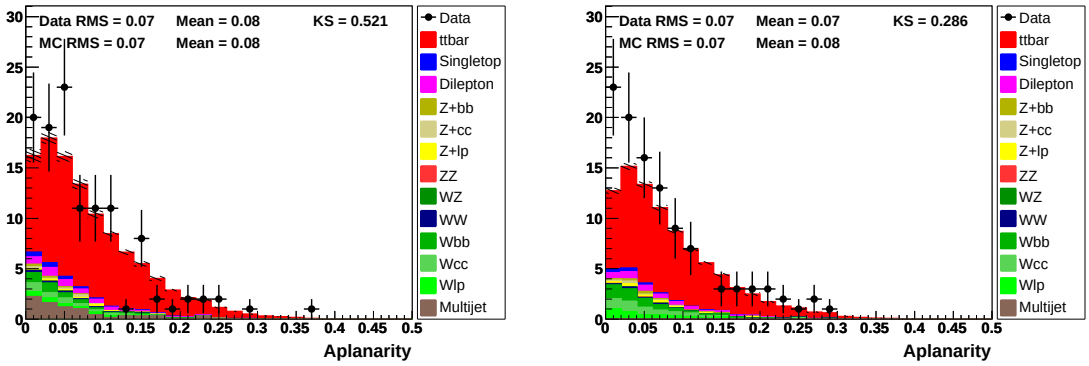

Figure C.122: Aplanarity, e+jets (left) and μ+jets (right), NN-medium = 1 b-tag bin. Signal model: ALPGEN.

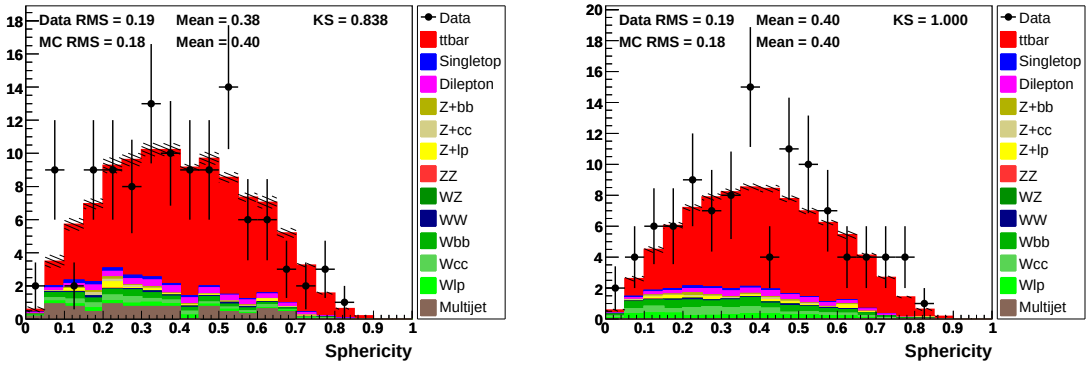

Figure C.123: Sphericity, e+jets (left) and μ+jets (right), NN-medium = 1 b-tag bin. Signal model: ALPGEN.

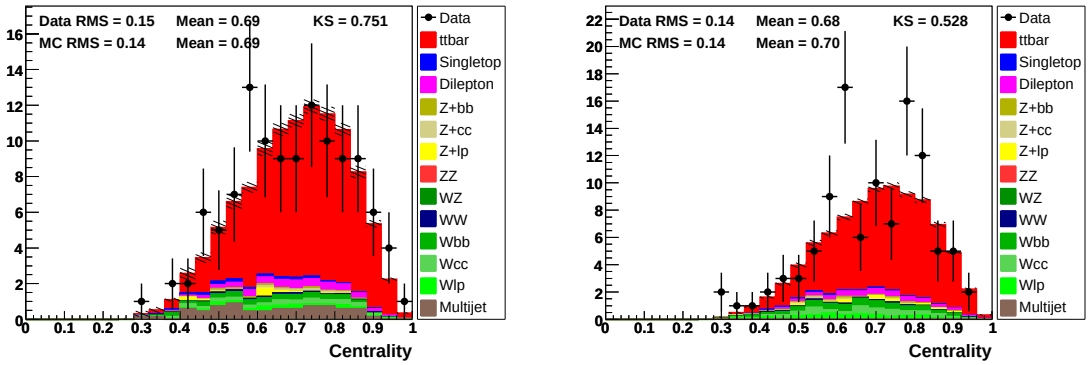

Figure C.124: Centrality, e+jets (left) and μ+jets (right), NN-medium = 1 b-tag bin. Signal model: ALPGEN.

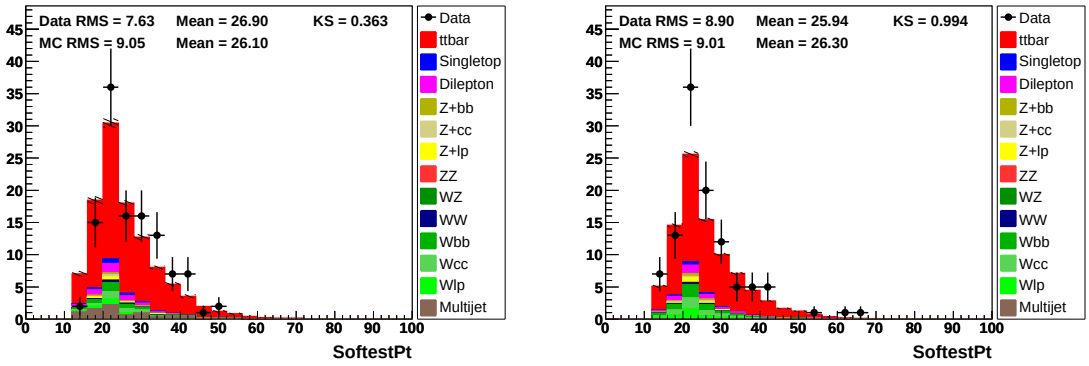

Figure C.125: Softest p_T, e+jets (left) and μ+jets (right), NN-medium = 1 b-tag bin. Signal model: ALPGEN.

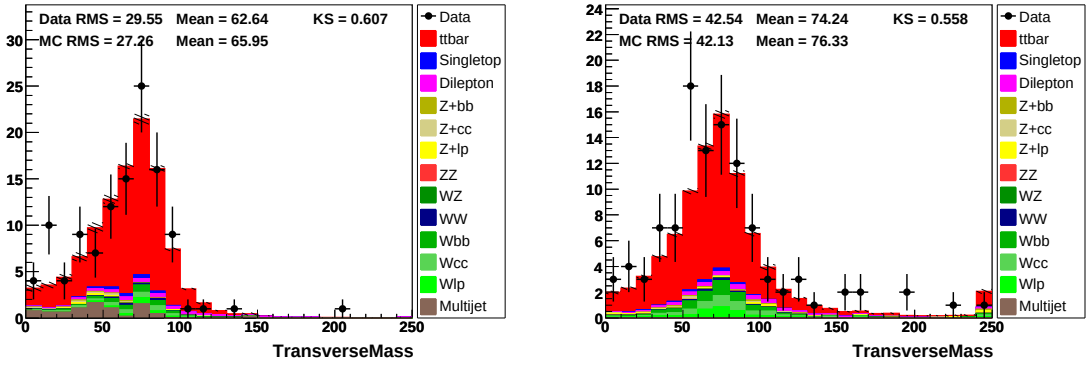

Figure C.126: Transverse mass, e+jets (left) and μ+jets (right), NN-medium = 1 b-tag bin. Signal model: ALPGEN.

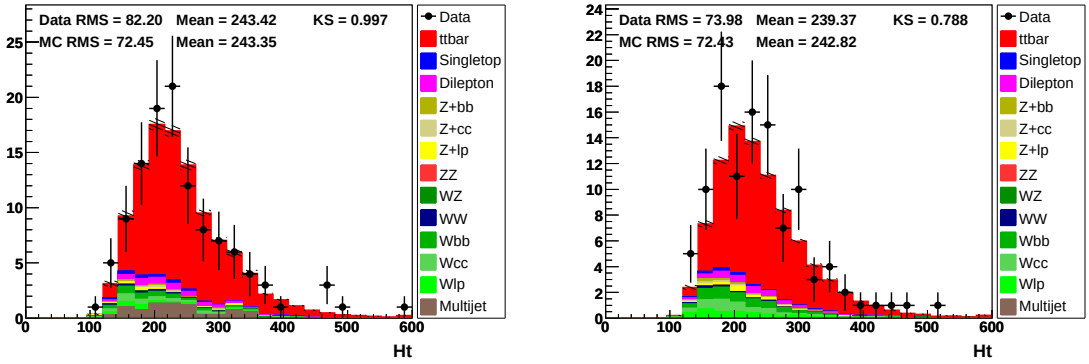

Figure C.127: H_T, e+jets (left) and μ+jets (right), NN-medium = 1 b-tag bin. Signal model: ALPGEN.

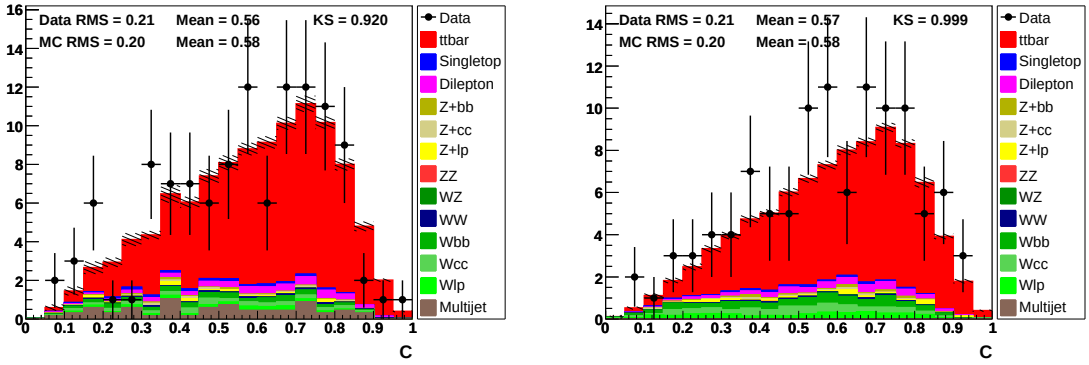

Figure C.128: $\mathcal{C}$, e+jets (left) and μ+jets (right), NN-medium = 1 b-tag bin. Signal model: ALPGEN.

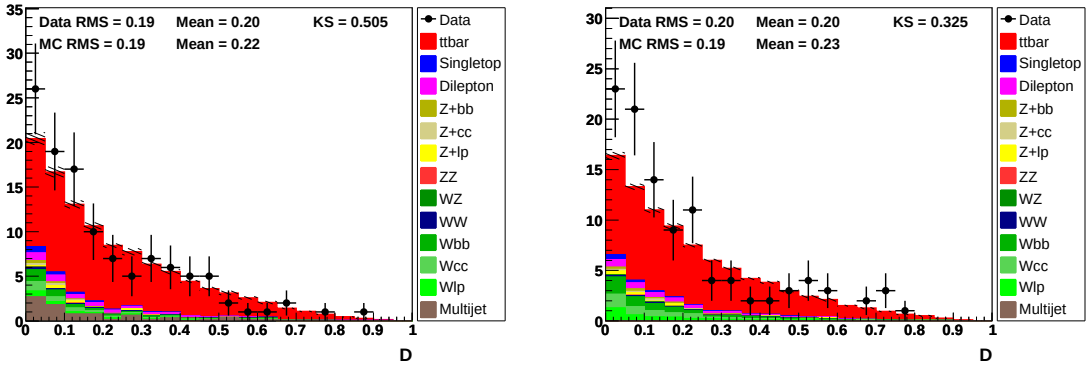

Figure C.129: $\mathcal{D}$, e+jets (left) and μ+jets (right), NN-medium = 1 b-tag bin. Signal model: ALPGEN.

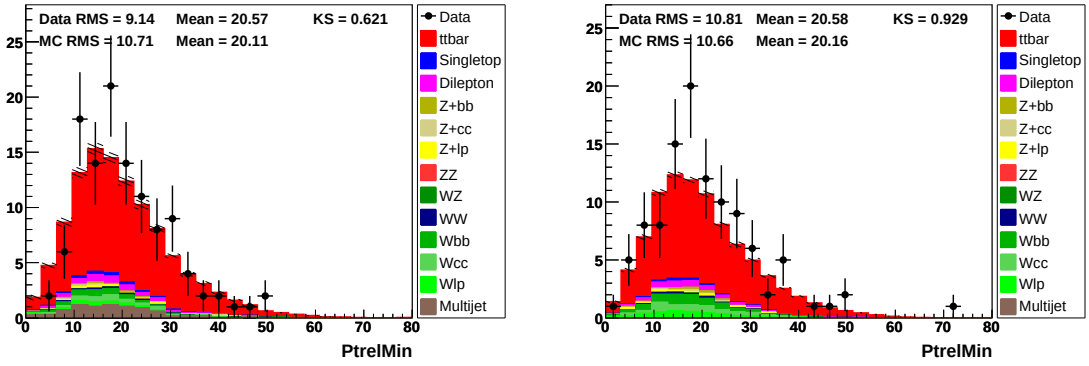

Figure C.130: $p_{Trel.}^{\min}$, e+jets (left) and μ+jets (right), NN-medium = 1 b-tag bin. Signal model: ALPGEN.

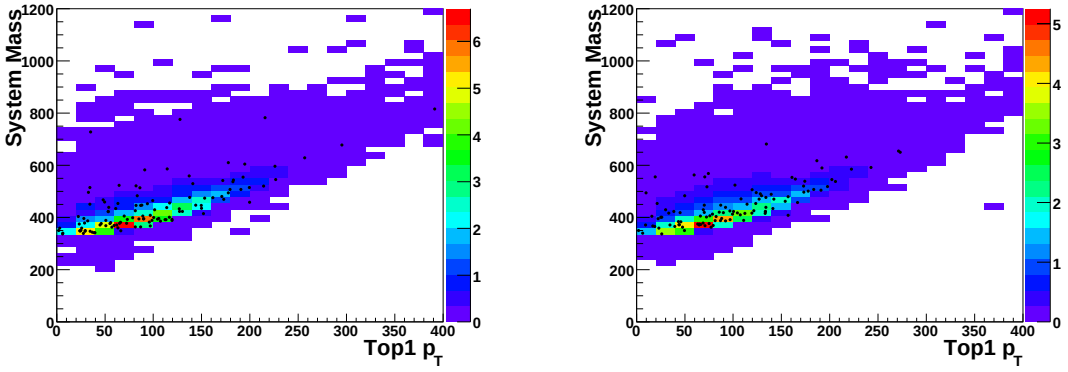

Figure C.131: $t\bar{t}$ system mass vs. leptonic top $p+T$, e+jets (left) and μ+jets (right), NN-medium = 1 b-tag bin. Signal model: ALPGEN.

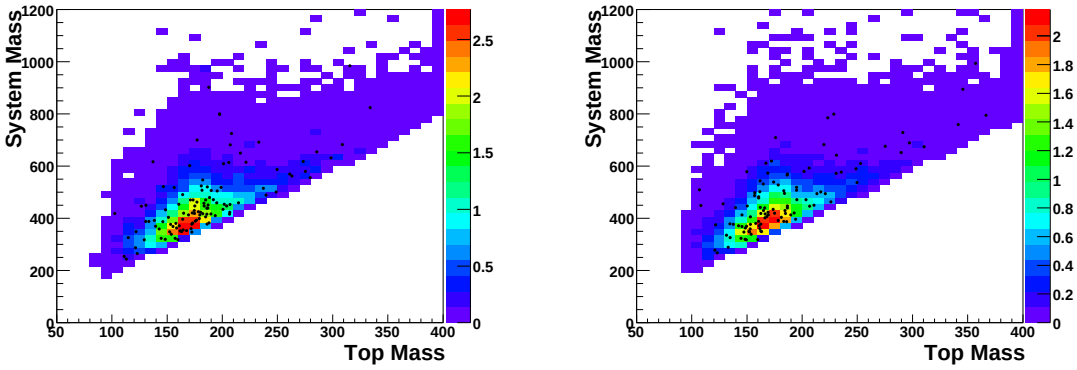

Figure C.132: $t\bar{t}$ system mass vs. top mass, e+jets (left) and μ+jets (right), NN-medium = 1 b-tag bin. Signal model: ALPGEN.

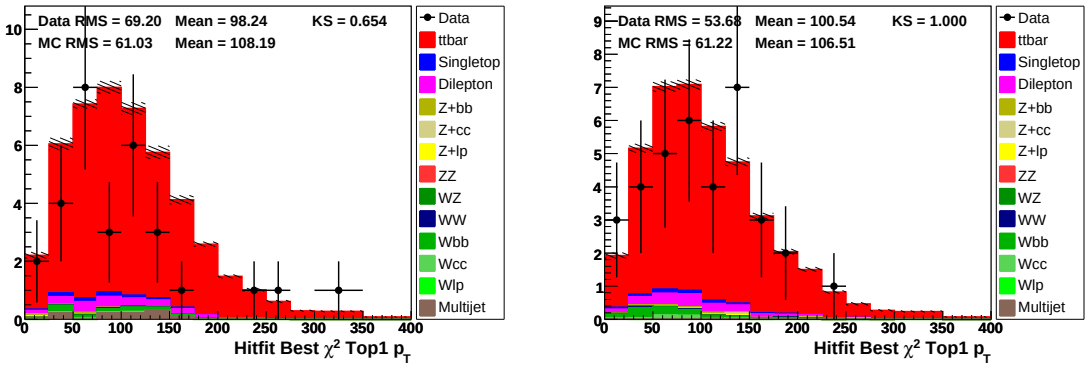

Figure C.133: Leptonic top p_{T}, e+jets (left) and μ+jets (right), NN-medium ≥ 2 b-tag bin. Signal model: ALPGEN.

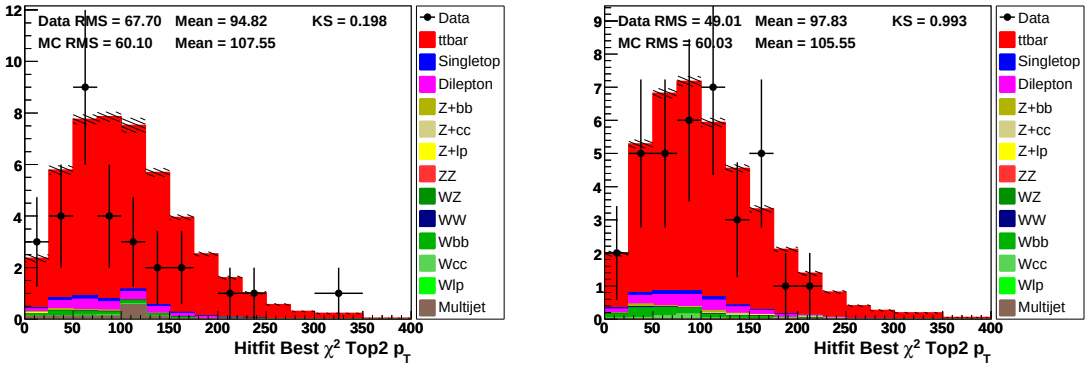

Figure C.134: Hadronic top p_{T}, e+jets (left) and μ+jets (right), NN-medium ≥ 2 b-tag bin. Signal model: ALPGEN.

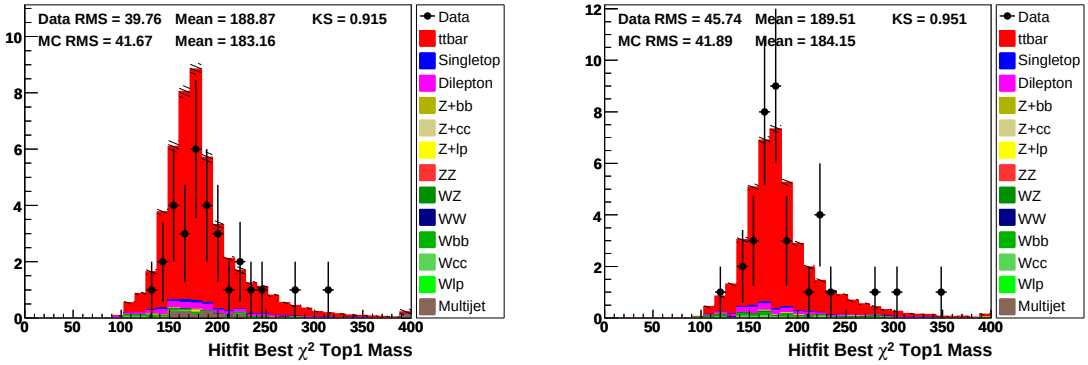

Figure C.135: Fitted top mass, e+jets (left) and μ+jets (right), NN-medium ≥ 2 b-tag bin. Signal model: ALPGEN.

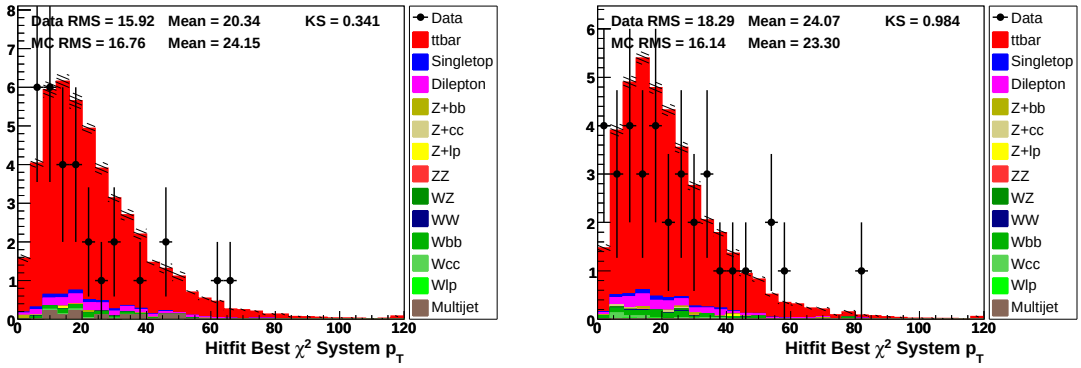

Figure C.136: $t\bar{t}$ p_{T}, e+jets (left) and μ+jets (right), NN-medium ≥ 2 b-tag bin. Signal model: ALPGEN.

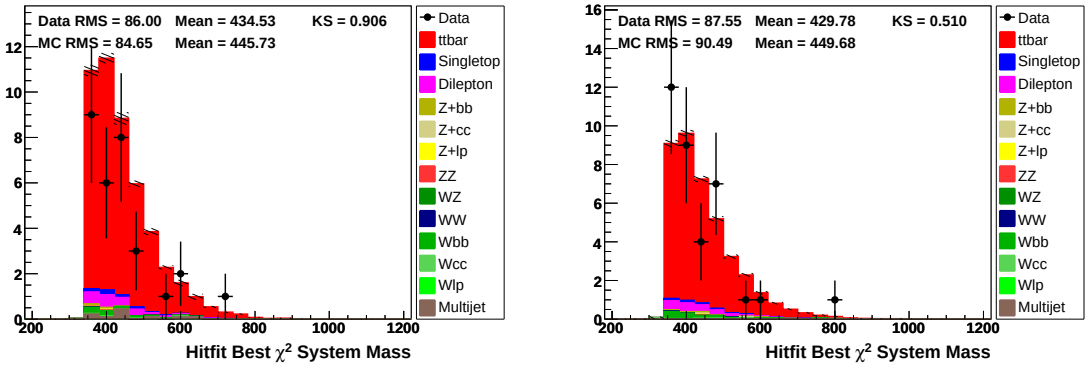

Figure C.137: $t\bar{t}$ mass, e+jets (left) and μ+jets (right), NN-medium ≥ 2 b-tag bin. Signal model: ALPGEN.

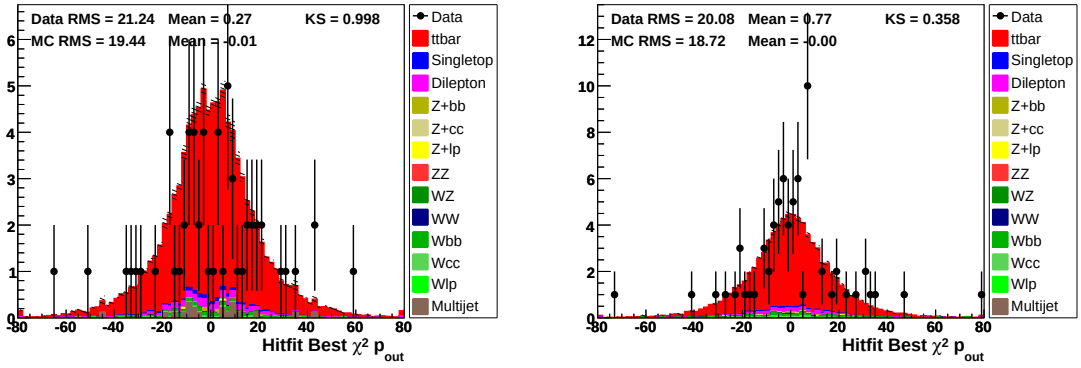

Figure C.138: p_{out}, e+jets (left) and μ+jets (right), NN-medium ≥ 2 b-tag bin. Signal model: ALPGEN.

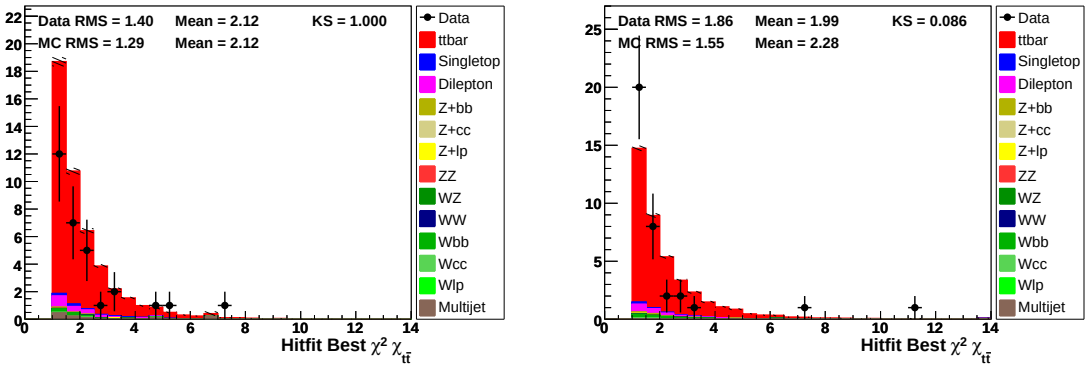

Figure C.139: $\chi_{t\bar{t}}$, e+jets (left) and μ+jets (right), NN-medium ≥ 2 b-tag bin. Signal model: ALPGEN.

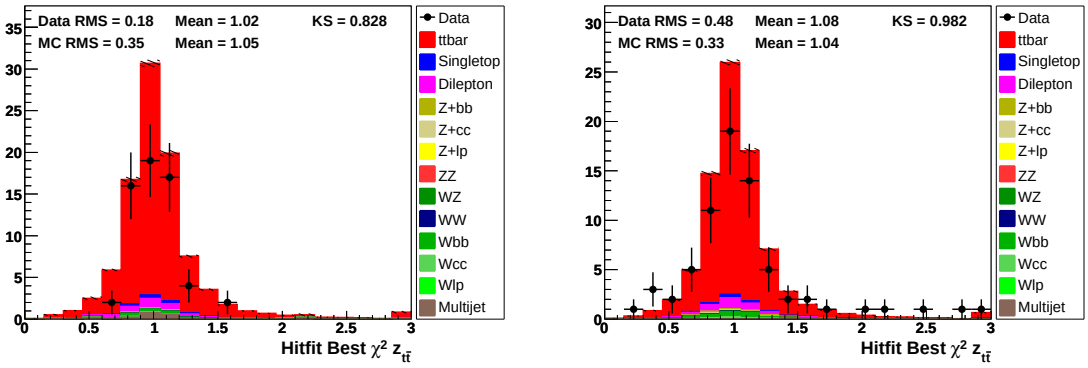

Figure C.140: $z_{t\bar{t}}$, e+jets (left) and μ+jets (right), NN-medium ≥ 2 b-tag bin. Signal model: ALPGEN.

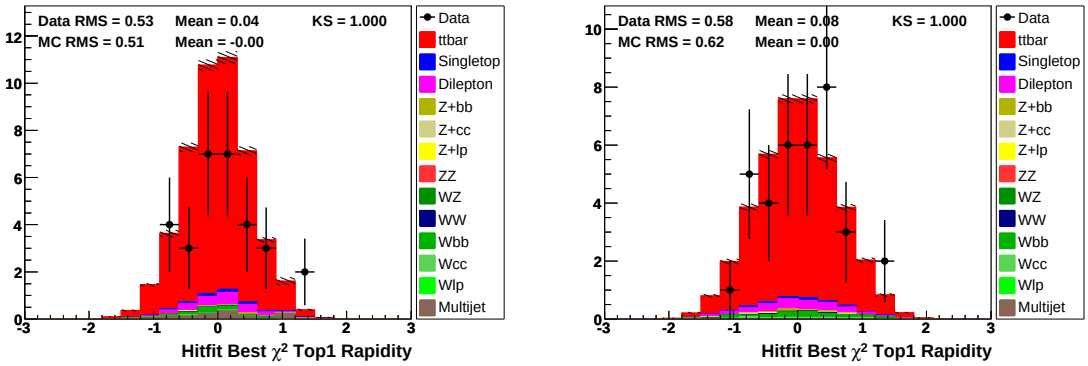

Figure C.141: Leptonic top rapidity, e+jets (left) and μ+jets (right), NN-medium ≥ 2 b-tag bin. Signal model: ALPGEN.

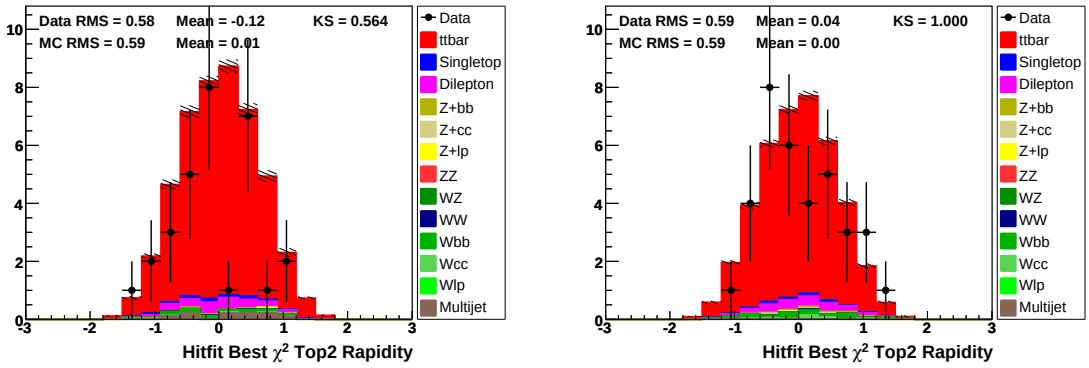

Figure C.142: Hadronic top rapidity, e+jets (left) and μ+jets (right), NN-medium $\geq$ 2 b-tag bin. Signal model: ALPGEN.

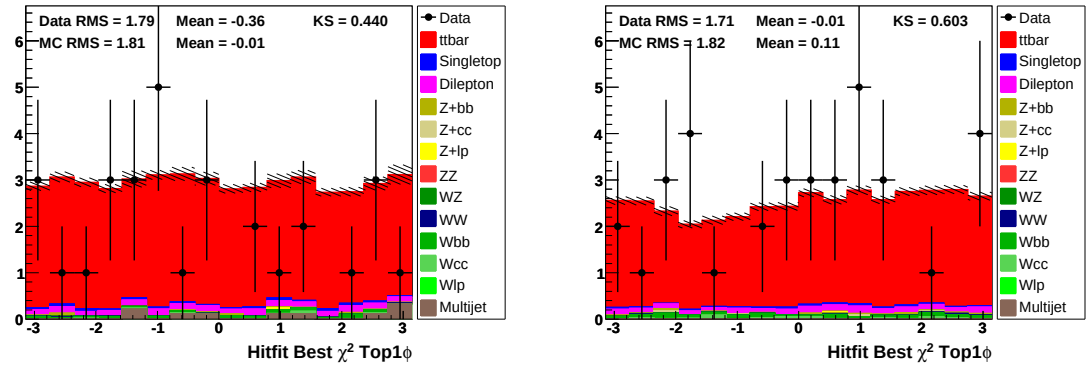

Figure C.143: Leptonic top ϕ, e+jets (left) and μ+jets (right), NN-medium $\geq$ 2 b-tag bin. Signal model: ALPGEN.

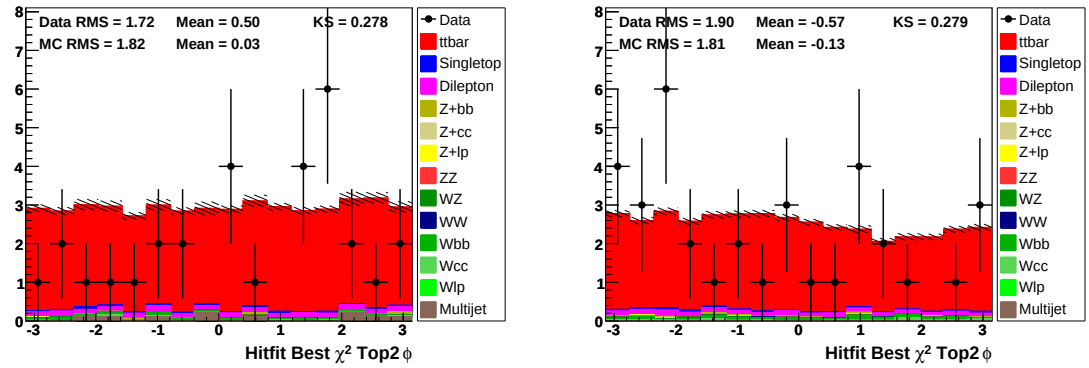

Figure C.144: Hadronic top ϕ, e+jets (left) and μ+jets (right), NN-medium $\geq$ 2 b-tag bin. Signal model: ALPGEN.

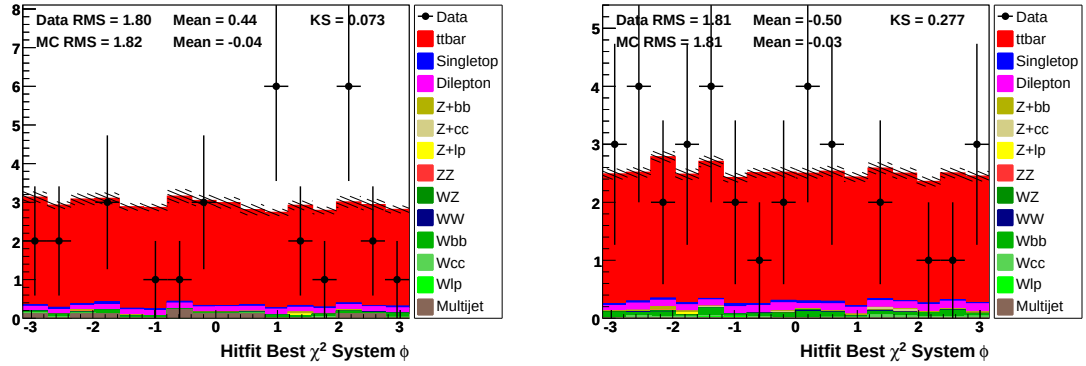

Figure C.145: $t\bar{t}$ ϕ, e+jets (left) and μ+jets (right), NN-medium ≥ 2 b-tag bin. Signal model: ALPGEN.

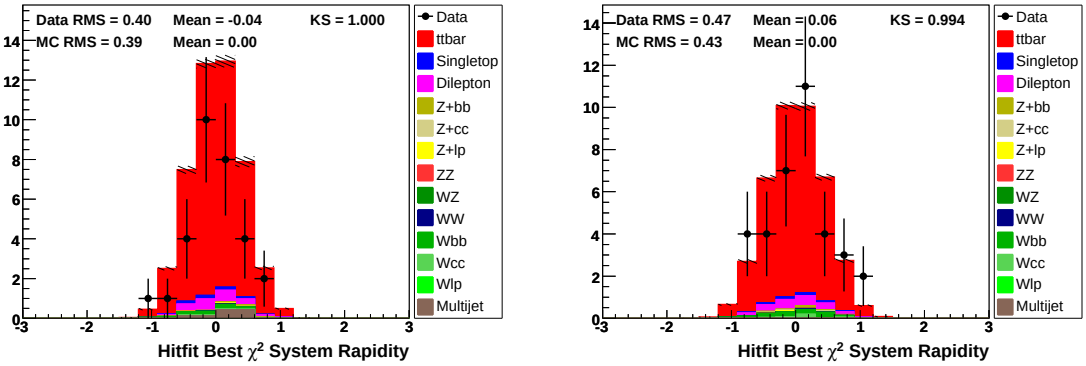

Figure C.146: $t\bar{t}$ rapidity, e+jets (left) and μ+jets (right), NN-medium ≥ 2 b-tag bin. Signal model: ALPGEN.

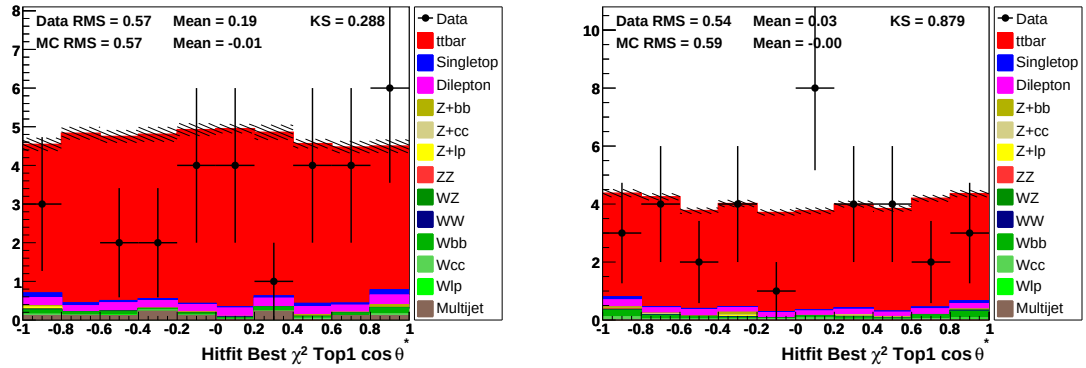

Figure C.147: Leptonic top $\cos\theta^*$, e+jets (left) and μ+jets (right), NN-medium ≥ 2 b-tag bin. Signal model: ALPGEN.

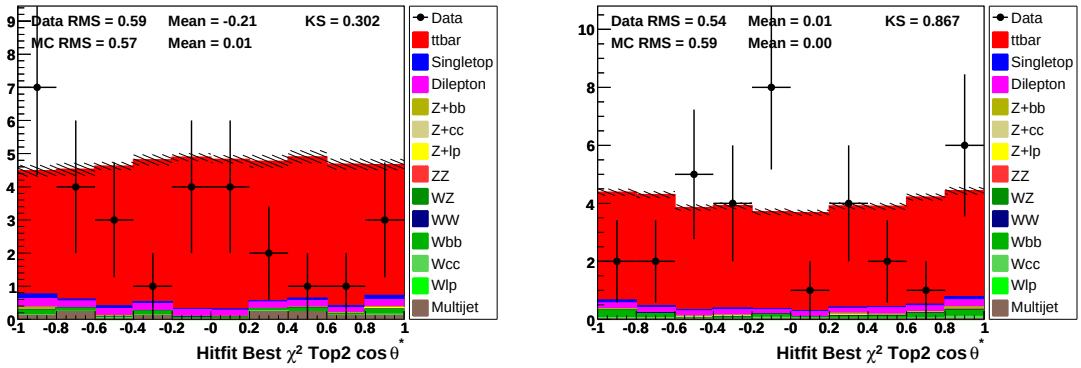

Figure C.148: Hadronic top $\cos\theta^*$, e+jets (left) and μ+jets (right), NN-medium ≥ 2 b-tag bin. Signal model: ALPGEN.

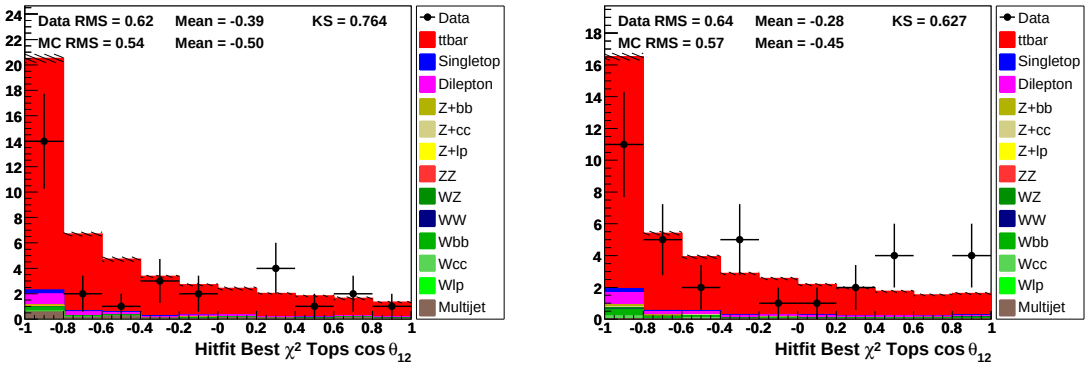

Figure C.149: Opening angle between top quarks, e+jets (left) and μ+jets (right), NN-medium ≥ 2 b-tag bin. Signal model: ALPGEN.

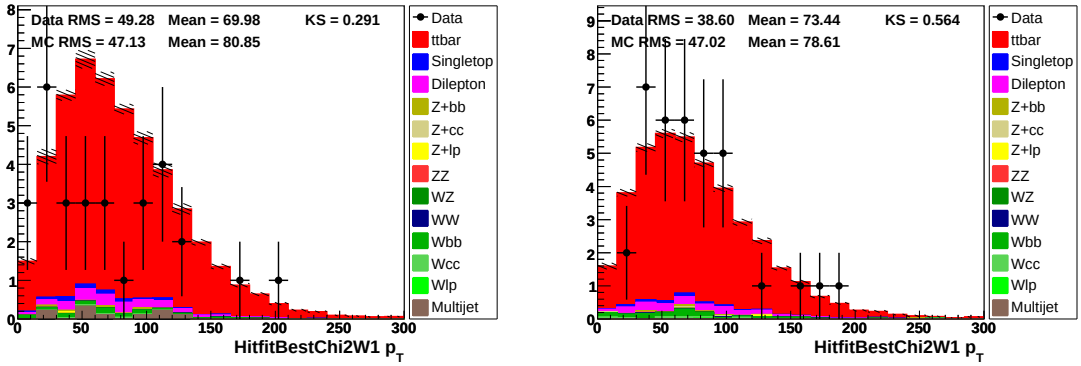

Figure C.150: Leptonic W p_{T}, e+jets (left) and μ+jets (right), NN-medium ≥ 2 b-tag bin. Signal model: ALPGEN.

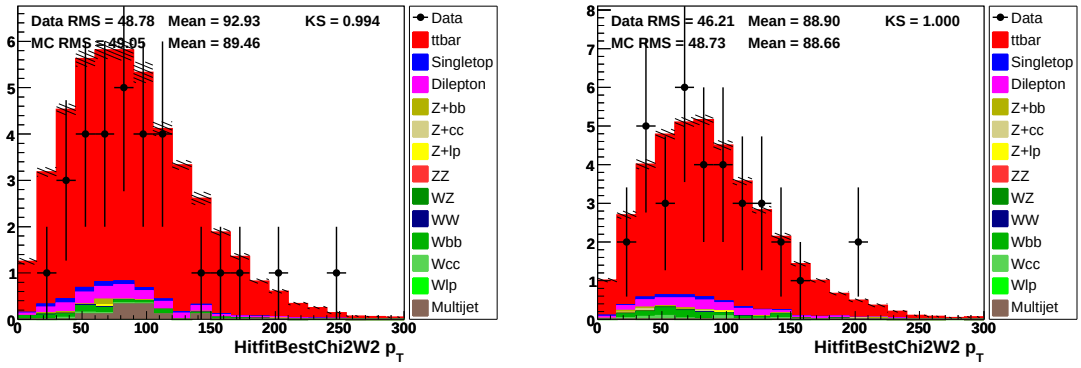

Figure C.151: Hadronic W p_{T}, e+jets (left) and μ+jets (right), NN-medium ≥ 2 b-tag bin. Signal model: ALPGEN.

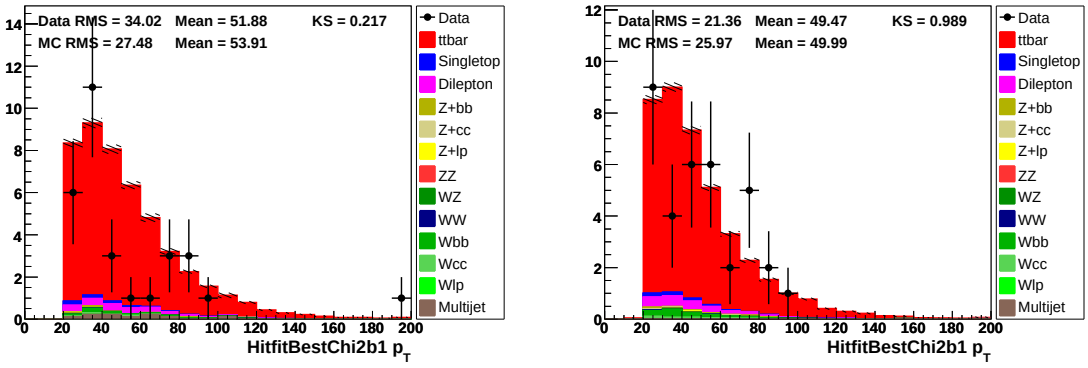

Figure C.152: Leptonic b p_{T}, e+jets (left) and μ+jets (right), NN-medium ≥ 2 b-tag bin. Signal model: ALPGEN.

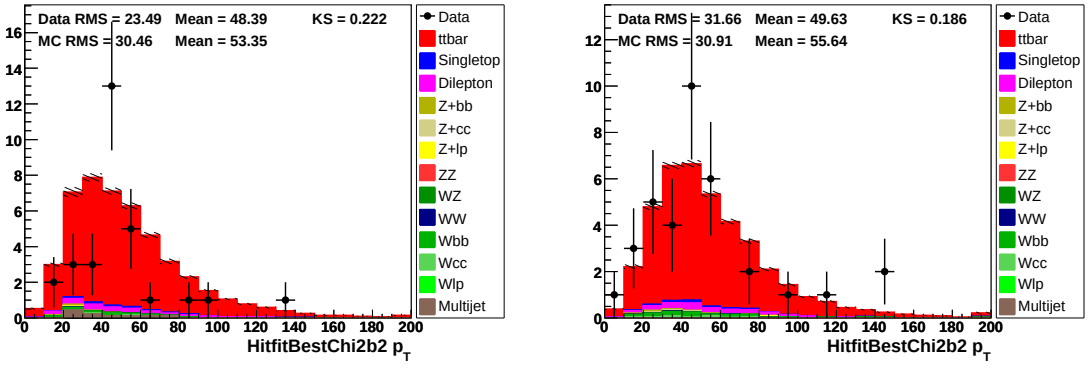

Figure C.153: Hadronic b p_{T}, e+jets (left) and μ+jets (right), NN-medium ≥ 2 b-tag bin. Signal model: ALPGEN.

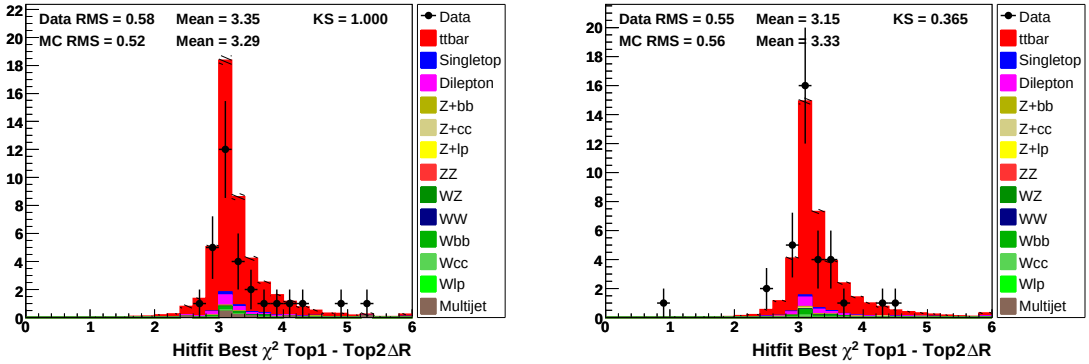

Figure C.154: $\Delta\mathcal{R}_{t\bar{t}}$, e+jets (left) and μ+jets (right), NN-medium ≥ 2 b-tag bin. Signal model: ALPGEN.

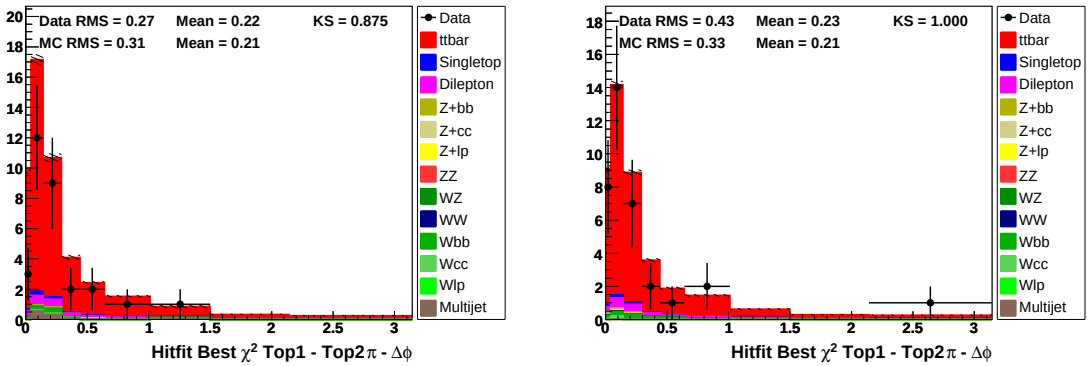

Figure C.155: $\Delta\phi_{t\bar{t}}$, e+jets (left) and μ+jets (right), NN-medium ≥ 2 b-tag bin. Signal model: ALPGEN.

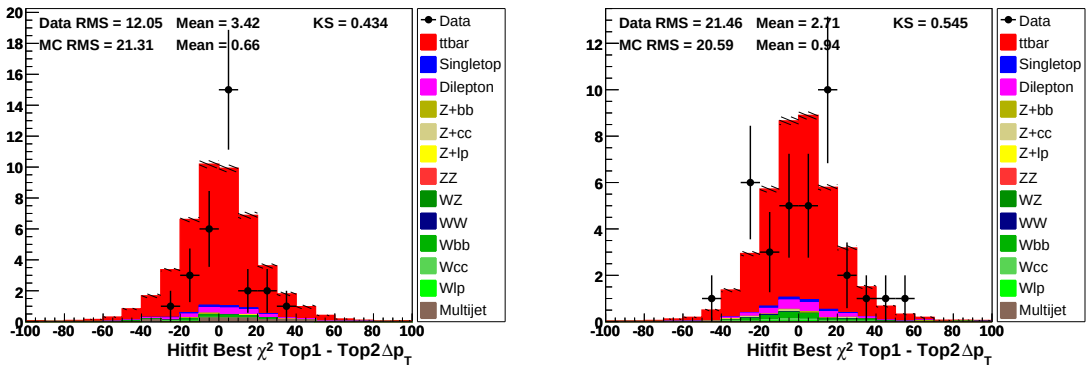

Figure C.156: $\Delta p_{\mathrm{T}}^{t\bar{t}}$, e+jets (left) and μ+jets (right), NN-medium ≥ 2 b-tag bin. Signal model: ALPGEN.

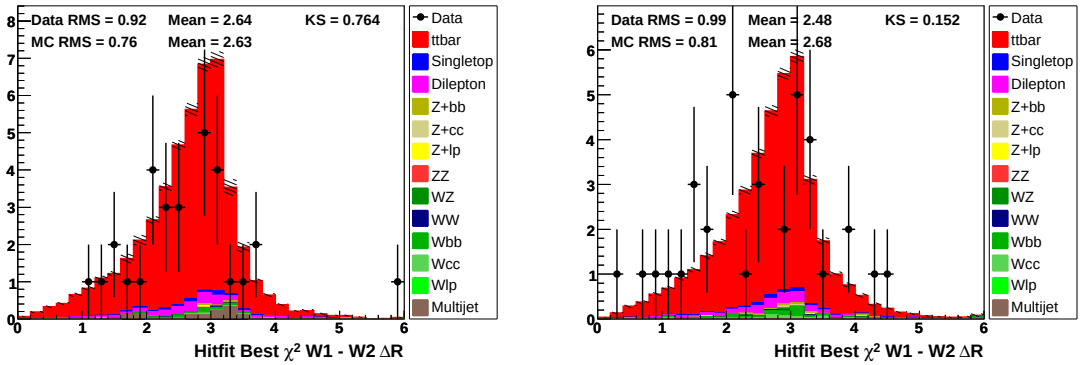

Figure C.157: $\Delta\mathcal{R}_{WW}$, e+jets (left) and μ+jets (right), NN-medium $\geq$ 2 b-tag bin. Signal model: ALPGEN.

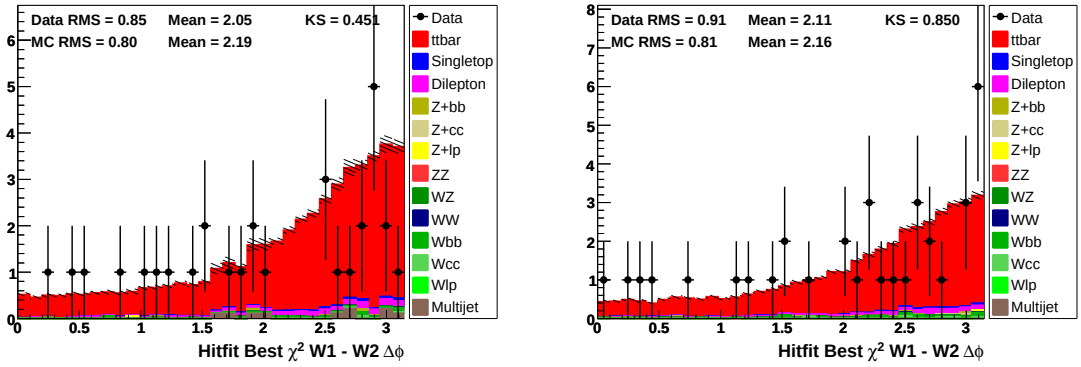

Figure C.158: $\Delta\phi_{WW}$, e+jets (left) and μ+jets (right), NN-medium $\geq$ 2 b-tag bin. Signal model: ALPGEN.

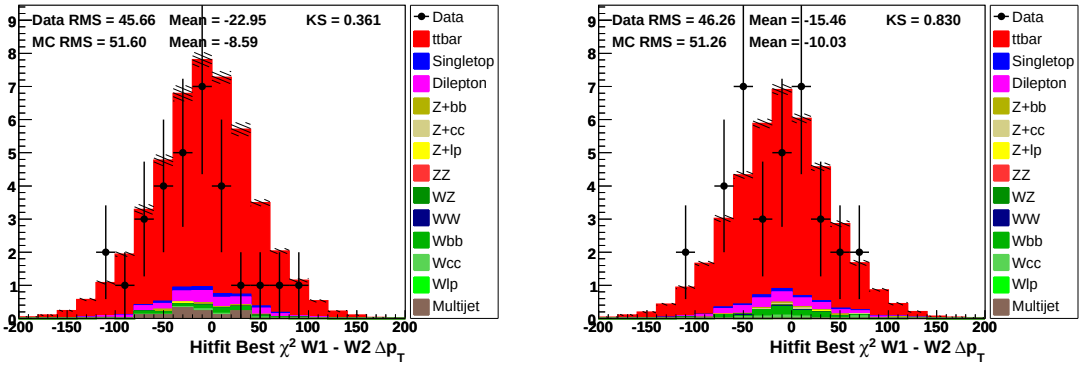

Figure C.159: $\Delta p_{\mathrm{T}}^{WW}$, e+jets (left) and μ+jets (right), NN-medium $\geq$ 2 b-tag bin. Signal model: ALPGEN.

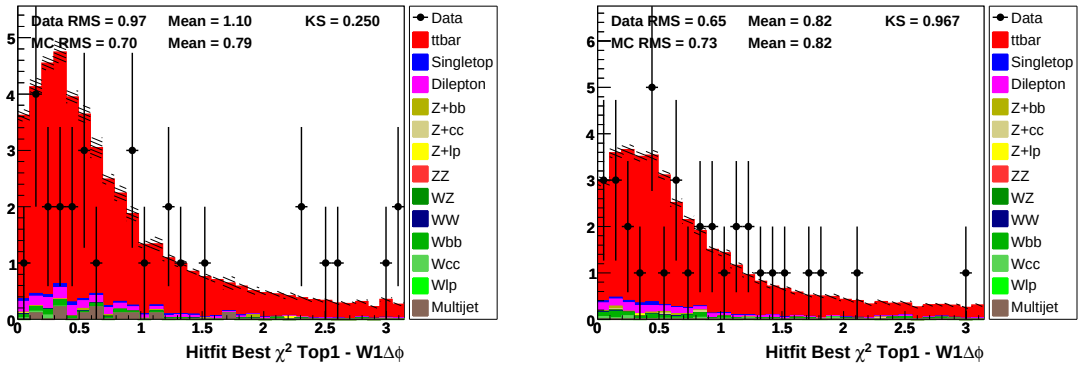

Figure C.160: $\Delta\phi_{t1W1}$, e+jets (left) and μ+jets (right), NN-medium $\geq$ 2 b-tag bin. Signal model: ALPGEN.

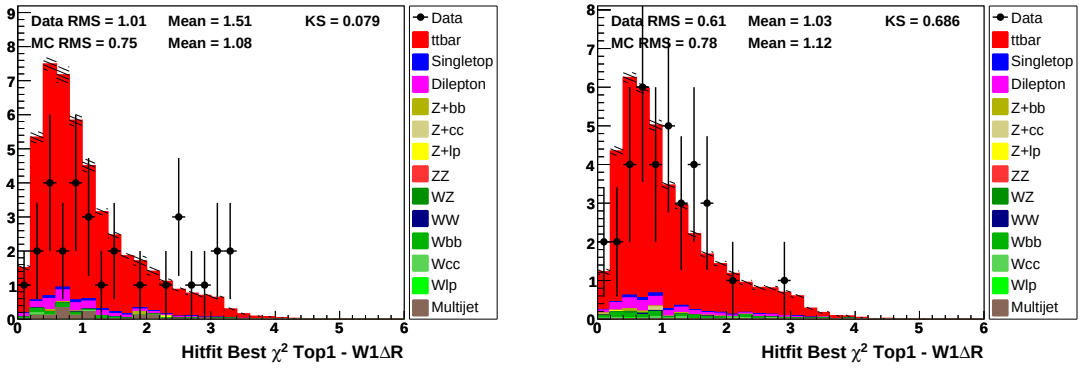

Figure C.161: $\Delta\mathcal{R}_{t1W1}$, e+jets (left) and μ+jets (right), NN-medium $\geq$ 2 b-tag bin. Signal model: ALPGEN.

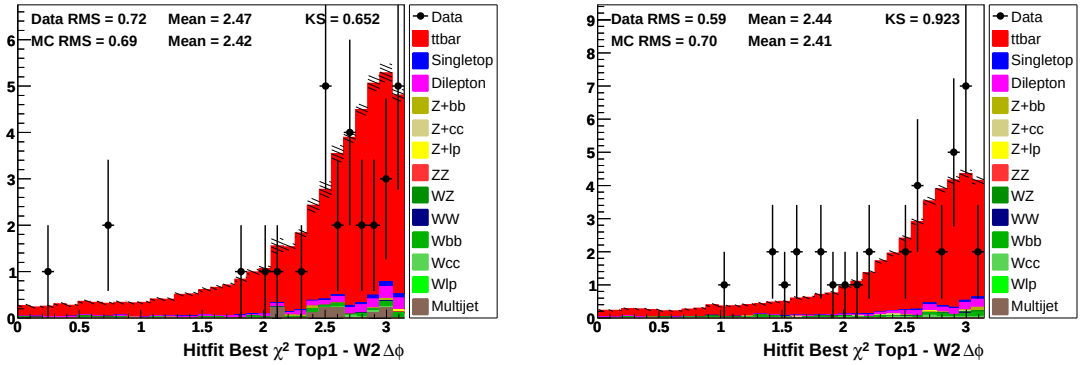

Figure C.162: $\Delta\phi_{t1W2}$, e+jets (left) and μ+jets (right), NN-medium $\geq$ 2 b-tag bin. Signal model: ALPGEN.

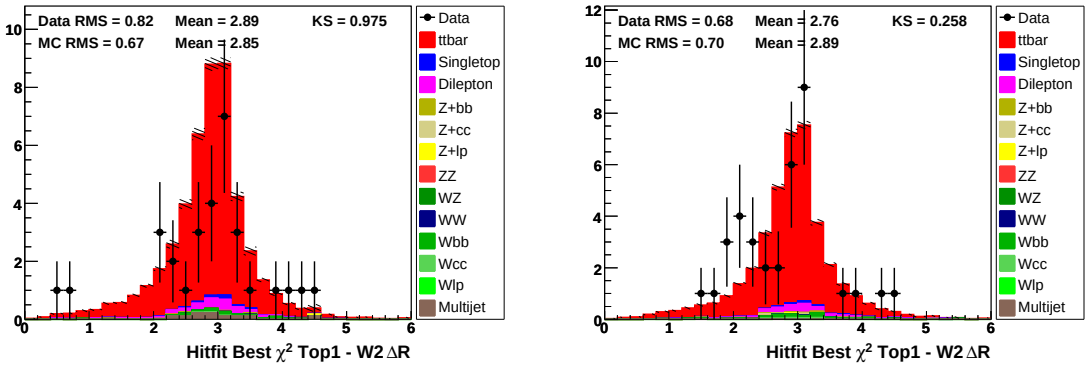

Figure C.163: $\Delta\mathcal{R}_{t1W2}$, e+jets (left) and μ+jets (right), NN-medium $\geq$ 2 b-tag bin. Signal model: ALPGEN.

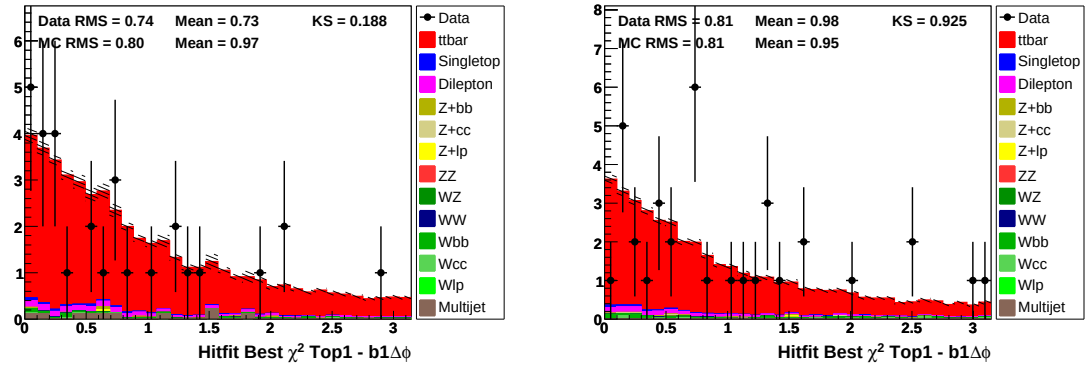

Figure C.164: $\Delta\phi_{t1b1}$, e+jets (left) and μ+jets (right), NN-medium $\geq$ 2 b-tag bin. Signal model: ALPGEN.

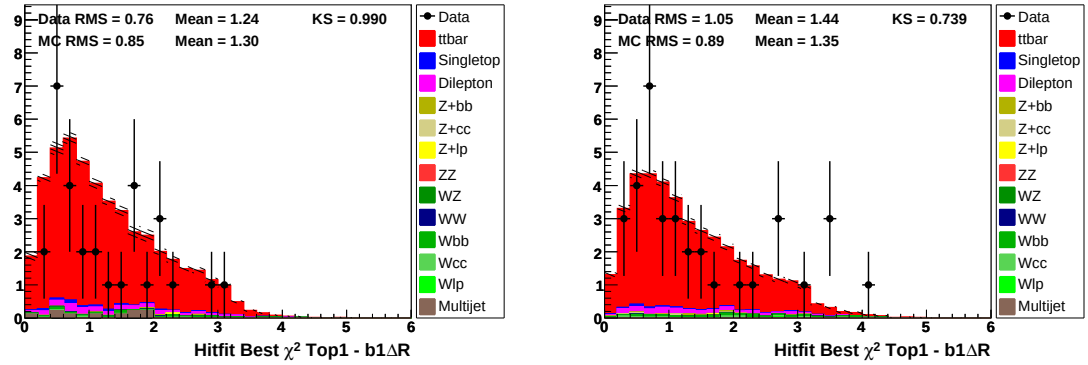

Figure C.165: $\Delta\mathcal{R}_{t1b1}$, e+jets (left) and μ+jets (right), NN-medium $\geq$ 2 b-tag bin. Signal model: ALPGEN.

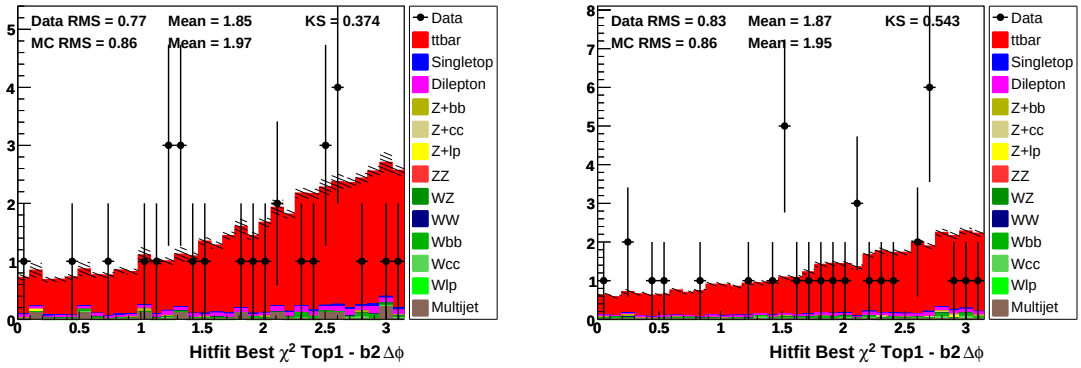

Figure C.166: $\Delta\phi_{t1b2}$, e+jets (left) and μ+jets (right), NN-medium $\geq$ 2 b-tag bin. Signal model: ALPGEN.

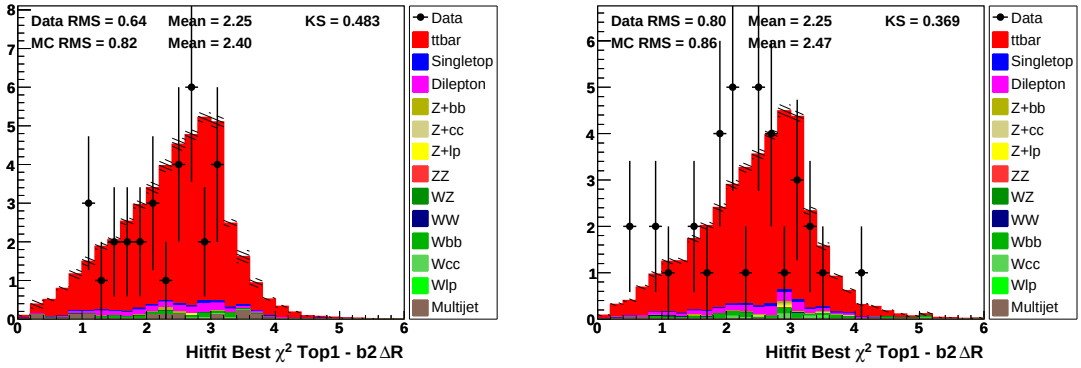

Figure C.167: $\Delta\mathcal{R}_{t1b2}$, e+jets (left) and μ+jets (right), NN-medium $\geq$ 2 b-tag bin. Signal model: ALPGEN.

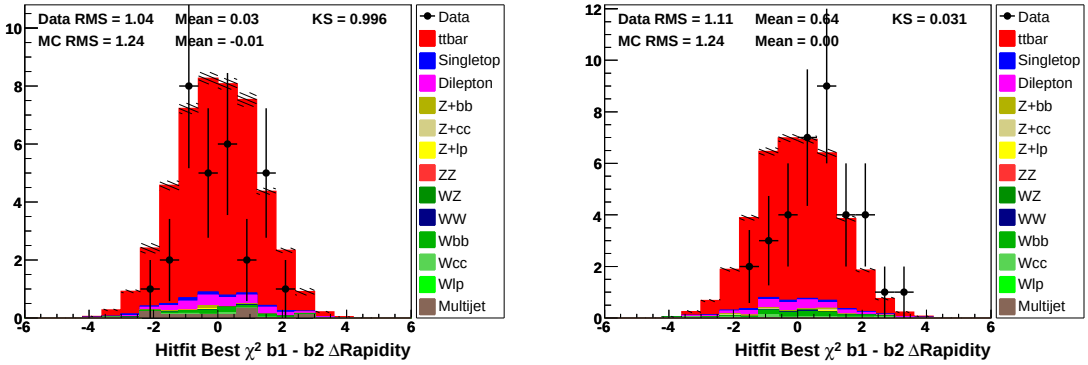

Figure C.168: $\Delta\text{Rapidity}_{b1b2}$, e+jets (left) and μ+jets (right), NN-medium $\geq$ 2 b-tag bin. Signal model: ALPGEN.

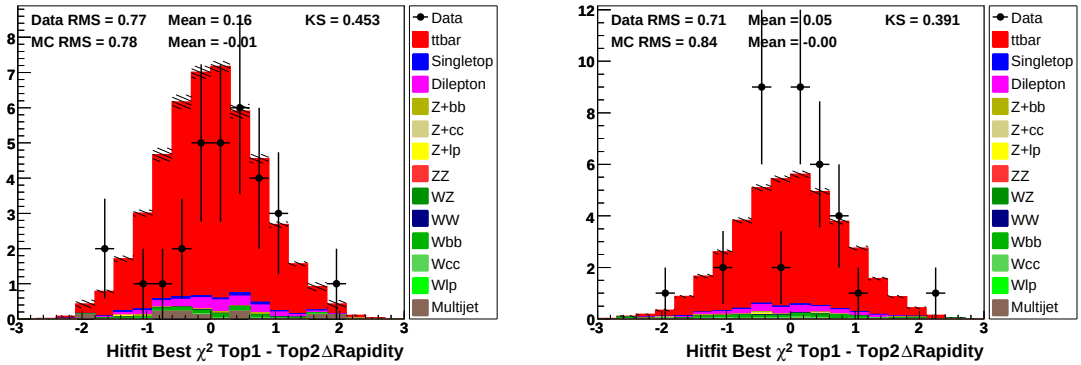

Figure C.169: $\Delta\text{Rapidity}_{t\bar{t}}$, e+jets (left) and μ+jets (right), NN-medium ≥ 2 b-tag bin. Signal model: ALPGEN.

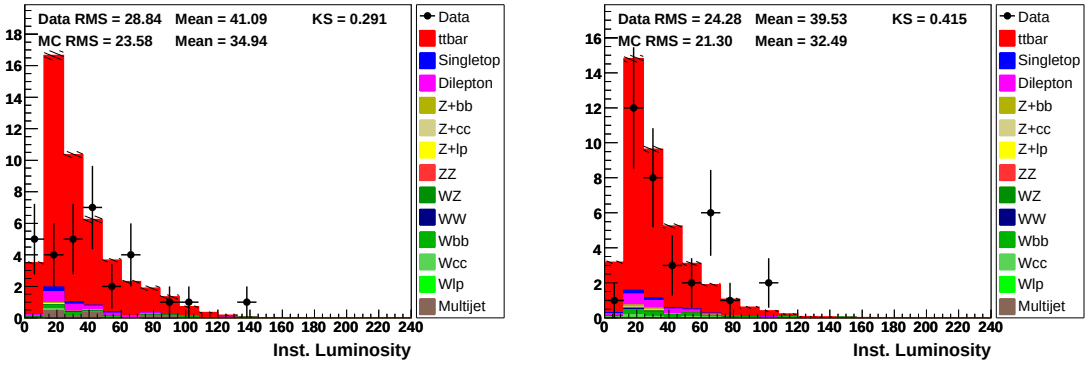

Figure C.170: Instantenous luminosity [$10^{30}\text{cm}^{-2}\text{s}^{-1}$], e+jets (left) and μ+jets (right), NN-medium ≥ 2 b-tag bin. Signal model: ALPGEN.

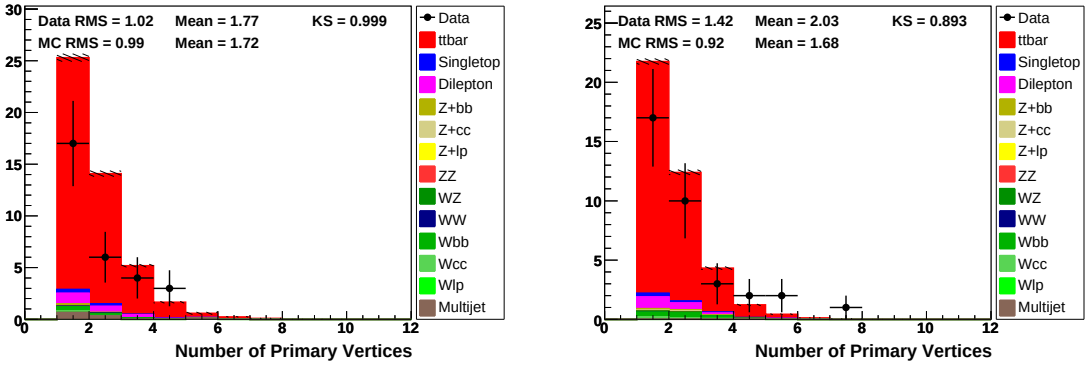

Figure C.171: Number of primary vertices, e+jets (left) and μ+jets (right), NN-medium ≥ 2 b-tag bin. Signal model: ALPGEN.

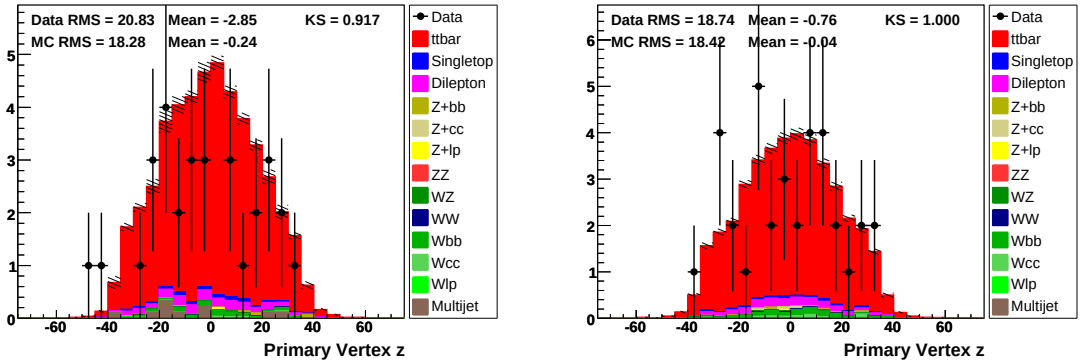

Figure C.172: Primary vertex z coordinate, e+jets (left) and μ+jets (right), NN-medium ≥ 2 b-tag bin. Signal model: ALPGEN.

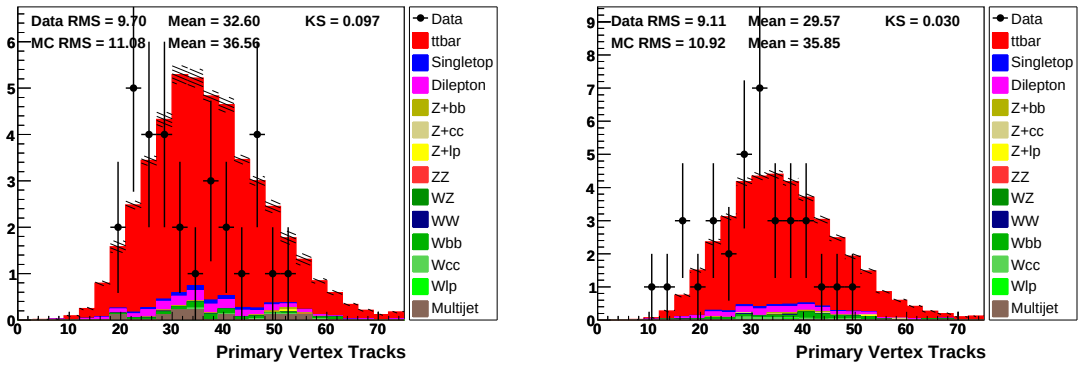

Figure C.173: Number of PV tracks, e+jets (left) and μ+jets (right), NN-medium ≥ 2 b-tag bin. Signal model: ALPGEN.

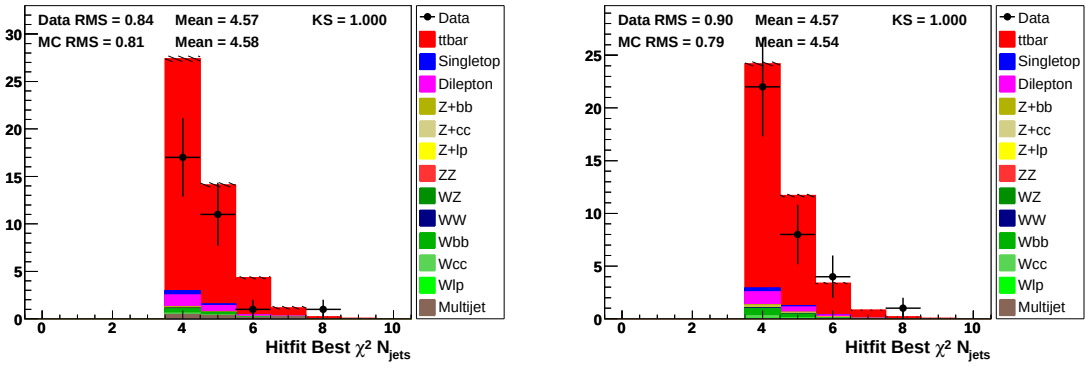

Figure C.174: n_{jets}, e+jets (left) and μ+jets (right), NN-medium ≥ 2 b-tag bin. Signal model: ALPGEN.

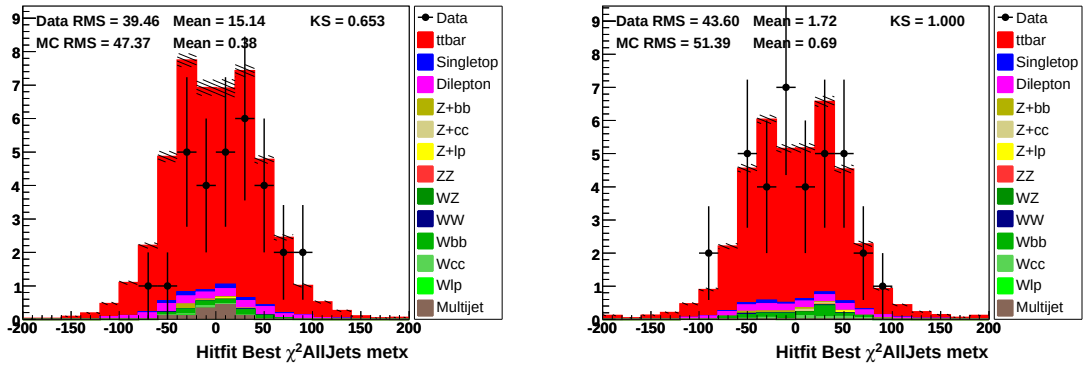

Figure C.175: Missing transverse energy x component, e+jets (left) and μ+jets (right), NN-medium ≥ 2 b-tag bin. Signal model: ALPGEN.

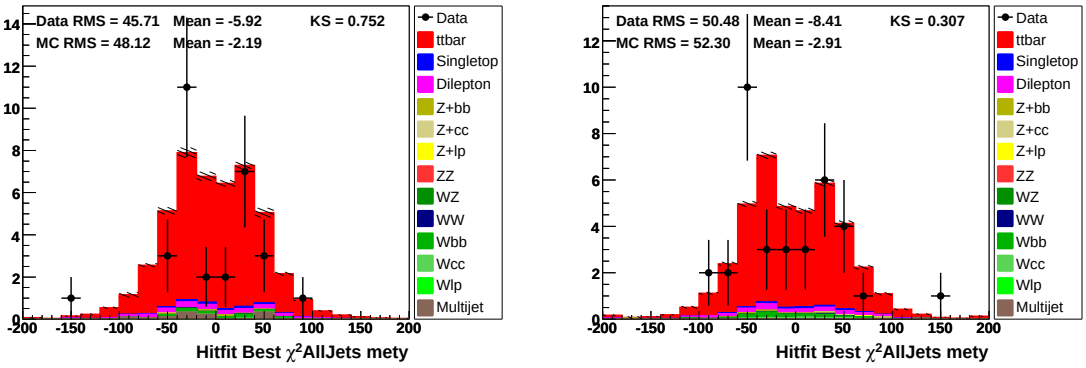

Figure C.176: Missing transverse energy y component, e+jets (left) and μ+jets (right), NN-medium ≥ 2 b-tag bin. Signal model: ALPGEN.

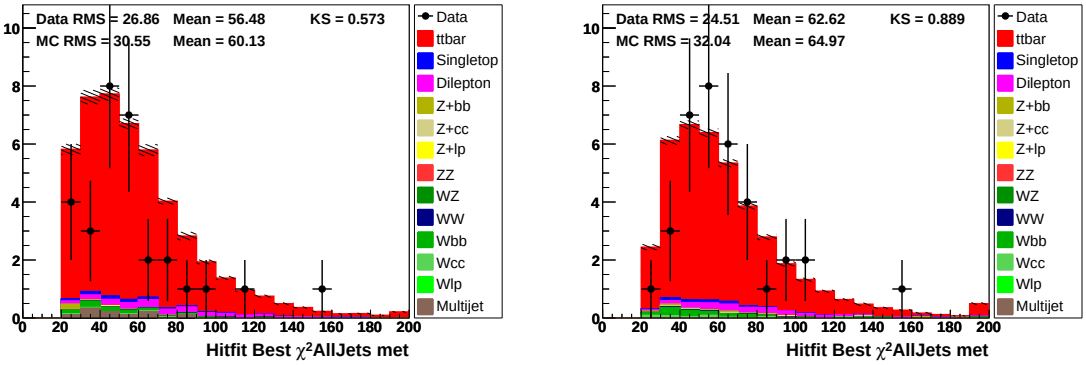

Figure C.177: Missing transverse energy, e+jets (left) and μ+jets (right), NN-medium ≥ 2 b-tag bin. Signal model: ALPGEN.

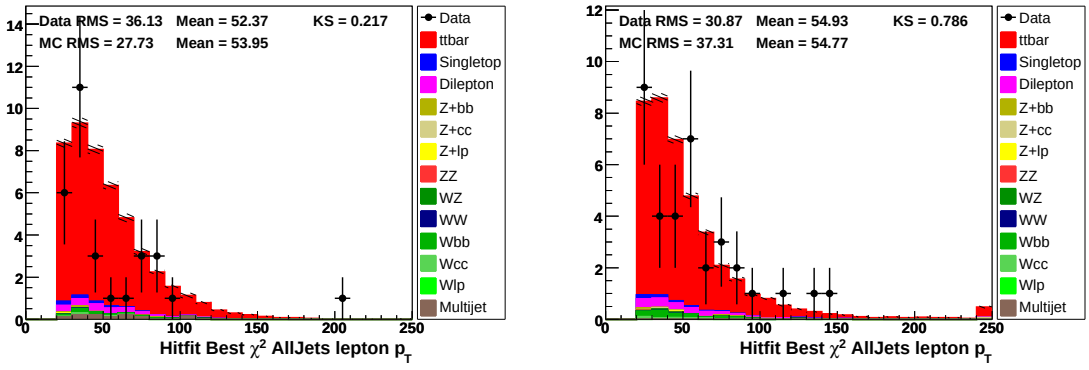

Figure C.178: Lepton p_{T}, e+jets (left) and μ+jets (right), NN-medium ≥ 2 b-tag bin. Signal model: ALPGEN.

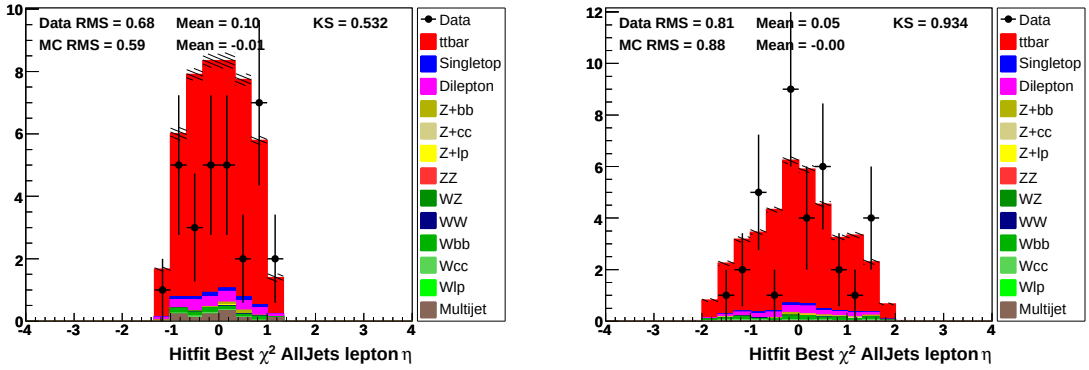

Figure C.179: Lepton η, e+jets (left) and μ+jets (right), NN-medium ≥ 2 b-tag bin. Signal model: ALPGEN.

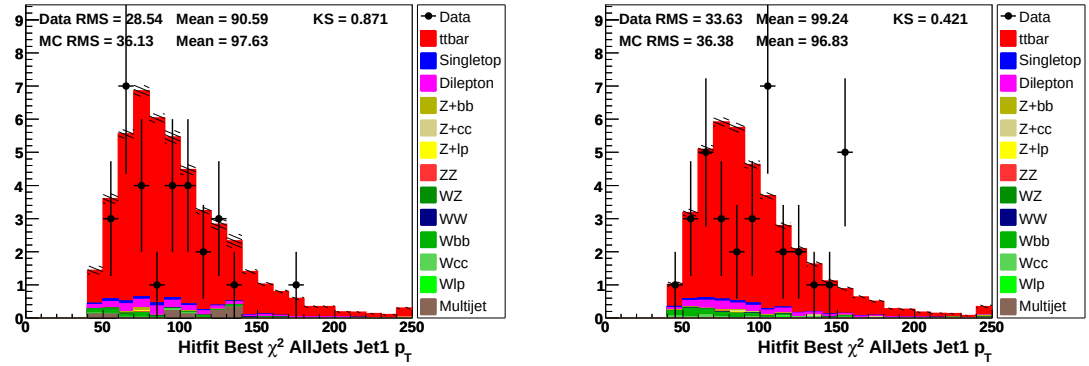

Figure C.180: 1st Jet p_{T}, e+jets (left) and μ+jets (right), NN-medium ≥ 2 b-tag bin. Signal model: ALPGEN.

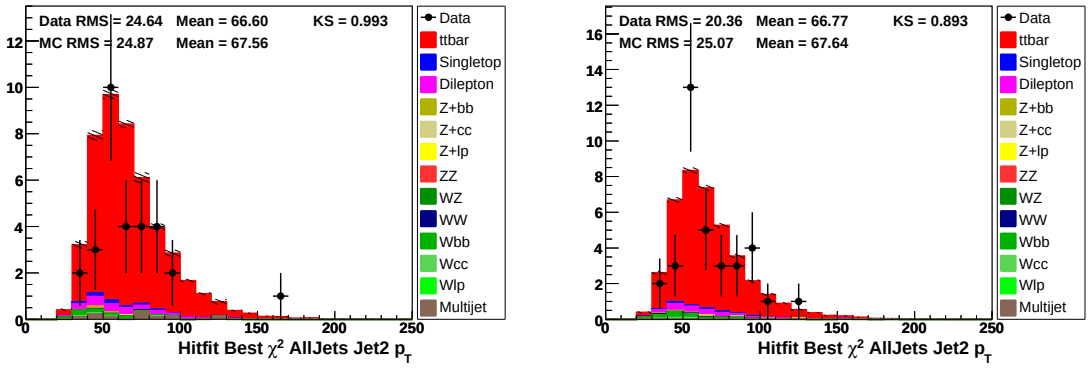

Figure C.181: 2nd Jet p_{T}, e+jets (left) and μ+jets (right), NN-medium ≥ 2 b-tag bin. Signal model: ALPGEN.

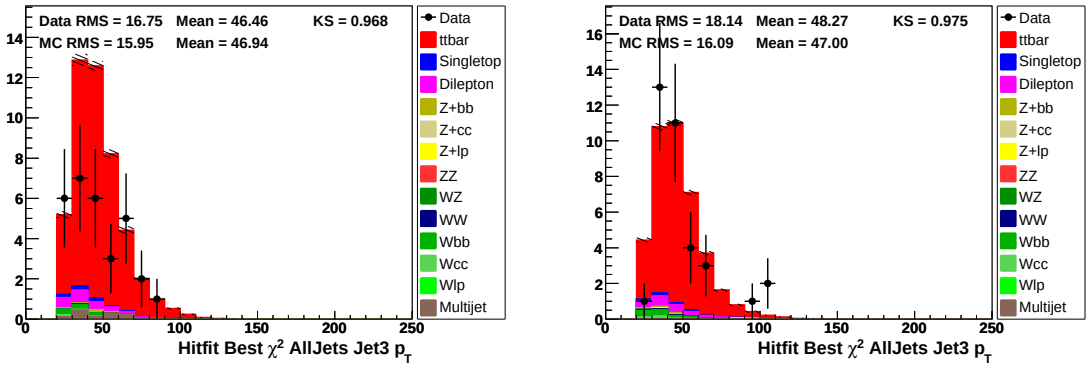

Figure C.182: 3rd Jet p_{T}, e+jets (left) and μ+jets (right), NN-medium ≥ 2 b-tag bin. Signal model: ALPGEN.

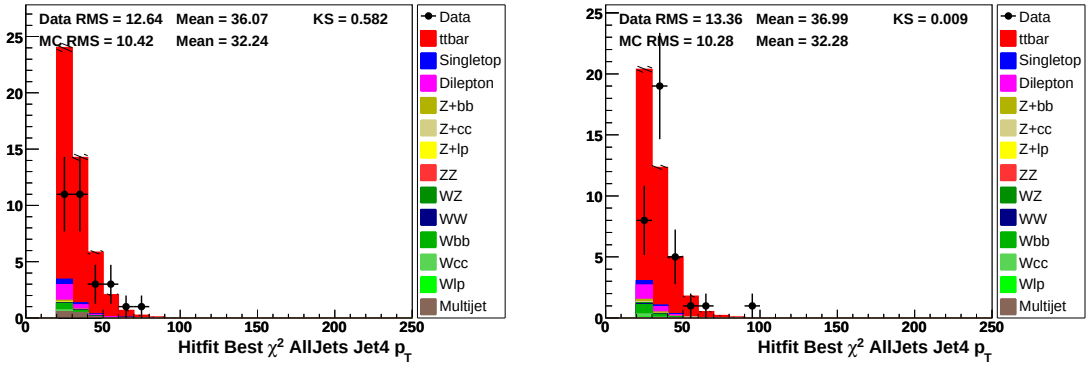

Figure C.183: 4th Jet p_{T}, e+jets (left) and μ+jets (right), NN-medium ≥ 2 b-tag bin. Signal model: ALPGEN.

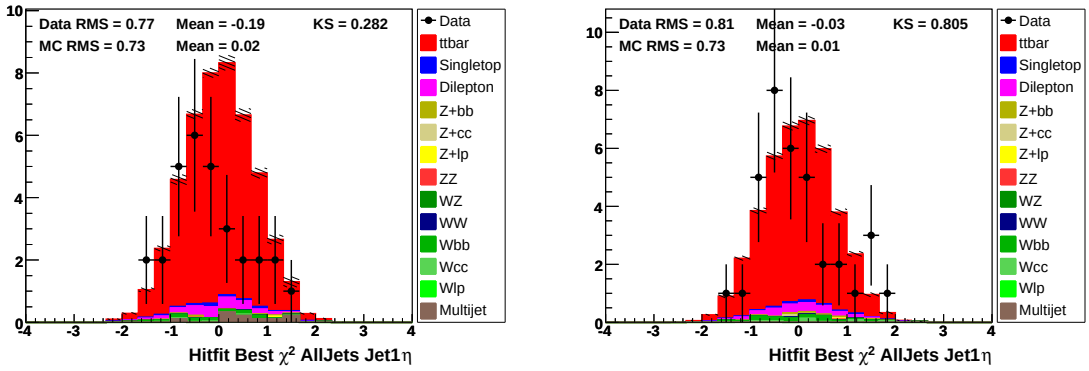

Figure C.184: 1st Jet η, e+jets (left) and μ+jets (right), NN-medium $\geq$ 2 b-tag bin. Signal model: ALPGEN.

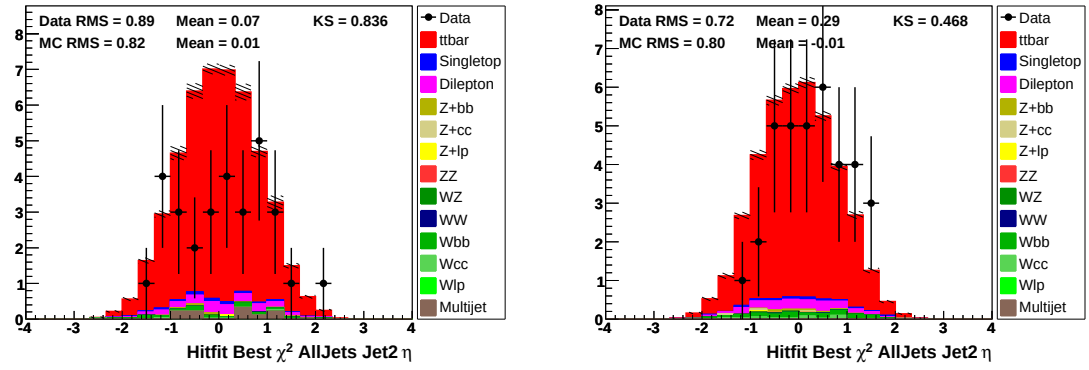

Figure C.185: 2nd Jet η, e+jets (left) and μ+jets (right), NN-medium $\geq$ 2 b-tag bin. Signal model: ALPGEN.

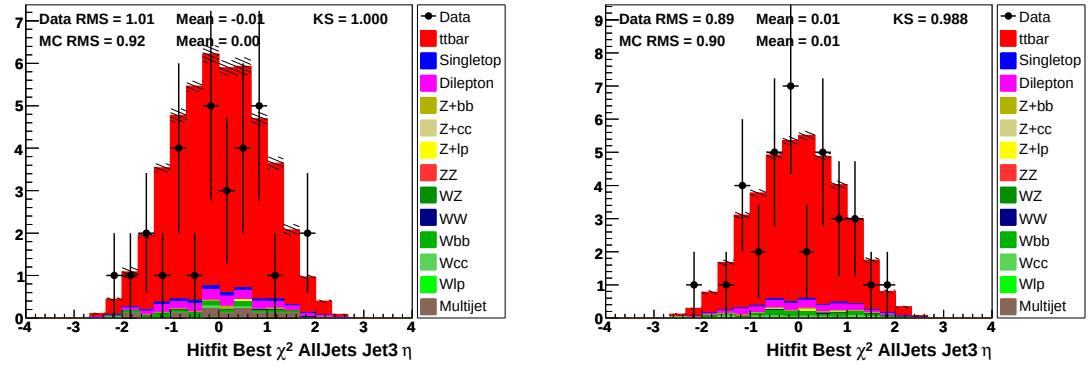

Figure C.186: 3rd Jet η, e+jets (left) and μ+jets (right), NN-medium $\geq$ 2 b-tag bin. Signal model: ALPGEN.

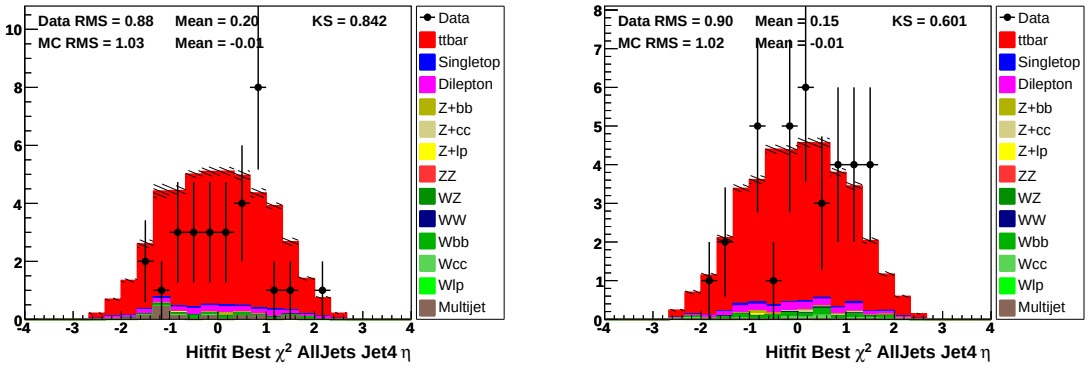

Figure C.187: 4th Jet η, e+jets (left) and μ+jets (right), NN-medium $\geq$ 2 b-tag bin. Signal model: ALPGEN.

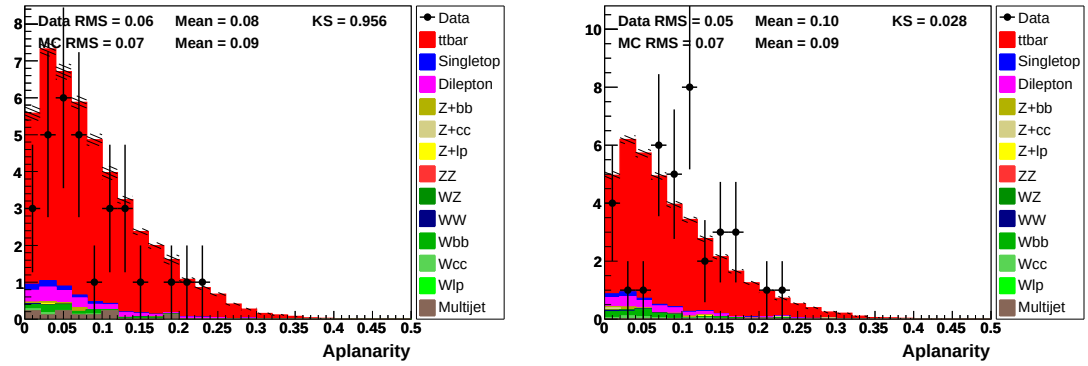

Figure C.188: Aplanarity, e+jets (left) and μ+jets (right), NN-medium $\geq$ 2 b-tag bin. Signal model: ALPGEN.

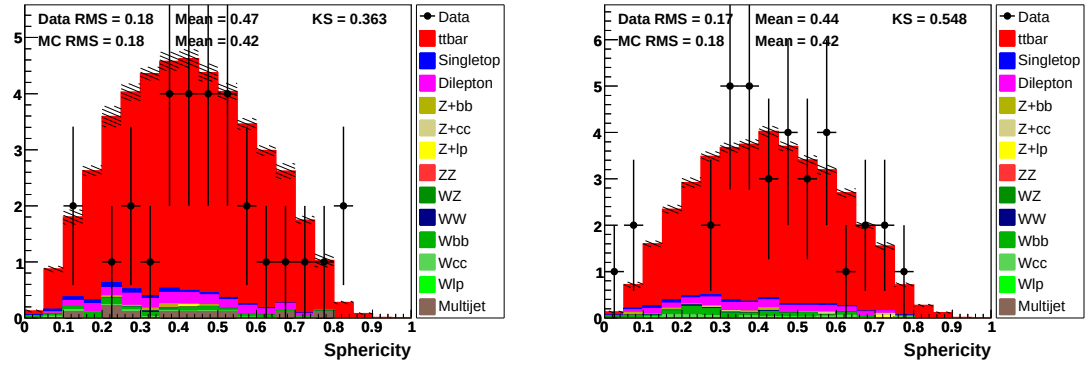

Figure C.189: Sphericity, e+jets (left) and μ+jets (right), NN-medium $\geq$ 2 b-tag bin. Signal model: ALPGEN.

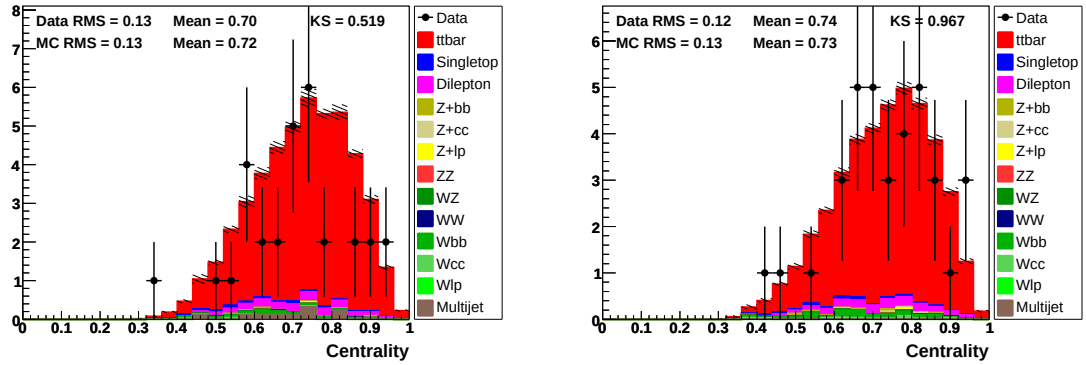

Figure C.190: Centrality, e+jets (left) and μ+jets (right), NN-medium ≥ 2 b-tag bin. Signal model: ALPGEN.

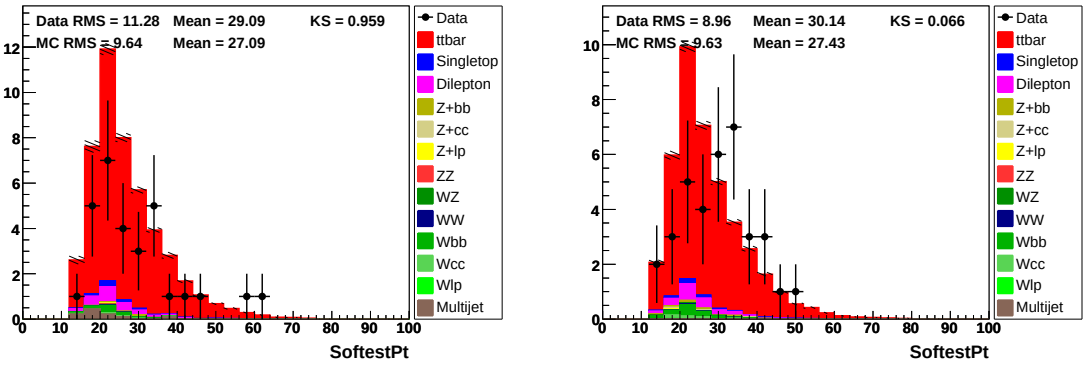

Figure C.191: Softest p_T, e+jets (left) and μ+jets (right), NN-medium ≥ 2 b-tag bin. Signal model: ALPGEN.

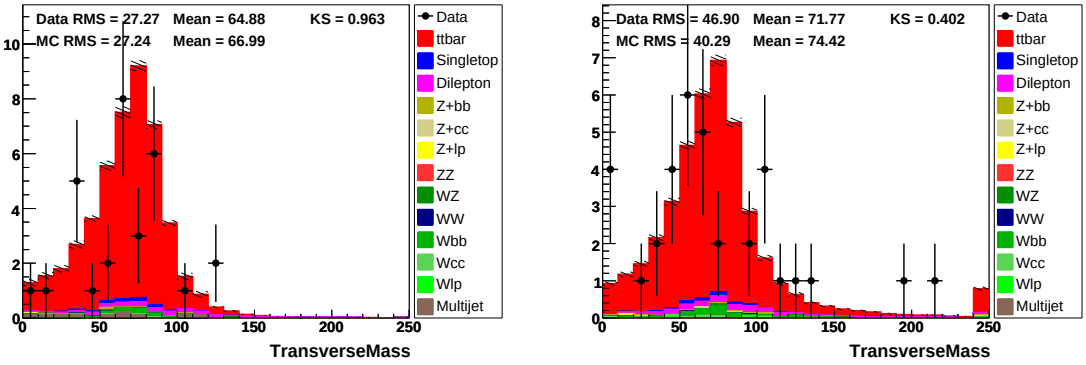

Figure C.192: Transverse mass, e+jets (left) and μ+jets (right), NN-medium ≥ 2 b-tag bin. Signal model: ALPGEN.

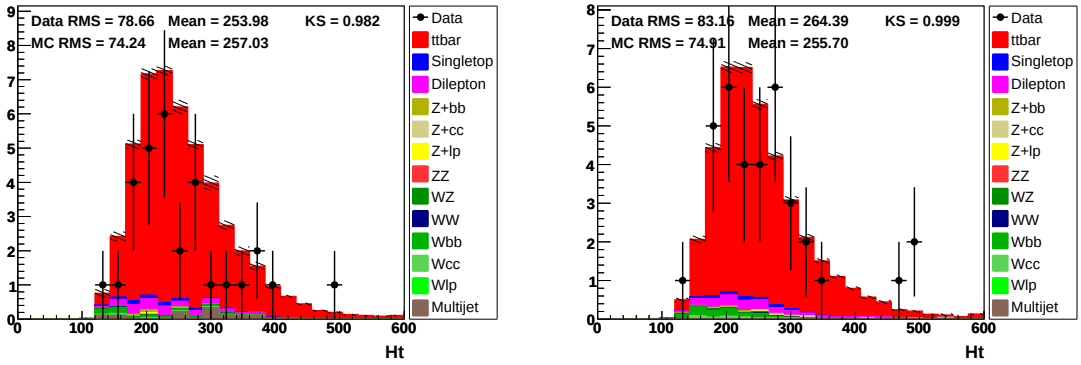

Figure C.193: H_T, e+jets (left) and μ+jets (right), NN-medium ≥ 2 b-tag bin. Signal model: ALPGEN.

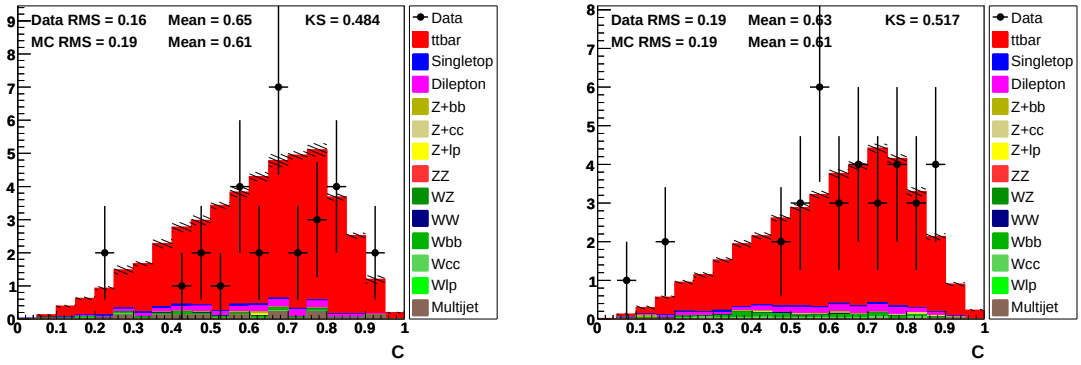

Figure C.194: $\mathcal{C}$, e+jets (left) and μ+jets (right), NN-medium ≥ 2 b-tag bin. Signal model: ALPGEN.

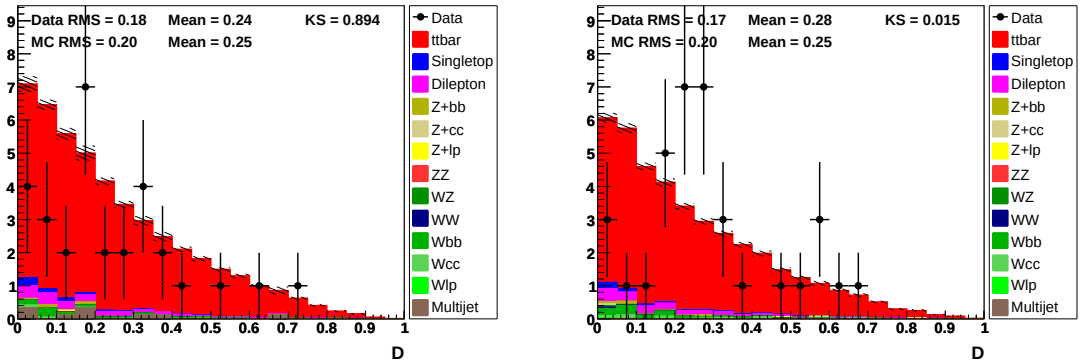

Figure C.195: $\mathcal{D}$, e+jets (left) and μ+jets (right), NN-medium ≥ 2 b-tag bin. Signal model: ALPGEN.

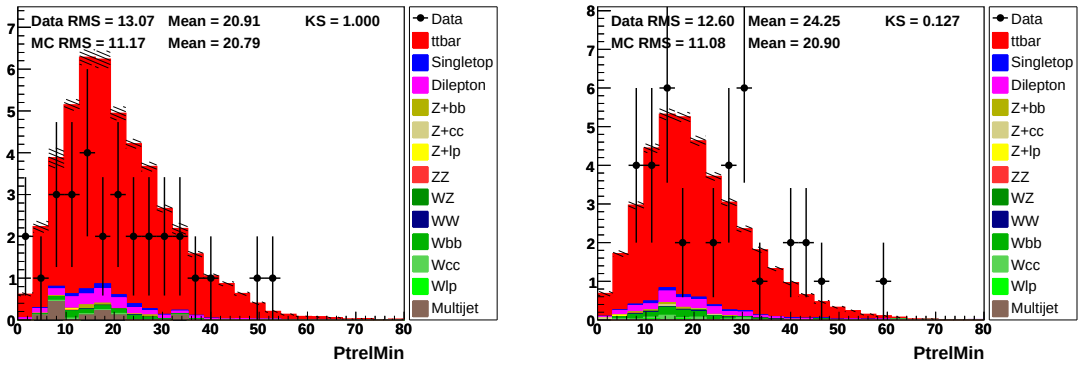

Figure C.196: $p_{Trel.}^{\min}$, e+jets (left) and μ+jets (right), NN-medium ≥ 2 b-tag bin. Signal model: ALPGEN.

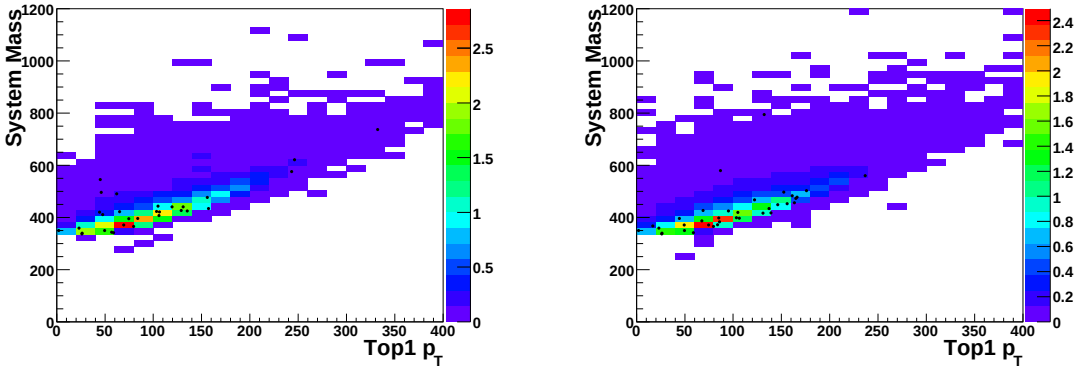

Figure C.197: $t\bar{t}$ system mass vs. leptonic top $p+T$, e+jets (left) and μ+jets (right), NN-medium ≥ 2 b-tag bin. Signal model: ALPGEN.

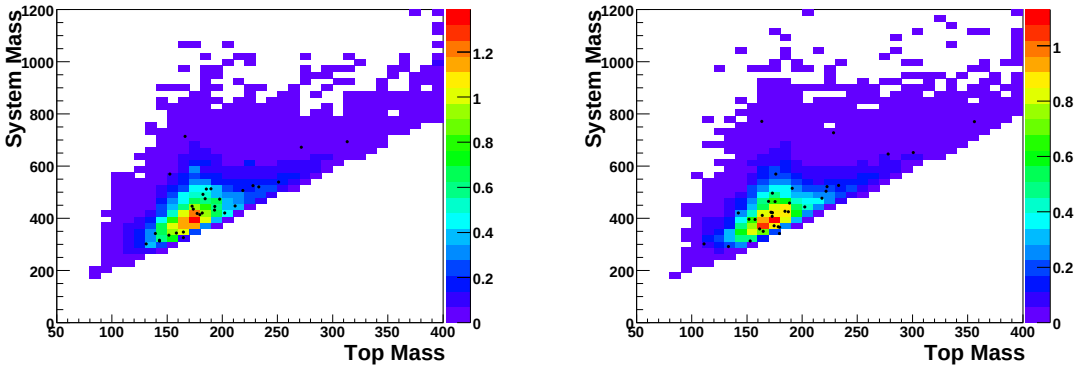

Figure C.198: $t\bar{t}$ system mass vs. top mass, e+jets (left) and μ+jets (right), NN-medium ≥ 2 b-tag bin. Signal model: ALPGEN.

Appendix D

$t\bar{t}$ Event Displays and Event Characteristics

Figures D.1–D.9 each provide three views of the DØ detector corresponding to the transverse $(x-y)$ and longitudinal $(r-z)$ views, as well as "lego" plot of calorimeter objects in the $\eta \times \phi$ space, for selected interesting events. Electromagnetic and hadronic calorimeter regions are depicted by red and blue colors respectively, missing transverse energy by yellow, electrons by brown and muon particle by green. Track jets are drawn as circles or cones depending on the projection while central tracking detector tracks themselves are black. Also, depicted are the three-moment of fitted four-vectors of the W bosons and top quarks, together with the $t\bar{t}$ system direction.

Selected events characteristics with large top quark p_{T} or high $t\bar{t}$ system mass are summarised in this section before the set of corresponding event displays.

Large top quark p_{T} in e+jets

Run 207072, event 11066941
Lumi: 1.568, MET: 35.8395
$t\bar{t}$ Mass: 624.854
Top mass: 170, $p_T^{t\bar{t}}$: 9.14441
Leptonic p_T^t: 245.32,
Hadronic p_T^t: 240.509
$\Delta\phi^{t\bar{t}}$: -3.10958, b-tags: 1
nPV: 3, χ^2_{HitFit}: 1.83708

Run 168523, event 7224247
Lumi: 0.6001, MET: 111.556
$t\bar{t}$ Mass: 672.705
Top mass: 170, $p_T^{t\bar{t}}$: 5.55723
Leptonic p_T^t: 285.799,
Hadronic p_T^t: 281.947
$\Delta\phi^{t\bar{t}}$: 3.12748, b-tags: 1
nPV: 1, χ^2_{HitFit}: 0.359645

Run 190057, event 19298213
Lumi: 1.495, MET: 103.011
$t\bar{t}$ Mass: 821.606
Top mass: 170, $p_T^{t\bar{t}}$: 29.3787
Leptonic p_T^t: 381.829,
Hadronic p_T^t: 352.537
$\Delta\phi^{t\bar{t}}$: 3.13547, b-tags: 1
nPV: 4, χ^2_{HitFit}: 45.3081

Large top quark p_{T} in μ+jets

Run 189402, event 69996854
Lumi: 0.468, MET: 43.0078
$t\bar{t}$ Mass: 580.495
Top mass: 170, $p_T^{t\bar{t}}$: 21.551
Leptonic p_T^t: 244.223,
Hadronic p_T^t: 225.039
$\Delta\phi^{t\bar{t}}$: -3.0997, b-tags: 1
nPV: 3, χ^2_{HitFit}: 0.710138

Run 211523, event 53043518
Lumi: 0.9332, MET: 102.131
$t\bar{t}$ Mass: 668.239
Top mass: 170, $p_T^{t\bar{t}}$: 32.4121
Leptonic p_T^t: 272.046,
Hadronic p_T^t: 239.711
$\Delta\phi^{t\bar{t}}$: -3.13284, b-tags: 1
nPV: 2, χ^2_{HitFit}: 31.75

Run 213084, event 13703807
Lumi: 1.389, MET: 175.341
$t\bar{t}$ Mass: 654.475
Top mass: 170, $p_T^{t\bar{t}}$: 16.8442
Leptonic p_T^t: 268.076,
Hadronic p_T^t: 251.639
$\Delta\phi^{t\bar{t}}$: 3.12741, b-tags: 1
nPV: 2, χ^2_{HitFit}: 22.2141

Large $t\bar{t}$ system mass in e+jets

Run 175919, event 46961265
Lumi: 0.4142, MET: 89.7435
$t\bar{t}$ Mass: 720.874
Top mass: 170, $p_T^{t\bar{t}}$: 36.0667
Leptonic p_T^t: 37.5474,
Hadronic p_T^t: 73.3291
$\Delta\phi^{t\bar{t}}$: 3.05532, b-tags: 1
nPV: 2, χ^2_{HitFit}: 2.61387

Run 195073, event 19419757
Lumi: 1.098, MET: 22.6979
$t\bar{t}$ Mass: 772.319
Top mass: 170, $p_T^{t\bar{t}}$: 7.75355
Leptonic p_T^t: 132.035,
Hadronic p_T^t: 124.476
$\Delta\phi^{t\bar{t}}$: -3.12813, b-tags: 1
nPV: 3, χ^2_{HitFit}: 1.96236

Run 188904, event 21333789
Lumi: 0.9323, MET: 71.8254
$t\bar{t}$ Mass: 786.881
Top mass: 170, $p_T^{t\bar{t}}$: 7.36746
Leptonic p_T^t: 203.921,
Hadronic p_T^t: 202.997
$\Delta\phi^{t\bar{t}}$: 3.10567, b-tags: 1
nPV: 2, χ^2_{HitFit}: 8.22248

Run 190057, event 19298213
Lumi: 1.495, MET: 103.011
$t\bar{t}$ Mass: 821.606
Top mass: 170, $p_T^{t\bar{t}}$: 29.3787
Leptonic p_T^t: 381.829,
Hadronic p_T^t: 352.537
$\Delta\phi^{t\bar{t}}$: 3.13547, b-tags: 1
nPV: 4, χ^2_{HitFit}: 45.3081

Large $t\bar{t}$ system mass in μ+jets

Run 208431, event 24883004
Lumi: 0.9952, MET: 48.0477
$t\bar{t}$ Mass: 625.062
Top mass: 170, $p_T^{t\bar{t}}$: 12.3505
Leptonic p_T^t: 212.83,
Hadronic p_T^t: 207.316
$\Delta\phi^{t\bar{t}}$: 3.08897, b-tags: 1
nPV: 1, χ^2_{HitFit}: 29.126

Run 213084, event 13703807
Lumi: 1.389, MET: 175.341
$t\bar{t}$ Mass: 654.475
Top mass: 170, $p_T^{t\bar{t}}$: 16.8442
Leptonic p_T^t: 268.076,
Hadronic p_T^t: 251.639
$\Delta\phi^{t\bar{t}}$: 3.12741, b-tags: 1
nPV: 2, χ^2_{HitFit}: 22.2141

Run 211523, event 53043518
Lumi: 0.9332, MET: 102.131
$t\bar{t}$ Mass: 668.239
Top mass: 170, $p_T^{t\bar{t}}$: 32.4121
Leptonic p_T^t: 272.046,
Hadronic p_T^t: 239.711
$\Delta\phi^{t\bar{t}}$: -3.13284, b-tags: 1
nPV: 2, χ^2_{HitFit}: 31.75

Run 211872, event 15258963
Lumi: 2.163, MET: 45.9566
$t\bar{t}$ Mass: 676.797
Top mass: 170, $p_T^{t\bar{t}}$: 11.2867
Leptonic p_T^t: 132.68,
Hadronic p_T^t: 142.231
$\Delta\phi^{t\bar{t}}$: -3.09782, b-tags: 1
nPV: 4, χ^2_{HitFit}: 2.90212

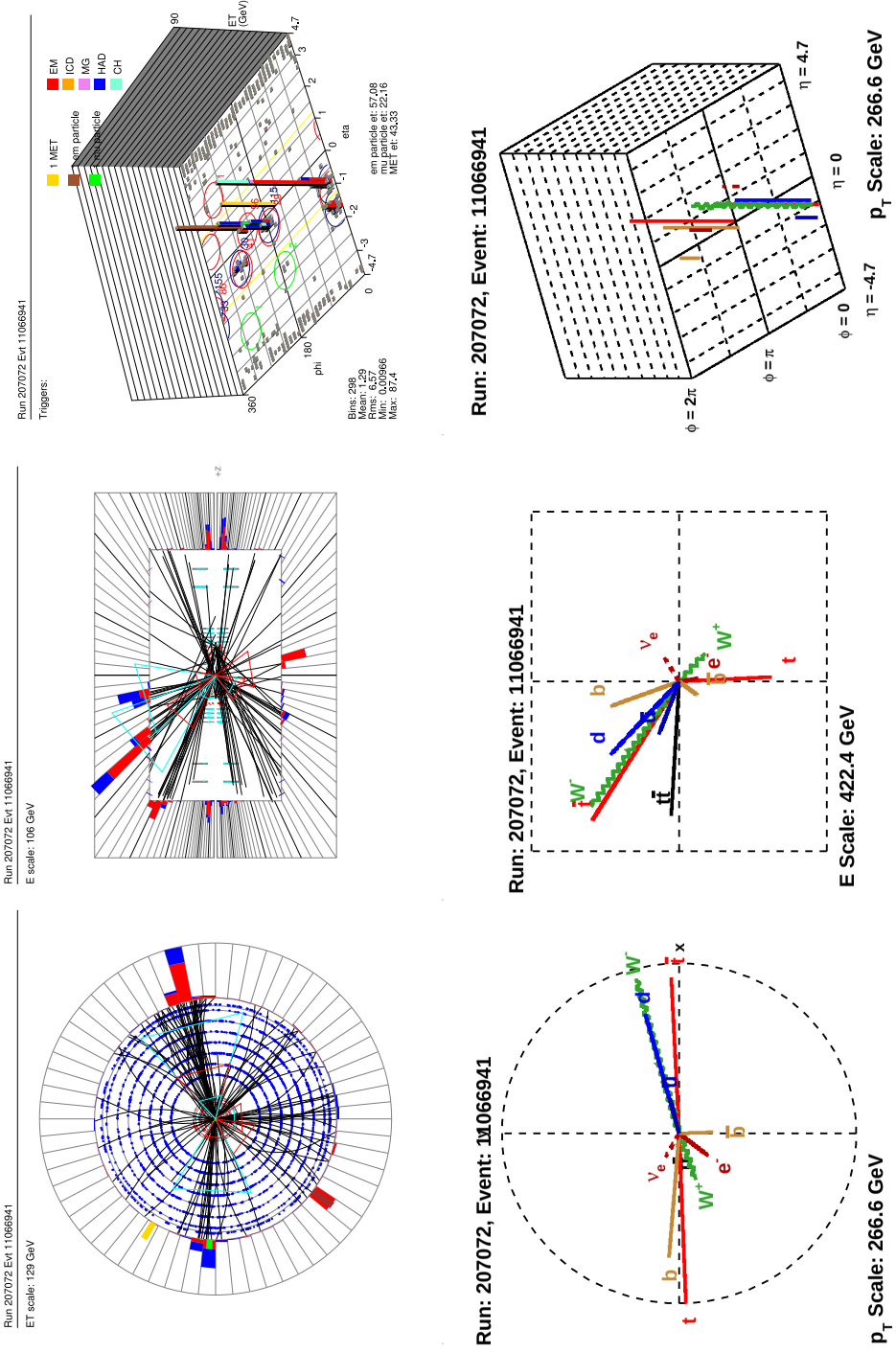

Run 207072, event 11066941
Lumi: 1.568, MET: 35.8395
$t\bar{t}$ Mass: 624.854
Top mass: 170, $p_T^{t\bar{t}}$: 9.14441
Leptonic p_T^t: 245.32,
Hadronic p_T^t: 240.509
$\Delta\phi^{t\bar{t}}$: -3.10958, b-tags: 1
nPV: 3, χ^2_{HitFit}: 1.83708

Figure D.1: Run 207072, Event 11066941.

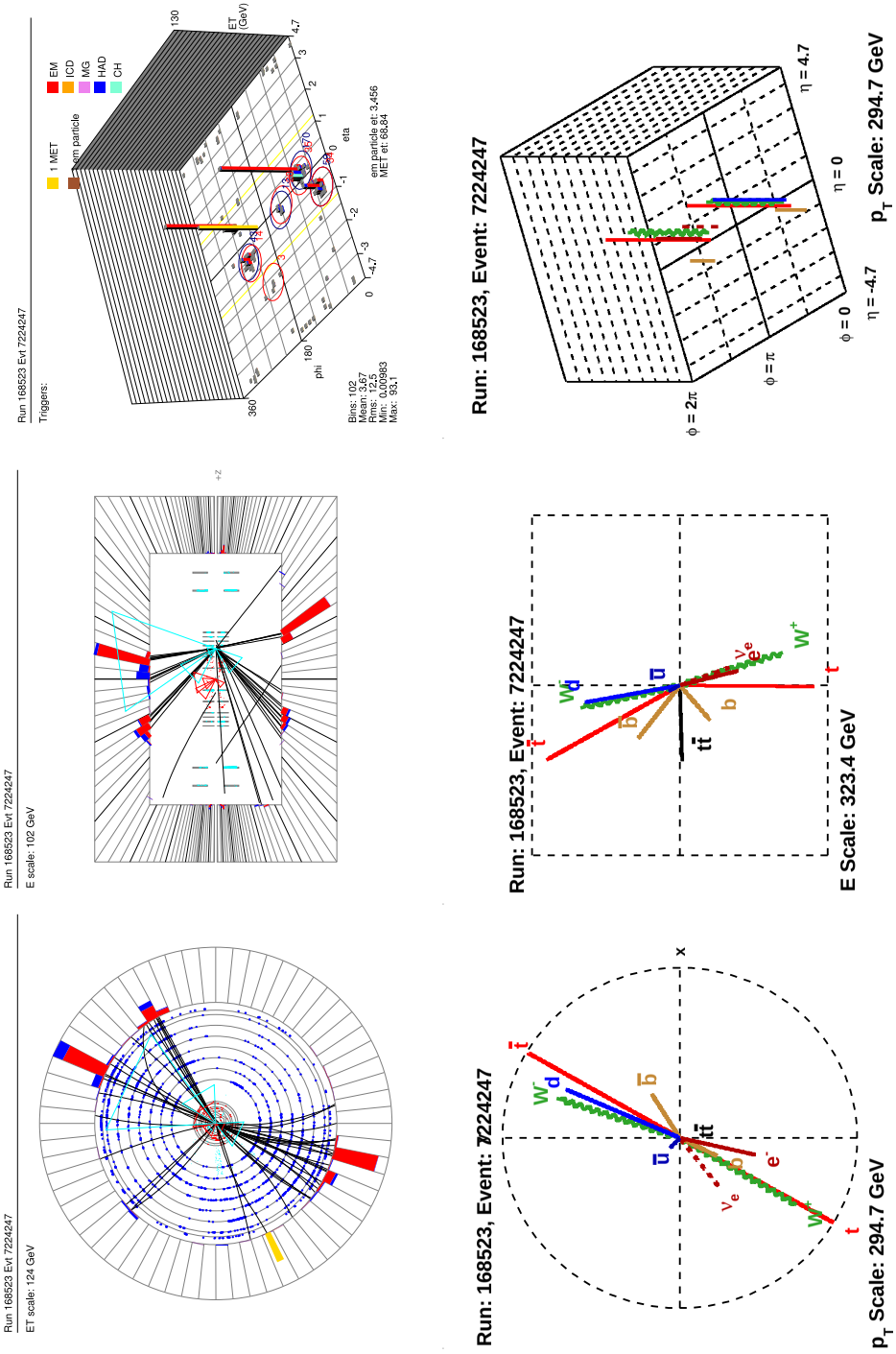

Run 168523, event 7224247
Lumi: 0.6001, MET: 111.556
$t\bar{t}$ Mass: 672.705
Top mass: 170, $p_T^{t\bar{t}}$: 5.55723
Leptonic p_T^t: 285.799,
Hadronic p_T^t: 281.947
$\Delta\phi^{t\bar{t}}$: 3.12748, b-tags: 1
nPV: 1, χ^2_{HitFit}: 0.359645

Figure D.2: Run 168523, Event 7224247.

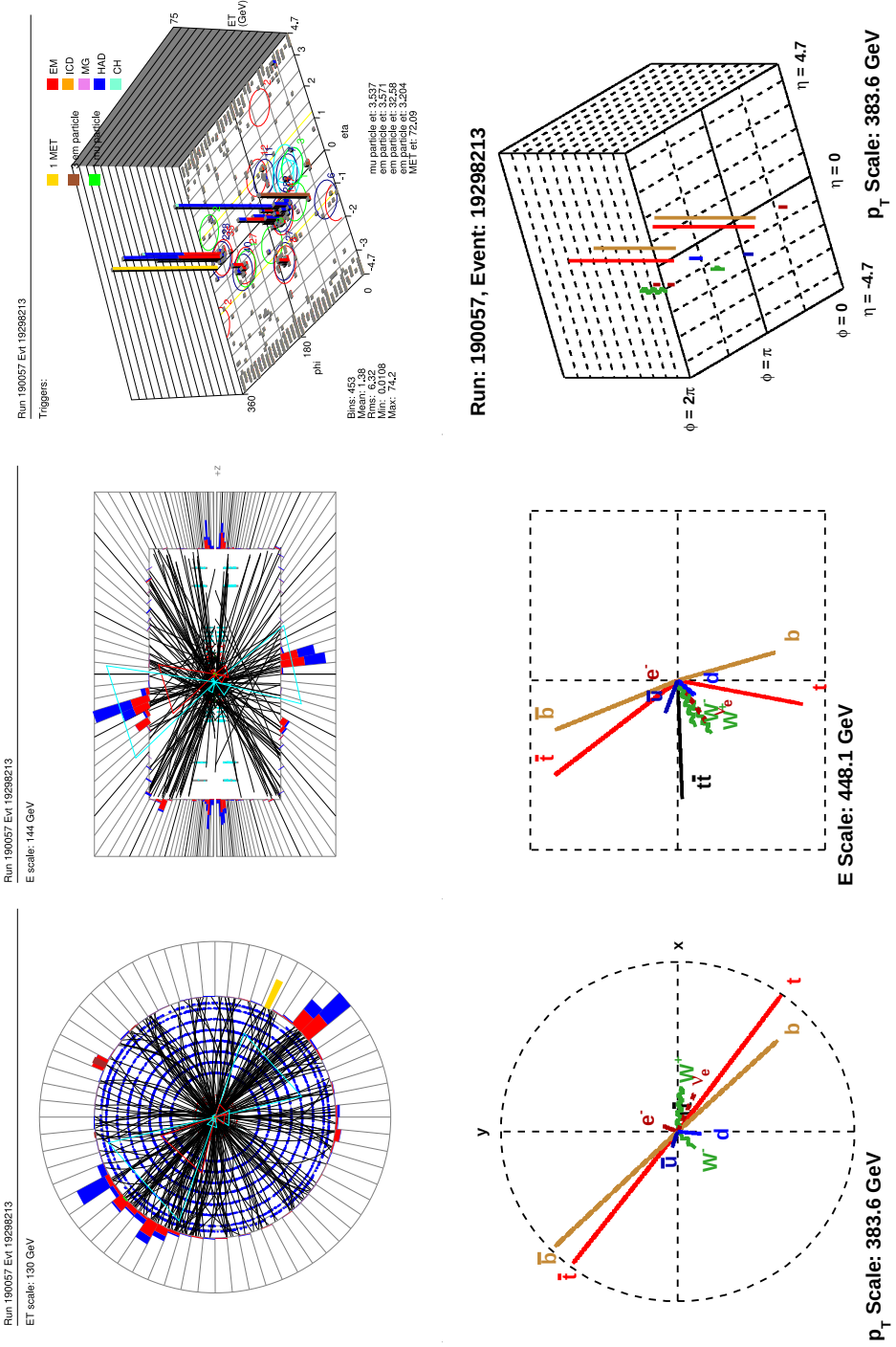

Run 190057, event 19298213
Lumi: 1.495, MET: 103.011
$t\bar{t}$ Mass: 821.606
Top mass: 170, $p_T^{t\bar{t}}$: 29.3787
Leptonic p_T^t: 381.829,
Hadronic p_T^t: 352.537
$\Delta\phi^{t\bar{t}}$: 3.13547, b-tags: 1
nPV: 4, χ^2_{HitFit}: 45.3081

Figure D.3: Run 190057, Event 19298213.

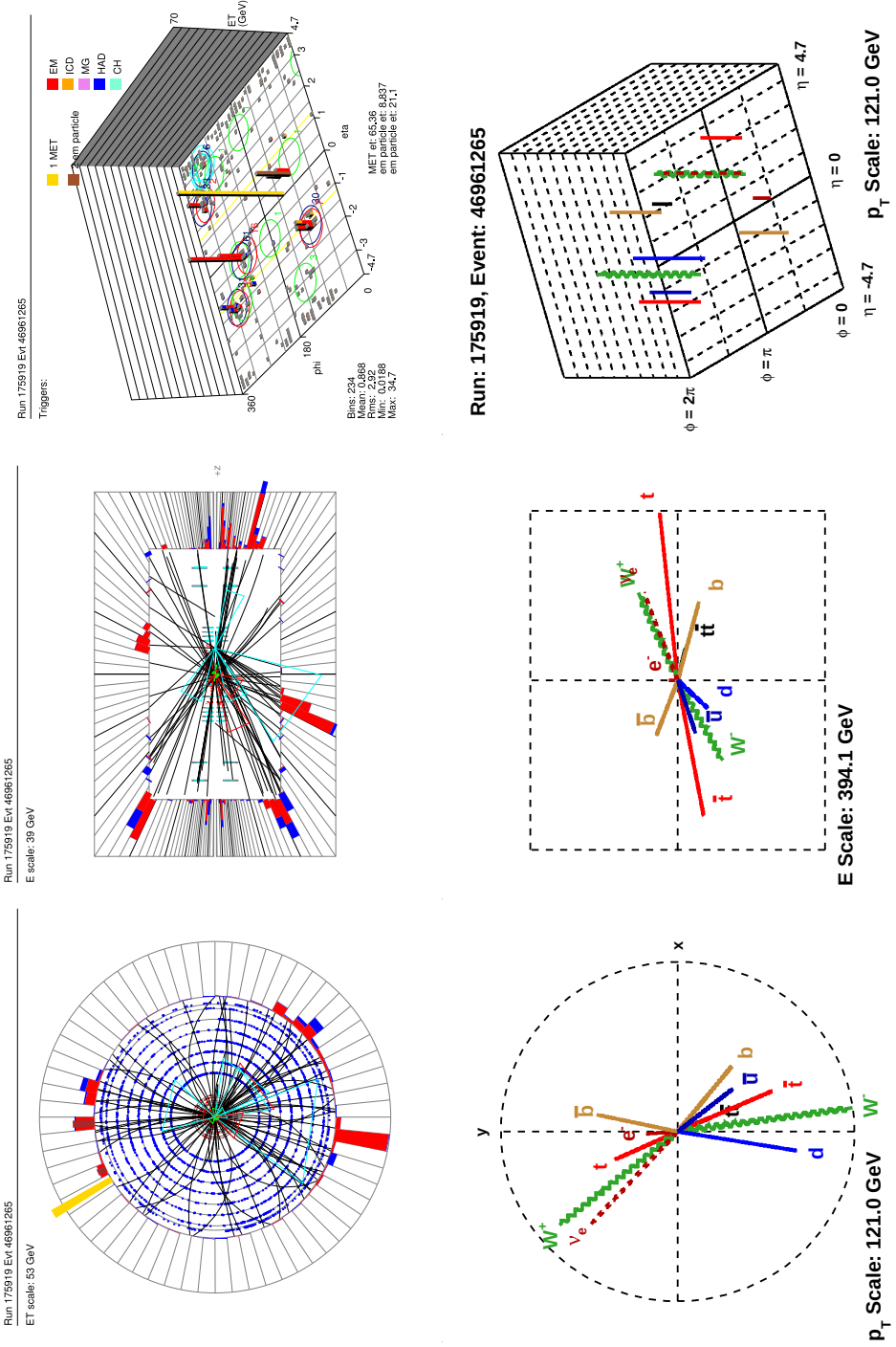

Run 175919, event 46961265
Lumi: 0.4142, MET: 89.7435
$t\bar{t}$ Mass: 720.874
Top mass: 170, $p_T^{t\bar{t}}$: 36.0667
Leptonic p_T^t: 37.5474,
Hadronic p_T^t: 73.3291
$\Delta\phi^{t\bar{t}}$: 3.05532, b-tags: 1
nPV: 2, χ^2_{HitFit}: 2.61387

Figure D.4: Run 175919, Event 46961265.

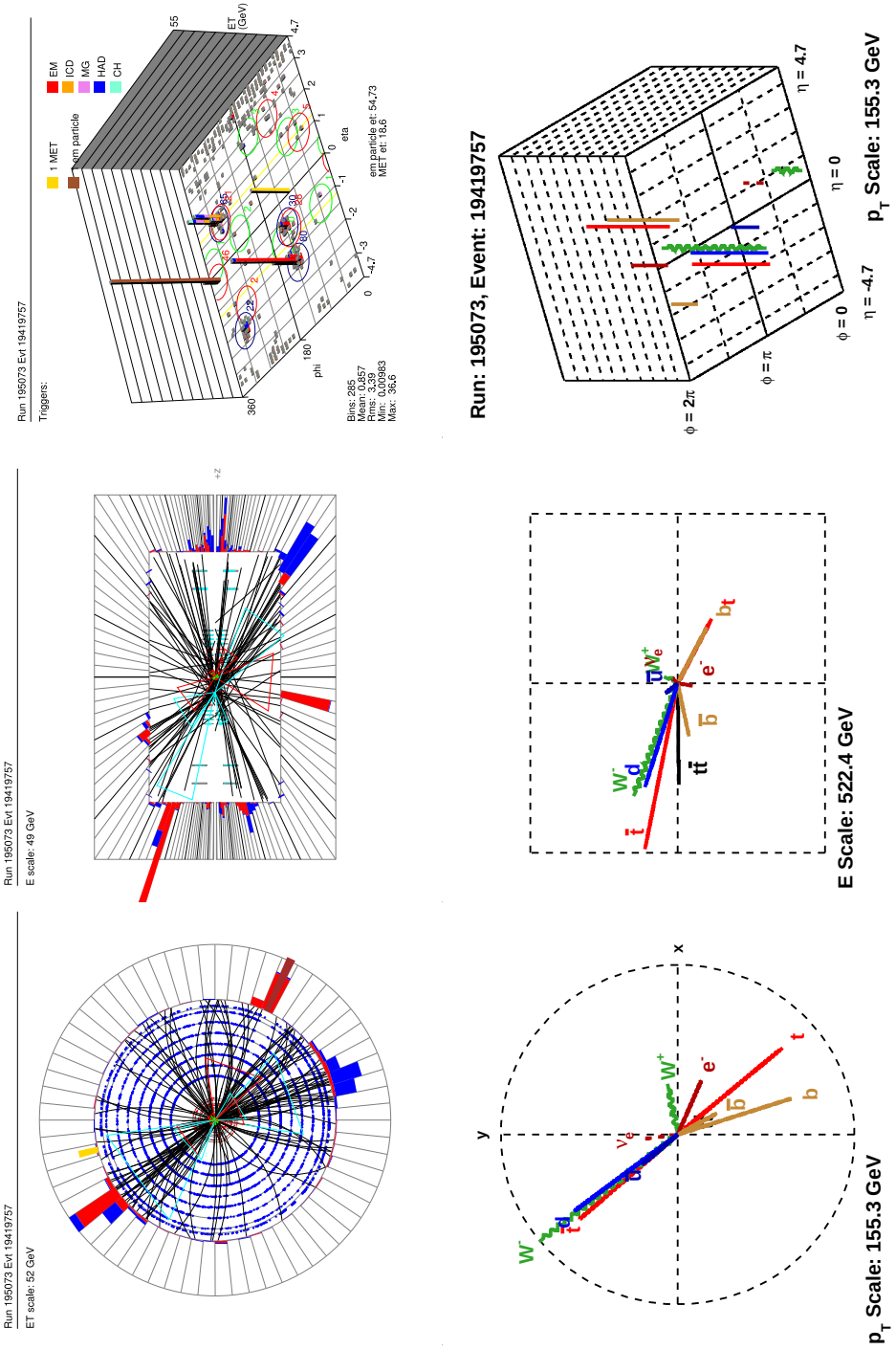

Run 195073, event 19419757
Lumi: 1.098, MET: 22.6979
$t\bar{t}$ Mass: 772.319
Top mass: 170, $p_T^{t\bar{t}}$: 7.75355
Leptonic p_T^t: 132.035,
Hadronic p_T^t: 124.476
$\Delta\phi^{t\bar{t}}$: -3.12813, b-tags: 1
nPV: 3, χ^2_{HitFit}: 1.96236

Figure D.5: Run 195073, Event 19419757.

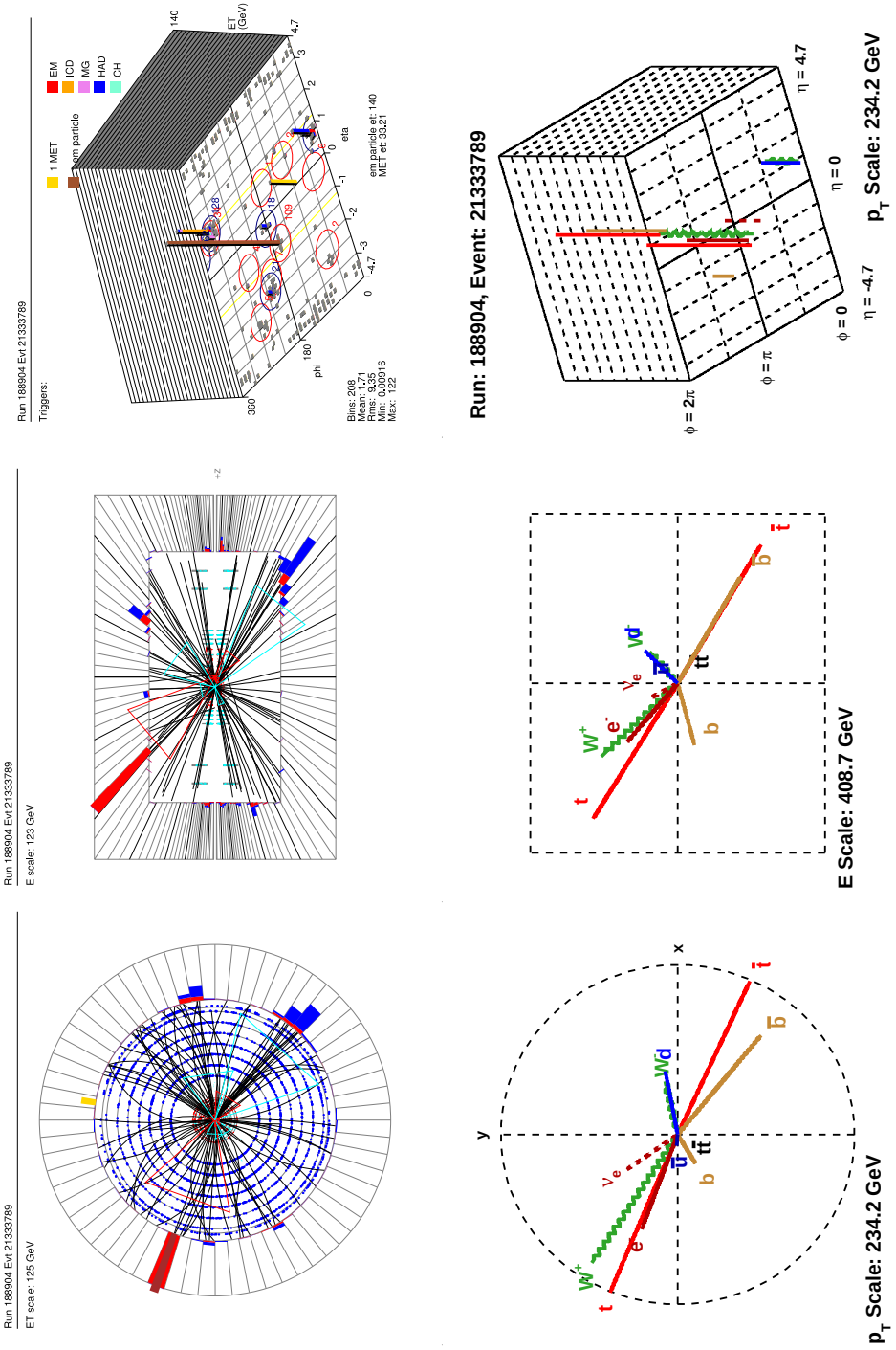

Run 188904, event 21333789
Lumi: 0.9323, MET: 71.8254
$t\bar{t}$ Mass: 786.881
Top mass: 170, $p_T^{t\bar{t}}$: 7.36746
Leptonic p_T^t: 203.921,
Hadronic p_T^t: 202.997
$\Delta\phi^{t\bar{t}}$: 3.10567, b-tags: 1
nPV: 2, χ^2_{HitFit}: 8.22248

Figure D.6: Run 188904, Event 21333789.

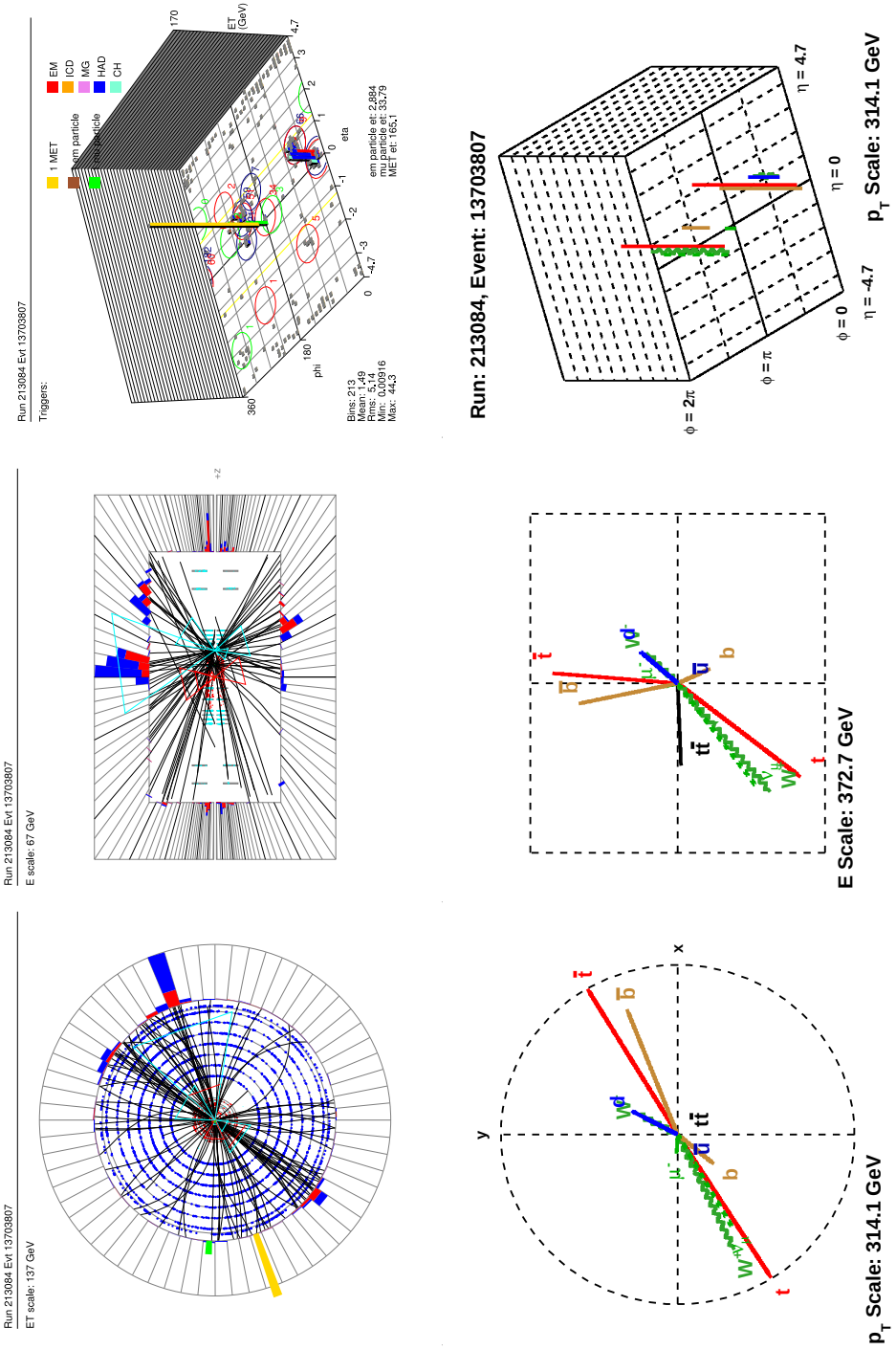

Run 213084, event 13703807
Lumi: 1.389, MET: 175.341
$t\bar{t}$ Mass: 654.475
Top mass: 170, $p_T^{t\bar{t}}$: 16.8442
Leptonic p_T^t: 268.076,
Hadronic p_T^t: 251.639
$\Delta\phi^{t\bar{t}}$: 3.12741, b-tags: 1
nPV: 2, χ^2_{HitFit}: 22.2141

Figure D.7: Run 213084, Event 13703807.

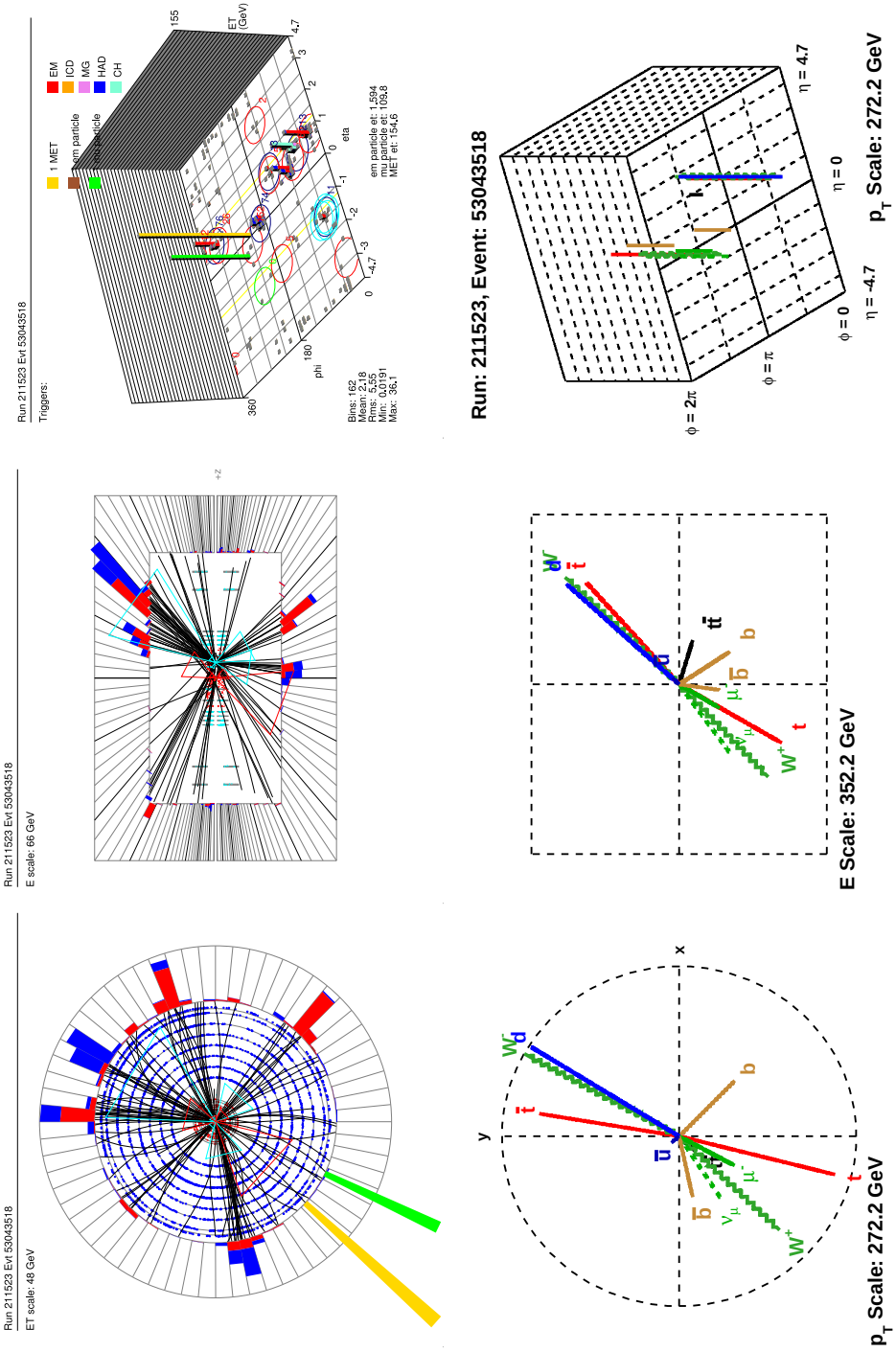

Run 211523, event 53043518
Lumi: 0.9332, MET: 102.131
$t\bar{t}$ Mass: 668.239
Top mass: 170, $p_T^{t\bar{t}}$: 32.4121
Leptonic p_T^t: 272.046,
Hadronic p_T^t: 239.711
$\Delta\phi^{t\bar{t}}$: -3.13284, b-tags: 1
nPV: 2, χ^2_{HitFit}: 31.75

Figure D.8: Run 211523, Event 53043518.

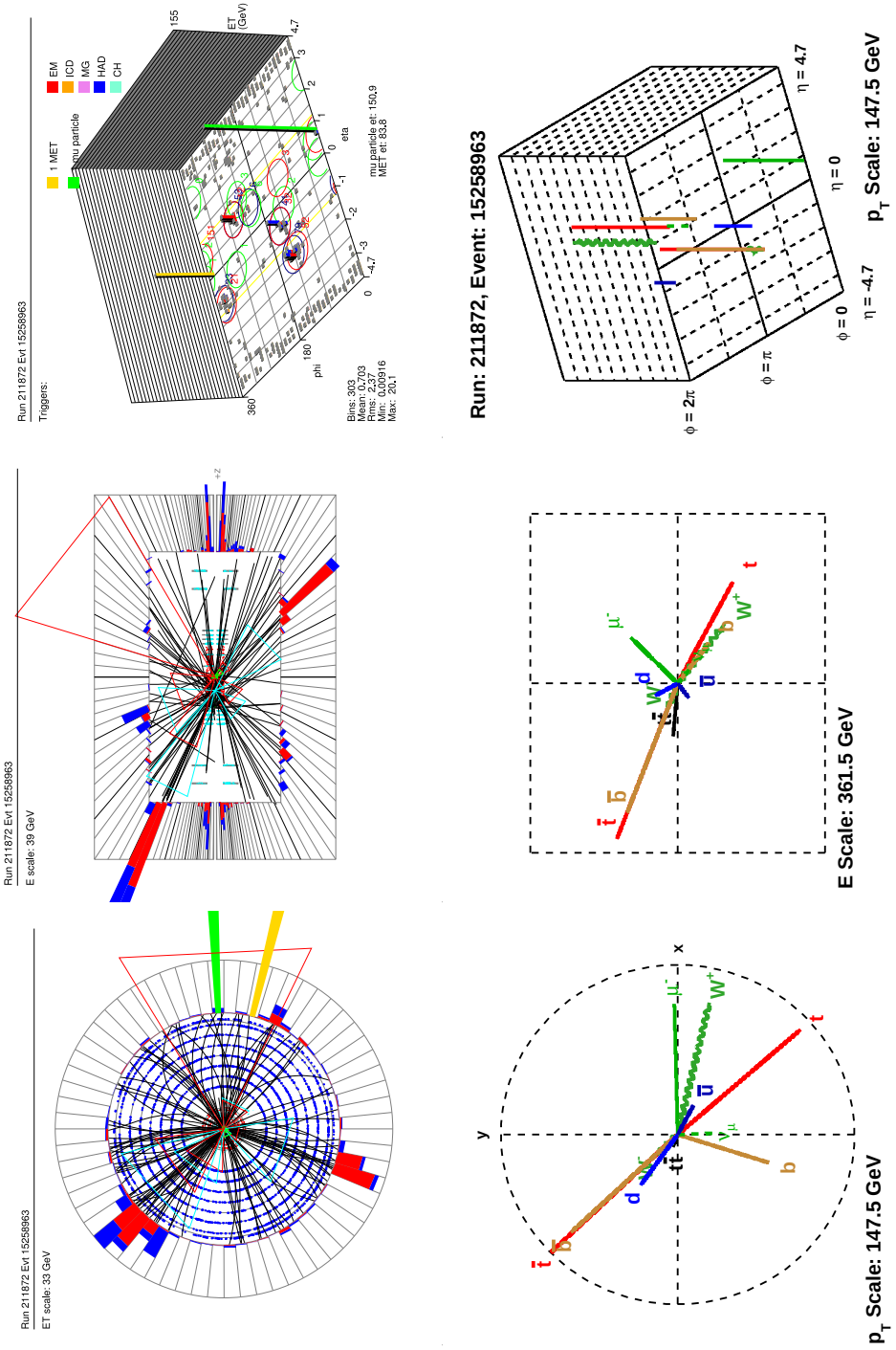

Run 211872, event 15258963
Lumi: 2.163, MET: 45.9566
$t\bar{t}$ Mass: 676.797
Top mass: 170, $p_T^{t\bar{t}}$: 11.2867
Leptonic p_T^t: 132.68,
Hadronic p_T^t: 142.231
$\Delta\phi^{t\bar{t}}$: -3.09782, b-tags: 1
nPV: 4, χ^2_{HitFit}: 2.90212

Figure D.9: Run 211872, Event 15258963.

Selected List of Publications

[APS08] J. Kvita, "Study of differential distributions of top quarks at DØ", APS Meeting Abstract J12.00004, 2008.

[CALOR06] J. Kvita, "Jet energy scale determination at the D0," AIP Conf. Proc. **867** (2006) 43.

[APS05] J. Kvita, "Measurement of the Top Quark Transverse Momentum Spectrum at DØ", APS Meeting Abstract BAPS.2005.APR.R7.8, 2005.

[UnfoldTop] Unfolding Differential Distributions in the $t\bar{t} \to \ell$+jets Channel at $\sqrt{s} =$ 1.96 TeV with $1\,\mathrm{fb}^{-1}$ DØ Data, DØ 5775 (Michael Begel, Jiří Kvita).

[JetID] "p20 JetID Efficiencies and Scale Factors", DØ Note 5634 (Amnon Harel, Jiří Kvita).

[p17Top] "Measurement of top quark differential distributions in the lepton+jets channel at sqrts=1.96 TeV using the neural network tagger", DØ Note 5442 (Michael Begel, Jiří Kvita).

[p17JES] "Jet Energy Scale Scale Determination at DØ Run II (final p17 version)", DØ Note 5382 (p17 JES group).

[ϕCalib] "Run II Phi-Intercalibration of the Fine Hadronic Calorimeter", DØ Note 5005 (Jiří Kvita, Krisztián Peters).

[p14JES] "Jet Energy Scale at DØ Run II", DØ Note 4720 (Jean-Laurent Agram, Subhendu Chakraborti, Pavel Demine, Kazu Hanagaki, Ia Iashvili, Alexander Kupco, Jiri Kvita, Vivian O'Dell, Nirmalya Parua, Christophe Royon, Jyothsna Rani, Markus Wobisch).

[p14Top] "Measurement of the Top Quark Transverse Momentum Distribution in $t\bar{t}$ Decays in the Lepton+Jets Channel at $\sqrt{s} = 1.96$ TeV using the Secondary Vertex Tagger", DØ Note 4693 (Jiří Kvita).

Full List of Publications

[1] **"Search for admixture of scalar top quarks in the ttbar lepton+jets final state at sqrt(s)=1.96 TeV"**
V. M. Abazov *et al.* [D0 Collaboration]
arXiv:0901.1063 [hep-ex]
FERMILAB-PUB-09-005-E(2009)

[2] **"Measurement of photon+b+X and photon+c+X production cross sections in ppbar collisions at sqrt(s)=1.96 TeV"**
V. M. Abazov *et al.* [D0 Collaboration]
arXiv:0901.0739 [hep-ex]
FERMILAB-PUB-08-582-E(2009)

[3] **"Search for associated production of charginos and neutralinos in the trilepton final state using 2.3 fb-1 of data"**
V. M. Abazov *et al.* [D0 Collaboration]
arXiv:0901.0646 [hep-ex]
FERMILAB-PUB-09-003-E(2009)

[4] **"Search for anomalous top quark couplings with the D0 detector"**
V. M. Abazov *et al.* [D0 Collaboration]
arXiv:0901.0151 [hep-ex]
FERMILAB-PUB-08-583-E(2009)

[5] **"Evidence for decay $B_s^0 \to D_s^{(*)} D_s^{(*)}$ and a measurement of $\Delta\Gamma_s^{CP}/\Gamma_s$"**
V. M. Abazov *et al.* [D0 Collaboration]
arXiv:0811.2173 [hep-ex]
FERMILAB-PUB-08-518-E(2008)

[6] **"Search for the lightest scalar top quark in events with two leptons in ppbar collisions at sqrt(s)=1.96 TeV"**
V. M. Abazov *et al.* [D0 Collaboration]
arXiv:0811.0459 [hep-ex]
FERMILAB-PUB-08-508-E(2008) (Submitted to Phys.Lett.B)

[7] **"Search for neutral Higgs bosons at high tan(beta) in the b(h/H/A)→btautau channel"**
V. M. Abazov *et al.* [D0 Collaboration]
arXiv:0811.0024 [hep-ex]
FERMILAB-PUB-08-451-E(2008)

[8] **"Evidence of $WW + WZ$ production with lepton + jets final states in proton-antiproton collisions at $\sqrt{s}$ =1.96 TeV"**
V. M. Abazov *et al.* [D0 Collaboration]
arXiv:0810.3873 [hep-ex]
FERMILAB-PUB-08-457-E(2008)

[9] **"Measurement of the angular and lifetime parameters of the decays $B_d^0 \to J/\psi K^{*0}$ and $B_s^0 \to J/\psi\phi$"**
V. M. Abazov *et al.* [D0 Collaboration]
arXiv:0810.0037 [hep-ex]
FERMILAB-PUB-08-418-E(2008)

[10] **"Search for charged massive stable particles with the D0 detector"**
V. M. Abazov *et al.* [D0 Collaboration]
arXiv:0809.4472 [hep-ex]
FERMILAB-PUB-08-409-E(2008)

[11] **"Search for Large extra spatial dimensions in the dielectron and diphoton channels in $p\bar{p}$ collisions at $\sqrt{s}$ =1.96 TeV"**
V. M. Abazov *et al.* [D0 Collaboration]
arXiv:0809.2813 [hep-ex]
FERMILAB-PUB-08-368-E(2008) (Submitted to Phys.Rev.Lett.)

[12] **"Observation of the doubly strange b baryon Ω_b^-"**
V. M. Abazov *et al.* [D0 Collaboration]
Phys. Rev. Lett. **101**, 232002 (2008) [arXiv:0808.4142 [hep-ex]]

[13] **"Search for pair production of second generation scalar leptoquarks"**
V. M. Abazov *et al.* [D0 Collaboration]
arXiv:0808.4023 [hep-ex]
FERMILAB-PUB-08-334-E(2008) (Submitted to Phys.Lett.B)

[14] **"A Search for associated W and Higgs Boson production in $p\bar{p}$ collisions at $\sqrt{s}$ = 1.96 TeV"**
V. M. Abazov *et al.* [D0 Collaboration]
arXiv:0808.1970 [hep-ex]
FERMILAB-PUB-08-297-E(2008) (Submitted to Phys.Rev.Lett.)

[15] **"Measurement of $\sigma(p\bar{p} \to Z + X)$ Br$(Z \to \tau^+\tau^-)$ at $\sqrt{s}$ = 1.96 TeV"**
V. M. Abazov *et al.* [D0 Collaboration]
arXiv:0808.1306 [hep-ex]
FERMILAB-PUB-08-295-E(2008) (Submitted to Phys.Lett.B)

[16] **"Measurement of differential Z/γ^* + jet + X cross sections in $p\bar{p}$ collisions at $\sqrt{s}$ = 1.96 TeV"**
V. M. Abazov *et al.* [D0 Collaboration]
Phys. Lett. B **669**, 278 (2008) [arXiv:0808.1296 [hep-ex]]

[17] **"A Search for the standard model Higgs boson in the missing energy and acoplanar b^- jet topology at $\sqrt{s}$ = 1.96 TeV"**
V. M. Abazov *et al.* [D0 Collaboration]
Phys. Rev. Lett. **101**, 251802 (2008) [arXiv:0808.1266 [hep-ex]]

[18] **"Observation of ZZ production in $p\bar{p}$ collisions at $\sqrt{s}$ = 1.96 TeV"**
V. M. Abazov *et al.* [D0 Collaboration]
Phys. Rev. Lett. **101**, 171803 (2008) [arXiv:0808.0703 [hep-ex]]

[19] **"Search for scalar leptoquarks and T-odd quarks in the acoplanar jet topology using 2.5 fb^{-1} of $p\bar{p}$ collision data at $\sqrt{s}$ = 1.96 TeV"**
V. M. Abazov *et al.* [D0 Collaboration]
Phys. Lett. B **668**, 357 (2008) [arXiv:0808.0446 [hep-ex]]

[20] **"$ZZ \to \ell^+\ell^-\nu\bar{\nu}$ production in $p\bar{p}$ collisions at $\sqrt{s}$= 1.96 TeV"**
V. M. Abazov *et al.* [D0 Collaboration]
Phys. Rev. D **78**, 072002 (2008) [arXiv:0808.0269 [hep-ex]]

[21] **"Measurement of the electron charge asymmetry in $p\bar{p} \to W+X \to e\nu+X$ events at $\sqrt{s} = 1.96$ TeV"**
V. M. Abazov *et al.* [D0 Collaboration]
Phys. Rev. Lett. **101**, 211801 (2008) [arXiv:0807.3367 [hep-ex]]

[22] **"Precise measurement of the top quark mass from lepton+jets events at D0"**
V. M. Abazov *et al.* [D0 Collaboration]
Phys. Rev. Lett. **101**, 182001 (2008) [arXiv:0807.2141 [hep-ex]]

[23] **"Search for anomalous Wtb couplings in single top quark production"**
V. M. Abazov *et al.* [D0 Collaboration]
Phys. Rev. Lett. **101**, 221801 (2008) [arXiv:0807.1692 [hep-ex]]

[24] **"Search for charged Higgs bosons decaying to top and bottom quarks in $p\bar{p}$ collisions"**
V. M. Abazov *et al.* [D0 Collaboration]
arXiv:0807.0859 [hep-ex]
FERMILAB-PUB-08-229-E(2008) (Submitted to Phys.Rev.Lett.)

[25] **"Search for third generation scalar leptoquarks decaying into τb"**
V. M. Abazov *et al.* [D0 Collaboration]
Phys. Rev. Lett. **101**, 241802 (2008) [arXiv:0806.3527 [hep-ex]]

[26] **"Search for long-lived particles decaying into electron or photon pairs with the D0 detector"**
V. M. Abazov *et al.* [D0 Collaboration]
Phys. Rev. Lett. **101**, 111802 (2008) [arXiv:0806.2223 [hep-ex]]

[27] **"Search for a scalar or vector particle decaying into $Z\gamma$ in $p\bar{p}$ collisions at $\sqrt{s} = 1.96$ TeV"**
V. M. Abazov *et al.* [D0 Collaboration]
arXiv:0806.0611 [hep-ex]
FERMILAB-PUB-08-154-E(2008) (Submitted to Phys.Lett.B)

[28] **"Search for neutral Higgs bosons in multi-b-jet events in $p\bar{p}$ collisions at $\sqrt{s} = 1.96$ TeV"**
V. M. Abazov *et al.* [D0 Collaboration]
Phys. Rev. Lett. **101**, 221802 (2008) [arXiv:0805.3556 [hep-ex]]

[29] **"Measurement of the lifetime of the $B_c^{\pm}$ meson in the semileptonic decay channel"**
V. M. Abazov *et al.* [D0 Collaboration]
arXiv:0805.2614 [hep-ex]
FERMILAB-PUB-08-136-E(2008) (Submitted to Phys.Rev.Lett.)

[30] **"Relative rates of B meson decays into ψ_{2S} and J/ψ mesons"**
V. M. Abazov *et al.* [D0 Collaboration]
arXiv:0805.2576 [hep-ex]
FERMILAB-PUB-08-134-E(2008) (Submitted to Phys.Rev.D)

[31] **"Search for Higgs bosons decaying to τ pairs in $p\bar{p}$ collisions with the D0 detector"**
V. M. Abazov *et al.* [D0 Collaboration]
Phys. Rev. Lett. **101**, 071804 (2008) [arXiv:0805.2491 [hep-ex]]

[32] **"Search for $t\bar{t}$ resonances in the lepton plus jets final state in $p\bar{p}$ collisions at $\sqrt{s} = 1.96$ TeV"**

V. M. Abazov *et al.* [D0 Collaboration]
Phys. Lett. B **668**, 98 (2008) [arXiv:0804.3664 [hep-ex]]

[33] **"Measurement of the forward-backward charge asymmetry and extraction of $sin^2Theta_W^{eff}$ in $p\bar{p} \to Z/\gamma^* + X \to e^+e^- + X$ events produced at $\sqrt{s} = 1.96$ TeV"**
V. M. Abazov *et al.* [D0 Collaboration]
Phys. Rev. Lett. **101**, 191801 (2008) [arXiv:0804.3220 [hep-ex]]

[34] **"Measurement of the polarization of the $\Upsilon(1S)$ and $\Upsilon(2S)$ states in $p\bar{p}$ collisions at $\sqrt{s}$ =1.96 TeV"**
V. M. Abazov *et al.* [D0 Collaboration]
Phys. Rev. Lett. **101**, 182004 (2008) [arXiv:0804.2799 [hep-ex]]

[35] **"Measurement of the differential cross-section for the production of an isolated photon with associated jet in $p\bar{p}$ collisions at $\sqrt{s} = 1.96$ TeV"**
V. M. Abazov *et al.* [D0 Collaboration]
Phys. Lett. B **666**, 435 (2008) [arXiv:0804.1107 [hep-ex]]

[36] **"Search for W' Boson Resonances Decaying to a Top Quark and a Bottom Quark"**
V. M. Abazov *et al.* [D0 Collaboration]
Phys. Rev. Lett. **100**, 211803 (2008) [arXiv:0803.3256 [hep-ex]]

[37] **"Measurement of the $t\bar{t}$ production cross section in $p\bar{p}$ collisions at $\sqrt{s}$ = 1.96 TeV"**
V. M. Abazov *et al.* [D0 Collaboration]
Phys. Rev. Lett. **100**, 192004 (2008) [arXiv:0803.2779 [hep-ex]]

[38] **"Search for scalar top quarks in the acoplanar charm jets and missing transverse energy final state in $p\bar{p}$ collisions at $\sqrt{s} = 1.96$ TeV"**
V. M. Abazov *et al.* [D0 Collaboration]
Phys. Lett. B **665**, 1 (2008) [arXiv:0803.2263 [hep-ex]]

[39] **"Measurement of the ratio of the $p\bar{p} \to W+c$-jet cross section to the inclusive $p\bar{p} \to W+$jets cross section"**
V. M. Abazov *et al.* [D0 Collaboration]
Phys. Lett. B **666**, 23 (2008) [arXiv:0803.2259 [hep-ex]]

[40] **"Search for large extra dimensions via single photon plus missing energy final states at $\sqrt{s} = 1.96$ TeV"**
V. M. Abazov *et al.* [D0 Collaboration]
Phys. Rev. Lett. **101**, 011601 (2008) [arXiv:0803.2137 [hep-ex]]

[41] **"Search for pair production of doubly-charged Higgs bosons in the $H^{++}H^{--} \to \mu^+\mu^+\mu^-\mu^-$ final state at D0"**
V. M. Abazov *et al.* [D0 Collaboration]
Phys. Rev. Lett. **101**, 071803 (2008) [arXiv:0803.1534 [hep-ex]]

[42] **"Search for decay of a fermiophobic Higgs boson $h_f \to \gamma\gamma$ with the D0 detector at $\sqrt{s} = 1.96$ TeV"**
V. M. Abazov *et al.* [D0 Collaboration]
Phys. Rev. Lett. **101**, 051801 (2008) [arXiv:0803.1514 [hep-ex]]

[43] **"Evidence for production of single top quarks"**
V. M. Abazov *et al.* [D0 Collaboration]
Phys. Rev. D **78**, 012005 (2008) [arXiv:0803.0739 [hep-ex]]

[44] **"First study of the radiation-amplitude zero in $W\gamma$ production and limits on anomalous $WW\gamma$ couplings at $\sqrt{s}$ = 1.96- TeV"**
V. M. Abazov *et al.* [D0 Collaboration]
Phys. Rev. Lett. **100**, 241805 (2008) [arXiv:0803.0030 [hep-ex]]

[45] **"Observation of the B_c Meson in the Exclusive Decay $B_c \to J/\psi\pi$"**
V. M. Abazov *et al.* [D0 Collaboration]
Phys. Rev. Lett. **101**, 012001 (2008) [arXiv:0802.4258 [hep-ex]]

[46] **"Study of direct CP violation in $B^{\pm} \to J/\psi K^{\pm}(\pi^{\pm})$ decays"**
V. M. Abazov *et al.* [D0 Collaboration]
Phys. Rev. Lett. **100**, 211802 (2008) [arXiv:0802.3299 [hep-ex]]

[47] **"Measurement of the inclusive jet cross section in $p\bar{p}$ collisions at $\sqrt{s}$ =** 1.96TeV"
V. M. Abazov *et al.* [D0 Collaboration]
Phys. Rev. Lett. **101**, 062001 (2008) [arXiv:0802.2400 [hep-ex]]

[48] **"Measurement of B_s^0 mixing parameters from the flavor-tagged decay $B_s^0 \to J/\psi\phi$"**
V. M. Abazov *et al.* [D0 Collaboration]
Phys. Rev. Lett. **101**, 241801 (2008) [arXiv:0802.2255 [hep-ex]]

[49] **"Simultaneous measurement of the ratio B($t \to Wb$) /B($t \to Wq$) and the top quark pair production cross section with the D0 detector at $\sqrt{s}$ = 1.96 TeV"**
V. M. Abazov *et al.* [D0 Collaboration]
Phys. Rev. Lett. **100**, 192003 (2008) [arXiv:0801.1326 [hep-ex]]

[50] **"Search for excited electrons in $p\bar{p}$ collisions at $\sqrt{s}$ = 1.96 TeV"**
V. M. Abazov *et al.* [D0 Collaboration]
Phys. Rev. D **77**, 091102 (2008) [arXiv:0801.0877 [hep-ex]]

[51] **"Search for squarks and gluinos in events with jets and missing transverse energy using 2.1 fb-1 of ppbar collision data at sqrt(s)=1.96 TeV"**
V. M. Abazov *et al.* [D0 Collaboration]
Phys. Lett. B **660**, 449 (2008) [arXiv:0712.3805 [hep-ex]]

[52] **"Measurement of the B_s^0 semileptonic branching ratio to an orbitally excited D_s** state, Br($B_s^0 \to$ Ds1(2536) mu nu)"**
V. M. Abazov *et al.* [D0 Collaboration]
arXiv:0712.3789 [hep-ex]
FERMILAB-PUB-07-659-E(2007) (Submitted to Phys.Rev.Lett.)

[53] **"First measurement of the forward-backward charge asymmetry in top quark pair production"**
V. M. Abazov *et al.* [D0 Collaboration]
Phys. Rev. Lett. **100**, 142002 (2008) [arXiv:0712.0851 [hep-ex]]

[54] **"Measurement of the shape of the boson transverse momentum distribution in ppbar → Z/gamma* → ee+X events produced at sqrts=1.96 TeV"**
V. M. Abazov *et al.* [D0 Collaboration]
Phys. Rev. Lett. **100**, 102002 (2008) [arXiv:0712.0803 [hep-ex]]

[55] **"Search for ZZ and $Z\gamma^*$ production in $p\bar{p}$ collisions at $\sqrt{s}$ = 1.96 TeV and limits on anomalous ZZZ and $ZZ\gamma^*$ couplings"**
V. M. Abazov *et al.* [D0 Collaboration]
Phys. Rev. Lett. **100**, 131801 (2008) [arXiv:0712.0599 [hep-ex]]

[56] **"A combined search for the standard model Higgs boson at sqrts=1.96 TeV"**
V. M. Abazov *et al.* [D0 Collaboration]
Phys. Lett. B **663**, 26 (2008) [arXiv:0712.0598 [hep-ex]]

[57] **"Search for sneutrino particles in e + mu final states in ppbar collisions at sqrts =1.96 TeV"**
V. M. Abazov *et al.* [D0 Collaboration]
Phys. Rev. Lett. **100**, 241803 (2008) [arXiv:0711.3207 [hep-ex]]

[58] **"Model-independent measurement of the W boson helicity in top quark decays"**
V. M. Abazov *et al.* [D0 Collaboration]
Phys. Rev. Lett. **100**, 062004 (2008) [arXiv:0711.0032 [hep-ex]]

[59] **"Observation and properties of the orbitally excited B^*_{s2} Meson"**
V. M. Abazov *et al.* [D0 Collaboration]
Phys. Rev. Lett. **100**, 082002 (2008) [arXiv:0711.0319 [hep-ex]]

[60] **"Search for Supersymmetry in Di-Photon Final States at sqrts = 1.96 TeV"**
V. M. Abazov *et al.* [D0 Collaboration]
arXiv:0710.3946 [hep-ex]
FERMILAB-PUB-07-560-E(2007)

[61] **"Search for Randall-Sundrum gravitons with 1 fb-1 of data from ppbar collisions at sqrt(s)=1.96 TeV"**
V. M. Abazov *et al.* [D0 Collaboration]
Phys. Rev. Lett. **100**, 091802 (2008) [arXiv:0710.3338 [hep-ex]]

[62] **"Search for W' bosons decaying to an electron and a neutrino with the D0 detector"**
V. M. Abazov *et al.* [D0 Collaboration]
Phys. Rev. Lett. **100**, 031804 (2008) [arXiv:0710.2966 [hep-ex]]

[63] **"Measurement of the muon charge asymmetry from W boson decays"**
V. M. Abazov *et al.* [D0 Collaboration]
Phys. Rev. D **77**, 011106 (2008) [arXiv:0709.4254 [hep-ex]]

[64] **"Measurement of the $p\bar{p} \to WZ + X$ cross-section at $\sqrt{s} = 1.96$ TeV and limits on WWZ trilinear gauge couplings"**
V. M. Abazov *et al.* [D0 Collaboration]
Phys. Rev. D **76**, 111104 (2007) [arXiv:0709.2917 [hep-ex]]

[65] **"Search for $B_s \to \mu^+\mu^-$ at D0"**
V. M. Abazov *et al.* [D0 Collaboration]
Phys. Rev. D **76**, 092001 (2007) [arXiv:0707.3997 [hep-ex]]

[66] **"Search for the lightest scalar top quark in events with two leptons in $p\bar{p}$ collisions at $\sqrt{s} = 1.96$ TeV"**
V. M. Abazov *et al.* [D0 Collaboration]
Phys. Lett. B **659**, 500 (2008) [arXiv:0707.2864 [hep-ex]]

[67] **"Measurement of the $Lambda^0_b$ lifetime using semileptonic decays"**
V. M. Abazov *et al.* [D0 Collaboration]
Phys. Rev. Lett. **99**, 182001 (2007) [arXiv:0706.2358 [hep-ex]]

[68] **"Direct observation of the strange b baryon Xi^-_b"**
V. M. Abazov *et al.* [D0 Collaboration]
Phys. Rev. Lett. **99**, 052001 (2007) [arXiv:0706.1690 [hep-ex]]

[69] **"Measurement of the $t\bar{t}$ production cross-section in $p\bar{p}$ collisions using dilepton events"**
V. M. Abazov *et al.* [D0 Collaboration]
Phys. Rev. D **76**, 052006 (2007) [arXiv:0706.0458 [hep-ex]]

[70] **"Observation and Properties of $L = 1B_1$ and B_2^* Mesons"**
V. M. Abazov *et al.* [D0 Collaboration]
Phys. Rev. Lett. **99**, 172001 (2007) [arXiv:0705.3229 [hep-ex]]

[71] **"Measurement of the $t\bar{t}$ production cross section in $p\bar{p}$ collisions at $\sqrt{s}$ = 1.96 TeV using kinematic characteristics of lepton + jets events"**
V. M. Abazov *et al.* [D0 Collaboration]
Phys. Rev. D **76**, 092007 (2007) [arXiv:0705.2788 [hep-ex]]

[72] **"$Z\gamma$ production and limits on anomalous $ZZ\gamma$ and $Z\gamma\gamma$ couplings in $p\bar{p}$ collisions at $\sqrt{s}$ = 1.96- TeV"**
V. M. Abazov *et al.* [D0 Collaboration]
Phys. Lett. B **653**, 378 (2007) [arXiv:0705.1550 [hep-ex]]

[73] **"Search for third-generation leptoquarks in $p\bar{p}$ collisions at $\sqrt{s}$ = 1.96 TeV"**
V. M. Abazov *et al.* [D0 Collaboration]
Phys. Rev. Lett. **99**, 061801 (2007) [arXiv:0705.0812 [hep-ex]]

[74] **"Search for stopped gluinos from $p\bar{p}$ collisions at $\sqrt{s}$ = 1.96 TeV"**
V. M. Abazov *et al.* [D0 Collaboration]
Phys. Rev. Lett. **99**, 131801 (2007) [arXiv:0705.0306 [hep-ex]]

[75] **"Measurement of the Λ_b lifetime in the exclusive decay $\Lambda_b \to J/\psi\Lambda$"**
V. M. Abazov *et al.* [D0 Collaboration]
Phys. Rev. Lett. **99**, 142001 (2007) [arXiv:0704.3909 [hep-ex]]

[76] **"Search for a Higgs boson produced in association with a Z boson in $p\bar{p}$ collisions"**
V. M. Abazov *et al.* [D0 Collaboration]
Phys. Lett. B **655**, 209 (2007) [arXiv:0704.2000 [hep-ex]]

[77] **"Measurement of the branching fraction Br($B^0(s) \to D_s^{(*)} D_s^{(*)}$)"**
V. M. Abazov *et al.* [D0 Collaboration]
Phys. Rev. Lett. **99**, 241801 (2007) [arXiv:hep-ex/0702049]

[78] **"Combined D0 measurements constraining the CP-violating phase and width difference in the B/s0 system"**
V. M. Abazov *et al.* [D0 Collaboration]
Phys. Rev. D **76**, 057101 (2007) [arXiv:hep-ex/0702030]

[79] **"Measurement of the shape of the boson rapidity distribution for $p\bar{p} \to Z/gamma^* \to e^+e^- + X$ events produced at $\sqrt{s}$ of 1.96 TeV"**
V. M. Abazov *et al.* [D0 Collaboration]
Phys. Rev. D **76**, 012003 (2007) [arXiv:hep-ex/0702025]

[80] **"Measurement of the top quark mass in the lepton + jets channel using the ideogram method"**
V. M. Abazov *et al.* [D0 Collaboration]
Phys. Rev. D **75**, 092001 (2007) [arXiv:hep-ex/0702018]

[81] **"Search for production of single top quarks via flavor-changing neutral currents at the Tevatron"**
V. M. Abazov *et al.* [D0 Collaboration]
Phys. Rev. Lett. **99**, 191802 (2007) [arXiv:hep-ex/0702005]

[82] **"Jet energy scale determination at the D0"**
J. Kvita
AIP Conf. Proc. **867**, 43 (2006)
Prepared for 12th International Conference on Calorimetry in High Energy Physics (CALOR 06), Chicago, Illinois, 5-9 Jun 2006

[83] **"Lifetime difference and CP-violating phase in the B_s^0 system"**
V. M. Abazov *et al.* [D0 Collaboration]
Phys. Rev. Lett. **98**, 121801 (2007) [arXiv:hep-ex/0701012]

[84] **"Measurement of the charge asymmetry in semileptonic B_s decays"**
V. M. Abazov *et al.* [D0 Collaboration]
Phys. Rev. Lett. **98**, 151801 (2007) [arXiv:hep-ex/0701007]

[85] **"Evidence for production of single top quarks and first direct measurement of —V(tb)—"**
V. M. Abazov *et al.* [D0 Collaboration]
Phys. Rev. Lett. **98**, 181802 (2007) [arXiv:hep-ex/0612052]

[86] **"Measurement of the $p\bar{p} \to t\bar{t}$ production cross section at $\sqrt{s} = 1.96$ TeV in the fully hadronic decay channel"**
V. M. Abazov *et al.* [D0 Collaboration]
Phys. Rev. D **76**, 072007 (2007) [arXiv:hep-ex/0612040]

[87] **"Search for techniparticles in e + jets events at D0"**
V. M. Abazov *et al.* [D0 Collaboration]
Phys. Rev. Lett. **98**, 221801 (2007) [arXiv:hep-ex/0612013]

[88] **"Search for single production of scalar leptoquarks in p anti-p collisions decaying into muons and quarks with the D0 detector"**
V. M. Abazov *et al.* [D0 Collaboration]
Phys. Lett. B **647**, 74 (2007) [arXiv:hep-ex/0612012]

[89] **"Search for the pair production of scalar top quarks in the acoplanar charm jet topology in p anti-p collisions at $\sqrt{S} = 1.96$ TeV"**
V. M. Abazov *et al.* [D0 Collaboration]
Phys. Lett. B **645**, 119 (2007) [arXiv:hep-ex/0611003]

[90] **"Measurement of the t anti-t production cross section in p anti-p collisions at $\sqrt{S} = 1.96$ TeV using secondary vertex b tagging"**
V. M. Abazov *et al.* [D0 Collaboration]
Phys. Rev. D **74**, 112004 (2006) [arXiv:hep-ex/0611002]

[91] **"Measurement of the top quark mass in the dilepton channel"**
V. M. Abazov *et al.* [D0 Collaboration]
Phys. Lett. B **655**, 7 (2007) [arXiv:hep-ex/0609056]

[92] **"Measurement of the top quark mass in the lepton + jets final state with the matrix element method"**
V. M. Abazov *et al.* [D0 Collaboration]
Phys. Rev. D **74**, 092005 (2006) [arXiv:hep-ex/0609053]

[93] **"Measurement of the W boson helicity in top quark decay at D0"**
V. M. Abazov *et al.* [D0 Collaboration]
Phys. Rev. D **75**, 031102 (2007) [arXiv:hep-ex/0609045]

[94] **"Measurement of B_d mixing using opposite-side flavor tagging"**
V. M. Abazov *et al.* [D0 Collaboration]
Phys. Rev. D **74**, 112002 (2006) [arXiv:hep-ex/0609034]

[95] **"Measurement of the CP-violation parameter of B0 mixing and decay with p anti-p → mu mu X data"**
V. M. Abazov *et al.* [D0 Collaboration]
Phys. Rev. D **74**, 092001 (2006) [arXiv:hep-ex/0609014]

[96] **"Measurement of the ratios of the Z/G* + ¿= n jet production cross sections to the total inclusive Z/G* cross section in ppbar collisions at sqrt(s) = 1.96 TeV"**
V. M. Abazov *et al.* [D0 Collaboration]
Phys. Lett. B **658**, 112 (2008) [arXiv:hep-ex/0608052]

[97] **"Experimental discrimination between charge $2e/3$ top quark and charge 4e/3 exotic quark production scenarios"**
V. M. Abazov *et al.* [D0 Collaboration]
Phys. Rev. Lett. **98**, 041801 (2007) [arXiv:hep-ex/0608044]

[98] **"Search for pair production of scalar bottom quarks in p anti-p collisions at $\sqrt{S}$ = 1.96 TeV"**
V. M. Abazov *et al.* [D0 Collaboration]
Phys. Rev. Lett. **97**, 171806 (2006) [arXiv:hep-ex/0608013]

[99] **"Limits on anomalous trilinear gauge couplings from W W → e+ e-, W W → e+- mu-+, and W W → mu+ mu- events from p anti-p collisions at $\sqrt{S}$ = 1.96 TeV"**
V. M. Abazov *et al.* [D0 Collaboration]
Phys. Rev. D **74**, 057101 (2006) [Erratum-ibid. D **74**, 059904 (2006)] [arXiv:hep-ex/0608011]

[100] **"Search for W' boson production in the top quark decay channel"**
V. M. Abazov *et al.* [D0 Collaboration]
Phys. Lett. B **641**, 423 (2006) [arXiv:hep-ex/0607102]

[101] **"Search for associated Higgs boson production WH → WWW* → $\ell^{\pm}\nu\ell'$+- ν' + X in $p\bar{p}$ collisions at $\sqrt{s}$ = 1.96 TeV"**
V. M. Abazov *et al.* [D0 Collaboration]
Phys. Rev. Lett. **97**, 151804 (2006) [arXiv:hep-ex/0607032]

[102] **"Search for neutral, long-lived particles decaying into two muons in $p\bar{p}$ collisions at $\sqrt{s}$ = 1.96 TeV"**
V. M. Abazov *et al.* [D0 Collaboration]
Phys. Rev. Lett. **97**, 161802 (2006) [arXiv:hep-ex/0607028]

[103] **"Search for the Standard Model Higgs Boson in the $p\bar{p}$ → ZH → $\nu\bar{\nu}b\bar{b}$ channel"**
V. M. Abazov *et al.* [D0 Collaboration]
Phys. Rev. Lett. **97**, 161803 (2006) [arXiv:hep-ex/0607022]

[104] **"Search for scalar leptoquarks in the acoplanar jet topology in $p\bar{p}$ collisions at $\sqrt{s}$ = 1.96 TeV"**
V. M. Abazov *et al.* [D0 Collaboration]
Phys. Lett. B **640**, 230 (2006) [arXiv:hep-ex/0607009]

[105] **"Search for a heavy resonance decaying into a Z+ jet final state in $p\bar{p}$ collisions at $\sqrt{s}$ = 1.96 TeV using the D0 detector"**
V. M. Abazov *et al.* [D0 Collaboration]
Phys. Rev. D **74**, 011104 (2006) [arXiv:hep-ex/0606018]

[106] **"Search for particles decaying into a Z boson and a photon in $p\bar{p}$ collisions at $\sqrt{s} = 1.96$ TeV"**

V. M. Abazov *et al.* [D0 Collaboration]
Phys. Lett. B **641**, 415 (2006) [arXiv:hep-ex/0605064]

[107] **"Search for resonant second generation slepton production at the Tevatron"**
V. M. Abazov *et al.* [D0 Collaboration]
Phys. Rev. Lett. **97**, 111801 (2006) [arXiv:hep-ex/0605010]

[108] **"Search for neutral Higgs bosons decaying to τ pairs in $p\bar{p}$ collisions at $\sqrt{s} = 1.96$ TeV"**
V. M. Abazov *et al.* [D0 Collaboration]
Phys. Rev. Lett. **97**, 121802 (2006) [arXiv:hep-ex/0605009]

[109] **"Search for R-parity violating supersymmetry via the LL anti-E couplings λ_{121}, λ_{122} or λ_{133} in $p\bar{p}$ collisions at $\sqrt{s} = 1.96$ TeV"**
V. M. Abazov *et al.* [D0 Collaboration]
Phys. Lett. B **638**, 441 (2006) [arXiv:hep-ex/0605005]

[110] **"A Precise measurement of the B_s^0 lifetime"**
V. M. Abazov *et al.* [D0 Collaboration]
Phys. Rev. Lett. **97**, 241801 (2006) [arXiv:hep-ex/0604046]

[111] **"Search for excited muons in $p\bar{p}$ collisions at $\sqrt{s} = 1.96$- TeV"**
V. M. Abazov *et al.* [D0 Collaboration]
Phys. Rev. D **73**, 111102 (2006) [arXiv:hep-ex/0604040]

[112] **"Search for squarks and gluinos in events with jets and missing transverse energy in $p\bar{p}$ collisions at $\sqrt{s} = 1.96$ TeV"**
V. M. Abazov *et al.* [D0 Collaboration]
Phys. Lett. B **638**, 119 (2006) [arXiv:hep-ex/0604029]

[113] **"Multivariate searches for single top quark production with the D0 detector"**
V. M. Abazov *et al.* [D0 Collaboration]
Phys. Rev. D **75**, 092007 (2007) [arXiv:hep-ex/0604020]

[114] **"Search for the rare decay $B_s^0 \to \phi\mu^+\mu^-$ with the D0 detector"**
V. M. Abazov *et al.* [D0 Collaboration]
Phys. Rev. D **74**, 031107 (2006) [arXiv:hep-ex/0604015]

[115] **"First direct two-sided bound on the B_s^0 oscillation frequency"**
V. M. Abazov *et al.* [D0 Collaboration]
Phys. Rev. Lett. **97**, 021802 (2006) [arXiv:hep-ex/0603029]

[116] **"Measurement of $B(t \to Wb)/B(t \to Wq)$ at $\sqrt{s} = 1.96$ TeV"**
V. M. Abazov *et al.* [D0 Collaboration]
Phys. Lett. B **639**, 616 (2006) [arXiv:hep-ex/0603002]

[117] **"Search for pair production of second generation scalar leptoquarks in p anti-p collisions at $\sqrt{s} = 1.96$ TeV"**
V. M. Abazov *et al.* [D0 Collaboration]
Phys. Lett. B **636**, 183 (2006) [arXiv:hep-ex/0601047]

[118] **"Measurement of the isolated photon cross section in $p\bar{p}$ collisions at $\sqrt{s} = 1.96$ TeV"**
V. M. Abazov *et al.* [D0 Collaboration]
Phys. Lett. B **639**, 151 (2006) [Erratum-ibid. B **658**, 285 (2008)] [arXiv:hep-ex/0511054]

[119] **"Search for the Higgs boson in H → W W(*) decays in p anti-p collisions at $\sqrt{S}$ = 1.96 TeV"**
V. M. Abazov *et al.* [D0 Collaboration]
Phys. Rev. Lett. **96**, 011801 (2006) [arXiv:hep-ex/0508054]

[120] **"The upgraded D0 detector"**
V. M. Abazov *et al.* [D0 Collaboration]
Nucl. Instrum. Meth. A **565**, 463 (2006) [arXiv:physics/0507191]

[121] **"Measurement of the lifetime difference in the B/s0 system"**
V. M. Abazov *et al.* [D0 Collaboration]
Phys. Rev. Lett. **95**, 171801 (2005) [arXiv:hep-ex/0507084]

[122] **"Measurement of semileptonic branching fractions of B mesons to narrow D** states"**
V. M. Abazov *et al.* [D0 Collaboration]
Phys. Rev. Lett. **95**, 171803 (2005) [arXiv:hep-ex/0507046]

[123] **"Search for large extra spatial dimensions in dimuon production at D0"**
V. M. Abazov *et al.* [D0 Collaboration]
Phys. Rev. Lett. **95**, 161602 (2005) [arXiv:hep-ex/0506063]

[124] **"Measurement of the t anti-t production cross section in p anti-p collisions at $\sqrt{S}$ = 1.96 TeV in dilepton final states"**
V. M. Abazov *et al.* [D0 Collaboration]
Phys. Lett. B **626**, 55 (2005) [arXiv:hep-ex/0505082]

[125] **"Search for single top quark production in p anti-p collisions at $\sqrt{S}$ = 1.96 TeV"**
V. M. Abazov *et al.* [D0 Collaboration]
Phys. Lett. B **622**, 265 (2005) [arXiv:hep-ex/0505063]

[126] **"Measurement of the W boson helicity in top quark decays"**
V. M. Abazov *et al.* [D0 Collaboration]
Phys. Rev. D **72**, 011104 (2005) [arXiv:hep-ex/0505031]

[127] **"Search for Randall-Sundrum gravitons in dilepton and diphoton final states"**
V. M. Abazov *et al.* [D0 Collaboration]
Phys. Rev. Lett. **95**, 091801 (2005) [arXiv:hep-ex/0505018]

[128] **"Measurement of the t anti-t production cross section in p anti-p collisions at $\sqrt{S}$ = 1.96 TeV using lepton + jets events with lifetime b-tagging"**
V. M. Abazov *et al.* [D0 Collaboration]
Phys. Lett. B **626**, 35 (2005) [arXiv:hep-ex/0504058]

[129] **"Measurement of the t anti-t production cross section in p anti-p collisions at $\sqrt{S}$ = 1.96 TeV using kinematic characteristics of lepton + jets events"**
V. M. Abazov *et al.* [D0 Collaboration]
Phys. Lett. B **626**, 45 (2005) [arXiv:hep-ex/0504043]

[130] **"Search for supersymmetry via associated production of charginos and neutralinos in final states with three leptons"**
V. M. Abazov *et al.* [D0 Collaboration]
Phys. Rev. Lett. **95**, 151805 (2005) [arXiv:hep-ex/0504032]

[131] **"Production of W Z events in p anti-p collisions at $\sqrt{S} = 1.96$ TeV and limits on anomalous W W Z couplings"**
V. M. Abazov *et al.* [D0 Collaboration]
Phys. Rev. Lett. **95**, 141802 (2005) [arXiv:hep-ex/0504019]

[132] **"Search for neutral supersymmetric Higgs bosons in multijet events at $\sqrt{S} = 1.96$ TeV"**
V. M. Abazov *et al.* [D0 Collaboration]
Phys. Rev. Lett. **95**, 151801 (2005) [arXiv:hep-ex/0504018]

[133] **"Measurement of the p anti-$p \to$ W gamma + X cross section at $\sqrt{S} = 1.96$ TeV and W W gamma anomalous coupling limits"**
V. M. Abazov *et al.* [D0 Collaboration]
Phys. Rev. D **71**, 091108 (2005) [arXiv:hep-ex/0503048]

[134] **"Study of Z gamma events and limits on anomalous Z Z gamma and Z gamma gamma couplings in p anti-p collisions at $\sqrt{S} = 1.96$ TeV"**
V. M. Abazov *et al.* [D0 Collaboration]
Phys. Rev. Lett. **95**, 051802 (2005) [arXiv:hep-ex/0502036]

[135] **"Measurement of inclusive differential cross sections for Upsilon(1S) production in p anti-p collisions at $\sqrt{S} = 1.96$ TeV"**
V. M. Abazov *et al.* [D0 Collaboration]
Phys. Rev. Lett. **94**, 232001 (2005) [Erratum-ibid. **100**, 049902 (2008)] [arXiv:hep-ex/0502030]

References

[1] www.ftpi.umn.edu/dsu07/talks/dsuLinder.pdf

[2] J. Hořejší, "Fundamentals of electroweak theory," Prague, Czech Republic: Karolinum Press (2002) 351 p.

[3] J. Chýla, Quarks, Partons and Quantum Chromodynamics, http://www-hep2.fzu.cz/~chyla/lectures/text.pdf

[4] S. Moch, "Hard QCD at hadron colliders," J. Phys. G **35** (2008) 073001, arXiv:0803.0457 [hep-ph].

[5] CTEQ Summer school 2005, 2007.

[6] "Measurement of the Run II Luminosity Monitor Efficiency" (Tamsin Edwards), DØ note 4504.

[7] Pbar Rookie Book, http://www-bdnew.fnal.gov/pbar/documents/PBAR_Rookie_Book.pdf

[8] Run II Tevatron Handbook, http://www-bd.fnal.gov/lug/runII_handbook/RunII_index.html

[9] "Determination of the Effective Inelastic p pbar Cross-Section for the DO Luminosity Measurement Using Upgraded Readout Electronics", DØ note 4958 (Brendan Casey, Yuji Enari, Thorsten Kuhl, Thomas Nunnemann, Rich Partridge, Pavel Polozov, Heidi Schellman, Markus Wobisch).

[10] "Determination of the D0 RunIIb Luminosity Constants", DØ note 5559 (Brendan Casey, Marj Corcoran, Yuji Enari, Michelle Prewitt, Greg Snow).

[11] S. Abachi *et al.* [DØ Collaboration], "The D0 Detector," Nucl. Instrum. and Methods A **338**, 185 (1994).

[12] V.M. Abazov, et al. (DØ Collaboration), "The upgraded DØ detector", Nucl. Instrum. and Methods A **565**, 463-537 (2006).

[13] "Luminosity and Performance of D0 during the first year of Run 2", DØ note 3973.

[14] DAQ shifter tutorial presentations 2006-2008.

[15] W Bernreuther 2008 J. Phys. G: Nucl. Part. Phys. 35 083001 (56pp), "Top-quark physics at the LHC".

[16] A. Hoang *et. al.*, Infrared Renormalization Group Flow for Heavy Quark Masses, hep-ph/0803.4214

[17] I.I. Bigi *et. al.* Pole mass of the heavy quark: Perturbation theory and beyond, Phys. Rev. D 50, 2234 - 2246 (1994)

[18] DØ Collaboration, Physical Review Letters **98**, 181802 (2007), "Evidence for Production of Single Top Quarks and First Direct Measurement of $|V_{tb}|$".

[19] F. Deliot [CDF and D0 Collaboration], "Top Quark Cross Sections," arXiv:0810.5473 [hep-ex].

[20] S. Dittmaier, P. Uwer and S. Weinzierl, "Hadronic top-quark pair production in association with a hard jet at next-to-leading order QCD: Phenomenological studies for the Tevatron and the LHC," arXiv:0810.0452 [hep-ph].

[21] M. Cacciari, S. Frixione, M. L. Mangano, P. Nason and G. Ridolfi, "Updated predictions for the total production cross sections of top and of heavier quark pairs at the Tevatron and at the LHC," JHEP **0809** (2008) 127 [arXiv:0804.2800 [hep-ph]].

[22] Particle Data Group, Top Quark Review, `http://pdg.lbl.gov/2008/reviews/topquark_q007.pdf`

[23] V. M. Abazov *et al.* [D0 Collaboration], "Search for $t\bar{t}$ resonances in the lepton plus jets final state in $p\bar{p}$ collisions at $\sqrt{s} = 1.96$-TeV," Phys. Lett. B **668** (2008) 98 [arXiv:0804.3664 [hep-ex]].

[24] T. Aaltonen *et al.* [CDF Collaboration], "Search for resonant $t\bar{t}$ production in $p\bar{p}$ collisions at $\sqrt{s} = 1.96$-TeV," Phys. Rev. Lett. **100** (2008) 231801 [arXiv:0709.0705 [hep-ex]].

[25] V. M. Abazov *et al.* [D0 Collaboration], "First measurement of the forward-backward charge asymmetry in top quark pair production," Phys. Rev. Lett. **100** (2008) 142002 [arXiv:0712.0851 [hep-ex]].

[26] T. Aaltonen *et al.* [CDF Collaboration], "Forward-Backward Asymmetry in Top Quark Production in $p\bar{p}$ Collisions at $sqrts = 1.96$ TeV," Phys. Rev. Lett. **101** (2008) 202001 [arXiv:0806.2472 [hep-ex]].

[27] V. M. Abazov *et al.* [D0 Collaboration], "Model-independent measurement of the W boson helicity in top quark decays," Phys. Rev. Lett. **100** (2008) 062004 [arXiv:0711.0032 [hep-ex]].

[28] A. Abulencia *et al.* [CDF II Collaboration], "Measurement of the Helicity Fractions of W Bosons from Top Quark Decays using Fully Reconstructed $\boldsymbol{t\bar{t}}$ Events with CDF II," Phys. Rev. D **75** (2007) 052001 [arXiv:hep-ex/0612011].

[29] N. Kidonakis and R. Vogt, Phys. Rev. D **68**, 114014 (2003), available also as hep-ph/0308222.

[30] R. P. Feynman, R. D. Field, G. C. Fox, Phys. Rev. D **18**, 3320-3343 (1978).

[31] Direct Measurement of the Top Quark Mass at DØ, Phys. Rev. **D58**, 052001, hep-ex/9801025, pg. 39-41.

[32] A. A. Affolder *et al.* [CDF Collaboration], Measurement of Top Quark $\boldsymbol{p_T}$ Distribution, Phys. Rev. Lett. **87**, 102001 (2001), Fermilab PUB-00-101-E, CDF 5193 (2001).

[33] S. Frixione and B.R. Webber, Matching NLO QCD computations and parton shower simulations, JHEP **0206** (2002) 029 [hep-ph/0204244];

[34] S. Frixione, P. Nason and B.R. Webber, Matching NLO QCD and parton showers in heavy flavour production, JHEP **0308** (2003) 007 [hep-ph/0305252].

[35] Herwig 6.5, G. Corcella, I.G. Knowles, G. Marchesini, S. Moretti, K. Odagiri, P. Richardson, M.H. Seymour and B.R. Webber, JHEP 0101 (2001) 010 [hep-ph/0011363]; hep-ph/0210213.

[36] Amnon Harel, private communication.

[37] First Measurement of Dijet Angular Distributions in the TeV Regime and Searches for Quark Compositness and Extra Dimensions, N. Parua – M. Wobish for the DØ collaboration, to be published.

[38] `http://www-d0.fnal.gov/d0dist/dist/releases/development/haryo/libfeynman/`

[39] The Feynmf packagag, Thorsten Ohl, `http://xml.web.cern.ch/XML/textproc/feynmf.html`

[40] "Primary Vertex Reconstruction by Means of Adaptive Vertex Fitting", DØ note 4918 (Ariel Schwartzman, Chris Tully).

[41] "Probabilistic Primary Vertex Selection", DØ note 4042 (Ariel Schwartzman and Meenakshi Narain).

[42] Run II Jet Physics, hep-ex/0005012.

[43] "Jet ID optimization", DØ note 4919 (Amnon Harel).

[44] "Improved L1 Confirmation", DØ note 4932 (Amnon Harel Robert Wagner).

[45] Single Electron Efficiencies in p17 data and Monte-Carlo using p18.05.00 `d0correct`, DØ note 5105 (J. Hays, J. Mitrevski, C. Schwanenberger and T. Toole).

[46] "Electron Likelihood Study", DØ note 4769 (Ashish Kumar, Brajesh Choudhary, Joseph Kozminski, Robert Kehoe, Jon Hays, Jan Stark).

[47] Georg Steinbrück, PhD Thesis, `http://www-d0.fnal.gov/results/publications_talks/thesis/steinbrueck/thesis.ps`

[48] "Muon Identification Certification for p17 data", DØ note 5157 (Philippe Calfayan, Thomas Gadfort, Gavin Hesketh, Vincent Lesne, Mark Owen, Raimund Stroehmer, Viatcheslav Sharyy, Boris Tuchming)

[49] "Towards a Coherent Treatment of Calorimetric Energies: Missing Transverse Energy, Jets, E.M. Objects and the T42 Algorithm", DØ note 4124 (Ursula Bassler and Gregorio Bernardi).

[50] Performance of the NN ***b***-tagging Tool on p17 Data, DØ note 5213 (Miruna Anastasoaie, Stephen Robinson, Tim Scanlon).

[51] "Studies of Taggability vs. nPV for p17", DØ note 5240 (Ioana Anghel, Cecilia Gerber, Lisa Shabalina, Timour Ten).

[52] B. Abbott *et. al.* [DØ Collaboration], "Determination of the Absolute Jet Energy Scale in the DØ Calorimeters", Nucl. Instrum. and Methods A, **424**, 352 (1999).

[53] DØ note 5609 "SSR for p17" (C. Ochando and J.-F. Grivaz); the jet shift+smear+removal procedure for simulation-based jet to match data in resolution and efficiencies.

[54] `https://www-d0.fnal.gov/Run2Physics/cs/skimming/fixPass2p170903.html`

[55] ALPGEN, a generator for hard multiparton processes in hadronic collisions, M.L. Mangano, M. Moretti, F. Piccinini, R. Pittau, A. Polosa, JHEP 0307:001,2003, hep-ph/0206293.

[56] PYTHIA The complete PYTHIA 6.301 manual, LU TP 03-38 [hep-ph/0308153], T. Sjostrand, P. Eden, C. Friberg, L. Lonnblad, G. Miu, S. Mrenna and E. Norbin, "High-energy-physics event generation with PYTHIA 6.1," Comput. Phys. Commun. **135**, 238 (2001) [arXiv:hep-ph/0010017].

[57] R. Field and R. C. Group [CDF Collaboration], "PYTHIA Tune A, HERWIG, and JIMMY in Run 2 at CDF," arXiv:hep-ph/0510198.

[58] "Tevatron-for-LHC Report of the QCD Working Group", arXiv:hep-ph/0610012.

[59] `http://www.phys.ufl.edu/~rfield/cdf/tunes/py_tuneA.html`

[60] The CTEQ Collaboration, J. Pumplin, D. R. Stump, J. Huston, H. L. Lai, P. M. Nadolsky and W. K. Tung, "New generation of parton distributions with uncertainties from global QCD analysis," JHEP **0207** (2002) 012, arXiv:hep-ph/0201195.

[61] "Measurement of the Electron and Muon Fake Rates in Lepton+Jets Datasets", DØ note 5469 (Marc-André Pleier)

[62] F. Maltoni, Top 2008 symposium.

[63] Matching Parton Showers and Matrix Elements, hep-ph/0602031.

[64] Simultaneous measurement of $B(t \to Wb)/B(t \to Wq)$ and $\sigma(p\bar{p} \to t\bar{r}) * B(t \to Wq)^2$ with p17 data, DØ note 5422 (Yvonne Peters, Elizaveta Shabalina).

[65] "Measurement of the ttbar production cross section at sqrt(s)= 1.96 TeV in the ee final state using p17 data set", DØ note 5386 (Bertrand Martin, Yannick Arnoud, Gerard Sajot, Elizaveta Shabalina).

[66] E. E. Boos, V. E. Bunichev, L. V. Dudko, V. I. Savrin and A. V. Sherstnev, "Method for simulating electroweak top-quark production events in the NLO approximation: SingleTop event generator," Phys. Atom. Nucl. **69** (2006) 1317 [Yad. Fiz. **69** (2006) 1352].

[67] Combination of the top quark pair production cross section, DØ note 5597 (Todd Adams, Jochen Cammin, Frederic Deliot, Amnon Harel, Jens-Peter Konrath, Bertrand Martin, Yvonne Peters, Christian Schwanenberger, Elizaveta Shabalina, Viatcheslav Sharyy, Haryo Sumowidagdo, Daniel Wicke).

[68] ROOT: An Object-Oriented Analysis Framework, `http://root.cern.ch/`.

[69] CAF, Common Analysis Format, `http://www-d0.fnal.gov/Run2Physics/working_group/data_format/caf/`.

[70] Rochester trees format (ROC trees) by Jochen Cammin, `https://plone4.fnal.gov/P1/D0Wiki/Members/cammin/index_html/view?searchterm=Cammin`.

[71] Microsoft Excel `http://office.microsoft.com/en-gb/excel/default.aspx`.

[72] DØ Data Quality Group, `http://www-d0.fnal.gov/computing/data_quality/`

[73] Yvonne Peters, private comunication.

[74] Efficiency of the Data Quality Calorimeter Flags, DØ note 5324 (Su-Jung Park, Michael Begel).

[75] A Search for $ZH \to \ell^+\ell^- bb$ Production at D0 with 0.84-0.92 $\mathbf{pb^{-1}}$ Integrated Luminosity, DØ note 5275 (Shaohua Fu, Andy Haas).

[76] Study of the W+Jets heavy flavor scale factor in p17, DØ note 5406 (Yvonne Peters, Michael Begel, Elizaveta Shabalina, Daniel Wicke).

[77] Scott Snyder, "Measurement of the Top Quark Mass at DØ", DØ PhD Thesis.

[78] Particle Data Group, `http://pdg.lbl.gov/`

[79] DØ Note 5418 Title: p17 parton level corrections and resolutions for hitfit (Marcel Demarteau, Pieter Houben, Marcel Vreeswijk and Michele Weber).

[80] "Jet pT resolution using v7.1 JES for p17 data", DØ note 5381 (Mikko Voutilainen, Christophe Royon).

[81] "Production of high mass pairs of direct photons and neutral mesons in a Tevatron fixed target experiment", Michael Begel (Rochester U.) . FERMILAB-THESIS-1999-05, UMI-99-60725, 1999. 376pp. Ph.D. thesis.

[82] L. Apanasevich *et al.* [Fermilab E706 Collaboration], Phys. Rev. Lett. **81** (1998) 2642 [arXiv:hep-ex/9711017], FERMILAB-PUB-97-351-E

[83] GURU Unfolding Method, Vakhtang Kartvelishvili, `http://www.lancs.ac.uk/users/spc/staff/kartvelishvili.htm`

[84] SVD Approach to Data Unfolding, hep-ph/9509307, A. Hoecker, V. Kartvelishvili.

[85] G. Hesketh, private communication, `http://www-d0.fnal.gov/~ghesketh/unfolding/`